2024 International Maha Fluid Power Conference

West Lafayette, IN, USA

September 3-5, 2024

Conference Proceedings



PURDUE UNIVERSITY | Maha Fluid Power Research Center

2024 International Maha Fluid Power Conference

West Lafayette, IN, USA

September 3-5, 2024

Dr. Andrea Vacca, Purdue University
Dr. Lizhi Shang, Purdue University
Dr. Jose Garcia-Bravo, Purdue University

Dear Colleagues,

We are pleased to present the Proceedings for the 2024 International Maha Fluid Power Conference, a event dedicated to sustainable fluid power and motion control technologies and systems. The Maha Fluid Power Conference is one of the most impactful gatherings in the field, bringing together professionals, researchers, and innovators to exchange ideas and showcase the latest research trends.

This year's conference features 10 keynote lectures from leading experts representing off-road vehicle OEMs, fluid power system suppliers, universities, and local governments. In addition, there are 58 technical presentations covering a broad spectrum of topics, including novel fluid power components and systems, solutions for system electrification, condition monitoring, noise and vibration, alternative prime movers, tribology, and fluids. Of these presentations, 19 have been submitted as full conference papers, while the remaining contributions are presented as presentations only.

This conference proceedings collection includes these 19 full papers, carefully selected based on thorough reviews by the conference's scientific committees and field experts. Each paper was further refined in response to reviewers' feedback. We hope the concepts, methodologies, results, and conclusions presented in this 2024 Maha Fluid Power Conference Proceedings will contribute to advancing fluid power technology for a sustainable future.

Scientific Committee

From Academia:

- Torben Ole Andersen, University of Aalborg, Denmark
- Eric Bideaux, National Institute of Applied Sciences of Lyon, France
- Paolo Casoli, University of Parma, Italy
- Marcello Canova, Ohio State University, US
- Victor J. De Negri, Federal University of Santa Catarina, Brazil
- Ali Erdemir, Texas A&M, US
- Liselott Ericson, Linköping University, Sweden
- Wieslaw Fiebig, Wrocław University of Science and Technology, Poland
- Emma Frosina, University of Sannio, Italy
- Pedro Javier Gamez Montero, The Technical University of Catalonia, Spain
- José Gaspar, University of Lisbon, Portugal
- Kalevi Huhtala, Tampere Universities, Finland
- Nigel Johnston, University of Bath, UK
- John Lumkes, Purdue Universtiy, US
- Bernhard Manhartsgruber, Johannes Kepler University Linz, Austria
- Paul Michael, Milwaukee School of Engineering, US
- Tatiana Minav, Tampere Universities, Finland
- Damiano Padovani, Guangdong Technion-Israel Institute of Technology, China
- Fabrizio Paltrinieri, University of Modena and Reggio Emilia, Italy
- Massimiliano Ruggeri, Italian National Research Council, Italy
- Massimo Rundo, Polytechnic University of Turin, Italy
- Kazushi Sanada, Yokohama National University, Japan
- Katharina Schmitz, RWTH Aachen University, Germany
- John Schueller, Univeristy of Florida, US
- Adolfo Senatore, University of Naples Federico II, Italy
- Nariman Sepehri, University of Manitoba, Canada
- Andrzej Sobczyk, Cracow University of Technology, Poland
- Brian Steward, Iowa State University, US
- Scott Sudhoff, Purdue University, US
- James Van de Ven, University of Minnesota, US
- Juergen Weber, Dresden University of Technology, Germany
- Travis Wiens, University of Saskatchewan, Canada

- Bing Xu, Zhejiang University, China
- Barbara Zardin, University of Modena and Reggio Emilia, Italy

From Industry:

- John Bekker, Bucher Hydraulics
- Pierre Bernard, Poclain Hydraulics
- Filippo Boiardi, Settima Meccanica
- Enrique Busquets, Bosch Rexroth
- Germano Franzoni, Parker Hannifin
- Matthew Kaldor, Bobcat
- Antonio Lettini, Casappa
- John Mahrenholz, John Deere
- Uli Melchinger, CNH Industrial
- Davide Mesturini, Walvoil
- Steve Weber, Sun Hydraulics
- Catherine Zhuang, Hengli

Contents

1. Facilitating the Development of a Novel Heavy-Duty Offroad Vehicle Exploiting Hardware-in-the-Loop Technique
2. Improving transmission efficiency via a novel radial piston cam lobe motor architecture
3. Efficiency Improvements in a Servoless Swash Plate Pump: Experimental and Simulation Results
4. Robust Multivariate Air Handling Control for an Electrified Off Road Diesel Powertrain
5. Centralized Pressure Control and Displacement Quantization with Digital Displacement Pumps
6. Implement-Only Implementation of a Multi Pressure Rail System to an Agricultural Planter
7. Transforming Excavator Operation: Fusing teleoperation, Digital twin, and fluid power system for optimal performance and safety conditions
8. Reduction of dynamic loads in piston compressors through the use of mechanical resonance
9. Innovative Hyper-thin Sensor for Cartridge Valves Diagnostics and Predictive Diagnosis
10. Thermal Insights and Predictive Modeling of Axial Piston Pumps: A Journey to a High-Fidelity Digital Twin
11. Electronified Open Circuit Drive Concept for Compact Loaders
12. Electrification of a compact skid-steer loader – redesign of the hydraulic functions
13. A numerical modeling procedure to reduce the noise emitted by External Gear Pumps
14. Causal Condition Monitoring for Axial Piston Pumps: Prediction of Different Faults Under Variable Operating Conditions
15. Design Strategy for Noise Reducing Particle Dampers on Hydraulic Pumps
16. Simultaneous Transfer Path Analysis of Axial Piston Pump Lumped Parameter Model Results
17. Enhancing System Performance in Subsea and Off-Highway Applications: A High-Fidelity, Transient Dynamic CFD Analysis Approach
18. Analysis of the incomplete filling of a positive displacement pump due to undissolved gas involving experiments and simulations
19. Optimal designs of a hydromechanical hybrid transmission by minimizing fuel consumption and damage to human health

Facilitating the Development of a Novel Heavy-Duty Offroad Vehicle Exploiting Hardware-in-the-Loop Technique

Weijin Qiu [1], Shubham Ashta [1], Gregory M. Shaver [1], Scott Johnson [2], Bryan C. Frushour [3]

[1] Ray W. Herrick Laboratories, Mechanical Engineering, Purdue University, West Lafayette, IN, USA 47907

[2] John Deere Intelligent Solutions Group, Fargo, ND, USA 58102

[3] John Deere Electric Powertrain, Waterloo, IA, USA50701

Abstract

Stricter emissions regulations have placed unprecedented pressure on off-road OEM companies to reduce the fuel consumption of their products. This has led to the adoption of powertrain electrification as a viable solution. The increased complexity associated with powertrain electrification necessitates a more reliable and efficient testing approach to assess the control performance of off-road vehicles with electrified powertrains. In this study, a real-time hardware-in-the-loop (HIL) simulation platform was developed for validating a novel heuristics-based vehicle power management (VPM) strategy to be implemented on a novel heavy-duty offroad wheel loader featuring battery-hybrid powertrain configuration. The platform incorporates a vehicle power management strategy for power distribution, component-level controllers to oversee actuator functions, and physics-based models of powertrain components to mimic vehicle performance. This HIL simulation platform enables the safe and efficient testing and validation of a controller board comprising the VPM strategy and a DC/DC converter control system. Results from simulations conducted on the HIL platform demonstrate that the studied battery hybrid wheel loader can achieve over 10% fuel savings.

Keywords. Off-road vehicles, vehicle power management, hybrid vehicles, hardware-in-the-loop simulation.

1. INTRODUCTION

Electrifying off-road vehicles is necessary to address critical environmental and operational challenges facing the industrial and agricultural sectors. By transitioning to electric powertrains, off-road vehicles can significantly reduce harmful emissions, contributing to improved air quality and reduced environmental impact. Furthermore, electrification offers the potential to enhance operational efficiency, lower operating costs, and mitigate the reliance on fossil fuels, thereby promoting sustainability and resource conservation. The shift towards electrification also aligns with evolving regulatory standards and societal expectations regarding carbon emissions and environmental stewardship. Additionally, electric powertrains can provide off-road vehicles with improved torque characteristics, precise power delivery, and quieter operation, enhancing overall performance and operator comfort. Embracing electrification in off-road vehicles represents a crucial step towards building a cleaner, more sustainable future for industrial and agricultural machinery, ensuring a healthier environment and more efficient operations for years to come [1].

As one of the largest manufacturing corporations in the US, John Deere introduced its first production electric wheel loader, the 644k, in 2012, wherein its powertrain was transitioned from a conventional transaxle with a hydraulic torque converter to a series electric powertrain without an energy storage system. This very first evolution of this type of machine reduced its engine size from 9.0 L to 6.8 L, and provided a 30% gain in fuel efficiency. The presented work is part of a research effort aiming at developing a battery-hybrid wheel loader for John Deere based upon this production 644k series electric wheel loader by furthering downsizing the engine and adding an electric energy storage system. Note that the incorporation of a battery requires a vehicle power management (VPM) to regulate the power flows between power sources and power consuming units, which raises the demand for appropriate simulation tools to test its algorithm rapidly and safely before being implemented on a demo vehicle for in-field testing.

Hardware-in-the-loop (HIL) testing is a method utilized for controller validation, involving the interaction of actuating signals from an actual controller with a test rig that replicates real-world physical systems to simulate the

controller's performance in an assembled product. One significant advantage of utilizing this method is its ability to notably reduce the cost, time, and safety risks associated with controller development, verification, and debugging [2]. Given the characteristics of HIL testing, it is well-suited for validating the VPM strategy proposed in this study. As there is limited existing literature on the establishment of a comprehensive hardware-in-the-loop simulation platform for the hybrid electric wheel loader application, the content presented in this paper would partially address this gap.

2. SYSTEM MODELING & CONTROL DEVELOPMENT

2.1. Powertrain

Fig. 1 showcases the configuration of the baseline wheel loader examined in this research. A 6.8 L diesel engine is linked to a generator motor and a hydraulic pump responsible for bucket operations via a planetary gearbox. The generator motor, powered by the engine, generates AC power, which is subsequently transformed into DC power by a rectifier. For simplicity, a DC-link between the rectifier and the inverter has been omitted. When the generator motor supplies electricity, the inverter has the capability to extract direct currents from the DC-link and convert them back into alternative currents to drive the electric motor for vehicle propulsion.

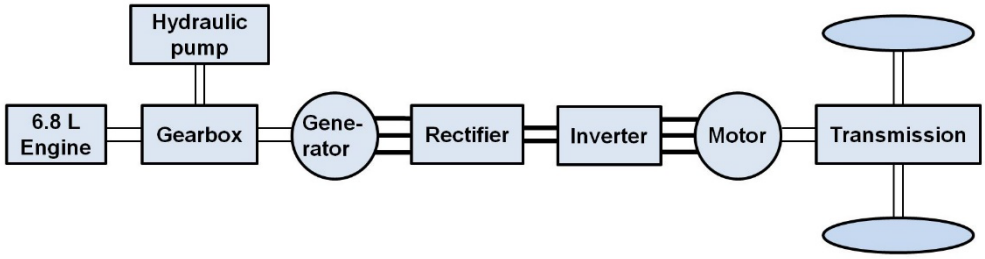

Figure 1. Baseline powertrain architecture

The powertrain of the envisioned wheel loader depicted in Figure 2 undergoes a transformation from this arrangement by reducing the engine size from 6.8 L to 4.5 L and integrating a battery pack to compensate for the diminished torque and power capability resulting from the engine reduction. Additionally, an electrically-driven pressure charging device, known as an "eBooster," is introduced to enhance boost pressure and transient engine performance.

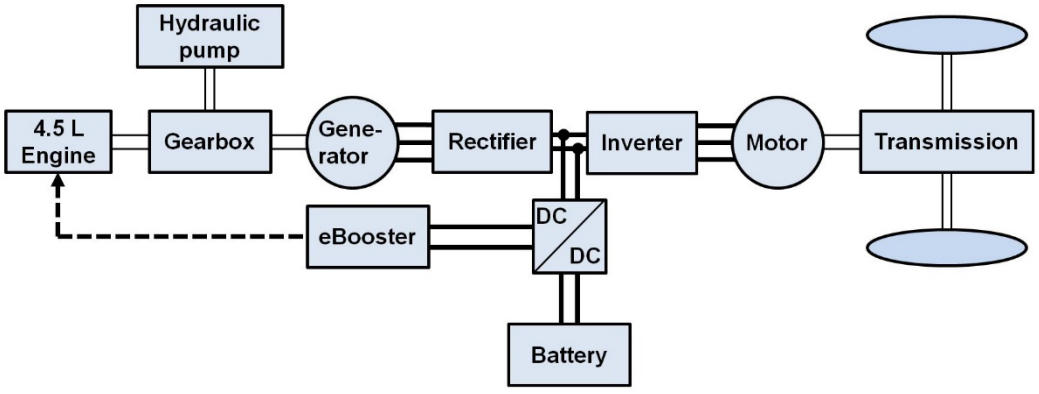

Figure 2. Proposed powertrain architecture

2.2. Engine

The 4.5 L turbocharged diesel engine, utilized as one of the two primary power sources for the proposed wheel loader, is integrated into the architecture illustrated in Fig 3. To model the engine's performance and fuel

consumption, a state-space form nonlinear engine model can be developed based on fundamental principles [3, 4]. It is important to acknowledge that, for the sake of simplicity in the model, the dynamics of the eBooster were omitted, although the engine's torque and power properties have accounted for the influence of the eBooster.

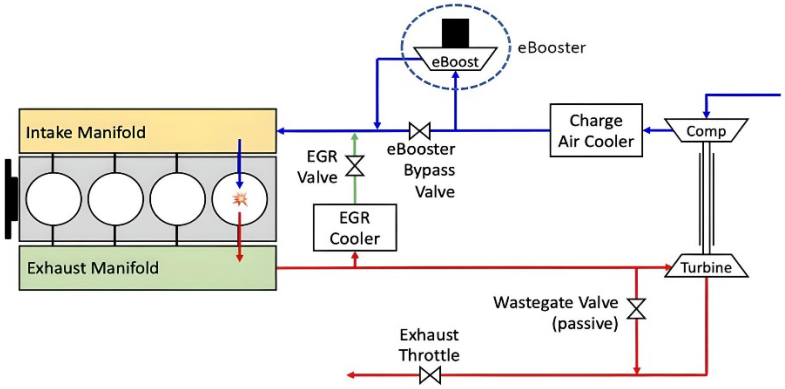

Figure 3. Engine schematic

Determining the actual engine speed involves conducting a torque balance analysis on the crankshaft [5] of the engine under investigation, resulting in:

$$\frac{d\omega_{eng,act}}{dt} = \frac{1}{J_{eng}}(T_{ind} - T_{hyd} - T_{gm}) \tag{1}$$

In the expression above, J_{eng} denotes moment of inertia of the engine crankshaft. T_{ind}, T_{hyd}, and T_{gm} represents indicated torque, load torque applied by the hydraulic system, and load torque applied by the generator motor, respectively. The indicated torque T_{ind} is a controller output generated by a production engine speed controller in PI form.

Furthermore, engine fuel consumption can be calculated as shown below per [6]:

$$\dot{M}_{fuel} = \frac{\omega_{eng,act} T_{ind}}{\eta_{therm} Q_{LHV}} \tag{2}$$

In the above expression, Q_{LHV} stands for gas lower heating value of diesel fuel, which is treated as a constant. η_{therm} denotes brake thermal efficiency and can be modeled as a function of actual engine speed and air-fuel ratio (AFR) [7]. Fig. 4 demonstrates an illustrative diagram of the engine model and control strategy deployed in this study.

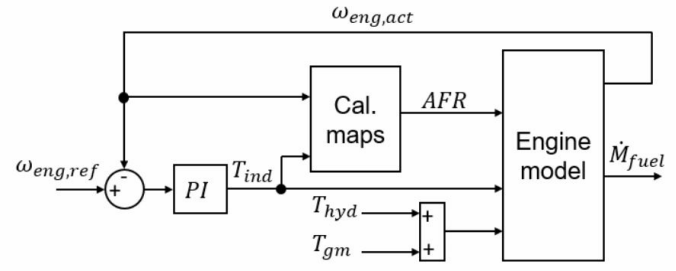

Figure 4. Engine model & control diagram

2.3. Battery

The battery model employed in this study is relatively straightforward, aiming primarily to forecast the state-of-charge (SOC) of the battery at any given moment and the system voltage of the battery. This study utilizes the Coulomb counting method to compute the battery SOC, which necessitates the input of battery current and initial battery SOC to proceed. Here, C represents the battery capacity, and $I(t)$ denotes the battery current.

$$SOC(t) = SOC(t_0) + \frac{1}{C}\int_{t_0}^{t} I(t)dt \tag{3}$$

The system voltage of the battery can be acquired by referencing a specification data sheet supplied by the battery manufacturer, which establishes a correlation between battery SOC and system voltage. Additionally, the specification data sheet from the battery manufacturer includes current restrictions for charging and discharging based on battery SOC, represented as $I_{chg,max}$ and $I_{dis,max}$, respectively. Fig. 5 depicts an illustrative diagram for the battery model.

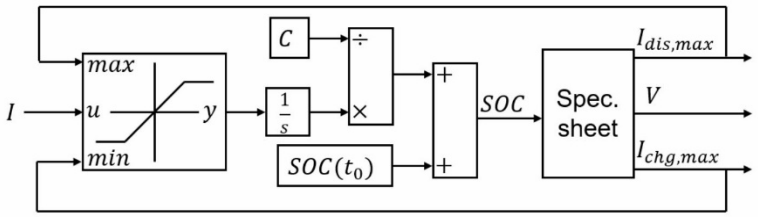

Figure 5. Battery model diagram

Table 1 presents essential specifications of the acquired battery pack utilized to establish the battery model. It is worth noting that the maximum discharge C-rate of the battery is 5 C, equating to a maximum discharge power of 177.5 kW. The battery is not designed for operation at this power level for more than 10 seconds; hence, this maximum discharge C-rate is labelled as "pulse." Conversely, the maximum continuous discharge C-rate of the battery is 3 C, corresponding to a discharge power of 106.5 kW. Temperature represents another crucial factor influencing battery properties. For the purposes of this study, it is assumed that the battery and thermal management systems can maintain the battery temperature at approximately 300 K.

Table 1. Specifications of sourced battery

Specification	Value
Nominal voltage	355 V
Min/Max voltage	288 V/403 V
Rated capacity	100 Ah
Rated energy	35.5 kWh
Max discharge C-rate (pulse)	5 C
Max discharge C-rate (continuous)	3 C
Max charge C-rate	2 C

2.4. Power Electronics

The power electronics components examined in this study encompass a generator motor and its associated controlling rectifier, a traction motor and its corresponding controlling inverter, and a DC/DC converter for battery management. To replicate their behaviors during operation within the vehicle under investigation, an electrical circuit for this power electronics system is formulated using the eHS solver, which is a real-time power electronics

simulation solver that facilitates simulation of an electric circuit on a FPGA, without needing to write mathematical equations. Fig. 6 displays a visual representation of the created electrical circuit.

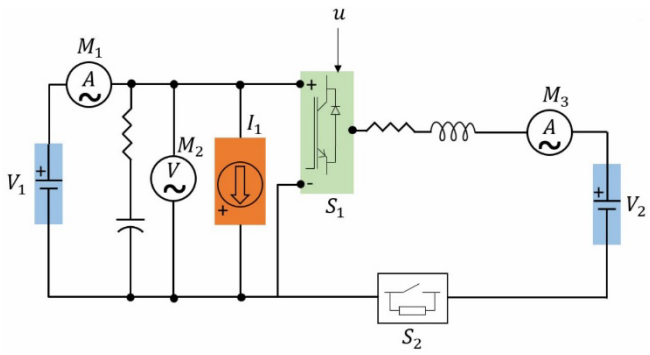

Figure 6. Illustrative layout of designed electrical circuit

Within the circuit, an ideal voltage source V_1 is utilized to simulate the generator and its corresponding bidirectional rectifier, as the rectifier is configured to operate in voltage control mode for the proposed hybrid vehicle design. During the operation of the proposed hybrid vehicle, any activity involving the traction motor or the battery, whether it entails power consumption or power supply, leads to fluctuations in the DC-link voltage, reflecting a power imbalance. By configuring the rectifier in voltage control mode, the generator is prompted to provide or absorb an appropriate amount of electrical power to or from the DC-link, thereby compensating for the power imbalance. The ideal voltage source is adjusted to supply a constant 700 V voltage. Typically, the generator supplies electrical power to the DC-link, resulting in the imposition of an electromagnetic load torque on the engine, denoted by the term T_{gm} in Eq. 1. To model this electromagnetic load torque, the current supplied by the generator I_{gm} and the DC-link voltage V_{dc} are measured, for which a current sensor M_1 and a voltage sensor M_2 are incorporated into the circuit, respectively. This load torque can then be formulated as demonstrated in Eq. 4, where η_{gm} represents the generator motor efficiency, and r signifies the gear ratio between the engine and the generator, and is utilized for further simulation purposes.

$$T_{gm} = \frac{I_{gm} V_{dc} \eta_{gm}}{\omega_{eng} r} \tag{4}$$

To model the traction motor and its associated bidirectional inverter, an ideal current source labelled as I_1 is utilized within the circuit. This approach is adopted to simulate two specific scenarios: vehicle propulsion, during which the traction motor draws current from the DC-link, and vehicle braking, where the traction motor injects current into the DC-link. The magnitude of the current passing through this ideal current source I_{tm} is contingent upon the power required by the operator for propulsion or braking P_{tm}, and the efficiency of the traction motor η_{tm}, as outlined below.

$$I_{tm} = \frac{P_{tm} \eta_{tm}}{V_{dc}} \tag{5}$$

The accuracy of the DC/DC converter model for battery control in this study, denoted as S_1 in the circuit, surpasses that of the other power electronics models, as it is intended to validate an actual controller governing battery current during simulation. Therefore, the fidelity of its model was increased and Fig. 7 presents a more intricate layout of the converter model.

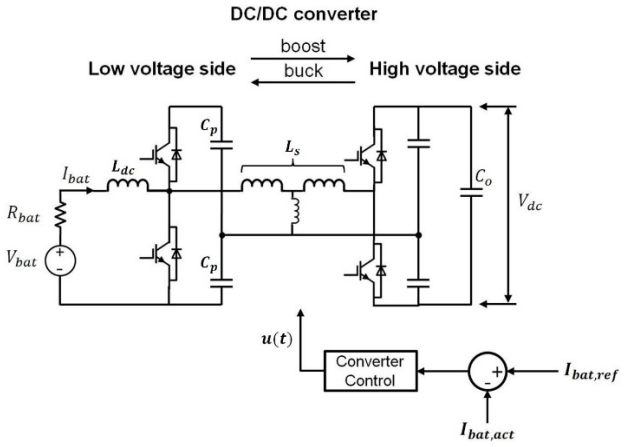

Figure 7. Illustrative layout of converter model

The proposed hybrid vehicle necessitates a high-power bidirectional DC/DC converter to interface with the vehicle's battery, given the substantial voltage differential between the 700 V DC-link (high voltage side, HVS) and the battery, which has a nominal voltage of 350 V (low voltage side, LVS). When power transfers from the battery to the DC-link, the DC/DC converter operates as a boost converter. Conversely, when the power flow direction is reversed, the DC/DC converter functions as a buck converter. The magnitude and direction of power flow between the battery and DC-link are regulated by a converter controller, which operates as a PI controller in current control mode. The input to the converter controller constitutes the error between the reference battery current and the actual battery current, compelling the converter controller to respond and generate appropriate gating signals $u(t)$ to achieve an instantaneous desired phase angle shift between LVS and HVS voltages. This is accomplished by a specific gating pattern, assuming a constant drive cycle and switching frequency. Ultimately, this phase angle shift ϕ, as depicted in the equation below, aligns the actual battery current with the reference battery current, where ω denotes the converter's switching frequency.

$$\frac{dI_{bat}}{dt} = \frac{\int \left(\frac{I_{bat}}{2C_p} - \frac{\phi(\pi-\phi)V_{dc}}{2C_p\omega L_s}\right) dt + V_{bat} - I_{bat}R_{bat}}{L_{dc}} \tag{6}$$

To verify the DC/DC converter's ability to effectively monitor battery current, a current sensor M_3 is integrated into the circuit to compare its measurement with the corresponding reference value. Additionally, another ideal voltage source, denoted as V_2, is introduced to simulate the battery voltage and complete the circuit, with the voltage value derived from the previously described battery model.

3. VEHICLE POWER MANAGEMENT

For certain component-level controllers to operate effectively, a supervisory-level vehicle power management (VPM) strategy must provide the necessary reference signals. At the system level, this VPM strategy governs the regulation of power flows within the vehicle by generating directives for the component-level controllers to execute. The control architecture of the proposed hybrid vehicle is depicted in Fig. 8. Notably, the control variables derived from the power management strategy chosen for this hybrid vehicle consist of the commanded engine speed ω_{eng} for the engine controller, the commanded battery current I_{bat} for the converter controller, and the available torque limit $T_{tm,max}$ for the inverter controller.

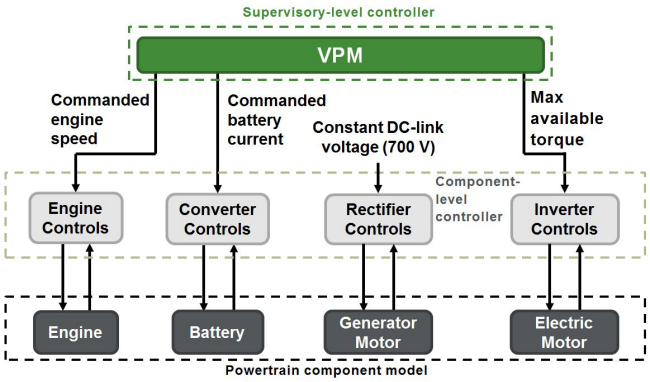

Figure 8. Control architecture of the battery-hybrid vehicle

Fundamentally, the developed VPM strategy for this research should have the ability to distribute the power demanded by the operator from multiple power sources to various power-consuming units of the proposed vehicle (within physical constraints), optimize engine operation for maximum efficiency, and manage battery operation to maintain battery state of charge (SOC). Fig. 9 illustrates the heuristic-based algorithm of the designed VPM strategy for calculating the commanded engine power $P_{eng,cmd}$ and the commanded battery current $I_{bat,cmd}$. In the algorithm, $P_{hyd,req}$, $P_{trac,req}$, and $P_{load,para}$, represent the hydraulic power requested by the operator, the traction power requested by the operator, and the auxiliary load power estimated by the vehicle's transmission control unit (TCU), respectively. It is noteworthy that these requested power terms are predominantly positive, although $P_{trac,req}$ may be negative during energy regeneration. Additionally, $P_{bat,max}$, $P_{bat,min}$, $P_{dis,max}$, and $P_{chg,max}$ can be defined as follows:

$$
\begin{aligned}
P_{dis,max} &= I_{dis,max} V_{bat} \\
P_{chg,max} &= I_{chg,max} V_{bat} \\
P_{bat,max} &= \begin{cases} P_{dis,max}, SOC_{act} > SOC_{ref} \\ P_{SOC}, SOC_{act} < SOC_{ref} \end{cases} \\
P_{bat,min} &= \begin{cases} P_{SOC}, SOC_{act} > SOC_{ref} \\ P_{chg,max}, SOC_{act} < SOC_{ref} \end{cases}
\end{aligned} \tag{7}
$$

In the above equation, P_{SOC} is defined as a tuneable control limit of the battery in the format of a PI controller, with the differential value between target SOC SOC_{ref} and actual SOC SOC_{act} being the controller input, and battery power control limit P_{SOC} being the controller output.

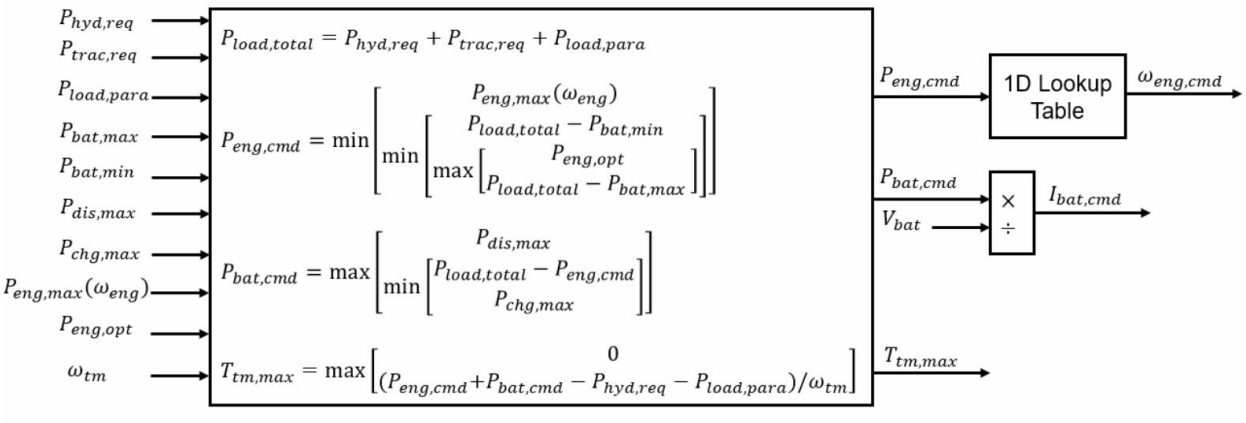

Figure 9. Vehicle power management strategy

Additional terms requiring clarification in the algorithm include the maximum engine power $P_{eng,max}$ at the current engine speed, the optimal engine power $P_{eng,opt}$ indicating the power level at which the engine achieves the lowest brake specific fuel consumption (BSFC) value, and the traction motor speed ω_{tm}.

After determining the commanded engine power $P_{eng,cmd}$, the VPM strategy will choose a commanded engine speed based on the engine efficiency map. This selected engine speed aims to achieve the best fuel economy while operating at the specified power level. Nevertheless, the chosen engine speed may be constrained by various factors, such as the operational speed limit of the hydraulic pump [8], leading to a suboptimal engine speed as the ultimate result.

Through the generation of a commanded engine power $P_{eng,cmd}$ and commanded battery current $I_{bat,cmd}$, the VPM strategy can compute the available power limit for the electric motor with the aid of the TCU. This calculated value is then transformed into a maximum torque value that the electric motor can deliver for vehicle propulsion, serving as the third output. Further detailed explanation about this algorithm can be found in [9].

4. HAREDWARE-IN-THE-LOOP TESTING

4.1. Experimental Setup

In this research, a novel HIL simulation platform has been established, and Fig.10 displays an actual image of the deployed HIL simulator. To provide a clearer depiction of its structure and the interactions between each element, Fig.11 illustrates a layout of the platform. This simulation platform comprises four main components: a physical controller board housing the designed VPM strategy and a converter controller for the battery, which serves as the "hardware" under examination in this system; an FPGA module utilized for executing the eHS solver to simulate the power electronics employed in this study; a CPU module responsible for executing the plant model; and a host PC used as a console and monitor.

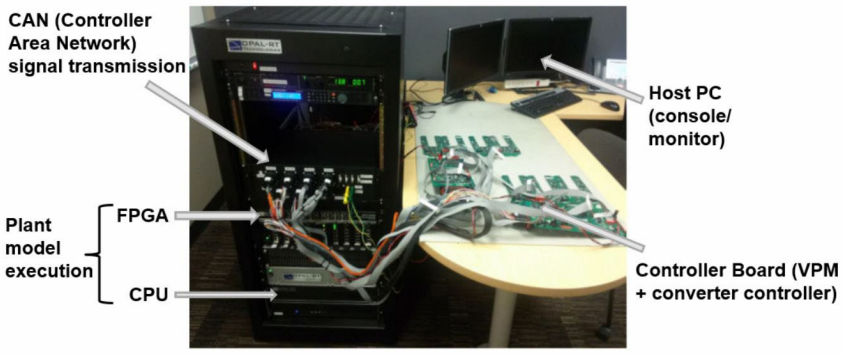

Figure 10. Image of the deployed HIL simulator

By employing the innovative HIL simulation platform, the following three objectives can be safely and efficiently accomplished: (1) executing the VPM strategy on actual hardware in real time to evaluate its functionality, specifically its ability to operate in real time on a vehicle implementable controller board and communication bus; (2) validating the converter controller's capacity to regulate battery current; (3) evaluating the potential fuel savings of the proposed battery hybrid electric wheel loader in comparison to the baseline wheel loader. To enable a valid comparison between the baseline vehicle and the proposed vehicle, a typical production drive cycle of the baseline wheel loader known as "Stockpile" is replicated in the HIL simulation platform for the proposed wheel loader. This is achieved by inputting the experimental load (power) data obtained from an actual baseline wheel loader running the "Stockpile" drive cycle into the HIL simulation platform via the host PC, prompting the platform to simulate vehicle performance. The simulation results of the proposed vehicle can then be compared to the experimental results of the baseline vehicle for validation and assessment purposes.

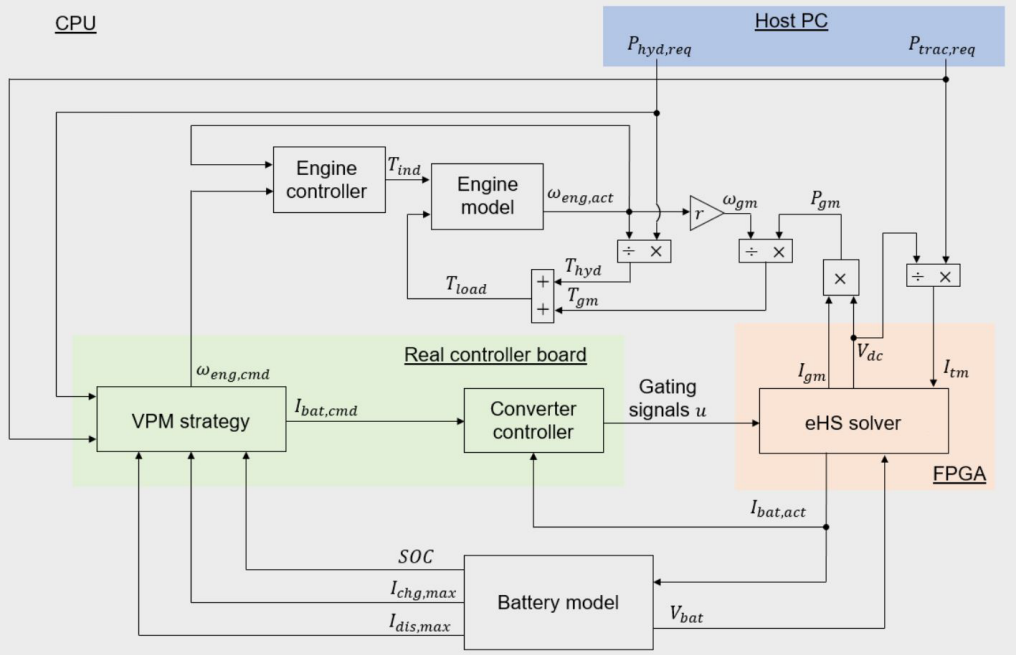

Figure 11. Configuration of HIL simulator setup

Fig. 12 illustrates the concept of replicating a real production drive cycle performed by a baseline vehicle on the HIL simulation platform for the proposed vehicle. Additionally, it also provides an explanation of the procedure for the "Stockpile" drive cycle. It is important to note that when simulating the proposed vehicle on this HIL simulation platform, there is a specific consideration to be addressed. Despite the VPM strategy's ability to direct the engine controller to follow a target engine speed, enabling efficient engine operation, currently the (proposed) demo vehicle assembled by John Deere for ground testing lacks the capability to freely adjust engine speed. Consequently, within the HIL simulation setup, the target engine speed is fixed at 1800 RPM, which is generally an efficient speed for the engine installed in the proposed vehicle.

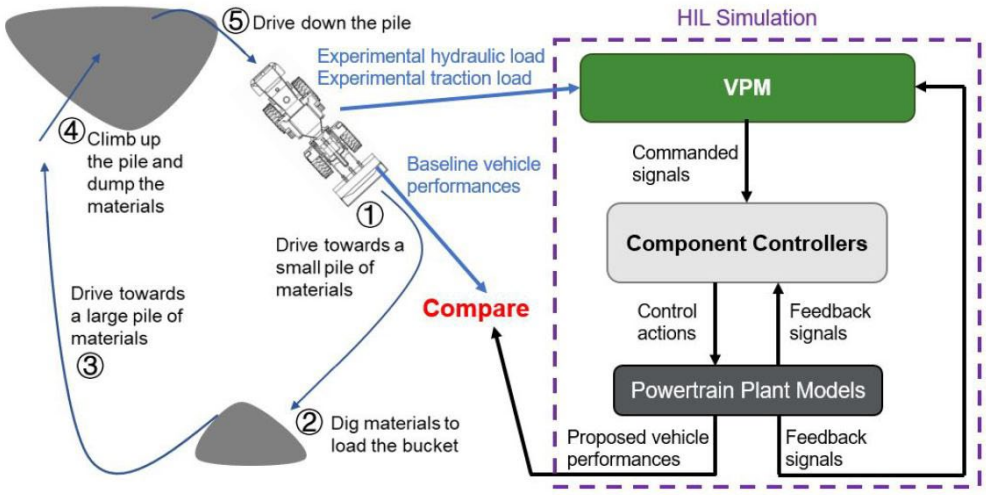

Figure 12. Illustration of reproducing a "Stockpile" drive cycle in the HIL simulator

4.2. Experimental Results

Fig. 13 illustrates the instantaneous power consumption of the two primary power-consuming components on the analyzed wheel loaders as simulated on the HIL platform: the traction motor and hydraulic pump. A positive power value indicates power consumption by the respective unit, while a negative power value indicates power generation by the unit. It is noteworthy that the solid red line represents the actual traction/hydraulic power measured from the baseline vehicle during experimentation, which also serves as the "requested power" inputs ($P_{trac,req}$, $P_{hyd,req}$) for the proposed vehicle (denoted as “Next-gen vehicle” in the figure) in the HIL simulation platform. Meanwhile, the dashed blue line represents the measured simulated traction/hydraulic power delivered by the proposed vehicle in the HIL simulation platform. It is evident that the dashed blue line closely aligns with the solid red line for both power-consuming units across the entire drive cycle. Since traction power signifies vehicle propulsion and hydraulic power indicates the vehicle's bucket operation, this figure leads to the conclusion that despite the proposed wheel loader featuring a downsized engine, it is still capable of delivering equivalent vehicle performance to the baseline wheel loader with the assistance of the battery.

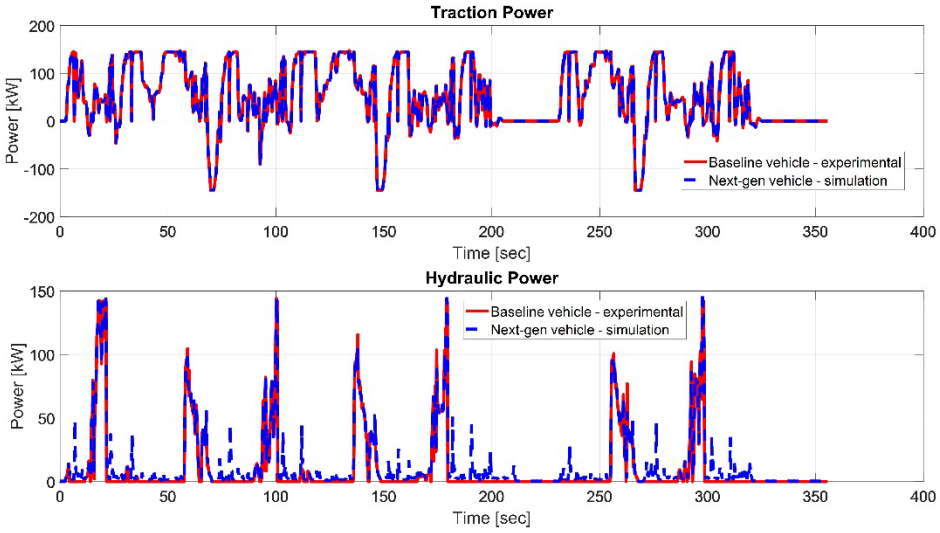

Figure 13. HIL simulation result - power consuming unit performances

Fig. 14 evaluates the performance of the battery in the proposed vehicle during the "Stockpile" drive cycle. The first and second subplots depict the commanded battery power by the VPM strategy, and the actual battery power measured from the plant model, respectively. It is important to note that the commanded battery power is derived from the real controller board, which records simulation results as data points, while the actual battery power is obtained from the CPU module, which records simulation results as time-series data. Consequently, there is not a perfect alignment on the x-axis between the two subplots. However, the two subplots are presented in a manner that reflects correspondence throughout the simulated drive cycle. Analysis of these subplots reveals that the actual battery power closely follows the trend and magnitude of the commanded battery power, notwithstanding some spikes and dips during transients, which are expected. This observation confirms that the DC/DC converter controller effectively regulates the actual battery current in response to commands from the VPM strategy. The third subplot in Fig. 14 illustrates the battery State of Charge (SOC) condition. It is noted that the battery SOC value at the end of the drive cycle matches the initial battery SOC value of 70%, demonstrating that the VPM and component-level control strategies effectively maintain the battery SOC by appropriately discharging and charging the battery without violating its physical limits. Furthermore, the conservation of battery SOC enables a valid comparison between the baseline wheel loader and the proposed wheel loader in terms of engine fuel consumption.

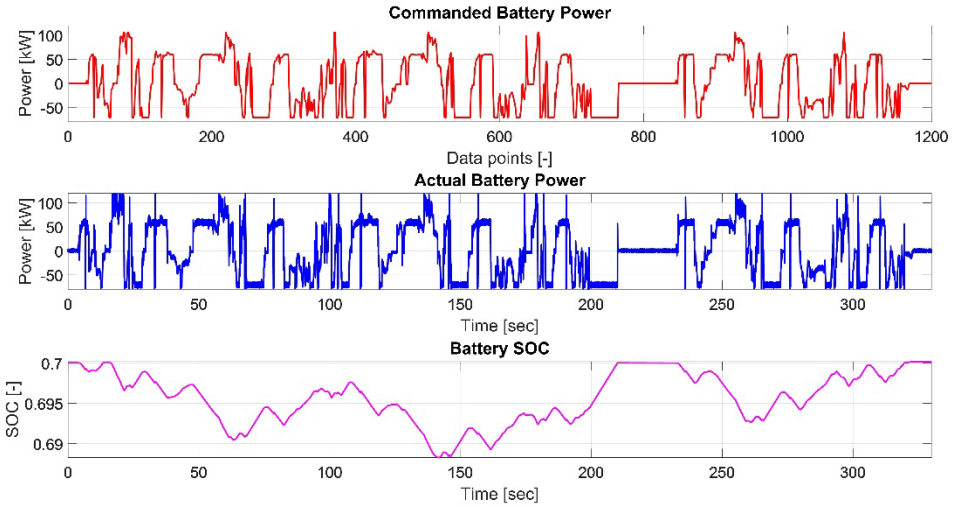

Figure 14. HIL simulation result - battery performances

In Fig. 15, the simulation results of the downsized engine for the proposed hybrid vehicle are analyzed. Similar to the battery, the first two subplots depict the commanded engine power measured from the VPM strategy (in the real controller board) and the actual engine power measured from the engine model (in the CPU module), respectively. It is noteworthy that although engine power is not a direct control variable of the VPM strategy, the close match between actual engine power and commanded engine power throughout the entire drive cycle suggests that the VPM strategy effectively manages power distribution within the proposed hybrid vehicle, without consistently drawing extra power from the engine to compensate for power deficiencies. The third and fourth subplots display engine speed and engine torque, respectively. It is observed that the engine speed controller promptly and accurately regulates the engine speed around 1800 RPM in the simulation, instilling confidence in its deployment on a real controller board for testing the demonstration vehicle. Additionally, it is evident that the commanded engine power remains at 85 kW for the majority of the time, which represents the optimal power level for the engine at 1800 RPM. This insight underscores one of the key objectives of the VPM strategy: to operate the engine efficiently for the purpose of fuel savings.

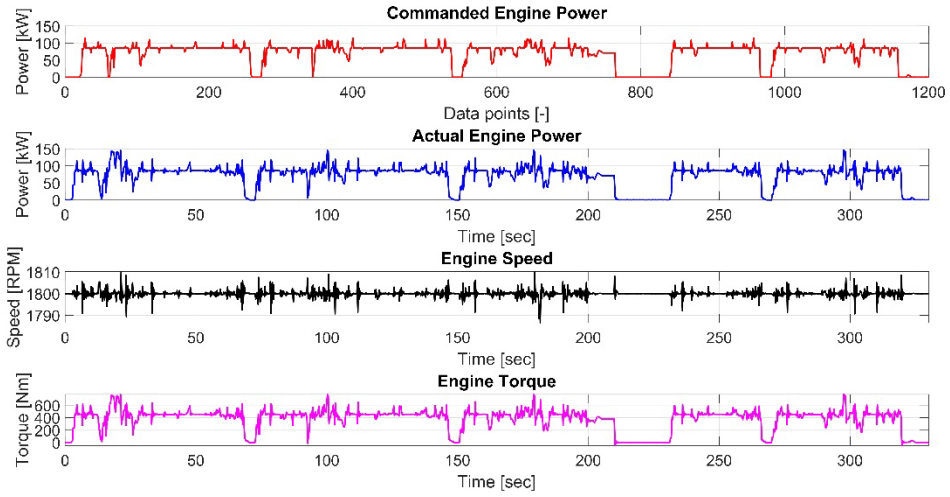

Figure 15. HIL simulation result - engine performances

Fig. 16 examines the fuel consumption of the downsized engine utilized in the proposed vehicle, as depicted by the orange line in both subplots. The top subplot displays the instantaneous engine fueling rate at each time instant. Integrating the instantaneous engine fueling rate over time yields the cumulative engine fuel consumption, which is illustrated in the bottom subplot. For reference, corresponding data of the original engine used in the baseline vehicle are also included, represented by the blue line. It is evident that at the end of the same drive cycle, the original engine of the baseline vehicle consumes 1.82 kg of fuel, whereas the downsized engine of the proposed vehicle consumes only 1.58 kg of fuel, resulting in a 13% fuel saving achieved by the proposed vehicle.

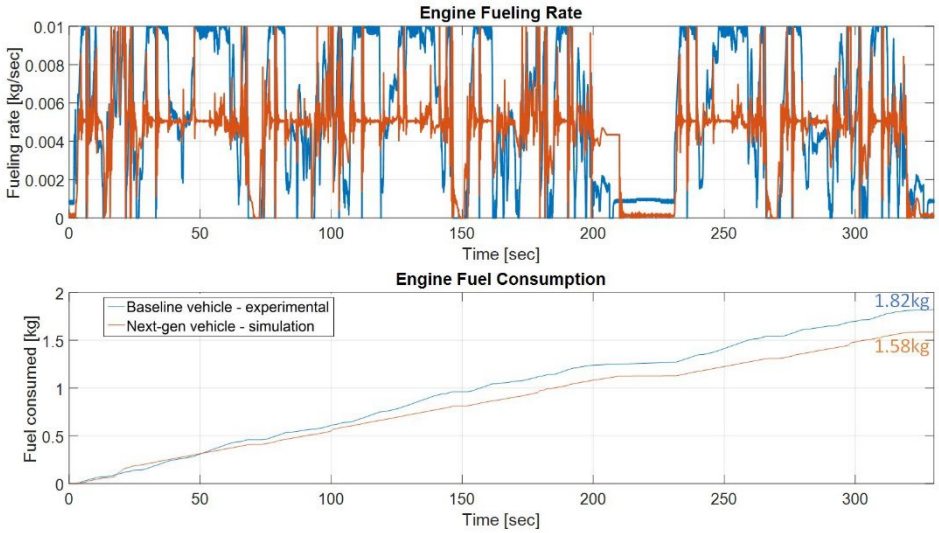

5. CONCLUSIONS

The increasing demand for hybrid wheel loaders in the off-road construction vehicle industry over the past decade is driven by concerns about global warming, rising fuel prices, and stricter government regulations. This heightened demand underscores the necessity for advanced testing methodologies that can facilitate the design of next-generation hybrid wheel loaders. In this research, a cutting-edge hardware-in-the-loop (HIL) simulation platform, comprising a supervisory-level vehicle power management (VPM) strategy, component-level controllers, and vehicle powertrain plant models, has been established for a battery-hybrid wheel loader currently under investigation at John Deere. This HIL simulator enables the safe and efficient real-time validation of an actual controller board that integrates the VPM strategy and a DC/DC converter controller. Additionally, it allows for the evaluation of potential fuel savings achievable with the battery-hybrid wheel loader in comparison to its baseline counterpart.

The results of the HIL simulation demonstrate that the VPM strategy effectively delivers the power demanded by operators from power sources to power consuming units, ensures efficient engine operation, and maintains a balanced battery State of Charge (SOC). Moreover, the ability of the DC/DC converter controller to promptly and accurately regulate battery current to match the target value is confirmed. As a result of engine downsizing and powertrain hybridization, it is anticipated that the proposed battery hybrid electric wheel loader will achieve fuel savings of over 10% in comparison to a baseline wheel loader.

6. REFERENCES

[1] Zhao, Dezong, et al. "Real-time energy management for diesel heavy duty hybrid electric vehicles." IEEE Transactions on Control Systems Technology 23.3 (2014): 829-841.

[2] Fathy, Hosam K., et al. "Review of hardware-in-the-loop simulation and its prospects in the automotive area." Modeling and simulation for military applications. Vol. 6228. SPIE, 2006.

[3] Rayasam, Sree Harsha, et al. "Robust Switching MIMO Control of Turbocharged Lean-Burn Natural Gas Engines." IFAC-PapersOnLine 55.24 (2022): 7-12.

[4] Rayasam, Sree Harsha, et al. "Robust model-based switching MIMO air handling control of turbocharged lean-burn SI natural gas variable speed engines." International Journal of Engine Research 24.6 (2023): 2783-2804.

[5] Qiu, Weijin, et al. "Modeling and Robust Coordinated Control of Turbocharged Natural Gas Engine with Genset Application." IFAC-PapersOnLine 55.24 (2022): 39-44.

[6] Harsha Rayasam, Sree, et al. "Control-oriented modeling, validation, and interaction analysis of turbocharged lean-burn natural gas variable speed engine." International Journal of Engine Research 24.2 (2023): 738-754.

[7] Qiu, Weijin, et al. "Control design-oriented modeling and μ-synthesis-based robust multivariate control of a turbocharged natural gas genset engine." International Journal of Engine Research 24.9 (2023): 3905-3921.

[8] Qiu, Weijin. AN INTEGRATED FRAMEWORK FOR MODELING, ROBUST COORDINATED CONTROL, AND POWER MANAGEMENT OF ADVANCED POWERTRAINS FEATURING TURBOCHARGED ENGINES. Diss. Purdue University Graduate School, 2023.

[9] Qiu, Weijin, et al. "System configuration, control development, and in-field validation of a hybrid electric wheel loader featuring electrically-boosted engine." Control Engineering Practice 150 (2024): 105989.

Improving transmission efficiency via a novel radial piston cam lobe motor architecture

Pierre Bernard *, Vincent Langlois, Maxime Maurer

Poclain Hydraulics Industrie, pierre.bernard@poclain.com

Abstract

This paper presents the energy efficiency optimization of a closed loop hydrostatic transmission, using the example of a heavy tandem roller compactor application. An innovative concept of radial piston cam lobe motor is proposed, which allows a paradigm shift in hydrostatic transmissions sizing, essentially moving away from breakout torque as the entry point to sizing and refocusing the transmission sweet spot on its most used conditions. The comparative simulation of a standard machine and the same machine equipped with the new concept of hydraulic motor is realised using a 1D simulation software. The energy consumption of both machines is simulated over a reference usage profile derived to represent long-term machine use. On this usage profile, simulations demonstrate a fuel consumption reduction of 7.7% using the updated design of hydraulic motor.

Keywords: efficient transmission, radial pistons motor, cam-lobe, energy efficiency optimization, hydraulic evolution.

River Journal, 1–19.
© 2024 *River Publishers. All rights reserved.*

1 Introduction

Climate change and energy management are at the heart of preoccupations and innovations in all sectors. The road construction sector accounts for approximately 5% of global GHGs emissions in Europe [1], and off-road machinery in Europe is subject to the European Commission's *Green Deal* [2], which targets net zero emissions of GHGs by 2050. Road compaction equipment participates to the CO2 emissions and global GHGs of the construction sector [3]. To the knowledge of the authors, no study has investigated the energy efficiency of compaction equipment and specifically heavy tandem rollers. However, as will be shown in the coming sections, their operation is quite repeatable, which makes them a good candidate for a study of fuel consumption over a representative mission profile.

The concept of hydraulic motor proposed in this paper is designed to refocus the sizing of the transmission towards efficiency, treating the maximum breakout torque requirement of the machine as a separate issue.

After giving an overview of the application and its usage profile, a standard system currently in use on this type of machine will be used as a reference case for the energy efficiency study. Then, the novel radial piston cam lobe motor architecture will be introduced, and the sizing philosophy it allows will be described. In simulation studies, this upgraded motor and its optimized transmission will be substituted for the reference machine transmission, and the energy efficiency evolution will be evaluated.

2 Heavy tandem roller compactors

2.1 Function, purpose

A heavy compaction tandem roller is a compaction machine for road creation or refurbishment. These machines are used to compress the asphalt's support and top layers in order for the pavement to carry the traffic loads and to resist to weather and temperature induced stresses. Several compaction methods and machine exist, each dedicated to specific conditions and types of soil. The machine studied in the present work is a vibratory heavy articulated tandem roller, meaning that a vibration of the drums is induced by an off-centred mass, driven in rotation by a high speed hydraulic motor. As explained in [4], the vibration of the drums drastically increases compaction efficiency by reducing internal friction in the mix.

The choice of the type of compactor to use is based on several parameters. Vibratory tandem rollers are adapted to the base and sub-base layers, as well as to the top asphalt layer (see [5]).

2.2 Hydraulic system

The hydrostatic transmission commonly used on such machines is a standard closed loop circuit with two hydraulic motors fed in parallel by a variable displacement pump, usually an axial piston type. Each drum is equipped with one fixed-displacement motor, which is responsible for the forward and reverse motion of the machine. An auxiliary closed loop circuit is used for the vibration function. The targeted machine speed is defined by the operator, and regulated by the on-board electronics, which also manages the acceleration and deceleration ramps.

2.3 Standard use

The machine is brought on a trailer from the contractor's parking site to the work site. Then, asphalt compaction is achieved in several passes, the first of which is made just after the mix has been laid-down. The standard lay-down temperature is approximately 130 to $160°C$, and the first compaction pass is made right away, in order to finish it with mix temperatures still higher than $115°C$, a temperature above which bitumen is more fluid and compaction using vibration is efficient. Subsequent compaction passes (generally between 2 and 4) are then made before the mix cools down to temperatures lower than $60°C$ and becomes stiffer and harder to compact.

For the reasons described above, a standard compaction pass, a description of which is given in Figure 1, is made in a specific pattern on a 30 to 60 m long strip behind the paver (the machine depositing the asphalt mix), with a slight overlap of 10 to 20 cm between each strip. To preserve compaction homogeneity, during the start and stop phases of the compaction, smooth acceleration and decelerations are mandatory, and a constant compaction speed during the passes is required. Suitable compaction speeds range between 2 and 6 km/h depending on the mix composition and layer thickness. On a worksite, the compaction machine also has to travel from one point to another, be it from its parking site to the location of the compaction strip start, or between road sections. These travels are made at higher speeds, up to 12 km/h, and the rolling resistance is much less than during compaction passes.

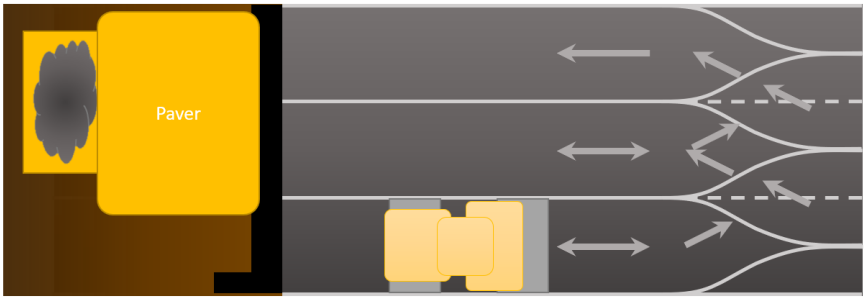

Figure 1 Illustration of the optimised pattern of a compaction pass.

2.4 Simplified reference duty-cycle

In order to estimate the energy efficiency of a heavy tandem roller, a simplified drive cycle is elaborated to represent the use of the machine on a worksite, including travel and work periods. The reference duty-cycle includes portions of flat, uphill and downhill travel for both transfer and work periods. While the gradability of vibratory heavy tandem rollers is usually between 30 and 40% (see for example [6], [7]), it is rare to find roads with this kind of gradient, and smaller compaction machines are used for mountain roads. As a reference, the European Road Safety Observatory [8] defines motorways as a road with, amongst other characteristics, maximum gradients of 4 to 5%. Therefore, an arbitrary value of uphill/downhill slope of 7.5% is chosen for the reference mission profile to represent an average value of the slopes encountered by the heavy tandem roller.

A real worksite in southern France was used to consolidate the different time ratios between work and travel modes, as well as between flat, uphill, and downhill sections. A proportion of approximately 10% of the time is allocated as "7.5% slope" on our reference mission profile.

Figure 2 shows the speed, slope (both on left ordinate axis) and rolling resistance (right ordinate axis) in function of time for the heavy tandem roller duty-cycle. The reference profile is nearly 20 minutes long, which is due to the importance of the acceleration and deceleration phases. Indeed, measurements on a machine have shown acceleration ramps defined to reach the targeted speed in 2 to 3 seconds, whether for working speeds of 5 kph, or travelling speeds of 12 kph. As a result, acceleration and deceleration times of 2.5 seconds have been set in the reference mission profile.

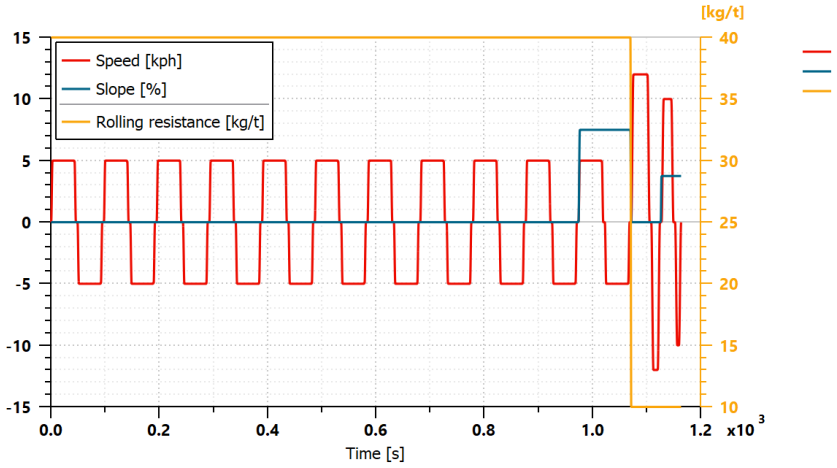

Figure 2 Reference mission profile for heavy compaction energy efficiency determination.

2.4.1 A note on rolling resistance

Sun et al. in [9], give several definitions of rolling resistance, from an energy and a force standpoint. In the context of a compaction roller rolling on fresh, not yet compacted, asphalt, the asymmetry in force distribution at the contact line can be attributed to the asphalt mix deformation. This deformation is closely linked to the apparent viscosity of the asphalt mix, a characteristic that varies with mix temperature, and thus with time. Different situations of the compactor roller are shown, a low rolling resistance travel situation in Figure 3 (a) ; what could be a first compaction pass with hot, low viscosity, asphalt in Figure 3 (b), leading to a high rolling resistance ; and what could be a finishing, higher viscosity, pass in Figure 3 (c), with intermediate rolling resistance.

These different conditions mean that the rolling resistance would evolve with time during compaction, and especially in the different compaction passes. To simplify the mission profile, only two values are used for the coefficient of rolling resistance C_{rr}: 40 kg/t for compaction mode, and 10 kg/t for travel mode. The 40 kg/t work value of rolling resistance is taken as a representative value for all compounded compaction passes. Separating compaction phases would lead to values between 50 kg/t for the first compaction pass, and 35 kg/t for finishing compaction passes.

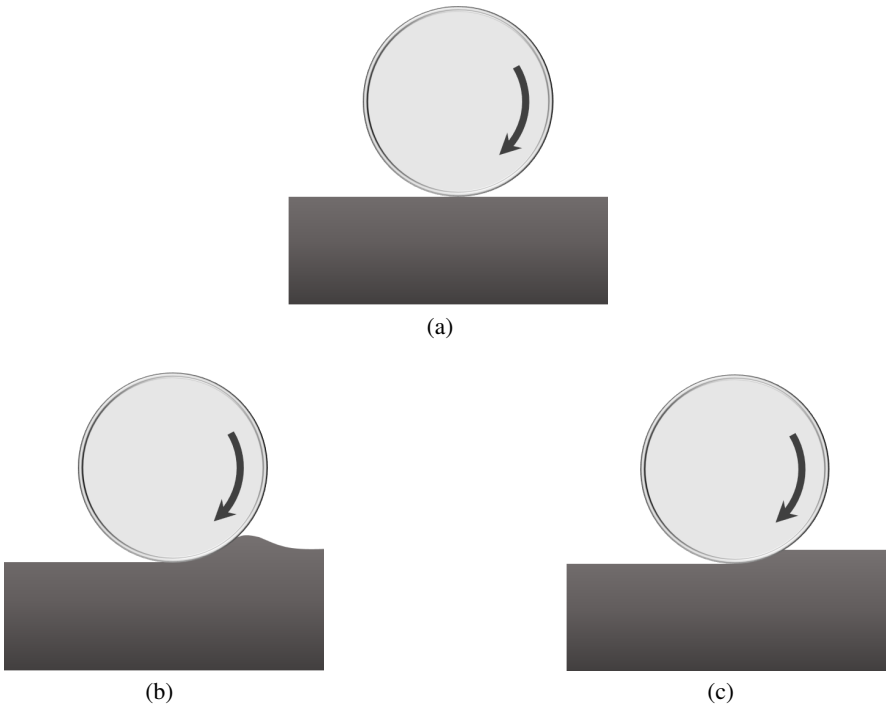

Figure 3 Roller rolling on road (a), on hot asphalt mix (b), on "cold" mix (c).

3 Current situation

3.1 Transmission sizing

As exposed in the previous sections, the compactor's transmission and mission profile are rather simple, and for these reasons, a heavy tandem roller's performance level assessment is unlikely to be based on the sole hydrostatic transmission capability. When evaluating a compaction machine, the focus is on compaction efficiency, which encompasses speed stability, compaction ability, as well as vibration frequencies and amplitudes.

3.1.1 Machine gradability

The main characteristic used for sizing the hydraulic motors of the compactor is the gradability of the machine, which means that the maximum slope to be climbed defines the torque requirement on the motors. From this, the displacement D_M of the motor is obtained by the standard formula: $D_M = \frac{T}{\Delta P}$, with T the torque and ΔP the differential pressure at the motor's ports. Using

this displacement, and knowing the maximum required speed, drum rolling circumference, and internal combustion engine (ICE) speed, one is able to define the required pump displacement D_P. As mentioned in §2.4, the gradability of heavy tandem rollers is in the 30–40% range. Due to the mass of the machine, and the incline of such a slope, this max climbable slope is driving the maximum torque requirement on the hydraulic motors installed in the drums. The torque T required for each of the two drum motors in order to climb a slope s is given by:

$$T = \frac{1}{2} M \cdot g \cdot R_{Drum} \cdot (\sin(\arctan(s)) + C_{rr} \cdot \cos(\arctan(s))) \quad (1)$$

where M is the mass of the machine, and R_{Drum} is the radius of the drums.

3.1.2 Application

Applying the previously described method, without considering efficiencies, to a real case with the machine parameters listed in Table 1, representative of a heavy tandem roller available for test, gives a required torque on the motor $T_M \approx 17000 N.m$.

Table 1 Machine parameters.

M	[kg]	13300	Compactor mass
s_{max}	[%]	39	Gradability
C_{rr}	[kg/t]	10	Rolling resistance coefficient on max slope
R_{Drum}	[m]	0.7	Drums radius
p_{max}	[bar]	400	Max system pressure
p_{charge}	[bar]	20	System charge pressure

With the available differential pressure in the system (differential pressure $\Delta P = p_{max} - p_{charge}$), this gives a displacement of $D_M = 2800 cc/rev$ for each of the two motors in the system.

3.2 Fuel consumption over reference cycle

Simulation of this machine over the reference mission profile described in §2.4 is performed using the AMESim 1D-simulation software.

3.2.1 Model description

The model, the sketch of which is shown in Figure 4, makes use of the capabilities of AMESim to implement vehicle, ICE, and hydraulic circuitry and components in the same model. The vehicle model calculates the longitudinal

acceleration, velocity and displacement of the machine based on road profile, wheels (in our case, drums) torque. The implemented model accounts for rolling friction and road slope. The machine speed is controlled by way of

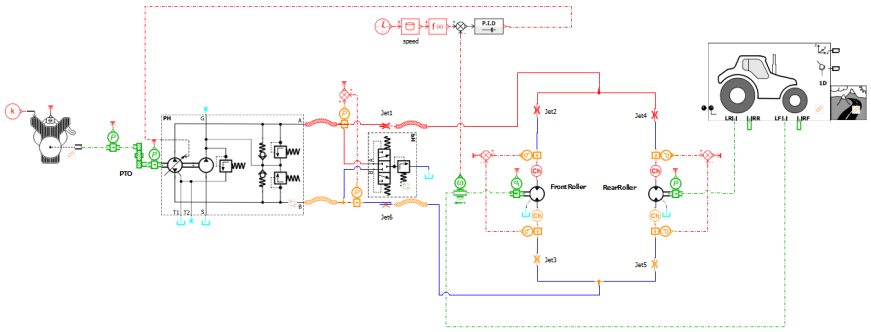

Figure 4 Model for reference machine energy efficiency simulation.

a PID controller on the pump displacement, the internal combustion engine speed target being fixed at 2300 rpm. The engine model manages acceleration ramps of the engine to avoid stalling, and returns fuel consumption based on tabulated values function of engine speed and torque. The hydraulic system is modelled using physical models of the pump and motors, including tabulated data for hydro-mechanical and volumetric losses, and pipes including pressure drops and compressibility. The pump and motor losses models are based on elementary measurements and advanced simulation results, aggregated in simplified models for energy analysis.

3.2.2 Reference machine energy efficiency analysis

The simulation of the AMESim model of the machine described in the previous paragraph over the reference mission profile described in §2.4 gives several results, of which the fuel consumption of the machine over the complete cycle is the metric chosen in this study. Figure 5 shows the mechanical energy in Wh on the pump's shaft and the differential hydraulic energy on the pump's ports, as well as the fuel consumption in L over the nearly 20 minutes reference mission profile described previously.

The total fuel consumption for the machine is $2.5L$ over this duty-cycle. The energy and fuel consumption are plotted over time, and it can be seen that the instantaneous energy consumption is greater near the end of the mission profile, during phases of compaction in slope, and travel.

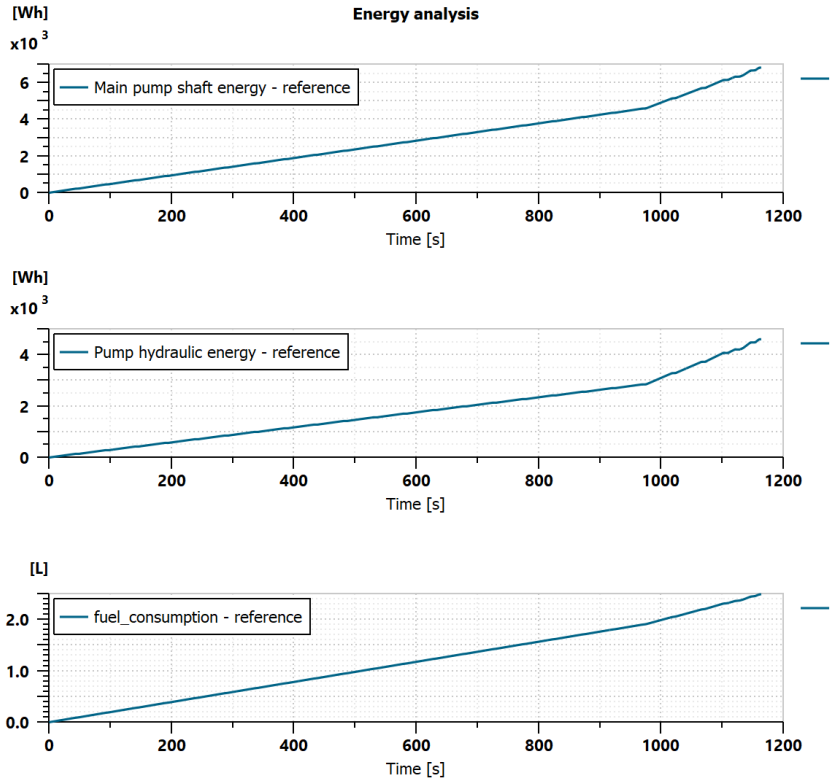

Figure 5 Energy analysis of reference solution over reference mission profile.

4 Proposed system improvement

As described in §3.1.1, the current standard situation for the hydrostatic transmission of a heavy tandem roller, is to size the hydraulic motors for the maximum duty point. This can largely be generalized to other hydrostatic transmissions, and the maximum duty point can be referred to as the maximum breakout torque, which in the case of the heavy tandem roller, has been shown to be the torque required to climb the maximum gradable slope of the machine. The sizing of the hydrostatic transmission is therefore made while disregarding the number of occurrences of, or time spent at, this maximum breakout torque condition, thus ignoring energy efficiency.

4.1 Sizing philosophy

In order to bring energy efficiency into focus, a new "sizing philosophy" is required. Sizing a hydrostatic transmission for maximising energy efficiency entails to size the hydraulic motors to try minimising system losses for the most frequent working conditions of the machine. In the case of the heavy tandem roller, the most time is spent in compaction mode, at low speed, on the flat, or on moderate slopes. Using Equation 1, it is possible to determine the motor torque required for stabilised conditions, but torque is also required to accelerate the machine up to the stabilised speeds depicted in Figure 2. This acceleration torque is added to Equation 1 to yield:

$$T = \frac{M \cdot R_{Drum}}{2} \cdot \left(g \cdot (\sin(\arctan(s)) + C_{rr} \cdot \cos(\arctan(s))) + \frac{\mathrm{d}V}{\mathrm{d}t} \right) \tag{2}$$

From this, and the maximum available differential pressure in the system, the minimum hydraulic motor displacement required at all times can be computed. Figure 6 displays a normalised time distribution of this required displacement, with the discrete distribution in the thin blue stair plot, and an approximated distribution in thick blue line. It shows that the required displacement very seldom exceeds half of the displacement determined in §3.1.1. In fact, 90% of the time, a displacement of 1370 cc/rev is sufficient to realise the mission of the machine.

By setting the motor displacement to 1370 cc/rev, the flow in the hydraulic circuit is reduced, and the pressure is increased, which brings hydraulic components into more efficient operating conditions zones. However, this efficiency increase is at the cost of the unattainable operating points that the lower motor displacement forbids.

4.2 Characteristics of the new radial pistons cam-lobe motor

To solve the problem of these heavy duty operating points, a new radial pistons cam-lobe motor (RPCLM) is designed, which is able to provide additional torque for limited periods of time.

4.2.1 RPCLM operating principle

A radial pistons cam-lobe motor is a kind of fixed displacement hydraulic motor, on which pistons are arranged radially in a cylinder-block which is acting as the rotor. The stator is placed around the rotor, and has a specific internal profile designed to force a reciprocating movement of the pistons in

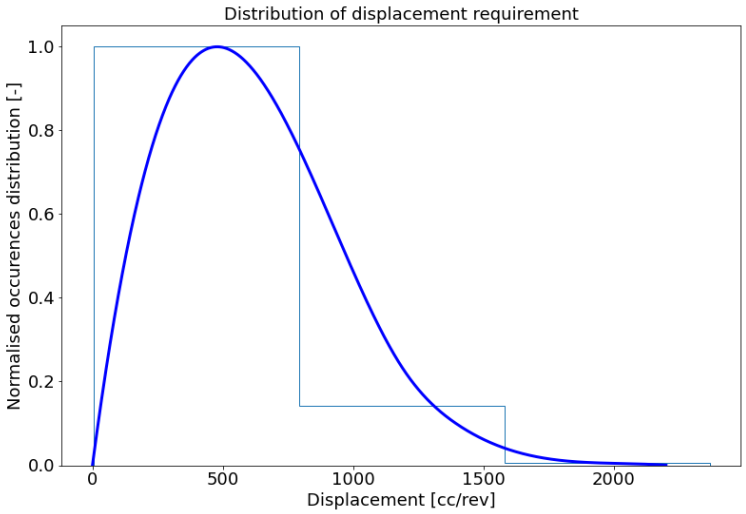

Figure 6 Normalised distribution of displacement requirement over the reference mission profile.

their chambers several times per rotation of the rotor. Isaksson in [10], and Giavarini in [11], provide descriptions of the operating principle of examples of such hydraulic motors. Figure 7 shows a cut-view schematics of the central part of the hydraulic motor. On this illustration, the cam (stator) is coloured to represent the zones on which pistons are submitted to high (dark grey) and low (light grey) pressure. In the position depicted, the rotor is rotating in the counter-clockwise direction, the high pressure zones corresponding to a piston moving out of its chamber.

A RPCLM is a fixed displacement motor, but it is possible to make use of internal symmetries to create several "sub-motors": by creating an internal bypass loop, the motor can work with a reduced apparent displacement. It is frequent to have RPCLMs with two discrete displacements, and some commercially available RPCLMs have up to four distinct displacements. As an example, the RPCLM shown on Figure 7 is able to work with a second displacement by bypassing three of the six cam lobes.

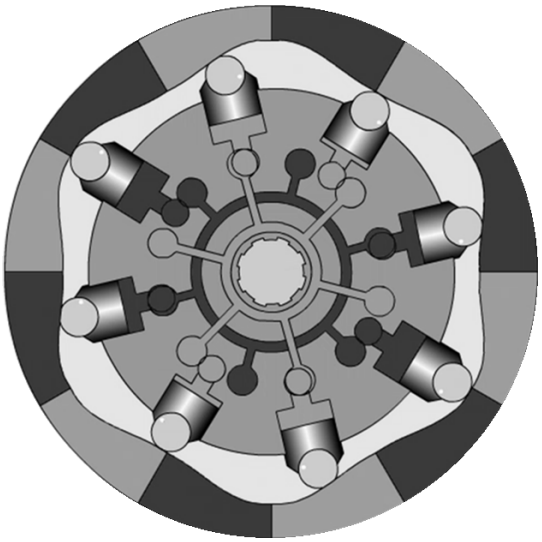

Figure 7 Illustration of the RPCLM "torque module" in cut view.

4.2.2 Particularities of the new RPCLM

The proposed new RPCLM design is a fixed one-displacement motor of the type described in the previous paragraph. The torque provided by a hydraulic motor is:

$$T = \Delta P_M \cdot D_M \tag{3}$$

From Equation 3, two ways of modifying the provided torque appear:

1. Changing the displacement of the motor D_M.
2. Changing the differential pressure at the motors ports ΔP_M.

While the usual way of dealing with torque requirements is to increase the displacement of the motor, the approach taken in the new RPCLM design is to act on the differential pressure. The maximum pressure in a system being enforced by several parameters (all components, be it the pump, the pipes and hoses, or the valves, have a maximum sustainable pressure value), an internal pressure modifier is used to locally change the pressure in the hydraulic motor without affecting other components of the hydrostatic transmission. This pressure modifier is used to amplify ΔP_M when – and only when – the differential pressure in the system is insufficient to provide the required torque.

The pressure modifier is entirely integrated to the RPCLM, and its use is transparent to the system. Figure 8 shows a schematics view of the new

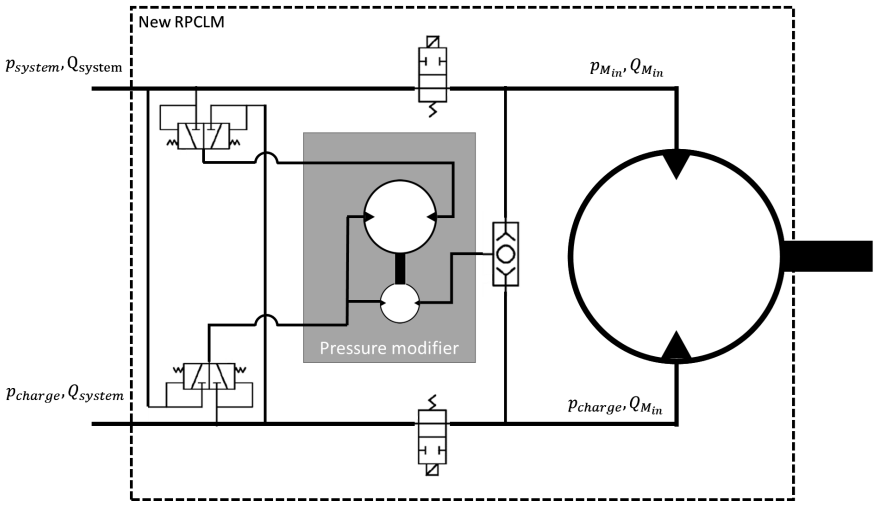

Figure 8 Schematics of the new RPCLM principle.

component, with the dashed line depicting the bounding box of the motor. A control block is included inside the motor, which commands the pressure amplifier's activation automatically when a pressure higher than can be supplied by the hydraulic circuit is required. The details of the exact design being currently in a patenting process, it is not detailed further in this paper.

When the amplifier is inactive, the pressure and flow at the motor's inlet $(p_{M_{in}}, Q_{M_{in}})$, are equal to the pressure and flow in the system (p_{system}, Q_{system}) and the same is true for the outlet: $(p_{M_{out}}, Q_{M_{out}}) = (p_{charge}, Q_{system})$. Because the RPCLM design ensures that $p_{M_{out}}$ is always equal to p_{charge}, and $Q_{M_{out}}$ is always equal to $Q_{M_{in}}$, both variables have been directly substituted on Figure 8.

When the pressure modifier is activated, there is a conversion of flow and pressure, where:

$$p_{M_{in}} = p_{system} \times r_{amp} \tag{4}$$

$$Q_{M_{in}} = Q_{system} \times \frac{1}{r_{amp}} \tag{5}$$

Due to the law of power conservation, the pressure modifier transforms a low pressure and high flow rate power into a high pressure and low flow rate power: $p_{M_{in}} \cdot Q_{M_{in}} = p_{system} \cdot Q_{system}$. In addition to this reduced flow, the amplification of pressure comes at the cost of the transformation efficiency η_{amp}. However, there is no impact of the pressure modifier when

it is inactive, only the control block incurs some small pressure losses, which means that the motor efficiency is preserved during standard use phases.

4.3 Integrating the new RPCLM in the system

A version of the new "boosted radial pistons cam-lobe motor" (bRPCLM) is designed to fit the heavy tandem roller application described in §3.1.2 and this bRPCLM is substituted to the motors in the system shown in Figure 4. According to the required displacement derived in §4.1 based on the normalised time distribution of required displacement shown in Figure 6, the bRPCLM displacement is set to 1370 cc/rev, and an effective amplification ratio $r_{eff} = 2.1$ is targetted. The model described in §3.2.1 is otherwise unchanged. The bRPCLM model replacing the RPCLM model of the reference system includes the pressure modifier model, itself including physical models for hydro-mechanical and volumetric losses, as well as the control block and pressure losses incurred by its valves.

4.4 Modified machine energy efficiency analysis

The modified model of the machine is made to run over the reference mission profile of §2.4, and the same results as for the reference simulation of §3.2.2 are extracted.

The total fuel consumption for the machine equipped with two bRPCLM motors is $2.3L$ over this duty-cycle.

5 Comparison and discussion

Both the standard solution described in §3.2.1, and the proposed concept of bRPCLM introduced in §4.3 have been simulated over the reference mission profile of §2.4.

5.1 Fuel consumption reduction

As the results of §3.2.2 and §4.4 show, the fuel consumption of the proposed solution is reduced from 2.5 to $2.3L$ over the reference mission profile. Figure 9 shows the two systems fuel consumption in function of the time. The integration of the two bRPCLM instead of standard motors allows a 7.7% reduction of the fuel consumption of the heavy tandem roller over its reference mission profile.

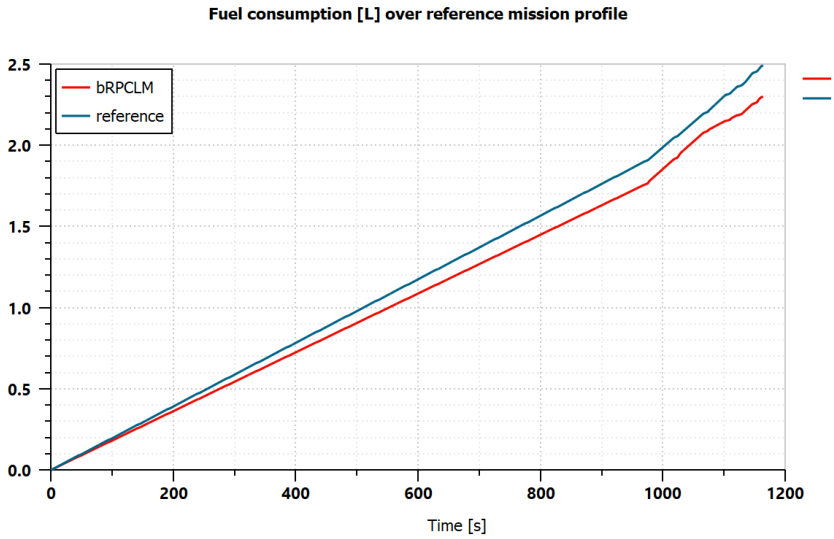

Figure 9 Comparative fuel consumption of reference and improved solutions.

5.2 Efficiency gain

The fuel consumption improvement brought about by the proposed bRPCLM concept can be attributed to the principles introduced in §4.2. The re-focusing of the hydraulic motors efficiency towards the work conditions of the machine bring efficiency improvements on the component itself, and the reduced displacement reduces losses in the hydraulic system. During the compaction work at stabilised speed, the bRPCLM efficiency is improved by 3.3% over the standard hydraulic motors of the reference solution.

Looking at the hydraulic energy at the outlet of the pump shows the total efficiency improvement allowed by the modified system. The bottom part of Figure 10 shows the differential hydraulic energy at the pump's ports in Wh in function of the time for the reference and modified solutions. At the end of the mission profile, the proposed solution has required 22.4% less hydraulic energy than the reference solution, for the same energy at the machine's drums. The top part of Figure 10 shows the energy at the pump's shaft, for which the bRPCLM equipped machine has required 17.3% less energy at the end of the cycle. Further gains in fuel consumption are therefore possible, by reducing the pump's and the thermal engine's displacements to fully convert the 22.4% hydraulic energy improvement into fuel consumption reduction.

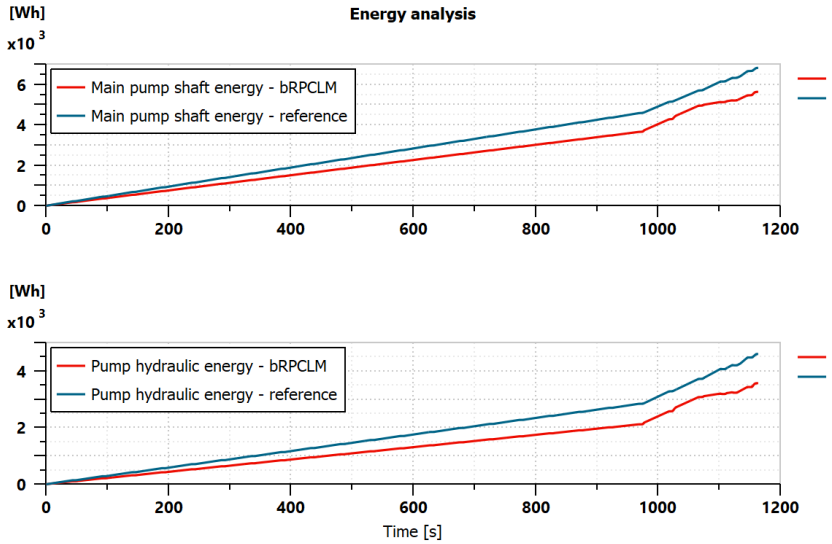

Figure 10 Comparative energy analysis of reference and improved solutions.

5.3 Comparative strengths and weaknesses of the sizing approaches

Radial piston cam-lobe motors are fixed displacement motors, with the possibility to create sub-displacements. Alternative technologies, comprising an infinitely variable axial piston motor coupled to a reducer (APMGB) also allow the reduction of the motors displacement to best fit the operating point. In the case of the bRPCLM, the displacement is smaller, but pressure is amplified when additional torque is required.

The standard sizing methodology described in §3.1 applies to both RPCLM and APMGB, while the bRPCLM is designed to apply the sizing methodology introduced in §4.1. As highlighted by the mission profile of §2.4, most of the time is spent at lower duty points, making the efficiency of the transmission on these operating points an important part of the energy efficiency of the machine. This is the purpose of the bRPCLM, which targets maximum efficiency during work mode, when lower torque levels are required, and tries to moves any inefficiencies to the maximum duty points, when the pressure amplifier is activated.

The amplification ratio of the pressure modifier implies a limitation of the rotation speed of the motor in high torque mode. For example, with an amplification ratio r_{amp} of 2.5, the transformation efficiency will mean the

flow available for motor rotation $Q_{M_{in}}$ is less than $\frac{Q_{system}}{2.5}$, and the pressure available to create torque is less than $2.5p_{system}$. With an efficiency of 80% for the transformation, this means an amplification of pressure by a factor of 2, while the rotation speed of the motor is divided by 3.125. This limitation of the proposed concept seems acceptable for the heavy tandem roller application, as operating points requiring high torque are low speed points. For other applications, it could lead to lower speeds than would ideally be wished for, a concession that is to be put on the balance in front of the expected energy efficiency gains.

The pressure modifier being autonomous in its activation, it brings simplicity into the system's control when compared to a multi-displacement RPCLM or an APMGB, both of which require some degree of control algorithms and valves to control the displacement value.

6 Experimental validation

The machine modelled and simulated in this study has been selected because of its availability to be tested with the two hydraulic system configurations. As no road is available to be compacted, the testing and correlations are done on a simplified use cycle, using flat asphalted ground and a concrete ramp with a 20 % slope. Figure 11 shows the heavy tandem roller equipped for testing.

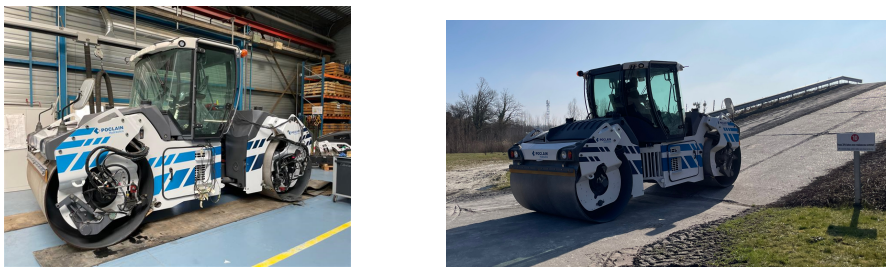

(a) (b)

Figure 11 Test machine parked (a), and in a 20 % slope (b).

These tests have confirmed the fuel consumption improvements witnessed in the simulation results. They were also used to fine-tune the machine characteristics for the simulation (head loss in the pipes for example), and test the hypotheses concerning rolling resistance values discussed in §2.4.1.

Fuel consumption was measured at 0.11 L in average for a 50 m run on the flat asphalted test road at 5.5 km/h. This result was obtained by averaging a number of runs of the same cycle. The machine equipped with bRPCLM showed improvements in the fuel consumption over the same duty-cycle, with an average of 0.07 L of diesel used over the 50 m. This improvement, more consequent than what the model predicts over the mission profile used in this study (§5), is partly due to a reduced engine speed, from 2300 to 1800 rev/min for the bRPCLM test, a behaviour the model is able to reproduce, and an avenue of improvement that will be part of the next steps in the study. Adjusting for the ICE speed using the model, a fuel consumption reduction of 6% can be inputted to the bRPCLM, the rest of the improvement coming from the lower speed permitted by the smaller displacement of the bRPCLM.

The tests available at the moment of writing were performed with a prototype version of the bRPCLM, the efficiency of which is not up to par with the design used in this study, which might explain the slightly lower gain in testing (6% in testing vs 7.7% in this study). Testing this improved bRPCLM design is the next step in the project.

7 Conclusion

In this paper, a new radial pistons cam lobe motor integrating a pressure amplifier and a control block is proposed. This bRPCLM aims at refocusing the sizing of the hydraulic transmission towards its most frequent usage points. The traditional sizing point of the transmission for required breakout torque is addressed by the inclusion of the pressure amplifier, which allows a punctual increase of the output torque of the motor by an increase of the internal pressure in the component, pressure rise which is invisible to the system itself, allowing the use of standard components (e.g. pump, valves, pipes).

The demonstration of the energy efficiency gains obtainable through this new hydraulic motor concept is made via the simulation of the energy efficiency of a heavy tandem roller over a reference duty-cycle constructed for the study. The comparative simulations show a 7.7% reduction of fuel consumption on the machine over the twenty minutes reference cycle. The simulation results also indicate that further fuel economies could potentially be made by adapting the pump and diesel engine, as the mechanical energy required on the pump's shaft is reduced by 17.3% by the use of the bRPCLM.

Appendix

Table 2 Full machine parameters.

M	[kg]	13300	Compactor mass
s_{max}	[%]	39	Gradability
C_{rr}	[kg/t]	10	Rolling resistance coefficient on max slope
R_{Drum}	[m]	0.7	Drums radius
d_{drums}	[m]	3.9	Wheel base
p_{max}	[bar]	400	Max system pressure
p_{charge}	[bar]	20	System charge pressure
$\mathcal{D}_{pump}$	[cc/rev]	90	Pump max displacement
$\mathcal{D}_{RPCLM}$	[cc/rev]	2812	Initial motor displacement
$\mathcal{D}_{bRPCLM}$	[cc/rev]	1370	Improved motor displacement

References

[1] Sustainable roads — about the project. [https://sustainableroads.eu/about-the-project/]

[2] The European Green Deal - European Commission. [https://commission.europa.eu/strategy-and-policy/priorities-2019-2024/european-green-deal_en]

[3] The role of construction equipment in decarbonising Europe. Committee for European Construction Equipment. Position Paper, 2021.

[4] BOMAG GmbH, Fayat Group. Basic Principles of Asphalt Compaction.

[5] MM Communications AB, Sweden. Compaction and paving theory and practice.

[6] AMMANN Group. *Datasheet for ARP & ARX HEAVY TANDEM ROLLERS*, 2023

[7] HAMM AG, Wirtgen Group. *Datasheet for Heavy Duty tandem roller HD+ 140i VO* , 2023

[8] European Commission. Motorways. *European Commission*, Directorate General for Transport, February 2018.

[9] Sun et al. A state-of-the-art review on rolling resistance of asphalt pavements and its environmental impact. In *Construction and Building Materials*, 2024.

[10] P. Isaksson. Simulation of tribology in hydraulic motors. PhD Thesis, Luleå University of Technology, 2010.

[11] F. Giavarini. Analysis and Simulation of a Radial Piston Hydraulic Motor. Master's degree Thesis, University Politecnico di Torino, 2022.

Efficiency Improvements in a Servoless Swash Plate Pump: Experimental and Simulation Results

Nathaniel J. Fulbright[1]*, Samuel Hall[2], Matthew Creswick[3], Stanislav Smolka[4], Robert Rahmfeld[5]

[1]*Danfoss Power Solutions, Hydrostatics Engineering, 14615 Lone Oak Rd, Eden Prairie, MN, 55344, USA*
[2]*Danfoss Power Solutions, Research and Development, Centers of Excellence, 2800 E 13th St, Ames, IA, 50010, USA*
[3]*Danfoss Power Solutions, Open Circuit Pumps Engineering, 14615 Lone Oak Rd, Eden Prairie, MN, 55344, USA*
[4]*Danfoss Power Solutions, Hydrostatics Engineering, 2800 E 13th St, Ames, IA, 50010, USA*
[5]*Danfoss Power Solutions, Hydrostatics Engineering, Krokamp 35, 24539 Neumünster, Germany*

*Corresponding author. Email: nate.fulbright@danfoss.com

Abstract

Variable displacement axial piston units conventionally use a servo system (consisting of a servo piston and valve) to adjust and control their displacement. In a novel design approach, the traditional servo system is removed, and the displacement is adjusted only by the loads on the swash plate. By employing specialized valve plate porting and control logic, the design allows for the displacement to be controlled without a servo system, improving efficiency and reducing complexity and size, and also introduces the ability to adjust the cross-port area profile of the valve plate. This adaptability significantly reduces cross-port flow and its associated losses, particularly in low-flow, high-pressure conditions, and it enables tunability in efficiency and noise. Previous work has demonstrated the controllability of a servoless swash plate pump. In this work, theorized efficiency improvements are confirmed by experimental data indicating up to an 18% improvement in overall pump efficiency. A 1D simulation modeling approach is presented, detailing the unique considerations that must be considered for a servoless pump. The simulation model produces efficiency improvement predictions that are generally within ±3% of the experimental results and are often within ±2%.

1 INTRODUCTION

Swash plate type axial piston units are ubiquitous in industrial and mobile fluid power systems due to their high efficiency, robustness, and high power-density. While fixed displacement swash plate units are used in many applications, variable displacement units offer enhanced flexibility to support a wide range of operating conditions. Conventionally, variable displacement units use a hydraulic servo piston that must overcome all internal forces that act to change the displacement of the unit[1]. As the internal forces increase, either the size of the servo piston must increase (increasing the package size of the unit) or the servo piston must run at higher pressures (leading to increased power consumption). Additionally, mechanical feedback methods used in variable displacement units, like the complex feedback linkage found in many swash plate pumps, further complicates the design. Despite these challenges, servo pistons persist as the *de facto* choice due to limited availability of alternative solutions capable of effectively controlling the immense and varying internal forces applied to the swash plate. However, a shift in perspective to view the internal forces as a potential asset rather than something to overcome allows more solutions to emerge.

One potential solution is to completely remove the servo piston and use the loads on the swash plate to control the stroke of the unit. Removing the servo piston leads to a smaller package, reduced hardware complexity, and a complete removal of servo system losses, but it also yields tangible performance enhancements. Several patents present designs that remove the servo piston [1,2,3], but available scientific research is limited. Cho presented a servoless pump that utilized valve plate indexing to vary the moments on the swash plate [4]. That work focused on developing control methodologies using a reduced order model, but it did not examine the effects of the control strategy on efficiency. Furthermore, the design deviates from a traditional swash plate pump design by introducing a valve plate that rotates to change the indexing.

The most promising approach to achieving a servoless pump was introduced by Tvarůžek with the concept of a "dynamic valve plate" [5]. By adding additional ports feeding into control valves at each dead center position, the cross-port area profile can be dynamically adjusted throughout the operating range of the unit. In contrast to a

[1] Direct displacement control is another approach to enabling variable displacement in swash plate units, but this paper only focuses on units with a servo system.

conventional “static” valve plate, the dynamic valve plate enables tunable efficiency and noise levels and the ability to change the operating characteristics (e.g., switch between high-efficiency and low-noise modes). Furthermore, the variable cross-porting can greatly reduce cross-port flow and associated losses, especially at low-flow high-pressure operating conditions. This design requires only minimal modifications to existing production pump hardware, although it does introduce the requirement for a microcontroller to select the appropriate control valve opening for a given operating condition. The fluid power industry is looking for more efficient technologies but cannot easily support drastic changes in architecture [6], so the dynamic valve plate approach is well aligned with industry desires.

The proof-of-concept design presented in [5] demonstrated controllability of a servoless swash plate pump using only forces generated by the rotating kit. While these initial achievements demonstrate the feasibility and benefits of displacement control without a servo piston, further considerations are needed for a production-ready unit. Efficiency, noise, stability, and dynamic response to commands must be well-understood and optimized. To expedite this design work and guide control-logic optimization, simulation is the ideal tool.

In this work, the efficiency improvements of a servoless pump are demonstrated. The operating principles of the dynamic valve plate that enable the servoless pump displacement control are summarized, and the 1D modeling approach that is required for a servoless pump is discussed. Experimental results are presented and used to determine the accuracy of the simulation model.

2 Dynamic Valve Plate and Servoless Unit Operating Principles

Note: For a detailed explanation of the dynamic valve plate and servoless unit operating principles, refer to [5].

The servoless swash plate unit concept eliminates the servo piston and uses the moments applied to the swash plate by the rotating kit to control the position of the swash plate. This is accomplished by manipulating the piston chamber pressure during the transition between the high- and low-pressure ports. Pressure during the transition between ports is regulated via a control port connected to a variable valve, collectively referred to as the dynamic valve plate (Figure 1). The effect of the control valve is the same as that of conventional porting features on a static valve plate: connect the piston chamber to the oncoming pressure port. For a given operating condition, the valve opening is constant and does not change during individual piston transitions.

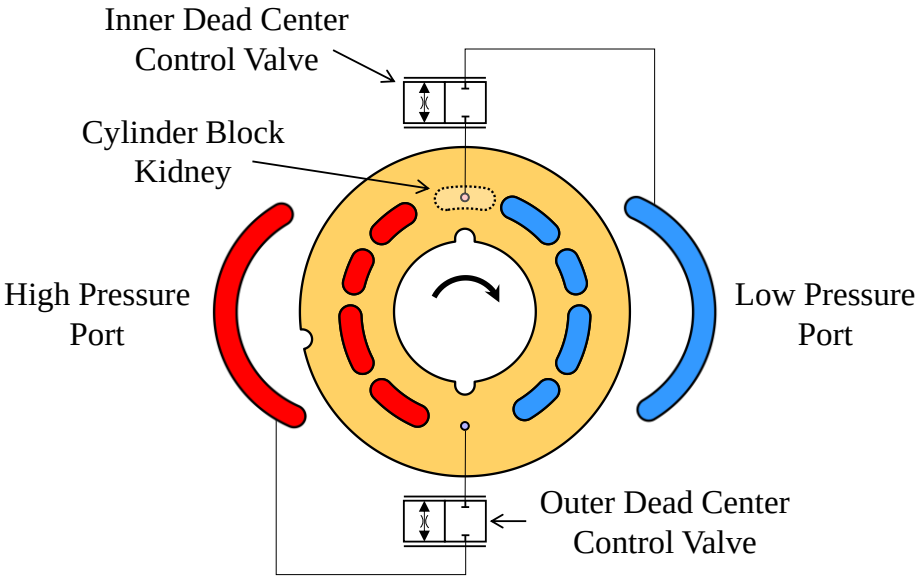

Figure 1 Dynamic Valve Plate Showing Valve Connections to Transitions [2]

The behavior of the piston chamber pressure profile during the transition is primarily influenced by the interaction between the control valve opening and the compressibility of the fluid. Throughout the pressure transition, the volume of the piston chamber remains relatively constant. At inner dead center (IDC), the piston chamber transitions from high to low pressure, while at outer dead center (ODC), it transitions from low to high pressure. When the control valves are open (as depicted in the top panel of Figure 2), the IDC piston maintains low pressure during

the transition and the ODC piston maintains high pressure. The larger the control valve opening, the faster the piston chamber pressures transition. The net effect of the pressure forces on the swash plate causes the swash plate angle to increase, causing on-stroking behavior. Conversely, when the control valves are closed (as shown in the bottom panel of Figure 2), the IDC piston prematurely rises to high pressure and the ODC piston prematurely drops to low pressure, de-stroking the pump. Leakage and the small changes in the piston chamber volume during the transition also impact the pressure profiles, though to a lesser degree. Achieving stable displacement under specific operating conditions involves commanding the valves to appropriate openings that balance all piston forces on the swash plate (including pressure, friction, and inertia) with other external moments, such as those from springs.

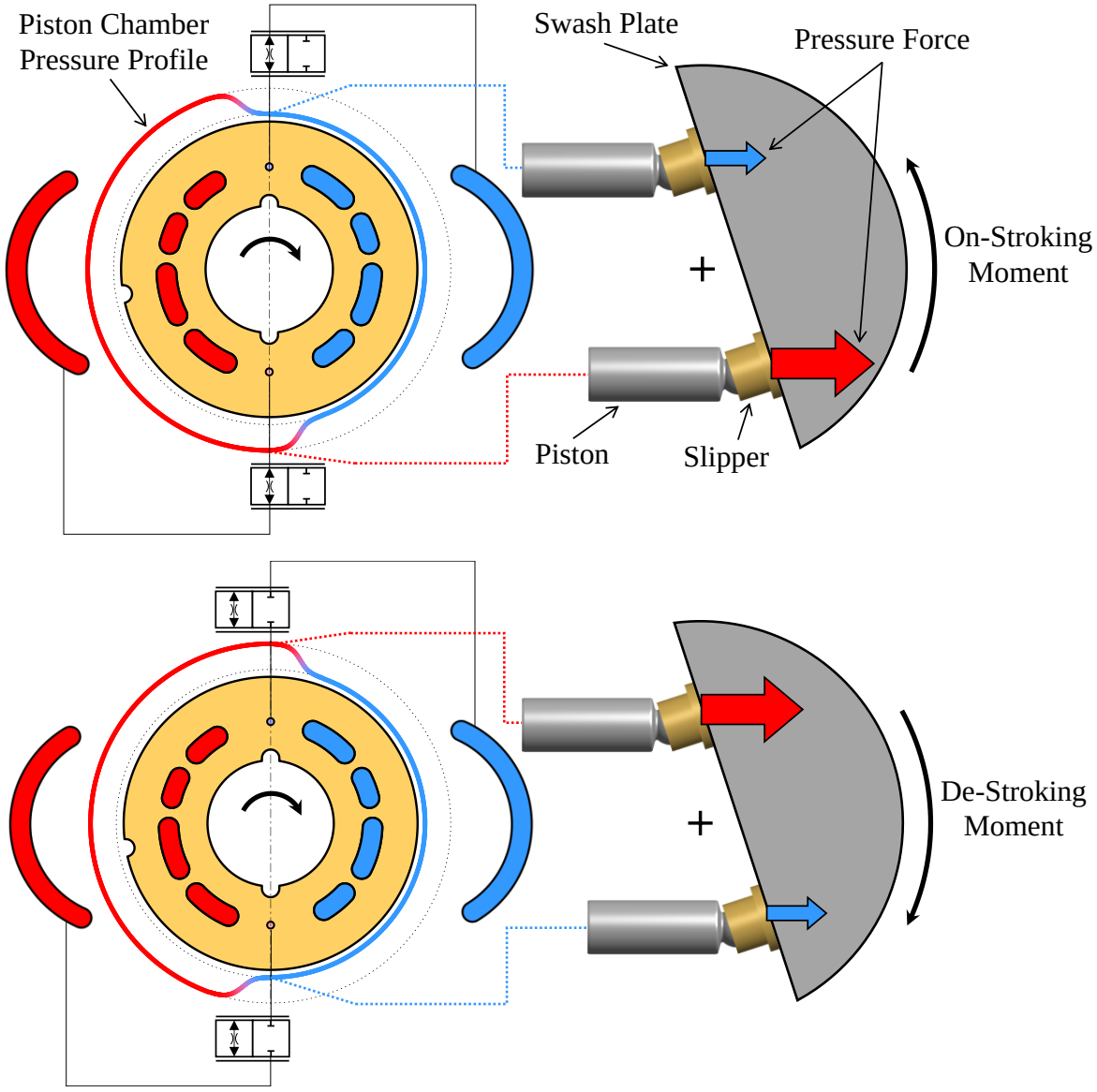

Figure 2 Pressure Transition Variation with IDC and ODC Valves Open (Top) and Closed (Bottom)

When the control valves are closed, there is little to no cross-port flow, resulting in reduced loss compared to conventional pump valve plates. Conventional pump valve plates often incorporate cross-porting for noise reduction, prevention of cavitation, or modification of the swash plate moments. As the control valves open, cross-port flow increases, leading to increased loss. The efficiency improvement in a servoless pump primarily stems from the decreased cross-port flow.

3 SIMULATION MODEL

In a conventional swash plate unit with a servo piston, the rotating kit can be simulated and analyzed relatively independently from the servo system. This allows for models with lower complexity while maintaining fidelity for the relevant metrics such as efficiency and pressure ripple for the rotating kit and step-response and stability for the servo system. For a servoless unit, the rotating kit *is* the servo system, requiring the single model to contain additional dynamic degrees of freedom for the displacement adjustment. For example, instead of predefining the motion of the swash plate, the swash plate motion is calculated given the forces applied to it. Mechanical and hydraulic losses, typically only used for efficiency predictions and treated as noise to be rejected by the servo system, now play an important role in determining the control behavior of the unit.

Many modeling approaches exist, ranging from simple equations for theoretical flow rate to complex 3D multiphysics modeling. A useful middle ground between these two extremes is 1D modeling, which provides significant insight into the dynamics of the system while being substantially less computationally expensive than 3D multiphysics modeling.

3.1 Fundamental Modeling Techniques

Each piston chamber is considered its own control volume with multiple fluid flow paths to and from the volume. Flow between the piston chamber and the end cap passes through the valve plate, which is modeled as an orifice with a constant or flow-dependent discharge coefficient. Additional flow between the piston chamber and the pump case occurs due to leakage between the piston and the bore, the slipper and the swash plate, the cylinder block and valve plate, and the valve plate and the end cap. The volumes of the piston chambers and the kinematics of the pistons are calculated as a function of the pump geometry, shaft motion (position, velocity, and acceleration), and swash plate motion (position, velocity, and acceleration). These kinematic calculations are closed form and are formulated to allow for time-varying swash plate motion. The instantaneous pressure (p) within each piston chamber is calculated by solving the pressure build-up differential equation shown in Equation (1), which accounts for fluid stiffness (β), piston chamber volume (V), and the net flow into or out of the piston chamber ($q_{V,net}$):

$$\frac{dp}{dt} = \frac{\beta}{V}\left(q_{v,net} - \frac{dV}{dt}\right) \tag{1}$$

The various flow rates for the next time step of the model are calculated using this new instantaneous piston chamber pressure, and the process iterates. Some simulation models do not model any more physics beyond those that have already been mentioned, especially those that are only concerned with pump hydraulic performance. However, the fluid-related aspects of the model are only the first aspect needed to accurately model a servoless swash plate pump.

The internal forces and moments of a swash plate pump provide the next level of information to analyze a servoless swash plate pump. The most basic approach is to include the pressure force on the pistons and the inertial forces of the piston-slipper assemblies. For some conventional pump models, this is sufficient for tasks like sizing a servo piston because the remaining non-ideal behavior is considered a noise factor to be robust against. However, for a servoless pump, these noise factors (i.e., friction) can have a large impact on the resulting swash plate moments. Piston-bore friction and slipper-swash plate friction are both substantial sources of friction in a swash plate pump, and during portions of the cycle, their effects compound and increase the overall piston friction force. Given that the swash plate reacts all axial force applied to the piston including pressure, inertia, and friction, accurate swash plate moment predictions necessitate considering all axial forces. Frictional losses such as valve plate-cylinder block friction, bearing friction, and shaft seal friction are unnecessary for swash plate moment predictions, but these losses are still useful for making more accurate pump efficiency predictions.

At this point, many pump models are considered complete; the hydraulic and mechanical behavior of the pump is well understood, including losses, and useful performance predictions can be made. Simulated performance maps can be generated, partial efficiencies can be determined, and the servo piston can be sized to maintain control authority for any operating condition. However, such a model is only marginally useful for a servoless swash plate unit. The swash plate motion must still be prescribed and cannot react to changes in the swash plate moment, a fundamental requirement dictated by the principles of servoless pump operation.

3.2 Dynamic Swash Plate

Instead of the swash plate angle being defined before the simulation, it is calculated based on the net moment applied to the swash plate. This net moment of course consists of the forces from the pistons and can also include forces and moments from other elements like springs, or for a conventional pump, the servo piston. Frictional moments and hysteresis can also be incorporated into the swash plate dynamics calculation. The introduction of a dynamic swash plate to the model enables prediction of the dynamic response of the pump to changes in displacement commands, and it also improves the fidelity of the predictions at steady-state conditions.

To hold the swash plate at a given angle, the mean moment on the swash plate must be zero, but that does not mean the instantaneous swash plate moment will be equal to the mean moment. Even in the most ideal case (no losses, no fluid compressibility, ideal valve timing, etc.), the finite number of pistons in a swash plate pump guarantees that the moment on the swash plate will not be a constant value throughout a revolution. For an unconstrained swash plate, like that found in a servoless pump, this means the swash plate will have instantaneously unbalanced moments and will oscillate about a mean angle. This behavior is also observed in pumps with a servo piston because the servo piston and the associated fluid volumes are not infinitely stiff.

The potentially larger swash plate oscillations in a servoless unit affect the kinematics of the piston, especially at the dead center positions where the piston velocity due to shaft rotation is near zero and the piston velocity due to swash plate rotation is the greatest. With the additional consideration that the flow area near the dead center positions is at a minimum, even relatively small changes in swash plate angle can significantly affect the piston pressure, especially if those changes are fast enough to outpace valve plate and leakage flow. Pistons at the dead center positions have the largest moment arm on the swash plate, further amplifying the effect of the pressure changes. The IDC and ODC pistons are inversely affected (e.g., swash plate motion that increases the IDC piston pressure will decrease the ODC piston pressure), leading to an oscillatory feedback loop between the swash plate motion and the dead center piston pressures.

The effects of the swash plate oscillation combined with all other effects in the model result in a sufficiently detailed understanding of the net moment applied to the swash plate. With this information, a control valve opening map can be generated for different operating conditions, linking each condition to the corresponding valve opening and ensuring a mean swash plate moment of zero. To change displacement, the control valve opening is changed following the map, and the “macro-level” dynamic swash plate behavior of the model is observed. Traditional control metrics such as rise time, settling time, and overshoot can be calculated for this behavior. Finally, the control valve opening map can be used to develop control algorithms.

4 EXPERIMENTAL RESULTS

4.1 Hardware Modifications

The same prototype closed-circuit servoless swash plate pump used in [5] was used to gather steady-state pump performance data. The pump is a variable displacement 130 cc swash plate pump with EDC control, and was tested in its unmodified state to gather benchmark data. The following modifications were made to the pump to make it a servoless pump:

- Grooves were added in the end cap to drain the servo piston oil to case. All other supply passages of control flow were also blocked. With no control pressure applied to the servo piston, the servo piston assembly acts as a damper to the motion of the swash plate.
- Internal passages were added in the end cap to connect the control ports on the valve plate to the respective control valves and to connect the control valves to the respective pump ports.
- Two control spool valves driven by proportional solenoids were added. The control valves mount to the servoless pump end cap.

All rotating kit components remained identical between the tests. A representative image of a servoless pump is shown in Figure 3.

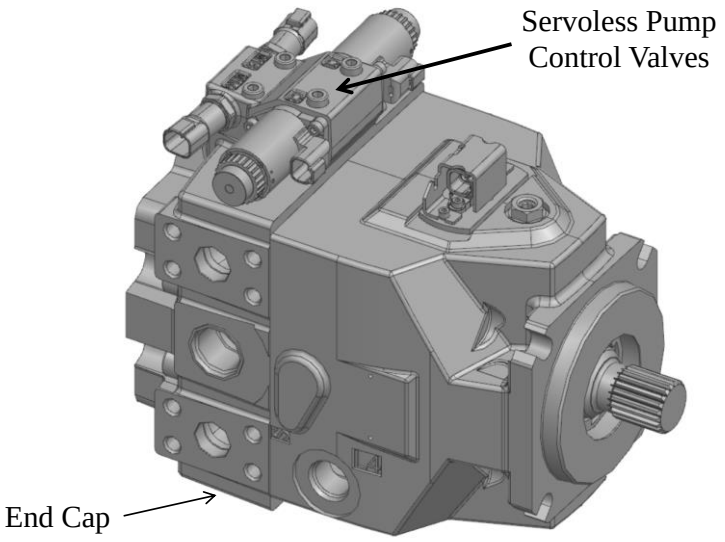

Figure 3 Servoless Pump

4.2 Operating Conditions and Data Collection

A total of four pressure and speed combinations were used to compare the servoless pump to the production pump in pumping mode: 100 and 200 bar pressure differentials and 1,000 and 2,000 RPM shaft speeds. For each combination, five swash plate angles (4, 8, 12, 16, and 18 degrees) were examined. The production pump used the EDC control to maintain the swash plate angle. The servoless pump used open-loop control of the control valves to hold the swash plate at the desired angle. Both control valves were opened the same amount for a given operating condition. For the servoless pump, effort was made to ensure minimal impact on the swash plate moments from the servo piston. No command was sent to the EDC control, the servo cans were drained to case, the servo gauge ports were connected to each other, and the control supply port was plugged – the servo piston and servo piston springs were only serving as a neutral return mechanism for the swash plate.

Testing was done in accordance with ISO 4409 using “class A” measurement accuracy [7]. All tests were done using Shell Tellus 46 S2 MX oil at 50 °C. The following measurements were recorded: swash plate angle, shaft angular velocity and torque, port pressures, outlet flow rate, and inlet fluid temperature. Sensors were sampled for 2 seconds at 2,000 Hz with an anti-aliasing filter applied and the readings were averaged. An external charge pump was used to supply 26 bar of charge pressure at 26 LPM (nominal).

4.3 Results

4.3.1 Servoless Pump Control Valve Solenoid Current

Figure 4 shows the current provided to the solenoids controlling the servoless pump control valves. The solenoid current trends upwards as swash plate angle increases. An increase in solenoid current corresponds to an increase in control valve opening area, although flow forces can also impact the current required to maintain a given valve opening area.

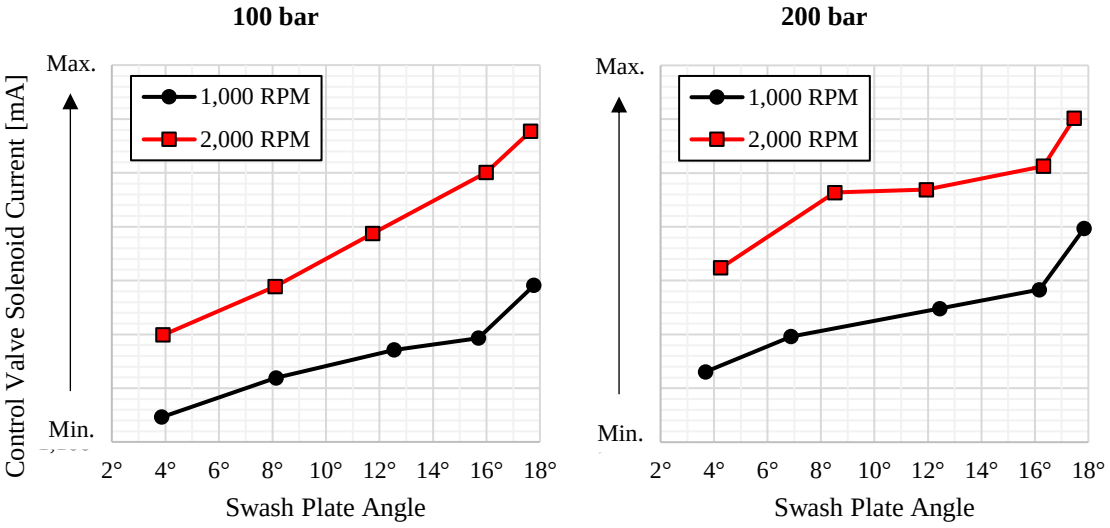

Figure 4 Servoless Pump Control Valve Solenoid Current

4.3.2 Overall Efficiency

Figure 5 shows the difference in overall efficiency between the servoless pump and the production pump. Overall efficiency, η_τ, is calculated as:

$$\eta_\tau = \frac{P_{out}}{P_{in}} \tag{2}$$

where P_{out} is the output power and P_{in} is the input power. Only the pump power is included in the efficiency calculations – power lost via the servo system and the power needed to drive the control valves are not included. For a pump, the output power is hydraulic power (Equation (3)) and the input power is mechanical power (Equation (4)):

$$P_{out} = \Delta p q_V \tag{3}$$

$$P_{in} = Tn \tag{4}$$

where Δp is the pressure differential between the primary ports of the pump, q_V is the volumetric flow rate at the outlet of the pump, T is the shaft torque, and n is the angular velocity of the shaft. The error bars in Figure 5 represent the uncertainty in the overall efficiency difference due to sensor accuracy compounding through the calculations.

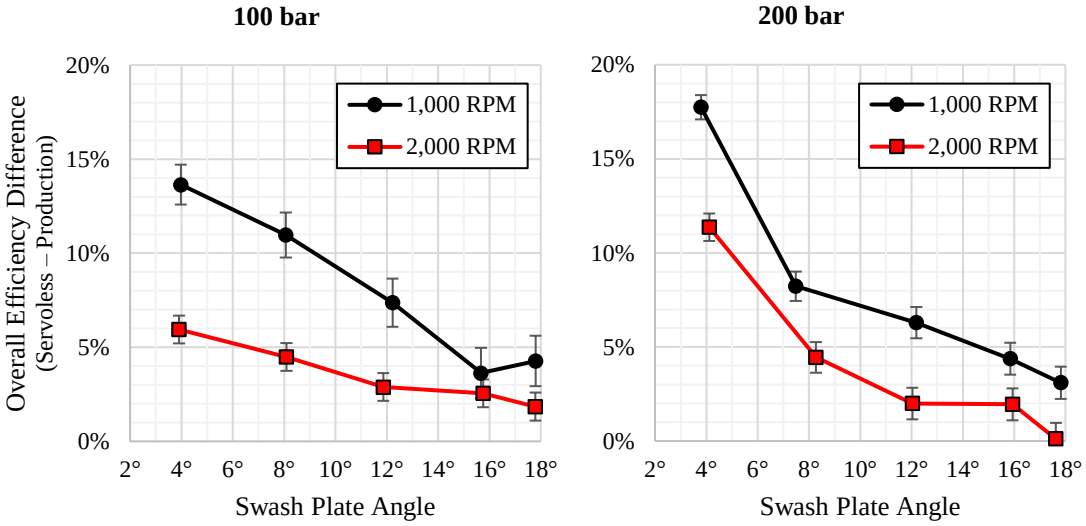

Figure 5 Overall Efficiency Difference Between Servoless Pump Prototype and Production Pump

Across all conditions, the servoless pump consistently outperforms the production pump, boasting a peak overall efficiency improvement of nearly 18%. This improvement in efficiency is more pronounced at lower shaft speeds and swash plate angles. The greatest efficiency improvements are at the minimum tested swash plate angle (4°) and highest pressure (200 bar) for both shaft speeds. However, as the swash plate angle increases, the efficiency difference for the high-pressure conditions becomes lower than the efficiency difference for the low-pressure conditions. Notably, the low-speed (1,000 RPM) results show a higher overall efficiency difference than the high-speed (2,000 RPM) results at all swash plate angles and pressure differentials.

4.3.3 Power Loss

Figure 6 shows the power loss reduction of the servoless pump relative to the production pump. Power loss, P_{loss}, is defined as:

$$P_{loss} = P_{in} - P_{out} \tag{5}$$

Just as with the overall efficiency, the servoless pump has reduced power loss relative to the production pump at all tested conditions. For most operating conditions, the power loss is at least 1 kW lower than the production pump, with a peak power loss reduction of over 2 kW. The power loss is roughly constant across the range of swash plate angles for the 100 bar data sets, showing a consistent power loss reduction of approximately 1 kW. Conversely, the power loss comparison for the 200 bar data sets is more varied, with both data sets beginning with a 2 kW power loss reduction at the lowest swash plate angle (4°), followed by diminishing power loss reductions as the swash plate angle increases. The data set at 1,000 RPM and 200 bar demonstrates a 1.5 kW power loss reduction at full stroke, while the data set at 2,000 RPM and 200 bar data set exhibits minimal change in power loss (relative to the production pump) at full stroke.

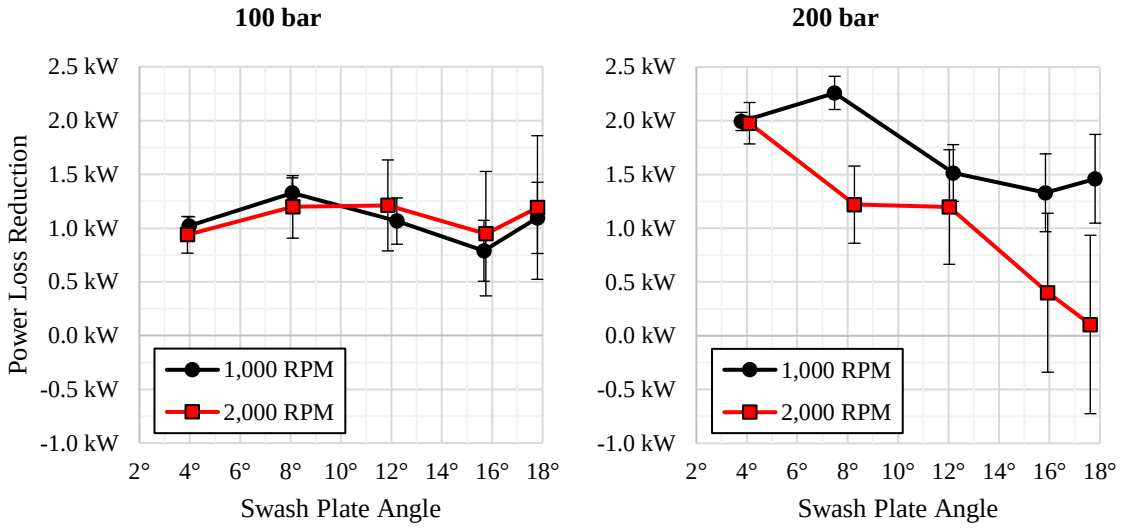

Figure 6 Power Loss Reduction for Servoless Pump Prototype Relative to Production Pump

4.4 Discussion

The experimental results align with the anticipated trends based on the servoless pump operating principles outlined in Section 2. As the swash plate angle and shaft speed increases, the increasing control valve solenoid currents indicate a larger control valve opening area is required. The overall efficiency difference is most significant at lower speeds and swash plate angles and higher pressure-differentials, conditions where the efficiency of conventional swash plate pumps is typically low.

Especially at low speeds and swash plate angles, some of the efficiency improvements of the servoless pump can be attributed to reduced cross-port flow, though the additional new dynamics of the servoless pump can also affect efficiency. For example, for the 100 bar operating conditions shown in the left panel of Figure 6, the power loss reduction is relatively constant, even as the swash plate angle and shaft speed vary. Figure 4 for the same conditions indicates that the control valve opening areas increase as both the swash plate angle and shaft speed increase. Therefore, the cross-port flow at a given speed increases as the swash plate angle increases, leading to a decrease in power loss reduction when considering cross-port flow alone. However, because the observed power loss reduction remains relatively constant, there are clearly other effects beyond just cross-port flow reduction involved that affect the power loss reduction in the servoless pump.

Upon initial inspection of the 100 bar results of Figure 6, it seems as if the efficiency improvement of the servoless pump should be constant across swash plate angles, not trending downwards as shown with the 100 bar results of Figure 5. This behavior can be explained by substituting Equation (5) into Equation (2), reformulating the overall efficiency to be a function of the input power and power loss:

$$\eta_\tau = \frac{P_{in} - P_{loss}}{P_{in}} = 1 - \frac{P_{loss}}{P_{in}} \tag{6}$$

The overall efficiency difference, $\Delta\eta_\tau$, between two pumps with the same rotating kit that are running at the same operating conditions (swash plate angle, shaft speed, pressure differential, and temperature) can be rewritten as:

$$\Delta\eta_\tau = 1 - \frac{P_{loss,2}}{P_{in}} - \left(1 - \frac{P_{loss,1}}{P_{in}}\right) = \frac{P_{loss,1} - P_{loss,2}}{P_{in}} = \frac{\Delta P_{loss}}{P_{in}} \tag{7}$$

where ΔP_{loss} is the power loss reduction of the second pump relative to the first pump. When the rotating kit is unchanged between the pumps and the primary efficiency improvements are due to hydraulic efficiency improvements (as is the case for the servoless pump prototype), the input power should not change significantly between the pumps. As the swash plate angle increases, so does the shaft torque, leading to an increased input power. Inspection of

Equation (7) shows that a constant power loss reduction leads to a reduced efficiency improvement as the input power increases.

The servoless pump prototype used in the tests is a proof-of-concept intended to show displacement controllability of a servoless swash plate pump and was designed with the sole intent of demonstrating that the pump displacement could be controlled using only forces generated by the rotating kit. It is likely that the efficiency of the pump can be improved beyond the results shown here, especially at the higher swash plate angles.

5 Comparison of Simulation Model to Experimental Results

A simulation model was constructed in Simulink, mirroring the assumptions and functionality outlined in Section 3. The simulations were conducted at the same nominal operating conditions and with the same oil properties as those used in the experimental tests. Both the production pump and servoless pump were simulated. Nominal dimensions and values were used for both pumps.

5.1 Overall Efficiency Difference Comparison

Figure 7 demonstrates the simulation predictions of overall efficiency difference between the servoless pump and production pump to the experimental results. The simulation results follow the same trends as the experimental results and are generally within measurement accuracy of the experimental data at swash plate angles 12° and above. Apart from the 1,000 RPM, 200 bar operating conditions, the simulation tends to underpredict the overall efficiency difference.

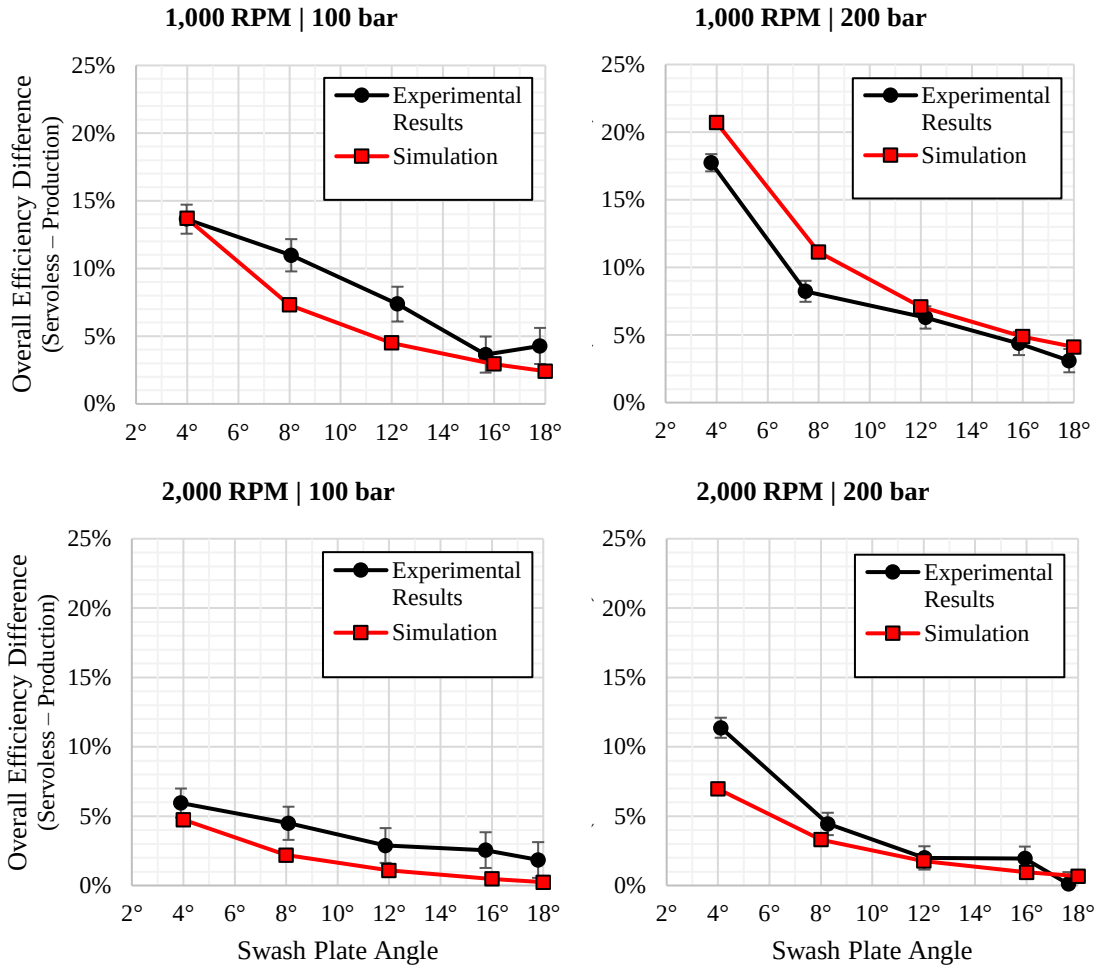

Figure 7 Overall Efficiency Difference, Simulation vs. Experimental Results

5.2 Discussion

The correlation between the simulation results and experimental results is impressive considering the modeling approach and early stage of investigation of the servoless pump concept. Although 1D modeling is a powerful tool, there are many aspects of a pump it cannot fully capture that have an impact on performance (for example, deformations and fluid film thicknesses/gap heights). That said, such close agreement validates the servoless pump theory and enhances confidence in the predictive capabilities of the simulation model. Even with the discrepancies between the model predictions and the experimental results, the accuracy is sufficient for design and optimization purposes because of good qualitative and quantitative agreement, especially at high swash plate angles. The servoless pump is a new concept, and the accuracy of the models is reasonable given the early stages of investigation.

Further work to improve the correlation between the simulation and experimental results is planned. The operating conditions in this comparison are only a subset of the operating conditions of a typical pump. Higher pressures and speeds and motoring operating conditions are also important. Additionally, improved correlation with the current model would likely be recognized by using measurements of the tested hardware rather than nominal values. Tuning friction and loss coefficients to the tested hardware can also be done. With these improvements in mind, there is significant potential for improved correlation between the simulation and experimental results, especially at low swash plate angles.

6 CONCLUSION

The servoless swash plate unit is an innovative technology that replaces a traditional servo piston for stroke control with a dynamic valve plate that controls swash plate moments. Controllability of a servoless swash plate pump was demonstrated in previous work, but that work did not investigate the potential efficiency improvements. The servoless/dynamic swash plate approach theoretically provides improved efficiency due to elimination of servo system losses and reduction of cross-port flow, and that theory was validated in this work. A production 130 cc swash plate pump was tested, modified to function as a servoless pump, and retested. The servoless pump showed improved efficiency over the production pump at all tested conditions, peaking at an overall pump efficiency improvement of nearly 18%. Similarly, the servoless pump shows a power loss reduction between 1 and 2 kW when compared with the production pump. The efficiency improvements and power loss reductions presented in this paper apply only to the rotating kit of the pump – they do not account for the power loss of the production pump servo system or the electrical power needed to drive the control valves. Note that the servoless pump used in this experimentation was a proof-of-concept design intended to demonstrate controllability. It has not been optimized for efficiency, and further improvements are likely.

Simulating a servoless swash plate unit and a conventional swash plate unit are largely the same, but shortcuts sometimes used in conventional pump modeling cannot always be taken. Moments applied to the swash plate by the rotating kit are now the control force instead of disturbances, and care must be taken to account for effects such as piston inertia, friction, and leakage. Furthermore, the swash plate must dynamically respond to the moments applied to it within the model. Such a model was implemented in Simulink and the simulations were conducted to mirror the experimental operating conditions. The simulation predictions for overall efficiency difference between the servoless and production pumps follow the same trends as the experimental results and are generally within ±3% of the experimental results and often within ±2%. This correlation is impressive for a 1D simulation model that lacks subtleties such as deflection and non-uniform gap heights, and the simulation results are well within the range of being useful for design and optimization work.

The advancements showcased in this work underscore the promising potential of servoless swash plate pumps, offering not only significant efficiency improvements but also aligning well with industry megatrends of sustainability and emissions reduction. With minimal modifications to existing production pump hardware, the adoption of this technology presents a compelling pathway towards improved efficiency and reduced environmental impact, marking a significant stride forward in fluid power systems innovation.

7 REFERENCES

[1] R. W. Reynolds, "ROTARY PUMP WITH DISPLACEMENT CONTROL". United States Patent US3727521A, 17 April 1973.

[2] K. Miki and Y. Kotake, "VARIABLE DISPLACEMENT PISTON MACHINE". United States Patent US4918918A, 24 April 1990.

[3] T. A. Watts, "VARIABLE DISPLACEMENT AXIAL PISTON HYDRAULIC UNIT". United States Patent US005554007A, 10 September 1996.

[4] C. Junhee, "Dynamic Modeling and Analysis for Swash-Plate Type Axial Pump Control Utilizing Indexing Valve Plate," ProQuest, 2000.

[5] J. Tvarůžek, R. Rahmfeld, C. Fiebing, A. Krahn and W. Göllner, "DYNAMIC VALVE PLATE DESIGN FOR AN AXIAL PISTON PUMP (SERVO-LESS PUMP)," in *14th IFK Proceedings*, Dresden, 2024.

[6] R. Rahmfeld, "Displacement Machines – Key Elements of Future Technology (General Lecture)," in *12th International Fluid Power Conference (12. IFK)*, Dresden, 2020.

[7] "Hydraulic fluid power – Positive-displacement pumps, motors, and integral transmissions – Methods of testing and presenting basic steady state performance," ISO 4409:2019(E), 2019.

Empowering Off-Road Diesel Powertrains: Advanced Multivariate Air Handling Control for Electrified Performance

Shubham Ashta, Nicholas Vang, Weijin Qiu, Chisom Emegoakor, Sree Harsha Rayasam, Tyler Swedes, Jacob Mazanec, Giraldo Luis, Bryan Frushour, Gregory Shaver, Sage Kokjohn, Jaal Ghandhi and David Rothamer

Abstract

This conference paper delves into the advantages of employing an electrified intake boosting system in a 4.5L John Deere diesel engine. The electrified intake system (eBooster) strategically activates solely during transient operations to mitigate drops in the air-to-fuel ratio (AFR) that may result in smoke emissions. To adeptly oversee the electrified air handling system, we introduce a two-degree-of-freedom robust H_∞ single-input single-output (SISO) eBooster controller and a robust model-based H_∞ multiple-input multiple-output (MIMO) controller. These controllers are engineered to regulate the desired AFR, engine speed, and diluent air ratio (DAR) through the manipulation of various air handling actuators (exhaust throttle and EGR valve) and fueling strategies.

The robust SISO controller is crafted utilizing a linear plant model derived through system identification, while the robust MIMO controller is developed based on a physics-based mean value engine model meticulously calibrated to accurately replicate high-fidelity engine simulation software. Both controllers are subjected to simulation using high-fidelity engine simulation software, followed by validation through experimental testing on an engine dynamometer at the University of Wisconsin. Results are benchmarked against a non-eBoosted engine, serving as the baseline. While both the SISO and MIMO controllers exhibit improvements in AFR, DAR, and engine speed recovery during load transients, the robust MIMO controller outperforms them, showcasing superior overall engine performance. This superiority is attributed to its nuanced understanding of the coupling between each actuator input and the model output.

Operating in tandem with the electrified intake boosting system, the MIMO controller brings about significant enhancements. The engine not only recovers to a steady state 70% faster than the baseline but also mitigates engine speed droop by 45%. Consequently, the engine's ability to accommodate load torque sees a substantial increase, underscoring the benefits of an electrified air handling system governed by a robust MIMO controller.

Keywords. Heavy Duty Diesel Engine Operation, Robust Multivariate Control, Electrified Air Handling System

1. INTRODUCTION

Diesel engines have gained extensive traction in heavy-duty off-road applications owing to their robust torque output, durability, and fuel efficiency [1]. These engines demonstrate remarkable performance in tasks demanding substantial power and resilience in harsh environments. Recognizing the substantial emissions associated with diesel engines [2], prioritizing fuel efficiency emerges as a pivotal consideration in the development of heavy-duty diesel powertrains.

In response to stringent emission regulations and fuel economy objectives, engine downsizing utilizing turbomachinery has emerged as a prevalent strategy to meet these imperatives. Downsizing facilitates reduced fuel consumption while upholding equivalent power and torque compared to non-downsized engines. Moreover, downsized engines typically exhibit reduced weight, contributing to overall vehicle weight reduction. This reduction translates into diminished energy requirements for acceleration and maintaining velocity, thereby yielding noteworthy fuel savings.

Moreover, under part load operating conditions, downsized engines offer the potential to enhance fuel efficiency [3]. Turbochargers frequently feature in downsized diesel engines, enhancing fuel efficiency, bolstering low-end torque, and mitigating emissions [20].

Boosting technologies are pivotal in facilitating engine downsizing, thereby enhancing thermal efficiency and brake mean effective pressure (BMEP) [4]. In pursuit of further enhancing the capabilities of these downsized powertrains, electrified boosting technologies emerge as a promising solution [5]. Electrified intake boosting systems provide immediate boost pressure, eliminating the typical turbo lag associated with conventional mechanical turbochargers. This instantaneous boost substantially improves engine responsiveness, particularly during transient load operations, by minimizing air-fuel ratio (AFR) recovery delays.

Integrating electrified boosting systems into hybridized powertrains represents a significant advancement in enhancing fuel efficiency. By harnessing energy from regenerative braking and repurposing wasted engine exhaust gas, this integration optimizes fuel conservation [6][7][8]. Previous endeavors, including those detailed by Nazari [9][10], underscore the significance of decentralized control schemes in air handling systems featuring electrified boosting, with a focus on diminishing turbo lag to enhance engine speed response. Moreover, innovations like frequency separation controllers [11], SISO AFR controllers for electric turbochargers [12], and SISO AFR controllers for downsized gasoline engines [13] contribute to the dynamic landscape of engine control strategies. Nonetheless, the intricate and nonlinear characteristics of air handling systems in diesel engines, incorporating various actuators like exhaust throttles and EGR valves, pose challenges. These systems often exhibit MIMO characteristics, emphasizing the complex interplay between actuators and outputs.

The Relative Gain Array (RGA) analysis offers a method for assessing the degree of Multiple Input Multiple Output (MIMO) coupling in a system [14]. In the study conducted by Harsha et al. [15], the focus lies on developing such a MIMO system and analyzing various couplings using RGA analysis. Despite the benefits of decentralized controllers for MIMO systems, the overall engine performance might still fall short of optimal. This situation calls for exploring multivariate control strategies to effectively handle such intricate air handling systems. An example of such an approach is demonstrated in the work highlighted in [16] and [18], where a robust multivariate controller is devised for a turbocharged natural gas engine and switching algorithms are developed to use multiple controllers at different operating points [17][19].

Addressing the requirement for downsized, e-boosted, power-dense Internal Combustion (IC) engines used in demanding commercial vehicle applications, this paper discusses the creation and deployment of robust Single Input Single Output (SISO) and MIMO H_∞ feedback controllers for a heavy-duty diesel powertrain equipped with an electrically driven intake boosting system for a downsized 4.5L John Deere diesel engine. The electrified compressor (eBooster) from BorgWarner is selected for implementation on the downsized diesel engine. These controllers aim at managing multiple outputs: engine speed for torque/power regulation, air-fuel ratio (AFR) for controlling smoke emissions, and diluent air ratio (DAR) to regulate engine NOx emissions. H_∞ controller tuning is iterative and it requires a certain methodology to get the optimal results [21].

The initial emphasis of this research is on the robust SISO eBooster controller, which aims to maintain the desired AFR by specifically controlling the eBooster speed during load changes. Subsequently, a robust MIMO eBooster controller is developed. A nonlinear state space mean value model is constructed to represent the engine's air handling system, which is validated against engine simulations. This nonlinear model is then linearized for robust MIMO controller synthesis.

To showcase the effectiveness of these control strategies, the SISO and MIMO controllers are experimentally verified on the engine coupled to a dynamometer, and their performance is compared against the baseline non-eBoosted engine, illustrating the benefits of multivariate control strategies for air handling systems.

2. ROBUST SISO EBOOSTER CONTROL DEVELOPMENT

The initial phase in the development of an eBooster controller involved synthesizing a SISO H_∞ feedback controller. Implementing this controller is comparatively simpler than integrating the MIMO controller with the stock ECM (Engine Control Module). The SISO eBooster controller aims to recover the Air-Fuel Ratio (AFR) by adjusting eBooster speed during transients, while the ECM manages the remaining aspects of the engine's air handling system.

2.1. Controller Configuration

The primary objective of the robust SISO controller is to restore the engine's Air-Fuel Ratio (AFR) during transient load operations. As engine load increases, the fueling commanded by the ECM rises to generate more brake torque, thereby maintaining engine speed. However, this increased fueling can lead to a temporary dip in the engine's AFR, potentially resulting in unwanted smoke emissions. By introducing additional air through an electrically driven intake boosting system, the AFR can be restored more rapidly during transient operations.

Figure 2.1 illustrates the configuration of the controller utilized to synthesize the SISO eBooster controller. This configuration entails a 2-degree of freedom controller with inputs consisting of Desired and Measured AFR, while the controller output dictates the commanded eBooster speed. Multiplicative uncertainty for the output was incorporated during controller synthesis. The Desired AFR serves as the exogenous input to the system, while the weighted AFR and weighted eBooster Speed serve as the exogenous outputs.

Further elucidation on the controller configuration will be provided in the subsequent discussion on the Development of Robust MIMO eBooster Controller.

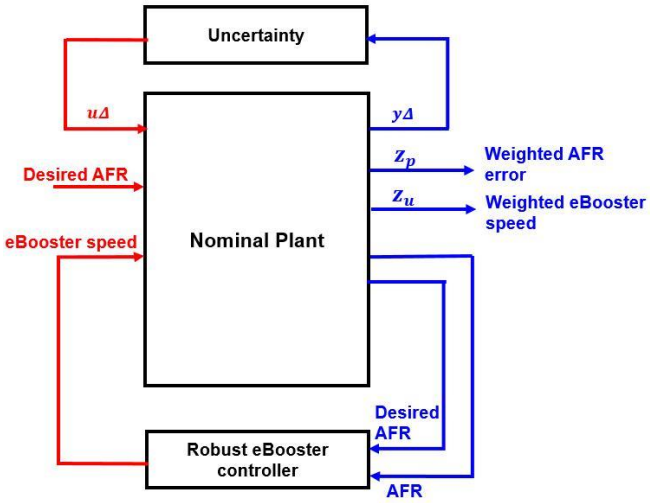

Figure 2.1. Controller Configuration for SISO eBooster controller

2.1.1. System Identification for Plant Model Development

A nominal plant model is derived via the system identification process to relate the effect of eBooster speed on the AFR of the engine. The relationship is defined as

$$G(s) = \frac{Y(s)}{U(s)} \tag{2.1}$$

where G(s) represent the transfer function for the plant model, Y(s) is the plant output representing the engine's AFR response and U(s) is the plant input representing the commanded eBooster speed. For system identification of the plant model, we utilize the 4.5L single turbo engine housed in the engine test cell as a truth reference (Fig. 2.2). The engine operates in closed-loop control mode at the desired torque and speed within the test cell. Once a steady state is attained, a step change in the eBooster speed is commanded to transition from 2000 rpm to 50000 rpm (with the eBooster's maximum speed capped at 70000 rpm) for the system identification procedure. The engine's Air-Fuel Ratio (AFR) response is logged via dSPACE, employing a wideband lambda sensor to discern the plant dynamics accurately. This process is iterated across various operating points of the engine for comprehensive analysis and model estimation.

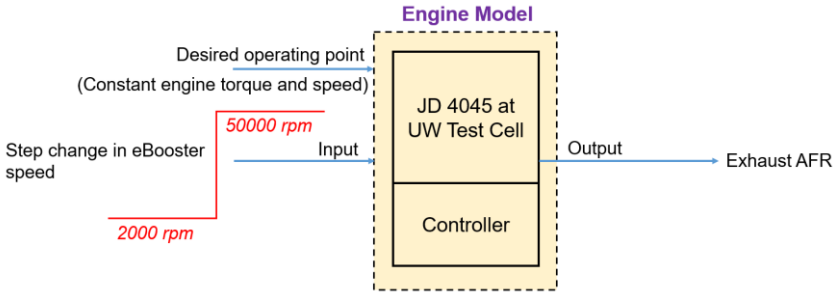

Figure 2.2. System Identification Process

The AFR responses of the engine indicate that a first-order plant transfer function ($G(s) = \frac{K}{(\tau s+1)}$) serves as a suitable approximation for illustrating the engine's dynamics across different load and speed points.

2.2. Plant Uncertainty Weight

Several plant models were developed using the system identification process above in order to estimate the plant dynamics of the engine. Using these transfer functions, a nominal plant model is estimated:

$$G(s) = \frac{7.61 \times 10^{-4}}{(0.4627s + 1)} \tag{2.2}$$

The nominal plant model developed loses accuracy at different operating points. To account for this uncertainty the plant model output, a multiplicative uncertainty weight is defined as a frequency dependent weight.

$$w_i = \frac{(0.25s + 0.35)}{(0.45s + 1)} \tag{2.3}$$

Figure 2.4 shows various samples of possible relative uncertainties and w_i chosen to be greater than these relative uncertainties.

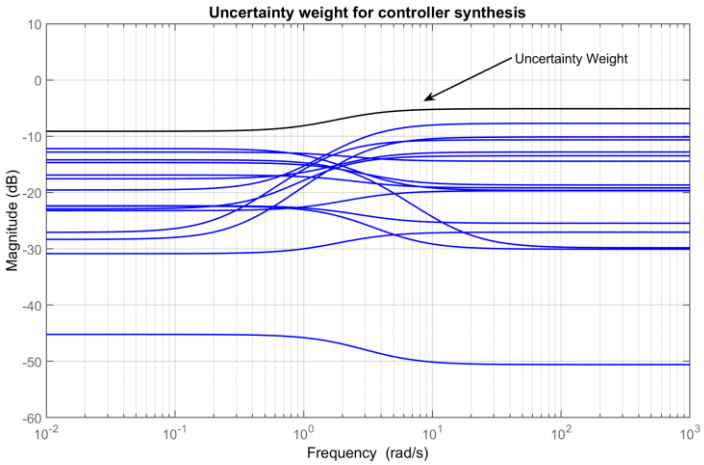

Figure 2.4. Plant Model Uncertainties

2.3. Performance and Actuator Weighting Functions

The performance (W_p) and actuator weighting (W_u) functions are designed to control shape the AFR error and penalize control usage respectively. The performance weighting function provides the upper bound to the complimentary transfer function of the system while actuator weighting function helps provide physical limitations to the commanded eBooster speed.

To shape the AFR error, the performance weighting function in frequency domain is defined as

$$W_p = \left(\frac{\frac{s}{M} + \omega_B}{s + \omega_B A} \right) \tag{2.4}$$

where M represents max error at high frequency, A represents the steady state error in AFR, ω_B represents the frequency at which the error is 100%.

The tuned values for the above parameters are shown below.

$$M = 8 \quad A = 0.7 \quad \omega_B = 4 \frac{rad}{s}$$

Similarly, the actuator weighting function is defined as

$$W_u = \left(\frac{\frac{s}{3.7} + 1}{\frac{s}{370} + 1} \right) \tag{2.5}$$

Figure 2.5 shows the bode magnitude plots of the inverse performance weight $W_P^{-1}$and inverse actuator weight W_u^{-1}.

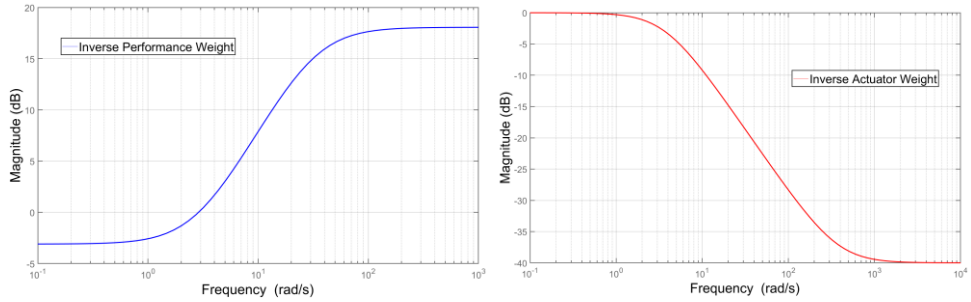

Figure 2.5. Inverse Performance and Actual Weighting Functions

Although SISO eBooster control showcases the benefits of eBoosting during load transient operation, the air handling system is also affected by other actuators in the system (EGR and Exhaust throttle valve). There is a need to develop a robust multiple input multiple output (MIMO) controller that can handle all the actuators while being able to the track the desired reference targets. The following section discusses the development of a robust MIMO controller.

3. ROBUST MIMO CONTROL DEVELOPMENT

A robust multiple input multiple output controller is hypothesized to provide the most optimal control action for the electrified air handling system of the downsized diesel engine as shown in the figure 3.1. To develop such a controller, a non-linear state space (NLSS) representation is developed to model the dynamics of various actuators and their effect on various outputs. The NLSS model is described in the figure 3.2 with various states that affect the air handling system of the diesel engine.

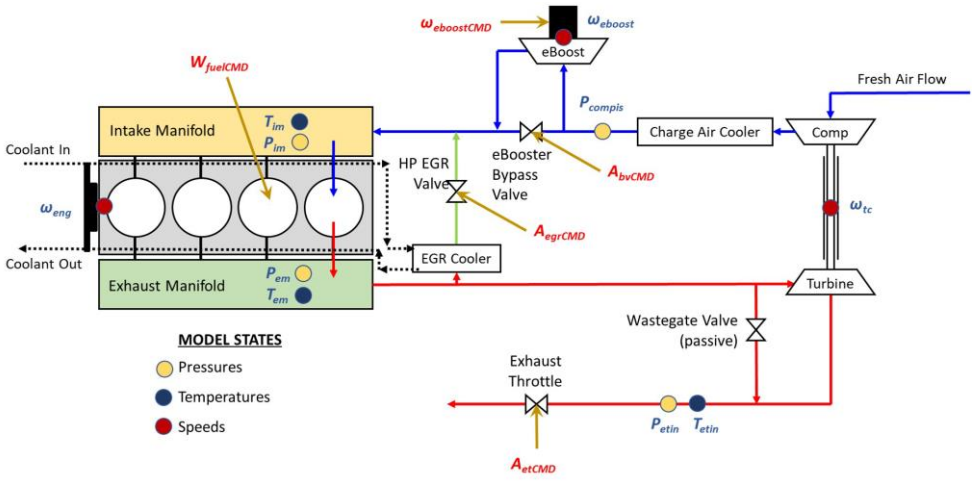

Figure 3.1. Electrified Air Handling System Architecture

3.1. NLSS Model Development

These NLSS model states are described using the following equations.

$$\dot{x} = f(x, u, u_d)$$

$$y = g(x, u)$$

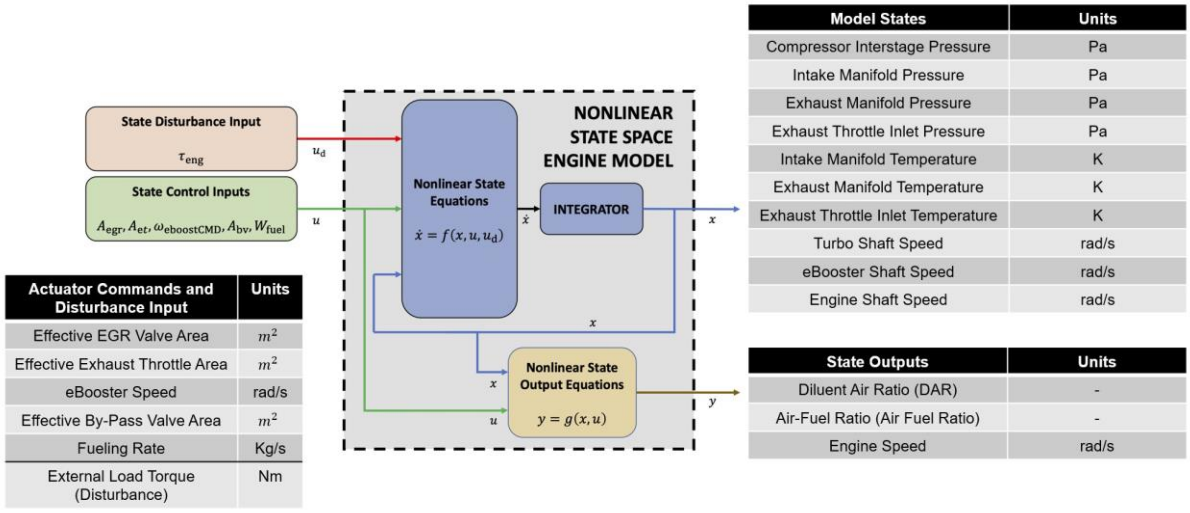

Figure 3.2. NLSS Model Representation

Where x represents the model states, u represents the actuator inputs, u_d represents the disturbance input (load torque) and y represents the state outputs.

The ten model states and the model outputs are governed by the dynamic equations as shown in figure 3.3. The pressure and temperature states are derived by conducting a thermodynamic analysis for various manifolds. Torque analysis around the crankshaft and turbocharger shaft is used to estimate the dynamics of the speed states. While some variables are considered as constants (e.g. manifold volumes, inertias), others are represented as internal sub models based upon various model states and inputs (as shown in figure 3.3). These sub models are derived as parameterized curve fits using the high-fidelity engine simulation software as truth reference.

The tuned high-fidelity model is used as a truth reference for the non-linear model validation process. This is an open loop validation and is represented in figure 3.4. The desired engine speed and load torque are simulated in GT Power (running with various internal controllers). The actuator commands generated from the controllers are used as actuator inputs to the non-linear state space model.

Dynamic Equations (Model States)

$$\dot{x}_1 = P_{\dot{compis}} = \frac{\gamma_{amb} R}{V_{compis}} \left[W_{comp} T_{CAC} + W_{eBoost} T_{CAC} - W_{bv} T_{CAC} \right]$$

$$\dot{x}_2 = P_{\dot{im}} = \frac{\gamma_{im} R}{V_{im}} \left[W_{egr} T_{egr} + W_{eBoost} T_{eBoost,out} + W_{bv} T_{CAC} - W_{cyl} T_{im} \right]$$

$$\dot{x}_3 = P_{\dot{em}} = \frac{\gamma_{ex} R}{V_{em}} \left[W_{cylout} T_{cylout} - W_{turb} T_{em} - W_{wg} T_{em} - W_{egr} T_{em} \right]$$

$$\dot{x}_4 = P_{\dot{etin}} = \frac{\gamma_{ex} R}{V_{etin}} \left[W_{wg} T_{em} + W_{turb} T_{turb,out} - W_{et} T_{etin} \right]$$

$$\dot{x}_5 = T_{\dot{im}} = \frac{R_{im} T_{im}}{P_{im} V_{im}} \left[W_{eBoost} \left(\gamma_{amb} T_{eBoost,out} - T_{im} \right) + W_{egr} \left(\gamma_{ex} T_{egr} - T_{im} \right) + W_{bv} \left(\gamma_{amb} T_{CAC} - T_{im} \right) - W_{cyl} \left(\gamma_{im} T_{im} - T_{im} \right) \right]$$

$$\dot{x}_6 = T_{\dot{em}} = \frac{R_{em} T_{em}}{P_{em} V_{em}} \left[W_{cylout} \left(\gamma_{cylout} T_{cylout} - T_{em} \right) - \left(W_{turb} + W_{wg} + W_{egr} \right) \left(\gamma_{ex} T_{em} - T_{em} \right) \right]$$

$$\dot{x}_7 = T_{\dot{etin}} = \frac{R_{etin} T_{etin}}{P_{etin} V_{etin}} \left[W_{wg} \left(\gamma_{ex} T_{em} - T_{etin} \right) + W_{turb} \left(\gamma_{ex} T_{turb,out} - T_{etin} \right) - W_{et} \left(\gamma_{ex} T_{etin} - T_{etin} \right) \right]$$

$$\dot{x}_8 = \omega_{\dot{tc}} = \frac{Z_{turb} - Z_{comp}}{I_{tc} \omega_{tc}}$$

$$\dot{x}_9 = \omega_{\dot{eBoost}} = \frac{\omega_{eBoostCMD} - \omega_{eBoost}}{\tau_{eBoost}}$$

$$\dot{x}_{10} = \omega_{\dot{eng}} = \frac{C_{trq} P_{im} - \tau_{eng}}{I_{eng}}$$

Summary of Submodels Used

Parameter	Description	Submodel
W_{eBoost}	eBooster Compressor Flow	$fcn(x_1, x_2)$
W_{comp}	Turbocharger Compressor Flow	$fcn(x_1)$
W_{bv}	eBooster Bypass Flow	$fcn(x_1, x_2, u_4)$
W_{cyl}	Cylinder-In Flow Rate	$fcn(x_2, x_5, x_{10})$
W_{egr}	EGR Flow Rate	$fcn(x_2, x_3, u_1)$
W_{turb}	Turbine Flow Rate	$fcn(x_3, x_4, x_6)$
W_{et}	Exhaust Throttle Flow Rate	$fcn(x_4, x_7, u_2)$
Z_{comp}	Compressor Power	$fcn(x_1, x_8)$
Z_{turb}	Turbine Power	$fcn(x_3, x_4, x_6, x_8)$
$T_{eBoost,out}$	eBooster Outlet Temperature	$fcn(x_1, x_2)$
T_{cylout}	Cylinder Outlet Temperature	$fcn(x_2, x_3, x_5, x_{10}, u_5)$
C_{trq}	Engine Torque Coefficient	$fcn(x_1, x_5, x_{10}, u_5)$

Dynamic Equations (Model Outputs)

$$y_1 = DAR = \frac{(AFR_{stoich} + 1) W_{fuel}}{W_{fuel} + W_{comp}} \cdot \left(\frac{W_{egr} + W_{res}}{W_{egr} + W_{res} + W_{comp} - \frac{(AFR_{stoich}+1)(W_{fuel}(W_{egr}+W_{res}))}{W_{fuel}+W_{comp}}} \right)$$

$$y_2 = AFR = \frac{W_{comp}}{W_{fuel}}$$

$$y_3 = \omega_{eng} = x_{10}$$

Figure 3.3. Dynamic Equations for the NLSS Model

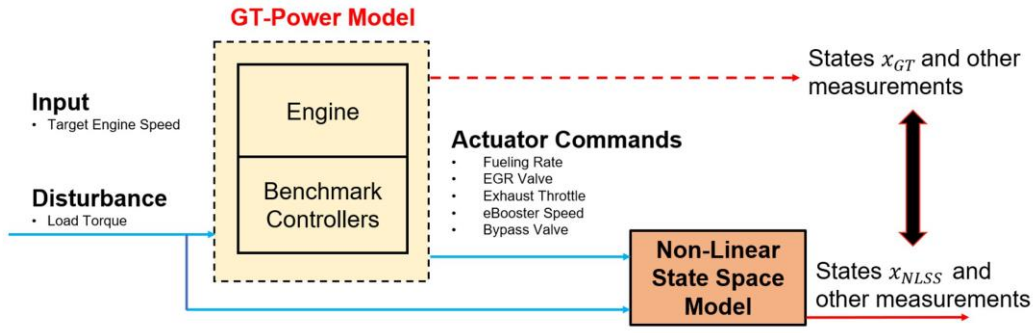

Figure 3.3. NLSS Model Validation

3.2. Model Linearization

The NLSS model is then linearized around the equilibrium of our choice to be used as plant model for controller synthesis. This linearized plant model is represented as:

$$\dot{x} = \delta\dot{x} = A\delta x + B\delta u + F\delta u_d$$

$$\delta y = C\delta x + D\delta u$$

$$\delta x = x - x_e \qquad \delta y = y - y_e \qquad \delta u = u - u_e \qquad \delta u_d = u_d - (u_d)_e$$

Here, x, y, u and u_d are the model state inputs and outputs as discussed in 2.3.3. The variables x_e, u_e, y_e and $(u_d)_e$ represent the equilibrium values around which the non-linear state space model is linearized. The variables δx, δy, δu, and δu_d are the linear model state inputs and outputs. The state space matrices A, B, C, D, and F are estimated by taking the Jacobian of the non-linear differential equations.

The equilibrium values around which the model is linearized, are presented in table 3.1 below.

State/Input	**Parameter**	**Equilibrium Value**	**Units**
x_1	Compressor Interstage Pressure	155.83	kPa
x_2	Intake Manifold Pressure	174.39	kPa
x_3	Exhaust Manifold Pressure	211.61	kPa
x_4	Exhaust Throttle Inlet Pressure	127.62	kPa
x_5	Intake Manifold Temperature	323.37	K
x_6	Exhaust Manifold Temperature	756.95	K
x_7	Exhaust Throttle Inlet Temperature	663.94	K
x_8	Turbo Shaft Speed	85.7	krpm
x_9	eBooster Shaft Speed	45	krpm
x_{10}	Engine Shaft Speed	1800	rpm
u_1	EGR Valve Area	1.07 (24% of max)	m^2
u_2	Exhaust Throttle Area	5.65 (23% of max)	m^2
u_3	eBooster Speed	55000 (78% of max)	rpm
u_4	eBooster By-pass Valve Angle	0 (0% of max)	Degrees
u_5	Total Fueling	3.6	g/s
u_d	Load Torque	300	Nm

Table 3.1 Equilibrium Point for Model Linearization

The equilibrium values are selected to linearize the nonlinear plant model within the midrange of the engine's operating spectrum, where uncertainties will be assigned to account for potential inaccuracies. This engine operates within a hybridized powertrain, maintaining a constant speed of 1800 rpm while handling load torque from both the hydraulic system and the generator used to charge the battery [22]. Accordingly, the equilibrium point was set at 1800 rpm and a load torque of 300 Nm.

3.3. Model Uncertainty Weights

The linearized state space model is used as the nominal plant model for controller synthesis. This nominal model is accurate at the equilibrium point (table 3.1) but loses accuracy at operating points away from its equilibrium. To account for these inaccuracies, multiplicative output uncertainty is assigned to the model outputs as a diagonal matrix. Each element is this matrix is a frequency dependent transfer function and is expressed in the equation below.

$$\delta y = \delta\overline{y_o}\left(1 + W_y\Delta_y\right) \qquad (2.6)$$

Here, $\Delta_y = diag\{y_1, y_2, y_3\}$ and $\delta y_i \in [-1,1]$

$$W_y = \begin{bmatrix} \left(\frac{\frac{s}{20}+1}{\frac{s}{4}+1}\right) & 0 & 0 \\ 0 & \left(\frac{\frac{s}{20}+1}{\frac{s}{4}+1}\right) & 0 \\ 0 & 0 & \left(\frac{\frac{s}{20}+1}{\frac{s}{4}+1}\right) \end{bmatrix}$$

3.4. Performance and Actuator Weighting Functions

The exogenous outputs for various actuators (z_u) and target errors (z_p) are defined using equation 2.7 below.

$$z_u = W_u e \qquad z_p = W_p e \tag{2.7}$$

Where e represents the target error ($y - r$), u represents the actuator command, W_u and W_p represent the actuator and performance weighting functions respectively. To shape the respective errors in frequency domain, the following performance weight (n^{th} order) is used.

$$W_p = K\left(\frac{\frac{s}{M} + \omega_B}{s + \omega_B A}\right)^n \tag{2.8}$$

Where, M represents max error at high frequency, A represents the steady state error in AFR, ω_B represents the frequency at which the error is 100%, n represents the order of the weighting function, K is the scalar multiplied to increase/decrease the weightage to the tracking performance. Table 3.2 below shows the value of each parameter for each of the three outputs (AFR, DAR, Engine Speed) used in simulation as well as on the engine in the engine test cell.

y_i	Implementation in Simulation					Implementation in Engine Test Cell				
	ω_B	M	A	n	K	ω_B	M	A	n	K
DAR	3	0.5	0.001	2	1	8	0.5	0.01	1	1
AFR	1	5	0.1	1	0.5	1	5	0.5	1	0.5
Engine Speed	2.5	0.4	0.01	1	1	2	0.5	0.01	1	4

Table 3.2 Performance Weighting Functions

The actuator weighting function is defined using the equation below.

$$W_u = \frac{1}{N} * \frac{\frac{s}{\left(\frac{\tau}{N}\right)} + 1}{\frac{s}{\left(\frac{\tau}{\epsilon}\right)} + 1} \tag{2.9}$$

Where, N represents control action at low frequencies, ϵ represents control action at high frequencies, and τ represents the response time of the actuator command.

Table 2.23 below shows the various parameters for the actuator weighting function for each actuator command used both for simulation as well as experimental setup.

u_i	Implementation in Simulation			Implementation in Engine Test Cell		
	τ	N	ϵ	τ	N	ϵ
EGR Valve	20	3.33	0.00303	10	1	0.00303
Exhaust Throttle Valve	25	14	0.00303	25	14	0.00303
eBooster Speed	3.7	25	0.01	1	10	0.001
eBooster By-Pass Valve	30	1	0.0091	30	1	0.0091
Fueling	2	1	3.3e-05	4	1	3.3e-05

Table 3.3 Actuator Weighting Functions

The controller configuration along with the nominal plant and its associated uncertainty can be seen in figure 3.4. The controller is designed to track AFR, DAR, and engine speed with the help of the electrified air handling system for the 4.5L engine.

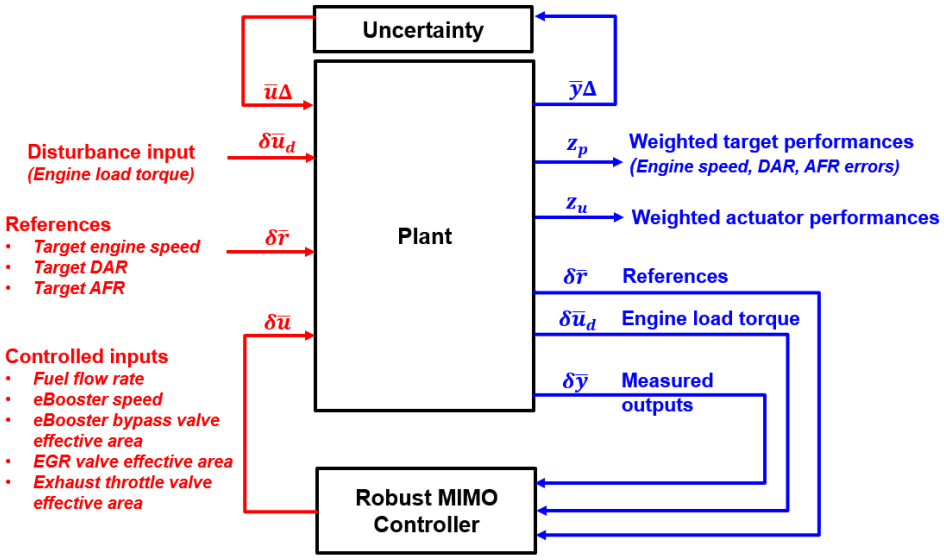

Figure 3.4. Controller Configuration for the robust MIMO controller

3.5. Results and Discussion

This section discusses results (both simulation and experimental) and comparison of engine responses for the three configurations.

1. Non eBoosted Case: This consists of the baseline 4.5L diesel engine running with the stock engine control module (ECM) without an electrified air handling system. In this case, the decoupled PID controllers are implemented to track DAR, AFR and engine speed via EGR valve, exhaust throttle valve and fueling command respectively.
2. SISO eBoosted Case: In this configuration, the 4.5L diesel engine is equipped with the baseline ECM and an electrified eBooster, which supplies additional fresh air into the cylinders during transient conditions. Additionally, a bypass valve is incorporated in parallel with the eBooster to enable fresh air intake when the eBooster is deactivated.
3. MIMO eBoosted Case: This configuration features the electrified 4.5L diesel engine with a robust MIMO controller maintaining the air handling system. The MIMO controller ensures precise tracking of DAR, AFR, and engine speed by utilizing multiple actuators, including the EGR valve, exhaust throttle valve, eBooster speed, eBooster bypass, and fueling.

3.5.1. Simulation Results

The three outlined setups are simulated within a co-simulation framework that employs both Simulink and GT-Power. Within this arrangement, the robust single-input single-output (SISO) and multiple-input multiple-output (MIMO) controllers are configured within Simulink, while the benchmark controllers and the engine model (plant) are established within GT-Power. During simulation, load torque is applied at 1800 rpm and 1600 rpm approximately 8 seconds into the simulation, transitioning from 100Nm to 500Nm at a rate of 1200Nm/s.

Figure 3.5 depicts the outcomes of implementing the controller at 1800 rpm. Given that the plant model's equilibrium was set at 1800 rpm and 300 Nm, the MIMO controller is anticipated to demonstrate sufficient robustness in managing the load transient at this speed. The left-side subplots exhibit reference tracking for Diluent Air Ratio (DAR), Air Fuel Ratio (AFR), and engine speed. Meanwhile, on the right, five subplots illustrate the actuator commands utilized by the controllers to track the desired variables. As the load ramps up, the engine speed decreases, prompting the fueling controllers to respond by increasing fueling during the transient operation. Among the three configurations, the robust MIMO controller shows the most effective engine speed recovery, with a 43% lower engine speed droop and a 65% faster recovery time compared to the non-eBoosted case. The SISO eBoosted case demonstrates better recovery than the non-eBoosted case but still lags behind the MIMO eBoosted case. In terms of Air Fuel Ratio (AFR) recovery, the MIMO eBoosted case surpasses the other configurations, with AFR dropping to approximately 18.24, whereas the SISO eBoosted and non-eBoosted cases show AFR drops to 17.79 and 16.26, respectively. The MIMO controller also exhibits a similar trend in Diluent Air Ratio (DAR) recovery. During transients, the EGR valve reduces DAR, which then returns to normal once the engine reaches a steady state after the load transient. Additionally, the exhaust throttle area remains relatively open for the MIMO eBoosted case compared to the other cases.

Figure 3.6 presents the results for SISO and MIMO controller implementation at 1600 rpm, with a similar load transient applied to the engine across all three configurations. The choice of 1600 rpm aims to showcase the controller’s robustness and stability at operating points away from the equilibrium point. The MIMO eBoosted case outperforms the other configurations, demonstrating a 47% lower droop in engine speed and a 72% shorter recovery time to return the engine speed to 1600 rpm. However, it's noteworthy that there is an overshoot in engine speed, causing it to reach steady state at approximately the same time as the other cases. This observation confirms that while the MIMO controller remains stable, its performance at 1600 rpm is not as optimal as it is at 1800 rpm.

Furthermore, the MIMO controller showcases faster recovery in Diluent Air Ratio (DAR) and Air Fuel Ratio (AFR) compared to the SISO eBoosted and non-eBoosted cases. During the MIMO eBoosted case at 1600 rpm,

the exhaust valve remains relatively open. This behavior primarily results from the measured engine AFR being lower than the desired AFR, prompting the MIMO controller to adjust accordingly.

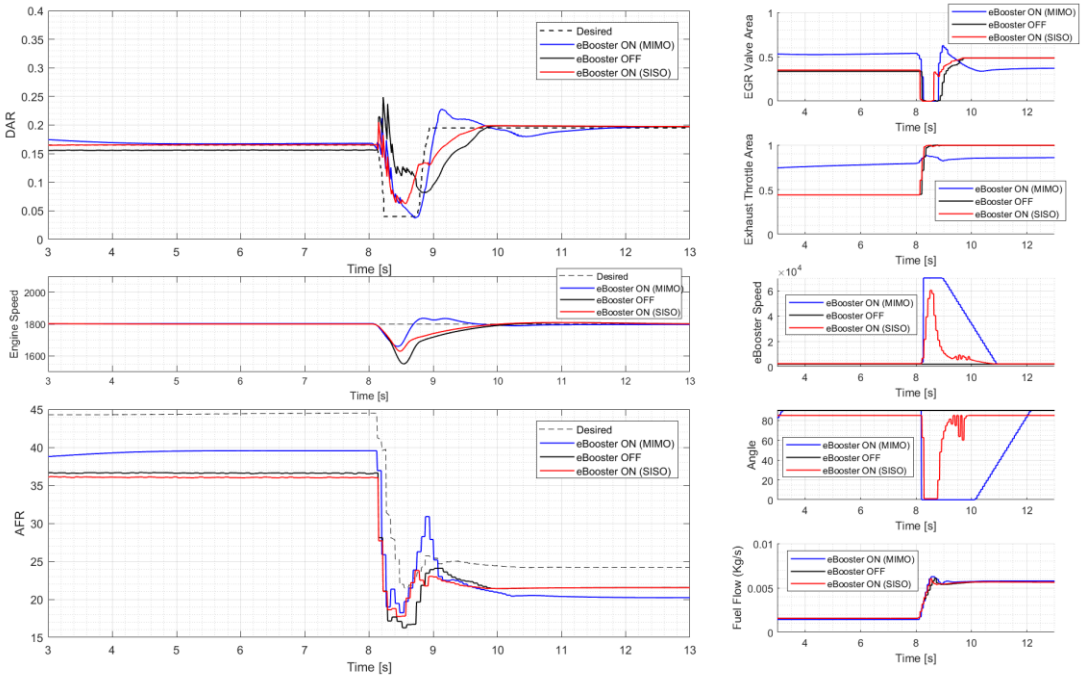

Figure 3.5. MIMO Implementation at 1800 rpm [100 Nm to 500 Nm at 1200 Nm/s]

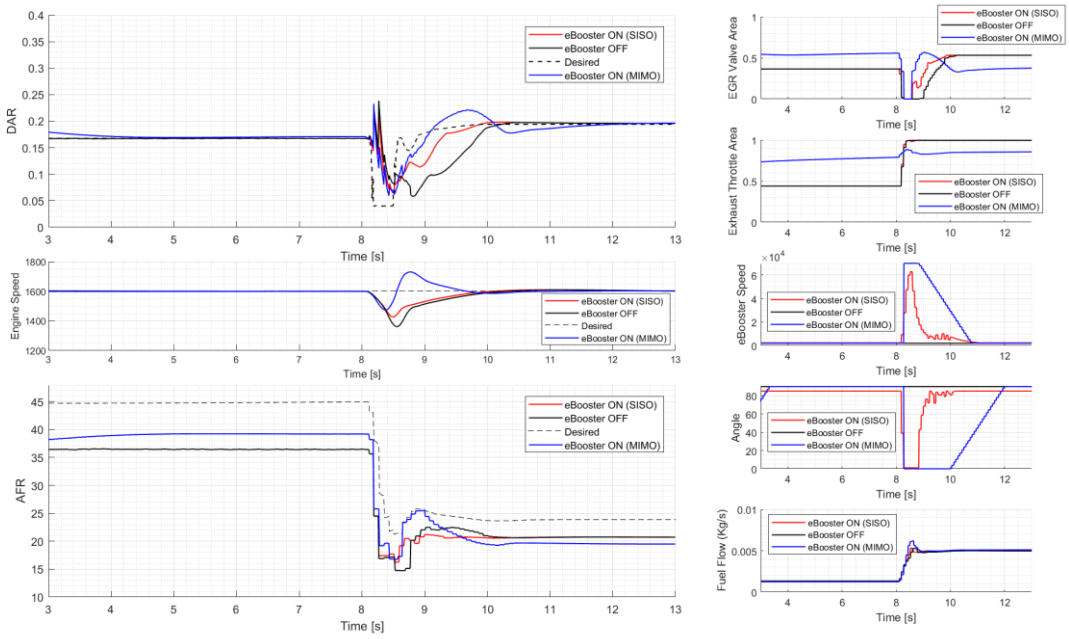

Figure 3.6. MIMO Implementation at 1600 rpm [100 Nm to 500 Nm at 1200 Nm/s]

3.5.2. Experimental Results

The SISO and MIMO controllers undergo implementation and experimental validation within the engine test cell at the University of Wisconsin. This process involves configuring the controller architectures in Simulink and then deploying them onto the engine using a dependable in-vehicle prototyping system (AutoBox) via dSPACE. The controller matrices and architectures are seamlessly integrated into the AutoBox system, facilitating communication with the baseline engine control module (ECM) and effectively superseding the actuator commands sent to the engine. To apply the load transient, an engine dynamometer coupled to the 4.5L diesel engine is utilized, ensuring a controlled and reproducible environment for the tests. Data from the test cell is captured using a high-speed data acquisition system, which is subsequently employed to generate comparison plots for the three configurations.

Figure 3.7 illustrates the results of implementing both SISO and MIMO controllers on the engine operating at 1800 rpm, alongside comparisons with other configurations. A load step ranging from 100Nm to 500Nm was applied at a rate of 1200 Nm/s. The experimental findings demonstrate the successful implementation of both SISO and MIMO controllers, clearly showcasing the superiority of the MIMO controller over the other configurations.

The MIMO eBoosted case showcases a notable 45% reduction in engine speed droop compared to the non-eBoosted case, with its recovery time impressively shortened by 70%. Furthermore, it displays superior recovery in both Diluent Air Ratio (DAR) and Air Fuel Ratio (AFR) during transient operations. The EGR valve closes during load transients to match the desired DAR, reopening when the engine speed returns to 1800 rpm. To maintain the desired AFR, the exhaust throttle valve is partially open at low loads. This throttling of air at low loads assists in heating the exhaust gas entering the aftertreatment system, aiding in the passive regeneration of the Diesel Particulate Filter (DPF).

During low-load conditions, less fueling is necessary to maintain engine speed, enabling the partial closure of the exhaust throttle while still achieving an appropriate AFR and effectively heating up the exhaust gas. The eBooster is activated solely during the load transient and promptly deactivated once the engine reaches a steady state. Additionally, the bypass valve closes during the transient to fully utilize the capabilities of the eBooster. The fueling from the MIMO controller reacts faster to the drop in engine speed than the other cases, thereby aiding in improving the speed response.

Figure 3.8 presents the experimental results for SISO and MIMO implementation at 1600 rpm, with a similar load transient ranging from 100 Nm to 500 Nm applied at 1200 Nm/s. The choice of 1600 rpm helps demonstrate the robustness of the MIMO controller in performing at an operating point away from the equilibrium range. At 1600 rpm, the MIMO controller emerges as the superior configuration. It exhibits a remarkable 55% reduction in engine speed droop, along with a 69% shorter recovery time compared to the non eBoosted case. Although the droop in engine speed for the SISO eBoosted case matches that of the MIMO eBoosted case, the SISO eBoosted case takes roughly twice as much time to recover.

In summary, both the MIMO and SISO controllers are effectively implemented and experimentally verified on the engine, underscoring the benefits of employing an electrified compressor during transient load operations. The experimental findings from the engine test cell align closely with the results obtained from simulations. The decoupled SISO system for the eBooster is found to be suboptimal due to its limited understanding of other actuators that can impact the air handling system. Leveraging the knowledge of interconnections among various actuator inputs and model outputs, the MIMO controller emerges as the most efficient solution for the engine's air handling system, enhancing the engine's capability to handle transient operations through the integration of an electrified compressor.

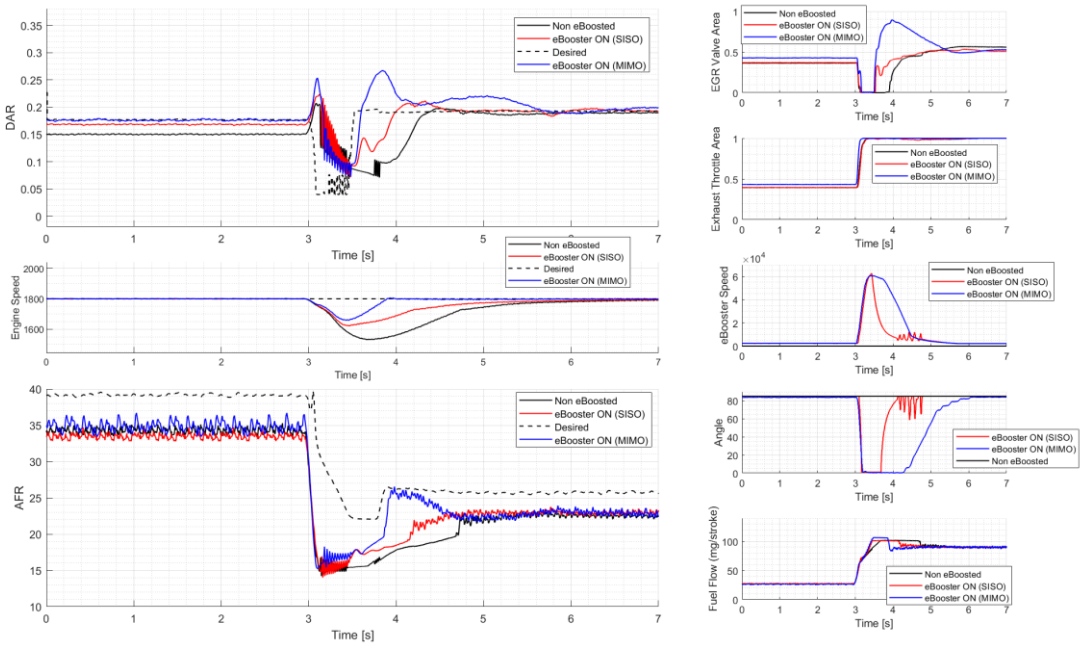

Figure 3.7. MIMO Implementation at 1800 rpm [100 Nm to 500 Nm at 1200 Nm/s]

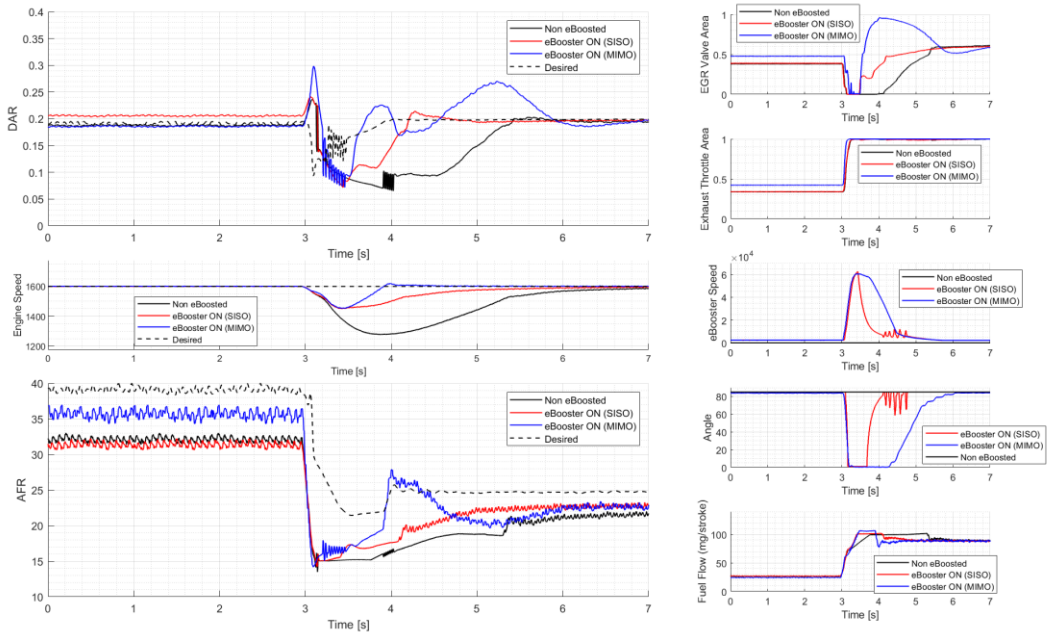

Figure 3.8. MIMO Implementation at 1800 rpm [100 Nm to 500 Nm at 1200 Nm/s]

4. CONCLUSIONS

This paper discusses the benefits of developing robust coordinated control strategies for a highly non linear air handling system over the conventional decoupled controllers that we see in today's industry. Overall, both the MIMO and SISO controllers were successfully implemented and experimentally tested on the 4.5L diesel engine. The experimental results obtained from the engine test cell align well with the simulation outcomes. The results for the implementation of the SISO eBooster controller demonstrates the benefits of deploying an electrified air handling system to improve the engine performance for load transient operation. By utilizing the knowledge of coupling between various actuator inputs and model outputs, the MIMO controller proves to be the most effective for the engine's air handling system, enhancing the engine's load acceptance during transient operations through the use of an electrified compressor.

5. REFERENCES

[1] Dallmann, T., & Menon, A. (2016). Technology pathways for diesel engines used in non-road vehicles and equipment. *International Council on Clean Transportation (ICCT): Washington, DC, USA*.

[2] Kean, A. J., Sawyer, R. F., & Harley, R. A. (2000). A fuel-based assessment of off-road diesel engine emissions. *Journal of the Air & Waste Management Association*, *50*(11), 1929-1939.

[3] Ecker, H. J., Schwaderlapp, M., & Gill, D. K. (2000). *Downsizing of diesel engines: 3-cylinder/4-cylinder* (No. 2000-01-0990). SAE Technical Paper.

[4] Ricardo, M. B., Apostolos, P., & Yang, M. (2011). Overview of boosting options for future downsized engines. *Science China Technological Sciences*, *54*, 318-331.

[5] Alshammari, M., Alshammari, F., & Pesyridis, A. (2019). Electric boosting and energy recovery systems for engine downsizing. *Energies*, *12*(24), 4636.

[6] Kiwan, R., Middleton, R., & Stefanopoulou, A. (2018). *Thermodynamic and practical benefits of waste energy recovery using an electric turbo-generator under different boosting methods* (No. 2018-01-0851). SAE Technical Paper.

[7] Nazari, S., Siegel, J., & Stefanopoulou, A. (2019). Optimal energy management for a mild hybrid vehicle with electric and hybrid engine boosting systems. *IEEE Transactions on Vehicular Technology*, *68*(4), 3386-3399.

[8] Zhao, D., Stobart, R., Dong, G., & Winward, E. (2014). Real-time energy management for diesel heavy duty hybrid electric vehicles. *IEEE Transactions on Control Systems Technology*, *23*(3), 829-841.

[9] Nazari, S., Stefanopoulou, A., Kiwan, R., & Tsourapas, V. (2016, October). A coordinated boost control in a twincharged spark ignition engine with high external dilution. In *Dynamic Systems and Control Conference* (Vol. 50701, p. V002T20A003). American Society of Mechanical Engineers.

[10] Nazari, S., Siegel, J., & Stefanopoulou, A. (2021). Control of hybrid boosting in highly diluted internal combustion engines. *International Journal of Engine Research*, *22*(6), 1794-1807.

[11] Xiao, B., Buckland, J. H., & Karnik, A. (2017, October). Frequency separation control of series sequential boosting system with electric supercharger and turbocharger. In *Dynamic Systems and Control Conference* (Vol. 58295, p. V003T34A004). American Society of Mechanical Engineers.

[12] Ekberg, K., & Eriksson, L. (2017). Improving fuel economy and acceleration by electric turbocharger control for heavy duty long haulage. *IFAC-PapersOnLine*, *50*(1), 11052-11057.

[13] Villegas, J., Gao, B., Svancara, K., Thornton, W., & Parra, J. (2011, September). Real-time simulation and control of an electric supercharger for engine downsizing. In *2011 IEEE Vehicle Power and Propulsion Conference* (pp. 1-6). IEEE.

[14] Bristol, E. (1966). On a new measure of interaction for multivariable process control. *IEEE transactions on automatic control*, *11*(1), 133-134.

[15] Harsha Rayasam, S., Qiu, W., Rimstidt, T., Shaver, G. M., Van Alstine, D. G., & Graziano, M. (2023). Control-oriented modeling, validation, and interaction analysis of turbocharged lean-burn natural gas variable speed engine. *International Journal of Engine Research*, *24*(2), 738-754.

[16] Qiu, W., Rayasam, S. H., Shaver, G. M., Rimstidt, T. G., & Van Alstine, D. G. (2023). Control design-oriented modeling and μ-synthesis-based robust multivariate control of a turbocharged natural gas genset engine. *International Journal of Engine Research*, *24*(9), 3905-3921.

[17] Rayasam, S. H., Qiu, W., Rimstidt, T., Shaver, G. M., & Van Alstine, D. G. (2023). Robust model-based switching MIMO air handling control of turbocharged lean-burn SI natural gas variable speed engines. *International Journal of Engine Research*, *24*(6), 2783-2804.

[18] Qiu, W., Rayasam, S. H., Shaver, G. M., Rimstidt, T., Van Alstine, D. G., & Graziano, M. (2022). Modeling and Robust Coordinated Control of Turbocharged Natural Gas Engine with Genset Application. *IFAC-PapersOnLine*, *55*(24), 39-44.

[19] Rayasam, S. H., Qiu, W., Shaver, G. M., Rimstidt, T., & Van Alstine, D. G. (2022). Robust Switching MIMO Control of Turbocharged Lean-Burn Natural Gas Engines. *IFAC-PapersOnLine*, *55*(24), 7-12.

[20] Qiu, W. (2023). AN INTEGRATED FRAMEWORK FOR MODELING, ROBUST COORDINATED CONTROL, AND POWER MANAGEMENT OF ADVANCED POWERTRAINS FEATURING TURBOCHARGED ENGINES (Doctoral dissertation, Purdue University Graduate School).

[21] Chen, Z., Chen, Z., & Yao, B. (2021). Modeling and H∞ position control of a spreader in the gantry crane. IFAC-PapersOnLine, 54(20), 592-597.

[22] Qiu, W., Ashta, S., Shaver, G. M., Mazanec, J., Kokjohn, S., Johnson, S. C., ... & Frushour, B. C. (2024). System configuration, control development, and in-field validation of a hybrid electric wheel loader featuring electrically-boosted engine. Control Engineering Practice, 150, 105989.

Centralized Pressure Control and Displacement Quantization with Digital Displacement Pumps

Jordan Pascale - *Danfoss Power Solutions, jpascale@danfoss.com*

Chris Williamson – *Danfoss Power Solutions, cwilliamson@danfoss.com*

Jim Hennen – *MTS Systems - jim.hennen@mts.com*

Paul Rindahl – *MTS Systems – paul.rindahl@mts.com*

Abstract

Danfoss Power Solutions has developed a centralized pressure control solution for multi-pump hydraulic power units in the industrial market. This system architecture has been developed around the use of the Digital Displacement Pump® (DDP) which is highly efficient over a wide range of operating conditions and has typically shown a >30% decrease in electrical input energy over similar systems using axial piston pumps.

MTS Systems expanded this centralized control to work in a harmonized fashion with other pumping technologies housed within unique motor-pump modules; some containing DDP and others containing conventional axial piston pumps. This arrangement provided several benefits and empirically demonstrated the DDP module efficiency over the axial piston pump module in supplying fluid power to dynamic downstream force and motion systems that replicate real-world automotive drive files and test track profiles.

Special consideration was required when implementing DDP in a system with multiple pumps' (maximum of 6) outlet flow combined in parallel. Allowing each individual pump controller to operate in pressure control mode caused compounding complexity in tuning, and noisy, unstable flow pulsations. As a solution, a centralized pressure control scheme was implemented in which a system level microcontroller evaluated user inputs, pressure signals from a transducer, executed logic, and output displacement commands to each pump controller as required to meet the system demand. What makes this control scheme unique is that in a multi-pump system, one pump has a continuously variable displacement fraction with any value from 0 to 100%. The other pump displacements were controlled in a quantized manner with stepped values of displacement (for example: 0%, 25%, 75%, 100%). Hose resonant frequencies were also avoided in this manner.

Testing and implementation of this control scheme has proven to be effective in reducing system tuning complexity and undesirable flow pulsations in the system. Measured results indicate that the average pressure ripple power was reduced by 28% to 94% and the average pressure ripple band power by 61% to 98% (pump module dependent).

Successful implementation of the centralized control allowed MTS to demonstrate through an energy efficiency study that HPUs equipped with DDP consume up to 37.5% less energy than those with swashplate pumps for a given test cycle.

Keywords. Digital Displacement, Hydraulic Power Units, Centralized Pressure Control.

1. INTRODUCTION

1.1. Motivation

Energy conservation to reduce CO2 emissions becomes increasingly prominent for industrial equipment. Last year, the EU adopted European Sustainability Reporting Standards, which require publicly traded EU companies to disclose CO2 emissions in their annual reports, beginning in fiscal year 2024.

The economic benefits of energy efficiency are also compelling, particularly in European countries where the price of electrical power has increased dramatically in recent years. The United States government finds that pumps represent 27% of the electricity used by industrial systems [1]. Energy is the largest cost of ownership of an industrial pump system, representing 50% to 90% of total life cycle costs, depending on the technology.

1.2. Background

Digital Displacement Pump (DDP) technology was invented at the University of Edinburgh [2]. The basic DD principle is activating cylinders individually with an electronic controller, varying the pump displacement volume by on/off control rather than by reducing the piston stroke. This method enables high energy efficiency and fast, precise flow control. Innovation in Scotland led to numerous successful demonstrations of digital fluid power for renewable energy, industrial machinery, on-highway and off-highway vehicles, and more. Danfoss Power Solutions acquired Artemis Intelligent Power and its DDP portfolio in 2021. Danfoss brought DDP to market with the DDP096 pump [3], and Danfoss continues to introduce new DD components and systems. Digital pumps and motors also have been a research topic at multiple universities over the last 20 years, and new contributions to the field are published continuously. A full bibliography of the state of the art would be too large for this paper. The interested reader can find extensive references in [4] and a few interesting examples of more recent works in [5] through [8].

Hydraulic Power Units (HPU) are a mainstay of many industrial installations. HPUs convert electrical power to fluid power with one or more hydraulic pumps driven by electric motors. HPUs include associated components such as a reservoir, filters, control valves, accumulators, sensors, controllers, and so on. A typical HPU has AC induction motors driving variable displacement, pressure-compensated piston pumps. Large installations with multiple pumps in parallel may have trouble with pressure control stability if each pump is individually pressure-compensated. Consequently, a multi-pump HPU may synchronize pump commands with a single hydro-mechanical pressure control and a common pilot line connected to all pumps.

If an HPU has periods of low power demand, motors with variable frequency drives are an energy-efficient alternative by adjusting motor speed to reduce standby power loss. However, it is important to note that VFD efficiency decreases with decreasing motor load and the decline in efficiency is more pronounced with drives of smaller horsepower ratings [9]. Additionally, a VFD system requires slightly more energy when the motor is running at rated speed and load due to higher losses within the drive.

MTS Systems is a leading global supplier of test and simulation systems. This testing relates to applying precision forces and motions to help understand the physical properties of structures, components, materials, and the accuracy of model-based designs. The HPU is the backroom fluid power producer that feeds fluid power through a network of pipes and valves to the front room test operations. The actuator system in the front room imparts forces and motions into the test article, such as a vehicle or structure. MTS SilentFlo™ HPU are designed to be used with servocontrolled, electro-hydraulic systems. MTS HPU are scalable with multiple pump/motor modules arranged in single, 3-module and 6-module arrays. The pump/motor modules are submerged in the hydraulic reservoir to save space and reduce noise.

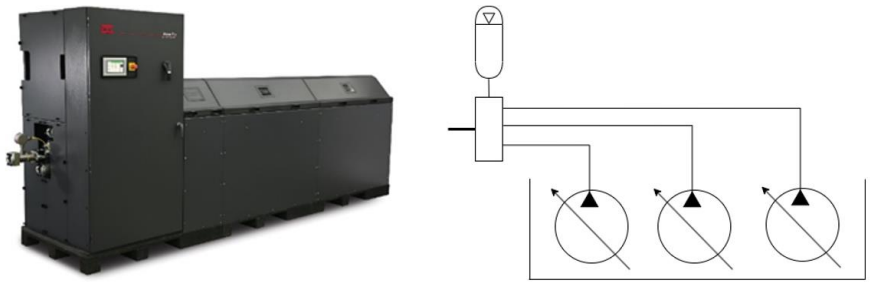

Figure 1: MTS SilentFlo™ HPU

Total energy efficiency of a test system is rather low. Efficiencies at each stage of power transmission from electrical to fluid to mechanical domains are multiplied together to realize the overall efficiency of the physical test system. For example, if each power conversion step is 90% efficient, then the overall efficiency = 90% x 90% x 90% = 73%. Efficiencies based on conventional technologies in these three phases of transmission need to consider the full operating range from idling to full power consumption. Total system efficiency in the range of 30% to 60% is typical with conventional swash-plate piston pumps in the HPU.

1.3. Project Goals

With the goal of gaining substantial efficiency improvements, and to differentiate themselves in the market, MTS began investigating the use of Danfoss DDP technology for their newest models of HPU. The industry-leading efficiency and control was a key driver for MTS in pursuing the technology. An MTS HPU utilizing DDP technology could reasonably expect a 3 to 5 year payback time based on lower operating cost but would vary depending on the cost of energy and other factors.

The system must be able to deliver the peak flow, but, from an economic point of view, it is also important to know at what flow rates the system is going to operate most of the time. To find the total cost of operating the HPU, the running cost at each operating condition must be calculated and summated. A duration diagram helps estimate HPU energy costs via a histogram distribution of how many hours during an annual period required a given flow rate.

As the project developed, significant challenges became apparent. Because of its digital flow control principle, DDP produces larger flow and pressure ripple output than conventional piston pumps. Flow pulsations can cause control instability and undesirable noise and vibration. A system architecture combining up to 6 DDP modules in parallel, each operating separately in pressure control mode, amplified the pressure oscillations. Quiet, smooth operation was a major goal of the project and a requirement for bringing DDP to production in MTS HPU.

The present paper describes two sets of experiments with the same DDP HPU. The pressure ripple test (see section 4.1) compares the first prototype control system with distributed pressure control to a more sophisticated, centralized pressure control system. The energy test (see section 4.2) compares the energy efficiency of the DDP HPU with centralized pressure control to a traditional HPU with swash-plate type pumps.

2. SYSTEM CONTROL DESCRIPTION

As previously mentioned, the hydraulic power units built by MTS presented a unique challenge in combining outlet flow in parallel while coordinating the pressure control of up to 6 DDP units in a single HPU. Initially, a distributed pressure control was attempted by relying on an embedded pressure transducer at each pump's outlet in conjunction with its DPC12 pump microcontroller. However, there were difficulties in matching pressure setpoint levels between pumps due to variations in transducer tolerances. DDP pressure ripple and interactions between pumps produced substantial noise and hose vibration.

Through testing and analysis, an alternative solution was established through incorporating a stand-alone Danfoss Plus+1 system controller. A unique software architecture was successfully developed around the system controller and implemented in coordination with the DPC12 (pump controllers). The system controller received user setpoint information from the HPU user interface display (pressure setpoint, and maximum flowrate) along with a pressure transducer measurement taken at a single location at the HPU's outlet. The software in the system controller then calculated appropriate displacement values for each DDP in the system and sent the necessary commands to the pump controllers, thus "centralizing" the control. Figure 4 shows the control system architecture; note that HPU outlet pressure is measured by two sensors for redundancy.

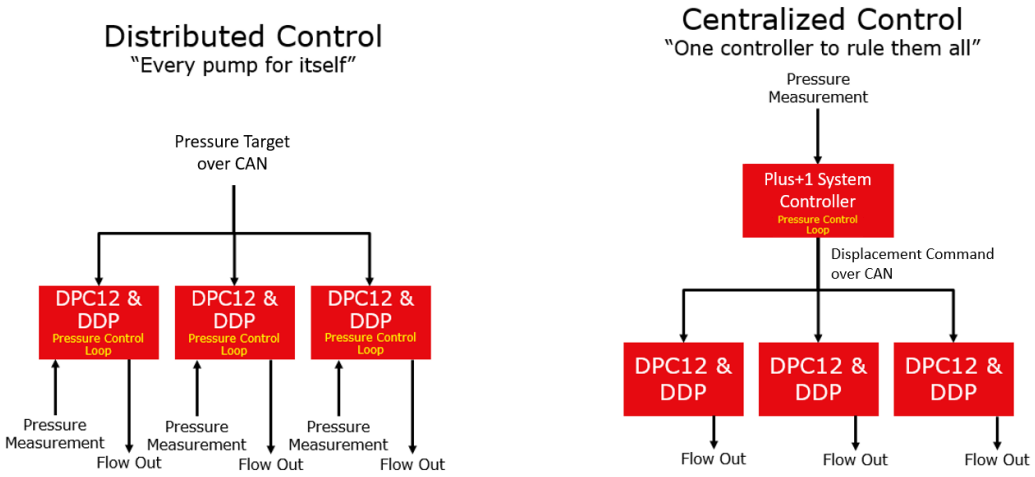

Figure 2: Distributed Pressure Control vs Centralized Pressure Control

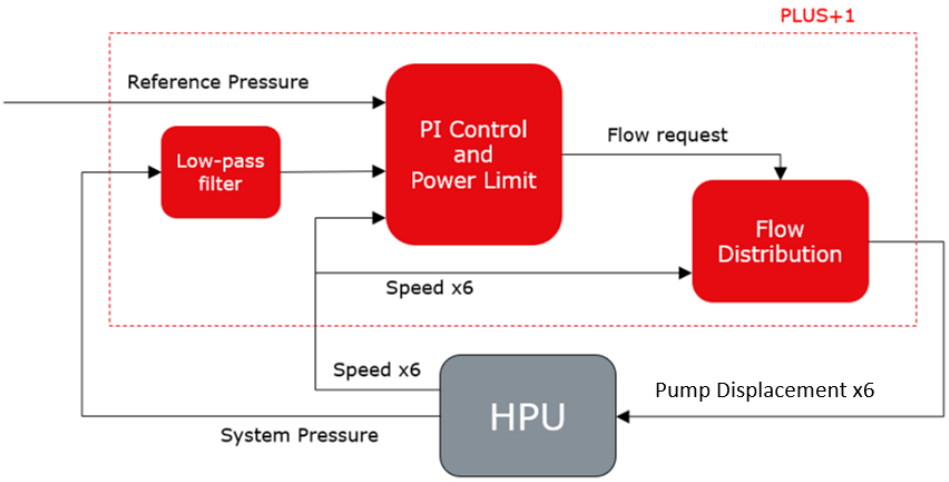

Figure 3: Centralized Control Software Flowchart

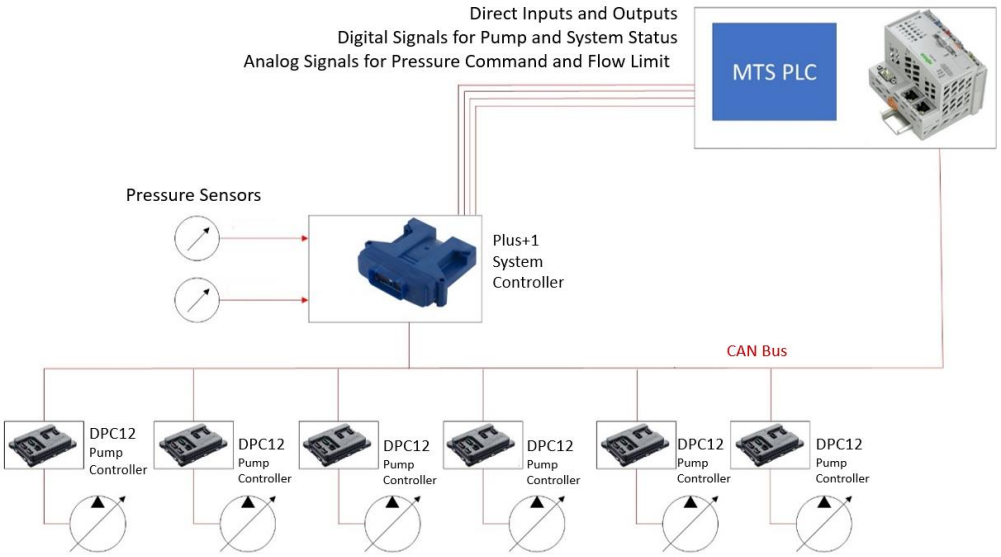

Figure 4: HPU Physical Control System Network Diagram with Centralized Control

DDP's flow output inherently produces low-frequency pressure ripple [10]. The pressure ripple frequency spectrum depends on operating condition, specifically the shaft speed and fractional displacement. Pump pressure ripple caused several problems in the distributed multi-pump system. Pump pressure ripple output due to the digital flow algorithm was amplified by the pressure control loop, so-called "self-excitation". There were undesirable interactions between the pressure control loops with each DPC12 controller responding to pressure changes from other pumps in the circuit. Furthermore, pressure pulsation at certain resonant frequencies caused standing waves in the hydraulic hoses, particularly for the longest hoses in the circuit. Altogether, the distributed control system suffered from significant noise and vibration.

Based on line resonance theory, Danfoss was able to understand and calculate the fundamental theoretical frequency at each module based on an "open on one end" boundary condition. From test results, the quarter wave, "one end open" boundary condition was selected as the ideal case approximation for the pump outlet hoses on the HPU. The hydraulic circuit downstream of the HPU junction manifold has very low hydraulic stiffness; it includes high-pressure filters, accumulators, and long 2-inch diameter distribution pipes. Pressure waves generated at the pumps reflect back from the junction manifold, almost like a pipe with one end open. The 4x factor in the fundamental frequency equation below gives insight as to why the HPU is so sensitive to line length.

Table 1: Line resonance with ideal boundary conditions. The "open on one end" case is a good approximation of the DDP outlet hoses on the HPU.

Boundary Conditions	Wavelength	Fundamental Frequency	Graph (wave displacement)
Open on both ends	$\lambda = 2L$	$f = \frac{c}{2L}$	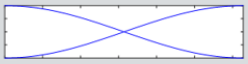
Closed on both ends	$\lambda = 2L$	$f = \frac{c}{2L}$	
Open on one end	$\lambda = 4L$	$f = \frac{c}{4L}$	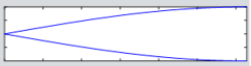

$c = speed\ of\ sound\ (m/s)$
$L = Hose\ Length\ (m)$

Table 2: Calculated fundamental frequency of pump modules based on line resonance theory.

	Module 1	Module 3	Module 4	Module 6
Fundamental frequency from theory (Hz)	54	69	79	112

assume c = 1000 m/s

Table 3: Summary of improvements with centralized pressure control.

Problem	**Solution**
Extensive tuning due to part-to-part variation between pressure transducers	Centralized control measures pressure at a single point in the circuit
Interaction between pumps increases pressure oscillation	Centralized control has one pressure feedback loop with the measurement point at the junction manifold rather than at a pump outlet port
"Self-excitation": pressure feedback loop amplifies pressure ripple	Low-pass signal filter on measured pressure
Pump pressure ripple excites line resonance	Quantization scheme: pumps with longer lines run at constant displacement levels to avoid resonant frequencies.

With the knowledge of each line's calculated fundamental frequency, a displacement quantization algorithm was developed and applied to the Centralized Pressure Control that avoids exciting resonant frequencies [11]. Operating pumps at any displacement fraction between 0 and 100% results in a range of fundamental frequencies between 0 and 12 times speed (360 Hz at 1800 rpm). These include enabling frequencies (1) which are pulsations generated by cylinders as they are activated and used. Also present, are disabling frequencies (2) which are generated by the pump as cylinders are deactivated and unused.

The quantization scheme allows one pump to continuously vary its displacement while all other pumps operate in quantized displacement steps (in this case, 0%, 25%, 75%, and 100%). The quantization scheme also considers the relative proximity of each pump to the junction manifold; the pump closest to the junction is continuously variable. Quantizing displacement commands at selected fractions produced smooth flow and low pressure ripple compared to less favorable displacement fractions. The pressure and flow requirements of the hydraulic system are still maintained by activating and phasing in pump modules as they are needed.

$$f_{enable} = \frac{n}{60} N_p F_d \tag{1}$$

$$f_{disable} = \frac{n}{60} N_p (1 - F_d) \tag{2}$$

$$n = shaft\ speed\ (rev/min)$$

$$N_p = number\ of\ pump\ pistons$$

$$F_d = fraction\ of\ total\ pump\ displacemet\ (0\ to\ 1)$$

Below, Figure 5 shows the enabling and disabling frequency outputs while operating in quantized steps. As can be seen, the quantized steps avoided outputting low frequency content below 90Hz which is in the resonant frequency range of the hoses.

Table 4: Enabling and disabling frequencies based on pump quantization value.

Displacement (%)	F_d	n (rev/min)	N_p	f_{enable} (Hz)	$f_{disable}$ (Hz)
0	0	1800	12	0	360
25	0.25	1800	12	90	270
50	0.5	1800	12	180	180
75	0.75	1800	12	270	90
100	1	1800	12	360	0

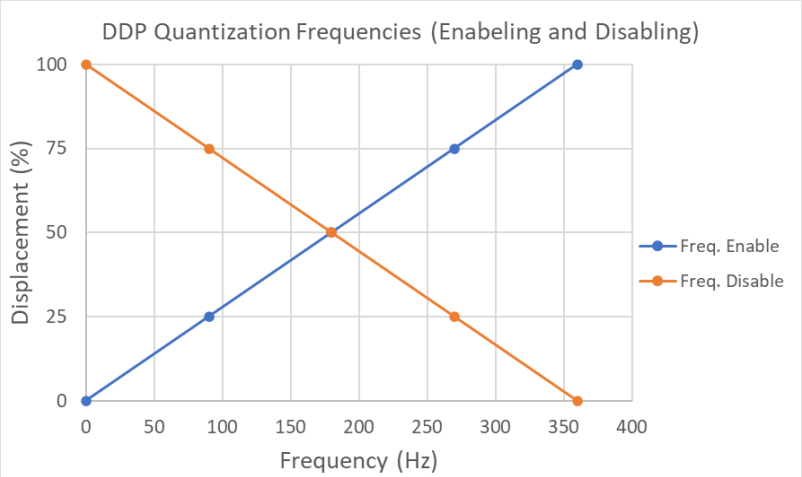

Figure 5: Quantized DDP Enabling and Disabling Frequency Outputs

3. PRESSURE RIPPLE TEST

3.1. Setup

In addition to the Ames HPU, Danfoss had periodic access to a 6-bay HPU at MTS' facility in Eden Prairie, Minnesota. This HPU dubbed "HPU62" was used for development purposes as well as to provide downstream hydraulic flow for internal test stands at MTS. As this was the only accessible 6-bay, all DDP HPU, it was essential in tuning and validating the production intent version of the centralized pressure control software architecture.

A series of controlled displacement sweep tests at 3,000 psi (207 bar) were performed utilizing a servo-controlled load valve downstream of the HPU (not pictured in Figure 7). The following pressure ripple results are an analysis of these tests.



Figure 6: MTS HPU62 (6 bay DDP)

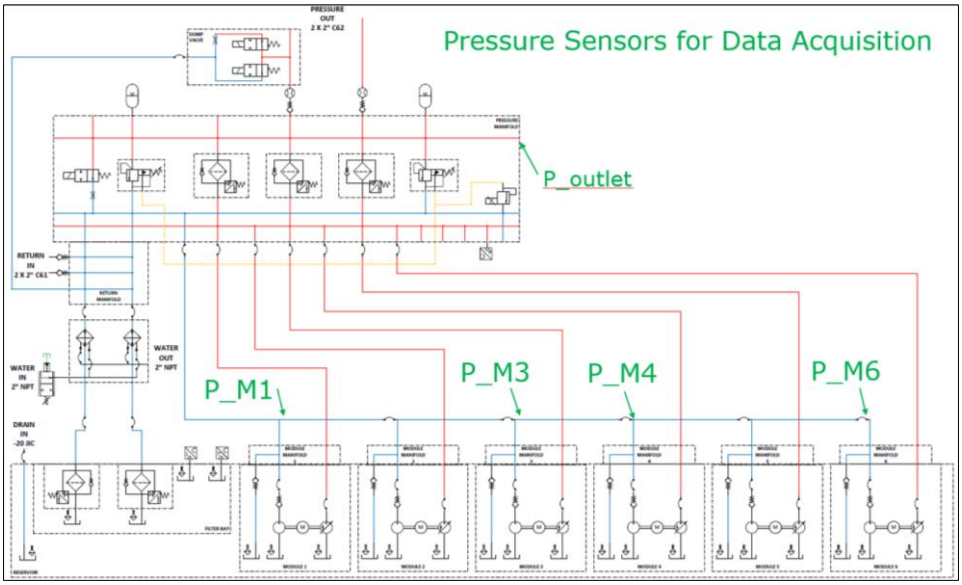

Figure 7: Hydraulic Schematic, MTS HPU62

3.2. Results

Frequency spectrum results are shown to relay the effectiveness of the centralized pressure control and how quantization changes the frequency profile of the pressure pulsations. The results presented represent data collected on MTS' HPU62. As previously show in Figure 6, module 1 is the furthest from the control cabinet and consequently has the longest hose length. Due to its length, resonance frequencies generated in this hose were the greatest source of noise and vibration when using the distributed pressure control. Much of the focus and marks of success in applying the Centralized Pressure Control revolved around improving or eliminating resonant frequencies in this module.

Power spectral density of the pressure signals is presented to show the power of the periodic signals in the frequency domain. Also shown are the post-processed average power and average band power of module pressures in the 0 to 100 Hz domain. Using this method allows for a visual and quantifiable representation of the improvements made by the Centralized Pressure Control.

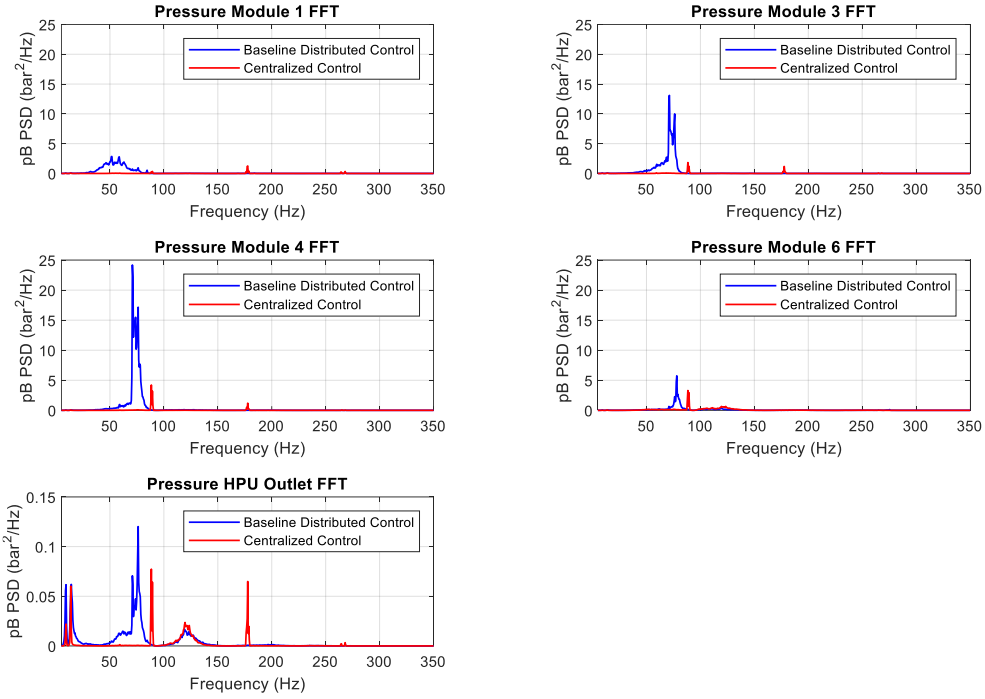

Figure 8: Pressure Spectral Density FFT Results, MTS HPU62

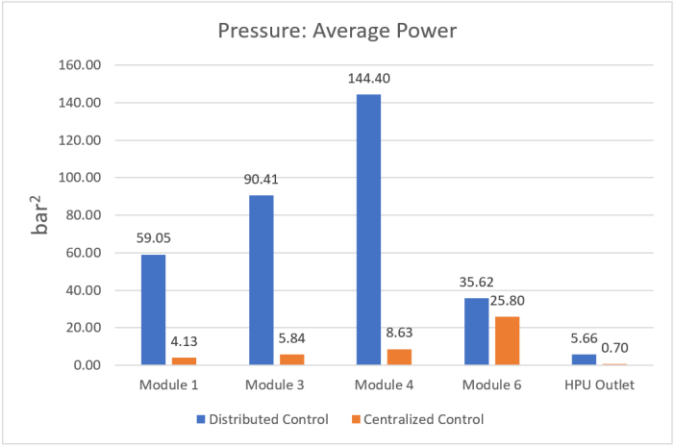

Figure 9: Average signal power (pressure ripple) per module

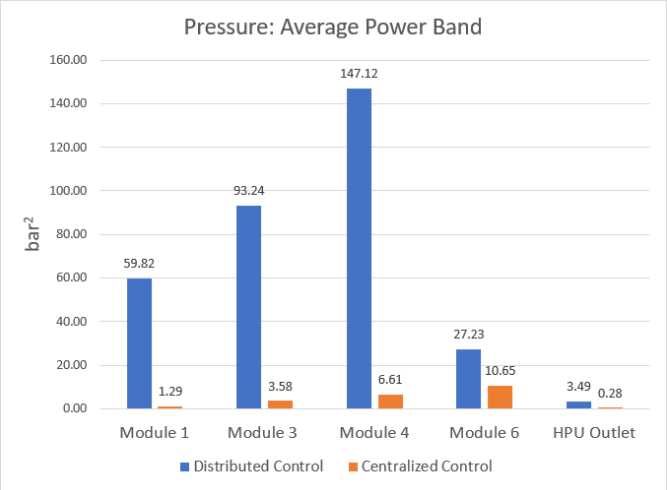

Figure 10: Average band power <100 Hz (pressure ripple) per module

Table 5: Resulting Percent Improvement by Centralized Control

Percent Improvement

Location	Pressure: Average Power (bar^2)	Pressure: Average Band Power (bar^2)
Module 1	**93%**	**98%**
Module 3	**94%**	**96%**
Module 4	**94%**	**96%**
Module 6	**28%**	**61%**
HPU Outlet	**88%**	**92%**

Figures 11 and 12 below show comparative displacement sweep tests from HPU 62. With the distributed control, the peak to peak displacement of the pumps was large as each pump controller (DPC12) tried to maintain a pressure setpoint of the DDP it controlled. The result was a high level of pressure ripple. With the centralized control utilizing quantization, a much smoother displacement characteristic could be achieved in addition to decreasing pressure ripple.

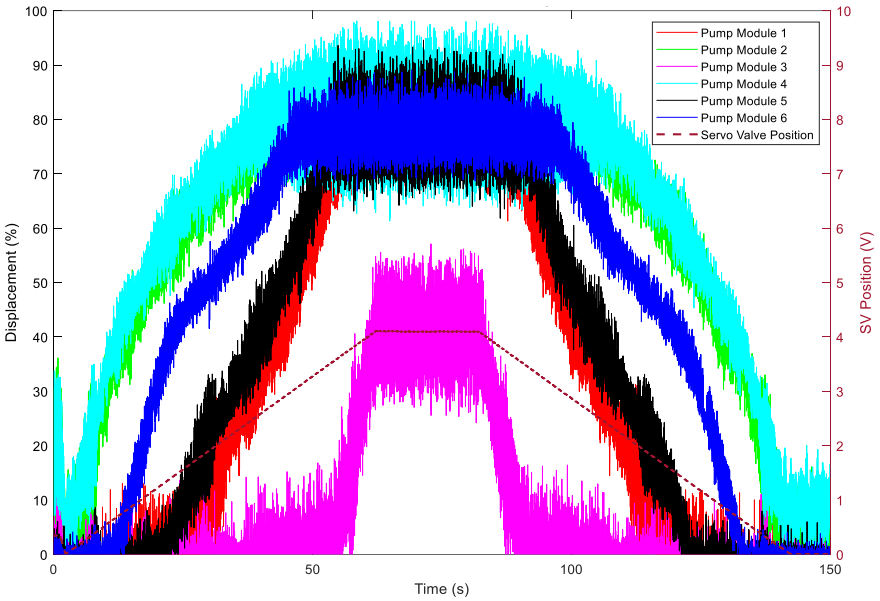

Figure 11: MTS HPU62 (6 DDP) Displacement Sweep with Distributed Control (All modules operate in continuously variable mode)

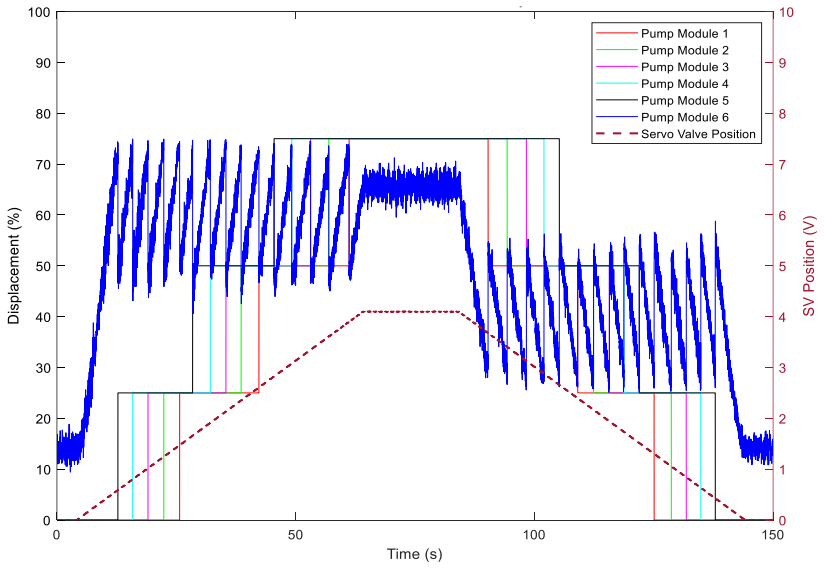

Figure 12: MTS HPU62 (6 DDP) Displacement Sweep with Centralized Pressure Control (module 6 operates in continuously variable mode while all other modules are quantized)

4. ENERGY EFFICIENCY TESTS

4.1. Drive Profile Test Setup and Results

An energy efficiency study was performed using MTS 329 Test Rig (Figure 13) running a specific repeating drive file. The rig was first powered by HPU61 which is a 6-bay HPU utilizing only swashplate pumps. The output flow, pressure, and total electrical power was recorded over the test duration (10 minutes) and then the test was repeated powered only by HPU62 which as mentioned previously, is a 6-bay HPU utilizing only DDP. HPU62 required **37.5%** less electrical energy to produce the same flow demand.

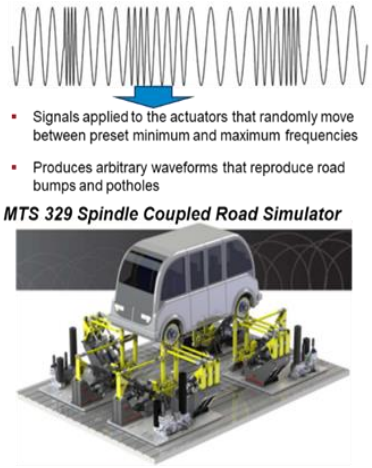

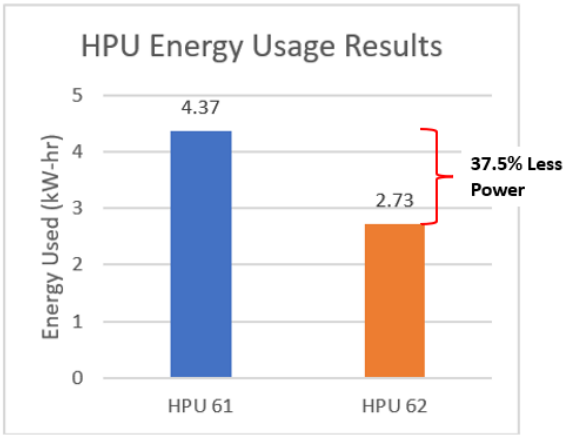

Figure 13: MTS Energy Audit Results

4.2. Calander Year Comparison Test Setup and Results

Over a calendar year of plant operations, HPU 61 and 62 were used to supply the fluid power to the MTS hydraulic distribution system (HDS). By capturing the total kW-hrs of electrical energy the HPUs consumed per day, the hours in operation per day, the total fluid output (in gallons) per day, and a consistent pressure setpoint of 3,000 psi (207 bar), the overall energy efficiency of each HPU could be calculated. Figure 14 shows the recorded fluid flow and the related HPU efficiency based on consumed electrical power analysed over the year.

HPU efficiency is the ratio of fluid energy output to electrical energy input. The observed data shows that HPU62 (All DDP) is increasingly more efficient than HPU61 (all swash) as the flow output increases.

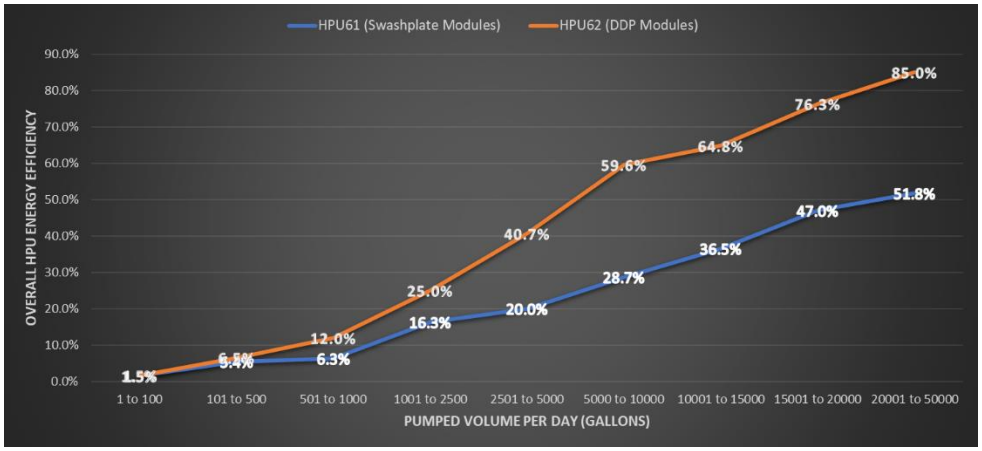

Figure 14: HPU Efficiency Based on Flow Output

5. DISCUSSION

As can be seen in the testing results, low frequency pressure pulsations in the 30 – 80 Hz range were noticeably reduced. As the primary resonance frequencies for the pump modules lie within this range, there was a significant improvement the stability of the HPU. Though it was not quantified in the report, audible noise levels seem to be lower as a result of reducing resonance frequencies, and it can be estimated that the life of mechanical components in the system (hoses, brackets, etc) will be improved. There is evidence that the magnitude of some higher frequencies were slightly increased by moving to the centralized pressure control with quantization, however, their influence on the noise and vibration of the HPU was not nearly as noticeable. With quantization, pressure wave energy still exists, but what is there shifts outside of the resonant frequency range of the hoses. This explains the reduction of lower frequency content in Figure 8, in exchange for some increases at higher frequencies.

Noticeable efficiency improvements of HPU 62 (DDP) over HPU 61 (Swashplate) were seen in both a controlled test scenario and in accumulated data over a calendar year. With a lower power consumption compared to swashplate pumps across the displacement range (0 to 100%), the HPUs equipped with DDP benefit from a compounding effect that increases with the number of DDP pumps used. This explains the larger difference between the two HPU's energy efficiencies as flow increases and the number of active DDP modules increases. As a result, HPUs with DDP can produce more fluid flow per kW-hr of energy consumed.

6. CONCLUSION

In conclusion, it has been shown through a multitude of tests, and analysis that the centralized pressure control with quantization was able to solve a large potential issue associated with pressure pulsations of DDP in the MTS HPU system. Analysis proves that the control strategy measurably reduced the magnitude of average pressure ripple power by 28% to 94% and the average pressure ripple band power by 61% to 98% depending on the analysed pump module. These pressure pulsations in the resonant frequency range of the

hydraulic lines were reduced while still meeting the flow and pressure demands required of the system.

In application, the DDP equipped HPUs showed a 37.5% reduction in energy consumption when compared to a swashplate only HPU in a controlled test scenario. Based on output flow, pressure setpoint, and known energy usage captured over a calendar year of plant operations, efficiency improvements of up to 33% were observed on HPUs with DDP compared to those with swashplate only pumps.

7. ACKNOWLEDGMENTS

In addition to the authors of this paper, it is important to mention the following individuals for their contributions to the successful implementation of DDP with centralized pressure control at MTS. **From Danfoss**: Connor Szczepaniak and Andrew Hansen for creating the groundwork of system level control software. Jeremy Edmondson and Jeremie Lagarde for their contributions to quantization implementation. Ruoshui Zhang and Wyatt Brenneman for their development, testing, and implementation of production level software. Luke Wadsley for leading commercial discussions and establishing production agreements. William Funk for his assistance in lab testing and setup. Danfoss Scotland for their support, particularly in assembling DDP hardware and various improvements to DPC12 software. **From MTS:** Scott Johnson for managing the launch of HPUs equipped with DDP. Ian Kugel for portfolio and production launch efforts. Kurt Kvistberg and Kevin Thurmes for their help in electrical and software integration. Jim Sweet for on-site testing setup and assistance.

8. REFERENCES

[1] U.S. Department of Energy (15 March 2024). Improving Pumping System Performance: A Sourcebook for Industry, 2nd Ed. Publication date May 2006. https://www.energy.gov/sites/prod/files/2014/05/f16/pump.pdf

[2] Rampen, William. 1992. The Digital Displacement Hydraulic Piston Pump. PhD Thesis. University of Edinburgh. Edinburgh, UK.

[3] Danfoss Power Solutions (15 March 2024). Digital Displacement Data Sheet, DDP096 pump and DPC12 controller.
https://assets.danfoss.com/documents/361313/AI332064420016en-000201.pdf

[4] Williamson, C. and Manring, N. A more accurate definition of mechanical and volumetric efficiencies for Digital Displacement pumps. Proceedings of the ASME/Bath 2019 Symposium on Fluid Power and Motion Control, FPMC2019.

[5] Karnell, S. and Ericson, L. Analysis of a Digital Pump with Variable Speed Drive. Proceedings of the ASME/Bath 2022 Symposium on Fluid Power and Motion Control, FPMC2022.

[6] Huova, M. and Linjama, M. Control of Multi-Pressure Hydraulic Supply Line Using Digital Hydraulic Power Management System. Proceedings of the ASME/Bath 2022 Symposium on Fluid Power and Motion Control, FPMC2022.

[7] Jimenez, C.R., Reinertz, O. and Schmitz, K. A Novel Hydro-Mechanical Control Method for Digital Pumps. The 11th Workshop on Digital Fluid Power. Edinburgh, Scotland, 2022.

[8] Pate, K.; Marschand, J.R.; Breidi, F.; Salem, T.; Lumkes, J. Design and Sensitivity Analysis of Mechanically Actuated Digital Radial Piston Pumps. Processes 2024, 12, 504. https://doi.org/10.3390/pr12030504

[9] U.S. Department of Energy (12 April 2024). Adjustable Speed Drive Part-Load Efficiency: Energy Tips, Motor System Sheet #11. Publication date November 2012
https://www.energy.gov/eere/amo/articles/adjustable-speed-drive-part-load-efficiency

[10] Dumnov, D. and Caldwell, N. A cylinder enabling algorithm for reduction in low frequency pulsation from Digital Displacement pumps. Proceedings of the ASME/Bath 2022 Symposium on Fluid Power and Motion Control, FPMC2022.

[11] Szczepaniak, C. and Legarde, J. Hydraulic circuit arrangement and control system for ganged electronically-commutated pumps. PCT patent application WO2022/226026A1, 20 April 2022.

Implement-Only Implementation of a Multi Pressure Rail System to an Agricultural Planter

Jacob Lengacher[1], Xiaofan Guo[1], Ryan Jenkins[2], Andrea Vacca[1]

[1] Purdue University, , [2] CNH Industrial

1. Abstract

Tightening emissions regulations and rising fuel costs have driven a desire across many industries for more efficient actuation systems. This is particularly true of the agricultural sector. An extremely common arrangement in this sector is the tractor and implement pairing, in which actuators on an implement are powered by a hydraulic supply system on the towing tractor. This arrangement complicates the development of energy efficient hydraulic systems, as many new system designs require modification of both machines to reap efficiency benefits. Past work by the authors' team has demonstrated great potentials for Multi-Pressure-Rail (MPR) technology involving both the tractor and implement subsystems. However, applicability of this MPR technology in a more realistic scenario where only one vehicle is equipped with such technology was not addressed.

This work proposes an implementation of the MPR technology to an agricultural planter that allows significant savings, while only modifying the implement machine. This is done by manipulating the load sense network of a stock tractor to set system pressures to those required by the MPR system. This greatly reduces the barrier to implementation of MPR technology in agriculture. The work begins by outlining the reference machine for the system, then reviews the MPR system working principle. After this, the proposed expansion to the MPR concept is laid out, and applied to the reference system. Finally, experimental validation is carried out, demonstrating on average 37% reduction in system power consumption.

2. Introduction

A growing world population corresponds naturally with increased demand for food [1]. This increased demand will naturally require more effective agricultural machinery to meet. Simultaneously, however, growing economic, environmental, and social pressures demand a reduction in carbon emissions [2]. These demands can only be reconciled by the development of more efficient agricultural systems capable of meeting the needs of the future in a sustainable way. One particularly common arrangement in existing agricultural systems is the tractor / implement pair, in which a tractor supplies power to a towed working implement. This arrangement is popular for its cost effectiveness; the most expensive components of the system are kept aboard the tractor and can be reused across a variety of operations, such as planting, seeding, baling, and tillage, while the task specific actuators and tools are kept on the less expensive implement. The state of the art for this arrangement is the LS system, in which the tractor supplies flow at a pressure set by the highest load user. While it is very efficient for tightly grouped loads and single actuators, this system often suffers serious inefficiency when

supplying multiple actuators at widely spread pressure levels, as demonstrated for the case of an exavator by Zimmerman in [3]. All of this combines to give fluid power systems in agriculture an average efficiency of just 20%, as estimated by Oak Ridge National Laboratory [4].

A wide variety of solutions aiming to improve the efficiency of the LS system, or replace it entirely have been proposed. Madau dynamically minimizes the load-sensing margin of a wheel loader system in [5] to reduce regulation losses. Tian and Stump apply a similar logic to an agricultural system in [6] also varying the margin of the compensator to enable even greater reduction in pump pressure [7]. Independent metering, in which the meter in and meter out valves are controlled independently with the goal of reducing unnecessary metering are also a common method of reducing unwanted losses [8]. Wydra pairs an independent metering LS system with an accumulator rail to allow for some load recovery potential in [9], showing in simulation up to 18.7% reduction in system energy consumption. These solutions are effective in reducing the power consumption of systems with relatively closely grouped actuator loads. They do not address the issue of load imbalance described in [3], however. Solving this problem requires more radical modifications of the system.. The most natural and extreme modification is the addition of more pumps. Grouping actuators together by load and supplying these groups independently allows for reduction in regulation losses due to load imbalance. The natural conclusion of this is primary control hydraulics, in which one actuator is controlled by one pump, either by varying the speed or displacement of the pump. The latter method, displacement control, as implemented in [10] and [11] eliminates the need for throttling speed control, and ensures each actuator is supplied with exactly the pressure and flow required by the user. The former method has seen much interest in recent years as electrification, and thus variable-speed pumps (ePumps) have become a more common part of off-road actuation. Qu proposes an architecture for a small loader using an ePump for primary control of an actuator, reducing system power consumption by greatly reducing throttling losses and recovering energy from the lowering of a boom [12] [13]. All of these solutions have the potential to drastically reduce the power consumption of these hydraulic systems by doing away with regulation losses entirely, and enabling energy recovery from overrunning loads. The limitation of the system is cost, however. The more actuators a system has, the less affordable and plausible primary control methods become. Busquets attempts to resolve this, proposing a pump sharing algorithm that allows for fewer pumps to be used to supply the system's actuators in [14]. This strategy relies heavily on transient, well-characterized duty cycles, like those present in construction excavators, making them less suited for application to agricultural applications, where there may be many actuators with uncertain drive cycles.

Another option is switching to a pressure supplied logic. Pressure supplied systems decouple the flow requirements of the actuator and the pump, having the pump set a rail to a chosen pressure. This arrangement can be inefficient if poorly designed, but with proper design it can be quite efficient [15]. One option to reduce the throttling losses of pressure supplied systems is the use of hydraulic transformers. Proposed by Achten in [16], this concept mimics electrical

systems by utilizing a pair of variable displacement hydraulic pump/motors connected in tandem. One serves as the motor, taking flow from a fixed constant pressure rail, to power the second, which pumps up to the pressure and flow required by the actuator. This architecture does away with throttling losses entirely and enables load recovery, but at the cost of somewhat increased component losses. This concept can be implemented in smaller, less dynamic forms as well, to generate multiple fixed rails from one main supply as seen in [17]. Li et al propose an architecture in which a constant pressure system is used, with small ePumps boosting or bucking pressure to that required by the actuators [18] [19], following a similar strategy to this.

A middle ground can be found in multi-pressure rail systems (MPR). These systems split the hydraulic supply into multiple pressure-supplied rails, then use selection valve sets to dynamically adjust the rails attached to each actuator inlet and outlet. In [20], Lumkes proposed this idea with the goal of improving the controllability of pressure supplied systems, though power savings potential and controller design were not considered. It was then utilized to great effect by the STEAM excavator in [21] where the MPR system's decoupling of actuator and prime mover speed enabled not only reduction in throttling losses, but engine management strategies and energy recovery as well.

Relevant to this work, the authors of this work propose an implementation of an MPR architecture specific to the agricultural implement case in [22], using a stationary test rig to assess several options for the hydraulic supply and control logic. Then, in, [23] the proposed architecture was fully fleshed out and demonstrated in simulation. Finally, in [24] the system's functionality and power savings potential were demonstrated on a full-scale prototype machine. This implementation of the architecture takes advantage of the slow dynamics of the agricultural system to further optimize throttling losses by dynamically selecting the rail pressures. This enables the potential for a reduction of up to 48% in system power consumption. However, one limitation of this work, and much of the rest of the prior work done towards improving the efficiency of hydraulic systems, is that it requires the modification of both the hydraulic supply and the valving. As discussed above, one of the fundamental advantages of the tractor / implement system utilized in agriculture is that one tractor can supply and work with a wide range of implements, keeping costs lower. Most of the previously discussed solutions require modifications to both the supply system- the tractor- and the valving – the implement. This represents a significant barrier to adoption of such systems, as the costs of replacing both the tractor and the implement simultaneously is restrictive.

This work aims to address this challenge by proposing an MPR architecture for an agricultural implement that improves system efficiency using only modifications to the implement and can be supplied by an unmodified state of the art tractor. Such a system could serve as a "bridge" implement, capable of working first with existing tractors, and gaining some savings potential, and gaining even further benefits when paired with a purpose-built MPR Tractor. This allows for a staggered adoption of MPR technology, lowering the cost barrier to entry and likely

improving adoption rate. To do this, first, the reference tractor/implement system will be outlined, and the MPR architecture proposed in [24] will be briefly reviewed. After this, the working principle of the proposed expansion to the system will be laid out. This principle is applied to the reference case, and then validated via experiments taken on a full-scale prototype machine in real field conditions.

3. Reference System

The reference machine for this work is a Case-IH 2150 Agricultural Planter supplied by a New Holland T8.435 Agricultural Tractor. This implement pairing is representative of the sort of system used across a wide range of North American farms for planting operations on soybeans and corn, and is a worthwhile case for consideration as a result. The tractor is outfitted with a simple pre-compensated load-sensing circuit able to supply implements via two different types of connections. The primary method is the Remote Valves, which are pre-compensated load-sensing valves with quick connections at the outlet and internal load-sense pickups. The second is the Power Beyond Manifold, which uses a larger quick-connect, no control valve, and an external load-sense connection, relying on the actuator to control the amount of flow required. The hydraulic architecture of the tractor can be seen in Figure 1 below.

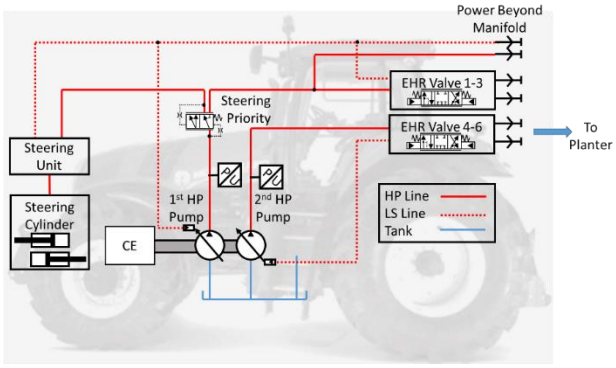

Figure 1: Simplified Tractor Schematic

The planter uses hydraulic motors and cylinders to carry out the majority of the actuations assorted with planting, as shown in Figure 2 below.

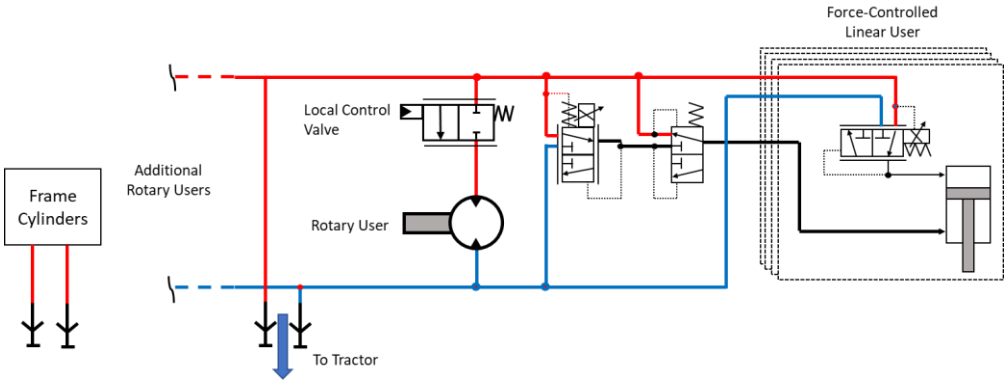

Figure 2: Simplified Planter Schematic

The actuators in use on the planter are outlined below. The steady state rotary and steady state linear functions run continuously during planter operation carrying out a range of operations, such as providing planting material to the planting row units (Bulk and Vacuum fans, Fertilizer pump), powering the row units (compressor and alternator), and ensuring consistent ground contact and planting depth (HDPCs and WMCs). The transient linear functions run far less consistently, serving only to raise and lower the planter toolbar during headland turns, and reconfigure the frame arrangement for transport.

Table 1: Hydraulically Actuated Planter Functions

Steady State Rotary Functions	**Purpose**
Alternator	Power planter electronics
Bulk Fill Fan	Move seed to row units
Compressor	Power planter pneumatics
Fertilizer Pump	Provide fertilizer to row units
Vacuum Fan	Provide suction for planting
Steady State Linear Functions	**Purpose**
Hydraulic Down Force Cylinders (HDPCs)	Maintain consistent planting depth
Weight Management Cylinders (WMCs	Keep wings in contact with ground
Transient Linear Functions	**Purpose**
Frame Cylinders	Raise and lower toolbar to begin / end planting process

The planter has a large number of actuators that must run continuously, so to reduce the number of connections between the tractor and planter, it supplies all of the steady state planting functions via a pair of hydraulic quick connects, connected to the remote valves on the tractor. The remote valves are opened fully, and flow is then controlled via the local flow control valves on the planter. The frame cylinders are then supplied more traditionally using the remote valve for metering control. This arrangement allows for more complex control on the planter and makes the planter largely independent of the control capabilities of the tractor, but it comes at the cost of system efficiency. A conflict in control occurs due to the position of the load-sense pickup between the two control valves. As shown in Figure 3 below, the load-sense pump attempts to maintain a fixed margin across the remote valve, effectively controlling flow through that valve. Simultaneously, the local flow control valves, either via hydraulic compensation or an electronic controller, attempt to control flow to the actuators by throttling from the outlet of the remote valves. This leads to a conflict; the pump upstrokes, increasing flow through the remote valve to try to meet its margin. Simultaneously the control valve compensators close down, trying to maintain their own margins leading to a net increase in the line pressure between the valves. This increase in pressure is passed through the LS network to the pump, causing it to further increase its displacement, and continue the cycle. Equilibrium is reached when the LS pressure reaches the LS pressure for the system. For most applications, pressure saturation is reached first, with the relief valve in the LS line limiting the pump displacement and system pressure. This leads the system to behave not like an LS system, but like a constant pressure system, with the rail pressure set at the pump's maximum pressure, leading to very low system efficiency but good control characteristics. These control benefits owe to the decoupling of the supply flow rate from the actuator flow rate which allows actuator speed to be controlled entirely by the local flow control valve.

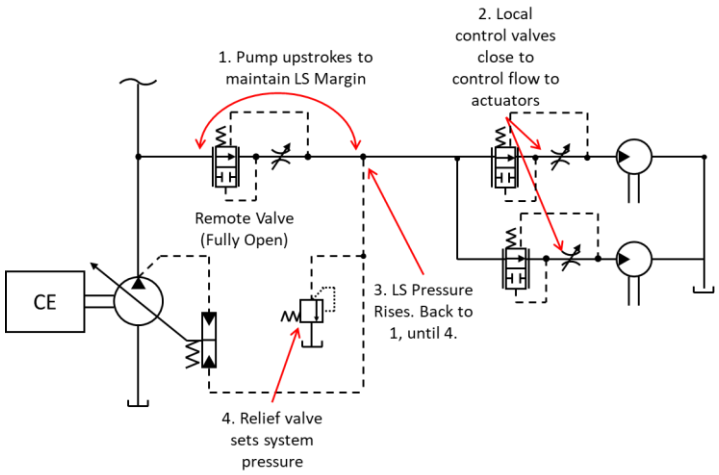

Figure 3: Control Conflict due to Series Control Valves

4. MPR Architecture Review

The MPR Architecture, as presented in [24] aims to improve the system efficiency while maintaining its good controllability by switching from a flow-controlled logic like LS to a pressure-controlled logic. The proposed system, shown in Figure 4 is supplied by 2 pressure rails whose pressure can be controlled by varying the flow provided to them. Thanks to the long lines and large capacitance of the planter case, this can be achieved without the need for accumulators. Rotary actuators are supplied via pressure selection and control valve manifolds which control what rails are connected to the inlet and outlet of each actuator, and then control the speed of the actuator by throttling flow from those rails. The force controlled linear actuators (the HDPCs and WMCs) are connected permanently from HP to LP due to their continuous high load requirements.

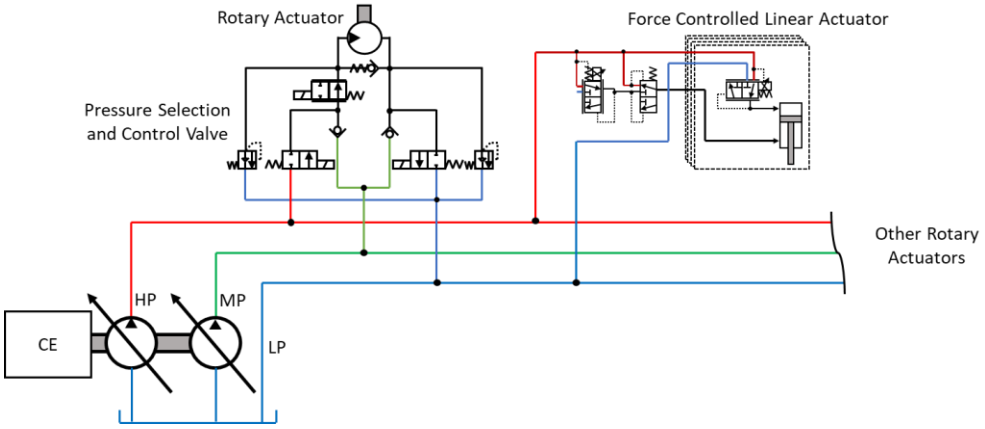

Figure 4: MPR Architecture Overview

The pressure levels of the different rails are optimized to minimize the total system throttling losses while ensuring all actuators get the required flow, following a logic laid out in [24]. In this work, two control logics were proposed. The first varies both the high and medium pressure levels to fully optimize the system throttling losses, called “Variable HP MPR”. The second logic stemmed from the recognition that the downforce system always requires close to maximum pressure, resulting in the high-pressure rail spending most of its time very close to that level. This fact is leveraged by the second control logic, called “Fixed HP MPR” to reduce control effort and improve system stability by locking the high-pressure rail at the maximum system pressure and only optimizing the medium pressure rail. [24] demonstrates that this logic improves dynamic behavior at only a slight cost in terms of reduced savings. To optimize the pressure levels and operating modes of the system a controller was devised. It assigned the HP rail to either a pressure just exceeding the required pressure of the highest load user (for Variable HP MPR), or to the system maximum pressure (for Fixed HP MPR). The medium pressure rail was then selected by calculating the system losses at key points based on the pressure requirements of the actuators and discontinuities in the loss cost function. After the rail pressures were selected, each actuator was assigned to the rail combination that minimized system loss. The previously proposed architecture required modification to both the tractor and the implement, with the control logic and switching being carried out on the planter, and the tractor being relied upon to provide the required pressures. This represents a substantial barrier to potential implementation, due to requiring changes to both systems. This work proposes an alternative method of achieving the Fixed HP MPR control logic on an implement that can be achieved using an unmodified, state-of-the-art tractor.

5. Compatible MPR System

There are some requirements for this unmodified tractor. Principally, it must have remote valves, a power beyond manifold, and a two-pump, divided LS system. This is true of the

reference tractor for this work, and a wide range of other machines currently on the market within the 300-400 hp size range of the reference system, and in larger vehicles. The pressure control is then implemented by "tricking" the tractor's LS system into enacting MPR logic. The high-pressure level is set by exploiting the control conflict discussed previously; the HP rail is connected to one of the LS circuits via the remote valves, and the remote valves are opened fully. The control conflict drives the LS pump to maximum pressure, giving the HP rail its desired pressure level. The MP rail still requires variable control, however, which is achieved using the power-beyond manifold. The MP rail is supplied by the power beyond port, and thus the second LS pump, and uses an electronically regulated pressure to control the LS pressure seen by the power beyond manifold's LS port. This working principle applied to the reference machine is shown in Figure 5 below.

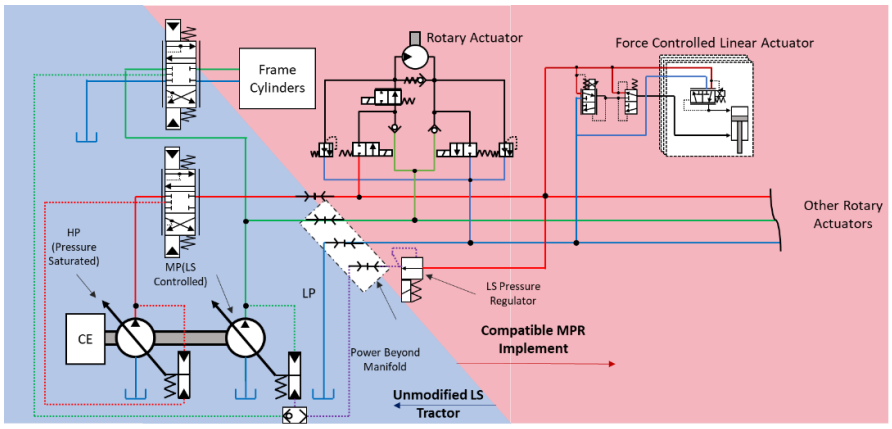

Figure 5: Implement-Only MPR Working Principle

As can be seen, the HP and MP rails are connected and controlled as outlined above. Notably, the transient linear functions are connected to the same pump as the MP system, ensuring their LS functionality is maintained. With this supply arrangement, the MPR implement can be left largely unchanged from that previously outlined, using pressure selection and control valves to handle speed control and mode switching for the rotary functions, while the force controlled linear functions are connected continually from HP to LP.

It is worth noting that this implement architecture also be compatible with an older-model tractor, via an expansion to the onboard control system, switching the system to use only HP and LP rails. Such a system would likely gain very few savings but would still be able to function as usual. This potential is valuable, and represents a direction for further investigation.

6. Experimental Setup

To validate system functionality and savings potential, the proposed architecture was then implemented on the reference machine. This modification was done in addition to the

modifications presented in [24]. Figure 6 below shows the ISO schematic of the modified planter, including key sensor locations, along with the structure of the DAQ and control system for both the tractor and planter.

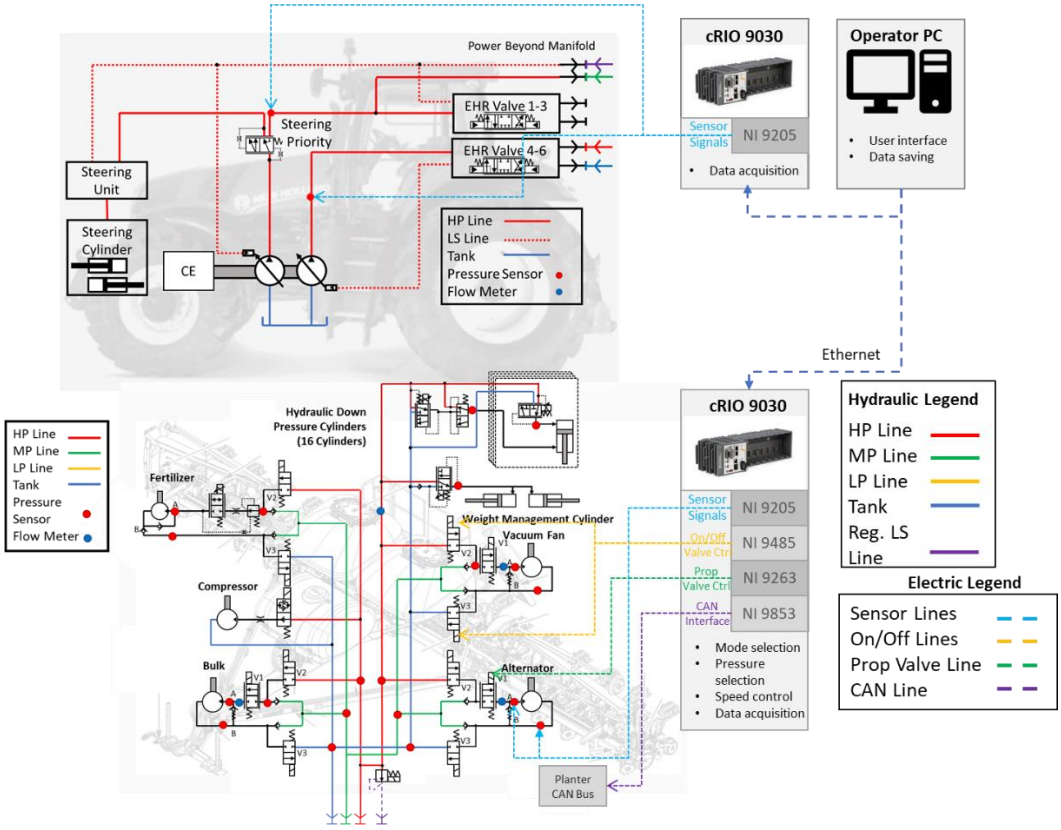

Figure 6: Implement-Only MPR Architecture Applied to Reference Machine

As can be seen above, the control logic was implemented using an NI CRio system. As in previous work, two CRios were used, one on the planter and one on the tractor. For this system, however, all control was carried out on the planter, with the tractor system serving only to monitor the behavior of the tractor hydraulic supply. The hydraulic modifications to the implement, beyond those shown in prior work, are shown in Figure 7 below. The hydraulic modifications made are implemented as a sort of adapter, connecting the MPR implement's quick connectors to the correct ports on the tractor and siphoning flow from the HP line to run the regulator

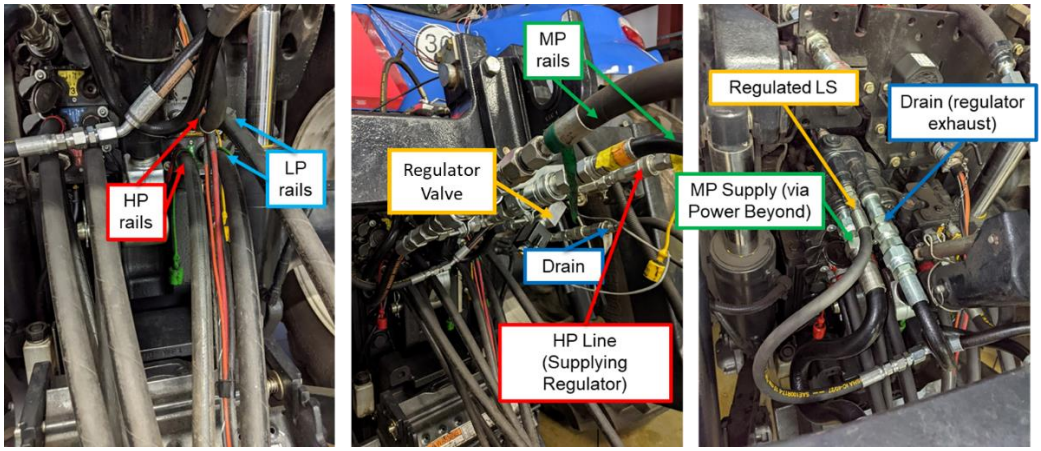

Figure 7: Compatible MPR Adapter Hydraulic Implementation

To assess the effectiveness of the system, and ensure a fair comparison against prior work could be made, the same working cycle as used in [24] was used. This cycle was provided by the vehicle manufacturer and contains two common working conditions; one corresponding to normal planting conditions, and one corresponding to a more aggressive high-speed planting case. Each test case was run at several engine speeds. The overall test set is shown in Table 2 below.

Table 2: Normalized Validation Drive Cycle

Drive Cycle Name	Crop	Vehicle Speed (%)	EngineSpeed (%)	Vacuum (%)	Alternator (%)	HDPC Force (%)	Wing Force (%)	Bulk Fill (rpm)	Liquid Fert. (gal/ac)
Baseline - Popcorn	Popcorn	50%	71%	57%	60%	50%	55%	70%	13%
			86%						
			100%						
High Speed - Popcorn	Popcorn	83%	86%	71%	80%	100%	55%	70%	13%
			100%						

Tests were taken in a similar method to prior work, on a quarter-mile test field strip at a Purdue farm, as shown in Figure 8. Each test was begun by starting the recording software, lowering the planter toolbar, planting for the length of the field, then raising the toolbar before stopping the recording. This ensured that ample steady state regions could be recorded to assess the power savings potential of the system at each condition.

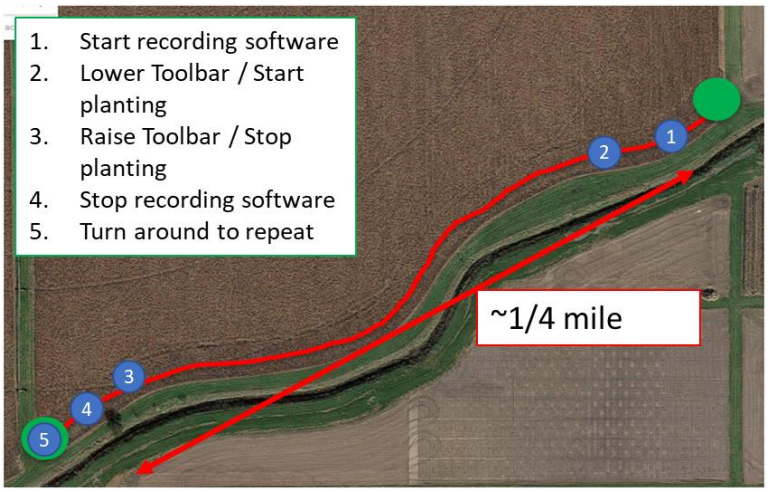

Figure 8: Test Field and Plan

7. Experimental Results

Figure 9 below shows the time series behavior of the MPR system, including several actuator modes and rail pressure levels. The system pressure behavior is as expected, with the HP rail locked at maximum pressure, and the MP rail settling to roughly 50% of the system maximum pressure. Initially, all the rotary actuators connect from MP to LP, however once the fertilizer has reached its target speed, it no longer needs to accelerate, but only to keep spinning, dropping its load enough to switch to connecting from HP to MP. Meanwhile the HDPCs are supplied from HP to LP.

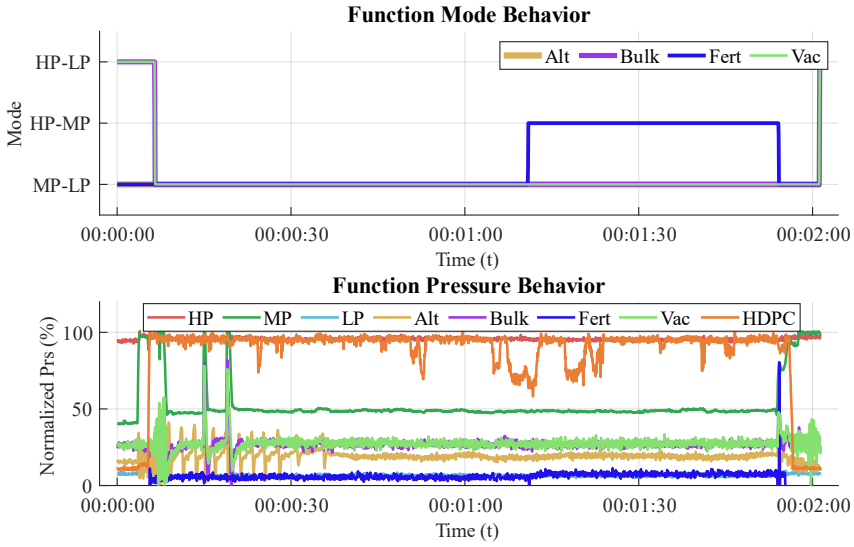

Figure 9: Time Series Results for Implement-only MPR System

All functions switch to be supplied by HP to LP at the beginning (0:00-0:10) and end (1:55-2:00) of the cycle. This coincides with the toolbar of the planter, which is powered by the MP pump (as shown in Figure 5) being lowered and raised, and occurs because the MP pump's LS functionality is maintained. When the bar is moved, the MP pump pressure rises, placing the MP and HP rail pressures close together and leading the system to function at a suboptimal point. This is only a transient region, however, and the system quickly stabilizes and returns to more optimal operation. Table 3 below shows the system's improvement in power consumption over the baseline system, compared with the two-machine, Fixed HP MPR version of the system presented in [24] averaged across the tests taken.

Table 3: Pump Power Consumption Results Compared with Tractor / Implement MPR

Operating Condition	**Pump Power Reduction (%)**	
Solution:	Tractor / Planter MPR [24]	Implement-Only MPR
Normal	*49.9*	*39.3*
High-Speed	*37.1*	*34.5*

As can be seen, the implement-only MPR architecture does not achieve the same level of savings as the two-machine MPR system. There are several reasons for this. The first is that where the implement-only system supplies the HP rail via the remote valves, which have compensators, metering areas, lock check valves, and other features to ensure breadth of

usability, the two-machine system uses specially made MPR quick connects which bypass these features. This allows for smaller pressure losses from the pump to the actuator, allowing the two-machine system to operate at a slightly lower pump pressure to maintain equivalent rail pressures. The second source of this loss is the LS regulator, which siphons a small amount of flow from the HP rail continuously. This flow is small, but since it comes from the HP line it does have a noticeable impact on the overall system efficiency.

8. Conclusion

This work set out to design an MPR-based architecture capable of improving the efficiency of a tractor-planter system while only modifying the implement. An expansion to the basic agricultural MPR architecture was proposed allowing the system to function in tandem with a standard LS tractor that met certain requirements. The system working principle was detailed and a schematic presented. This architecture was then implemented on a full-scale prototype planter and tested with an unmodified tractor. Field test results demonstrated an average 37% power savings over the unmodified system. This improvement was less than that demonstrated in [24] for a two-machine MPR system, but still substantial, and its requiring modifications to only one machine represents a significantly smaller barrier to adoption.

9. Acknowledgement

This work was carried out in partnership with CNH Industrial, and funded by DOE Project DE-EE0009201, *A New Approach for Increasing Efficiency of Agricultural Tractors and Implements.*

10. References

[1] D. Wrachien, B. Schultz and M. Goli, "Impacts of population growth and climate change on food production and irrigation and drainage needs: A world-wide view," *Irrigation and Drainage*, pp. 981-995, 2021.

[2] A. Masia, "Greenhouse Gas Emissions-Off Highway Vehicles Solutions and Future Trends," Maha Fluid Power Research Center , Lafayette, IN, 2022.

[3] J. Zimmerman, M. Pelosi, C. Williamson and M. Ivantysynova, "Energy Consumption of an LS Excavator Hydraulic System," in *ASME International Mechanical Engineering Congess and Exposition*, 2009.

[4] L. J. Love, E. Lanke and P. Alles, ""Estimating the impact (energy, emissions and economics) of the US fluid power industry,"," Oak Ridge National Laboratory, Oak Ridge, TN, 2012.

[5] R. Madau, A. Vacca and F. Pintore, "Energy Saving on a Full-Size Wheel Loader Through Variable Load Sense Margin Contro," *J. Dyn. Sys., Meas., Control.,* 2021.

[6] X. Tian, P. Stump, A. Vacca, S. Fiorati and F. Pintore, "Power-Saving Solutions for Pre-Compensated Load-Sensing Systems on Mobile Machines," in *Transactions of the ASABE. 64(5),* 2021.

[7] P. Stump, X. Tian, J. Lengacher, R. Jenkins and S. Fiorati, "Combined Pump and Compensator Margin Control for Pre-Compensated Load Sensing Architecture: Implementation and Experiments," in *Fluid Power Systems Technology*, Sarasota, FL. USA, 2023.

[8] Z. e. a. Quan, "A Survey of Powertrain Technologies for Energy-Efficient Heavy-Duty Machinery," *Proceedings of the IEEE,* vol. 109, no. 3, pp. 279-308, 2021.

[9] M. Wydra, G. M. and B. Weiss, "An Approach to Combine an Independent Metering System with an Electro-Hydraulic Flow-on-Demand Hybrid-System," in *The 15th Scandinavian International Conference on Fluid Power*, Linköping, Sweden, 2017.

[10] J. Zimmerman, Toward Optimal Multi-Actuator Displacement Controlled Mobile Hydraulic Systems, West Lafayette: PhD Thesis: Purdue University, 2012.

[11] N. Daher and M. Ivantysynova, "Yaw stability control of articulated frame off-highway vehicles via displacement controlled steer-by-wire," *Control Engineering Practice,* pp. 46-53, 2015.

[12] S. Qu and e. al., "A high-efficient solution for electro-hydraulic actuators with energy regeneration capability.," *Energy,* vol. 216, 2021.

[13] S. Qu, D. Fassbender, E. Busquets and A. Vacca, "Formulation, Design and Experimental Verification of an," in *Global Fluid Power Symposium*, 2020.

[14] E. Busquets, Advanced control algorithms for compact and highly efficient displacement-controlled multi-actuator and hydraulic hybrid systems, West Lafayette: Purdue University: PhD Thesis, 2016.

[15] W. Shen, H. Huang, Y. Pang and X. Su, "Review of the Energy Saving Hydraulic System," *IEEE Access,* pp. 665-669, 2017.

[16] P. Achten, Z. Fu and G. Vael, "Transforming future hydraulics: a new design of a hydraulic transformer," in *The Fifth Scandinavian International Conference on Fluid Power*, Linkoping, Sweden, 1997.

[17] J. Lengacher, P. Stump, A. Vacca, R. Jenkins, F. Pintore and S. Fiorati, "Application of the Hydraulic Transformer Concept to Reduce Throttling Loss in a Multiple-Function Load Sensing System," in *ASME/BATH 2023 Symposium on Fluid Power and Motion Control*, Sarasota, Florida, 2023.

[18] P. Li, J. Siefert and D. Bigelow, "A HYBRID HYDRAULIC-ELECTRIC ARCHITECTURE (HHEA) FOR HIGH POWER OFF-ROAD MOBILE MACHINES," in *Proceedings of the ASME/BATH 2019 Symposium on Fluid Power and Motion Control*, Longboat Key, FL, USA, 2019.

[19] J. Siefert and P. Li, "Optimal Control of the Energy-Saving Hybrid Hydraulic-Electric Architecture (HHEA) for Off-Highway Mobile Machines," *IEEE TRANSACTIONS ON CONTROL SYSTEMS TECHNOLOGY*, 2021.

[20] J. Lumkes and J. Andruch, "Hydraulic Circuit for Reconfigurable and Efficient Fluid Power Systems," in *The 12th Scandinavian International Conference on Fluid Power*, Tampere, Finland, 2011.

[21] M. Vukovic, R. Leifeld and H. Murrenhoff, "STEAM - A hydraulic hybrid architecture for excavators," in *10th Int. Fluid Power Conference*, Dresden, Germany, 2016.

[22] X. Guo, R. Madau, J. Lengacher, A. Vacca and R. Cardosa, "Multi-Pressure Rail System Design with Variable Pressure Control Strategy," in *The 13th International Fluid Power Conference*, Aachen, Germany, 2022.

[23] X. Guo, J. Lengacher and A. Vacca, "A Variable Pressure Multi-Pressure Rail System Design for Agricultural Applications," *Energies*, vol. 15, 2022.

[24] X. Guo, J. Lengacher and A. Vacca, "Quantification of energy savings due to the adoption of of Multi-Pressure Rail technology in an Agricultural Tractor – Implement system through experiments," *Energies*, 2024 (Under review; draft available upon request).

An Innovative Approach for Controlling Fluid Power Systems Using Extended Reality

Marvin R. Durango[1], Jose A. Solorio[1], Gina C. Baquero[2], Andres Rincon[3], Jose Garcia-Bravo[1*]

1. *School of Engineering Technology, Purdue University, West Lafayette, IN., USA.*
2. *Mechanical Engineering, Universidad Javeriana de Colombia, Bogotá, Colombia.*
3. *Computer Engineering, Universidad de Los Andes Bogotá, Bogotá, Colombia.*

** Corresponding author: jmgarcia@purdue.edu*

Abstract.

This article showcases the application of Mixed Reality (MR) technology for communicating and controlling a fluid power system. The proposed system uses a combination of virtual and physical elements to provide users with an interactive and immersive experience with the HoloLens 2, a head-mounted device that overlays digital information onto the real-world environment allowing them to control components in real-time through a computational model developed through the Unity game engine. Visual Studio 2022 and Windows 11 SDK are the other tools implemented to generate a digital twin that can be used to manipulate a pneumatic excavator. In this system, the user can receive immediate feedback from the actions performed by the system while displaying process variables (e.g., pressure, flow, and acceleration). In addition, the project includes a physical component in the form of a hydraulic cylinder, which serves as the output of the mixed reality control system. This system requires establishing a bilateral connection between the HoloLens 2 and the microcontroller, for example, the ESP232 boardbase. Therefore, the electronic hardware will communicate wirelessly using a Wi-Fi network connection (API).

Additionally, the proposed interface is designed to be intuitive, easy to use, and versatile, allowing for a wide range of fluid power system applications (e.g., manufacturing, mobile, industrial, and robotics). The project demonstrates the potential of mixed reality technology for enhancing how humans interact with machines and equipment in the real world. The inherent traditional risks of using hydraulic technology will be mitigated.

Keywords. Mixed Reality, IoT, Fluid Power Systems, HoloLens 2.

NOMENCLATURE

API	Application Programming Interface
AR	Augmented Reality
MR	Mixed Reality

VR	Virtual Reality
VA	Virtual Annotations
SDK	Software Development Kit
HDM	Head Mounted Device
MRTK	Mixed Reality Tool Kit
PWM	Pulse Width Modulation
P_{out}	Output pressure after pressure regulator
P_{in}	Input pressure before pressure regulator
K_1	Pneumatic resistance of orifice 1
K_2	Pneumatic resistance of orifice 2
C	Compressibility of the system
q_1	Inlet flow in pressure regulator
q_2	Outlet flow from pressure regulator
F	External cylinder force
k	Spring constant
x	Piston displacement
v	Piston velocity
A	Area of piston bore

1. INTRODUCTION

When speaking of fluid power, one prominent example comes to mind: Excavators. A heavy-duty machine that exemplifies quite well the systems and principles characteristic of this field. They can dig, carry, and move heavy loads, benefiting from one principle, Pascal's law. In most hydraulic applications, the fluid medium is usually oil. However, some commercial machines leverage air power when the application involves grabbing or crushing light objects.

Hydraulic excavator have been studied and analyzed at length, whether if is for better efficiency, controllability or safety, studies in tele-operation have focused on remotely operating excavators, however, the use of Head Mounted Devices (HMD) for doing so is unheard off. The number of personnel qualified to operate fluid power equipment is decreasing more and more. Moreover, even when personnel is available to be trained, safety and cost are other drawbacks to overcome. To bridge the gap between lack of skilled workers and the increasing demand for these jobs, researchers [1],[2],**Error! Reference source not found.** have resorted to the use of Virtual Reality (VR) and other simulated experiences to train and upskill employees. In fact, the aviation industry has successfully used this approach to train pilots for decades [4].

Interaction with a fluid power system comes with certain risks and costs. For example, the pressure handles in these systems are around 4,500 psi for a commercial one when working with oil. Even if the process fluid is air, the risk is not mitigated. Consequently, the risks associated with an excavator operation are a constant factor regardless of the fluid process. As for the required skills to operate heavy equipment, the user should account for time needed for training, this time amounts to increased cost of operation and reduced allocation of resources which decreases productivity. In addition, the location where the training is carried out is expected to ensure safety. These factors lead to an increment in cost and productivity, not to mention that traditional training is not engaging. The virtualization of the training is an appealing alternative to lower operation costs, develop new skills, and provide a safe learning environment. However, a common concern when proposing a virtual learning environment is the inclusion of hands-on experience. This kind of virtualization is supposed to secure a platform with hands-on experience and teleoperation. Although non-technology replaces the need to interact with physical objects, it is through interaction that users acquire new skills. In combination with teleoperation, users can grab new skills and develop them in a safe environment as often as required.

Some companies have adopted virtual training modalities with a long track record in fluid power applications. These virtual modules or packages are intended to be used in virtual environments, specifically head-mounted devices (HDM). For instance, Festo [5] has a training program where MR assists in assembling pneumatic circuits and more complex systems. This company also reinforces that computer-aided systems prevent users from life-threatening or hazardous situations (environment and machinery). Furthermore, CIRO VR, a package developed by Festo, provides an experience close to real-life situations by enabling real-time simulation.

Other companies, such as Bosch, are pioneers in developing Mixed Reality packages. They conduct maintenance programs remotely, such as those reported by Neges et al. [6]. As a result, workers can execute tasks without using physical manuals or devices to interfere with their job. The company claims that mixed reality reduces the cost of training, keeps trainees safe, and, more importantly, the experience combines the real world and the 3D representation of the fluid power system [7].

These cases only address one side of the problem; they provide a safe way to interact with machines to minimize inherent risk for operation. However, the teleoperation of components is missing: the capacity to operate the machine remotely from a distance away from the equipment. Teleoperation in a mixed reality environment integrates different fields, communication protocols, digital twins, and control. Some researchers have successfully implemented and documented various architectures for the remote operation of actuators and fluid-power systems reliably and safely using different AR methods. An example of work in this field is the work presented by Fu et al. [8]. They proposed an integrated digital twin approach to support optimal excavation trajectory generation. The proposed architecture included the simulation of machine motion in a virtual environment to verify the feasibility of the generated trajectory and prevent accidents caused by structural interference. The effectiveness of the proposed approach was demonstrated via field tests with a scaled UCS prototype. The results showed that the proposed digital twin-based trajectory generation procedure could generate the optimal excavation trajectory in real-time and achieve better performance than manual operation [8].

Teleoperation has become a popular way to enhance worker safety in hazardous construction workplaces. Lee et al. [9] identified and presented the challenges, tasks, and opportunities in teleoperating excavators through rigorous analysis of past studies. The outcomes provide insights into future directions for teleoperation in construction workplaces, emphasizing the need for human-centered research to develop seamless human-robot interaction. Despite the complex and uncertain nature of construction workplaces, there has been an increasing interest in automation [9]. Hong et al. [10] examined the effects of virtual annotations (VAs) on the teleoperation performance of an excavator in a virtual environment. They performed some tests with an experimental group finding that the use of VAs helped the users to have significantly fewer collisions under adverse visual conditions compared to the control group without VAs. Their research suggests that VAs can improve an operator's situational awareness. However, they acknowledged the observed adverse effects, such as increased collisions on the back of the equipment. They concluded that further research is necessary to understand the mechanisms of forming a visual base and assessing an operator's cognitive load.

Sekizuka et al. [11] developed a system to remotely control a hydraulic excavator using virtual reality to evaluate operator skills. The results are promising. They can tell if the excavator is operated by an expert or not. However, the setup consists of several pieces of hardware, such as: a laptop computer, a joystick, camera, and excavator. All these devices limited the operator's range of motion and the remote control's windows.

A Mixed Reality headset can overcome the above shortcomings. A camera, virtual buttons, and the laptop’s compute power are embedded in one Head Mounted Device (HMD), HoloLens 2.

The present study aims to create a teleoperation model for controlling a scaled pneumatic excavator from a mixed-reality environment, to the best of the author’s knowledge no other experimental work in literature has reported the remote operation of an excavator using a HDM, other teleoperation applications have relied on cabins and screens to replicate the movements of the excavator, however the use of MR technology allows the user to be immersed in a real environment (i.e. construction site) without the need to be onboard the machine. For this proof of concept, the HoloLens2 device is used to manipulate one of the actuators of a miniature model of an excavator. In addition, the ESP232-based board serves as a bridge to enable communication between the HMD and the excavator. Finally, a user interface is designed to track operational variables, such as inlet pressure and displacement of the actuator, in real time.

This article is divided into four major sections, the second section discusses in detail the materials needed to build a prototype fluid machine and the necessary mechanical and electronic components as well as the software needed to demonstrate control of the fluid power system. The third section presents the reader with the qualitative demonstration of the integration of a physical pneumatic system and the means to control such system trough a wireless connection using mixed reality. This third section also proposes a methodology for improving the control of the system. A subsection of part three is dedicated to describing and testing a simple proportional control architecture to move the actuators in the pneumatic arm. The fourth and final section of the paper provides concluding remarks from this research and ideas for the improvement of this project.

2. MATERIALS AND METHODS

The present study focuses on the remote operation of the actuators of the scale model pneumatic excavator shown in Figure 1. The excavator model is partially operated from a Mixed Reality (MR) environment (Figure 4). The full system has four degrees of freedom or operation modes: swing, boom, arm, and bucket [12]. The valves control the compressed air flow to the cylinders, which power the excavator's arms and bucket movement. Thus, it is possible to move the pneumatic excavator in four directions: Boom lift and drop, arm curl in and out, bucket curl in and out, and swing arm to rotate the whole machine just as a real excavator would.

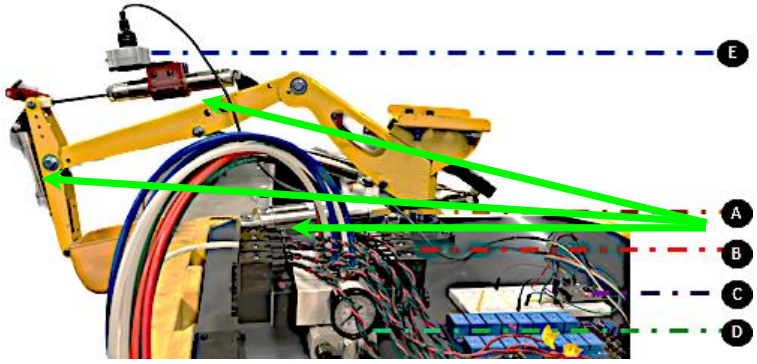

Figure 1 Pneumatic excavator model.

The model system comprises four pneumatic directional valves, four actuators, a Wi-Fi microcontroller module, and a pressure gauge. The position of each cylinder is set based on the differential pressure between its two chambers. The schematic diagram of the excavator shown in Figure 1 shows the various components of the machine and their connections (Table 1).

Table 1 Components and description of system elements

Part	Component	Reference	Qty	Description
A	Pneumatic actuators	A24040D	4	Double Acting with different diameters
B	Directional valves	AVS-523C1-120A	4	3-position 5-port (4-way) spool valve, center-closed
C	Wi-Fi microcontroller Module	ESP232	1	Provide Wi-Fi functionality.
D	Pressure gauge	G15-BD160-8LB	1	Monitor and control pressure [0-160 PSI]
E	String Potentiometer	SPD-4-3	1	Measure linear position using a flexible cable

A string potentiometer allows measuring the position of the piston as the cylinder extends; the string is attached to a stationary object mounted on the arm as shown in Figure 2. As the cylinder moves, it pulls the wire, which causes the spool to rotate and change the resistance value of the potentiometer. In addition, the string potentiometer is parallel to the cylinder's direction of movement, so when the cylinder moves, it causes the potentiometer's core to move along with it, changing its resistance value to track the position of the arm, a calibration process was conducted and shown later in Figure 5.

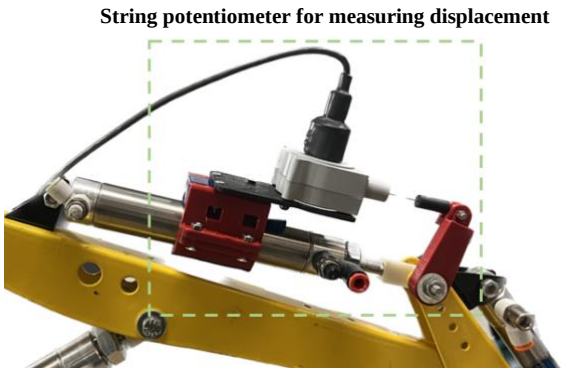

Figure 2 String potentiometer linear measurement.

To achieve this goal, a communication protocol via Wi-Fi is established between a microcontroller, ESP232 baseboard, and the HMD device, HoloLens 2, the configuration used for configuring this system is detailed in the next section.

2.1. System communication

The ESP232 Development Kit module bridges the Wi-Fi network and the relays on the electronics board to drive the valves. This development board includes a microcontroller, and a WIFI module, allowing it to connect to a WIFI network and communicate with other devices. An 8-relay module board is physically connected to the ESP232 module, where each solenoid is connected to a separate relay. When activated, the relay closes the circuit, enabling the voltage to pass to the solenoid to open or close the valves.

Virtual buttons created in the game engine Unity, are wirelessly connected to the ESP232 module to provide a user interface for controlling the valves and movement of the excavator. Each button is virtually connected to a separate pin on the ESP232, which is programmed to activate the corresponding relay and control the solenoid. With the levers for each solenoid, the user can quickly start the valves and control the movement of the excavator. Specifying the IP address and port number in the Unity code is essential to establish the connection to send commands to the ESP232 microcontroller module to operate the cylinders via the relay board.

2.2 Electronics and control

In addition to its mechanical components, the system shown in Figure 3 included a Wi-Fi module microcontroller, this device enabled the connection to a wireless network and, thus, two-way data transmission between a HoloLens 2 headset and the ESP232 microcontroller. Furthermore, the 8-relay module and the ESP232 Wi-Fi module, which are integral components of the system, have a shared operating voltage of 5V. This advantageous feature eliminates the need for additional hardware to couple the voltages, simplifying the wiring process and reducing the system's complexity. In addition, each relay serves the purpose of activating a corresponding solenoid controlling the corresponding valve's opening and closing, enabling reliable control of the flow through the system. It is worth noting that the pneumatic valves used in this excavator demonstrator model are not proportional, this fact makes the realization of precise displacement of the actuators nearly impossible.

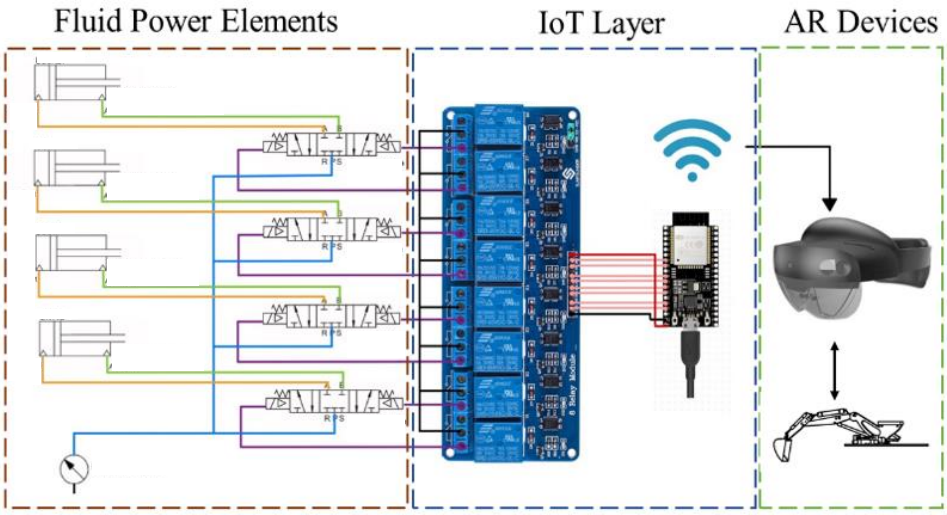

Figure 3 System architecture.

2.3 Mixed Reality scene

For this project, creating a visual interface that allowed the user to send and receive data from the hydraulic system was crucial. Therefore, a development tool such as Unity was an excellent choice for implementing a mixed-reality application. Unity is a game engine that allows developers to create virtual environments and immersive experiences for multiple platforms. Furthermore, Unity has a physics engine that enables user interaction with virtual objects, on top of easy integration of third-party tools such as Microsoft Mixed Reality Toolkit (MRTK), which receives user input solely using hand gestures from a HoloLens headset [6]. Hence, allowing users to manipulate digital content to control external physical machines, such as the excavator model in the present study. With this tool, the user can teleoperate the excavator and visualize an overlaid digital representation of the excavator position measurements, or others such as operating pressure or as in this study, the stroke of the main pneumatic actuator, the boom.

3. RESULTS AND DISCUSSION

3.1. User Interface

The fluid power system was divided into four segments, each controlled by a pneumatic cylinder with three states: extended, retracted, and at rest. To control the different excavator parts, two buttons were assigned to each cylinder (arm, bucket, boom swing). Depending on the virtual button pressed by the operator, a unique coded variable was sent to the ESP232 baseboard microcontroller to execute the desired action (Figure 4). Additionally, a designated button was provided to clear all commands and set the pneumatic actuators at rest (all relays off). The displacement or position of the cylinder is displayed in real time on the HMD screen. The user can see the reading from the sensor in the excavator arm as time elapses. Similarly, the actuation of the solenoids to operate valves are all shown in the user interface as labeled in Figure 4. The buttons are color coded and numbered to imply extension (state 1, red) or retraction of the cylinders (state 2, blue).

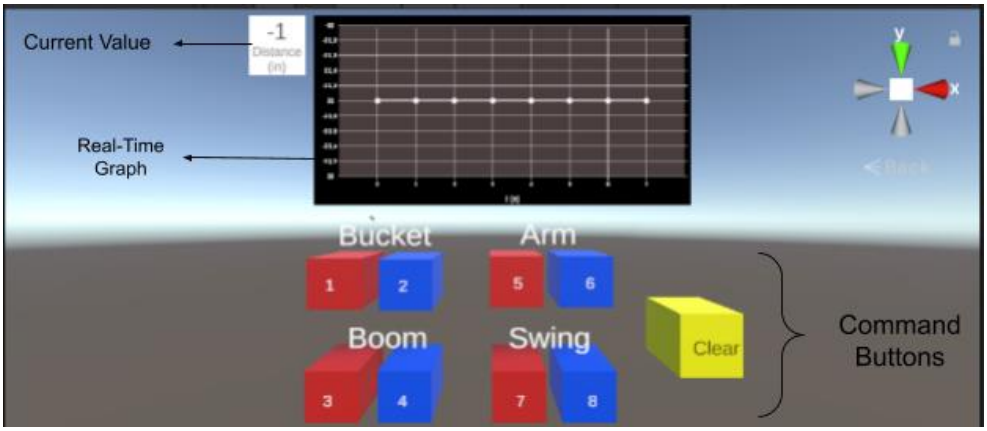

Figure 4 Unity interface with buttons and graph features.

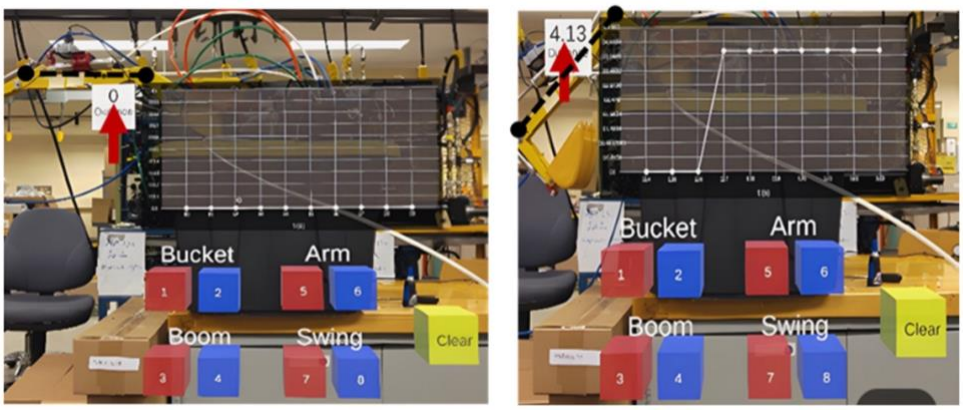

Figure 5 Retracted and extended position of the arm

Additionally, the application counts with a real-time graph that displays detailed relevant metrics of the arm. This attribute allows the users to keep track of the arm stroke in real-time, as seen on Figure 5. The instrumentation and control of the arm used on the microcontroller will be addressed in the subsequent sections.

3.2. Sensor Calibration

The potentiometer attached to the excavator's arm was used to determine the stroke of the pneumatic arm. A calibration process was conducted to convert the potentiometer's voltage into a displacement function that depends on the potentiometer output. The resulting position signal from the potentiometer is transmitted by the Wi-Fi module and presented as a virtual object in the MR environment on the HMD.

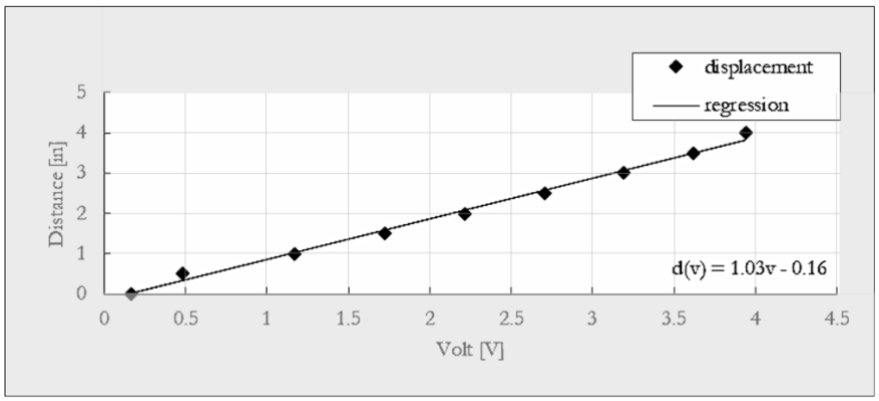

Figure 6 Calibration curve.

Figure 6 shows the calibration curve, the equation that correlates the voltage and the strokes is an input function coded on the microcontroller that, in return, sends the converted metric to HoloLens 2. The information can be displayed in real-time exactly as shown in Figures 4 and 5.

3.3. Modelling of Proportional Control

Given that the proportional control of the model excavator is not achievable using the available 5/3 pneumatic valves installed in the system, a pseudo digital approach is proposed to achieve accurate position control, Figures 6 and 7.

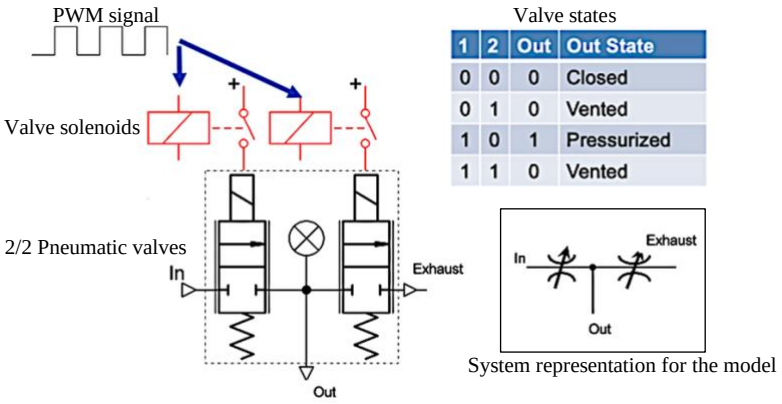

Figure 7 Electronic Pressure Regulator configuration.

This digital control is proposed to be implemented in a future iteration of the excavator model and consists of the installation of four electronic pressure regulators and single acting spring returned actuators, this, will have the objective of achieving precise position control by using PWM-like control (Figure 7). Initially, the system pressure is allowed into the inlet valve 1. The intermediate port connecting the inlet and exhaust valves is monitored by a pressure transducer, additionally a secondary control loop is added to monitor the position of the actuator (Figure 9) and simulated using Matlab Simulink.

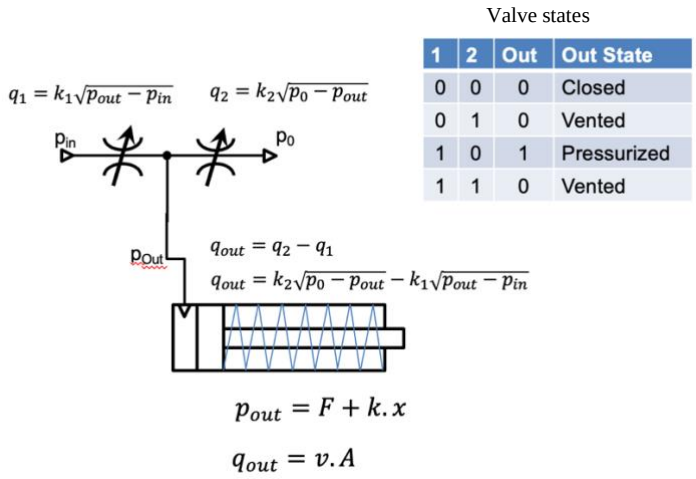

Figure 8 Pneumatic Position control using PWM regulation.

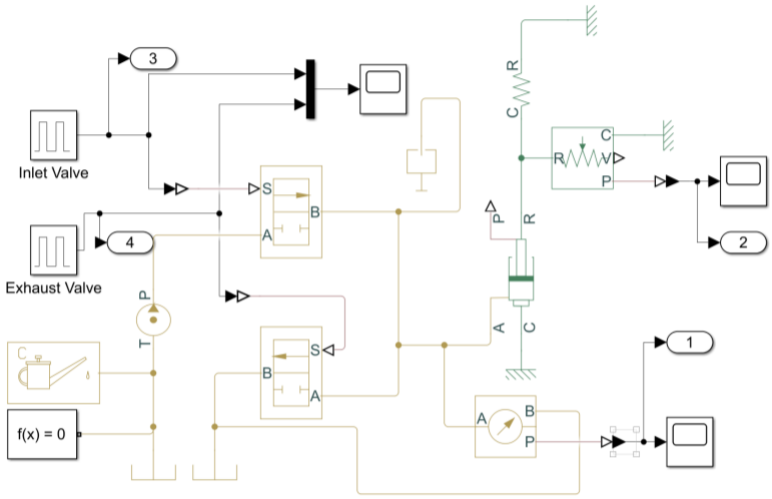

Figure 9 Simulink preliminary model of PWM position control.

Figure 10 shows the resulting simulation for the operation of the pressure regulator valves for achieving digital control of the system. This preliminary environment neglects the effects of compressibility of the pneumatic system. It is expected that this system will be implemented in the Unity environment to produce true remotely operated control of the position from a MR environment, including the compressibility effect with a first order system as shown in Equation 3.1.

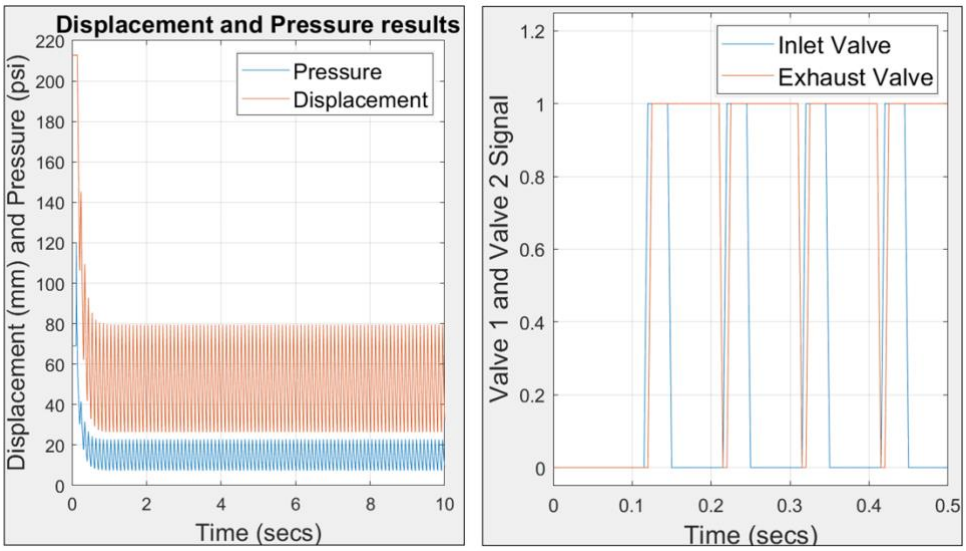

Figure 10 Preliminary position control.

$$\frac{dp_{out}}{dt} = \frac{K_1}{C}\sqrt{p_{in} - p_{out}} - \frac{K_2}{C}\sqrt{p_{out}} \qquad (3.1)$$

In this proposed physical model, an accumulator is used to simulate the effects of the system compressibility. An experimental validation model has been built to simulate and validate the model as shown in Figure 11. The resulting validated model will be input into the existing MR environment in the Unity MRTK to account for the effects of compressibility and for achieving pseudo proportional control using digital valves.

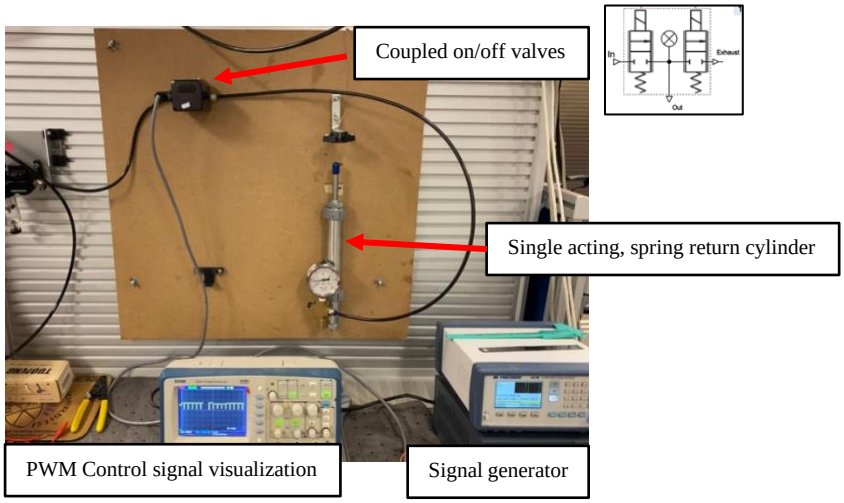

Figure 11 Experimental setup proposed to validate the compressibility effect.

4. CONCLUSIONS

Teleoperation of a pneumatic excavator was accomplished from the HoloLens 2 HMD. This is conducive to a safe operation because the user is not directly on board or in close contact with the physical scale model. Moreover, key performance indicators, namely the displacement is presented as a plot in real-time on the Mixed Reality environment.

The ability to visualize information in real-time from a safe control environment opens other paths. For example, as a future work, the XR tool can provide information of a fluid power system to evaluate its performance, or can help to take action timely in case of an impeding failure, additionally, this technology opens the door to a potential scenario where one operator may be able to control more than one machine, which would in turn increase productivity of certain lower risk operations. Another potential future work is the representation of the excavator as a digital twin. Then, the user can reproduce the different trajectories of the arm and obtain the optimal path from the digital twin. Thus, the operator can apply the optimal path of the physical object, reducing the operation's energy and time.

An approach for achieving precise position control of the actuators is explored and proposed and will be implemented as part of the future work and loaded into the Unity environment to produce a method for proportional control using Mixed Reality headsets.

5. REFERENCES

[1]. R. Sekizuka, M. Ito, S. Saiki, Y. Yamazaki and Y. Kurita, "Evaluation System for Hydraulic Excavator Operation Skill Using Remote Controlled Excavator and Virtual Reality," 2019 IEEE/RSJ International Conference on Intelligent Robots and Systems (IROS), Macau, China, 2019, pp. 3229-3234, doi: 10.1109/IROS40897.2019.8968213.

[2]. Wallmyr, M., Sitompul, T.A., Holstein, T., Lindell, R. (2019). Evaluating Mixed Reality Notifications to Support Excavator Operator Awareness. In: Lamas, D., Loizides, F., Nacke, L., Petrie, H., Winckler, M., Zaphiris, P. (eds) Human-Computer Interaction – INTERACT 2019. INTERACT 2019. Lecture Notes in Computer Science(), vol 11746. Springer, Cham. https://doi.org/10.1007/978-3-030-29381-9_44

[3]. Assaf, H., & Vacca, A. (2023). Virtual reality tool to support fluid power curriculum. Computer Applications in Engineering Education, 31(5), 1137-1158.

[4]. Allerton DJ. The case for flight simulation in general aviation. The Aeronautical Journal. 2002;106(1065):607-612. doi:10.1017/S0001924000018261

[5]. D. J. Chanchay, J. D. Feijoo, J. Llanos, and D. Ortiz-Villalba, "Virtual Festo MPS® PA Workstation for Level and Temperature Process Control," Lecture Notes in Electrical Engineering, vol. 762 LNEE, pp. 164–180, 2021, doi: 10.1007/978-3-030-72208-1_13/FIGURES/14.

[6]. M. Neges, S. Adwernat, and M. Abramovici, "Augmented Virtuality for maintenance training simulation under various stress conditions," Procedia Manuf, vol. 19, pp. 171–178, 2018, doi: 10.1016/J.PROMFG.2018.01.024.

[7]. J. R. Oliveira, "Insight About the Use of AR and VR for Trainees: The Case of Bosch Company," https://services.igi-global.com/resolvedoi/resolve.aspx?doi=10.4018/978-1-7998-2874-7.ch011, pp. 178–192, Jan. 1AD, doi: 10.4018/978-1-7998-2874-7.CH011.

[8]. T. Fu, T. Zhang, Y. Lv, X. Song, G. Li, and H. Yue, "Digital twin-based excavation trajectory generation of Uncrewed excavators for autonomous mining," Autom Constr, vol. 151, p. 104855, Jul. 2023, doi: 10.1016/J.AUTCON.2023.104855.

[9]. J. S. Lee, Y. Ham, H. Park, and J. Kim, "Challenges, tasks, and opportunities in teleoperation of excavator toward human-in-the-loop construction automation," Autom Constr, vol. 135, p. 104119, Mar. 2022, doi: 10.1016/J.AUTCON.2021.104119.

[10]. Z. Hong, Q. Zhang, X. Su, and H. Zhang, "Effect of virtual annotation on the performance of construction equipment teleoperation under adverse visual conditions," Autom Constr, vol. 118, p. 103296, Oct. 2020, doi: 10.1016/J.AUTCON.2020.103296.

[11]. R. Sekizuka, M. Ito, S. Saiki, Y. Yamazaki, and Y. Kurita, "System to Evaluate the Skill of Operating Hydraulic Excavators Using a Remote Controlled Excavator and

Virtual Reality," Front Robot AI, vol. 6, Jan. 2020, doi: 10.3389/FROBT.2019.00142.

[12]. Mishler, L. A., Garcia, J. M., & Lumkes, J. H. (2011). “Engaging Pre-College Students in Engineering Using Hands-on Micro-Processor Controlled Portable Fluid Power Demonstrators.” In 2011 Louisville, Kentucky, August 7-10, 2011 (p. 1). American Society of Agricultural and Biological Engineers.

Reduction of Dynamic Loads in Piston Compressors Through the Use of Mechanical Resonance

Wieslaw Fiebig and Willy Prastiyo

Wroclaw University of Science and Technology, Wroclaw, Poland
wieslaw.fiebig@pwr.edu.pl, willy.prastiyo@pwr.edu.pl

Abstract.

In reciprocating compressors that use the slider-crank mechanism, the input torque experiences significant fluctuations due to the inertial forces of the reciprocating components. In this paper, a technique to improve the dynamics of reciprocating compressors is presented using the phenomenon of mechanical resonance. The study involves a comparative analysis using multibody dynamics simulations (MBD), and comparisons of experimental investigations are performed in two main operating setups: 1. piston without an additional coil spring element; and 2. piston with an additional coil spring element. System performance is analyzed by examining the forces in the joints, the inertia torque, and the estimated power demand of the two main sets of components in various simulation scenarios considering different configurations of friction, pressure load, reciprocating mass, and spring stiffness. The MBD model is prepared and simulated in ADAMS. The findings of this study confirm that the resonance setup offers a significant advantage, exhibiting a lower inertia torque amplitude compared to the conventional setup, primarily attributed to the compensation of inertia forces by spring forces. Not only by the use of steel spring, in the case of the work of a compressor system, resonance can also be attained by the process of air compression. The stiffness of the air spring in the cylinder itself can be harnessed to achieve resonance. In this case, the influence of pressure on the natural frequency of the system is taken into account. To simulate the dynamics of fluid, an equivalent multidomain system of the model is made in Simcenter Amesim.

Keywords: resonance, vibration, slider-crank, mechanism, dynamics.

1. INTRODUCTION

Resonance is mostly known as an unwanted phenomenon in a mechanical system. Nevertheless, despite the common concern that the resonance phenomenon in most mechanical structures is undesirable, a number of studies show that resonance in a mechanical system can in fact be utilized to obtain a beneficial outcome. Franca & Weber [1] have studied the use of mechanical resonance in a drilling technique called resonance hammer drilling. In their study, the resonance phenomenon was used to increase the penetration rate (ROP) in hard rock drilling. Despotovic et al. [2] show that the vibratory

conveyor resonant mode with electromagnetic excitation consumed less energy when maintaining the system in the resonance state. Aiple, M., et al. [3] show that if the excitation frequency and the resonance frequency are the same, with a flexible (Series Elastic Actuator-based) hammer, teleoperators can reach peak velocities of more than 200% higher than peak velocities with a rigid hammer. Compared to a rigid hammer driven by the same velocity source, the peak velocity and peak energy of a flexible hammer are substantially higher when the mechanical resonance of the hammer is excited. Fiebig & Wróbel [4], based on their simulation and experiment, found that the impact machine that uses mechanical resonance with a resonant block and spring element has a significant reduction in energy demand compared to the conventional machine that uses slider-crank and flywheel coupling.

When a slider-crank mechanism is activated, in which the rotation of its crank drives the linear movement of the slider, the reaction torque arises when the slider translationally accelerates or decelerates [5]. A higher fluctuation of the reaction torque and forces on joints due to inertial forces [6] can, in fact, result in higher energy dissipation [7] that arises from joint friction and internal stresses of the components. In the end, higher energy dissipation will lead to lower system energy efficiency [8].

In this paper, the approach to improving the dynamics of the slider-crank mechanism will be done through the modification of the conventional slider-crank design [9, 10] and the arrangement of the system operation within the resonance frequency. In particular [11], the reciprocating compressor (or piston compressor) is discussed as a practical study example because it represents the common application of a slider-crank mechanism that has varying external loads [12, 13]. The numerical simulation method, which includes multibody dynamics (MBD), is used to model, analyze, and estimate the performance of the designed system. In addition, a physical prototype is built for verification. The contributions of this study are as follows: (a) The method of utilizing mechanical resonance in the slider-crank mechanism is described, especially for the case of a reciprocating compressor. (b) Comparative results of the system with and without the use of mechanical resonance are presented.

2. MODELING OF THE RECIPROCATING COMPRESSOR

As shown in Figure 1, the presented model consists of the crankshaft, as the crank; and the crosshead, push rod, and piston. The coil springs envelope the rails, fixed to the main frame and the crosshead so that, at equilibrium position, the slider is in the middle of the stroke. Moreover, since MSC ADAMS cannot simulate the dynamics of the fluid, the Simcenter Amesim model has been developed to obtain the compression forces on the piston.

The model in Simcenter Amesim will be shown in Fig. 2. The electric motor rotates the crankshaft, which is then converted by the connecting rod into translational motion to move the crosshead and the piston. When the piston moves from the TDC (top dead centre) to the BDC (bottom dead centre), the pressure differential causes the inlet valve to open; the air is sucked into the cylinder. The air inside the cylinder is then pumped out through the outlet valve into the tank. A relief valve is used to limit the upstream pressure within the pneumatic circuit, thus protecting the pneumatic components from overpressure. Each simulation step size and duration in the multidomain system should be synchronized with the multibody dynamics simulation.

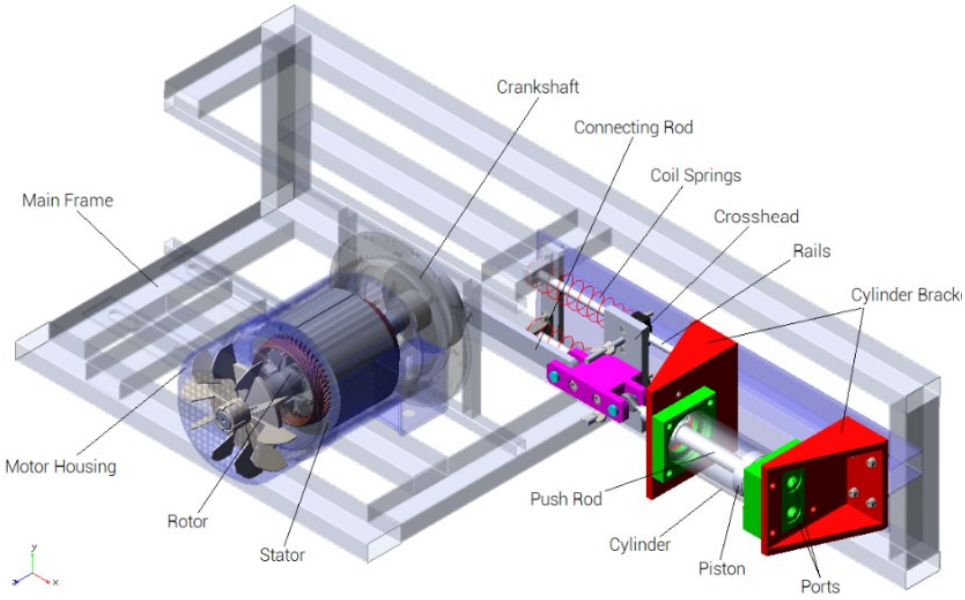

Figure 1: CAD-MBD model of the reciprocating compressor prototype. The electric motor is adapted from [7].

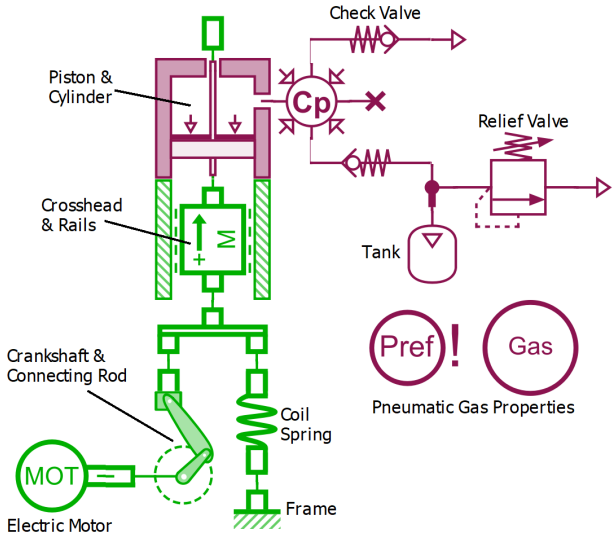

Figure 2: Sketch of the reciprocating compressor prototype.

The initial position of the crank (in Figure 2) is set at 0 °, which means that the piston is initially located at TDC. The cycle starts from the suction stroke, TDC to BDC (0° to 180 ° of the crank); followed by the compression stroke, BDC to TDC (180° to 360° of the crank). Compressed air is stored inside the tank and pressure builds gradually until the relief valve

cracks pressure. When the crack pressure of the relief valve is set at 8.7 bar, for example, the maximum pressure achieved inside the cylinder is about 8.84 bar and the force pushing down the piston reaches around 2500 N (Figure 3).

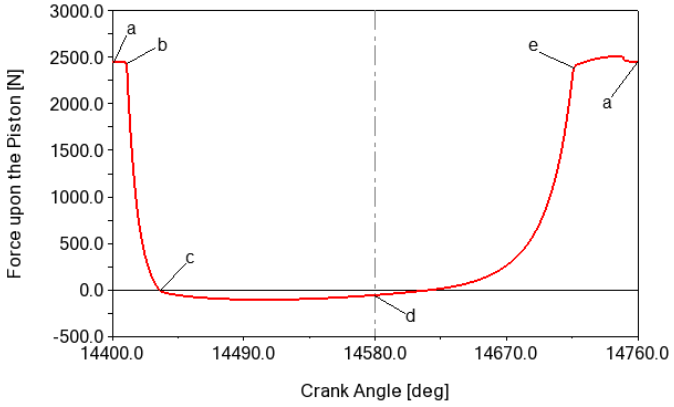

Figure 3: Force acting on the piston in one cycle (0° to 360 ° of crank), expansion (a-c), effective suction (c-d), compression (d-e), and discharge (e-a).

Table 1: Parameters of the simulations.

Components	Parameters	Value
Crankshaft & connecting rod	Initial angular position of the crank	0 degree
	Radius of the crank	50 mm
	Length of the connecting rod	168 mm
Piston & cylinder	Piston diameter	60 mm
	Chamber dead volume	0.62 L
Source of atmospheric pressure and temperature	Temperature	293.15 K
	Reference pressure	1.013 barA
Tank	Volume	1 L
Generic Gas Definition	Specific heat ratio	1.4
	Specific gas constant	287 J/kg/K
	Absolute viscosity	0.0182 cP
	Thermal Conductivity	0.0264 W/m/K
	Enthalpy of Formation	−125.53 J/mol
	Definition of properties	air, perfect gas

Part	Mass [kg]	Moment of Inertia [kg.mm^2]			Connected with	Joint
		I_{xx}	I_{yy}	I_{zz}		
Main frame	24.59	3.08×10^6	2.80×10^6	5.76×10^5	Ground	Fixed
Stator	2.80	1.103×10^4	8562.18	8555.26	Motor housing	Fixed
Connecting rod	0.15	451.95	441.64	12.76	Crankshaft	Revolute
					Crosshead	Revolute

Crankshaft	0.85	1350.89	798.75	772.66	Connecting rod	Revolute
					Rotor	Fixed
Cylinder	1.53	4056.40	4054.44	1688.46	Cylinder brackets	Fixed
					Piston	Cylindrical
Front cylinder bracket	4.13	1.59×10^4	1.07×10^4	7412.01	Main frame	Fixed
					Cylinder	Fixed
Motor housing	2.12	1.69×10^4	1.62×10^4	1.37×10^4	Main frame	Fixed
					Rotor	Fixed
Piston (including pin)	0.25[b]	335.87	292.34	290.84	Push rod	Fixed
					Cylinder	Cylindrical
Push rod	0.25[b]	2358.69	2357.44	35.95	Piston	Fixed
					Crosshead	Revolute
Rail	1.22	1.89×10^4	1.66×10^4	2664.15	Main frame	Revolute
					Crosshead	Translational
Rear cylinder bracket	3.93	1.90×10^4	1.09×10^4	1.01×10^4	Main frame	Fixed
					Cylinder	Fixed
Rotor	2.59	1.32×10^4	1.32×10^4	2554.61	Crankshaft	Fixed
					Motor housing	Revolute
Crosshead	*varied*	4850.21	4338.28	3509.18	Rail	Translational
					Connecting rod	Revolute
					Push rod	Revolute

3. SIMULATION RESULTS

3.1. Dynamic Torque without Load Pressure

Figure 4 shows that the setup without springs and without pressure has a progressive increase in dynamic torque as the angular velocity increases. On the other hand, the setup in which the springs are installed has a lower magnitude of dynamic torque at its resonant frequency of around 84.69 rad/s. At resonance frequency, the system effectively stores and transfers energy between the kinetic energy of the slider and the potential energy of the spring so that the torque and the required effort for the crankshaft to rotate are significantly lower than in any other angular velocity.

Figure 5 presents the graphs of power consumption vs. angular velocity, shown only in positive values that represent the magnitude of the power demand for the system to operate. The setup with spring shows that at a resonant frequency, the magnitude of power demand is about 0.3 kW, unlike the conventional one, which might require power at around 1.4 kW.

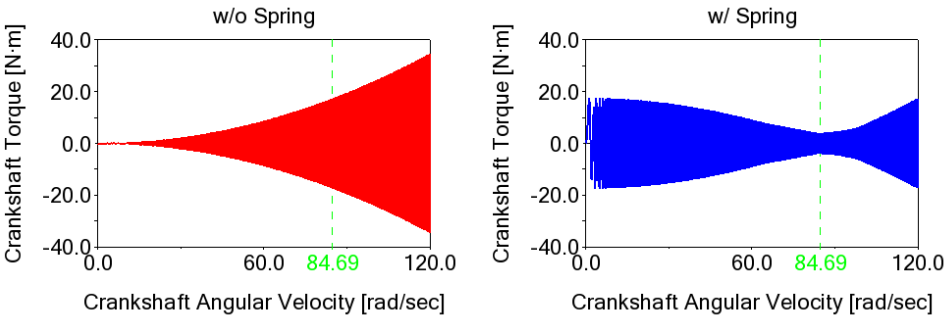

Figure 4: Torque vs. angular velocity curves without spring and with spring (data from Table 1, m=1.5 kg), without pressure load.

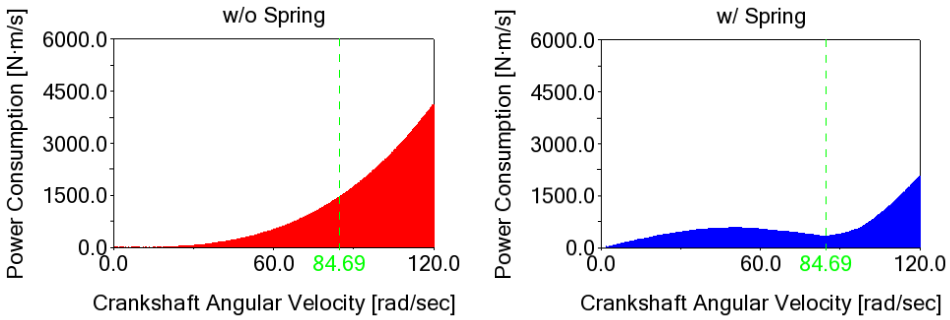

Figure 5: Instantaneous power demand vs. angular velocity curves, data from Table 1, m=1.5 kg), without pressure load

3.2. Dynamic Torque with Load Pressure

Several simulations are done to generate the force data in the example case of 0, 2.5, 5, 7.5 and 10 bar of air pressure. Figure 3 shows the force on the piston during the air suction and compression process within one cycle. Based on these simulations, the force data on the piston versus the angular position of the crank are imported into the MBD simulations, used as the input value of the applied force, which is placed at the top of the piston as a function of the angle of the crank.

Figure 6 shows the simulation results based on the data set defined in Table 1. It can be observed that when the crankshaft is operated at the resonant frequencies (denoted by the green line), the peak and RMS torque of the setup with spring is noticeably lower. Nevertheless, not only the setup with spring, it can be observed that the setup without spring also has a narrow torque region around its own resonant frequency since the compression of the air itself acts as the air spring compression. In this practical example, air compression can also be utilized to provide resonance, usually at lower frequencies. In case of working with a system that has an adjustable prime-mover angular velocity, if the resonance has been achieved at its own compression load, a spring might not be needed, and resonance can still be attained; otherwise, the installation of a spring with adjusted stiffness might be used to

match the resonance frequency with the available prime-mover angular velocity. In addition, the influences of both the mass of the reciprocating bodies and the resonance operating speed (that is adapted by the proper spring stiffness) are discussed in the paper [14].

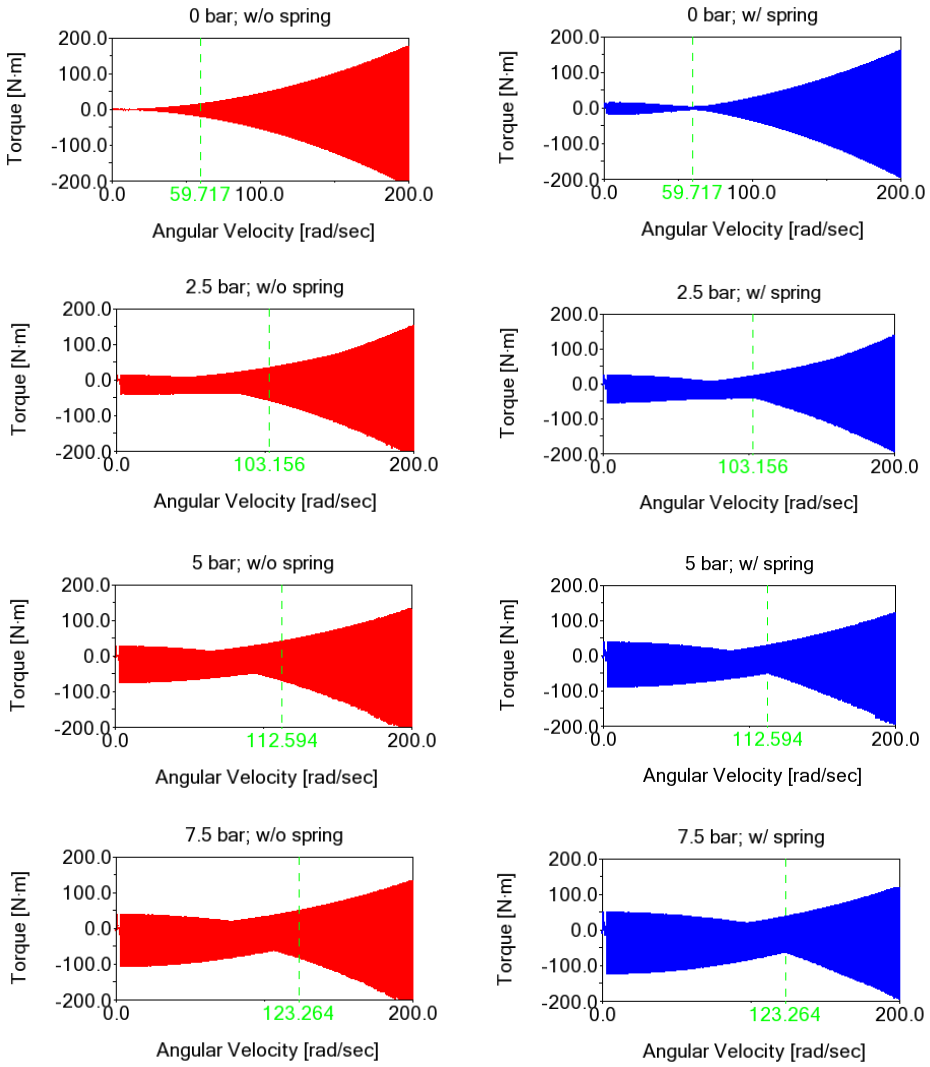

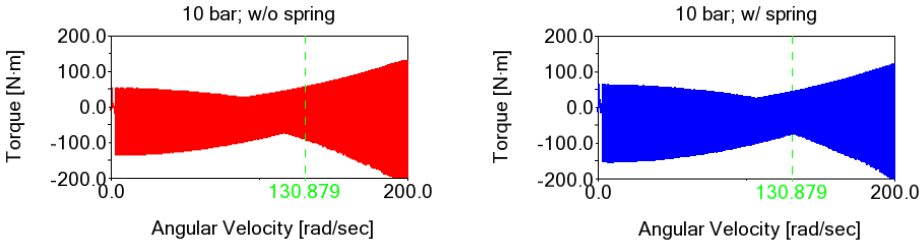

Figure 6: Torque vs. angular velocity graphs. Red- setup without spring, blue- setup with spring, data from the Table 1, M=3 kg, k= 6,25 N/m

If the resonance angular frequencies resulting from air springs in the compressor operating pressure range are too low, a steel spring should be used, ensuring a higher resonance frequency. In electric drives with variable speed, a control system can be used that adjusts the motor speed to the resonance. Selection of the appropriate stiffness in relation to achieving the resonance conditions is possible on the basis of the dynamic system simulation method presented in this paper. Equivalent spring stiffness is defined as:

$$k_e = k_s + k_g \tag{1}$$

where
k_s—mechanical spring stiffness;
k_g—gas spring stiffness.
The stiffness of the gas spring is nonlinear [7] and depends on the pressure and stroke of the piston $k_g = f(p, s)$.

$$k_g = E\frac{A^2}{V} \tag{2}$$

where:
E_p - bulk modulus depending on pressure.
A - piston surface
V - fluid volume depending on the position of the piston.

Depending on the required RPM of the electric motor (constant/variable), the equivalent spring stiffness can be obtained in the following way:

- For low-speed compressors, only a gas spring can be used, depending on the discharge pressure range.
- For high-speed compressors, an additional set of steel springs can be used to achieve resonance conditions.

The use of constant-speed motors requires a relatively exact selection of the equivalent stiffness in the compressor. By variable speed drives (VSD), resonance conditions can be achieved using, i.e. the appropriate frequency tracking control system [15].

4. EXPERIMENTAL INVESTIGATIONS

As shown in Figure 7, the physical prototype was built similar to the MBD model except for the drivetrain and the spring attachment. The prototype consists mainly of the compressor section and the electric drive section. The relief valve can adjust the level of external loads, that is, the magnitude of air pressure, on the slider.

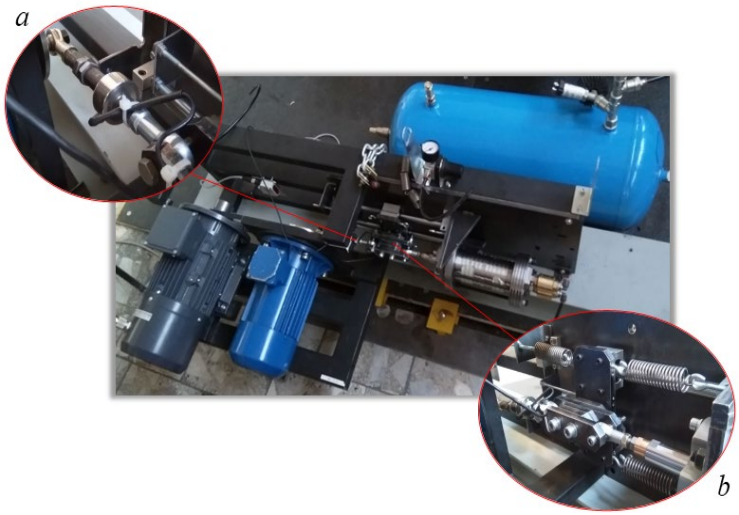

Figure 7: Physical prototype. Zoom in (a) force sensor on the joint of the connecting rod and (b) crosshead and springs.

The electric drive system consists of a three-phase motor, PLC, VFD, relay, circuit breaker, switches, cables, and control panel box. The assembled control unit in this system is programmed for the possibility of the motor to operate at a constant specified speed and steadily increasing speed (ramp function) to provide the sweep function to the slider. In the following, the resonance speed of the system can be identified. The force sensor was mounted on the connecting rod. Finally, sets with and without springs are tested to compare their forces on the joints of the connecting rod.

The test results are shown in Figure 8 and their essential data are presented in Table 2. It can be observed that all spring sets have a narrow force region around the resonance speed. Almost the same as in simulation, at the pressure 0 bar, the setup with spring provides about 60.34% reduction in the peak-to-peak force at resonance when no pressure load is involved (and no valves are installed). The attachment of the valves poses as an external load, so that the peak-to-peak force is reduced by 20.9%. This result underscores the important role of pressure losses that occur in the inlet and outlet valves in obtaining the highest positive resonance effect.

As demonstrated in the simulations, compression of the air itself takes effect as a spring compression. Even without any coil spring installed, a narrow force region can be observed in the setup without a spring. At 1 bar, the reduction of force goes down to 6.26% and 16.24% at 126.4 rad/s (1207 rpm) and 141.8 rad/s (1354 rpm) which are the resonance frequencies of both the setup without spring and the setup with spring, respectively. At the pressure 1 bar, if both sets are run and compared at their own resonant speed, that is, 126.4 rad/s for the conventional setup and 141.8 rad/s for the resonance setup, the difference in peak-to-peak force is less significant; about 1.53%. Therefore, in the air compression process, the spring may or may not be installed after the available system parameter. As long as the system is run at resonant frequency, enhancement of the system dynamics might be achieved.

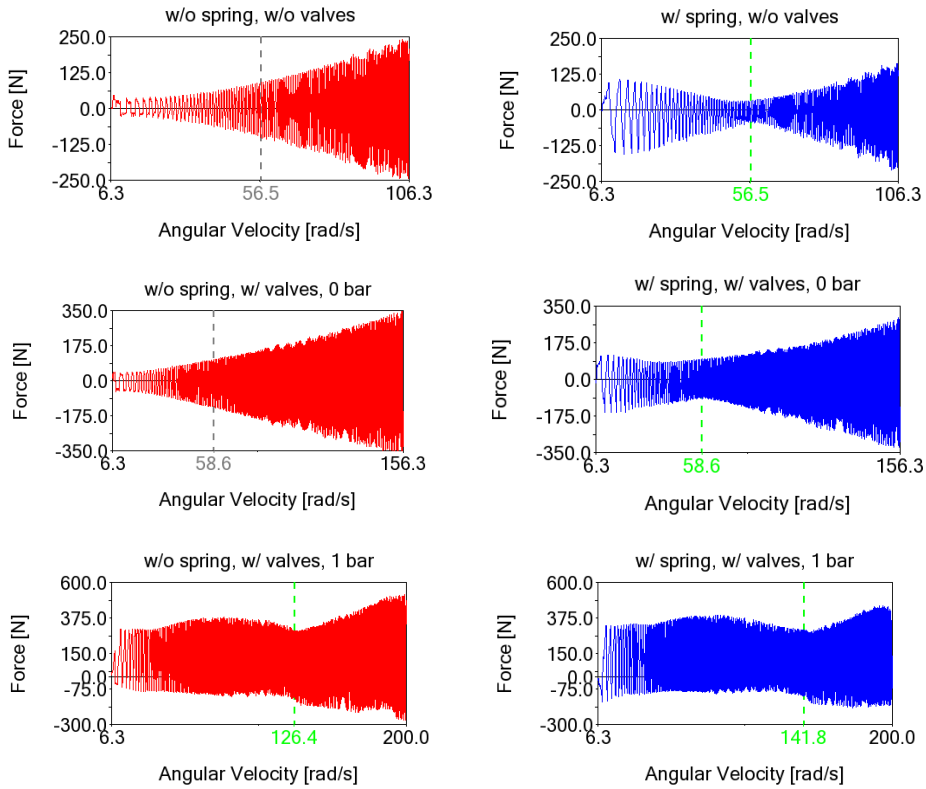

Figure 8: Force–angular velocity graphs of the set-up without spring (red) and with spring (blue). The force is measured on the connecting rod as shown in Figure 6(a). Reciprocating mass = 3.9 kg, spring stiffness = 2.5 kN/m.

Table 2. Comparison of the force on the connecting rod of the physical prototype.

Load [bar]	**Resonant frequency [rad/s]**	**Pulling force [N]**		**Pushing force [N]**		**Peak-to-peak force amplitude [N]**		**Decrease in the peak-to-peak amplitude of the force [%]**
		w/o spring	w/ spring	w/o spring	w/ spring	w/o spring	w/ spring	
w / no valves	56.5	−99.8	−43.9	93.2	32.6	193.0	76.6	60.3
0	58.6	−134.6	−92.0	106.1	98.3	240.7	190.4	20.9
1	126.4	−133.2	−84.0	295.0	317.4	428.3	401.5	6.3
1	141.8	−181.6	−121.0	321.8	300.7	503.5	421.8	16.2

5. CROSS-HEAD COMPRESSORS

The described method for reducing the force and torque pulsation can be used in industrial crosshead compressors. These types of compressors are often used i.e. for the compression and transportation of natural gas. In such compressors, the mass forces reach high values. The reciprocating movement is performed by pistons together with a crosshead, which are used to reduce the piston slap and increase the tightness. Due to the wear of individual elements related to friction in the joints, each reduction in the amplitude of variable loads contributes to reducing friction forces, wear, and thermal losses.

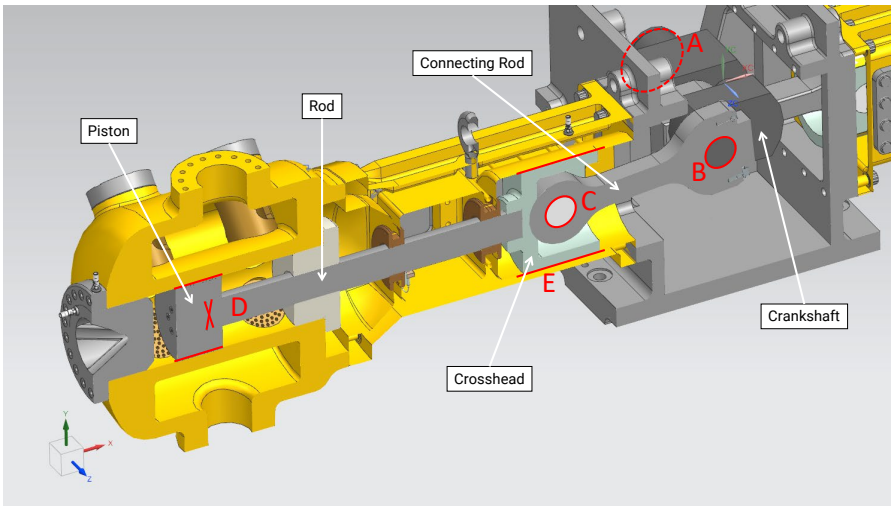

Figure 9. Cross section of the cross head compressor with the joints marked in red, Ariel compressor [16]. Reciprocating masses of 272.4 kg, crank length of 82.56 mm, connecting rod length of 533.4 mm, piston diameter of 254 mm, piston rod diameter of 101.4 mm

5.1. Dynamic Torque with Load Pressure

Industrial crosshead compressors are usually double-acting. The double-acting compressor compresses the air on both the up-stroke and the down-stroke of the piston, doubling the capacity of a given cylinder size.

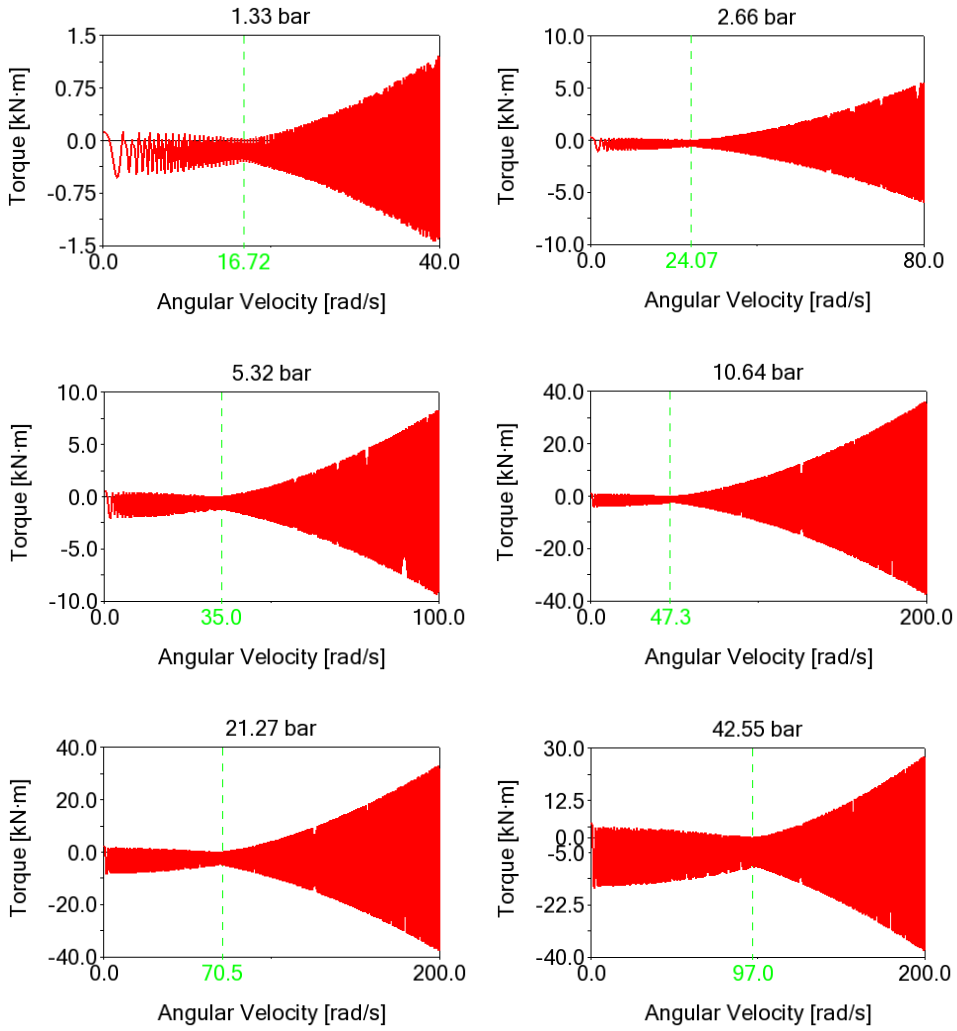

Figure 10: Torque vs. angular velocity graphs for a cross-head compressor without spring. Data from Figure 9.

The amplitudes of the torque and forces in the joints in the resonac are much smaller than for velocities above and below resonance. For higher resonance frequencies, this effect is even more visible in Figures 10 and 11.

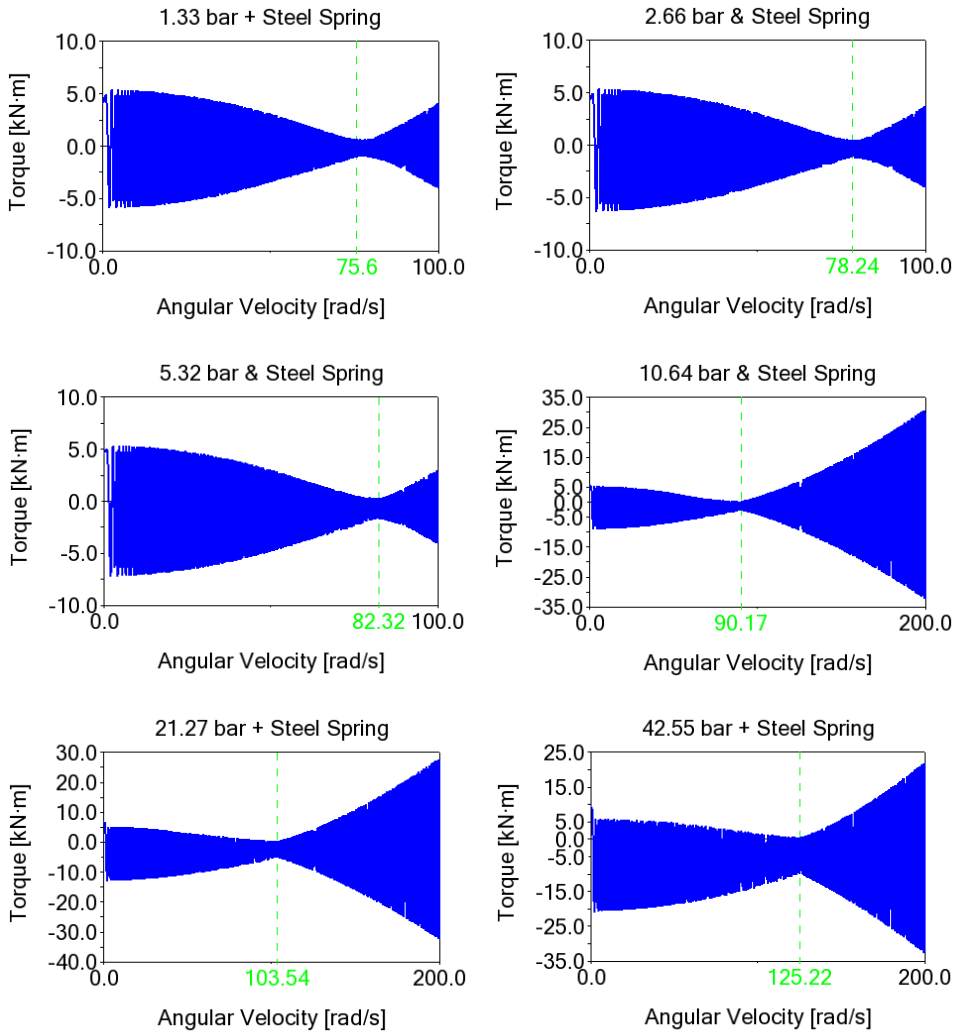

Figure 11: Torque vs. angular velocity graphs for the crosshead compressor with spring. Data from Figure 9, spring stiffness 1500 kN/m.

5.2. Dynamic Forces on Joints

Figure 12 shows the forces in the cross-head compressor joints before resonance (blue line), during resonance (green line) and after resonance (red line). It can be observed that in the resonance state the force amplitudes are much smaller (except for the connection between the piston and the piston rod).

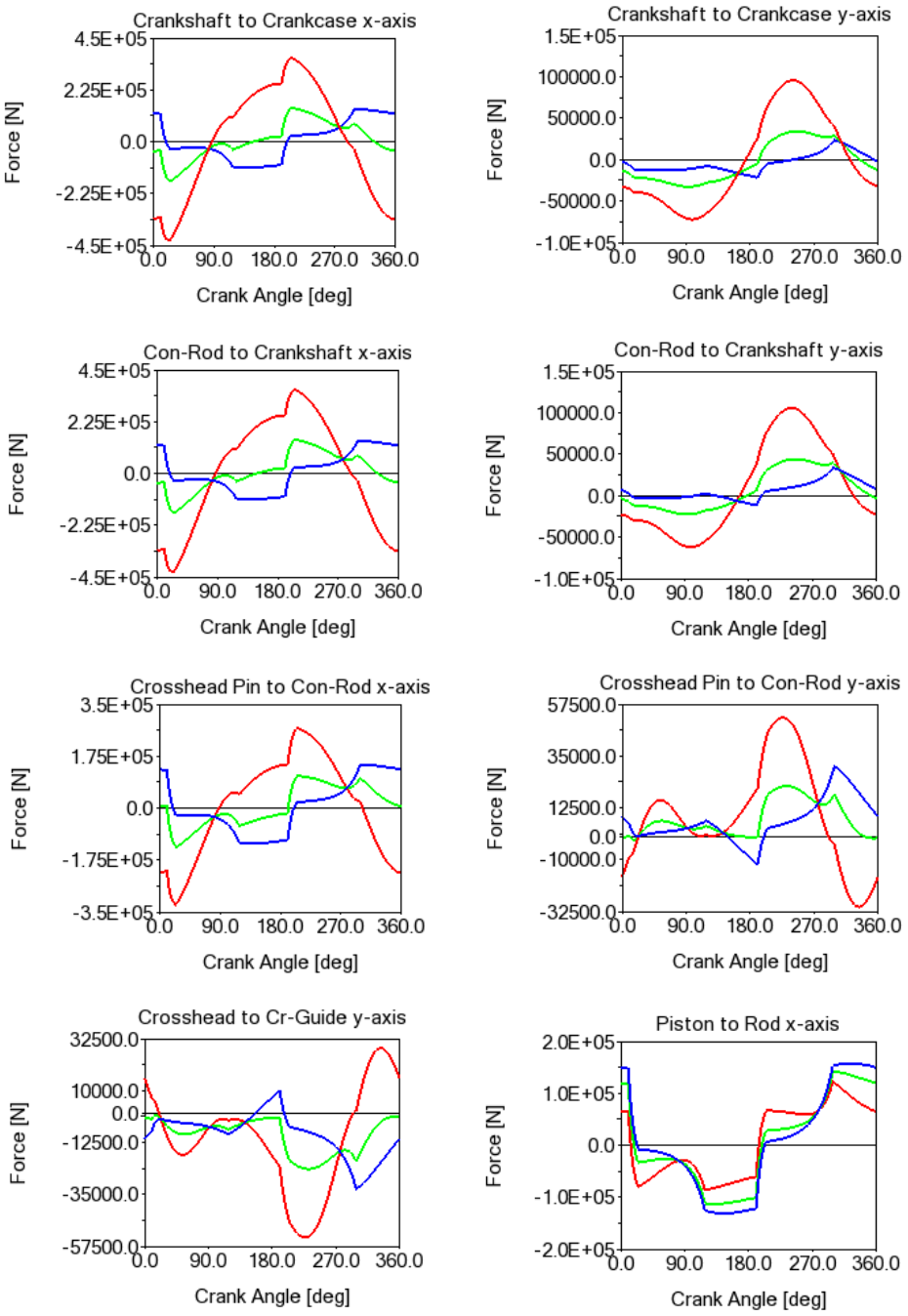

Figure 12: Forces on revolute and translational joints (arbitrary vs. resonance); no load and friction, stage 2 of compression. operating speed: red=135.5 rad/s, green=85.5 rad/s (narrowest region), blue=35.5 rad/s.

Figure 13 shows the dependence of the resonant angular velocity on the cylinder pressure for the versions without a spring and with a steel spring. In the absence of a steel spring, there is a nonlinear increase in angular velocity as a result of pressure. By using steel springs, higher resonance frequencies can be obtained. Therefore, their use would be appropriate for high-speed cross head compressors.

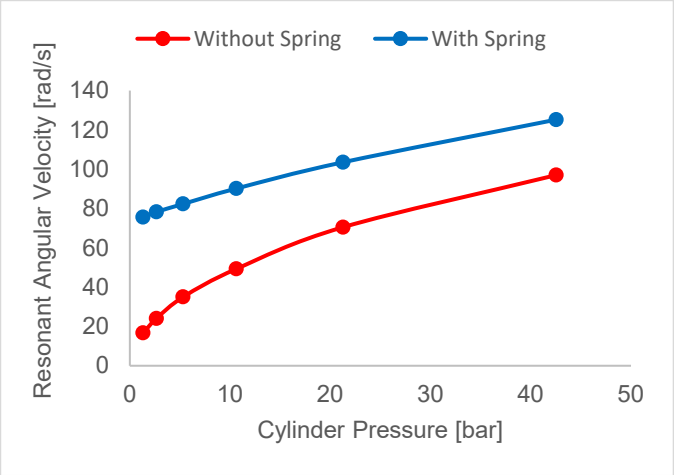

Figure 13: Resonant angular velocity vs. cylinder pressure of the crosshead compressor data from Figure 9, steel spring stiffness of 1500 kN/m

6. CONCLUSIONS

In this paper, a technique for improving the dynamics of the slider-crank mechanism is presented using the phenomenon of mechanical resonance. A comparative study towards the resonance and conventional operation is done using MBD simulations. A reciprocating compressor model is explored as a practical case study example, representing the application of a slider-crank mechanism.

It is found that the introduction of a spring element that can store and transfer back the potential energy in the slider-crank mechanism can provide a positive effect of resonance. The input torque on the crank shaft and the forces on all rotating joints of the setup run at resonance provide lower peak and RMS values (narrow region) compared to the conventional operation. The setup without a coil spring also presents a narrow torque region around the resonant frequency, since the process of air compression itself acts as the air spring compression. Whether or not the system uses the coil spring, as long as it is run at the resonant frequency, the advantageous result of resonance can be achieved.

If a particular pressure demand is required to maintain resonance, the angular velocity of the driving unit should be changed accordingly. In a future study, a control algorithm could be developed to improve the capability of the resonance slider-crank system presented, for example, using a frequency tracking control system [9]. Although the practical example presented in this article is only limited to the process of air compression, studying the use of resonance in the slider-crank mechanism for other applications would be very much worthwhile.

The simulation results indicate that an increase in equivalent spring stiffness (air spring plus steel spring) leads to higher power efficiency. Also the rotating joints at resonance exhibit lower peak and RMS values of forces. Finally, experimental verification of the slider-crank mechanism at resonance demonstrates a behavior equivalent to that in simulations. Based on the analysis, it can be concluded that controlled mechanical resonance can effectively reduce inertia load magnitudes in reciprocating compressors.

The innovative method proposed in the article has great application potential, especially in industrial cross-head compressors, in which the share of inertia forces is greater, and the forces occurring in the crank slider mechanism determine the wear and durability of these compressors.

7. REFERENCES

[1] Franca, L. F., & Weber, H. I. Experimental and numerical study of a new resonance hammer drilling model with drift. *Chaos, Solitons & Fractals,* **21**(4), 789-801, (2004).

[2] Despotovic, Z., Sinik, V., & Ribic, A. The impact of switch-mode-regulated vibratory resonance conveyors with electromagnetic drive on the power supply network. *2012 15th International Power Electronics and Motion Control Conference (EPE/PEMC)*, (2012).

[3] Aiple, M., Smisek, J., & Schiele, A. Increasing Impact by Mechanical Resonance for Teleoperated Hammering. *IEEE Transactions on Haptics*, **12**(2), 154–165, (2019).

[4] Fiebig, W. & Wróbel, J. Energy accumulation in mechanical resonance and its use in drive systems of impact machines. *Archives of Civil and Mechanical Engineering,* **20**(1), (2020).

[5] Ni, L., Huang, Y. Y., & Zhou, C. K. The dynamic simulation of Engine Slider-Crank mechanism based On ANSYS and Adams. *Advanced Materials Research, 842*, 347-350, (2013).

[6] Hroncová, D., Binda, M., Šarga, P., & Kičák, F. Kinematical analysis of crank slider mechanism using MSC ADAMS/View. *Procedia Engineering, 48*, 213-222, (2012).

[7] Bödrich, T. (2006). System and Component Design of Directly Driven Reciprocating Compressors with Modelica. Modelica 2006, September 4th – 5th

[8] Daniel, G.B.; Cavalca, K.L. Analysis of the dynamics of a slider–crank mechanism with hydrodynamic lubrication in the connecting rod–slider joint clearance. *Mech. Mach. Theory* **2011**, *46*, 1434–1452.

[9] Ni, L.; Huang, Y.Y.; Zhou, C.K. The dynamic simulation of Engine Slider-Crank mechanism based on ANSYS and ADAMS. *Adv. Mater. Res.* **2013**, *842*, 347–350.

[10] Arakelian, V. Design of Torque-Compensated Mechanical Systems With Two Connected Identical Slider-Crank Mechanisms. *J. Mech. Robot.* **2021**, *14*,

[11] Hroncová, D.; Binda, M.; Šarga, P.; Kičák, F. Kinematical analysis of crank slider mechanism using MSC ADAMS/View. *Procedia Eng.* **2012**, *48*, 213–222.

[12] Arakelian, V.; Briot, S. Simultaneous inertia force/moment balancing and torque compensation of slider- crank mechanisms. *Mech. Res. Commun.* **2010**, *37*, 265–269.

[13] Pishvaye Naeeni, I.; Keshavarzi, A.; Fattahi, I. Parametric Study on the Geometric and Kinetic Aspects of the Slider-Crank Mechanism. *Iran. J. Sci. Technol. Trans. Mech. Eng.* **2018**, *43*, 405–417.

[14] Fiebig W, & Prastiyo W. Utilization of Mechanical Resonance for the Enhancement of Slider-Crank Mechanism Dynamics in Gas Compression Processes. *Energies*, **15**(20):7769, (2022). https://doi.org/10.3390/en15207769.

[15] Xu, W., Wang, Q., Li, X., Liu, Y., & Zhu, J. A novel resonant frequency tracking control for linear compressor based on MRAS method. *CES Transactions on Electrical Machines and Systems*, **4**(3), 227–236, (2020).

[16] Troy. (2012). CAD File of Ariel 6 Throw Compressor. [Online] available: https://grabcad.com/library/ariel-6-throw-compressor.

Innovative hyper-thin sensor for cartridge valves diagnostics and prognostics

Massimiliano Ruggeri[1*], Francesco Maita[2], Luca Maiolo[2], Mattia Ferri[3], Christopher Rosi[4], Sara Baldoni[4]

1 STEMS-CNR, via canal bianco 28, 44124 Ferrara, Italy

2 IMM-CNR, Via del Fosso del Cavaliere 100, 00133 Roma, Italy

3 E.S.T.E: S.r.l., via Francesco Luigi Ferrari 34/2, 44122 Ferrara, Italy

4 VIS Hydraulics S.r.l. Innovation Center Via G. Marconi, 115, 41028 Serramazzoni (MO), Italy

E-mail: massimiliano.ruggeri@cnr.it

**Corresponding Author*

Abstract.

Functional Safety asks for diagnose-ability of systems and components in order to make the systems observable and to check for faults to be recovered in real time to avoid dangerous consequences of the faults themselves. At the same time, new technologies offer new materials and new production processes, which allow the creation of new sensors to meet the requirements of the functional safety certification procedures. Diagnostics and predictive diagnosis are not only related to functional safety, but rather to reliability and function availability, which represent two very important aspects of products quality. Finally, cartridge valves are widely used in many hydraulic systems, both in mobile and in industrial applications, and they are often part of systems that must meet functional safety requirements. Traditional sensors does not contain information on the state of health of the valve itself and its state with respect to the average life and the distance from a dangerous failure. This contribution deals with describing some type of failures of cartridge valves and describes how an innovative sensor is able to detect such failures before they can occur, also with a reasonable warning of the moment of failure. The innovation is described and both mechanical, electromagnetic, fabrication and installation problems are addressed.
A set of real tests on prototypes are reported, and it is shown that the tests prove the efficacy of the sensors in valve failures due to high pressure damages. Finally scenarios for new application ideas are described.

Keywords. Cartridge Valve, Fatigue breakage, Pole Tube, Strain Gauge, Valve Coil.

1. INTRODUCTION

In many electro-hydraulic applications nowadays, sensors are placed in manifolds and along the hydraulic circuits, as well as in pumps and motors, in order to acquire data useful for closed loop controls. As very well described in [1], the sensing technology has grown in the years in parallel to control techniques and, in recent years, in parallel with the need for health status of hydraulic components and, in special way, for the health information of valves.

Searching for special sensors "in valves", it is hard to find anything new, while it is very interesting to learn how much research has been done trying to deduce the health status or simply the status of valves using different inference techniques. Most of these techniques are using remote sensors and data collected from the effects of the valve status in the hydraulic circuit.

The reliability of hydraulic components it is a very heartfelt topic, but in many papers like in [2] it is treated using traditional pressure sensors, based on traditional strain gauges. In fact, reliability is one of the key arguments of safety, but safety is also related to faults and to be aware of faults, the component must be observable. Therefore, sensors are necessary for safety reasons, as it is demonstrated in [3], where traditional sensors placed in the hydraulic circuit are used to evaluate the valve faults in an independent metering system. Many different strategies have been developed to try to evaluate the health status of hydraulic components and, in particular, of valves, due to the difficulty of integrating sensors for a direct acquisition of the health status of the valve itself. In [4] authors propose a multi stage diagnosis based on sensor fusion, using accelerometers to analyse the vibration of the hydraulic directional valves. Even in this case, a direct acquisition of the status of the spool or of the health status of the valve is inferred using external and indirect sensors, i.e. sensors not acquiring the primary physical parameter responsible for the information to be collected. In [5] the importance of a real-time, accurate fault detection and isolation system is described for mobile hydraulic valves, and an inference method is proposed, using traditional pressure sensors and a reduced order model with adaptive thresholds. In the already cited [1] it is also described how the diagnosis of the valves is increased for the digital hydraulic valves. This is confirmed for example in [6] and [7], where authors propose an identification method for faulty valves recognition, based on combination of pressure measurements made during the normal operation of the machine and a mathematical model describing the flow balance of the hydraulic system, once again using traditional pressure sensors in the hydraulic circuit. The only experiences of integration of new thin sensors are in [8], where strain gauges are used to acquire and evaluate the correct functionality of a hydraulic clamping system, and in [9], where strain gauges are used to measure micro leakages of a hydraulic cylinder using internally installed strain gauges. This last experience is not a solution for the industrial production, but is useful in order to understand the strain gauges applicability even inside hydraulic components.

Based on the previously described experiences, the strain gauge technology seems the only one applicable to the problem the research wants to address, which represents an open issue as described in [10]. However, there are several problems to solve, in order to create a new type of sensors capable to cover the faults of the valve body. The proposed sensor is something that could represent a new sensitization methodology and technique for valves, applicable to both spool valves and cartridge valves. The main difference from the described experiences, in the case treated in this article, is that the aim of the proposed sensor is to

acquire directly the main physical phenomenon responsible for valve pole tube breakages. The main principle is to acquire the anomalies in the mechanical strain of the pole tube, using the electrical-mechanical properties of the strain gauges and a proper design of the sensors tailored on each valve model, in order to maximize the sensitivity and to adapt perfectly the temperature compensation. In next paragraphs it will be described the sensor and its production technology, the necessary adaptation of the electro-actuated cartridge valves and the practical experiences at test bench for sensor validation.

2. STRAIN GAUGE TECHNOLOGY

Among the different improvements implemented in the years in this branch of mechanical sensors, ultra-flexible and ultra-thin strain gauge sensors represent a class of devices with multiple advantages in terms of sensitivity, conformability, costs etc. Indeed, the conventional fabrication of strain gauges often relies on MEMS-based technology, where controlled environments and expensive microfabrication processes are requested, while roll-to-roll and printing techniques together with additive manufacturing can allow tuning production according by the case, thus reducing the costs of these devices [11]. Especially in biomedical applications and robotics, ultra-flexible strain gauge sensors embody a suitable choice, since a wearable device fits well with human body or garments and it can show proper conformability to non-conventional surfaces [12]-[13]. Depending by the high sensitivity of these sensors and by the specific range of strain requested, different materials can be implemented from elastic or stretchable substrates to extremely soft polymers (reaching strain >100%) [13]. To tune the conductivity and mechanical properties, nanocomposites usually based on carbon like materials or piezoelectric composites are used [14]-[15]. In this way, through percolation among conductive nanoparticles, it is possible to control the changes in conductivity during the sensors operation [16]. Alternatively, very stretchable polymers (e.g. PDMS) filled with metal nanoparticles can still be utilized to manufacture extremely long-range strain gauge sensors [17]. Generally, with the implementation of metal nanoparticles it is also possible to obtain very high gauge factors in specific sensor operation range (up to few thousands) [18].

3. THE CARTRIDGE VALVE AND ITS FAILURES

For this research, a proportional Flow regulation Cartridge Valve not pressure compensated, electronically controlled, of VIS Hydraulics was used.

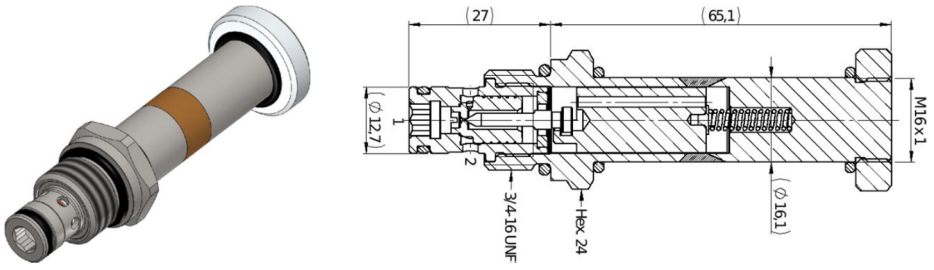

Figure 1. The Flow regulation Cartridge Valve and its section

The valve is one of the three new valves the company developed in the project, and this one was the first ready for the tests and it is shown in Figure 1, while its characteristic and symbol are shown in Figure 2. The Valve is actuated using a coil of 26 W either 12 or 24 VDC electronically controlled by a new electronic control unit directly connected to the coil connector.

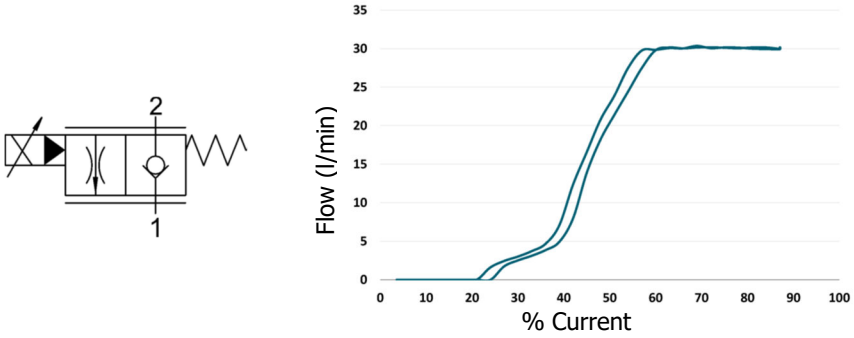

Figure 2. The valve hydraulic symbol and the Current vs Flow characteristic

There are several breakages of a cartridge valve to be analysed and that can occur during the valve operational life. Different types of breakages can be caused by excessive pressure in operation, which results higher in respect to the maximum pressure declared by the valve producer for the correct usage of the valve itself. Some of them can be caused by fatigue, due to excessive usage of the valve, exceeding the average or declared life of the valve. Others can be caused by mechanical stress, due to external factors or wrong installation of the valve. Finally few of them can be caused by production defects or process defects or material defects. These valve faults can lead to different types of malfunction, the ones we are interested in monitoring are the ones can lead to an oil loss with dangerous consequences, or with function unavailability that can cause damages and high cost consequences.

The faults we are discussing of are the faults that can provoke a breakage of the pole tube, whose consequences are shown in Figure 3.

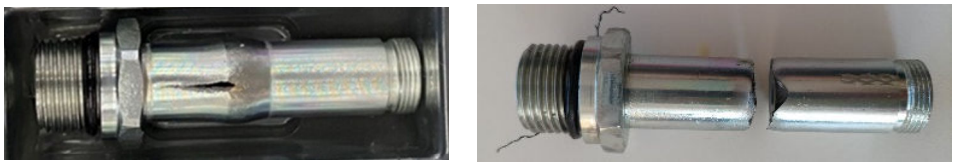

Figure 3. Excessive pressure breakage and process or fatigue breakage of the valve

The idea developed in this research is to apply sensors to the pole tube, which can directly monitor the health status of the valve. As discussed in the introduction, a sensor type that could fits the requirements, suitable to be installed in between the coil and coil enclosure and the pole tube, is the strain gauge. In fact, any mechanical deformation, or even an oil loss or oil spilling could lead to a sensor deformation and to a variation of the sensor value, then to a recognition of a malfunction of the valve. The different models available have a thickness that is not compatible with the available air gap in the valve. Moreover, it is impossible to find a strain gauge fitting perfectly the envelope of the cylindrical surface of

the pole tube. But in the last years the flexible electronics technology had interesting improvements both in materials and in processes, so it is likely possible to design and produce an ad hoc sensor for each valve model.

The opportunity of a specific design for each valve model will ensure that any type of breakage of the pole tube will be under the observation area of the sensor. Therefore, theoretically the sensor could reveal any type of breakage during the valve operation life. This is the thesis the research would like to demonstrate. The first step is to understand the sensor technology applied to the sensor prototypes made for this experiment.

4. THIN STRAIN GAUGE SENSOR

The flexible strain gauge sensor has been designed according to a classical meander configuration to obtain a total resistance in the range of [2; 4] kohm. For the manufacturing of the device, we started using a 3'' silicon oxidized wafer as carrier and we deposit a layer of 8 µm by spin coating. After a thermal treatment at 250°C for mechanical stabilization of the polymer, we patterned with a positive photoresist the metal track by using an EVG610 equipment. Then we evaporated a film of Aluminium of 150 nm and we removed the resin in an acetone bath for 2 h. To protect the sensor we deposit another layer of polyimide, 2 µm thick, and we photolithographically open vias to reach out the contacts by using an oxygen plasma treatment for 15 min. After this step, the sensor was cut from the wafer and mechanically peeled off, obtaining a thin freestanding device with a total thickness of about 10 um.

Prototype	Substrate thickness (µm)	Metal thickness (nm)	Sacrificial layer (nm)	Reference resistance
1	8	120	none	Yes
2	8	200	none	Yes
3	12	120	25	Yes
4	12	200	25	Yes

Table 1 Sensor Prototypes main characteristics

Different devices were tested with diverse thicknesses of Aluminium, ranging from 120 to 200 nm as shown in Table 1, and a sacrificial layer of chromium 25 nm thick to protect additionally the Aluminium film during the manufacturing process was implemented.

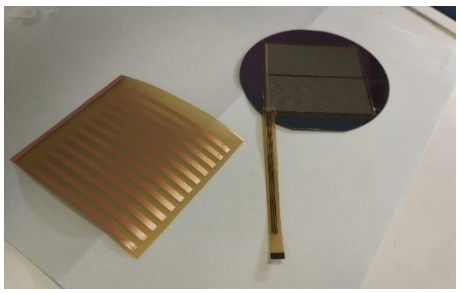

Figure 4. A photograph of the strain gauge with the adaptor.



Figure 5. The device wrapped around the valve

Additionally we fabricated for each device two equal sensors, in order to compensate the temperature variations during the testing procedure. The overall dimension of the sensor was designed for wrapping exactly the entire pole tube. To take out the signal from the sensor, a flexible adapter in copper was properly designed, manufactured and connected to the polyimide substrate through the usage of anisotropic conductive tape (Figure 4). Finally, the sensor was glued and wrapped around the valve to follow conformably the metal part subjected to the oil pressure (Figure 5).

The strain gauge sensor obviously reacts to any type of strain, so even to the temperature strain. It is then necessary to create a sensor capable of distinguish between pressure strain and temperature strain, in order to understand the part of the strain due to temperature and the part due to the normal pressure strain, or any abnormal strain, due probably to fatigue or excessive pressure, or pole tube defects. For this reason, a double strain sensor was designed, adapted to the structure of the valve. As shown in Figure 6, it can be noted that part of the pole tube is solid and part is hollow to allow the sliding of the mobile part. Consequently, the first part of the body will change its shape only for temperature, while the second one for both temperature and pressure or fatigue. Hence, the sensor was designed to have one resistance facing to the solid part of the pole tube (SG2), to be used as a reference for temperature strain, and a second resistance to be connected to the hollow part of the pole tube (SG1), sensitive to both pressure and temperature.

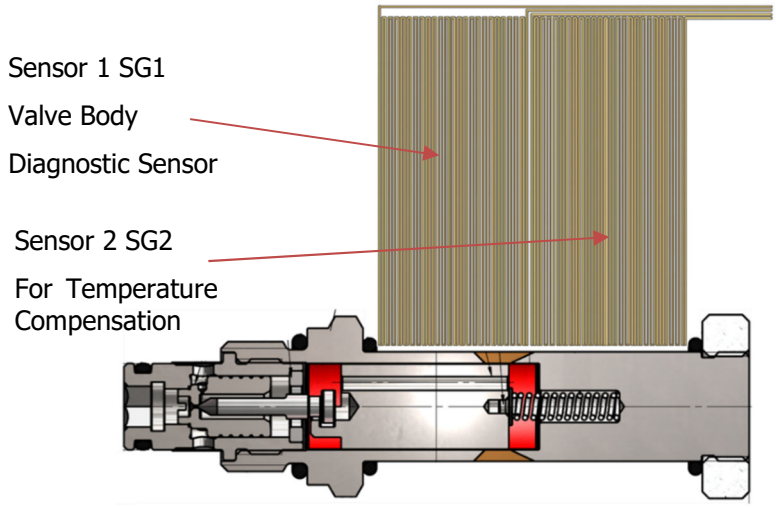

Figure 6. correspondence between pole tube structure and double sensor design

By a classic full bridge connection in the electronic readout system, it is possible to compensate the strain for temperature in the acquisition of the deformation of the SG1 sensor, subtracting the strain of the SG2 sensor, taking into account in the electronic circuit any difference in resistance of the two sensors. The same can be obtained using two half bridges readout circuitries and correcting the SG1 strain by a software function, with the advantage of reading both sensors values and having a more complete information on the valve. In this experience, we used this second approach due to the need to test different sensors with different characteristic resistances and the easiness of correcting Temperature strain by software.

5. THE NEW COIL SHAPE AND MAGNETIC FIELD ANALYSIS

Due to the specific design of the sensor, a problem that arose in the feasibility study related to the application of these sensors, was related to their installation on the valve. In particular, the strain gauge is placed above the pole tube, and the solenoid will be placed above the assembly of valve and strain gauge sensor. However, the solenoid enclosure is accurately designed in order to maximize the magnetic flux and part of the design is the minimization of the air gap between the valve coil and the pole tube. Consequently, the thickness of the sensor, although limited, requires a modification of the internal dimensions of the solenoid enclosure, to allow its insertion in between pole tube and coil enclosure. Figure 7 represents a sectional view of the valve and the solenoid. In the figure, a hypothetical magnetization path is highlighted with the dotted red line, which runs through the armature of the solenoid, the fixed core and the moving plunger and control cone.

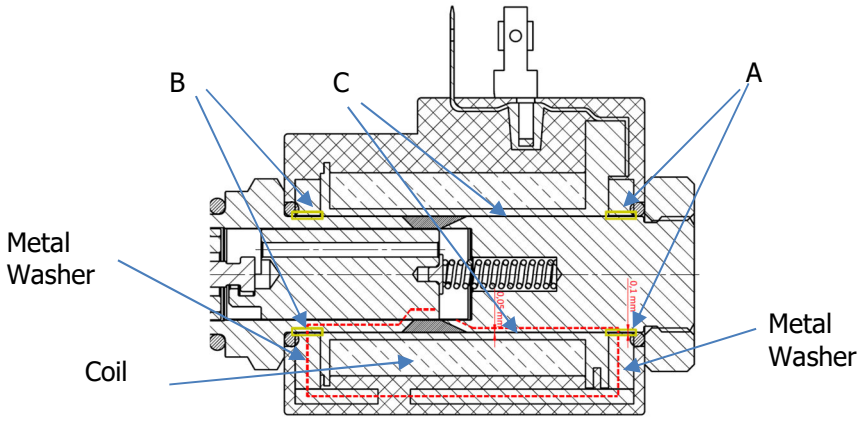

Figure 7. Valve section with Air Gaps Indication

This Figure shows also the air gaps that are to be redesigned, in order to allow the sensor placement. As it can be noted in red a very reduced air gap of 0,05 mm is available all along the pole tube and the coil, while in the two metallic rings at the end of the coil the air gap is 0,1 mm. The air gaps corresponding to the rings are highlighted in yellow in the figure. Each air gap represents a source of dispersion of magnetic flux that in these positions is not conduct in a magnetic guide. The magnetic flux dispersion ends in a reduced Coil force, proportionally. Then, the areas highlighted in yellow represent the air gaps along the path. The upper side, where the connector is placed, is not highlighted, nor the empty area on the lower side, since in reality the armature completely envelops the solenoid. Therefore, those areas are only "punctual" and are seen only in the plane chosen for the section, in the real valve the flow will pass around. Furthermore, the nominal thickness of the gaps between metal washers and tube, and between coil and tube, are shown, to indicate the space available for the sensor. The problem to be addressed in this case concerns the magnetic performance of the assembly, which is influenced by the presence of these air gaps, which introduce real losses. In fact, a circuit analogy can be made and the magnetic path can be represented as a sort of electrical circuit, where the various parts crossed are similar to electrical components. Each source of loss is schematized as a resistance, and all the air gaps encountered (for example the one between the metal washer that makes up the armature of the solenoid) will

therefore be resistances that oppose the passage of "current" that is the analog element of the magnetic flux.

Although the thicknesses involved seems sufficient compared to the thickness of the sensors (we are talking about 25 μm in the worst case), it must be considered that the sensor includes a plastic film that encloses the actual sensor, and the output cables. It is therefore necessary to obtain sufficient space for their accommodation, increasing these values. Losses will inevitably be introduced, and this is why a study was conducted using the EMS electromagnetic FEM (*EMS, Advanced Electromagnetic Design and Analysis Tool* dedicated add-on of the *Solidworks* suite), to evaluate the impact of any structural modifications to the coil on the electromagnetic performance of the valve. In order to understand how the analysis was performed and how the best configuration was chosen, the various case studies analyzed and the impact they had on the magnetic flux are reported. With reference to Figure 7, it is defined thickness A the thickness of the air gap between the tube and the upper armature of the solenoid, thickness B the thickness of the air gap between the tube and the lower armature of the solenoid, while thickness C the thickness of the air gap between the tube and the solenoid. The three air gap zones are shown in the Figure.

In order to define the range of use of the valve and to calculate the absolute stroke in the simulations, we consider the stop between the plunger and fixed core at the position of 4,5 mm stroke, with the valve completely closed at lower stop. Considering a core stroke of approximately 2,75 mm, reaching the mechanical stop in the shuttle part of the valve at 1,75 mm stroke with the valve fully open. This defines the range of use of the valve, since the equilibrium position between the force of the coil and the opposing force of the spring will necessarily be reached in this range of travel. In order to evaluate the worsening due to the modified coil enclosure in the air gaps, the steady state current was analyzed, which defines the "limit" of use in terms of current applicable to the solenoid.

case	Thickness A	Thickness B	Thickness C
Standard (Production)	0.1 mm	0.1 mm	0.05 mm
A	0.3 mm	0.3 mm	0.3 mm
B	0.4 mm	0.4 mm	0.4 mm
C	0.1 mm	0.4 mm	0.4 mm
D	0.1 mm	0.3 mm	0.3 mm
E	0.45 mm	0.45 mm	0.45 mm
F	0.1 mm	0.45 mm	0.45 mm
G	0.5 mm	0.5 mm	0.5 mm
H	0.1 mm	0.5 mm	0.5 mm

Table 2 Coil Air Gaps cases for Simulation

Various simulated cases with different air gaps were analyzed from the Electromagnetic point of view, calculating the electromagnetic field intensity, its dispersion and the field density in the area of the plunger movement control, especially near the control cone of the valve. All the analyzed cases are reported in Table 2.

All these cases were simulated, in order to understand the effect of an increased air gap and how the negative effect of the air gap can be reduced, using a washer with minimum air gap

in the critical area of the end of the coil. In fact, in this area the magnetic flux is conduct in a magnetic ring through the metal washer, in order to maximize the magnetic flux near the mobile core of the valve and the control cone. For that reason, a couple of cases are shown, to evaluate the dispersion of the magnetic flux and the consequent coil force reduction and its acceptability in function of valve functionality, energy balance and cost.

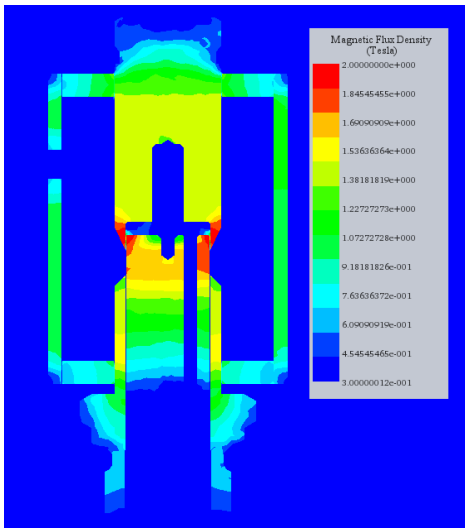

Figure 8. Case Std at maximum current

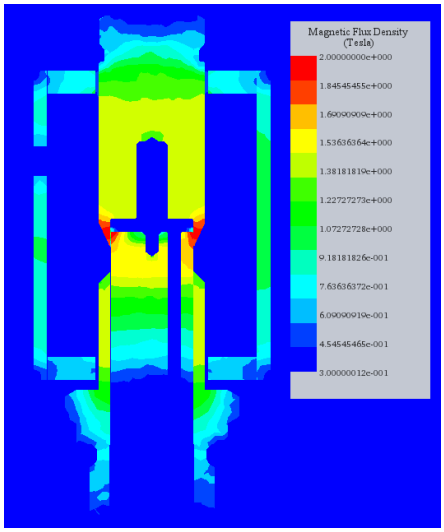

Figure 9. Case G at maximum current

In Figure 8 and Figure 9, it is evident the difference between the case standard, with minimum air gap, and the case G, which can be defined the worst case. As it can be observed, in correspondence of the metal washers, both upper and lower, in Figure 9, the field is interrupted and consequently the flux is dispersed. This is due to the larger air gap. The consequence is the reduction of the flux intensity also in the area of the control cone, where the field should be maximum, in order to control the valve plunger position. The yellow color, in respect to the orange available in the standard case, indicates that the field is lower. The final consequence is the reduction of the coil force and the impossibility to control properly the valve even at maximum current.

To justify mathematically this conclusion, the EMS simulator method shall be introduced. In particular, EMS solves the Maxwell equations of the electromagnetic interaction. In particular, it solves the two magneto-static analysis equations (7.1) and (7.2), which is the most useful for identifying the intensity characteristics of the magnetic field generated in each topology under study.

$$\tilde{N} \times H = J_S \tag{7.1}$$

$$\tilde{N} \cdot B = 0 \tag{7.2}$$

The simulator calculates the attraction force Fs between fixed and moving parts of the valve using the virtual work method and it calculates the value of the total magnetic energy when an object moves from a position 1 (W1) to a position 2 (W2) at a Δs distance (equation 7.3).

$$F_S = \frac{W_2 - W_1}{Ds} \tag{7.3}$$

$$W = \frac{1}{2}\int B \cdot H dv \tag{7.4}$$

$$B = \mu_0 \cdot \mu_r \cdot H \tag{7.5}$$

In the case of magnetic elements, the Work W is calculated in equation 7.4 in the Volume of the elements under study and the reason of the magnetic field flux density reduction is clear in equation 7.5. In this equation, B is the magnetic induction field or magnetic field flux density, H is the magnetic field, v is the volume, μ_0 is the magnetic air permeability and the μ_r is the magnetic permeability of the metal used for the valve (μ_r(AVP)≈1.000). It is then clear that, in case of a larger air gaps, the Fs is reduced of a μ_r factor in the incremental volume of the air gap in respect to the standard case. The magnetic field H does not change, because it depends on number of turns of the coil winding and the current, while B changes due to change of the air gap size.

The analysis justifies the reason higher currents are needed to control the valve plunger in all cases analyzed other than the Standard one. Then, in order to reduce as much as possible the deterioration of performance, it is necessary to optimize the air gap. From the analysis of the simulation results, it appears that the optimal case is case D, where it can be noted that metal washer that makes up the ring armor in area A (Figure 7), has the same air gap of the standard case, in order to not disperse the magnetic flux in that area. The case D is the one used for all the real tests.

6. TESTS OF FINAL VALVE ASSEMBLY

Once the coil and coil enclosure air gaps have been defined, the coils have been modified in order to assemble the prototypes. The air gaps have been modified by mechanical tooling enlarging only one ring, with the configuration of the case D. Furthermore two milled flats of the plastic layer in the rear part of the coil were made by mechanical tooling, to allow the housing of the flat cable which brings the poles of the two resistive sensors which make up the strain gauge to the outside (Figure 10 left).

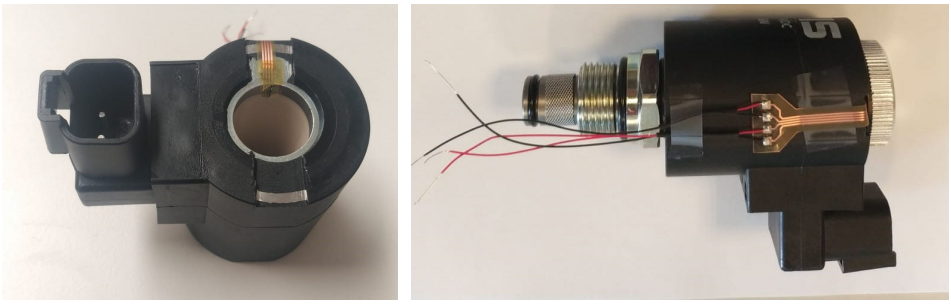

Figure 10. Modified coil and Valve Assembly

This was done to allow the fixing of the nut that holds the coil in place, once placed in the correct position with respect to the spaces available in the manifold, without risking

damaging the flat cable itself. The result of the assembly ready to be tested at the test bench is shown in Figure 10 right.

The Valve with the new sensor must be characterized and the expected behaviour is that the sensor should not detect signal variations during valve operation under nominal and healthy conditions, because of the very limited deformation of the valve body expected, while it should detect signal variation, if the valve is subject to higher-pressure levels.



Figure 11. Static Pressure Test Bench

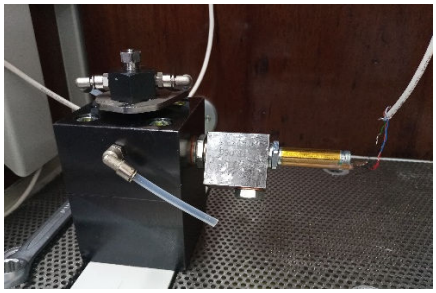

Figure 12. Dynamic Pressure Test Bench

The first tests have been conducted at the static test bench (Figure 11), in order to characterize the sensor resistances in nominal and ambient temperature conditions. In the range [0; 250] bar a barely detectable change in sensor resistance was observed, confirming that the sensor is not working in nominal conditions, exactly as other strain gauges used in past experiences. While the tests at the dynamic pressure bench (Figure 12), used for valve burst tests, made possible to fully characterize sensors in respect to valve deformation.

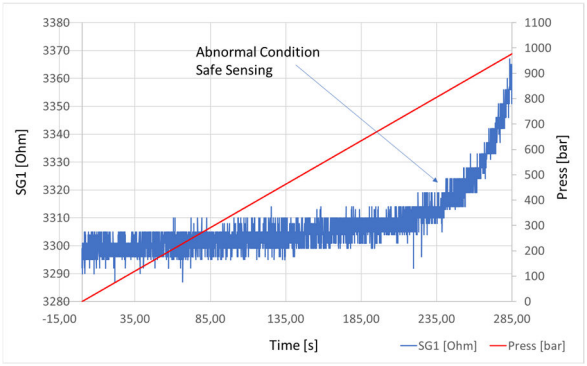



Figure 13. Pressure Transient Test

The tests were conducted in two different conditions: valve without coil and valve with coil. In fact, the coil presence changes the fault conditions for the sensor which, due to excessive deformation of the pole tube and the limited air gap, it is crushed between the pole tube and the coil. For that reason, the sensor often breaks in short circuit, resulting in a zero resistance measurement. On the contrary, without coil the more frequent fault for the sensor is case of excessive strain is in open circuit condition.

The described faults happen at the end of the burst tests or pressure tests, when the valve breaks with a consequent oil loss, or even before that condition if the sensor breaks due to an excessive pole tube deformation. The described tests were necessary to validate the capability of the sensor of providing a useful signal when in faulty conditions, to detect faults of the sensor itself, because of the valve failure or breakage.

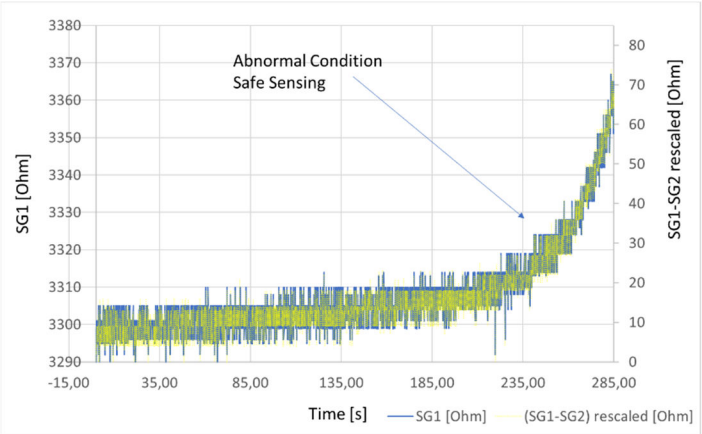

Figure 14. SG1 sensor signal comparison with (SG1-SG2) rescaled and referred to zero

However, the tests allowed recognizing abnormal conditions much earlier than valve failure conditions, so sensor breakage it represents a limit condition that should rarely be reached in real applications. In fact, a series of tests were conduct stopping the dynamic pressure test bench once the electronic control system was able to recognize a changing signal of the sensor in respect to its base line (Figure 13). In fact as it can be noted in Figure 13, the sensor in nominal working conditions is stable at a constant value, temperature dependent, while when for pressure or yielding of the pole tube, the tube shape changes, then the sensor acquire a signal that differs from the baseline of SG1 more than the 0,5% or 1% (15-30 Ω).

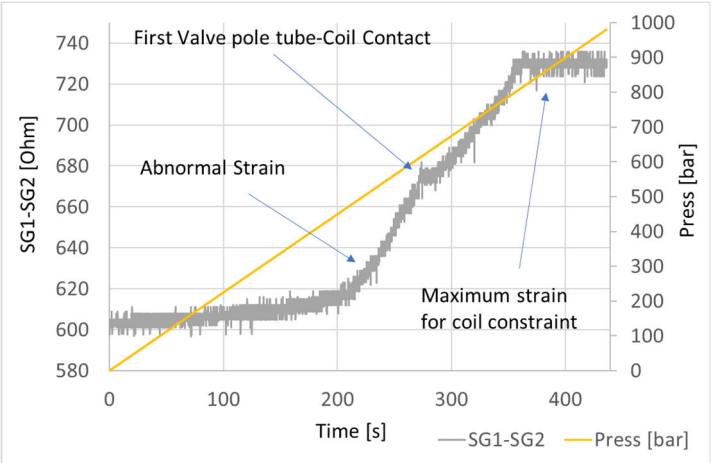

Figure 15. (SG1-SG2) in respect to Bench pressure in the test with Coil

The Electronic control is equipped with an analogue readout circuit adapted to the resistance of the sensor and with an amplification of the analogue signal, which is also adapted to the specific sensor. In these conditions 70 ohm can represent the 40 or 50% of the entire signal variation captured by the Analog to Digital converter (ADC) dedicated to the SG1 (sensor) input. The SG2 sensor is connected with a similar circuitry, so the resolution can be very high in respect to signal transition. In Figure 14, in fact it is represented how the two signals of SG1 and the signal SG1 referred to the SG2 sensor signal (SG1-SG2), which represent the pure temperature strain, are equivalent in shape and range. This consideration leads to prove that both configurations described (full bridge or two half bridges) are equivalent from the signal resolution point of view and are both functional for detecting anomalous deformations of the pole tube. The characterisation of the solution also analyses how the sensor reacts to the deformation in presence of the coil, which is a restraint in the pole tube expansion.

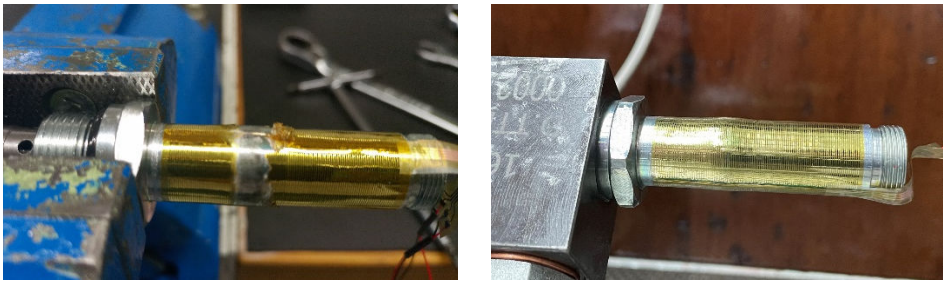

Figure 16. Valve pole tube in case of Coil and no coil

In Figure 15 it is shown a test on the dynamic pressure test bench where the test is stopped before the pole tube damage. In the chart, it is clearly visible the limit for sensor acquired strain that is also the limit of the pole tube enlargement due to small air gap available between pole tube and coil (and plastic coil enclosure). In addition, in this case, the sensor was able to capture the abnormal strain and the limited space did not affect the sensor's ability to detect an anomalous condition of deformation of the pole tube. Unfortunately, due to the hard contact, it is impossible to analyse the sensor after the test because the tube deformation is inelastic, and pole tube and coil are stuck and the sensor is crushed between the two elements. The described condition is shown in Figure 16, where it is visible the resulting deformation of the pole tube when the coil is extracted using a puller to overcome the resistance caused by the deformed pole tube. As it can be noted the shape of the pole tube deformation it is not rounded as in the case of no coil, so it is limited by coil presence.

7. CONCLUSIONS

The sensor presented is a specialized version of a strain gauge sensor. The sensor is not only special in its shape, but both materials and process are new. A very thin substrate and a nano-metric conductive material deposition allowed generating a sensor capable of sensing phenomena that normal strain gauges were unable to sense in past experiences. The sensor is a safety relevant sensor for cartridge valves, which allows detecting abnormal pole tube deformation at early stage, before valve breakage or oil leaks due to vale cracks. The sensor demonstrated its efficacy in static and dynamic conditions, both with and without coil, and

it has been characterized until sensor breakage and valve breakage. This research demonstrates that shape design freedom offered by flexible electronics technology represents an interesting opportunity to equip hydraulic components with new sensors, which can bring to electro-hydraulic systems an unseen diagnostic coverage level, matching with more stringent requirements of fault tolerant applications in various fields, like: submarine, avionics, autonomous systems, steering and braking, and in military applications. This project represents a first implementation of these new sensors to cartridge valves, the tests executed and the use cases are a part of the whole set of tests that can be planned and executed with valves and is of interest of the authors to validate sensors in all possible conditions, especially in endurance tests. These tests activities will be planned with the company for a full application characterization. Also the sensor itself will be revised in order to make it more robust in the connector part which had turned out to be delicate during the valve mounting phases at the test bench. Finally, the shape of the sensor and its resistive lines, as well as the number of resistive elements and the direction of resistive lines in respect to the direction of valve breakages will be deeply analysed and revised, in order to maximize the sensor response when under stress. In fact, based on strain gauge theory, each sensor element response is maximized, when the whole element is under stress due to incoming pole tube breakage. A sensor system with more than two independent elements as shown in this research, could maximize the sensor response. More in detail, authors will continue to develop the sensor by modifying its design and by applying it to other type of valves; from the tests side point of view, the authors will investigate the sensors response in endurance tests at rated pressure, to make them work under real conditions of use and to characterize them fully.

8. ACKNOWLEDGEMENT

The research was carried out under the financed project “Mechatronic hydraulic valves equipped with innovative intrinsically safe sensors” granted to VIS Hydraulics Company under the Italian Law 14/2014 for European funding for regional development.

9. REFERENCES

[1] Jingqi Liu, Chenggang Yuan, Lukas Matias, Chris Bowen, Vimal Dhokia, Min Pan, James Roscow, Sensor Technologies for Hydraulic Valve and System Performance Monitoring, Challenges and Perspectives. Advanced Sensor Research. 2024. doi: 10.1002/adsr.202300130

[2] A.I. Pavlov, I.A. Polyanin, K.E. Kozlov, Improving the Reliability of Hydraulic Drives Components, Procedia Engineering, Volume 206, 2017, Pages 1629-1635, ISSN 1877-7058, https://doi.org/10.1016/j.proeng.2017.10.689.

[3] B. Beck, J. Weber, Enhancing safety of independent metering systems for mobile machines by means of fault detection, The 15th Scandinavian International Conference on Fluid Power, SICFP’17, June 7-9, 2017, Linköping, Sweden, ISBN: 978-91-7685-369-6, ISSN: 1650-3686 (tryckt), 1650-3740 (online), http://dx.doi.org/10.3384/ecp1714492.

[4] Jinchuan Shi, Jiyan Yi, Yan Ren, Yong Li, Qi Zhong, Hesheng Tang, Leiqing Chen, Fault diagnosis in a hydraulic directional valve using a two-stage multi-sensor information fusion, Measurement, Volume 179, 2021, 109460, ISSN 0263-2241, https://doi.org/10.1016/j.measurement.2021.109460.

[5] Nurmi, J, & Mattila, J. "Detection and Isolation of Faults in Mobile Hydraulic Valves Based on a Reduced-Order Model and Adaptive Thresholds." Proceedings of the ASME/BATH 2013 Symposium on Fluid Power and Motion Control. Sarasota, Florida, USA. October 6–9, 2013. V001T01A020. ASME. https://doi.org/10.1115/FPMC2013-4435

[6] L. Siivonen, M. Huova, and M. Vilenius. Fault Detection and Diagnosis of Digital Hydraulic Valve System. The Tenth Scandinavian International Conference on Fluid Power, May 21-23, 2007 Tampere, Finland, Tampere, 2007.

[7] J Ersfolk, M Ahopelto, W Lund, J Wiik, M Waldén, M Linjama, J Westerholm, Online fault identification of digital hydraulic valves using a combined model-based and data-driven approach, arXiv preprint arXiv:1803.05644, 2018•arxiv.org, https://doi.org/10.48550/arXiv.1803.05644.

[8] Denkena, Berend & Dahlmann, Dominik & Kiesner, Johann. (2014). Sensor Integration for a Hydraulic Clamping System. Procedia Technology. 15. 10.1016/j.protcy.2014.09.006. https://doi.org/10.1016/j.protcy.2014.09.006

[9] Guo, Yuan & Zeng, Yinchuan & Fu, Liandong & Chen, Xinyuan. (2019). Modeling and Experimental Study for Online Measurement of Hydraulic Cylinder Micro Leakage Based on Convolutional Neural Network. Sensors. 19. 2159. 10.3390/s19092159.

[10] Michael Rannow, Fail Operational Controls for an Independent Metering Valve, 10th International Fluid Power Conference, Dresden 2016,

[11] A. K. Bose et al., "Screen-Printed Strain Gauge for Micro-Strain Detection Applications," in IEEE Sensors Journal, vol. 20, no. 21, pp. 12652-12660, 1 Nov.1, 2020.

[12] Araromi, O.A., Graule, M.A., Dorsey, K.L. et al. Ultra-sensitive and resilient compliant strain gauges for soft machines. Nature 587, 219–224 (2020).

[13] A. K. Bose et al., "Screen-Printed Strain Gauge for Micro-Strain Detection Applications," in IEEE Sensors Journal, vol. 20, no. 21, pp. 12652-12660, 1 Nov.1, 2020, doi: 10.1109/JSEN.2020.3002388.

[14] F. Maita, V. Piccialli, F. Pensa, M. Scatto, M. Ruggeri and L. Maiolo, "Application of Unconditioned Nanostructured Thermoplastic-Based Strain Gauge Sensor in Wearable Electronics," in IEEE Sensors Journal, vol. 22, no. 24, pp. 24019-24026, 15 Dec.15, 2022.

[15] Irani, F.S.; Shafaghi, A.H.; Tasdelen, M.C.; Delipinar, T.; Kaya, C.E.; Yapici, G.G.; Yapici, M.K. Graphene as a Piezoresistive Material in Strain Sensing Applications. Micromachines 2022, 13, 119.

[16] A. Pecora et al., "Strain gauge sensors based on thermoplastic nanocomposite for monitoring inflatable structures," 2014 IEEE Metrology for Aerospace (MetroAeroSpace), Benevento, Italy, 2014, pp. 84-88.

[17] Li, H., Zhang, J., Chen, J. et al. A Supersensitive, Multidimensional Flexible Strain Gauge Sensor Based on Ag/PDMS for Human Activities Monitoring. Sci Rep 10, 4639 (2020).

[18] E Aslanidis, E. Skotadis and D. Tsoukalas, Resistive crack-based nanoparticle strain sensors with extreme sensitivity and adjustable gauge factor, made on flexible substrates, Nanoscale, 2021, 13, 3263-3274.

Thermal Insights and Predictive Modeling of Axial Piston Pumps: A Journey to a High-Fidelity Digital Twin

Roman Ivantysyn and Jürgen Weber

Institute of Mechatronic Engineering, Technische Universität Dresden,
Helmholtzstrasse 7a, 01069 Dresden,
E-mail: roman.ivantysyn@tu-dresden.de, fluidtronik@mailbox.tu-dresden.de

Abstract.

This paper presents a novel investigation into the modeling of axial piston pumps, with a focus on identifying the essential and non-essential measures for achieving high accuracy in thermal and efficiency prediction. A notable highlight is the first-ever published dataset of simultaneous high-dynamic temperature and pressure measurements within the displacement chamber of an operating pump, accompanied by detailed monitoring of its thermal behavior. This unique experimental foundation provides unprecedented insight into the impact of various modeling assumptions on the predictive accuracy of digital twins.

Highlighting the critical balance between model complexity and computational efficiency, the study identifies which assumptions can be safely made without compromising model fidelity and which require more careful consideration. Through careful analysis, it demonstrates how specific measures, such as accounting for component wear, manufacturing tolerances, and incorporating real-world temperature variations, significantly improve the accuracy of the model.

This work not only advances theoretical understanding, but also sets new benchmarks for practical modeling strategies, paving the way for advances in hydraulic system optimization and predictive maintenance offering a physic-based model rather than complex black box models. The insights gained from this study underscore the importance of a nuanced approach to model development and mark a new phase in the precision engineering of axial piston pumps.

Keywords. Digital Twin, Thermal Modeling, Tribology, Efficiency, Thermal Boundary Conditions, High-Dynamic Temperature Measurements

1. INTRODUCTION

The hydraulic industry exhibits remarkable versatility, with positive displacement units gaining prominence due to their superior power density, efficiency, and durability. These attributes render them indispensable in a wide range of demanding environments, from space aviation to various mobile applications, continuous industrial manufacturing processes, and specialized domains like subsea robotics. A common thread among these applications is the

uncompromising need to avoid failure, coupled with an increasing emphasis on enhancing efficiency in response to escalating energy costs and the imperative to reduce emissions. Mobile machinery, which represents the largest market segment for hydraulic components, is undergoing a transformative shift towards sustainability, spurred by the electrification movement. In this new era, hydraulic pumps will be integrated within interconnected components, necessitating advanced feedback mechanisms for real-time efficiency monitoring and performance prediction across diverse operational conditions.

The advent of high-fidelity digital twins promises to revolutionize this landscape, offering a virtual repository for machine operators, controllers, and system optimization algorithms. The rise of powerful numerical tools now allows for a cost-effective creation of digital twins within a simulation environment, avoiding the need to acquire expensive test-rig experiments and difficult to gather field data sets for machine learning algorithms.

This paper will demonstrate how a digital twin framework can be build using Caspar FSTI and outlines the essential steps to ensure a precise alignment between empirical measurements and simulation outcomes.

2. PRIOR WORK AND RESEARCH GOAL

The primary objective of the presented research is to demonstrate the feasibility of building a digital twin for hydraulic components, specifically axial piston pumps, leveraging a physics-based numerical model. This approach prioritizes a physics-driven framework over traditional black box models, offering scalable predictability across an expansive spectrum of components without necessitating extensive data collection. The challenge of amassing sufficient training data to encompass all operational scenarios of piston pumps is particularly acute for smaller hydraulic suppliers. Therefore, a cycle and system independent approach is required to allow scaling between various sizes and manufactures all within a virtual environment.

Previous studies have underscored the potential of machine learning-based black box models, with several achieving noteworthy outcomes, some of which are currently in practical use [1], [2], [3]. However, these models are generally restricted to specific pump series and use cases, such as stationary hydraulics with repetitive cycles, heavily reliant on high-frequency data from sophisticated sensors, electronics, and rapid communication technologies. Minor alterations, like relocating a sensor or changing the system’s impedance, can significantly impact the systems' response characteristics, complicating the scalability of these solutions across a wide range of applications. An additional hurdle for the black-box models entails the requisite collaboration between machine Original Equipment Manufacturers (OEMs), responsible for implementing and operating these models, and the pump manufacturers, who have the knowledge about their components but typically lack access to the machine's field data. Moreover, the inherent nonlinearity of lubricating gaps — which are critical for the system losses — remains elusive to even advanced physics-informed machine learning techniques.

The author has published previous work that validated the predictive capability of numerical pump models and demonstrated the potential of using cost-effective, reliable, and low-bandwidth temperature sensors to accurately predict pump efficiency and power losses. [4], [5], [6], [7]. By creating a high-fidelity numerical model, the bulk of computational demands

can be transferred to a controllable virtual environment, minimizing the reliance on physical data collection, which remains feasible with current technology and is system agnostic. The use of temperature as an efficiency predictor, although not novel as evidenced by the work of Schlösser and Renius, is innovatively applied here to transient data analysis rather than solely steady-state conditions — a crucial distinction given the impracticality of maintaining steady-state operations in mobile machinery, a limitation that has precluded the implementation of existing models in real-world settings [8], [9], [10].

This paper will present the general feasibility of a physics-based numerical twin for axial piston pumps based on the numerical tool Caspar FSTI for real world applications. By being able to accurately predict the gap heights in the lubricating gaps within a digital twin allows for the prediction of the entire pump's power losses, forecasting thermal variations in both components and fluid, and adjusting for performance shifts due to manufacturing tolerances. In detail this paper will:

- Present novel measurements in a rotating cylinder block, allowing for a deeper look inside the pump rotating kit.
- Demonstrate the conversion of transient data into comparable steady-state conditions with a steady-state numerical twin.
- Outline the necessary modelling depth of the twin to accurately predict real world applications.
- Emphasize the importance of incorporating wear modeling due to its significant impact on pump performance.
- Examine the effects of manufacturing tolerances on power losses and how the model can be used to predict these factors.

3. MEASUREMENTS

This chapter will showcase the measurement setup, highlight key measurements, and then present interesting trends and patterns that can be used to validate the simulation, enhance the virtual model and in general broaden the thermal understanding of axial piston pumps.

3.1. Measurement Set-Up

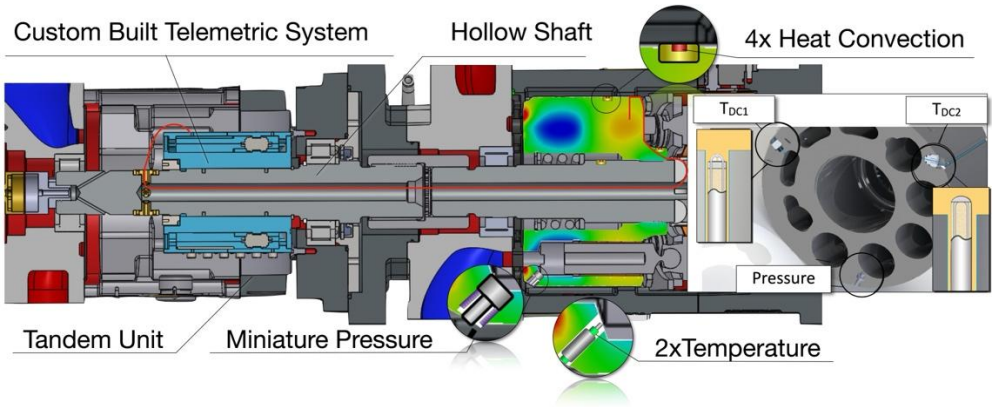

Figure 3.1. Measurement Set-up System Capturing 20x Temperature inside the Block, Pressure and Temperature in the Piston Chamber and Heat Transfer on the Surface.

A 160 cc open-circuit axial piston pump of the swash plate type was used as the test specimen for the temperature evaluation of the cylinder block. Prior publications have shown that measuring the cylinder blocks temperature is especially suitable for the efficiency evaluation of the entire pump, as it is the central element of the rotating kit and is affected by all lubricating gaps of the pump [4]. The utilized set-up is shown in Figure 3.1. An array of sensors was installed, including 20 temperature sensors capturing the cylinder block's temperature field, 4 heat-convection coefficients on the surface of the block (outside wall, shaft- and neck-surface) and high-speed pressure and temperature sensors monitoring the pressure build-up and corresponding transient temperature response of the compressed fluid. The locations of the thermocouples are illustrated in Figure 4.4. The data were transferred with an in-house built telemetric system that allowed for both the larger number of sensors and the fluent switch between high and low frequency data acquisition.
The heat convection coefficient sensors (h-sensors) capture the heat loss on the surface by heating a small resistance that also serves as a temperature sensor. The functionality was described in previous publications by Uffrecht et. al. [4], [11], [12], [13], [14]. The heat transfer was never measured in a working pump environment, allowing to validate CFD models in hydraulic fluid applications for the first time. A comprehensive comparison of different CFD-modeling techniques using various software approaches and comparing them to the measured trends will be published simultaneously to this paper in a different conference [15]. Figure 3.2 presents the measured trends for various surfaces with speed and change in displacement. The cylinder block (CB) outside wall surface only changes its heat exchange rate with speed and is independent of pressure and swash plate angle. The top region of the block however shows an increasing heat exchange rate with lower angles. Regions of high turbulences such as the piston or slipper can exceed the cylinder blocks convection rate due to local eddies increasing the boundary layer flow speed even though they have smaller angular velocities.

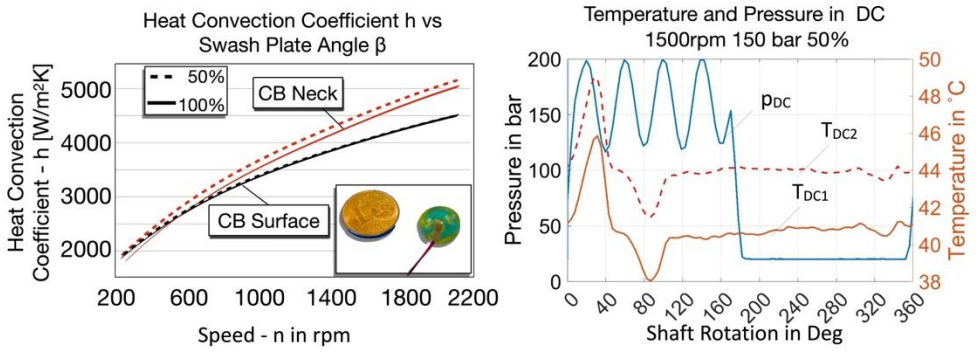

Figure 3.2. Sample Measurement of the Heat Convection and Pressure and Temperature inside the Displacement Chamber (DC)

By developing both the sensor and telemetry systems, as well as DAQ systems, in-house, it is possible to achieve high accuracy with maximum flexibility. This was demonstrated by capturing high-speed measurements simultaneous to the low-frequency temperature and h-sensors. By combining numerical gap results with FEM-Analysis it was possible to accurately predict the precise loading on the cylinder block and forecast the durability of the cylinder block for high pressure usage for each design option. The chosen design was designed to withstand at least 60 hours of testing at 300 bar. The resulting sensor

arrangement allowed the installation of two high-speed thermocouples and a high-speed miniature pressure sensor all within a cylinder block that featured over 30 other sensors, as some of the 20 temperature locations were installed redundantly. Two types of temperature sensors were used. The first sensor type (labeled 'T_{DC1}' in Figure 3.1) features an open tip, exposing the 0.1mm wire used to measure the temperature. This allowed for minimal heat capacity and enabling the capture of temperature changes in the nanosecond regime. Naturally, the tip is very fragile and cannot be placed inside the flow path. The second thermocouple, 'T_{DC2}', features the same small wire thickness as T_{DC1} but has a small protective cap. This added robustness allowed to protrude the sensor further into the flow, to capture different boundary layers. However, after inspecting the pump post-measurement, it was revealed that this second sensor was touching the wall, essentially measuring the wall temperature from the inside. Initially it was feared that the added robustness slightly increasing its heat capacity decreasing its reaction time slightly. However, the measurement results are conclusive that in this application, pump speeds up to 2100 rpm and pressure build-up rates of 150 bar/ms, both sensors yielded fast enough response rates to follow the pressurization inside the displacement chamber as can be seen for 1500 rpm and 150 bar in Figure 3.2. The measurement concluded shortly before this paper was written; therefore, a fundamental analysis will be published in the future.

However, several very interesting observations can be made at the current analysis stage. The temperature response of the fluid shows a small lag for both sensors of 1ms at high speed, by peaking later than the fluid pressure. However, the sensors are fast enough, as the reaction to pressure is immediate even at 2100 rpm. This lag seems to be independent of speed, indicating a geometrical cause. During the change from high to low pressure the fluid is confined for a short instance to one piston bore, before opening to the high-pressure (HP)-kidney of valve plate. During this time the temperature spikes considerably, but never peaks at the same time as the pressure, rather it continues to rise until the pistons opens to the HP-port. This indicates that the fluid temperature rise with pressure is not instantaneous. After re-connecting with the other HP-pistons through the HP-kidney the temperature in the fluid drops significantly, signally a thermodynamic loss. Surprisingly this temperature drop even falls below the suction stroke (180˚ - 360˚) temperature, in certain condition even below the 35˚C port temperature. This phenomenon occurs both in transient and steady state at all pressure and speed levels and is captured by both sensors ruling out a faulty sensor. This means that even during steady state operation the piston pressurization cannot be simplified as an adiabatic process. Another interesting finding is that while the temperature response to the pressurization is clearly visible and lies within 2-8K for pressures of 50-250 bar, there is no temperature change in the displacement chamber during the suction stroke. While all measurements were performed at 35˚C inlet temperature (measured directly at the inlet), the temperature in the displacement chamber was always several degrees above this value. One must assume that the turbulent flow through the suction port quickly heats the fluid by several degrees. This temperature increase as a function of speed is depicted in the blue curve in Figure 3.3.

The cylinder block temperature was captured both in transient and steady state conditions, where steady state was defined as <0.1K/min change in all installed sensors relative to the inlet temperature. This thermal equilibrium condition was typically reached in 10-15 min for small changes in the operating point or 15-30 min for larger speed or pressure changes. By analyzing the steady state temperature and efficiency one can gain a fundamental

understanding of the lubricating gaps, as all other transient effects can mostly be neglected, although the temperature dip inside the displacement chamber clearly suggests limits to these assumptions.

To illustrate how the cylinder block temperature level changes with speed for a given pressure level, the min. max, and mean block temperatures are shown in Figure 3.3 across the pumps' speed range for 100 bar. The total measured pump efficiency is shown in grey, while the measured fluid temperature in the suction stroke of the displacement chamber (T_{DC}) is depicted in blue and cyan. Both mean and maximum temperature rise significantly with speed, whereas the minimal temperature increases only slightly. The minimal block temperature is measured always near the displacement chamber (see Figure 4.5 and the cutout depicted). The minimum block temperature correlates exactly with the measured fluid temperature T_{DC1} (blue circles) indicating a rather large heat transfer rate in the displacement chamber. The second temperature sensor in the displacement chamber (T_{DC2} – shown in cyan color) turned out to touch the inside wall of the chamber. Hence it represents the temperature of the inside surface of the bore near the bottom of the displacement chamber, which shows a different trend with speed. It should be noted that the solid body temperature of the block is much higher in the area where the fluid temperature sensors were installed (bottom corner of the displacement chamber) as compared to further up towards the center of the middle of the chamber, where the minimal block temperature was captured. The shown graphic illustrates the temperature distribution at 1000 rpm and 100 bar around the displacement chamber. All measurements were standardized to 35˚C ±1˚C inlet temperature to guarantee uniformity across different operating conditions. Notably, the fluid temperature inside the displacement chamber never reaches this 35˚, indicating a high heat transfer rate in the suction port, increasing the fluid temperature notably. At 100 bar, the minimal block temperature decreases with speed, indicating that despite the block temperature increasing, the fluid temperature decreases. This is because the higher flow rate at increased speeds (with the fluid passing through the inlet port in roughly 15 ms at 2100 rpm) reduces the time the fluid remains in the pump. Consequently, the fluid has less time to absorb heat, resulting in a lower fluid temperature.

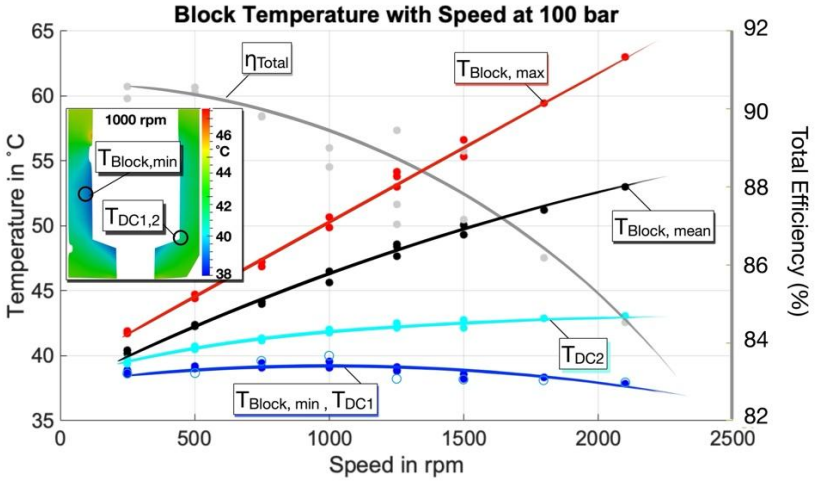

Figure 3.3. Measured Temperature and Efficiency Trend with Speed at 35˚C Inlet, 100 bar and Full Displacement.

The temperature increase in this pump is mainly due to speed and less affected by pressure, as can be seen in Figure 3.4. Shown on the left is the maximum measured cylinder block temperature with speed and pressure at 100% swash plate angle. The hydraulic power output is shown in the black contour lines. Shown are also the total and partial efficiencies for reference. While the temperature field is influenced by both viscous and volumetric losses occurring in the lubricating gaps, no discernible pattern emerges that aligns consistently with power output and efficiency lines. This suggests that, although temperature rise correlates with power output and losses, it intersects with both power and efficiency metrics in a manner that prevents a straightforward trend from being established. The method for leveraging this metric to accurately gauge efficiencies will be elaborated in the following section by means of simulation models that can link gap losses with efficiency and temperature.

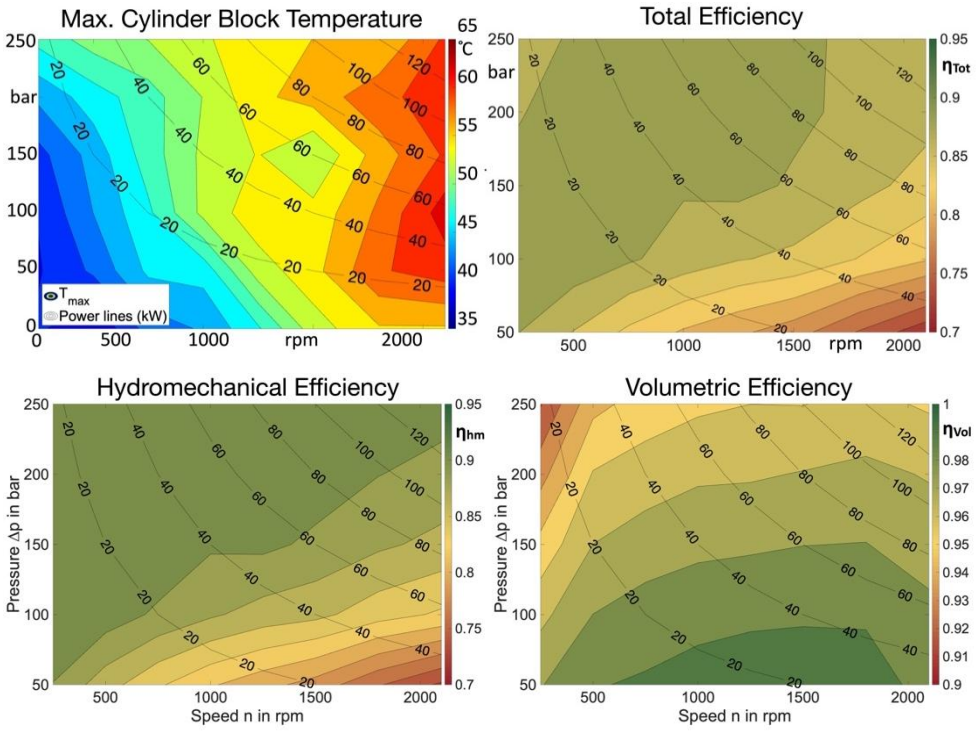

Figure 3.4. Captured Cylinder Block Temperature and Efficiency Field of an 160cc Axial Piston Pump at Full Displacement.

4. DIGITAL TWIN OF THE ROTATING KIT OF AN AXIAL PISTON PUMP

The numerical model used for predicting the power losses occurring in the lubricating gaps is called Caspar FSTI. The model was developed by Monika Ivantysynova and her team of researchers over a 30-year time span and several fluid power centers. It was specifically developed for piston pumps, enabling efficient modeling without the need for in-depth knowledge of numerical techniques and mesh studies. It captures the necessary micromotion and part deformation both due to pressure and temperature, which was shown to have a tremendous effect on the performance on the tribological interfaces [16]. The tool was

validated for each lubricating gap using both temperature and gap height measurements [4], [5], [17], [18], [19], [20], [21], [22]. While simulating just one gap interface is common practice and practical for relative improvement studies all three gaps need to be modelled to capture the entire pump efficiency and thermal behavior as the gaps affect each other.

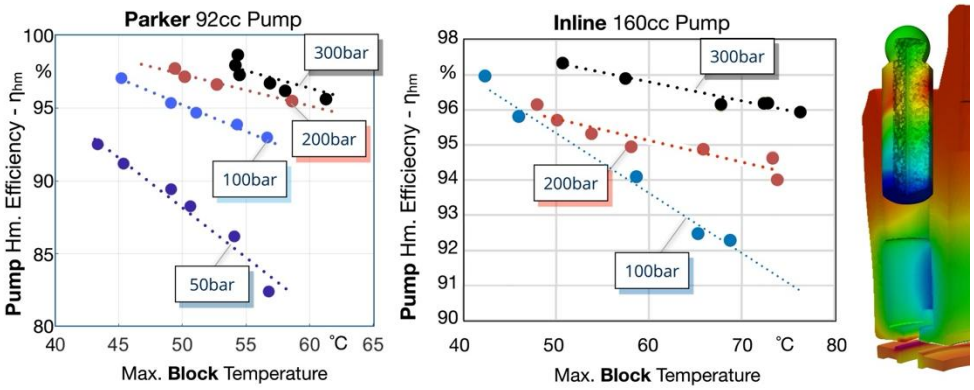

Figure 4.1 Digital Twin Predicts Pump Efficiency and Cylinder Block Temperature Correlation for Two Different Pumps.

Such a complete model was built for two different high-pressure axial piston pumps. A 92cc pump from Parker Hannifin and a 160cc pump from Inline Hydraulics were analyzed. Both pumps feature no special components such as inverse pistons, spherical valve plates or bushing less pistons and can therefore be taken as a good representation of the average piston pump on the market.

Both models predict a linear correlation between the hydromechanical efficiency of the entire pump and the max. cylinder block surface temperature. Shown in Figure 4.1 is the simulated trend for both pumps. As can be seen, there is a direct correlation between efficiency and temperature at each pressure. A similar trend can be made for the volumetric and total efficiency as was shown in [4]. In the same publication the trend was validated with steady state measurements, confirming that measuring the surface temperature of the cylinder block allows for a direct correlation with the total and partial efficiencies of the entire pump. A similar trend can also be made with the steady state leakage and housing temperature, as they follow the maximum block temperature quite well. However, for real world applications it is not feasible to wait for steady state. The cylinder block reacts instantly to any operational change, allowing for a transient model.

4.1. Efficiency Prediction using Transient Temperatures

A typical transient condition change is shown in Figure 4.2. The pump goes through a 250 rpm speed change in a 10 s time frame. While this change is not particularly dynamic, it greatly captures the temperature lag of the fluid and housing temperatures in comparison to the cylinder block. As can be seen in the thicker blue curve, the cylinder block reacts instantly and without any noticeable lag to the speed change, increasing its temperature by more than 2K in the 10 s time frame it took to change the speed. While it has not reached steady state, it exhibits an easily detectible temperature increase. Meanwhile, the fluid temperatures (inlet, outlet and leakage) change minuscule in this 60s time frame, not reliably

detectable for most temperature sensors. The housing temperature also does not change as it is reliant on the leakage temperature to conduct the heat generated in the rotating kit.

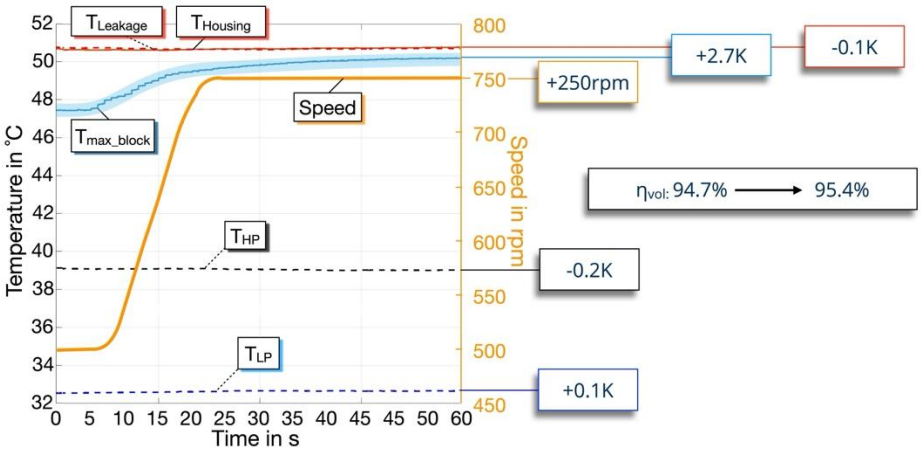

Figure 4.2 Fast Transient Response of the Cylinder Block in Comparison to the Fluid and Housing Temperatures.

While the speed change was small it caused a noticeable increase in volumetric efficiency, showcasing that the transient temperature is indeed capable of predicting transient efficiency changes. The volumetric efficiency η_{vol} exhibits an inverse trend with block temperature as compared to the hydromechanical efficiency η_{hm}. Higher viscous losses increase heat losses which increase local component temperatures, causing a positive correlation between η_{hm} and $T_{max,block}$. Higher volumetric efficiency means lower gap leakage, which causes less heat to be dissipated from the gap to the environment, causing an overall increase in component temperature. To be able to distinguish temperature increase due to higher friction or lower leakage, it is instrumental to predict the effect of gap height movement on distinct component temperature changes at various positions, e.g. where the hottest temperature occurs. In practice this means that at least 2-3 temperature locations need to be monitored on the cylinder block surface.

A digital twin allows for such a prediction, being trained on the physical behavior inside the lubricating gap, it can interpret each temperature change and predict even which component is causing the losses at this instance of time. As Caspar FSTI requires thermal equilibrium to keep simulation time reasonable, it is necessary to convert the transient temperature change to a steady state value, which can in turn be used with the digital twin.

Such transient model was developed using over 200 transient temperature rises/and falls with their corresponding measured steady state values. Such a rise is shown Figure 4.3 for the same 250 rpm increase as shown earlier. Left in the figure is the full 35 min of data, shown for one of the sensors inside the cylinder block. Steady state ($\Delta T/\Delta t$ <=0.1K/min) was reached for this operating condition after 30 min at 51.1˚C. The transient predictive model was fed with just 30 seconds of this data and predicts a steady state temperature of 51.2˚C after 25 min.

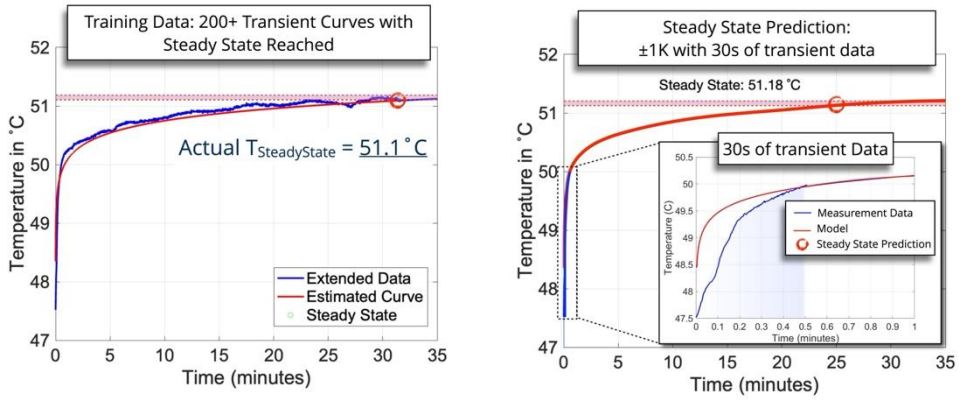

Figure 4.3. Prediction Model to Convert Transient Data to Steady State Data.

This model also works for temperature drops and can predict thermal steady state conditions with a ±0.1K accuracy, which was determined to be accurate enough as most efficiency changes cause temperature increase of more than 1K, as was demonstrated in Figure 4.2 for a less than 1% change in volumetric efficiency.

As was established in the previous section, it is quite feasible to monitor the current pump efficiency using the surface temperature of the cylinder block. There are multiple methods to capturing this temperature, whether through conduction (via a spring-loaded sensor), radiation (using an optical method) or by wireless transmission using an sender/receiver principle. The possibilities are endless and certainly do not require a complicated set up as was done for this research endeavor. The number of measurement locations could vary for each pump, but for the studied pumps two locations are sufficient to capture the maximum temperature. One sensor at the bottom near the valve plate and one towards the top on the cylinder block outside surface will suffice. While it is certainly possible to substitute some rotating sensors with non-moving stationary sensors such as on the valve plate, it will certainly require more sensors stationary sensors as compared to rotating ones. This is because the hot spots move on the valve plate between operating conditions as was shown in [5], [7], [22]. As the sensors-problem can certainly be solved with good engineering work, the question arises what model depth is necessary to build an accurate digital twin using Caspar FSTI or similar numerical models.

4.2. Required Model Accuracy and Boundary Conditions

As in every simulation model certain assumptions must be made to simplify reality. Caspar FSTI certainly is no exception and requires for example steady-state operating conditions and corresponding thermal boundary conditions including the port temperatures. In addition, the gap geometry needs to be defined using geometrical parameters such as diameters and notches. These components deviate within the manufacturing tolerance band in both shape and surface topology. Choosing the right dimension and determining which parameters are more important than others, requires experience. This paper is meant to give some helpful guidance in this process. To capture the deformation due to pressure loading or temperature expansion a mesh needs to be generated for each gap defining surface. As is typical for any FEM-Model, these meshes require geometrical simplifications and boundary conditions.

This section will show how the digital twin of the 160cc Inline pump was developed over time and what effect the model improvements had on the efficiency and temperature prediction. A mid speed and mid pressure operating condition will be used to showcase the changes throughout time, as extreme conditions can cause the model to numerically diverge due to mixed friction. The run-in process is period in the first couple of hours of the pump, where most pumps go through an abrasion process, which can vary from pump to pump in intensity. This run-process needs to be captured either by simulation prediction or by measuring part dimensions to capture the true efficiency and temperature.

Figure 4.4 shows the initial simulation result in terms of cylinder block temperature with speed for 100 bar and 100% displacement. In comparison is the measured temperature distribution. Shown are in red the maximum and in black the average block temperature. The simulation is in dashed and the measurement in full lines. The simulation shows a general good fit, especially at low speeds, however at high speeds the maximum temperature deviates significantly when comparing the simulation to measurement. For these first simulations there were no pump measurements available. Hence the boundary conditions were based on initial assumptions and experience. Other simplifications were no pressure and temperature deformation at the bushing, as there was an error in the part meshes, which had to be redone. All dimensions were based on CAD-information and all surfaces were flat, meaning no surface topology or edge rounding was applied.

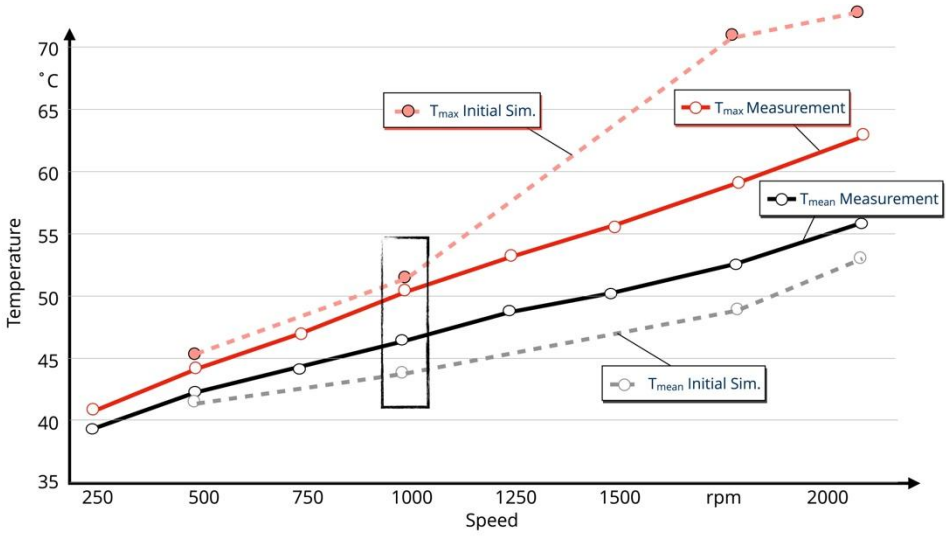

Figure 4.4. Initial Simulation Model Predicts Trend but does not Match Maximum Temperature at 100 bar and Full Displacement.

Despite these simplifications the initial simulation results were a good match between simulation and measurement in terms of overall temperature. 1000 rpm is highlighted as it will be discussed in more detail in the upcoming paragraphs. While the initial temperature level at this condition looks promising, a closer look shows significant deviations, exemplifying that not just one metric should be used to validate results.

Figure 4.5 shows the measured temperature field at the highlighted 1000 rpm 100 bar 100 % operating condition, along with the measured efficiency and steady state fluid temperatures. The colored dots on the left chart represent the 19 unique measurement locations, with one additional thermocouple being placed in the surrounding oil at the top of the block, to capture the leakage temperature near the block surface. On the right side is the initial simulated temperature field of the cylinder block and the predicted pump efficiency, based on the losses occurred in all three lubricating gaps. The overall temperature trend is similar, where the hottest temperatures occur on the valve plate gap, and the coldest around the displacement chamber. However, the temperature levels don't match. The upper half of the cylinder block is around 48˚C in measurement, where the simulation predicts no hot spots here with temperatures below 44˚C. False hot spots are being predicted by the simulation model at the bottom of the inner bushing. At this stage the simulation model did not account for bushing deformation, which caused contact and unrealistically high gap pressures and temperatures.

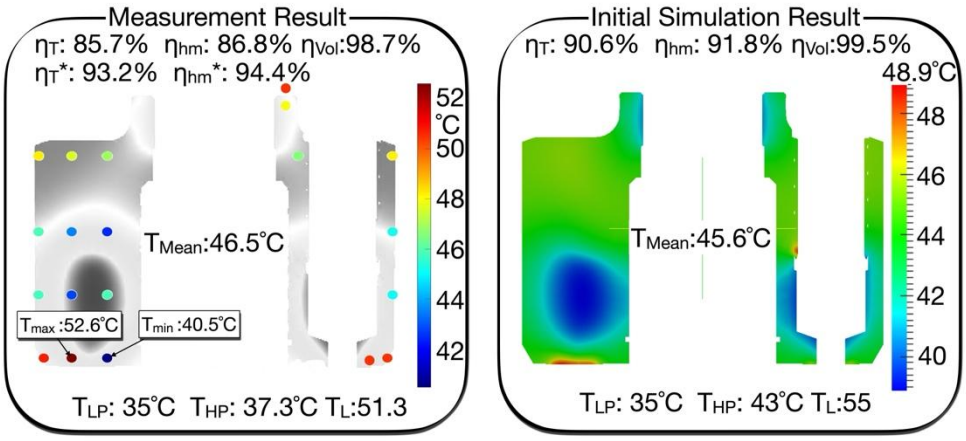

Figure 4.5. Measured (Left) Hot and Cold Spots are not Captured Accurately with Initial Simulation (Right) at 1000 rpm and 100 bar 100%.

For both the simulation and measurement the total and partial efficiencies are listed. For the measurement a second set of efficiencies is shown, marked with an asterisk(*). This adjusted efficiency is an estimated total and hydromechanical efficiency based on just the gap losses in the rotating kit, excluding the bearing and churning losses. This adjusted efficiency was estimated by subtracting the pump losses at the same speed at 0 bar, essentially subtracting estimated parasitic losses outside the rotating kit. This method cannot be applied at all operating conditions, as viscous friction also occurs without pressure especially at low or very high speed. However, at 1000 rpm 0 bar this pump exhibits nearly no tribological losses as confirmed by the simulation, measured block temperature and measured efficiency extrapolation (projecting η_{hm} to the 0 bar intersect), allowing for such an estimation. This estimated gap efficiency serves as a target for the simulation, allowing for a direct comparison between measurement and simulation.

The initial simulation model, which lacks bushing deformation and component wear, overestimates the losses, when compared to η_{total*}, which are mainly due to higher torque losses. In conclusion, the initial simulation gives a relatively good thermal preview, but lacks

the detail to predict the losses and temperature hot spots correctly, mostly due to the missing thermal and pressure deformation in the piston/bushing sealing gap.

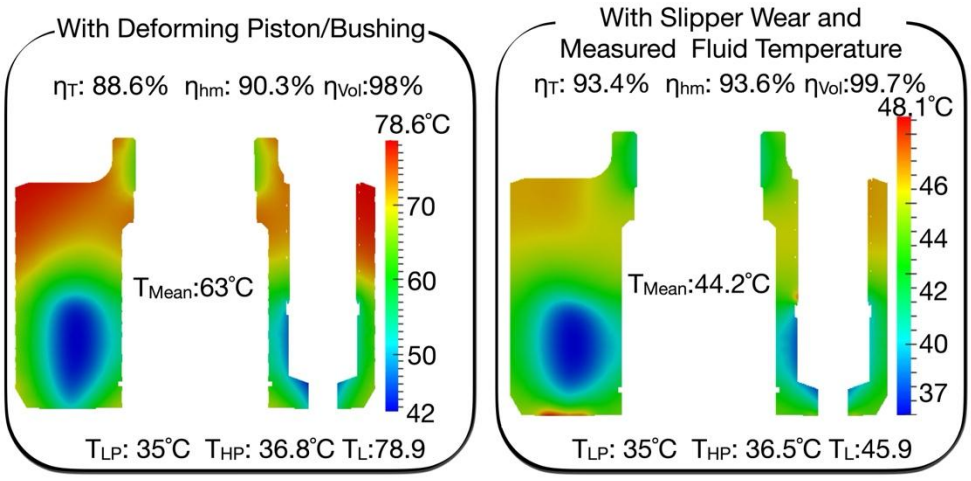

Figure 4.6. Influence of Increasing Modelling Complexity on the Predicted Temperature Field and the Efficiency at 1000 rpm 100 bar and 100%.

After including the elastic deformation of the bushing and piston, the overall temperature increased significantly mainly driven by the higher leakage temperature, as seen in Figure 4.6 on the left. While the efficiency now compares closer to the measured total efficiency, it lies well below the anticipated adjusted efficiencies, forecasting higher losses and higher temperatures. The hot spot locations however are now closer to the measurements, signaling that the gap behavior is now captured correctly just not at the correct power losses and thermal boundary conditions. The reason why the leakage temperature was much higher than the measurement can be explained by the fact that these simulations were performed before any pump measurements were recorded. Without any measurement data the inputs are reliant on an additional thermal model, which converts simulated gap losses to fluid temperatures [23]. As the losses were higher, the model predicted significantly increased leakage temperature levels. As this is an iterative process, the new boundary conditions are calculated after the simulation finished and then the simulation is restarted with the newly calculated temperatures. Several iterations are necessary to converge on a final solution. If the parts wear-in significantly this process can be quite lengthy without appropriate measurement data.

For the next simulation series (right temperature field in Figure 4.6), the first reference pump measurements were available. Thus, all simulation shown thus far relied on simulation models for their boundary inputs. As the reference pump was unmodified to ensure a reliable base, no cylinder block temperatures were available for validation or input. The measured fluid temperatures were now incorporated as the input for the simulation from here on out. Meanwhile it was discovered that the slipper performed poorly at several operating conditions, crashing with mixed friction and causing elevated friction losses. To improve this behavior, a wear model was used to predict the actual slipper surface geometry which was described in detail in [24], [25].

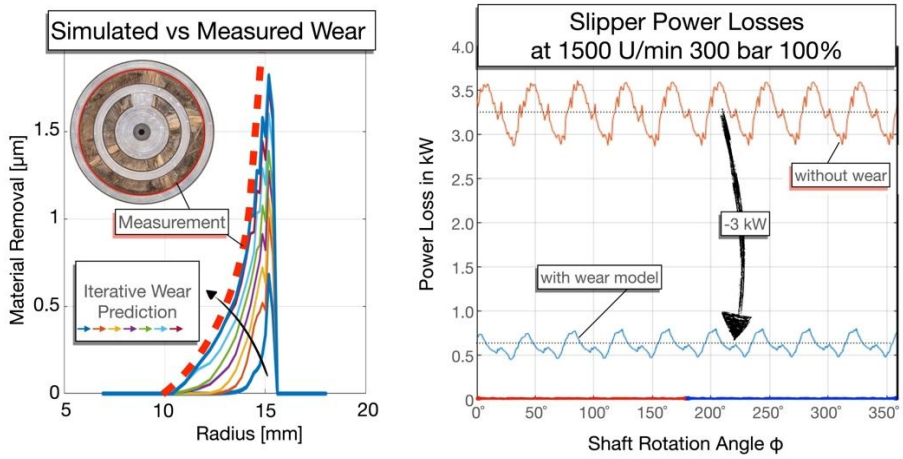

Figure 4.7. Slipper Edge Wear Decreases Power Losses Significantly.

The wear prediction is an iterative process, requiring a series of consecutive simulations slowly increasing wear with each step. The result of this pump was a 2 µm edge wear at the slipper sealing land. This edge wear seems rather miniscule, however the differences resulted in significant changes to the torque losses and power losses. As shown in Figure 4.7 on the right, the power losses decreased by over 3 kW for a high-speed high-pressure operating condition mostly due to a 50% reduction in viscous losses. The left graphic shows the predicted vs measured slipper sealing land geometry, as can be seen they match both in trend as well as in magnitude. However, as the iterative wear-in process is rather time consuming, it is recommended to measure these actual surface profiles if available. With measured fluid temperatures and the described slipper wear-in profile, the simulation results improved as shown on the right side of Figure 4.6. The simulation field now shows a better match with measurement, both showing the same trends and similar temperature magnitudes. With matching temperatures, the efficiencies also come closer to the measurement, both in hydromechanical and total efficiency. However, the leakage was underpredicted, which will be improved in the next section.

4.3. Correct Part Dimensions

To this point all shown simulation results were based on nominal CAD dimensions. To improve the simulation further all gap defining parts were measured both with a Keyence 3D optical profilometer and a 1D stylus-profilometer. A sample results for the relevant piston dimensions are shown in Figure 4.8

Shown are the piston length, diameter, and surface topology, which were averaged across all 9 pistons. These measurements were performed for both new and worn parts, albeit not from the same charge. During these measurements it is important to understand the limits of lubricating gaps. For example, the sealing length of the piston is only relevant for the first 100 µm as shown in the top figure. As the piston has chamfers for easier assembly, it is important to correctly determine the actual sealing length as any overestimation would cause a change in hydrodynamic pressure built up. To further improve the simulation, it is also recommended to input the actual sealing surface topology, as it also influences the results, as shown in the slipper wear.

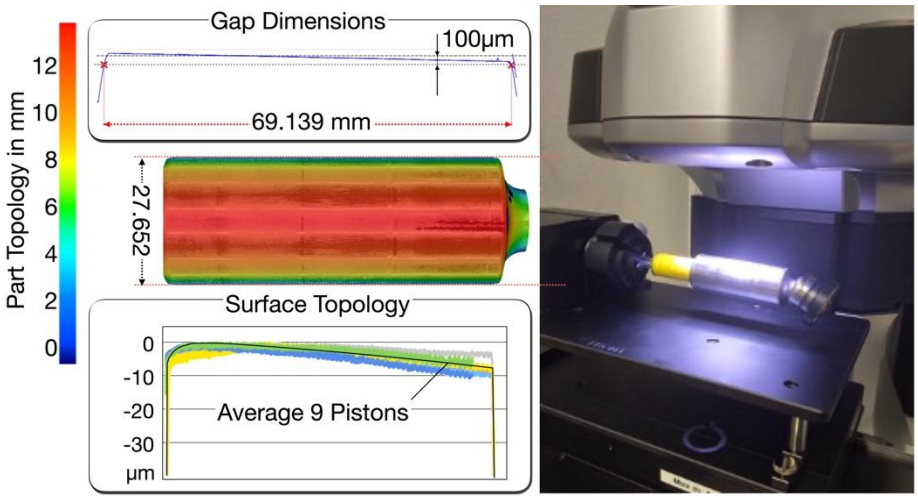

Figure 4.8. Actual Part Dimensions Measured with Profilometers

To demonstrate the effect miniscule dimensional changes, have on the efficiency and temperature, a dimensional case study was performed for the gap defining dimensions of the valve plate/cylinder block interface. Figure 4.9 shows the several simulation outputs for various dimensional inputs. The y-axis shows the power loss sum of 4 operating points, composed of two speed levels (500 rpm & 1800 rpm) and two pressures (100 bar and 300 bar) shown relative to the output power. The x-axis shows 5 different dimensional inputs: The minimum, maximum and nominal sealing land width, and the sealing land dimensions of a newly manufactured and a worn valve plate.

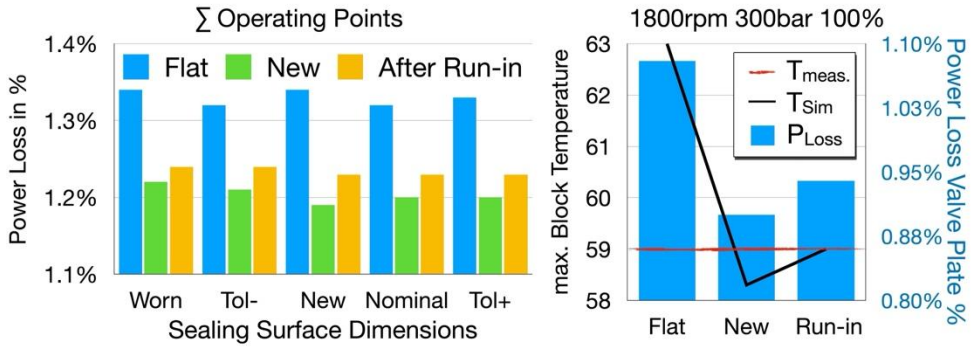

Figure 4.9. Change in Efficiency with Part Dimensions.

The different bar colors represent different surface definitions. The blue bar is a perfectly flat surface with sharp edges. The simulation results for the actual measured surface topology are represented by the green and orange bar for new and run-in respectively. There is a clear difference in power loss between the flat surface topology and the actual topologies. The magnitudes may not be significant, but a clear trend is shown: The actual geometry paired with the actual surface shape has the lowest power losses for this set of operating conditions. After run-in the power losses increase. The change between the different gap dimensions is not very large, the biggest influence on the power losses

simulation error is the false assumption that the surface is flat. While it shouldn't be assumed that the shown curves are true for every pump and every interface, they do illustrate the impact some simplifications have on the accuracy of the result.

As it is not possible to isolate power losses occurring in the valve plate/ cylinder block interface from the measured total pump losses, the validation will need to be made through the temperature level as thermocouples were placed near this gap. The right side of the graph shows the corresponding temperature changes in the cylinder block gap for the measured dimensions after wear-in for three different surface profiles (flat, newly manufactured and run-in). This is meant to demonstrate the impact of surface topology on maximum temperature prediction and how sensitive the temperature is to even the slightest efficiency changes. The bar height represents the power loss in % for the operating condition: 1800 rpm 300 bar 100% displacement angle. While the change in power loss seems insignificant, there is a clear impact on the maximum gap temperature. The actual gap temperature, measured 2 mm below the running surface, is shown in red for the given operating point. The black line represents the simulated temperature at the same location and depth. With the right surface dimensions (worn) but the wrong flat surface profile the powerloss is over-estimated and the temperature is off by several degrees. By providing the manufactured surface topology the temperature error decreased below 1K. Finally with the correct dimensions and the correct topology the temperature matches exactly, allowing for the assumption that the gap height and therefore power losses are simulated correctly.

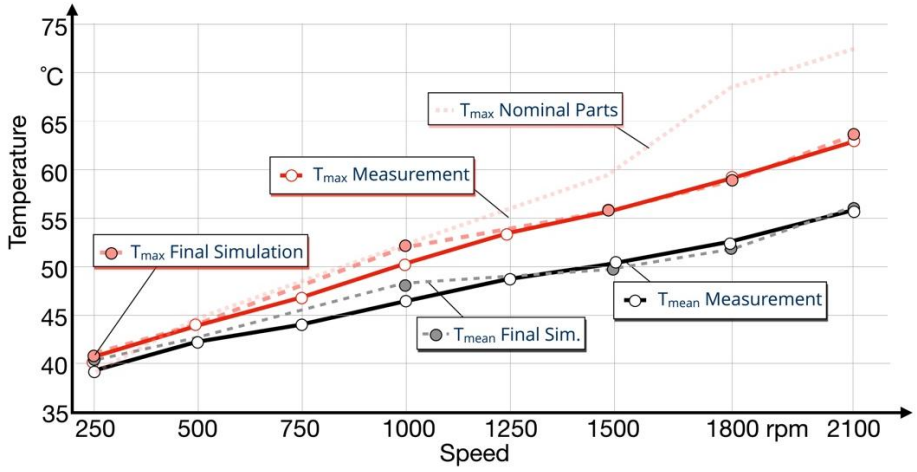

Figure 4.10. Final Output of the Digital Twin Compared to Measurement at Various Speeds at 100 bar and 100% Displacement Angle.

After improving the thermal boundary conditions by both incorporating the measured fluid temperatures and the measured heat convection coefficients, inputting the correct part dimensions and accounting for surface wear, the final simulated cylinder block temperatures can be seen in Figure 4.10 for various speeds as compared to measurement for 100 bar and 100% across the entire speed range of the pump. Now not only the temperature trends but also their magnitude match the measurement. This is true for both the average and the maximum temperature, with minor local differences. To demonstrate what impact the change to actual dimensions and measured surface topology has on the temperature, T_{max} is

also shown for nominal valve plate parts with the same thermal boundary conditions (light red dashed line). The highest impact of these model improvements is observed at high speed. There are a still a few simplifications such as a perfectly flat piston and cylinder block surface, however as both temperature and efficiency match quite well, it can be assumed that these have a smaller impact on this pump.

5. CONCLUSION

This paper demonstrates the impact various modeling assumptions have on the accuracy of the simulated efficiency and temperature predictions for the entire rotating kit of an axial piston pump. It was shown that general trends are matched quite well when considering nominal CAD dimensions when part deformation is considered. Achieving precise temperature predictions necessitates integrating accurate port temperatures (inlet, outlet, leakage), ideally through measurement. For prototypes where no measurements are available, these temperatures can also be estimated with a thermal model that uses pump losses, if part wear is factored into the analysis. Predicting surface wear using Caspar FSTI is feasible, albeit through a time-intensive, iterative process evidently affected by temperature and contingent on assumed thermal boundary conditions. If available it is recommended to measure the surface run-in using precise profilometers, which yields more accurate results in less time. The incorporation of measurement results, particularly measuring part dimensions and surface topology before and after operational tests, is strongly advocated. This study underscores the profound impact of surface topology on simulation fidelity, with wear on the slipper and valve plate notably altering power losses and temperature dynamics. It was shown that for the valve plate the gap dimensions are less impactful than modeling the correct surface topology.

The high-frequency temperature measurements conducted in this study revealed critical insights into the thermal dynamics within the axial piston pump's displacement chamber. These measurements demonstrated that the fluid temperature response highly dynamic, changing withing milliseconds but lags slightly behind pressure changes, indicating a non-instantaneous heat transfer process. There are significant differences in the fluid temperature levels between the inlet port, the suction stroke, and the delivery stroke, as well as between the fluid and the wall temperature. Moreover, the observed temperature spikes during the transition from low to high pressure, followed by significant temperature drops, highlight the complexity of the thermodynamic interactions within the pump. A key finding is that adiabatic assumptions for the rapid pressurization in the pump is false, as even in this short amount of time temperature is transferred to the environment, resulting in an energetic loss that cools the fluid.

Furthermore, the findings highlight the degree of simulation detail achievable with Caspar FSTI, distinguishing between assumptions that exert minimal impact and those that significantly influence the outcomes. The digital twin developed for this study successfully forecasts efficiencies and temperatures across a range of nominal part dimensions and the full spectrum of manufacturing tolerances. This capability underscores the model's robustness in accurately predicting pump performance under various manufacturing variations, highlighting its practical utility in engineering applications.

6. REFERENCES

[1] M. Oppermann, "An investigation into failure prediction for mobile hydraulic systems," TUHH, Hamburg, Hamburg, 2007.

[2] T. Torikka, "Bewertung von Analyseverfahren zur Zustandsüberwachung einer Axialkolbenpumpe," 2010.

[3] A. Emad, "Self-Learning Condition Monitoring for Smart Electrohydraulic Drives," 2019.

[4] R. Ivantysyn, J. Weber, A. Kunze, and W. Uffrecht, "Thermal Analysis of the Cylinder Block of an Axial Piston Pump – The Key to Monitoring Efficiency," in *IFK2024*, 2024, pp. 1–21.

[5] R. Ivantysyn and J. Weber, "Investigation of the Thermal Behaviour in the Lubricating Gap of an Axial Piston Pump with Respect to Lifetime," in *11. IFK 2018*, 2018.

[6] R. Ivantysyn, A. Shorbagy, and J. Weber, "An Approach to Visualize Lifetime Limiting Factors in the Cylinder block / Valve Plate Gap in Axial Piston Pumps," in *FPMC2017-4327*, 2017, pp. 1–12.

[7] A. Shorbagy, R. Ivantysyn, F. Berthold, and J. Weber, "Holistic analysis of the tribological interfaces of an axial piston pump - Focusing on pump' s efficiency," in *IFK2022*, Aachen, 2022.

[8] W. M. J. Schlösser and K. Witt, "Thermodynamisches Messen in der Ölhydraulik." VDMA, 1976.

[9] J. Schlösser, "Thermodynamisches Messen des Gesamtwirkungsgrades and hydrostatischen Antrieben," *O + P: Zeitschrift für Fluidtechnik*, pp. 285–287, 1973.

[10] H. J. Matthies and K. T. Renius, *Einführung in die Ölhydraulik*. 2014. doi: 10.1007/978-3-658-06715-1.

[11] W. Uffrecht and A. Günther, "Electro-thermal measurment of heat transfer coefficients," in *ASME Turbo Expo 2012*, 2012.

[12] W. Uffrecht, A. Günther, and V. Caspary, "Kleine Thermistoren zur Messung von Wärmeübergangskoeffizienten," *Technisches Messen*, vol. 79, no. 12, pp. 549–558, 2012, doi: 10.1524/teme.2012.0230.

[13] G. Eschmann, A. Kuntze, W. Uffrecht, and S. Odenbach, "Measurement if heat transfer coefficients un gaseous flow - first test of a recent sensor concept for stationary and oscillating flow," in *ASME Turbo Expo 2014*, 2014, pp. 1–11.

[14] W. Uffrecht, B. Heinschke, A. Günther, V. Caspary, and S. Odenbach, "Measurement of heat transfer coefficients at up to 25,500g - A sensor test at a rotating free disk with complex telemetric instrumentation," *International Journal of Thermal Sciences*, vol. 96, pp. 331–344, 2015, doi: 10.1016/j.ijthermalsci.2015.03.006.

[15] R. Ivantysyn, A. Shorbagy, A. Vedpathak, and J. Weber, "Investigation of the Heat Conduction in Axial Piston Pumps by Measurement and Simulation," in *IEE GFPS 2024*, Hurtigsval, Sweden, 2024.

[16] S. Horn, R. Ivantysyn, and T. Schmidt, "Tribological properties of different slipper designs of an axial piston pump," in *IFK2024*, 2024, pp. 1–18.

[17] U. Wieczorek and M. Ivantysynova, "Computer aided optimization of bearing and sealing gaps in hydrostatic machines—the simulation tool Caspar," *International Journal of Fluid Power*, vol. 3, no. 1, pp. 7–20, 2002, doi: 10.1080/14399776.2002.10781124.

[18] A. Schenk, "Predicting Lubrication Performance Between the Slipper and Swashplate in Axial Piston Hydraulic Machines," Purdue University, 2014.

[19] M. Pelosi, "An Investigation on the Fluid-Structure Interaction of Piston/Cylinder Interface," Purdue University, 2012.

[20] M. Zecchi, "A novel fluid structure interaction and thermal model to predict the cylinder block/valve plate interface performance in swash plate type axial piston machines," Purdue University, West Lafayette, IN, 2013.

[21] S. Horn, R. Ivantysyn, and J. Weber, "Validated efficiency improvements by implementation of structures on the slipper surface of an axial piston pump," in *IEEE GFPS 2022*, Naples, 2022.

[22] R. Ivantysyn and J. Weber, "'Transparent Pump' – An approach to visualize lifetime limiting factors in axial piston pumps," in *ASME 2016 9th FPNI Ph.D Symposium on Fluid Power*, Florianapolis, Brazil, 2016.

[23] L. Shang and M. Ivantysynova, "Port and case flow temperature prediction for axial piston machines," *International Journal of Fluid Power*, vol. 16, no. 1, pp. 35–51, 2015, doi: 10.1080/14399776.2015.1016839.

[24] R. Ivantysyn, A. Shorbagy, and J. Weber, "Investigation of the Wear Behavior of the Slipper in an Axial Piston Pump by Means of Simulation and Measurement," in *12. IFK 2020*, 2020.

[25] R. Ivantysyn, A. Shorbagy, and P. J. Weber, "Analysis of the Run-in Behavior of Axial Piston Pumps," in *IEEE GFPS 2018*, Samara, Russia, 2018.

Electronified Open Circuit Drive Concept for Compact Loaders

Xiaofan Guo, Shaoyang Qu, Rafael Cardoso, Enrique Busquets

Xiaofan Guo, Bosch Rexroth Corp., Xiaofan.Guo@boschrexroth-us.com

Shaoyang Qu, Bosch Rexroth Corp., Shaoyang.Qu@boschrexroth-us.com

Rafael Cardoso, Bosch Rexroth Corp., Rafael.Cardoso@boschrexroth-us.com

Enrique Busquets, Bosch Rexroth Corp., Enrique.Busquets@boschrexroth-us.com

Abstract.

The drive function of compact loader applications typically relies on closed-circuit hydrostatic transmission as a mature solution. This study adapts an innovative concept termed Electronified Open Circuit Drive (eOC-D), incorporating three open-circuit units, one pump to drive two motors, offering stepless speed control for the hydrostatic transmission. This innovative eOC-D concept is derived from the electronified open-circuit (eOC) unit by Rexroth. With four-quadrant capabilities in terms of displacement and speed, the eOC unit can smoothly transition from negative to position displacement, functioning as both a pump and a motor. Consequently, the eOC-D concept enhances drive performance through advanced electronic control of pressure, flow, torque, and power. In addition, the eOC-D approach leads to a significant reduction in component costs when compared to the closed-circuit architecture. To prove the concept, a simulation model is developed in the Simulink environment utilizing the lumped-parameter method with a 67kW power-rated compact loader as reference machine. Through simulations, the eOC-D system is sized considering an optimal combination of pump, motor, and gearbox. The performance of energy efficiency and dynamic response is evaluated from simulation. With baseline measurements as inputs, the eOC-D system demonstrates higher efficiencies and faster response compared to the baseline The efficiency improvement ranges from 5% to 10%, while the response time sees a reduction of over 50%.

Keywords. Open circuit drive, Hydrostatic transmission, Secondary control, Stepless speed control.

1. INTRODUCTION

1.1. State of the art

Hydrostatic transmission (HT) is a well-known solution for the transmission system of off-road vehicles [1] including construction machine, agriculture vehicle, forestry equipment and more. The advantages of simple design, robustness, and cost effectiveness is the key for its success. HT design normally has a variable displacement pump (P) close loop coupled (Line A and Line B) with a fixed or two-position motor (M) as depicted in Figure 1. A charge circuit (CP and PRC) is needed to provide control pressure for the pump and motor, as well

as replenish the close loop hydraulic circuit according to unit volumetric loss and flushing flow (FV). Two pairs of pressure relief (PRA and PRB) and check valves (CVA and CVB) are installed to protect the system from over-pressurize or cavitation.

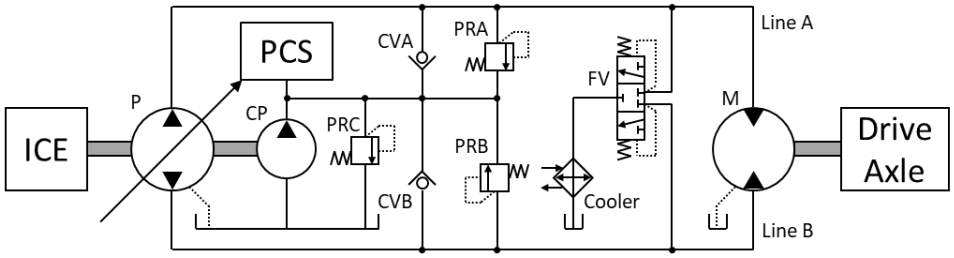

Figure 1. Hydrostatic Transmission Design

There are some significant alternatives on the design of the HT other than what is shown in Figure 1. Some great studies are [2] [3] [4] [5], and the difference are focus on charge circuit, different number of motors acting as multiple stage motor, configuration variation of series or parallel motor, and flushing, which does not change the fundamental design of the HT.

HT is a simple hydraulic circuit, but it still requires many components. For the reference machine in this study, compact track loader, there are two set of HT system. In total there are two primary units, two secondary units, four high pressure relief valves, four check valves, two flushing valves for cooling and recirculation, and two charge circuits. All these components cost money and take space. In addition to components, the charge circuits are always consuming power and creates parasitic loss [6].

To reduce the complexity and cost of the state-of-the-art transmission system with better system flexibility, the open-circuit drive concept has emerged as a great candidate motivated by increasing interest from the market thanks to the enormous improvement and cost reduction of the control unit and sensor technology. The innovative electronified open-circuit pump (eOC-P) technology from Rexroth makes the concept possible, termed Electronified Open Circuit Drive (eOC-D) in this study. Figure 2 illustrates the eOC-P technology, which uses the sensor feedback to accomplish for its capability in fast and accurate pressure and displacement control, as well as various working modes [7]. The most recent related work is done by Tetik and Brand [7]. They proposed an eOC-D system and control strategy for a small-sized tractor and showed great result on system performance.

The eOC units can serve as pump and motor with 4-quadrant operation in terms of speed and displacement. Consequently, the drive function can be achieved by one eOC pump and two eOC motors. In contrast to the traditional hydrostatic transmission, the eOC-D approach leads to a significant reduction in component costs. Only one drive pump is required instead of two, a single relief valve serves the open circuit instead of four, and the necessity for a charge pump is eliminated. Furthermore, the design enables the potential for energy regeneration during braking conditions, making use of the four-quadrant capability inherent in the EOC units.

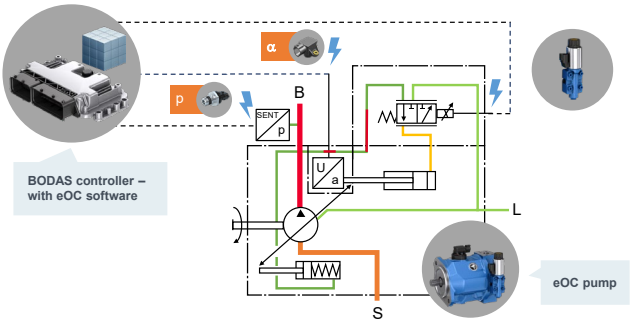

Figure 2. The electronified open-circuit pump (eOC-P) technology

For HT system control, the sequential control strategy is the most common way to manipulate the output speed of the drive. Machine starts at zero pump displacement at stand still. Then, increase the pump displacement to accelerate till hit maximum pump displacement, and the vehicle reaches maximum speed for fixed displacement motor. For two position motor, shift down to the lower motor displacement will reduce torque output but reach higher maximum vehicle speed. The eOC-D concept follows a similar control principle. However, compared to the conventional HT system, the eOC-D concept is capable of secondary control, offering stepless speed control for the transmission. Through advanced electronic control of pressure, flow, torque and power, an enhanced controllability can be achieved for the context of dynamic behavior and energy efficiency.

1.2. Goal and Structure

In contrast to the state-of-the-art architecture, the proposed eOC-D concept presents the following advantages:

- Reduced number of components and corresponding cost savings.
- Enhanced drive performance such as the faster response and better efficiencies.

The goal of this study is to define and optimize an all-in-one hydraulic system for mini-compact track loader (CTL) that powers transmission, implements, and aux systems using one supply pump equipped with secondary control strategy that could achieve same level of performance and efficiency.

This study is structured as follows: Chapter 2 showcases the proposed new one pump solution with hydraulic circuit design and sizing. Chapter 3 describes the control strategy for the secondary controlled transmission system and the implement systems. Chapter 4 lays out the simulation methodology adapted in this study and the simulation results, which reveal the drive cycle and compare both steady state driving system efficiency and dynamic driving performance. Finally, Chapter 5 concludes the study.

2. PROPOSED ARCHITECTURE

2.1. Reference Machine

The reference machine for this study is CAT 259D3 compact track loader as presented in Figure 3. It is a mid-power range CTL that equipped with duel hydrostatic transmission and closed centre load sensing implement hydraulic system.



Figure 3. Reference Machine CAT 259D3

The components and their details are listed in the Table 1.

Table 1. Component Information for Reference Machine.

Parameters	Description	Detail
Engine	Cat C3.3B DIT (turbo)	2500rpm rated speed
Hydrostatic Pump (V_P)	Axial piston variable displacement pump	45cc close-loop pump directly connect to engine
Hydrostatic Motor (V_M)	Axial piston two position motor	45cc close-loop motor connect to track drive through planetary gear set
Drive Gear (i_D)	Planetary Gear Set	18.47 gear ratio
Maximum Pressure Drop (Δp_{max})	-	350bar
Required Speed (v_{max})	Maximum speed for high and low gear	9.5km/h and 13.7km/h
Sprocket Radius (r_D)	-	0.2m

2.2. Proposed Architecture

This section will introduce the proposed architecture on hydraulic circuit and the component sizing.

2.2.1. Hydraulic Circuit

Figure 4 depicts the proposed eOC-D hydraulic circuit, highlighting the traction function. The target is to use one eOC unit for all functions, but this study mainly investigates the control of the drive track. Two eoc units are employed for the left and right track, and either of them can switch from positive to negative displacement for forwards or backwards movement.

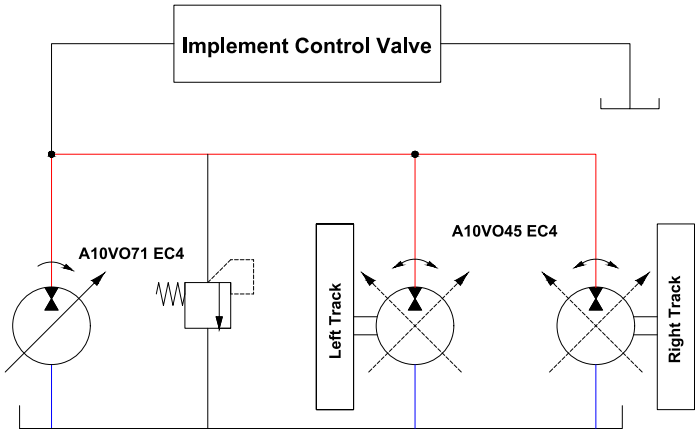

Figure 4. Proposed hydraulic schematic with simplified implement functions.

2.2.2. System Sizing

To ensure the proposed system achieve at least the same if not better performance, all the components need to be sized correctly. The benchmark is the vehicle travel speed and maximum traction force output.

The sizing starts from the maximum force output which determines the motor size and gear ratio. The pool for eOC unit, pump and motor, is 28cc, 45cc, 63cc, 71cc, and 88cc. The corresponding parameters of these units are in table below. The maximum pump flow q_P is calculated using equation (1), where the volumetric efficiency η_{VM} is assumed at 90%.

$$q_P = V_P \omega_P \eta_{VM} \tag{1}$$

Table 2. eOC Unit Pool and Key Parameters.

$V_{P/M}\left[\frac{cc}{rev}\right]$	28cc (P/M)	45cc (P/M)	63cc (M only)	71cc (P Only)	88cc (P Only)
$V_{M\,min}\left[\frac{cc}{rev}\right]$	8cc	12cc	16cc	-	-
$Max.\Delta p\ [bar]$	315	315	315	315	280
$Max.\omega_{P/M}\ [rpm]$	3000/4700	2600/4000	-/3300	2200/-	2100/-
$Max.q_P\ [lpm]$	75.6	105	-	141	166

Defining the gear ratio as i_D, the maximum traction force output is calculated from equation (2).

$$F_{tr} = T_M \frac{i_D \eta_i}{r_D} = \frac{V_M \Delta p_{max}}{2\pi} \eta_{HM} \frac{i_D \eta_i}{r_D} = \frac{V_M \Delta p_{max} i_D}{2\pi r_D} \eta_{HM} \eta_i \tag{2}$$

F_{tr} is the traction force generated by one hydrostatic transmission powered track, T_M is the motor output torque, η_i is the planetary gear set efficiency (assume to be 97%), η_{HM} is the hydromechanical efficiency of the motor (assume to be 90%). The maximum force output is around 20kN for one track from the reference machine data. From equation (2), the

gear ratio (i_D) to fulfil the traction force with given motor size could be calculated, as indicated in Table 3. Taking the maximum vehicle speed into consideration, the rotational speed with each motor could be calculated using equation (3), with the calculated gear ratio (i_D) from the traction force calculation. The results are summarized in Table 3.

$$\omega_{M_{max}} = \frac{v_{max}}{r_D} i_D \tag{3}$$

Table 3. Ideal Gear Ratio and Corresponding Maximum Motor Speed.

$V_M \left[\frac{cc}{rev}\right]$	28cc	45cc	63cc
$i_D\ [-]$	32.98	20.52	14.66
$\omega_{M_{max}}\ [rpm]$	5993	3729	2664

From the result and compared to Table 2, 28cc motor is out due to over speed at maximum vehicle velocity. 71cc and 88cc cannot operate as motor. From a quick search on possible size of the gearbox, a ratio of 20.88 is available. As a result, **45cc motor** and **20.88 gear ratio** is selected. To meet the maximal torque requirement, the pump needs 315bar as the nominal pressure. As the 88cc unit cannot meet the pressure requests yet, **71cc pump** is selected for the proposed eOC-D system. Figure 5 illustrates the FADI plots, where the black indicates the baseline machine, and the red represents the speed – traction of the selected eOC-D components. From point 1 to 2, the motor stays at the maximal displacement, while the pump displacement increases for higher vehicle velocity. At point 2 the pump reaches the maximum displacement. From point 2 to point 3, the motors displacement decreases until meeting the peak velocity of the vehicle (13.7km/h) on paper. Regarding the black curves, point 4 to 5 depicts the first gear, and point 6 to 7 represents the second gear option with maximal potential speed. It is possible to extend point 3 to cover point 7 as the eOC motor displacement can be decreased further, but here it follows the specifications on paper.

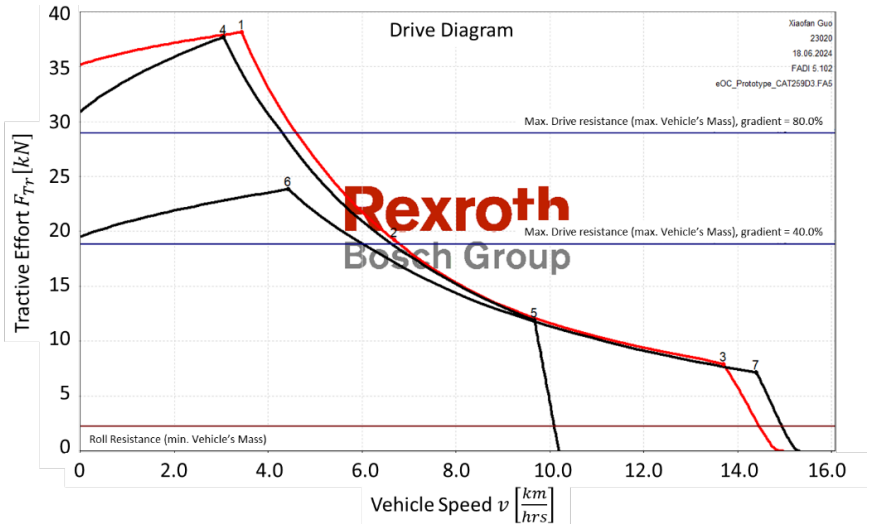

Figure 5. Sizing plots in FADI for the proposed eOC-D system.

The flow needed for the implement function is also taken into consideration. In this scenario, the minimum motor displacement of the motor (as shown in Table 2) is used for the calculation assuming the vehicle can run at maximum speed at this minimum motor displacement. Then the needed pump flow q_P could be calculated using equation (4). q_M is the required motor flow, q_{imp} is the required implement flow which is planned to be added in to the eOC system as next step. The selected 71cc pump can supply about 148lpm flow with a speed 2200rpm and 95% volumetric efficiency. For the baseline vehicle, the maximal speed of the first gear is 9.67km/h, which indicates a motor speed of about 2680rpm from equation (3). If the 45cc motor is commanded to the minimal displacement 12cc, both motors would need about 70lpm flow for the required speed, and about 78lpm flow is available for the implement functions. It fulfils the standard flow requests 76lpm for the reference machine implement functions.

$$q_P = \sum q_M + q_{imp} = \frac{2V_M \beta_M \omega_M}{\eta_{VM}} + q_{imp} \tag{4}$$

3. CONTROLLER DESIGN

This section introduces the control strategy adapted for the proposed eOC drive system in detail. Tetik et al. [7] did a great job on laying out the control strategy for a small-sized tractor which has one drive motor with torque-based drive controller. For the chosen application of CTL in this study, the controller need modification as it contains two drive motors and follows close-loop speed-based drive controller. The overall controller of the eOC drive system contains pump/motor displacement control, vehicle speed/steering control, supply pressure selection and control, anti-stall control for both the drive and engine, and the following sections explains each control design in detail.

3.1. Pump/Motor Displacement Controller

The base level control of the proposed architecture is the eOC unit displacement controller. As presented in Figure 6, it uses a PID controller with scheduled gains with respect to pump operation condition: displacement β_{act}, pump outlet pressure p_P, and rotational speed ω_{act}. It takes the commanded displacement β_{cmd} as input and the measured displacement as feedback to form a close-loop control. Control valve current i_{ctrl} to the eOC unit is the output of the controller that directly send to the control valve which regulates the pressure in the control piston chamber to move the swashplate.

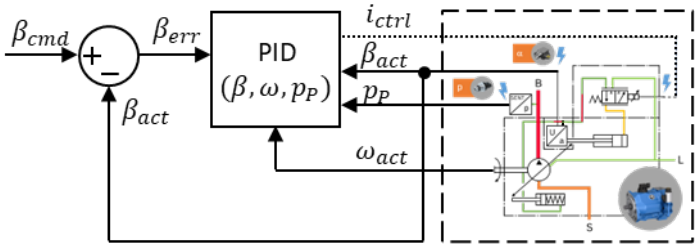

Figure 6. Pump/Motor Displacement Controller.

3.2. *Drive/Steering Controller*

This is the core controller for the CTL prototype. First, user will input desired drive/steering command using joystick. Then, these commands need to be converted to track desired speed for both left and right track. This is done through equation (5) and (6). cmd_{dr} and cmd_{st} indicating the user drive and steering command (from -100% to 100%), $v_{dr_{max}}$ and $\omega_{st_{max}}$ are the maximum drive speed (m/s) and steering rate (rad/s). $v_{cmd_{trL/R}}$ is the corresponding track speed (m/s) command from the drive and steering command. l_{tr} is the distance (m) between the centre line of left and right tracks.

$$v_{cmd_{trL}} = cmd_{dr} v_{dr_{max}} + cmd_{st} \omega_{st_{max}} l_{tr} \quad (5)$$

$$v_{cmd_{trR}} = cmd_{dr} v_{dr_{max}} - cmd_{st} \omega_{st_{max}} l_{tr} \quad (6)$$

If the drive and steering command cannot be met at the same time due to maximum speed limitation of the machine, the steering function holds priority. One example of this condition is the driver commands full speed forward and wants to steer to one side. Because the drive speed is the average of both track and neither track should exceed maximum speed, steering at full speed command will need to slow down one track to keep the speed difference between two tracks as demand to fulfil the steering command. In this situation, the drive speed will be lower than command, but the steering will execute successfully.

With the speed command for left and right track, Figure 7 illustrates the controller design. This controller is on the outer loop of the pump/motor displacement controller in green, so it is a cascade control structure. The command speed $v_{cmd_{tr}}$ and measured speed $v_{act_{tr}}$ are feed into the PID controller. The output of the controller is defined to be the command torque $T_{cmd_{tr}}$ for the motor to accelerate or decelerate the vehicle for speed tracking. Then, this torque is open-loop feedforward controlled to determine the corresponding motor displacement $\beta_{cmd_{tr}}$. This command displacement is sent to the pump/motor displacement controller introduced in section 3.1. With the actual displacement $\beta_{act_{tr}}$ at the motor and the supply pressure p_P, the actual torque $T_{act_{tr}}$ is sent to the track to manipulate machine speed.

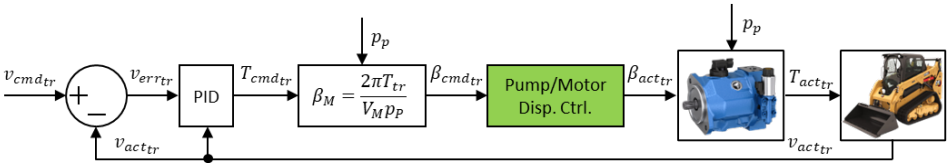

Figure 7. CTL Track Speed Controller.

In this controller, it is important for the PID controller output to be desired torque and go through one more calculation to get motor displacement command instead of directly commanding the motor displacement. The reason is twofold. On the one hand, without this step the system is oversimplified and missed the important coupling effect due to the supply pressure and will become very hard to reach an acceptable speed tracking performance. On the other hand, the desired torque could be used to determine the appropriate supply pressure for the drive system to achieve the best performance and system efficiency.

3.3. *System Supply Pressure Controller*

The supply pressure of the system determines how drive and implement system behaves and thus the overall performance and efficiency. The implement system required pressure $p_{cmd_{imp}}$ is straight forward, which is the highest load pressure $p_{imp_{max}}$ plus a certain margin p_{mar} to ensure the control valve has enough pressure drop to work properly as shown in equation (7).

$$p_{cmd_{imp}} = p_{imp_{max}} + p_{mar} \tag{7}$$

For the drive system, it is not that simple. The hydraulic motor can output same torque with infinite number of combinations of displacement and supply pressure. This provides the control freedom to choose the optimal pressure that provide maximum overall system efficiency. The hydraulic units are most efficient at high displacement and middle-to-high pressure [1]. As a result, the principle adapt in this study is to keep the motor displacement as high as possible. To find the corresponding pressure with maximum motor displacement, the desired torque from the track speed controller in section 3.2 is used. By assuming the motor at maximum displacement with 90% hydromechanical efficiency η_{HM}, equation (8) is used to calculate the desired supply pressure for the drive system. This calculation needs to be done for both left and right track motor.

$$p_{cmd_{dr}} = \max\left(\frac{2\pi T_{cmd_{tr_L}}}{V_M \eta_{HM}}, \frac{2\pi T_{cmd_{tr_R}}}{V_M \eta_{HM}}\right) \tag{8}$$

With both required pressure for implement and drive system, the final supply pressure is chosen using equation (9).

$$p_{cmd_P} = \max\left(p_{cmd_{imp}}, p_{cmd_{dr}}\right) \tag{9}$$

The system supply pressure control is critical for the proposed eOC drive system speed tracking performance. An accurate pressure controller can benefit the system on both efficiency and dynamic performance. Figure 8 depicts the pressure controller structure.

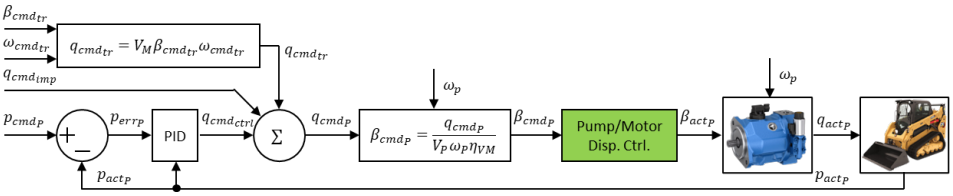

Figure 8. System Supply Pressure Controller.

It is a feedback-feedforward control structure based on flow logic. The total required flow q_{cmd_P} for both the drive $q_{cmd_{tr}}$ and implement $q_{cmd_{imp}}$ system is estimated from the command motor speed $\omega_{cmd_{tr}}$ with instantaneous command motor displacement $\beta_{cmd_{tr}}$ for both tracks and implement flow requirement $q_{cmd_{imp}}$. And a close-loop pressure PID controller is implemented to adjust the flow required $q_{cmd_{ctrl}}$ from the pump to match the command pressure. Then, the command pump displacement β_{cmd_P} is sent to the pump/motor displacement controller. Finally, the pump, with the actual displacement β_{act_P}, output flow q_{act_P} to the proposed eOC system.

3.4. *Engine Anti-Stall Controller*

Another advantage of the proposed one pump system is the ease of engine anti-stall control. With the one eOC pump with complete controllability and pressure feedback, the engine anti-stall could be implement based on the engine available torque output at any given engine speed. The idea is to add the anti-stall controller right between the controller put of the supply pressure controller and the eOC pump controller as shown in Figure 9. First, the actual engine speed is feed into the engine map for the specific machine to obtain the maximum available engine torque that will not stall the engine. Then, a back calculation is performed to find the maximum allowable supply pump displacement that will not stall the engine using equation (10). When the available engine torque is higher than the maximum pump torque, the limited pump displacement $\beta_{P_{lim}}$ is greater than 1 and will not be used. The original pump displacement command goes through. But, when the system pressure increased to a certain level that might stall the engine, the controller will limit the pump command displacement to prevent engine stall.

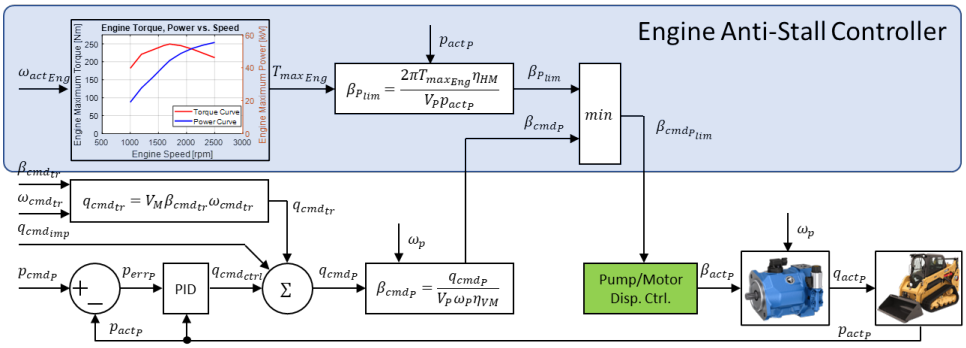

Figure 9. Engine Anti-Stall Controller.

$$\beta_{P_{lim}} = \frac{2\pi T_{max_{Eng}} \eta_{HM}}{V_P p_{act_P}} \tag{10}$$

3.5. *Flow Distribution Controller*

It is very likely that the total flow required by the drive system and implement exceed the maximum flow output of the pump. When that happens, the supply pressure will drop due to insufficient supply flow. Thus, the speed controller will command the motor to increase displacement to compromise for that pressure drop to keep the same torque output. This will lead to even worse flow deficit. This loop will happen very fast, and the pressure will crash and can never recover by its own. As a result, an anti-overflow controller must be added to prevent the system to go over the no-return point.

There are two rules defined in this controller. First, the implement holds the priority. Meaning when the total flow requirement exceeds the maximum supply flow, the drive system will automatically lower the motor displacement to free up more flow to ensure the implement can perform. In the meantime, the drive system required pressure will be recalculated with the limited motor displacement to compensate and keep same torque output. Second, when the limitation happens, the left and right track motor displacement limitation should hold same ratio $r_{L/R}$ to keep the flow balance between two tracks.

To achieve above rules, equation (11) - (15) are used to limit the motor displacement. The available flow for drive system $q_{dr_{lim}}$ is the lower one of the required flow $q_{cmd_{tr}}$ or what is left of the maximum pump flow subtract the implement system requirement $q_{cmd_{imp}}$. When flow saturation is happening, the motor beta command $\beta_{tr_{lim}}$ is scaled down with respect to the commanded speed ratio. In case of no limitation is needed, all terms will cancel out and leave $\beta_{tr_{lim}} = 1$, which means all 100% displacement is available.

$$r_L = \frac{\omega_{cmd_{tr_L}}}{\omega_{cmd_{tr_L}} + \omega_{cmd_{tr_R}}}, r_R = \frac{\omega_{cmd_{tr_R}}}{\omega_{cmd_{tr_L}} + \omega_{cmd_{tr_R}}} \tag{11}$$

$$q_{dr_{lim}} = min\left(\sum q_{cmd_{tr_{L/R}}}, q_{P_{max}} - q_{cmd_{imp}}\right) \tag{12}$$

$$q_{cmd_{tr_{L/R}}} = \omega_{cmd_{tr_{L/R}}} V_M \tag{13}$$

$$q_{P_{max}} = \omega_P V_P \tag{14}$$

$$\beta_{tr_{lim_L}} = \frac{q_{dr_{lim}} r_L}{V_M \omega_{cmd_{tr_L}}}, \beta_{tr_{lim_R}} = \frac{q_{dr_{lim}} r_R}{V_M \omega_{cmd_{tr_R}}} \tag{15}$$

4. SIMULATION AND RESULTS

4.1. Simulation Setup

A lumped parameter model is developed in Simulink environment as depicted in Figure 10. The model incorporates all controllers discussed in Section 3, along with the relevant components including the eOC units, engine, and vehicle. The models of these components are based on numerical expressions that account for efficiency losses and dynamic behaviours. While the focus of this study is on the controller design, the detailed modeling of each individual component is not covered in this section.

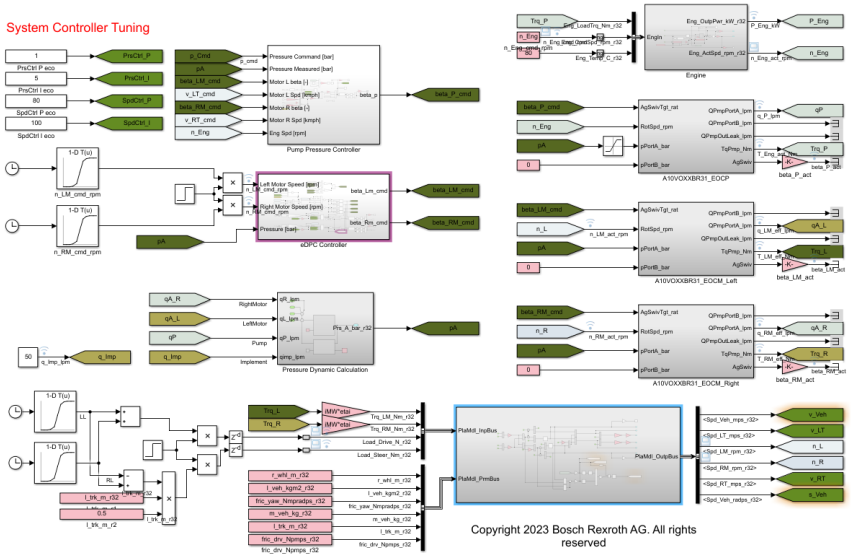

Figure 10. Simulation model developed in Simulink environment.

The inputs of the simulation are data from the baseline measurements on the reference vehicle. Figure 11 showcases a V-pattern drive cycle from the field. The first row shows the left and right motor load torque, and the second row shows the motor rotational speed.. For confidentiality of the baseline vehicle, the data are normalized according to the peak value. The torque is employed as the inputs to the kinematic model of the machine, and the motor speed is utilized as the user command. The target of the simulation is to investigate speed tracking performance with the complex loading conditions and compare the performance with the baseline regarding energy consumption and dynamic response.

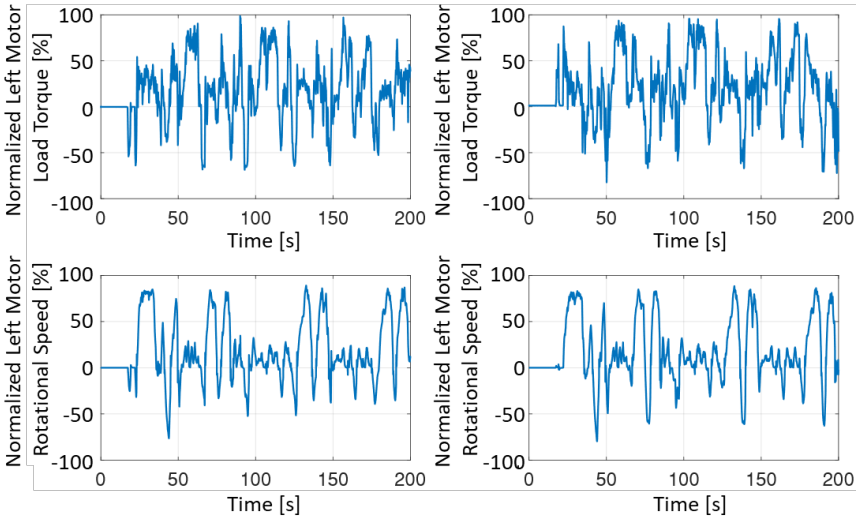

Figure 11. Baseline measurements of the track motor speed and torque.

4.2. Steady State Simulation and System Efficiency Comparison

Figure 12 depicts the system efficiency comparison between the proposed eOC-D system and the baseline machine. Focusing on the steady state performance, such as from 20s to 40s, the efficiency performance is fairly close and both are about 69%. However, this plot does not take power consumption of the charge pump into consideration. The eOC-D system does not require a charge circuit like the conventional closed-circuit. The reference machine employs a pilot pressure of 30bar with constant 55lpm flow, which results in about 2.8kW extra power consumption. If taking this value into account, the eOC-D system will have the overall efficiency advantage of 3% to 4%.

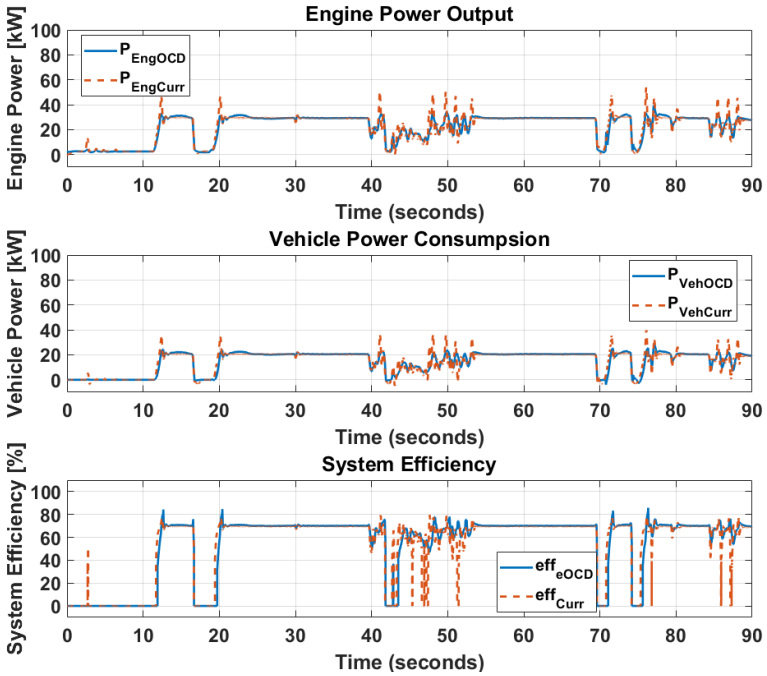

Figure 12. Steady-state simulation on the system efficiency comparison.

4.3. Dynamic Simulation and System Performance

4.3.1. No Implement Flowrate Performance

Figure 13 represents the simulation results based on the baseline measurements depicted in Figure 11. The three plots illustrate the pump displacement control, motor speed tracking, and system pressure, respectively. These results reflect the effective controller design detailed in Section 3 with proper parameters. In the second plot, the solid line is the command value and the dash line represents the simulated value. Overall, the motor speed tracking is good without apparent mismatch during all the transition phases.

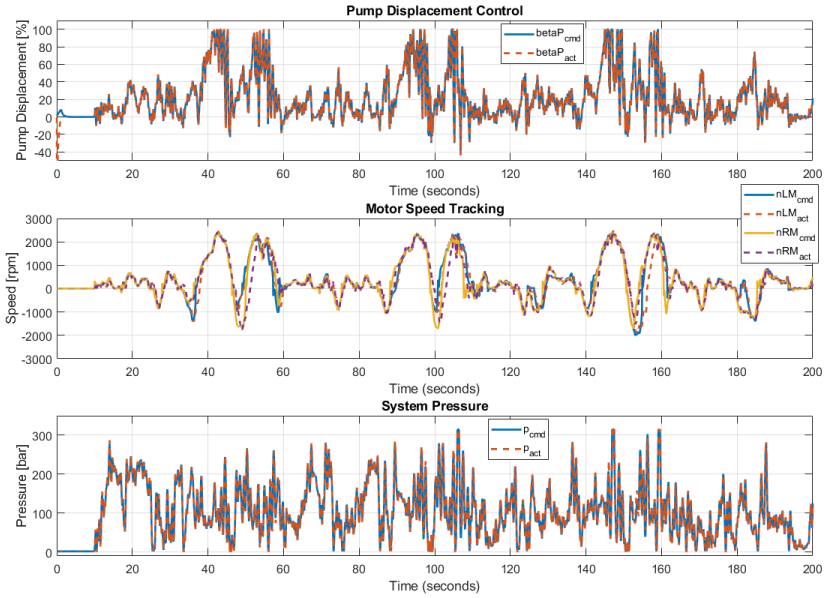

Figure 13. Simulation on dynamic performance, drive function only.

4.3.2. 50 lpm Implement Flowrate Performance

Figure 14 showcases another condition with drive and implement functions working at the same time. An extra 50lpm request is added to the pump with the same operation on the drive function. As explained in Section 3.5, the flow distribution controller gets activated. Compared to the results in Figure 13, the pump reaches the maximal pressure sometimes to meet the tractive torque demand with less motor displacement. With the proposed controller engaged, the speed tracking behaviour is still good and does not change obviously based on Figure 13.

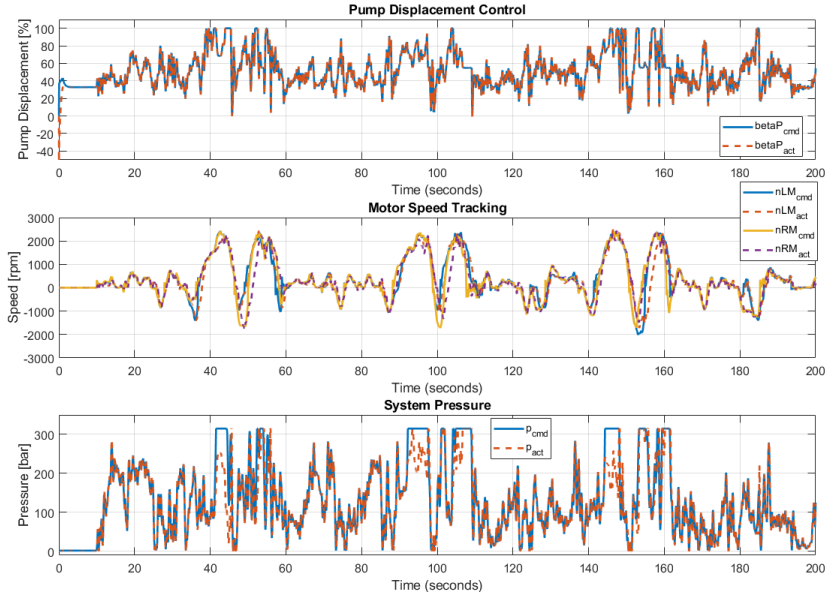

Figure 14. Simulation on dynamic performance, drive function and 50lpm implement requests.

5. CONCLUSION

This study proposed a novel eOC-D system aiming to improve the performance and reduce the component costs of the state-of-the-art hydrostatic transmission system. The development of the eOC-D architecture is based on a commercial compact loader. A comprehensive sizing study is conducted to determine the optimal combination of pump, motor and gearbox for the application, considering both the tractive torque and speed requirements. To overcome the control challenges of the new architecture, which uses only one pump for all functions, a detailed sequence of controller design is presented, from the component (eOC unit) level to the system level. The focus of this study lies in the controller, leveraging the capabilities of the eOC units to achieve the desired outcomes.

To evaluate the performance of the proposed architecture, a lumped-parameter model is built in Simulink environment. The simulation adapts the baseline measurements as inputs to reflect the realistic operating conditions. The simulation results indicate a comparable efficiency performance under steady-state scenarios. However, the simulation model does not include the charge circuit, which consumes extra power for the baseline system, thus giving a few percentage savings to the eOC-D architecture. On the other hand, the dynamic performance is remarkable due to the secondary control for the drive function.
At present, demonstration on the vehicle and more tests to validate the eOC-D design are undergoing. There are certainly some technical challenges to be addressed, especially for extreme loading conditions and simultaneously operation of the implement and traction. However, with the advantages of component costs reduction, the proposed architecture could be a popular solution to replace the traditional hydrostatic transmission system.

6. REFERENCES

[1] X. Guo and A. Vacca, "Advanced Design and Optimal Sizing of Hydrostatic Transmission Systems," *actuators,* vol. 10, no. 9, p. 243, 2021.

[2] N. Nervegna and M. Rundo, Passi nell'oleodinamica. Vol. 1-2., 2020.

[3] G. L. Zarotti, "Trasmissioni idrostatiche.," *Istituto per le Macchine Agricole e Movimento Terra,* pp. 707-2003, 2003.

[4] A. Vacca and G. Franzoni, Hydraulic Fluid Power: Fundamentals, Applications, and Circuit Design, Wiley, 2021.

[5] G. Costa and N. Sepehri, Hydrostatic Transmission and Actuators: Operation, Modelling and Applications, Hoboken, NJ, USA: John Wiley & Sons, 2015.

[6] N. Keller and M. Ivantysynova, "A New Approach to Sizing Low Pressure Systems," in *ASME/BATH Symposium on Fluid Power and Motion Control*, 2017.

[7] S. Tetik and M. Brand, "Secondary Control Based Hydraulic Architectures For Mobile Applications," in *The 13th International Fluid Power Conference*, Aachen, Germany, March 21-23, 2022.

Electrification of a compact skid-steer loader – redesign of the hydraulic functions

Shaoyang Qu*, Zifan Liu, Rafael Cardoso, Enrique Busquets

Bosch Rexroth, 100 Southchase Blvd, Fountain Inn, SC 29644

* Corresponding author email address: *Shaoyang.qu@bosch.com*

ABSTRACT

This study introduces an innovative design for the hydraulic implement system in electrified compact loader applications. The presented architecture is based on the pre-compensated load sensing system, incorporating electronified components with energy regeneration capabilities. The system employs an electronified open-center pump (eOC-P) and a load sensing pre-compensated valve sourced from Rexroth. The compensator for the boom function is re-designed to remain static, allowing a bidirectional path for regeneration during the boom lowering phase. The eOC-P offers pressure control, flow control, displacement control, and torque control modes, achieved by replacing the traditional mechanical load sensing feedback with sensor signals. Enhanced by a dedicated control strategy, the re-designed system adapts its operational modes to suit both single and multiple user conditions, aiming to achieve optimal energy performance. This system is designed to seamlessly integrate into the electric drive, reducing components and conserving space in the compact machine, also improving the energy performance. According to the simulation with baseline measurements on a 68kW rated power 5-ton compact loader, the proposed system can save up to 30% energy during a single boom cycle. Moreover, approximately 20% of the input energy can be recovered and stored in the battery, effectively extending the operating hours of the machine.

Keywords: Electrification, Energy regeneration, Load-sensing system.

1. INTRODUCTION

Compact skid-steer loaders stand as key players in the North American machinery market. In response to increased customer interest and more stringent regulations on exhaust emissions, a notable shift towards electrification has emerged within this sector. The electrification concept outlined in this paper includes the removal of the diesel engine and employing electric-hydraulic powertrain for the implement functions. This shift to a purely electric power source addresses emission concern. However, to unlock the full potential of the electrified powertrain, including energy regeneration, a redesign of the hydraulic system and control strategy is imperative.

In the context of compact loader applications, a predominant source of regenerative energy is derived during the boom lowering phase [1]. In traditional hydraulic systems, when the boom moves downwards, potential energy is typically dissipated at the control valve to regulate its lowering speed. This inefficient operation raises a significant challenge for battery-powered machines, impacting their operational longevity [2]. Thus, it is significant to maximize the usage of the regenerative energy for electrified compact loader.

Decentralization is one popular approach to enable energy regeneration. By employing one prime mover for each actuator, the control system can leverage the electric motor – hydraulic pump speed with minimal throttling losses. Additionally, the implementation of a regeneration mode is facilitated through the combination of a hydraulic motor and an electric generator, assuming the hydraulic machine supports two-quadrant operation [3]. The decentralized architecture has demonstrated notable advantages, with reported energy savings of up to 65% [4], and hydraulic efficiency reaching as high as 84% [5] from the previous research by the author. However, it is essential to acknowledge that while decentralized systems offer efficiency gains, they also pose challenges in terms of increased system costs [6]. This is attributed to the necessity of multiple electric and hydraulic machines to cater to all implement functions of the compact loader. To employ one prime mover for multiple functions, the compensated load-sensing (LS) hydraulic system is usually adopted for mobile applications. A cost-effective approach involves employing a single electric machine to directly drive the LS system, providing an intuitive means to control overall expenses [3]. With an electric drive, it becomes feasible to regulate both the drive speed and pump displacement, optimizing energy performance. Research by Lin. T. et al highlights the benefits of an electric load-sensing (e-LS) system, showcasing a reduction of over 20% in energy consumption through an adaptive variable speed and displacement control strategy [7]. However, a limitation of the LS system lies in its prohibition of energy regeneration, as the compensator only permits flow in one direction—from the pump to the actuator—while backflow is essential for energy recovery. Lin. Z. et al investigated the e-LS system and compared energy consumption between centralized LS systems and decentralized e-LS systems, revealing around 12% fuel savings [8]. Despite these efficiency gains, achieving energy regeneration remained elusive in both configurations. A patented hydraulic system uses extra valves on LS systems to enable energy regeneration [9], but not integrated with the electrified powertrain and a dedicated control algorithm as the authors [10].

From the state of the art, the electrification of compact loaders presents inherent trade-offs:

- High costs associated with decentralized architecture, offering enhanced energy performance.
- Absence of energy regeneration and operational inefficiencies with the e-LS system to limit the costs.

This study proposes a novel e-LS system that specifically targets the identified trade-offs. Two pivotal components, the electronified open-center pump (eOC-P) and the modified pre-compensated valve (RM-MPP) sourced from Rexroth, play a crucial role in enabling energy regeneration within the e-LS architecture. A key redesign involves the compensator for the boom function, strategically engineered to remain static, thereby creating a bidirectional path for regeneration during the boom lowering phase. The eOC-P offers pressure control, flow control, displacement control, and torque control modes, accomplished by replacing conventional mechanical load sensing feedback with sensor signals [11]. Consequently, the system attains energy regeneration capability by commanding the eOC-P into motor mode while simultaneously opening the valve section during the boom lowering phase. Through a comprehensive strategy, the proposed system adapts its operational modes based on sensors feedback to accommodate both single and multiple user conditions, with the overarching aim of achieving optimal energy performance.

The structure of this paper is organized as follows: In Section 2, the design and control strategy of the proposed e-LS system are detailed. Section 3 demonstrates the methods for this study, including the simulation model and baseline definition. Section 4 presents the simulation results and corresponding analysis. Finally, Section 5 concludes the study and offers insights into future perspectives.

2. SYSTEM DESIGN

2.1. Reference Vehicle

The reference machine for this study is the Bobcat T770 compact track loader, with the rated power of 68kW, as shown in Figure 1.



Figure 1. Reference vehicle Bobcat T770 compact track loader

Table 1 lists the key parameters of the reference machine. It is important to note that in the context of this electrification study, the diesel engine, along with all hydraulic and thermal components, has been eliminated from the reference machine This commercial compact loader establishes the sizing requirements but also serves as the benchmark for achieving the performance targets outlined in the electrification proof of concept.

Table 1: Main specifications of the reference vehicle

Specifications	***Values***
Engine Type	3.4L Bobcat Diesel Engine, 4 cylinders
Max power	92 hp [68 kW]
Max Standard flow	23 gpm [87 L/min]
Machine Weight	10,515 lb [4770 Kg]

Engine speed	1100-2600 rpm

This paper focuses on the control of two crucial implement functions of the vehicle, boom and bucket actuation. Figure 2 provides the parameters associated with these functions. The reference machine utilizes conventional pre-compensated LS system for its implement functions. Based on the actuation data, the electrified hydraulic system undergoes a redesign, with components sized to meet the demands of the original cycle requests.

Table 2: Parameters of the boom and bucket actuators.

Actuation parameters		***Value [unit]***
Boom cylinder and cycle time	Length of stroke L_{boom}	662.7 [mm]
	Diameter of piston D_{boom}	82.6 [mm]
	Diameter of rod d_{boom}	50.8 [mm]
	Raising arm time $t_{boom,ex}$	4.8 [s]
	Lowering arm time $t_{boom,re}$	3.4 [s]
Bucket cylinder and cycle time	Length of stroke L_{bucket}	349.0 [mm]
	Diameter of piston D_{bucket}	76.2 [mm]
	Diameter of rod d_{bucket}	38.1 [mm]
	Bucket dump time $t_{bucket,ex}$	2.34 [s]
	Bucket rollback time $t_{bucket,re}$	2.05 [s]

2.2. Proposed System

Figure 2 presents the hydraulic schematic of the implement system for the electrified tracked loader. For the sake of simplification and to maintain focus on the study's scope, certain elements such as the auxiliary section and functions like parking brake control are excluded from the illustration. The proposed architecture incorporates key components, including the eLION inverter and electric motor as the prime mover, the A10VO eOC unit capable of 4-quadrant operation, and the RM pre-compensated LS valve. Notably, the boom control section is enhanced with a static compensator, a modification crucial for enabling energy regeneration. The modification on the compensator with an extra shim to keep it open statically, but this valve section is still capable with other RM sections without any change on the platform. The schematic emphasizes the inclusion of essential sensors, such as pressure sensors, displacement sensors at the actuators, and the angle sensor of the eOC-P. These sensors play a vital role in providing feedback necessary for effective control.

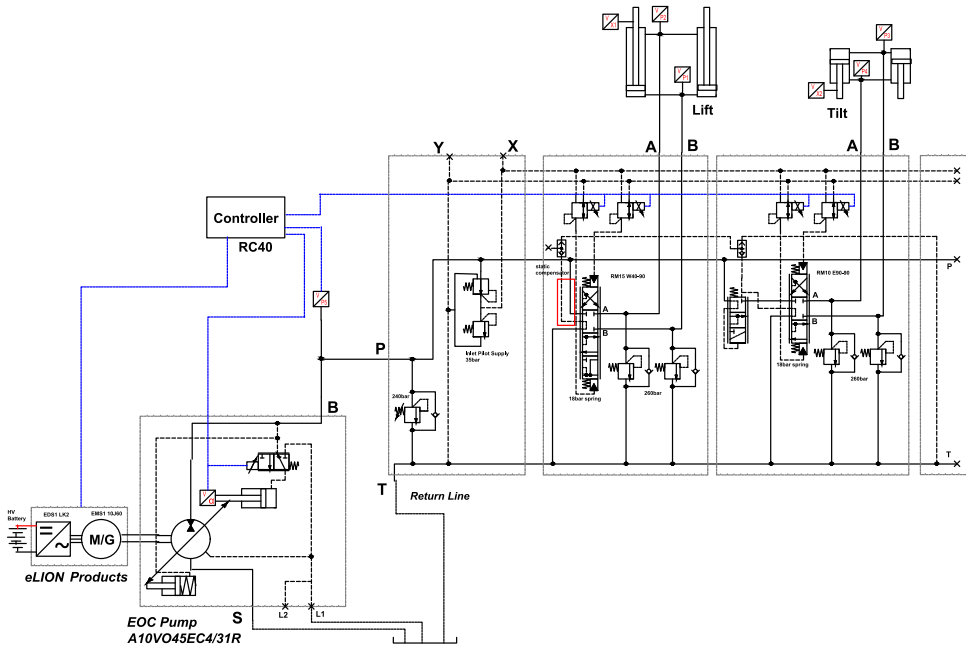

Figure 2. Hydraulic schematic of the proposed system

Figure 3 provides a visual representation of the working principle behind boom control with energy regeneration. The modification of the compensator to a static, always wide-open configuration allows for the implementation of displacement control for the boom function with the eOC-P capable of 2-quadrant operation, which covers both positive and negative displacement. The velocity of the boom actuation is governed by the pump displacement α, dictating the flow rate Q to the system in both directions. Simultaneously, this controls the power flow P to the electric machine and inverter, assuming an unchanged shaft speed. Notably, the valve can be fully opened, a design feature that serves to minimize throttling losses.

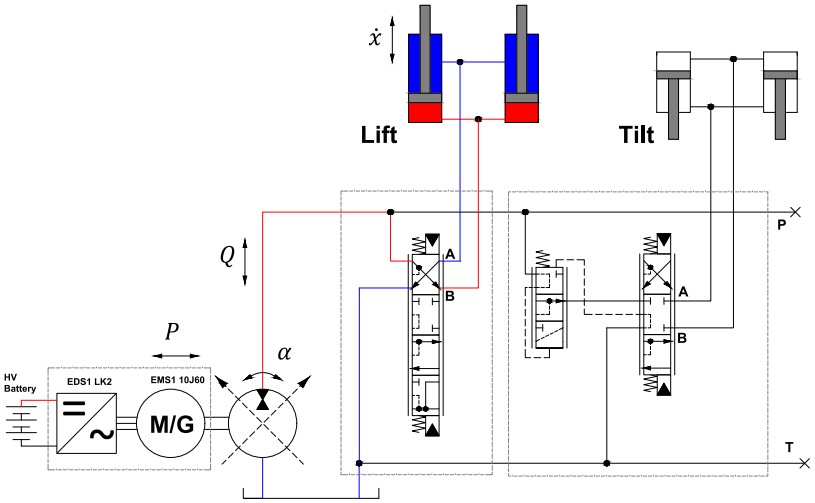

Figure 3. Regeneration capability from the boom function

The flow rate delivered to the boom actuators is as equation (1), where V_d is the maximum displacement of the pump.

$$Q = n \cdot V_d \cdot \alpha \cdot \eta_{vol} \tag{1}$$

And the velocity of the boom cylinders follows equation (2). Thus, the velocity can be controlled by adjusting the pump ratio α as given in equation (3). The ratio α could be negative for regeneration mode when the boom cylinders retract with negative $\dot{x}$ too.

$$\dot{x} = \frac{Q}{2 \cdot A_{boom}} = \frac{Q}{2 \cdot \pi D_{boom}^2} \tag{2}$$

$$\dot{x} = \frac{n \cdot V_d \cdot \alpha \cdot \eta_{vol}}{2 \cdot \pi D_{boom}^2} \tag{3}$$

While the example above focuses on boom control in a single-user scenario, the introduced modifications in the LS architecture pose a control challenge when considering multiple-user conditions. Consequently, a novel control strategy is proposed to address this complexity.

2.3. Control Strategy

Figure 4 illustrates one multiple user condition, wherein both the boom operation and bucket rollback occur at the same time. The compensator of the bucket section regulates he flow rate to the bucket cylinders Q_j, and the pump output flow can be controlled using equation (1). As a result, the flow rate to the boom cylinders is derived as $Q_p - Q_j$. If the user requires Q_i for the boom, the pump flow is controlled according to equation (4). In contrast to the conventional LS system, the proposed system eliminates the need for a boom compensator, replacing its functionality by directly controlling the pump flow using the eOC-P. Other functions with compensators maintain the same control principles.

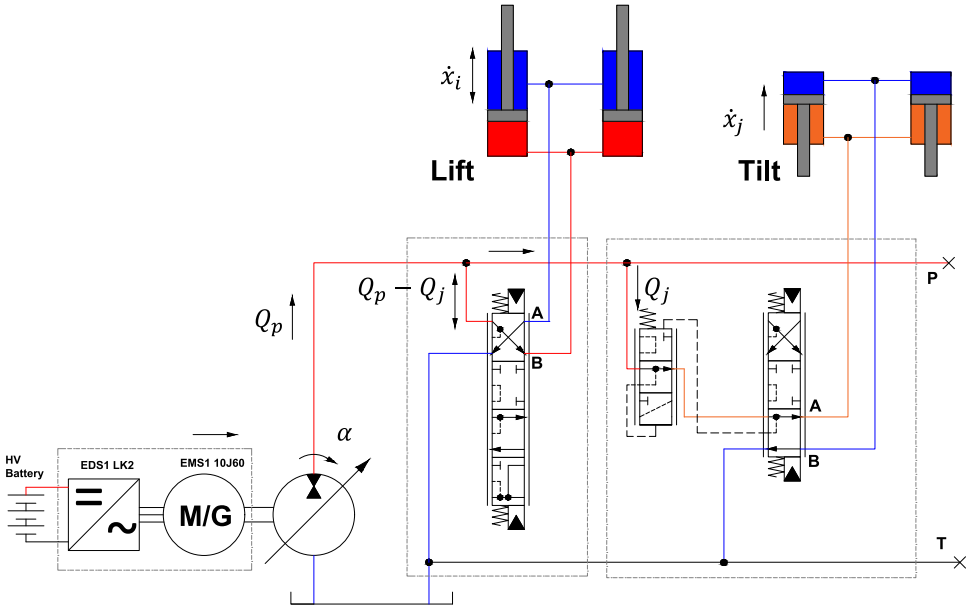

Figure 4. Control strategy for multiple users boom and bucket.

$$Q_p = Q_i + Q_j \tag{4}$$

One fact about this tracked loader application is that the load pressure of the boom cylinder p_i tends to be higher than that of the bucket cylinder p_j. Under this scenario, the valve for boom control can be fully opened to optimize efficiency, given that the flow typically aligns with the requests of the compensated bucket function, which operates at a lower pressure. Energy regeneration is feasible when $p_i > p_j$ when lowering the boom, utilizing backflow from the boom to fulfill the bucket's needs. The eOC-P would provide the rest of required flow. Conversely, if $p_i < p_j$, metering control of the boom valve may be applied to meet flow requests during the boom-raising phase. In instances where energy regeneration is not possible during boom lowering, the boom valve section can switch to the PA position, as depicted in Figure 5. The control principle is the same with Figure 4, but this scenario excludes energy regeneration due to the necessity for high pressure during downward boom movements, like in some piling operation. The mode presented in Figure 5 is similar to the conventional LS control in terms of overrunning the boom down but not regenerating from this operation phase.

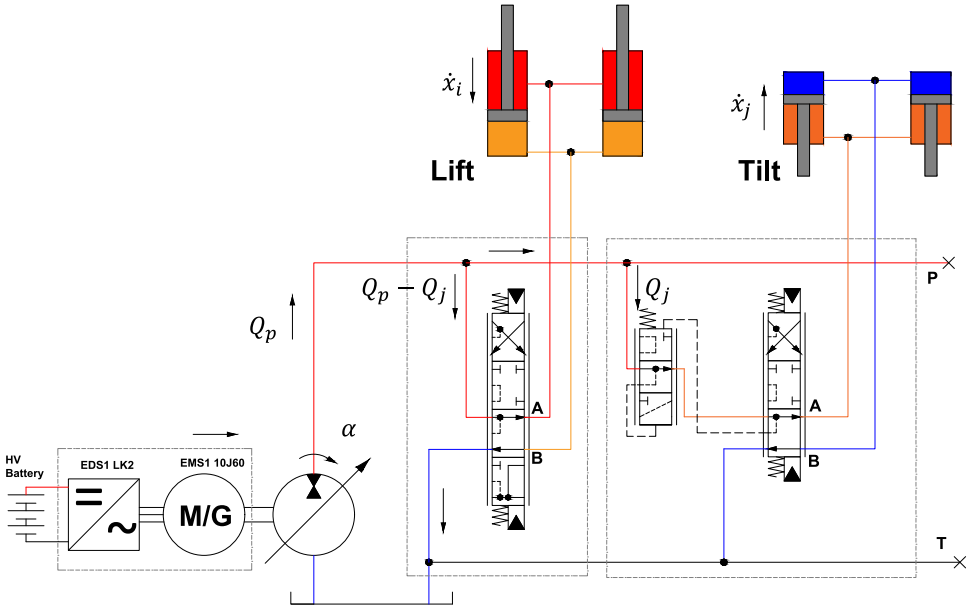

Figure 5. Control strategy for multiple users, lowering the boom without energy recovery.

An alternative method to control the boom lowering involves employing the float section of the valve, as presented in Figure 6. In this scenario, the flow control of the boom floating operates independently of the bucket control. This mode proves advantageous in situations where the load pressure of the boom is low, and energy regeneration is not attainable.

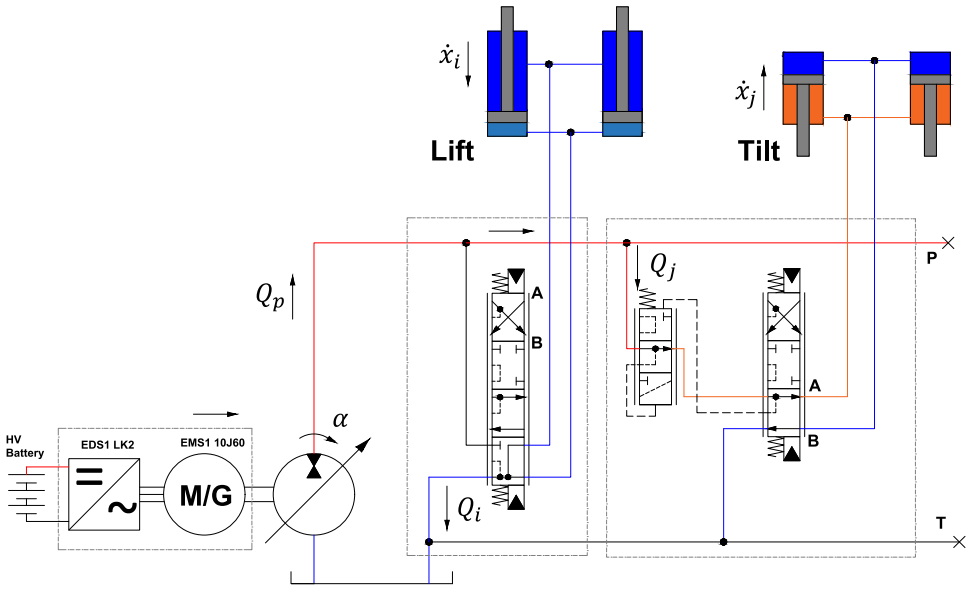

Figure 6. Floating mode of the boom control.

The control strategy is summarized in the flow chart presented in Figure 7. For single-user cases, employing displacement control for the boom is a straightforward approach, facilitating energy regeneration during boom operation. For multiple-user conditions, the compensator associated with the bucket regulates the flow rate along its path, while the pump delivers the required flow for all functions. Under different loading conditions with feedbacks from the sensors, the controller would switch the boom valve position, aiming to fulfil the functionality with optimal energy performance. Additionally, the boom section includes a float position designed for lowering the boom under specific conditions.

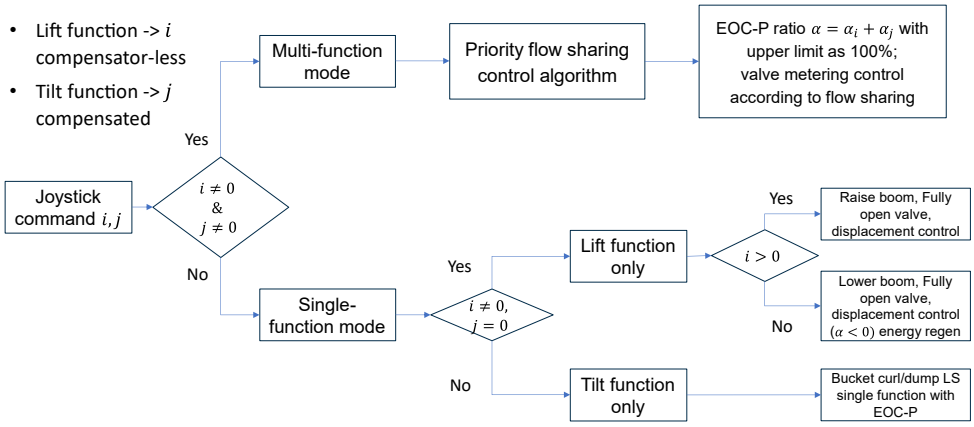

Figure 7. Flow chart of the control strategy for the proposed architecture.

3. METHODS

This study adapts both experimental and simulation methods. Initially, the baseline was established through on-field measurements with the reference machine. From the baseline data, a sizing study was conducted to choose suitable components for the proposed system, including the electric machine, hydraulic machine and valves. Subsequently, a lumped-parameter model was developed within AMESIM environment, with specifications of the chosen components as parameters, and baseline data as the model inputs. The simulation model incorporates the efficiency map of the pump and dynamic behaviours of the valves, creating a realistic environment for simulating and fine-tuning the control strategy in preparation for the vehicle demonstration. At present, the proposed system has been installed on the electrified compact loader, and ongoing tests are in progress. Therefore, this paper will focus on presenting simulation results.

3.1. Baseline and setup

Figure 8 presents a picture of the ongoing baseline measurements, undertaken at the test field at Bosch Rexroth in Fountain Inn, South Carolina. Various operating conditions were tested, such as fast traveling, Y-cycle, gradeability, etc. Specifically, the Y-cycle data obtained during these measurements serves as both a reference and inputs for the simulation of the hydraulic implement system.



Figure 8. Baseline measurements on the reference machine, Y-cycle operation.

The selected components and product number of those are listed in Table 3, including the Rexroth eLION products, eOC-P and the RM-MMP valve platform.

Table 3: Selected components for the proposed electrified system

Component	***Product Number***
Electric machine	EMS1-10J60LM7-RSCB-W1M7NNNNN
Inverter	EDS1-L0400 KNN-12 ECNM1RDNN-S03RSN9
Hydraulic machine	A10VO0045 EC4 000PL3/60DL VB2
Valve inlet plate	M4-12-2X / J 260 Y
Boom section	RM15 S1 S22ZZZ W040-090 H24H24 S00
Bucket section	RM10 S1 S22ZZZ E090-090 H24H24 S00
Auxiliary section	RM15 S1 S22ZZZ E110-110 H24H24 S00
Valve end plate	M4-12-2X / LA
Pressure sensors	PR4 280 U7 D SE/10, PR4 050 U7 D SE/10
Parking brake valve	SV08-30-6T-N-24ER
Oil filter	50LE0150-H10XLA00-V2,2-M

3.2. Simulation model

A lumped-parameter model was developed in AMESIM environment as depicted in Figure 9, it is evident that the architecture of the model aligns with the schematic illustrated in

Figure 2. The selected components have their parameters determined using measured data, ensuring the model reflects realistic performance to the maximum extent. These parameters include the efficiency map and simplified controller of the eOC-P, flow curves with pressure drops associated with the RM valve, and the lookup table of the load force derived from the Y-cycle baseline measurements. The primary outputs of the simulation focus on functionality within the compensator-less design and energy performance.

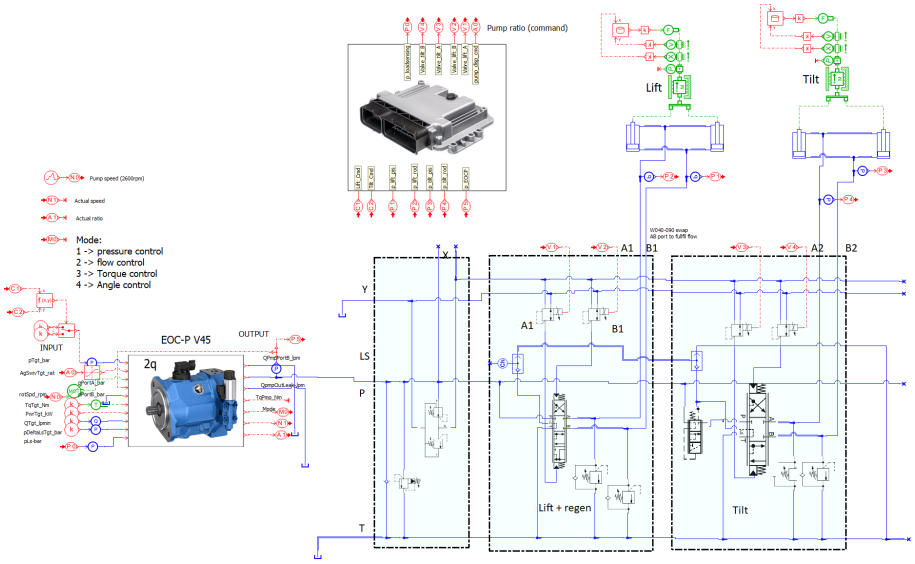

Figure 9. AMESIM simulation model of the electrified implement system.

4. RESULTS

4.1. Sizing study

Figure 10 represents the load force table of the boom actuators generated from the baseline data. During the boom up and down cycles, the load force F applied to the actuators is related to the displacement and the velocity. Equation (5) defines this relationship using measured pressures p_{pis}, p_{rod} at the piston and rod sides. The displacement alters the act angle between the actuators and the mechanism, consequently impacting the load force. In the case of the boom, an increase in displacement aligns the actuators more vertically, resulting in a decrease in load force. The velocity is related to the mechanism friction. When raising the boom, higher velocity leads to greater friction opposing the boom actuators, resulting in an increase in load force. Conversely, during boom lowering, the friction opposes in the opposite direction, causing a decrease in load force. These tables for boom and bucket work as the inputs of the AMESIM simulation model. The loading condition also provides reference for the sizing of the components.

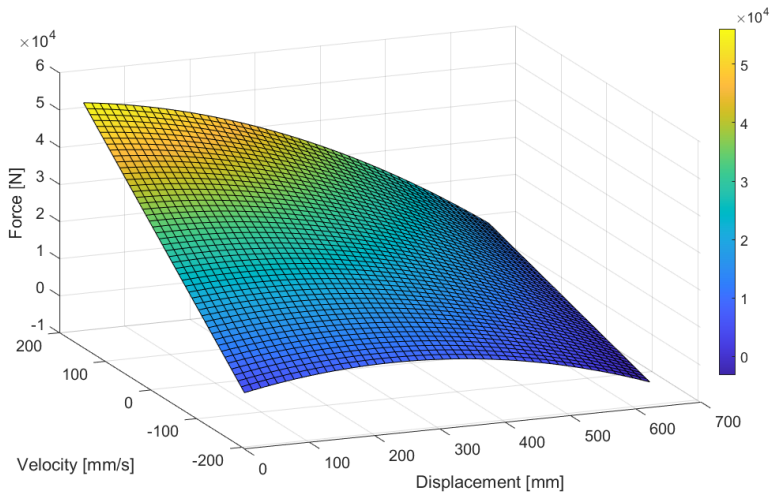

Figure 10. Load table generated from the baseline measurements, boom Y-cycle operation.

$$F = p_{pis}.\pi D^2 - p_{rod} \cdot \pi(D^2 - d^2) \qquad (5)$$

Figure 11 demonstrates the sizing considerations for the electric machine regarding the speed and torque performance. For electric machines, two curves serve as reference points: the continuous curve and the peak curve. The electric motor can run under the continuous line without limits. However, if the operation exceeds this curve, additional cooling measures may be necessary. The orange peak curve, indicating the limit for a 60-second duration, sets the boundary for operations beyond the continuous curve.

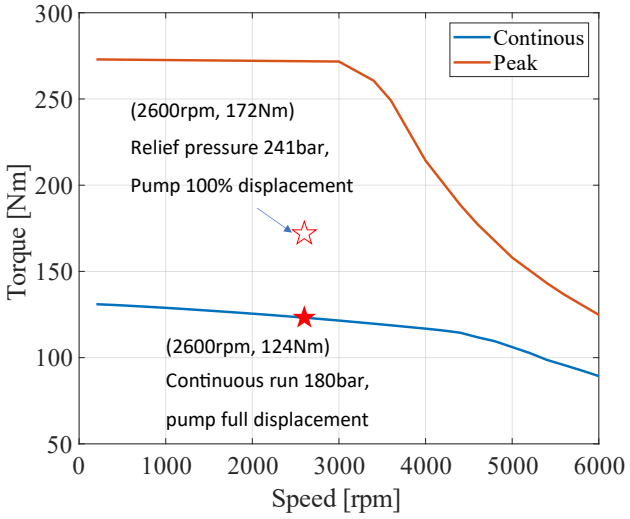

Figure 11. Sizing of the electric machine, EMS1-10J60 speed and torque curve

To select the proper electric machine for hydraulic implements often revolves around the consideration of maximum torque. The peak torque T of the hydraulic machine can be obtained using equation (6), where dp is the maximum pressure difference. Assumed relief pressure as dp and full displacement of the pump, the torque will reach the theoretical peak value. This point falls between the peak and continuous curve depicted in Figure 11 to avoid oversizing. Operating at continuous torque, the pump can function at 180bar with full displacement, or at relief pressure with about 75% displacement. This configuration aligns with operational requirements based on the baseline data.

$$T = dp \cdot \frac{V_d}{2\pi} \cdot \frac{1}{\eta_{mh}} \tag{6}$$

In terms of efficiency of the proposed system, the energy losses of the electric machine and inverter are not included in this study. Thus, the comparison is mainly about the hydraulic system.

4.2. Simulation results

Figure 12 represents an example of the AMESIM simulation results, capturing a complete boom raising and lowering cycle, like the mode illustrated in Figure 3. The first plot showcases the boom command and displacement, while the second provides the eOC-P ratio and the load pressure at the boom cylinder piston side. The third plot displays the power and energy consumption of the hydraulic systems, calculated at the pump shaft.

From the plots, the boom raising phase extends from 1s to approximately 6s, followed by the initiation of the lowering phase around 7s, persisting for about 4s. Notably, between the two black lines around 7s to 8s, the low load pressure disabled the energy regeneration, activating the float function to lower the boom instead, as indicated in Figure 6. The system requires a minimum of 18bar for pilot control, meaning energy regeneration is only enabled if the load pressure exceeds this threshold. Beginning at 8s, the ratio of the eOC unit becomes negative and works as a motor, energy regeneration starts and the power flow reverses direction as indicated in the third plot, until the cycle ends at about 11s.

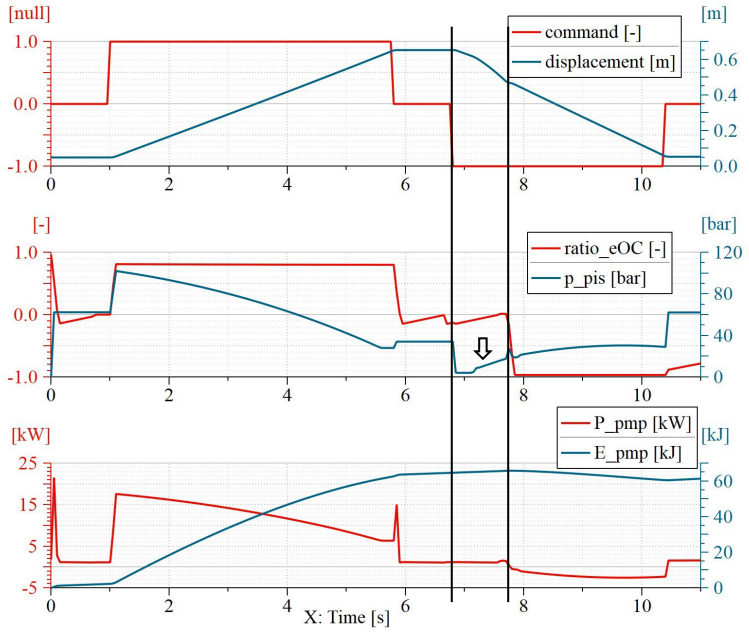

Figure 12. Simulation of one boom cycle with energy regeneration

For comparison, Figure 13 demonstrates the power and energy consumption in the cycle represented in Figure 12, where the speed command and actual displacement are presented. The baseline is the LS system with standard RM valves with loading conditions from the measurements on the vehicle, so the results should indicate the benefits from the energy regeneration with the electrified powertrain and modified compensator. Comparing the power consumption, the proposed electrified system saves energy during the lowering phase by regeneration. Moreover, because of its compensator-less design, the proposed architecture minimizes the throttling losses and additional energy saving is achieved during the raising phase as well. At approximately 7s, the baseline system experiences an extra power consumption spike due to insufficient load pressure at the piston side for assistive operation.

Regarding the energy consumption during one boom cycle, as depicted in the second plot, the baseline system records 90.4 kJ compared to the proposed system's 61.4 kJ, translating to a remarkable **32% energy saving** compared to the baseline system.

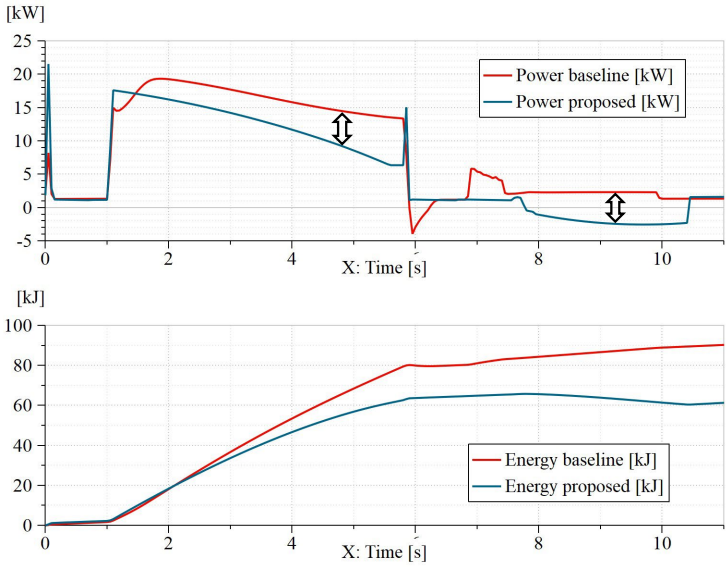

Figure 13. Power consumption comparison from the simulation

For multiple user conditions, Figure 14 represents the results with boom and bucket Y cycle operation. The first plot provides an overview of the cycle commands, with both actuators being commanded during the time slots of 2s-4s and 6.5s-7.5s. The second plot illustrates the displacement of the actuators, while the third plot presents the ratio of the eOC-P, offering insights into the flow control dynamics of the system.

During the period from 2s to 4s, the system operates in the control mode depicted in Figure 4. The pump is tasked with supplying the required flow for both the boom and the bucket. If the pump ratio reaches 100%, a flow sharing condition occurs, as seen between 3s to 4s. In this instance, an increased command to the bucket results in a decrease in the boom velocity. While this paper does not delve into specific control algorithms addressing flow sharing conditions based on user priority, it remains an option for further refinement. From 7s-7.5s, the boom drops down and the bucket rolls back. Throughout this time slot, the ratio of the eOC-P remains positive, indicating no energy regeneration with the bucket load pressure higher than that of the boom cylinders. After 7.5s, the system transitions into regeneration mode, specifically with boom lowering, causing the pump ratio to change to a negative value.

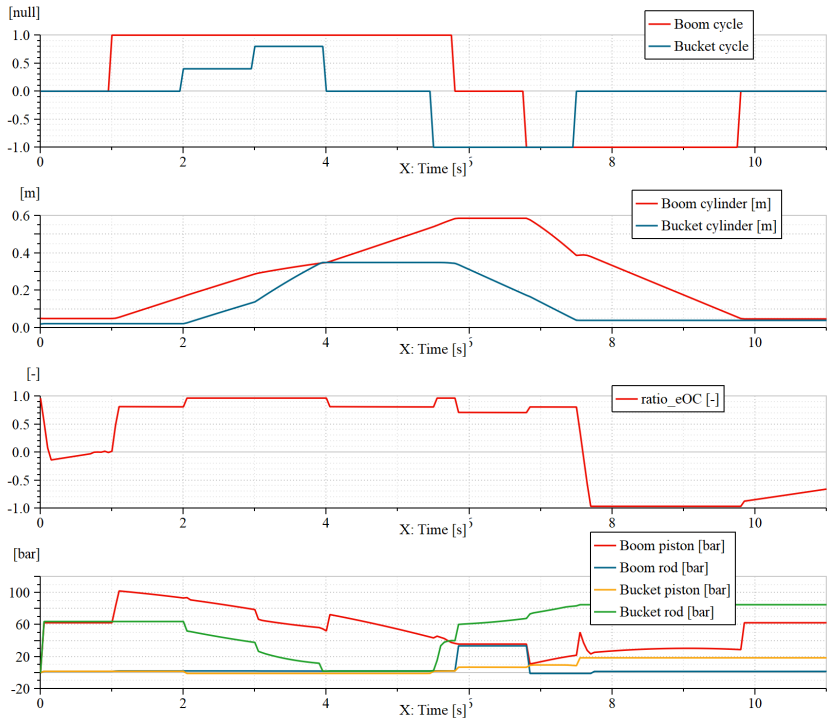

Figure 14. Simulation of the multiple user case, boom and bucket Y cycle operation

5. CONCLUSION

In this study, we introduced an innovative electrified hydraulic implement system based on conventional LS architecture. The modification of the boom function's compensator to a static state facilitates energy regeneration, and a corresponding control strategy has been devised. This strategy employs the capability of the eOC unit, incorporating displacement control and motoring mode to effectively address the complexities associated with multiple user conditions.

To investigate the proposed system, baseline measurements have been conducted on the reference compact track loader, leading to the selection of suitable components through a comprehensive sizing study. Subsequently, a lumped parameter model was developed in AMESIM environment. With the components' specifications and the measured loading conditions as the inputs, the simulation can reflect the realistic working conditions. The boom cycle simulation validates the displacement control strategy, revealing a remarkable energy savings of over 30% compared to the baseline LS system. Simulation results for multiple user conditions further explore various working modes as proposed, affirming the effectiveness of the control strategy.

As of now, tests on the proposed system are ongoing on the demonstration vehicle, and the gathering of additional data will contribute to refining the controller design, particularly in terms of dynamic behavior and handling extreme conditions. These ongoing tests aim to further enhance the overall performance and robustness of the proposed electrified hydraulic implement system.

REFERENCES

[1] Lin, T., Lin, Y., Ren, H., Chen, H., Chen, Q., & Li, Z. (2020). Development and key technologies of pure electric construction machinery. *Renewable and Sustainable Energy Reviews*, 132, 110080.

[2] Lin, T., Chen, Q., Ren, H., Huang, W., Chen, Q., & Fu, S. (2017). Review of boom potential energy regeneration technology for hydraulic construction machinery. *Renewable and Sustainable Energy Reviews*, 79, 358-371.

[3] Fassbender, D., Zakharov, V., & Minav, T. (2021). Utilization of electric prime movers in hydraulic heavy-duty-mobile-machine implement systems. *Automation in Construction*, 132, 103964.

[4] Qu, S., Zappaterra, F., Vacca, A., & Busquets, E. (2023). An electrified boom actuation system with energy regeneration capability driven by a novel electro-hydraulic unit. *Energy Conversion and Management*, 293, 117443.

[5] Qu, S., Fassbender, D., Vacca, A., & Busquets, E. (2021). A high-efficient solution for electro-hydraulic actuators with energy regeneration capability. *Energy*, 216, 119291.

[6] Qu, S., Fassbender, D., Vacca, A., & Busquets, E. (2021). A cost-effective electro-hydraulic actuator solution with open circuit architecture. *International Journal of Fluid Power*, 22(2).

[7] Lin, T., Lin, Y., Ren, H., Chen, H., Li, Z., & Chen, Q. (2021). A double variable control load sensing system for electric hydraulic excavator. *Energy*, 223, 119999.

[8] Lin, Z., Lin, Z., Wang, F., & Xu, B. (2024). A series electric hybrid wheel loader powertrain with independent electric load-sensing system. *Energy*, 286, 129497.

[9] WO24058689-A1, Hydraulic System, Lejonberg Robert, Maennistoe Ville, (2024). International patent

[10] US patent, E-Load sensing system with compensator-less design, Shaoyang Qu, Rafael Cardoso, Enrique Busquets, (2024), in prosess.

[11] US2021025414 (AA) - Hydraulic Pressurizing Medium Supply Assembly, Method, And Mobile Work Machine EOC patent, Geiger Daniel, Muehlbauer Florian, Golde Marcel, Brand Michael, An Minha, Tetik Salih, Wang Ximing, (2021)

A numerical procedure to reduce the noise emitted by External Gear Pumps

Emma Frosina[a], Francesca Pedrielli[b], Eleonora Carletti[b], Pietro Marani[b], Luca Romagnuolo[a], Adolfo Senatore[c]

[a]*Department of Engineering, University of Sannio, Italy, frosina@unisannio.it*

[b]*STEMS Institute - National Research Council of Italy, Ferrara, Italy*

[c]*Department of Industrial Engineering, University of Naples Federico II, Italy*

Abstract

External gear pumps offer very good performance at competitive costs, making them widely spread worldwide. On the other hand, these machines are generally characterized by high levels of vibrations and noise emissions. This article presents a numerical methodology based on lumped parameter approach to optimize both spur and helical External Gear Pumps (EGPs). The methodology was implemented in a multi-environment tool called EgeMATor MP+, developed by the Fluid Power Research Group of the Universities of Naples and Sannio. This tool executes a closed-loop procedure, which starts from the pump drawing. Thanks to several subroutines developed in different interconnected environments, it permits global analysis and later optimizes EGPs.

A reference pump was optimized, acting on the geometry of the pressure relief grooves of the wear plate, with the objectives of reducing flow ripple fluctuations, pressure spikes, and crossflow. Finally, both reference and optimized pumps were tested in the CNR-STEMS research institute laboratory in Ferrara, using a specific test rig, which physically isolates the pump from the prime mover. Sound pressure levels were measured in several points surrounding each pump and the results showed an effective reduction of the emitted noise for the optimized design.

Keywords. Helical EGPs; lumped parameter numerical approach; fluid-borne noise; flow ripple reduction; design optimization.

1. INTRODUCTION

Noise emission is increasingly becoming critical in selecting components for fluid power systems. The main noise sources in these systems are generally positive displacement machines such as external gear pumps (EGPs). They are usually chosen as the hydraulic power source for fluid systems thanks to their high volumetric efficiency, durability, compactness, and low manufacturing cost. These characteristics have allowed this type of pump to be widely used in the fluid power field for both industrial and mobile applications. One of the weak points of these pumps is the relatively high sound pressure level produced

in the different working conditions in which they are used. Reducing the noise emissions without impacting the global performance of the pumps is arduous. To reach this objective, the scientific community has devised two different approaches to decrease the pressure ripple, which is considered the main noise cause. The first utilizes a three-dimensional CFD approach to evaluate the overall flow behavior and the pressurization in the variable displacement chambers. The 3D-CFD approach was used by Frosina et al. [1] to investigate the performance of a high-pressure EGP with spur gears. Heisler et al. [2] and Qi et al. [3] used different methodologies based on the same approach to predict the behavior of a helical EGP. This methodology has demonstrated to obtain an exhaustive description of those pumps, with excellent accuracy in predicting the working characteristics. These outcomes require relevant computational power and time; thus, these models usually use some kind of simplification to reduce them. The second methodology implements a lumped parameter approach, where the pressure variations within the pump are obtained from the variations of interconnected control volumes with constant properties. This methodology only necessitates a small fraction of the computational capacity required by a 3D-CFD approach, therefore permitting it to run fast simulations. A lumped parameter model that predicts the general behavior of EGP was developed and validated by Borghi et al. [4]. A similar model was developed by Battarra e Mucchi [5] that is also capable of analyzing helical gears. Ransegnola et al. [6] used a lumped parameter approach in a multi-domain system to compare helical and spur EGPs, demonstrating the flexibility and accuracy of this methodology. The authors also explored the analysis of EGPs by means of a lumped parameter approach, developing a simulation tool [7][8] called EgeMATor MP+. This tool permits fully analyzing and predicting both the fluid dynamics and mechanical behavior of EGPs with both spur and helical gears. The software allows the evaluation of gear positions by calculating the bearing's force reactions, and it also includes a procedure to optimize the pump timing given a gear tooth profile. The developed tool was used to analyze a reference helical EGP manufactured by Hydreco Hydraulics Italia. The optimization subroutine was subsequently executed, hence identifying a new design for the pressure relief grooves. The new design was prototyped, and both reference and optimized pumps were tested in the CNR-STEMS laboratories in Ferrara using a specific test rig that physically isolates the pump from the prime mover. This experimental campaign measured both flow rate and sound pressure levels (SPLs). Sound pressure levels were measured at several points surrounding each pump. The results showed good agreement with the simulation results, pointing out an effective reduction of the emitted noise for the optimized design.

2. ANALYZED PUMP

The experimental campaign proposed in this paper was performed on two different EGPs: a reference helical external gear pump designed by Hydreco Hydraulics Italia company and a prototype optimized version that differs only in the design of the pressure relief grooves. The displacement of the tested pumps is 14.5 cm^3/rev, with a maximum continuous pressure of 260 bar and a maximum rotational speed of 3500 rev/min. An exploded view of the reference pump is shown in Figure 2.1. Pumps have a housing made from die-cast alloy, while the front and rear covers are made of cast iron, allowing them to reach higher pressure while maintaining a relatively small total weight, making them ideal for mobile applications.

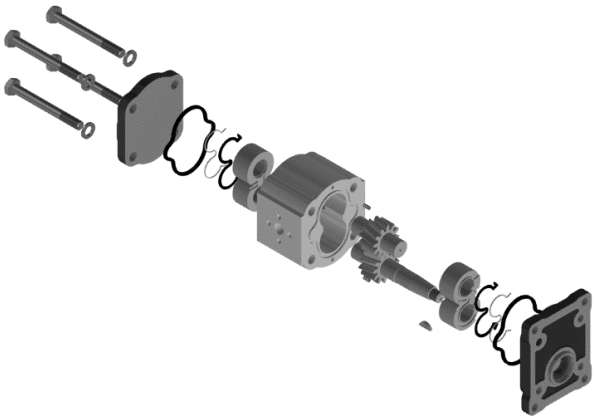

Figure 2.1. Exploded view of the reference pump

3. NUMERICAL MODEL

3.1. Overview of EgeMATor MP+

EgeMATor MP+ (External Gear Machine Multi Tool Simulator for Multiple Gears' Profiles) is a tool developed from scratch by the authors for the numerical simulations of external gear machines [7][8]. The tool consists of several subroutines developed in different environments, interconnected to each other, as shown by its workflow in Figure 3.1. Firstly, a subroutine called *Surface Tool*, written in the MATLAB® environment, is executed. It receives the pump geometrical data in Excel spreadsheet table format, while 2D CAD DXF files supply the tooth profile and the pressure relief grooves geometry to the subroutine. The subroutine first evaluates the meshing of the gears, checking for the presence of potential interference. After checking the gears' typology (spur or helical gear type), the *Surface Tool* calculates all the control volumes and their connections as a function of the rotation angle; then, it generates the data required. The hydraulic simulation main subroutine was developed in the simulation environment Simcenter Amesim®, based on the control volume approach. It computes the fluid-dynamic properties of the pump (pressure, flow rate, leakages, etc.) as a series of resistive and capacitive elements connected and ends up creating tables of the fluid-dynamic characteristics of the pump for post-processing and subsequent subroutines. Another subroutine was also written in the MATLAB® environment, where the forces and torques acting on the gears were evaluated. After this process, the data evaluated are passed to the "*fnest"* subroutine, which calculates the bearings reactions and thus estimates the position of the gears inside the case through an iterative finite element numerical simulation. *EgeMATor MP+* was developed to work in a closed loop; therefore, after this last subroutine, it compares the calculated gears' position with the previous step, and if the convergence is not reached, the loop procedure runs until the residuals are low enough. Further details are available in the authors' previous works [7][8].

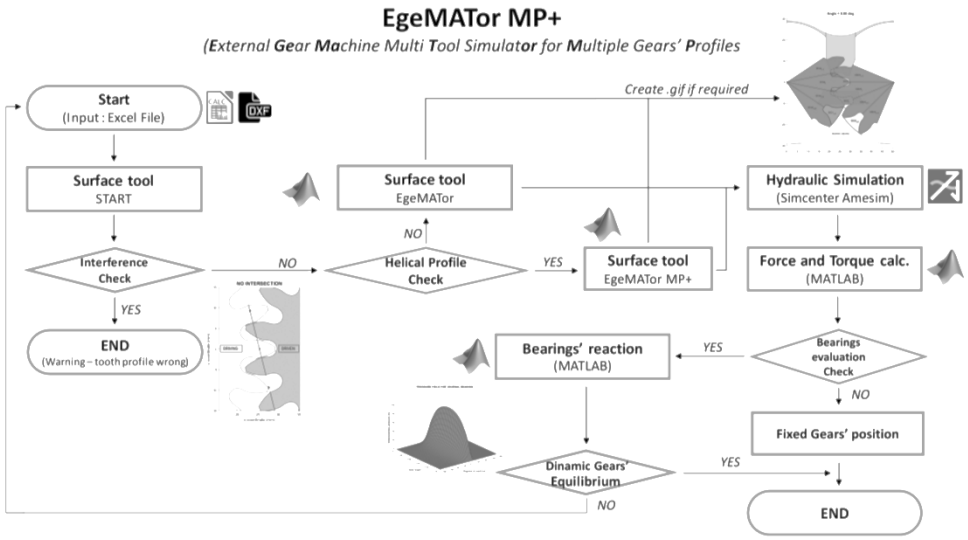

Figure 3.1. The EgeMATor MP+ (External Gear Machine Multi Tool Simulator for Multiple Gears' Profiles) workflow

3.2. Optimal groove design research methodology

The developed numerical model for studying and analyzing EGPs was also designed to include further capabilities, such as optimization procedures. The methodology implemented in the developed tool allows the optimization of the pressure relief grooves inside the pump wear plates for a given gear tooth profile. This procedure was based on geometric assumptions to minimize the crossflow between delivery and suction while limiting pressure spikes during the meshing of the gears. A brief description of the internal connections implemented in the lumped parameters model is required to describe the optimization methodology and its equations in more detail. Further details are available in the authors' previous works [7][8][9].

The previously mentioned *Surface Tool* estimates the volume of a displacement chamber as a function of the rotation angle φ. The optimization starts by finding the rotation angle value, which corresponds to the minimum value of the chamber volume. The identified angle, $\varphi_{DC\ MIN}$, represents the angle at which the instantaneous switch between delivery and suction pressure occurs, representing thus one of the defining parameters for a correct design of the pressure relief grooves. The optimization of the wear plate design around this angle value is of utmost importance to prevent high-pressure spikes and backflow. The next step implements the start of an iterative procedure. This procedure requires parametrizing the pressure relief grooves geometries, as shown. The relief grooves are manufactured into both wear plates, as shown in Figure 3.2. The parameterization was chosen to be normalized against the gear module m to be pump size independent and the grooves dimensions vary within the range shown in Table 3.1.



a) b)

Figure 3.2. Parameters for the groove shape design search: a) Parameters for the optimization procedure; b) Wear plate design with the relief grooves

Table 3.1. Grooves parametrization

DESCRIPTION	VALUE	MIN	MAX
Delivery Groove width	W	1	3
Suction Groove height	h	0.5	2
Delivery Groove reference distance	d_1	0	3
Suction Groove reference distance	d_2	0	3

To optimize the groove design, a simple rectangular-shaped groove design was chosen for both the delivery and inlet groove. The range of the parameters permitted the evaluation of a large number of designs that were tested within the iterative procedure against a series of target functions:

$$TF_1 = \left|\varphi_{DC_MIN} - \varphi_{GRV}\right| \tag{3.1}$$

$$TF_2 = \frac{1}{n}\sum_{i=1}^{n} A\left(\varphi_{DC_MIN} \mp n\Delta\varphi\right) - A_g\left(\varphi_{DC_MIN} \mp n\Delta\varphi\right) \tag{3.2}$$

The target function TF_1 in equation (3.1) was implemented to check the volumetric efficiency of the tested design. The TF_1 needs to be as small as possible to achieve high volumetric efficiency value. This implies reducing the angular difference between the rotation angle value of minimum chamber volume $\varphi_{DC\ MIN}$ and the characteristics rotation angle value for the grooves φ_{GRV}, thus reducing the amount of backflow from delivery to the inlet side. In particular, for the delivery groove, φ_{GRV} represents the rotation angle of connection closure between the groove and the delivery chamber. In contrast, φ_{GRV} represents the rotation angle of connection opening between the groove and the delivery chamber for the suction groove. The target function TF_2 in equation (3.2) was implemented to minimize the internal pressure peaks occurring during gears' meshing in the proximity of $\varphi_{DC\ MIN}$; the function evaluates the cross-sectional area in dark red in Figure 3.3 (called A_g) and the projection area of the displacement chamber volumes on the lateral side in green (called A). The reduction of the pressure peaks requires this difference to be as small as possible for a number n of points with an angular pitch distance from $\varphi_{DC\ MIN}$ equal to $\Delta\varphi$,

with both values chosen as user input. This ensures a more gradual transition between the delivery and inlet area around the $\varphi_{DC\,MIN}$, reducing thus the pressure peaks; sign minus or plus in equation (3.2) are respectively for the delivery or suction grooves. The iterative procedure checked all the designs and then selected the one that permitted obtaining the minimum total value for the sum of both target functions. In this way, the methodology allowed identifying the optimal starting and ending positions for the pump pressure relief groove design.

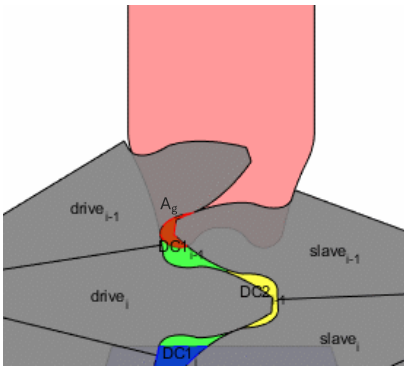

Figure 3.3. Areas evaluated in the optimal groove design methodology.

4. VALIDATION

The optimization procedure was tested on the reference pump, obtaining a new and optimized geometry. The results of this optimization procedure led to a radical change of the design philosophy: from a symmetrical design of the pressure relief grooves geometries, for the reference pump, to an asymmetrical one on which the front and rear wear plates exhibit pressure relief grooves with noteworthy geometric differences between them, as shown in Figure 4.1. The validation of the optimization methodology was carried out in two phases: in the first phase, the new design was compared to the reference pump through numerical models; in the second phase, an experimental campaign was performed, allowing to test and acquire the flow rate and the noise emissions of the tested pumps.

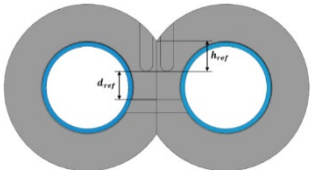

a)

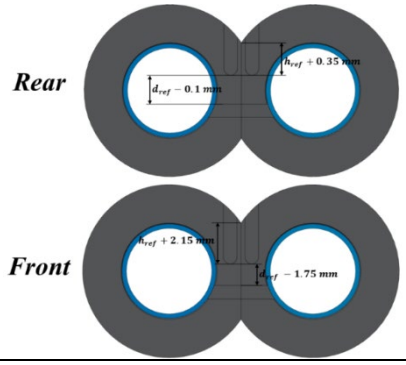

b)

Figure 4.1. Relief grooves design: reference pump (left) and optimized design (right).

4.1. Numerical model validation

The first phase was carried out by simulating several working conditions; the results of the two designs were compared. To focus on the primary aspects investigated by the optimization methodology, the comparison examined the mean flow rate value, the non-uniformity of the flow rate, and the pressure evolution inside the variable displacement chamber. This work shows only the comparison results obtained for a pump speed of 1500 rev/min and a system delivery pressure of 200 bar since the main target of the present work was the optimization of the design in this operating condition that was critical for the pump. However, the same analysis has been performed for different pressures and rotational speeds. The flow rate is normalized to a reference value, Q_{ref}, for confidential reasons. Figure 4.2 shows the numerical comparison between the reference and optimized design of the flow ripple for a particular operating condition.

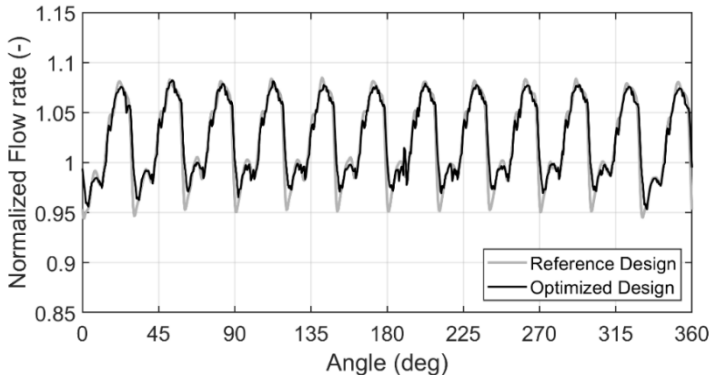

Figure 4.2. Numerical flow ripple comparison at n=1500 rev/min, Δp=200 barA

The comparison shows that the optimized design exhibits improved performances for both analyzed physical dimensions, with an increase of about 0.5% of the mean delivery flow rate and a reduction of the non-uniformity of the flow ripple of around 8%. In particular, the non-uniform rate reduction was mainly due to a higher minimum value of the flow ripples. This aspect implies a lower backflow rate value, one of the aspects on which the optimization methodology was focused.

Figure 4.3 presents another significant result: the comparison of the numerical pressure evolution inside the variable displacement chamber around the meshing zone between the reference and optimized pumps; in particular, on the left, there are results for the driving while on the right for the driven gear. The comparison highlights a reduction of the pressure spikes during the meshing of both gears, further suggesting the validity of the methodology employed. The reduction was mainly relevant for the driving gear chamber, with a reduction of about 10% of the pressure spikes. This result, coupled with the decrease in the non-uniformity rate of the flow ripple, hinted at the possibility of lower vibrations for the optimized design and, hence, a reduction in noise emissions.

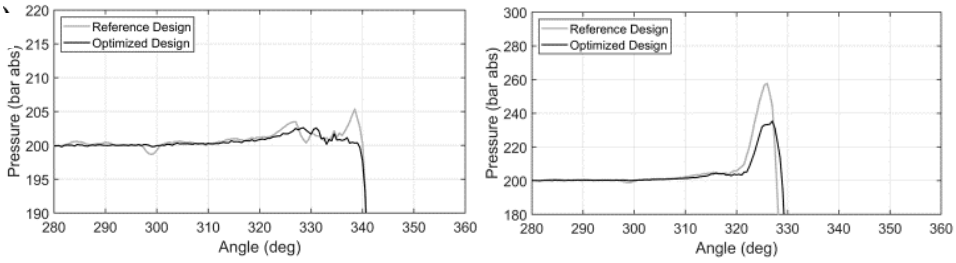

Figure 4.3. Numerical pressure evolutions comparison at n=1500 rev/min, Δp=200 barA: Driving gear (left); driven gear (right).

4.2. Experimental validation

This section focuses on the comparison between the noise emitted by a reference pump and an optimized one.

4.2.1. Test rig and experimental design

The experimental campaign to validate the model was performed on a dedicated test rig in the CNR-STEMS laboratories. This test rig was built for testing gear pumps, which are mounted on a metal plate and placed inside a large shed. It was explicitly designed to acoustically isolate the pump under test from the prime mover and all other hydraulic components placed outside the shed and separated by a concrete wall. This layout exclusively permits the acquisition of the noise radiated from the pump. The flow rate was acquired thanks to a screw-type flow meter installed on the pressure line; the circuit also integrates pressure and temperature transducers. The tests were conducted with an oil temperature of 40 °C ± 3 °C, thanks to an off-line cooling system. The environmental conditions were almost constant throughout the test, with air temperature ranging from 4 °C to 9 °C and relative humidity values ranging from 80 % to 94 %. The hydraulic scheme of the test rig is reported in Figure 4.4.

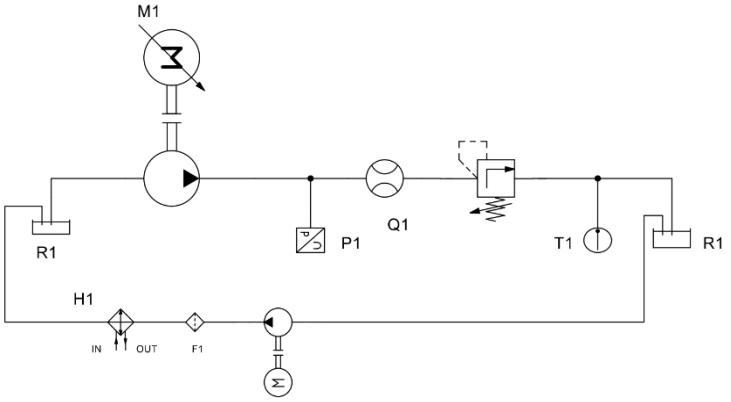

Figure 4.4. Test bench layout

For each pump type (reference and prototype), the tests were repeated on two different units to have a more reliable characterization and to compensate for possible production errors.

Noise tests were performed in 36 different operating conditions: six different rotational pump speeds (500, 1000, 1500, 1800, 2000, and 2200 rev/min) and, for each speed, six different delivery pressures (10, 50, 100, 150, 200, and 240 bar), from no-load condition to maximum continuous pressure. For each pump type and unit and each operating condition, the acquisition was repeated twice, the first run with an ascending delivery pressure and the second with a descending delivery pressure at fixed rotational speed.

4.2.2. Noise measurements

The noise tests consisted of the simultaneous acquisition of the SPL in five different positions arranged at a distance of 30 cm from the noise source in every direction (front, right, left, top, bottom) in order to account for the directivity of the noise emissions for each pump. Figure 4.5 shows the measurement layout.

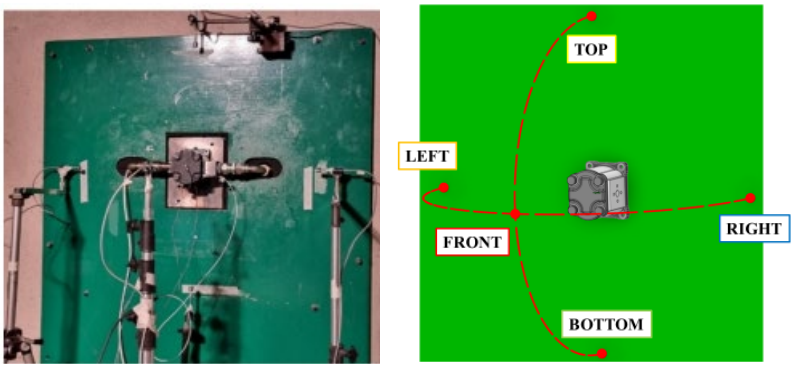

Figure 4.5. Noise measurement acquisition layout

The evaluation of the differences in noise emission between the reference pump and the optimized one (prototype) was based on a series of measurements of SPLs. 720 SPL spectra were acquired for each pump type: 2 units, 36 operating conditions, two runs and five measurement positions.

At each measurement point, the background noise was stationary, with SPLs always more than 15 dB lower than the corresponding SPLs of the noise sources under test.

The instrumentation included an 8-channel Siemens SCADAS analyzer (SCM-VM8.E module) coupled with Simcenter LMS TestLab software. The free-field ½ inch microphones (Brüel&Kjær 4181) and the measurement instrumentation met the requirements of class 1 instruments. Sound pressure measurements were performed in the frequency range of 20÷10000 Hz, and all the measurement chains were recalibrated several times during the tests with a pistonphone (Brüel&Kjær 4220). However, for this investigation, only the results in terms of linear overall SPL will be considered.

4.2.3. Measurement uncertainty

The uncertainties of sound pressure levels, in decibels, are estimated by the total standard deviation, σ_{tot}, in decibels, which should be obtained using the modeling approach described in ISO/IEC Guide 98-3 [10], which requires a mathematical model that can be replaced by results from measurements in case of lack of knowledge.

In this context, the total standard deviation is expressed by the standard deviation of reproducibility of the method, s_{R0}, in decibels, and the standard deviation due to the noise emission instability of the source, s_{ome}, in decibels, describing the uncertainty due to the instability of the operating and mounting conditions of the source under test, by equation (4.1).

$$s_{TOT} = \sqrt{{s_{R0}}^2 + {s_{omc}}^2} \tag{4.1}$$

The standard deviation values for s_{R0} and s_{omc} were estimated following the suggestions of the ISO Standard 3746:2010 [11]. The standard deviation s_{R0} was calculated using the existing knowledge on the noise emission of this family of machines (paragraph 9.3.2 of the Standard). In this regard, CNR-STEMS has been using this measurement method on external gear pumps for 20 years [12][13][14], and over time, researchers have had the opportunity to use the same method with different instrumentation and different operators. For this reason, a reasonable estimate of s_{R0} is 1 dB. The standard deviation s_{ome} was estimated considering a slight variation with time and properly defined measurement procedure (Note in paragraph 9.2 of the Standard). For this reason, a reasonable estimate of s_{ome} is 0.5 dB.

This leads to a total standard deviation value s_{tot} = 1.12 dB.

4.2.4. Noise measurement results

The first results, showing that the helical pump is quieter than the spur pump, were presented in Mazzei et al. [15]. In the following section, a comparison between the reference pump and its optimized prototype is given for each operating condition.

To evaluate the noise emission of the different pump types, an average sound pressure level SPL_{av} was taken between the two units, the two runs and the five measurement points.

Figure 4.6 shows the difference between the average SPL of the reference pump ($SPL_{av\text{-}REF}$) and the optimized pump ($SPL_{av\text{-}PROTO}$) for each operating condition. Positive differences indicate that the reference pump is noisier than the optimized one; negative differences show the opposite.

The shaded area indicates the uncertainty interval associated with these differences (± 1.58 dB), which is calculated following the propagation of the errors, with equation (4.2), assuming to have independent variables and assuming that the uncertainty of each quantity is quantified in terms of the total standard deviation value s_{tot}. For the results inside the shaded area, no indications can be deduced.

$$\delta SPL_{diff} = \sqrt{{\delta SPL_{REF}}^2 + {\delta SPL_{PROTO}}^2} \tag{4.2}$$

The graph in Figure 4.6 shows that the improvements occur from 1500 rev/min upwards, while below this rotational speed the differences are within the measurement uncertainty. In particular:

- Both at 1500 and 1800 rpm, the PROTO pump is less noisy than the REF pump at medium-high pressures. For 1500 rpm, the differences range between 2 and 3 dB (2.6 dB at 150 bar, 3.1 at 200 bar, and 2.5 dB at 240 bar), while for 1800 rpm, the differences are even higher (5.4 dB at 150 bar, 5.0 at 200 bar and 3.8 dB at 240

bar). The operating point on which the optimization was based (1500 rpm and 200 bar) presents good results.

- At 2000 rpm, the trend changes, and the differences are similar to those at 1500 rpm, in the range of 2-3 dB.
- At the maximum rotation speed (2200 rpm), the improvement appears increasingly apparent, especially at high pressures with differences of SPL up to almost 11 dB (6.7 dB at 150 bar, 9.2 dB at 200 bar, and 10.7 dB at 240 bar).

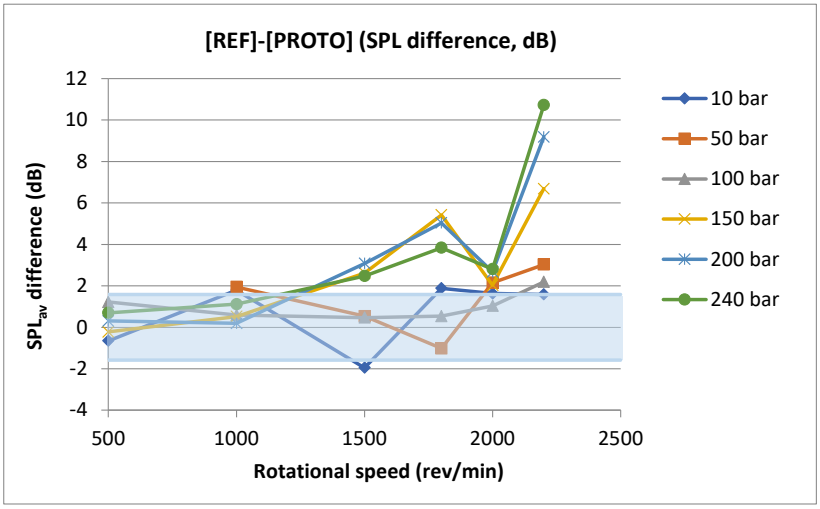

Figure 4.6. SPL_{av} difference between reference and optimized pumps for all the operating conditions

5. CONCLUSIONS

In this article, a novel numerical methodology for optimizing the noise and vibration emission of both spur and helical gear pumps was described. This methodology is based on lumped parameters approach and was implemented in a multi-environmental tool called EgeMATor MP+. This tool was developed entirely and validated by the authors; it consisted of tightly interconnected subroutines that worked in a closed-loop procedure.

The optimization subroutine was based on optimizing the design of the pressure relief grooves on the wear plates with the objective of finding the optimal design that reduces the pressure spikes, the flow ripple fluctuations, and the backflow during the meshing of the gears. The proposed methodology was employed to study and then optimize a reference helical gear pump. The optimization procedure determined a new asymmetric design that was first analyzed through the numerical tool, showing promising performances regarding noise and vibration emission reduction. The tool has been completely developed by the authors and demonstrated to be valid for optimizing EGPs. After prototyping the optimized design, an experimental campaign was organized in collaboration with the CNR-STEMS using a test rig physically isolating the tested pump from the prime mover. The results show that the proposed optimized pump has lower SPLs at 1500, 1800, and 2200 rpm with a

maximum reduction of almost 11 dB at higher rotational pump speed and pressure. This validates the methodology proposed. However, due to the complexity of the subject, specific tests and combined noise-vibration frequency analyses would be necessary to understand the reasons why, in certain conditions, there is a higher noise emission.

This will be investigated in a different specific study. Future work will also focus on further improving the optimization feature, implementing more complex pressure relief grooves designs and parametrization and target functions.

6. NOMENCLATURE

ACRONYM	DESCRIPTION
EGP	External Gear Pump
CFD	Computational Fluid Dynamic
EGM	External Gear Machine
SPL	Sound Pressure Level
SPL_{av}	Average sound pressure level

SYMBOL	DESCRIPTION	UNIT
A	Area of displacement chamber	[m^2]
A_g	Cross-sectional area of groove	[m^2]
B	Axial length of the gears	[m]
d_1	Delivery Groove reference distance	[-]
d_2	Suction Groove reference distance	[-]
h	Suction Groove height	[-]
m	Gear module	[m]
P	Pressure	[Pa]
p'	Non-dimensional pressure	[-]
Q_{ref}	Reference flow rate	[L/min]
s_{omc}	Standard deviation due to the noise emission instability of the source	
s_{R0}	Standard deviation of reproducibility	
s_{tot}	Total standard deviation	
W	Delivery Groove width	[-]
Z	Axial extension of the slices	[m]
z_1	Axial start position for the reference profile	[m]
z_2	Axial finish position for the reference profile	[m]

GREEK LETTER	DESCRIPTION	UNIT
B	Total helix rotation angle	[rad]
φ	Gear profile rotation angle	[rad]
φ_1	Axial profile angle start position for the reference profile	[rad]
φ_2	Axial profile angle finish position for the reference profile	[rad]
$\varphi_{DC\ MIN}$	Gear profile rotation angle of instantaneous commutation (minimum chamber volume)	[rad]
φ_{GRV}	Groove rotation angle characteristics	[rad]
$\Delta\varphi$	Angular pitch value for optimization function	[rad]

ACKNOWLEDGMENTS

The authors gratefully acknowledge the invaluable support provided by Duplomatic MS, in particular, to Simone Bulleri. The authors thanks also Pietro Mazzei.

7. REFERENCES

[1] E. Frosina, A. Senatore, M. Rigosi, “Study of a High-Pressure External Gear Pump with a Computational Fluid Dynamic Modeling Approach”, Energies, 2017, 10(8), 1113. 10.3390/en10081113

[2] A.S. Heisler, J.J. Moskwa, F.J. Fronczak, “Simulated Helical Gear Pump Analysis Using a New CFD Approach”, ASME 2009 Fluids Engineering Division Summer Meeting. Volume 1: Symposia, Parts A, B and C. Vail, Colorado, USA. August 2–6, 2009. pp. 445-455. 10.1115/FEDSM2009-78472

[3] F. Qi, S. Dhar, V. Nichani, C. Srinivasan, W. De Ming, L. Yang, B. Zhonghui, J.Y. Jinming, “A CFD study of an Electronic Hydraulic Power Steering Helical External Gear Pump: Model Development, Validation and Application”, SAE Int. J. Passeng. Cars - Mech. Syst. 9(1):346-352, 2016, 10.4271/2016-01-1376.

[4] M. Borghi, B. Zardin, E. Specchia, “External Gear Pump Volumetric Efficiency: Numerical and Experimental Analysis”, SAE Technical Papers, 2009. 10.4271/2009-01-2844.

[5] M. Battarra, E. Mucchi, “A method for variable pressure load estimation in spur and helical gear pumps”, Mechanical Systems and Signal Processing, Volumes 76–77, 2016, Pages 265-282, ISSN 0888-3270, 10.1016/j.ymssp.2016.02.020.

[6] T. Ransegnola, X. Zhao, A. Vacca, “A comparison of helical and spur external gear machines for fluid power applications: Design and optimization”, Mechanism and Machine Theory, Vol.142, 2019, 103604, ISSN 0094-114X, 10.1016/j.mechmachtheory.2019.103604.

[7] G. Marinaro, E. Frosina, A. Senatore, “A Numerical Analysis of an Innovative Flow Ripple Reduction Method for External Gear Pumps”, Energies, 2021, 14, 471. 10.3390/en14020471.

[8] P. Mazzei, E. Frosina, S. Bulleri, A. Senatore, “Numerical Modeling of Helical External Gear Pump Through a Lumped Parameter Approach”, 2022 IEEE GFPS Symposium, Naples, Italy 12-14 October 2022.

[9] P. Mazzei, E. Frosina, A. Senatore, 2023, Helical Gear Pump: A Comparison between a Lumped Parameter and a Computational Fluid Dynamics-Based Approaches, Fluids MPDI, 8(7).

[10] ISO/IEC Guide 98-3:2008, Uncertainty of measurement - Part 3: Guide to the expression of uncertainty in measurement (GUM:1995)

[11] ISO 3746:2010, Acoustics - Determination of sound power levels and sound energy levels of noise sources using sound pressure - Survey method using an enveloping measurement surface over a reflecting plane

[12] F. Pedrielli, E. Carletti, "Acoustical evaluation of power skiving gears for hydraulic pumps", 21st International Congress on Sound and Vibration, Beijing, China (13-17 July 2014), Session SS21, pp.1-8, ISBN 978-83-62652-66-2.

[13] F. Pedrielli, E. Carletti, G. Brambilla, “ISO 9614-2 applied to an external gear pump: determination of type A uncertainty”, 26th International Congress on Sound and Vibration ICSV26, Montreal, Canada (7-11 July 2019), pp. 1-8, ISBN 978-1-9991810-0-0, ISSN 2329-3675

[14] F. Pedrielli, E. Carletti, G. Brambilla, “ISO 9614-2 applied to an external gear pump: effect of geometric measurement parameters on the uncertainty”, 28th International Congress on Sound and Vibration ICSV28, Singapore (24-28 July 2022), pp. 1-8, ISBN 978-981-18-5070-7, ISSN 2329-3675

[15] P. Mazzei, E. Carletti, F. Pedrielli, E. Frosina, P. Marani, A. Senatore, “Acoustical characterization of external gear pumps: comparison of spur and helical gears”, 29th International Congress on Sound and Vibration ICSV29, Praha (9-13 July 2023), pp. 1-8, ISBN 978-80-11-03423-8, ISSN 2329-3675

CAUSAL CONDITION MONITORING FOR AXIAL PISTON PUMPS: PREDICTION OF DIFFERENT FAULTS UNDER VARIABLE OPERATING CONDITIONS

Svenja Horn, Ahmed Shorbagy, Michael Lenz, Simon Knoll, Moritz Winter, and Prof. Jürgen Weber

Institute of Mechatronic Engineering, Technische Universität Dresden,
E-mail: svenja.horn@tu-dresden.de, fluidtronik@mailbox.tu-dresden.de

Abstract.

The paper discusses a method for a targeted condition monitoring approach on key components of an axial piston pump. Three typical types of damage to an axial piston pump – valve plate cavitation, slipper wear and axial slipper-piston clearance - are artificially generated as realistically as possible. A variety of sensors were used to collect data on efficiencies, flow rates, temperatures, and accelerations of the new and the worn pump for 100 different operating conditions. The data was processed using signal analysis techniques to understand the influence of faults on the readings from different sensors. Two different machine learning algorithms – the support vector machine (SVM) and a gradient boost algorithm (XGBoost) - were used for fault detection. Several studies have been carried out to investigate which sensor gives the best accuracy and how many features are needed. This paper presents the first step towards a transferable and scalable condition monitoring concept, which should include the causal relationship between wear and load history to enable prediction of remaining life.

Keywords. Axial piston pumps, condition monitoring, machine learning, predictive maintenance, transferability, remaining lifetime.

1. INTRODUCTION

The ability to record large amounts of operating data with minimal effort and process it with intelligent algorithms opens up new ways for fluid technology, enhancing our understanding of component and system processes. This leads to a sustainable increase in the quality of future engineering and maintenance strategies. Current preventive maintenance guidelines prescribe the replacement of components at regular intervals to prevent spontaneous failures. While this approach improves failure safety, it causes high costs for the manufacture, replacement and disposal of components, as these parts often need to be replaced long before reaching their actual service life and are also designed to be oversized.
Predictive maintenance (PM) concepts aim to eliminate these disadvantages and enable needs-based, optimal maintenance. This requires knowledge of the current and past status of each component in the system, also known as condition monitoring (CM), and relating

this to process and machine data. Classic CM evaluates the wear tendencies to predict when technical usability is no longer guaranteed. Additionally, correlating wear with load history will allow, for the first time, causal statements about the reason for failure and the predictions of the remaining life.
This paper presents the first steps towards this vision, starting with the artificial wear of three pump parts in chapter 3. It explains in detail the artificial cavitation of the valve plate, the wear of the slipper sealing land, and the axial clearance between slipper and piston. Chapter 4 provides an overview of the measurement setup, the installed sensors and the measurement procedure. It concludes with measurement results showing the impact of the faults on the efficiencies, as well as a closer examination of the signal from the triax-y accelerometer in time and frequency domain. In Chapter 5, the data-driven analysis is explained, beginning with the pre-processing of the data, providing an overview of the feature engineering, and finally presenting the results of the model evaluation.

2. STATE OF THE ART

Table 1 provides an extensive overview of the literature on condition monitoring (CM) in axial piston pump systems, aiming to categorize and summarize key findings in a structured manner. The black bars are set to a maximum value to improve the visibility of the variation in the lower range, set to 16 for the column of operating conditions for example.

The literature review is organized into the following five main categories: investigated faults, data acquisition methods, employment of machine learning (ML) and CM techniques, and a judgment on predictive maintenance (PM) status. The first column in the table denotes the references to the literature sources, providing a comprehensive list of the studies reviewed. The second column categorizes the pump types, with the main focus on Axial Piston Units (APU). The subsequent block of the table details the investigated faults, divided into the components where the faults are applied, such as valve plate, slipper, or bearing faults. The number of fault levels investigated across all fault types is also given, offering insights into the scope and depth of fault analysis conducted in the literature. The section on data acquisition methods outlines the sensors used for measurements, along with the total number of sensors employed and the number of operating conditions considered. This provides a comprehensive understanding of the data collection strategies adopted in the reviewed studies. Regarding ML methods, “class” and “value” stand for using a classification or a regression algorithm. Additionally, it indicates whether ML or deep learning (DL) techniques were utilized to achieve these goals. An approach is classified as DL if it does not require separate feature extraction and engineering, as is often the case with various types of neural networks.

CM methods are classified into three categories: knowledge-based CM with ML/DL, functional CM integrating functional statistics of measurement data, and model-based CM incorporating digital twin concepts. This classification follows the VDI norm 2888 /Vdi99/, dividing diagnostic methods for data evaluation into functional, knowledge-based and model-based approaches, see **Figure 1**. The model-based approach is primarily used for system analyses, such as in investigations on valve-controlled drives, e.g. by /Chi04, Ise06, Kre02, Kho97, Mün06a+b, -07a+b, Raz07/ using parity equations or parameter estimates. For displacement units, the functional approach is particularly suitable, as it is based on the periodic signals of rotary machines. Such signal-based procedures are already used as

standard in the monitoring of rolling bearings, e.g., in wind turbines /Hac07, Wir04/. The knowledge-based approach mainly uses pattern recognition methods and processes input and output data with a learning algorithm without information about internal system correlations. Pure knowledge-based methods use vast amounts of field data to draw conclusions about the use and wear of a machine. The knowledge gained remains within the company and is not published. While the knowledge-based approach may provide general and imprecise estimates, robust and transferable algorithms can cope with the high variety of system and environmental influences, as demonstrated in the works of /Tor11/, /Cas19a,b/. This project aims to combine the advantages of functional methods with those of knowledge-based methods.

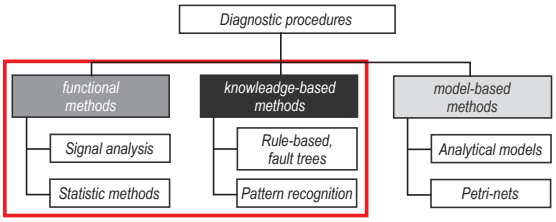

Figure 1: Classification of diagnostic procedures according to VDI standard 2888

Finally, Table 1 provides an assessment of PM status, offering an outlook on the transferability and remaining lifetime aspects of the CM approaches discussed in the literature.

Recent studies have aimed to optimize signal preprocessing by utilizing original sensor data in both time and frequency domains. They converted time series into Continuous Wavelet Transform (CWT) diagrams depicted in **Figure 2** and applied Deep Learning (DL) algorithms for analysis. Additionally, they've used Bayesian optimization to fine-tune Convolutional Neural Network (CNN) hyperparameters /Tan22, Tan24, Zhu23/.

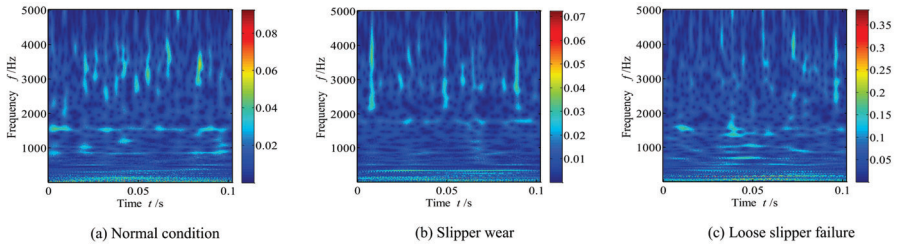

Figure 2: Continuous Wavelet Transformation (CWT) representation of vibration signal for CNN model /Tan22/

Another novel approach is the use of physics informed machine learning (PIML), which promises a better interpretation of the algorithm results. For this purpose, /Zhi23/ combines a neuronal network with the mass conservation equation in the exhaust pipe for different piston wear levels.

Table 1: Systematic literature overview of implementing CM in APUs

		Faults							Data Acquisition									ML methods		CM methods			PM	
		fault types							sensors															
source	device	valve plate	slipper	bearing	piston	cylinder	other	fault levels	vibration	acoustics	pressure	torque	efficiency	speed	flowrate	SP angle	number of sensors	number of operating conditions	goal	ML/DL methods	using ML/DL	functional CM	model based CM	transferability	remaining lifetime
/Ali16/	other							0									1	-	value	ML	●			-	-
/Ali18/	other						●	1						●	●		1	1	class	-		●		+	-
/Pau18/	APU							-									-	-	-	-				-	-
/Lu11/	APU	●	●					2	●	●						●	1	1	class	DL	●			+	-
/Gao05/	APU	●	●					2	●	●							1	1	class	-			●	-	-
/Has12/	APU	●				●		0	●				●				-	-	class	-			●	-	-
/Tor11/	APU		●	●		●		6		●	●		●			●	2	3	class	ML + DL	●	●		+	-
/Elt14/	other						●	0						●			1	0	class	-		●		+	-
/Li05/	APU				●			2				●					1	1	class	-		●		++	-
/Opp07/	APU			●				10			●					●	20	12	class	-		●		++	-
/Cas18/	APU		●	●		●		2		●	●		●			●	2	4	class	-		●		+	-
/Cas19a/	APU	●	●			●		5	●	●			●			●	2	9	class	ML	●			+	-
/Bed18/	APU	●	●			●		5	●	●			●				5	9	class	-		●		++	-
/Tan22/	APU		●				●	5		●				●		●	1	5	class	DL	●			+	-
/Kum19/	APU				●			4				●					3	3	value	-			●	-	-
/Zhu23/	APU		●				●	5		●				●		●	3	0	class	DL	●			+	-
/Cha21/	APU	●			●	●		4	●			●	●			●	9	1	class	ML	●			+	++
/Kel22/	APU	●						5	●								5	4	class	ML	●			+	-
/Don23/	APU		●			●		2		●			●				1	1	value	-			●	-	+
/He22/	APU	●	●		●		●	4	●	●		●		●		●	2	16	class	DL	●			++	+
/Tan24/	APU		●				●	5		●				●		●	3	1	class	DL	●			+	-
/Zhi23/	APU				●			4				●					1	1	class	DL	●		●	++	+
/Gne23/	APU	●	●					5	●	●						●	6	96	class	ML	●			++	-
this approach	**APU**	●	●		●			7	●	●	●	●	●	●	●	●	**24**	**120**	**value**	**ML + DL**	●			**+**	**++**

To summarise, previous investigations on displacement units have limitations, as they are restricted to one pump size and a few operating points, and no systematic investigation of the minimum sensor configuration has been carried out to date. The last row of Table 1 gives the perspective for this research: The overall aim of this project is to develop transferable and intelligent algorithms that function as reliably as possible for a holistic recording of the component condition, including load history, and the necessary minimum requirements for data generation.

This paper presents the first steps towards that perspective. It shows the development of two methods to artificially wear pump parts: one to cavitate a valve plate and another to enlarge the clearance between piston and slipper. Furthermore, it presents the analysis of the measurement data and the process steps of the implemented machine learning algorithms. Finally, it includes first results of the classification of three faults in the pump with respect to different sensor configurations and a representative set of operating conditions (OCs).

3. ARTIFICIAL WEAR OF PUMP COMPONENTS

Based on customer service data from past malfunction incidents from multiple axial piston pump manufacturers a compilation of common damage types to axial piston units has been

generated. These damages were sorted according to the following criteria: the location of damage, the damage mechanism and the intensity of the damage. From this study three different damage types were selected: damage in the slipper-piston joint, simulating a mechanical deformation damage, a cavitated valve plate surface and a mechanically damaged slipper surface. All three faults were artificially implemented into new pump parts, ensuring realistic form and location, and are presented in detail in the following chapter.

3.1. Axial slipper-piston clearance

For simulating a damaged slipper-piston joint, augmented joint clearance was induced by axial tensioning on a Schenck PE 40L hydraulic tensile testing machine up to a suitable amount of plastic deformation of the slipper brass material.

In order to estimate the necessary axial force, a finite element analysis (FEA) of the process was performed, employing bilinear isotropic hardening models to account for material plasticity of the slipper and piston, with values for yield strength and the tangent modulus derived from material supplier certificates. **Figure 3 a)** shows the resulting equivalent plastic strain resulting at a remaining clearance of 2 mm, which was set in the analysis to obtain an upper bound for the tensile force. It is visible that plastification occurs solely in the much softer slipper material. The picture also shows the specially designed fixture that mounts the piston and slipper to the tensile machine without damaging functional surfaces, allowing for the application of a controlled displacement u. The polymer disc was introduced in the actual experimental setup to provide a bump stop when measuring clearance. Figure 3 b) shows the experimental setup of the hydraulic tensile testing machine.

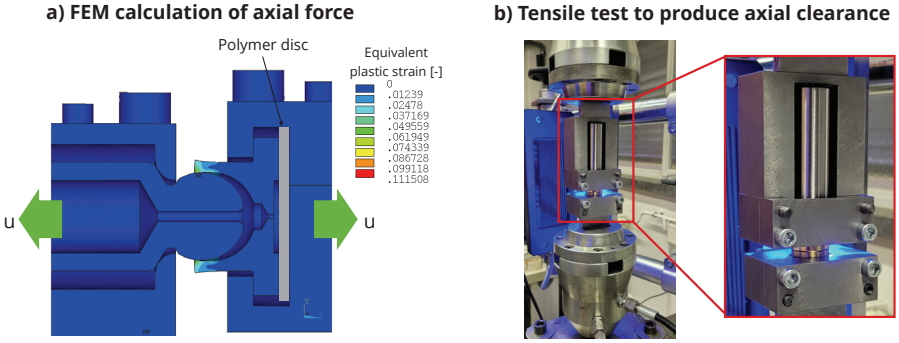

Figure 3: Simulation (left) and laboratory (right) setup for piston joint stretching

In a first run, an incremental step test of a slipper-piston assembly was performed, applying axial displacements of increasing magnitude to correlate the reaction force with the resulting permanent clearance, see **Figure 4 a)** and **b)**. In this context, measured clearance was defined as the axial deformation of the joint between -0.1 and 0.1 kN axial force.

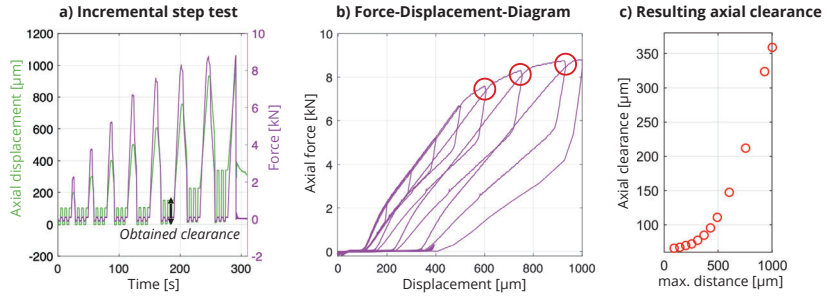

Figure 4: Incremental step cyclic loading of piston joint (left), force-displacement-diagram (middle) and obtained axial clearances (right)

A clearance of 180 µm was chosen to apply to the piston slipper assemblies, drawn from investigations of /Gne23/, in Figure 5 b). It was found that when subjecting new pistons to the force treatment, the resulting clearance did only roughly correspond to the function in Figure 4 b) and additional displacement had to be applied iteratively in order to achieve the desired clearance. At the same time, the reaction force after achieving the desired clearance was in the range of 10 to 11 kN, in contrast to the predicted 8 kN. Meanwhile, Figure 4 b) shows how during the cyclic run, the force appears to almost cap out below 9 kN for high deformation, approaching ideal plastic flow behaviour of the material. It is plausible that during cyclic loading and unloading the frictional contact attains a different configuration as compared to a straight loading ramp. Furthermore, material damage induced in the material during cyclic plastification is suspected. The marked regions in the diagram, where the axial force upon reloading does not reach the same value as during initial loading, point to either or a combination of these effects. A proper clarification will require further investigation and testing. The joint clearances obtained for ten pistons are depicted in **Figure 5 a).** A mean value of 179 µm was achieved, with a standard deviation of 7 µm. This compares to an initial mean clearance of 48 µm with a standard deviation of 11 µm. For the pump measurement, the outlier piston number 4 was discarded and the other nine were mounted, with an average clearance of 177 µm and a standard deviation of 3 µm. Figure 5 b) compares these values with those measured and reported in /Gne23/.

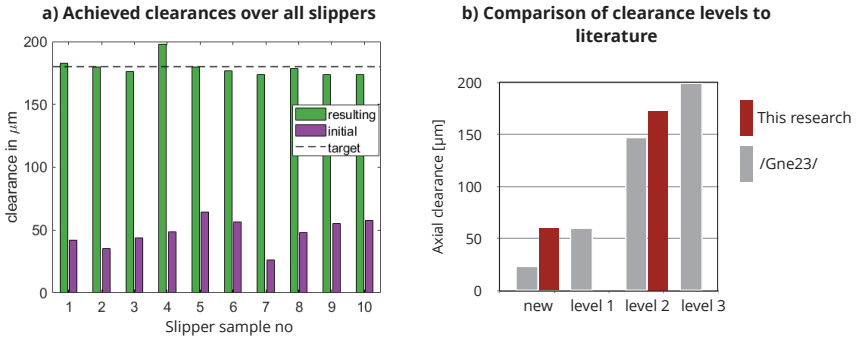

Figure 5: Obtained and initial values of axial clearance (left) and comparison to literature /Gne23/ (right)

3.2. Cavitated valve plate

Cavitation erosion damage on the surface of the valve plate is a very common damage especially in open-circuit pumps. In the case of a large damaged area on the valve plate, not only the volumetric efficiency is being affected, but also the pressure distribution over the entire surface of the valve plate, which leads to a change in the micro-motion of the cylinder block /Sho18/.

A computational fluid dynamics (CFD) model enables the localization of the cavitation erosion damage on the valve plate surface. The model predicts cavitation in the transition region between the high and low pressure kidneys of the valve plate. These locations were validated by deliberately inducing cavitation on the test rig after completion of the entire operating point grid. This was done by running the pump for at least 50 minutes at a speed of 2400 rpm, below its self-priming speed, and at a suction pressure of 0.9 bar absolute (the manufacturer's specification is 2300 rpm at 1.0 bar absolute to avoid cavitation). Good agreement was achieved between the predicted and the actual cavitation erosion damage locations.

After locating the cavitation erosion damage, different levels of damage were measured on several example valve plates from the field with a mean depth between 50 µm to 300 µm. Based on this study, three different damage levels are manufactured on three different valve plates. The manufacturing process is depicted in **Figure 6**. A mould with the location and shape of the fault was made. The mould was fixed to the surface of the valve plate to protect the surrounding areas. Using a high frequency sonotrode, the cavitation erosion damage was applied to the surface of the valve plate at three different intensities, see Figure 6 a). The surface measurement results qualify an excellent damage pattern corresponding to a real cavitation damage, compare Figure 6 b). In order to quantify the damage intensity of each valve plate, an optical surface measurement was performed. The surface measurement showed a clear correlation between the damage intensity and the volume removal of each valve plate, which is presented in Figure 6 c). Increasing damage intensity is associated with a rising volume removal.

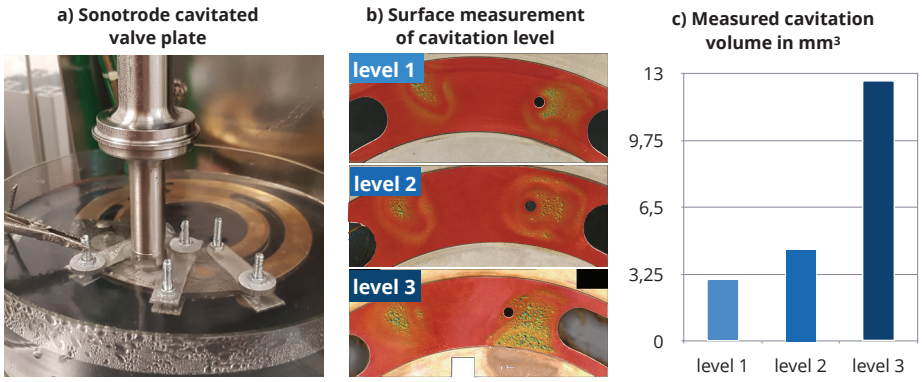

Figure 6: Artificial cavitation erosion damage on the valve plate surface

3.3. Worn slipper sealing land

A worn slipper sealing land produces an elevated leakage that decreases the volumetric efficiency. If the scratches of micro particles in the oil are deep enough, the entire hydrodynamic behaviour and the micro-motion of the slipper can be altered. This can lead to the destruction of the lubricating film between the slipper and the swash plate, resulting in increased friction and wear of the slipper /Iva20, 22/.

This fault was implemented manually using a filing tool. The target location, scratch shape and damage intensities were determined by analysing multiple worn slippers from different manufacturers. Filing was performed iteratively, with control of the achieved damage level by profilometer measurements. The result of an example surface scan is shown in **Figure 7**.

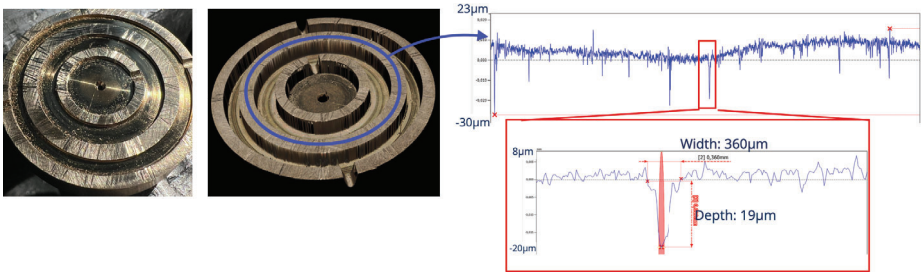

Figure 7: Artificial wear of slipper sealing land

4. EXPERIMENTAL

This section provides an overview and a detailed exploration of the test rig configuration, the sensors selected and positioned for data acquisition, followed by a description of the measurement procedure. The performance losses of the pump that can be attributed to the different faults are presented for several sensor data. For the triaxial accelerometer, the signal over one revolution in the time domain and the frequency spectrum are shown as example.

4.1. Test-Rig

A standard test rig setup capable of measuring pump characteristics was extended and modified. The upgraded version of the test rig used to perform the measurements was equipped with multiple sensors to capture high frequency pressure and acceleration signals. **Figure 8** shows a schematic of the hydraulic circuit of the test rig used.

This set-up of the test rig includes a suction pressure control to prime the specimen. A suction pressure of 1.8 bar was set to ensure that cavitation is avoided over the entire operating range. The implemented temperature control system helps to maintain a defined, consistent oil viscosity. The return flow is cooled by a heat exchanger and, if required, the oil in the tank can be heated by two electric heating cartridges. A coupling connects the pump to a variable speed electric motor with a maximum power rating of 270 kW. A torque transducer is also installed to measure the mechanical performance of the pump. Pressure and temperature sensors were strategically placed near the pump to facilitate accurate measurement and control of the desired operating conditions.

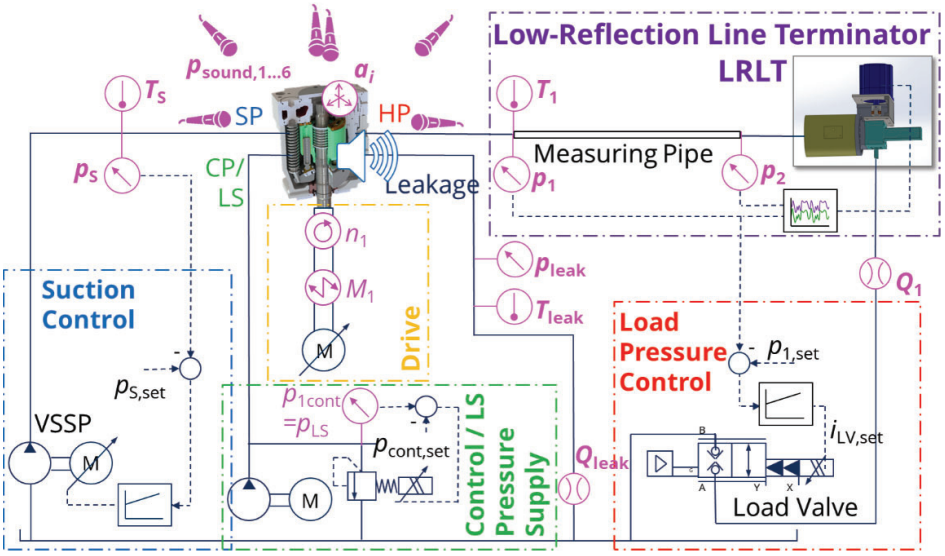

Figure 8: Hydraulic circuit of the pump test rig

A variety of high and low frequency sensors were used to monitor and record key parameters required for experimental analysis. **Figure 9** gives an overview of the installed sensors and their sampling frequency. The sensors were positioned to ensure accurate and reliable data acquisition. The pressure is recorded at high (HF) and low (LF) sampling rates. The sampling rate used for the evaluation for all high frequency sensors was 16.4 kHz.

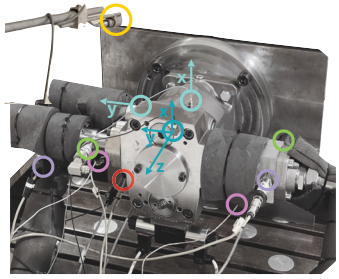

	Sensor	Sampling Frequency [kHz]	Location
	Acceleration Sensor	8	Pump casing, triaxial
	Acceleration Sensor	8	Pump casing, single Axis
	Pressure Sensor (HF)	25	Delivery & suction
	Pressure Sensor (LF)	1.2	Delivery, suction & leakage
	Temperature Sensor	0.3	Delivery, suction & eakage
	LVDT	16	Swash plate
	Microphones	50	According to DIN 45635

Figure 9: Overview on the installed sensors

4.2. Measurement Procedure

The pump measurements were carried out under different operating conditions using all available sensors. The measurements covered the entire operating range of the pump. In total, six pressure levels and four stroke angles were measured at four different speeds, resulting in 96 operating conditions. **Table 2** shows the reduced set of 28 OCs, that presents a representative selection to build and test the models. The findings of this paper are confined to the representative set, as a more sophisticated method, currently under development, is

being employed to reduce the features for the entire dataset due to the extensive number of features.

Table 2: Overview of representative set of 28 operating conditions (OCs)

100 %		75 %		50 %		25 %	
n [rpm]	Δp [bar]	n [rpm]	Δp [bar]	n [rpm]	Δp [bar]	n [rpm]	Δp [bar]
500	200	500	150	500	50	500	100
1000	100	500	250	1000	150	500	250
1000	250	1000	50	1000	300	500	300
1500	150	1000	200	1500	50	1000	150
1500	200	1500	100	1500	250	1500	50
2000	50	1500	300	2000	100	2000	200
2000	300	2000	150	2000	200	2000	250

In order to achieve a semi-equilibrium condition, a standby period of at least two minutes was allowed after setting up each operating point. The measurement period was chosen to be 10 seconds, which should be sufficient to capture several periodic motion cycles for each speed level. To maintain a constant oil viscosity and similar thermal conditions in the pump, the inlet temperature was regulated to 40°C+/-3°C for all measured operating conditions.

/Don23/ has shown that the flow pulsation changes due to faults, but is dependent on the pipeline length and therefore less transferable to other systems. In general, pressure pulsations emanating from a pump in a hydraulic system are influenced by reflections within the interconnected pipeline network. In the presented setup, a low reflection line terminator (LRLT) is used, which for each operating condition is steered to mimic the impedance of a pipeline of infinite length, thereby eliminating pressure pulsation reflections of the downstream hydraulic circuit. The LRLT guarantees that any change in pressure pulsations is attributed to the artificially added damage. This should ensure a robust transferability of the developed algorithm concerning the high pressure pulsation signal.

Initially, a reference measurement was conducted under healthy conditions without any damaged parts. This data serves as a baseline for comparison with subsequent measurements involving damaged parts. Each defect was measured separately, without combining multiple defects.

4.3. Performance Losses of the Pump due to worn components

This paragraph investigates the influence of wear on various performance parameters, including efficiencies, temperatures, and leakage, across the entire operating range. Mean values under different operating conditions are compared and depicted in Figure 10. The x-axis represents the operating conditions, sorted by increasing pressure blocks, each consisting of rising speed values.

Valve plate cavitation exhibits the lowest volumetric efficiency across all OCs. Since it does not have the lowest measured leakage, it can be assumed that internal leakage is also increased by valve plate cavitation, reducing the outlet volume flow. Simultaneously, valve plate cavitation shows the highest hydromechanical efficiencies. It is evident and physically expected that increased leakage occurs for all three types of wear. Slipper wear, in particular, negatively impacts friction losses, as indicated by lower hydromechanical efficiencies. This study provides insights into the relationship between wear-induced changes and hydraulic system performance, offering valuable information for predictive modelling and optimization strategies.

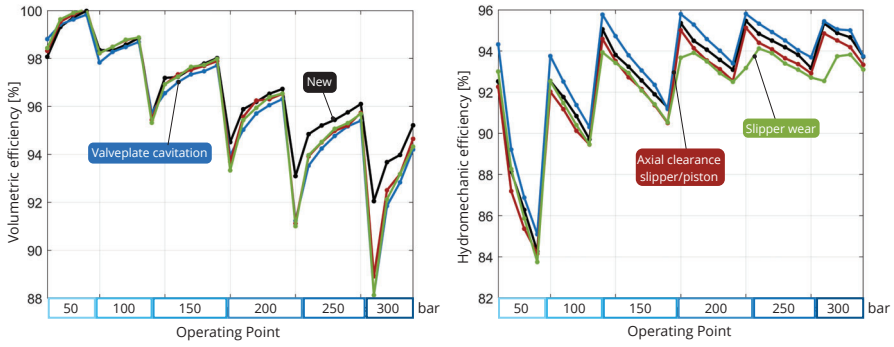

Figure 10: Influence of the faults on the volumetric and hydromechanic efficiencies over a broad operating range with rising speed for each pressure block

To understand the impact of the faults on different sensor signals, the data was evaluated in both the time and frequency domains. **Figure 11** exemplifies the accelerations of the triaxial-Y sensor over one revolution (left) and the corresponding FFT spectrum over 10 pump orders (right) for 500 rpm, 300 bar and 100 %.

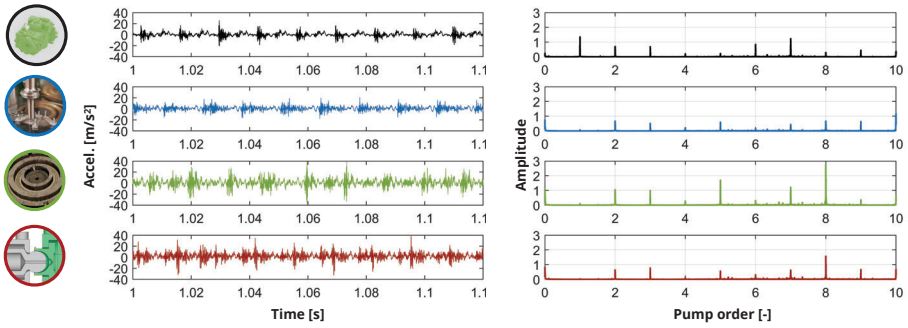

Figure 11: Accelerations over one revolution (left) and FFT (right) signal of the triaxial-Y sensor for 500 rpm, 300 bar and 100 %

While the new pump (first row in black) exhibits a dominant first pump harmonic resulting from the nine pulsating pistons, this harmonic is absent in the faulty signals. However, this observation is not consistent across all measurements; compare the results at 2000 rpm, 200 bar and 50 % in Appendix A, which display a completely different frequency spectrum.

In the time domain, higher amplitudes are observed for the slipper wear and the slipper-piston clearance fault, which is similar to the results in Appendix A. These examples illustrate the challenges of manual feature extraction and suggest the use of a powerful extraction tool like the TSFresh algorithm, which is used further in Chapter 5.

5. DATA-DRIVEN ANALYSIS

Figure 12 provides an overview of the individual steps for implementing ML algorithms. While all details about the data acquisition are described in chapter 4, the pre-processing of the data, the feature engineering and the model evaluation are explained in the next sections.

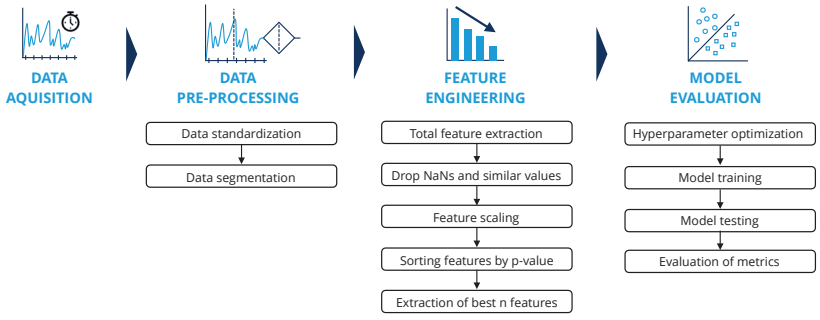

Figure 12: Methodical approach and individual steps for implementing ML algorithms

5.1. Pre-processing of the measurement data

The first step of data pre-processing involves formatting the measurement data into structures and file types that are accessible by the python-based algorithm. This includes segmenting the data and recombining it into new tables. In the rotary environment of an axial piston pump, effects of wear mostly appear cyclostationary, occurring with each revolution of the cylinder block or each piston (in this case nine times per revolution). Hence, the characteristic segment length depends on the speed of the pump. Longer time segments contain more precise information about repeating patterns or non-random anomalies. At the same time, to provide more information for training the algorithm, it is better to have as many segments as possible. The characteristic time segment length is chosen as twice the length of the inverted characteristic fault frequency, in which patterns and anomalies occur. It is calculated by equation 5.1, using the nominal speed of each OC $n_{OC,\mathrm{nominal}}$.

$$\Delta t_{\mathrm{seg}} = \frac{2 * 60 \frac{s}{min}}{n_{OC,\mathrm{nominal}}} \tag{5.1}$$

To ensure that all OCs are weighted equally, the number of time segments is set to 80. Unfortunately, the measurements at 500 rpm only contain 40 segments and are therefore slightly under-represented. Different sensors record different measurement ranges that may distort the calculation of the features. It is therefore common practice to standardise the raw data, carried out with the StandardScaler from the scikit-learn library centralizing the data around zero.

5.2. Feature extraction and evaluation

TSFresh is used to extract features from the time series /Chr18/. To ensure equal weighting of all features, a transformation into a common space is performed with the StandardScaler. Depending on the number of operating conditions and sensors, several hundred to thousands of features are calculated. For the vision of an onboard sensor system with microelectronics, minimizing the number of features is advantageous in terms of hardware requirements and computing time. Additionally, a balance needs to be found between fewer features for better generalization and more features for higher model accuracy.

The p-value is used to calculate the significance of each feature. Low p-values indicate a high importance of features for recognizing wear types by rejecting the null hypothesis. Furthermore, the significance of these features is evaluated using the Benjamini-Hochberg procedure /Ben95/. The procedure excludes irrelevant features from the analysis. The retained features in the relevance table are sorted by increasing p-value. **Figure 13** shows the best p-valued features for sets of [20, 50, 100, 200] features sorted by high and low frequency sensors for a set of 28 OCs, refer to Table 2. Over all feature sets, the high pressure sensor and the triaxial acceleration sensor contain the most important information, latter particularly in x and y directions. For higher numbers of features, sensors sampled at low frequencies also contain relevant information.

It should be noted that the p-value only provides a local correlation of *one* feature to the wear prediction and therefore allows only a rough estimate of its importance. The final accuracies of different feature sets can deviate from this, as they take into account the global relationships between many features and their interactions. Thus, features with lower p-values might not always result in the highest model accuracy when considered within the context of other features.

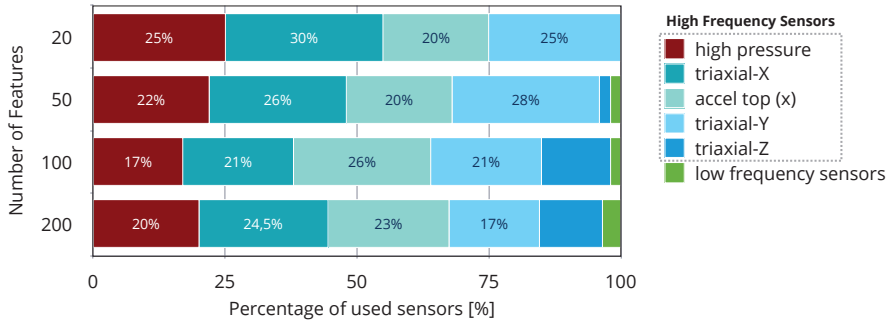

Figure 13: Best p-valued features for sets of [20, 50, 100, 200] features sorted by sensors

5.3. Model evaluation for fault detection

Many different algorithms for classifying features have been extensively developed, tested, and compared in the literature. Generally, a decision must be made whether to select a deep learning or a machine learning algorithm. Deep learning algorithms are excellent for large datasets, making them particularly advantageous for field data. They are complex to develop and can manage diverse types of data, unlike the simpler datasets examined in this study.

For this study, the two machine-learning algorithms, Support Vector Machine (SVM) and XGBoost, were chosen due to their power and robustness, while being relatively simple to implement and interpret. Both are supervised learning algorithms capable of wear type *classification* and wear depth *regression,* latter will be further investigated for valve plate cavitation levels.

SVM works by finding the hyperplane that best separates data points into different classes or predicts continuous outcomes. It aims to maximize the margin between classes, allowing for robust generalization to unseen data. By transforming input data into higher-dimensional feature spaces, SVM can effectively handle nonlinear relationships between variables. Additionally, SVM has regularization parameters that help prevent overfitting, making it suitable for datasets with high dimensionality and small sample sizes which is perfectly fitting to the data of this paper. SVM is popular in various machine learning applications and has been successfully applied to similar problems for the detection of faulty pumps parts (f.e. /Tor11, Cas19, Cha21/). XGBoost is a highly efficient and flexible implementation of gradient boosting. It builds an ensemble of decision trees sequentially, where each tree corrects the errors of the previous one, leading to highly accurate models. One of the key advantages of XGBoost is its robustness against overfitting, achieved through techniques such as regularization and shrinkage. Additionally, XGBoost is known for its scalability and speed, handling large-scale data efficiently.

For the hyperparameter optimization the optuna library is used. It is based on a bayesian optimization algorithm called “Tree-structured Parzen Estimator”. The hyperparameter optimization is performed on the total feature set of all sensors for the representative 28 OCs. The hyperparameters are used for all further accuracy calculations. A test of a further hyperparameter optimization for the 700 features of the high pressure sensor did not achieve any significant improvements in accuracy.

It is assumed that during one OC the features in the measurement data are very similar. If models are both trained and evaluated on the basis of this very similar data of the same set of OCs, overfitting to the given data cannot be ruled out. To prevent overfitting, the “GroupKFold” cross-validation strategy is therefore used. It ensures that the features from one OC occur either in the training or in the test data set, but not in both data sets at the same time. The data is split into training and test data with a typical amount of twenty percent proportion of test data using ten folds. To investigate the generalization of the results, the folds containing a different set of training and test data are calculated along with the corresponding accuracy results.

Figure 14 (left) provides a boxplot of the mean accuracies and their dispersion of different sensors, with a limitation of 700 features for both estimators, SVC and XGBC. Using all components of the triaxial acceleration sensor results in perfect fault prediction for the limited amount of test data. When examining the individual components (x, y and z), the data from the y-component of the triaxial sensor provides very high accuracy, also compared to the uniaxial acceleration sensors and the high-pressure sensor. The reason for those differences are not yet conclusively determined. One possible explanation, regarding the valve plate cavitation, is that cavitation influences the pressure build-up in the piston, thereby affecting the forces and torques on block and valve plate. Due to the torque

characteristics, this pump experiences significant torque fluctuations around the y-axis, which could be altered by the faults. Further investigations are pending.

The right plot in **Figure 14** shows the accuracy of the triaxial-Y sensor depending on the number of features. The SVC model already provides very high accuracies over 95 % for feature sets with more than 10 features, while the XGBC model achieves similarly high accuracy with more than 20 features.

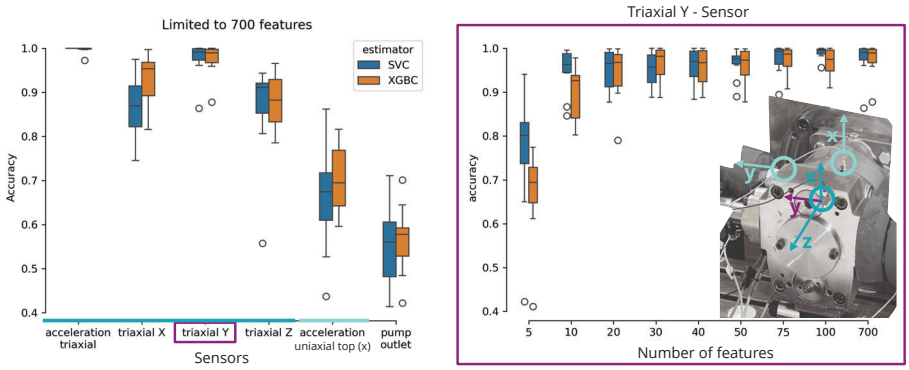

Figure 14: Accuracy results for different sensors with a total of 700 features (left) and accuracy results for different numbers of features of the triaxial-Y sensor (right)

The learning curves of both, the entire set of all features and sensors as well as the reduced set of 20 features of the triaxial-Y sensor are provided in appendix B showing that both models are not overfitted and well generalised.

6. SUMMARY AND OUTLOOK

This paper explains in detail how targeted and realistic artificial wear is applied to the valve plate, the slipper surface and the slipper-piston joint of an axial piston pump. With a sonotrode, cavitation has been applied to the valve plate surface in the area of the transition between low and high pressure. Axial clearance between slipper and piston of precisely defined values has been induced on a tensile test machine. A typical wear pattern was added to the slipper surface by filing.

Pump measurements have been conducted over a wide range of 96 operating conditions for each fault with a minimum of two repetitions. Results indicated that all faults resulted in higher leakage values and thus reduced volumetric efficiency. Notably, as valve plate cavitation progressed, volumetric efficiency decreased while hydromechanical efficiency increased, complicating system-side fault detection based on performance losses.

Feature extraction evaluation of a representative set of operating conditions (OCs) highlighted that the high-pressure sensor and accelerometers captured the most crucial information about the pump's condition. Further investigations will vary the set of OCs. The features are trained and tested with two algorithms, the SVC and the XGBoost, resulting in excellent accuracies of almost 100 % for the complete dataset of all sensors. Looking at the

results of single sensors, the triaxial-Y sensor achieves the best accuracies of 95 %, already for a small number of only 20 features.

The measurements were carried out under idealised conditions with constant inlet and outlet pressures and a constant inlet temperature. Such idealised conditions are not representative of the operating environments and could mean a deterioration in the prediction accuracies. Also, assembly and manufacturing tolerances may influence the results of the fault prediction. These controlled and reproducible conditions allow the investigation of defined disturbances on the model accuracies, which is planned for further development. Nevertheless, measurements on real machines in the field, collecting a large amount of data are necessary for a more general and robust model.

Regarding data segmentation across different OCs, low-speed conditions may be underrepresented due to their longer time periods per revolution, leading to fewer measurement segments compared to higher speed OCs. Future studies should select the same number of segments regardless of speed, increasing the measurement duration for low speeds to ensure a sufficient number of segments.

Further investigations include downsampling the sensor data within an optimization study to reduce sensor quantity and quality while determining the minimum sensor configuration and quality requirements necessary for maximum wear detection predictability. Measurements at different temperatures will provide more insights into data generalizability. The entire set of OCs will be analyzed, examining different subsets and their influence on prediction accuracy by various sensors.

The research aims to quantify multiple wear levels and types to achieve a comprehensive understanding of the degradation process in displacement units. Additionally, it will assess the transferability of developed monitoring techniques to other pumps of different sizes and manufacturers, ensuring broad industrial applicability. By addressing these objectives, this research aims to enhance the development of robust and adaptable condition monitoring strategies for displacement units, ultimately improving the reliability, efficiency, and lifespan of pump systems in industrial applications.

ACKNOWLEDGEMENT

The presented research activities are part of the project “Causal Condition Monitoring von Verdrängereinheiten durch Verschleiß- und Schadensdetektion in Korrelation zur Betriebs- und Lastsituation” (Ref. No. 22012 BR/1). The authors would like to thank the Fluid Power Research Fund of the VDMA for the funding and support.

Furthermore, a special thanks is given to Dr. Sven Werdin and the Institute of Solid Mechanics, TU Dresden, for facilitating machinery and guidance for the tensile test.

AUTHOR CONTRIBUTIONS

S.H. developed and organized the project concept. As the main author of the manuscript, S.H. was responsible for generating ideas and creating most of the figures and content. A.S. and M.L. conducted the investigation and implementation of the damaged pump parts. They were responsible for the setup and execution of the measurements and authored Chapter 3

and 4 of the manuscript. S.K. was responsible for feature analysis, hyperparameter optimization, model creation, training, and testing of the models. He also generated relevant figures. M.W. handled the data pre-processing using Matlab. J.W. was responsible for funding acquisition and supervision of the project. He provided critical revisions and valuable insights throughout the project.

APPENDIX A

Looking at the vibration levels of the three axes of the triaxial accelerometer over the entire operating range of the pump in **Figure 15**, it is clearly visible that the differences between the faults and the reference are more pronounced for the y and z direction. The trends suggest building two models, with one model exclusively classifying healthy from faulty and the second model identifying the fault. Different metrics could then also be used to evaluate the results and, for example, false-positive predictions could be penalized.

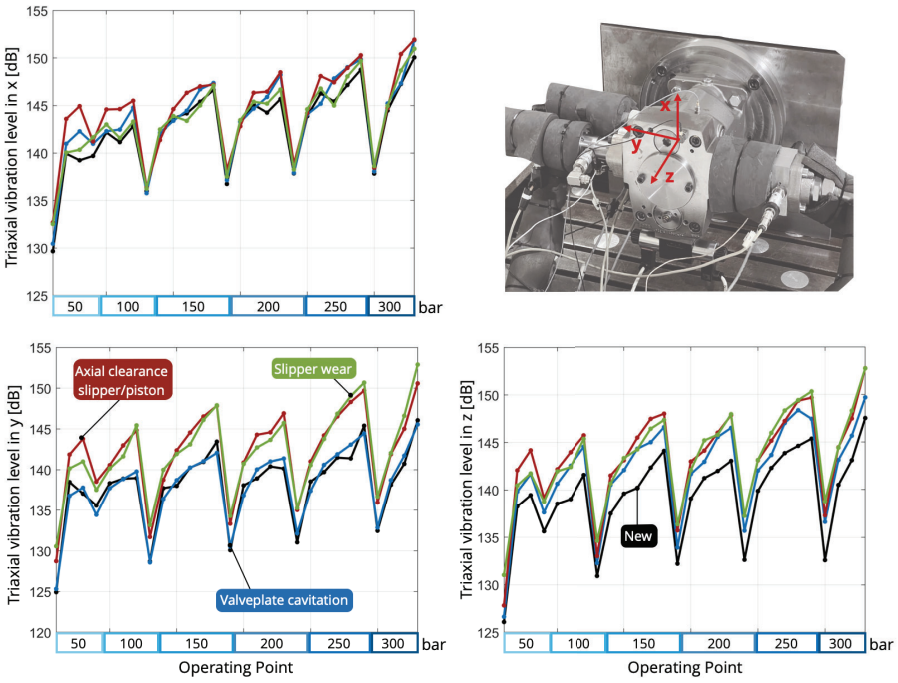

Figure 15: Influence of different faults on the three axes of the triaxial accelerometer

Figure 16 presents another example of signal analysis from the triaxial-Y accelerometer at 2000 rpm, 200 bar and 50 %. Notably, this sensor exhibits higher vibration levels for both slipper wear and axial clearance, consistent across all operating conditions shown in **Figure 15** and as previously observed in **Figure 11**. In the FFT spectrum, the pump order 8 stands out with a value of 27.7, more than three times higher than any other frequency.

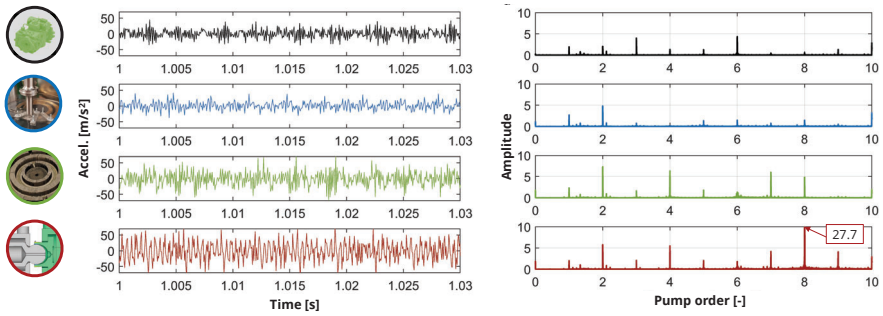

Figure 16: Accelerations over one revolution (left) and FFT (right) signal of the triaxial-Y sensor for 2000 rpm, 200 bar and 50 %

APPENDIX B

The learning curves of the support vector (SVC) and the XGBoost Classifier (XGBC) are depicted in **Figure 17** and **Figure 18**. In **Figure 17**, all of the several thousand features of all sensors are trained. Since the training and cross-validation accuracies are very close to each other and both values are very high, there is not much difference between the performance on the training data and the performance on the validation data. This indicates that the model is probably not overfitted but well generalised.

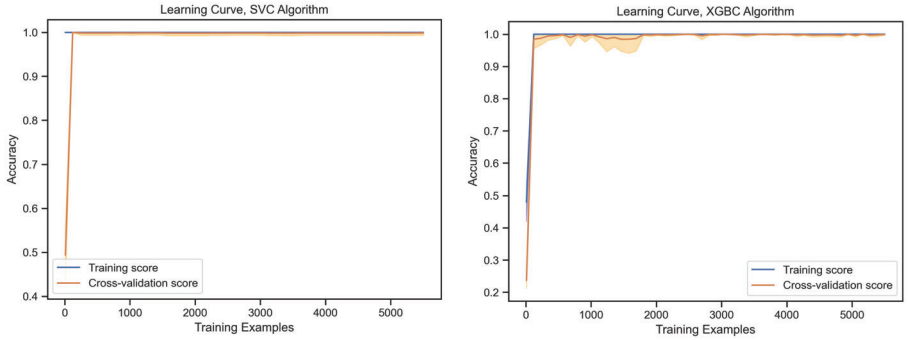

Figure 17: Learning curves of the SVC (left) and the XGBC (right) algorithm for the entire feature set of several thousand features of all sensors

Figure 18 shows the learning curve for the triaxial-Y acceleration sensor and a reduced feature set of the best p-valued 20 features each for one exemplary fold of the ten folds of the cross-validation. Reducing the number of features to 20 reduces the complexity of the model. This may result in the model being less able to fully learn the training data, but at the same time improve the ability to generalise to new data.

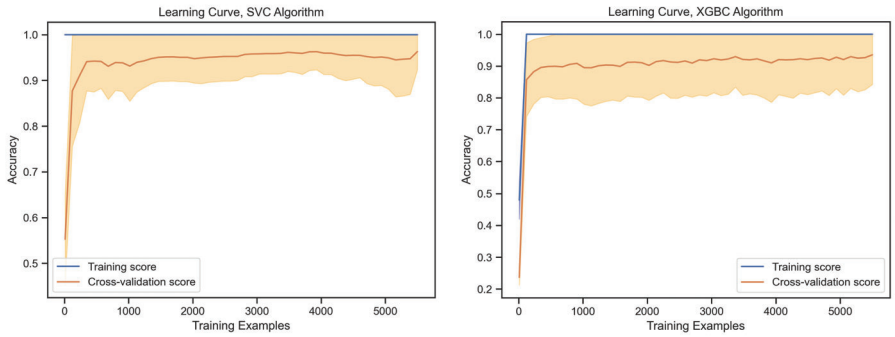

Figure 18: Learning curves of the SVC (left) and the XGBC (right) algorithm for the triaxial-Y acceleration sensor and a reduced feature set of the best p-valued 20 features

REFERENCES

/Ali16/ E. Ali, J. Weber, M. Wahler
A Machine Learning Approach for Tracking the Torque Losses in Internal Gear Pump - AC Motor Units, 10th International Fluid Power Conference, pp. 121–134, 2016.

/Ali18/ Emad Ali
Condition Monitoring of Wear Progress in Hydrostatic Pumps, International Journal of Trend in Scientific Research and Development, vol. 2, no. 6, pp. 139–142, 2018.

/Bed18/ A. Bedotti, M. Pastori, A. Lettini, P. Casoli
Condition Monitoring Based on Thermodynamic Efficiency Method for an Axial Piston Pump, Bath/ASME 2018 Symposium on Fluid Power & Motion Control, p. V001T01A004, 2018

/Ben95/ Y. Benjamini, Y. Hochberg
Controlling the False Discovery Rate: A Practical and Powerful Approach to Multiple Testing, Journal of the Royal Statistical Society: Series B (Methodological), Volume 57, Issue 1, Pages 289–300, Tel Aviv, 1995, https://doi.org/10.1111/j.2517-6161.1995.tb02031.x

/Cas18/ P. Casoli, A. Bedotti, F. Campanini, M. Pastori
A Methodology Based on Cyclostationary Analysis for Fault Detection of Hydraulic Axial Piston Pumps, *Energies*, vol. 11, no. 7, p. 1874, 2018

/Cas19a/ Casoli, P.; Pastori, M.; Scolari, F.; Rundo, M.
A Vibration Signal-Based Method for Fault Piston Pumps, In: *Energies*, 2019

/Cas19b/ Casoli P, Pastori M, Scolari F
A multi-fault diagnostic method based on acceleration signal for a hydraulic axial piston pump, AIP Conference Proceedings 2191, 020037 2019

/Cha21/ Q. Chao, Y. Shao, C. Liu, X. Yang
Health evaluation of axial piston pumps based on density weighted support vector data description, Reliability Engineering and System Safety, vol. 237, Sep. 2023

/Chi04/ Chinniah, Y.
Fault detection in the electrohydraulic actuator using extended Kalman Filter, Dissertation, University of Saskatchewan, 2004

/Chr18/ Christ, M., Braun, N., Neuffer, J., & Kempa-Liehr, A. W. (2018). Time Series FeatuRe Extraction on basis of Scalable Hypothesis tests (tsfresh – A Python package). *Neurocomputing*, *307*, 72–77. https://doi.org/10.1016/J.NEUCOM.2018.03.067

/Don23/ C. Dong, J. Tao, H. Sun, Q. Chao, C. Liu
Inverse transient analysis based calibration of surrogate pipeline model for fault simulation of axial piston pumps, Mechanical Systems and Signal Processing, vol. 205, Dec. 2023

/Elt14/ M. Eltabach
Condition monitoring of gear pumps using cyclostationarity, 9.IFK Aachen, 2014.

/Gao05/ Y. Gao, X. Kong, Q. Zhang
Wavelet Approach for Performance Monitoring and Diagnosis of a Hydraulic Pump, Proceedings of the 6th JFPS International Symposium on Fluid Power, Tsukuba, pp. 711–716, 2005.

/Gne23/ Gnepper, O., Hitzer, H., Enge-Rosenblatt, O.
Predictive Diagnosis in Axial Piston Pumps: A Study for High Frequency Condition Indicators Under Variable Operating Conditions, In: International Journal of Prognostics and Health Management, vol. 14, no. 1, 2023

/Hac07/ Hacke, B.; Reimers, E.; Hofmann, G.
Alles auf den Prüfstand – Neue Wege im Condition Monitoring, In: Antriebstechnik 12, 2007, S. 40 – 42

/Has12/ D. Hast, M. Gottfried, R. Findeisen,
A Method for the Interpretation of Parametric Faults in Model Based Condition Monitoring, vol. 45, no. 20. IFAC, 2012

/He22/ Y. He, H. Tang, Y. Ren, A. Kumar
A deep multi-signal fusion adversarial model based transfer learning and residual network for axial piston pump fault diagnosis, Elsevier B.V., Mar. 2022.

/Ise06/ Isermann, R.
Fault-diagnosis systems: an introduction from fault detection to fault tolerance, Berlin: Springer, 2006

/Iva20/ Ivantysyn, R.; Weber, J.; u.a.
Investigation of the Wear Behavior of the Slipper in an Axial Piston Pump by Means of Simulation and Measurement, 12. IFK 2020, Dresden, 2020

/Iva22/ Ivantysyn, R., Horn, S., Weber, J.
Design of a Lead-Free Slipper Bearing for Low Speed Axial Piston Pump Applications, In: IEEE GFPS 2022, 2022

/Kel22/ N. Keller, A. Sciancalepore, A. Vacca
Demonstrating a Condition Monitoring Process for Axial Piston Pumps with Damaged Valve Plates, International Journal of Fluid Power, vol. 23, no. 2, pp. 205–236, 2022

/Kho97/ Khoshzaban-Zavarehi, M.
Online condition monitoring and fault diagnosis in hydraulic system components using parameter estimation and pattern classification, Dissertation, University of British Columbia, Vancouver, 1997

/Kre02/ Kreß, R.
Robuste Fehlerdiagnoseverfahren zur Wartung und Serienabnahme elektrohydraulischer Aktuatoren, Dissertation, TU Darmstadt, 2002

/Kum19/ N. Kumar, R. Kumar, B. K. Sarkar, S. Maity
Condition monitoring of hydraulic transmission system with variable displacement axial piston pump and fixed displacement motor, in Materials Today: Proceedings, Elsevier Ltd, 2019, pp. 9758–9765.

/Li05/ Z. Li
Condition Monitoring of Axial Piston Pump, Master thesis at the University of Saskatchewan Saskatoon, no. November, p. 134, 2005, [Online]. Available: http://ecommons.usask.ca/bitstream/handle/10388/etd-11252005-202705/EricLithesis2005NovA.pdf

/Lu11/ C. Lu, N. Ma, Z. Wang
Fault detection for hydraulic pump based on chaotic parallel RBF network, EURASIP Journal on Advances in Signal Processing, pp. 1–10, 2011.

/Mün06a/ Münchhof, M.
Model-based fault management for a hydraulic servo axis, Dissertation, TU Darmstadt, 2006

/Mün06b/ Münchhof, M.
Model-based fault management for a hydraulic servo axis, In: The 5th International Fluid Power Conference (5. IFK), Bd. 3, S. 419-430, Aachen, 2006

/Mün07a/ Münchhof, M.
Fehlerdiagnose für hydraulische Servo-Achsen, In: Automatisierungstechnik, S. 96-103, 01/2007

/Mün07b/ Münchhof, M.
Modellbasierte Hydraulik-Überwachung - Übersicht über modellbasierte Verfahren zur Überwachung linearer Servo-Achsen, In: O+P Ölhydraulik & Pneumatik, S. 184-193, 04/2007

/Opp07/ M. Oppermann,
An investigation into failure prediction for mobile hydraulic systems, no. March. 2007.

/Pau18/ G. Paulmann, G. Mkadara
Condition monitoring on hydraulic pumps – lessons learnt, European Rotorcraft Forum (ERF 2017), p. 13, 2018.

/Raz07/ Razavi, B.
Condition monitoring in a hydraulic system of an industrial machine using unscented Kalman Filter, Master-Thesis, University of British Columbia, Vancouver, 2007

/Sho18/ Shorbagy A.; Ivantysyn R.; Weber J.
An experimental approach to simultaneously measure the temperature field and fluid film thickness in the cylinder block/valve plate gap of an axial piston pump. Proceedings of the 9th International Symposium On Turbulence, Heat and Mass Transfer, Rio de Janeiro, Brazil, 2018

/Tan22/ S. Tang, Y. Zhu, S. Yuan
Intelligent fault diagnosis of hydraulic piston pump based on deep learning and Bayesian optimization, ISA Transactions, vol. 129, pp. 555–563, Oct. 2022

/Tan24/ S. Tang, B. Cheong Khoo, Y. Zhu, K. Meng Lim, S. Yuan
A light deep adaptive framework toward fault diagnosis of a hydraulic piston pump, Applied Acoustics, vol. 217, Feb. 2024

/Tor11/ Torikka T.
Bewertung von Analyseverfahren zur Zustandsüberwachung einer Axialkolbenpumpe, Dissertation, Rheinisch-Westfälischen Technischen Hochschule Aachen, Fakultät für Maschinenwesen, Aachen, 2011

/Vdi99/ Verein deutscher Ingenieure
VDI 2888 1999-12, Zustandsorientierte Instandhaltung, Berlin, 1999

/Wir04/ Wirth, R.
Entwicklungstendenzen zur vollautomatischen Diagnose von Getriebeschäden, In: VDI Berichte 1826, 2004, S. 117 – 134

/Zhi23/ Z. Wang, Z. Zhou, W. Xu, C. Sun, R. Yan
Physics informed neural networks for fault severity identification of axial piston pumps, Journal of Manufacturing Systems, vol. 71, pp. 421–437, Dec. 2023

/Zhu23/ Y. Zhu, S. Tang, S. Yuan
Multiple-signal defect identification of hydraulic pump using an adaptive normalized model and S transform, Engineering Applications of Artificial Intelligence, vol. 124, Sep. 2023

Design Strategy for Noise Reducing Particle Dampers on Hydraulic Pumps

Michael Lenz, Peter Zuppke, Ahmed Shorbagy, and Prof. Jürgen Weber

Institute of Mechatronic Engineering, Technische Universität Dresden, Helmholtzstrasse 7a, 01069 Dresden, E-mail: michael.g.e.lenz@tu-dresden.de, fluidtronik@mailbox.tu-dresden.de

Abstract

Noise stands as a pivotal design criterion for displacement units, since it can limit their operability in a human environment. Particle damping promises a means of broadband mitigation of structural vibration and associated noise emissions. Cavities are introduced into the vibrating structure and partially filled with particles. Under oscillation, movement of the particles is induced, resulting in partially plastic impacts and friction, thus dissipating vibration energy. The damping effect is determined by a multitude of parameters; at the same time, simulation methods are still very limited in scope. Therefore, preliminary experimental studies are required for the targeted deduction of an integrated pump design.
To perform a flexible assessment, attachable particle damper components were designed and applied to an axial piston pump. The paper details the design process, manufacture, and the experimental setup and results of the parameter study.

Keywords. axial piston pumps, noise reduction, NVH, particle damping, FEA, experimental dynamics.

1. INTRODUCTION

Noise emission of machines is a determining factor for their acceptance with users and authorising bodies, as exposure to excessive noise causes annoyance and potential health hazards.

For hydraulic drives in particular, recent shifts in the industry are causing increased attention towards their acoustic properties. While classically hydraulic machines often had their noise masked by the louder combustion engines driving them, with electrification the hydraulic unit is often a primary cause of sound emission and vibration excitation. An ever present demand to increase power density carries with it the hazard of noise emissions increasing accordingly, while decentralized electrohydraulic drives make pump noise emission spots ubiquitous. Not only do hydraulic pumps emit significant airborne noise themselves, the transmission of their operating vibration into adjacent components through structure borne noise may cause these to emit even higher levels of noise, especially if thin walled structures such as found in vehicle bodies are affected. The attenuation of structural vibrations of

pumps and their associated sound emissions is therefore a central aspect of strategies to reduce hydraulic drive noise.

The intense vibration of displacement pumps has its origin in the periodic pressure build-up and suction processes which are inherent to their working principles. The pump drive can be optimized to reduce oil pressure pulsations and the consequential excitation of vibration, see e.g. [1], [2], [3]. However, this approach can affect pump performance and efficiency negatively, which is often not acceptable.

Active oscillation suppression either on the side of fluid [4] or structure borne noise [5] can provide substantial improvements, but may involve complex mechanisms and requires steering energy. In contrast, passive measures of structure borne noise suppression are typically achieved with rather simple components and require no energy input. The classical passive approach in machine dynamics is oscillation decoupling by resilient transmission elements. While the use of elastic hoses instead of rigid lines is a widespread application of this principle, the pump drive itself requires a high degree of rigidity for proper function. Further typical passive measures include insulation, barriers and mass-tuned dampers; however these come with the drawback of requiring significant additional installation space.

An emerging passive means of vibration attenuation is offered by particle damping. Figure 1 shows the basic setup of a particle damper, comprised of a cavity with solid walls which is filled with loose particles. The cavity may be attached to a vibrating structure as indicated in the figure, or integrated into it. When vibration is induced, its energy is partially transmitted to cause movement of the particles. This movement involves friction and partially plastic impacts of the particles with each other and the walls, upon which vibration energy is dissipated, leading to the damping effect. Damping by this method is effective over wide ranges of vibration frequency and amplitudes [6], [7], acting in arbitrary directions.

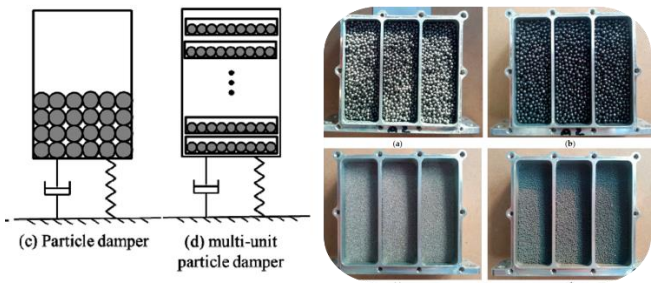

Figure 1: Principle of particle damping, from **[8]**

There is ample literature on the study of particle dampers in laboratory environments or with simulation tools, part of which will be discussed in Section 3. Reports on practical applications remain relatively rare, but often show significant success of the approach in reducing unwanted vibrations, [9], [10].

In the course of a research project, a modified design of an axial piston pump is being developed which incorporates cavities for particle damping into its structural parts. In the following, we present a preliminary study performed with attachable 3D printed particle damper casings. In a first section, an analysis of operational vibrations of the reference pump is reported. the next section details the design strategy for the dampers, based on this analysis

in correspondence with literature on particle dampers. In the final section, the experimental parameter study is described and results are reported.

2. OPERATIONAL VIBRATION MEASUREMENT AND FEA

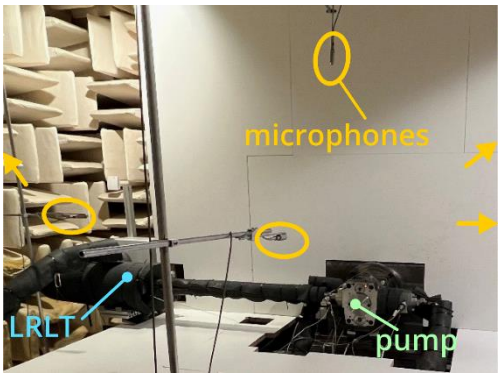

Figure 2: Sound power measurement setup in anechoic chamber

In order to design targeted noise reduction measures, the vibroacoustic behaviour of the pump in operation was studied. The pump was installed on a hydraulic test rig in an anechoic chamber as shown in Figure 2. The emitted sound power was measured at varying combinations of speed, working pressure and swivel angle according to Table 1. Also measured were surface accelerations and pressure pulsation in the low and high pressure lines and a trigger signal for the shaft rotation. The sound power measurement was carried out in an anechoic chamber according to the provisions set out in ISO 3744 / DIN 45635-1 and 26, using 6 microphones on a cuboid enclosing surface limited by 2 reflecting planes. A low reflection line terminator (LRLT) was used in order to suppress reflections of high pressure pulsations from the downstream hydraulic circuit.

Table 1: Operating points for reference measurements

	Revolutions per minute	**Working pressure / bar**	**Relative swiveling / %**
Sound power measurement (all combinations)	500; 1000, 1250, … 2000	50, 100, … 300	25, 50, 75, 100
Operational vibration measurement	1250	200	100
	1500	50, 200, 300	100
	1750	200	100

An in-depth assessment of the vibration was performed by means of an operational vibration measurement. For that, one hundred measurement points were defined, with four of them on the supporting flange and the others on the pump surface. At selected operating points (see Table 1), the stationary vibration at each measurement point was captured by a triaxial accelerometer. The sensor was mounted on a magnetic base to allow of fast and precise change of the measurement position. The measurement setup is shown in Figure 3, left.

After synchronization and Fourier transformation it is possible to give a phase-correct vector of complex acceleration amplitude $\vec{A}(f) = \vec{A}_{\mathrm{Re}} + j\vec{A}_{\mathrm{Im}}$, from which vectors $\vec{V}(f) = \frac{1}{j2\pi f}\,\vec{A}$ and $\vec{U}(f) = \frac{1}{j2\pi f}\,\vec{V}$ for surface velocity and displacement can be computed. From the vectors at all measurement points, an operational vibration shape can be deduced for each frequency, as shown in Figure 3, center.

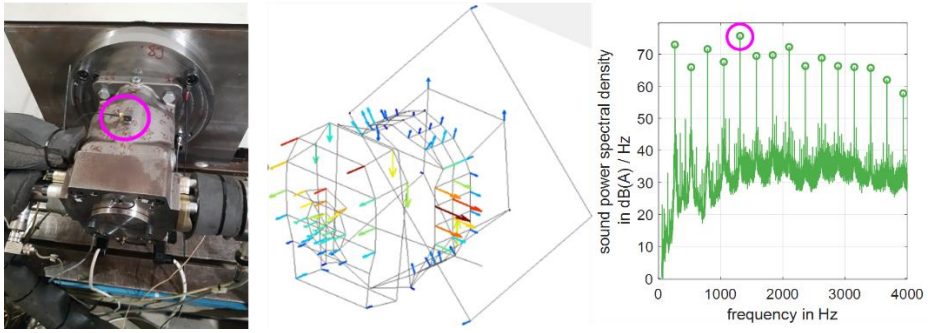

Figure 3: Operational vibration measurement setup, measured vibration shape at critical frequency, for 1750 rpm, 200 bar, and corresponding sound power level spectrum

The Fourier spectrum of A-weighted sound power is used to identify frequencies of critical sound emission. Due to the well-known characteristics of the vibration inducing pressure pulsation in axial piston pumps, the sound power is concentrated in several sharp peaks at frequencies $f_i = i \cdot n \cdot n_{\mathrm{p}}$, with n the revolution speed and n_{p} the number of pistons, as evidenced by the level spectrum shown on the right graph in Figure 3. Considering the logarithmic nature of the level value, there is little contribution from frequencies in between the peaks. It is concluded that vibrations at a few discrete frequencies cause most relevant sound emission at a given operating point, and targeted damping of these is therefore a promising means of reducing pump noise.

Consequently, the vibration shapes at those frequencies which contribute the most to sound power were evaluated different operating points, in order to determine locations of high normal surface velocity amplitude. Those were found to mainly fall in two groups: on the one hand, low frequency (300-1200 Hz) yaw, pitch and torsion oscillations of the whole pump body relative to the mounting flange, and on the other hand bending modes of the pump casing walls at higher frequencies (2-4 kHz). In the intermediate frequency range, a mix of both is observed. In the example shown in Figure 5, casing wall bending along with a pitching motion of the end case relative to the casing compose the vibration shape.

To support the analysis of operating vibrations, modal analysis of the pump in the test rig was performed both experimentally with the impulse hammer method, and by finite element analysis (FEA). For the latter, a basic model was used, with less detail compared to more advanced studies such as [11]. It doesn't account for hydraulic line admittances, contacts and joints of the lubricated gaps in the drive unit are defined with a simple frictionless condition, and a rigid boundary condition was set for the mounting points. This was deemed sufficient for the purpose of providing a point of reference for the operational vibration measurement, rather than precise quantitative predictions.

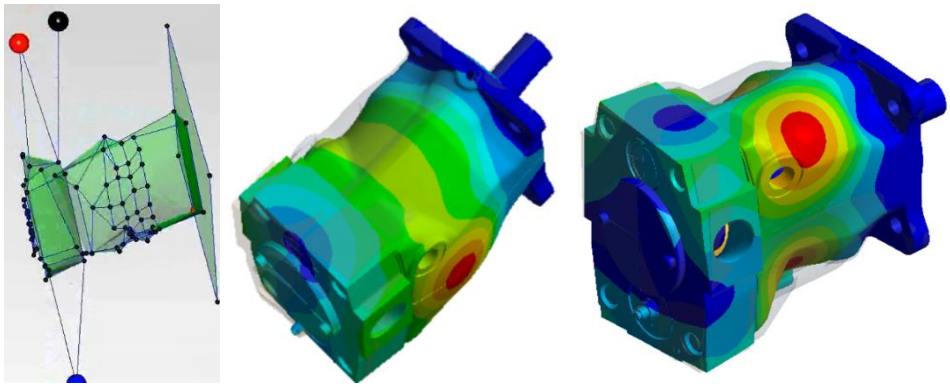

Figure 4: Modal analysis of pump mounted on test rig. Left: top view on yaw mode at 420 Hz, experimental. Middle and right: Whole pump bending at 2.3 kHz, and curved walls bending at 3.0 kHz, FEA.

The analysis found yaw and pitch modes at 3-400 Hz, a torsion mode at 1.2 kHz, and the first mode of elastic deformation of the casing, a bending mode of the pump as a whole, at 2.3 kHz. Further bending modes were observed at subsequent frequencies, first involving the lateral casing walls and subsequently the upper and lower curved walls with modes starting from 3.0 kHz. Experimentally and numerically determined natural frequencies were in accordance of 10% or better, which was deemed sufficient for this qualitative study.

The conclusions drawn from the presented experimental study will inform the placement of damper cavities in the following section.

3. ATTACHABLE PARTICLE DAMPER DESIGN AND MANUFACTURE

As was shown in Section 2, the pump noise emission, assuming variable speed operation, is driven by vibrations on a wide frequency range from a few hundred up to 4000 Hz. From reports in literature, particle dampers offer a promising means to attenuate such broad-band oscillation. The design of particle dampers poses challenges however:

- There are as of now relatively few industrial applications; most studies concern either idealized laboratory experiments, or simulations, as noted in [12]. Therefore, there is limited experience to draw upon.
- Simulation of particle dampers typically relies on discrete element method (DEM) models, which at present have prohibitive computational costs for practical numbers of particles, especially when finer particles are used. Calibrated concentrated or continuum models as in [7] are application-specific and cannot be generalized.
- There is a multitude of factors influencing particle damper performance, a non-exhaustive overview of which is shown in Figure 5.

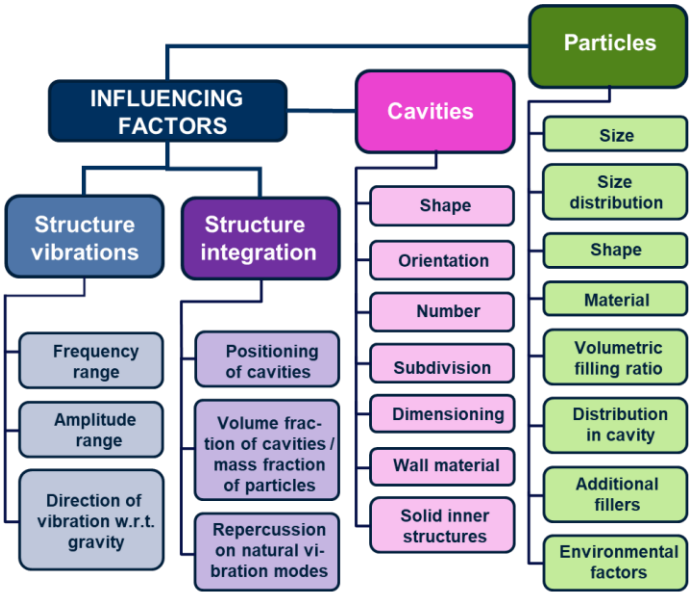

Figure 5: Parameters influencing particle damper performance

It was therefore decided to conduct a preliminary experimental study with the aim of exploring different configurations of the parameters from Figure 5 before embarking on a design for cast pump parts with integrated particle dampers,.

For that purpose, casings were designed and fabricated in 3D polymer print that could easily be attached to on a regular design pump. The casings can be filled with particles on the test rig, allowing for quick changes of both particle types or casings. The study aimed to provide insights for an integrated damper design; additionally, if the particle dampers proved to significantly reduce vibrations, these attachable units could also serve as retrofit solutions for noise reduction in existing pumps.

In a first step, the available literature on particle dampers both in laboratory settings and in practical applications was reviewed in order to deduce construction guidelines. The results are compiled in Table 2.

Table 2: particle damper construction guidelines from literature

Topic	Source	Finding
Cavity / structure volume ratio	[7]	Increasing damping performance with increasing volume ratio of the particle damper cavities relative to the overall structure up to a value of 10 %; beyond that rapidly diminishing returns
Particle size	[13]	Smaller particle size results in high damping effectiveness over a wider range of amplitudes
Particle material	[13]	Best results with tungsten particles, followed by steel; in contrast, polypropylene particles exhibit minimal damping
	[14]	Rubber particles perform well at relatively low frequencies;lead granulate has higher damping than steel chips and balls, tested for frequencies up to 350 Hz
Filling ratio	[15], [16]	Low filling ratios are beneficial at low frequencies, higher ratios at high frequencies
	[16]	Optimal filling ratio between 67 % (at 75 Hz) and 90 % (at 1500 Hz)
	[17]	Optimal filling ratio may reach values up to 98%
Cavity size	[18]	Higher damping at increasing dimensioning of the cavities in the direction of vibration
	[18]	Increasing damping effect with increasing cavity size in the vertical direction up to 30 mm, above that a slight decrease due to the effect of gravity on the particles
Cavity geometry	[19]	With spherical cavities, a more broadband damping effect is achieved as compared to a cubic shape, while peak values are lesser
Inner structures	[20], [9]	Damping increases when solid internal structures are included sinside the cavity

From the results of the operational vibration measurement presented in Section 2, specific areas on the pump surface were identified where significant vibrations occur at various operating points. The local vibration amplitudes at specific frequencies were put in relation to the maps of damping effect over frequency and vibration intensity from [6]. However, these cover only the frequency range up to 1 kHz. [7] documents transfer functions at high frequencies for damped and undamped hollow beams for a variety of configurations, using metallic sintering powder as damping particles. It is noted that these only describe frequency, but not amplitude dependency; still they provide a valuable guideline for the kilohertz frequency range.

Based on the literature survey and measurement results, the following preliminary design decisions were made:

- A target value of 10% of the pump casing and end case material volume was set for the cavities.
- Cavities were placed on the pump casing walls in areas where high amplitudes of bending modes were observed in the experimental study in Section 2, as well as on the end case where the yaw, pitch and torsion modes lead to significant amplitudes.
- The particles according to Table 3 were selected for experimental assessment. Focus was placed on cast iron particles, commonly used as blasting abrasives. These were chosen as a cost-effective alternative to the steel balls frequently mentioned in literature (e.g. [12], [8]). An additional damping effect was expected from the size distribution and rough surface, which [13] and [10] report as beneficial for particle damping, as well as from the material damping properties of cast iron. In addition, steel balls and tin granulate were included in the study, the latter with the aim to evaluate a softer metallic material.
- An ideal cavity dimension of 40x40x40 mm^3 was set based on the findings in [6]. In particular, the dimension in the vertical direction should not exceed this value so as to avoid the obstruction of particle movement by overlying layers.

Table 3: Particle selection for preliminary study

No.	Material	Size/mm
P1	Cast iron blasting agent	1.6-2.25
P2		0.8-1.25
P3		0.2-0.4
P4	Steel balls	2
P5	Tin granulate	2-4

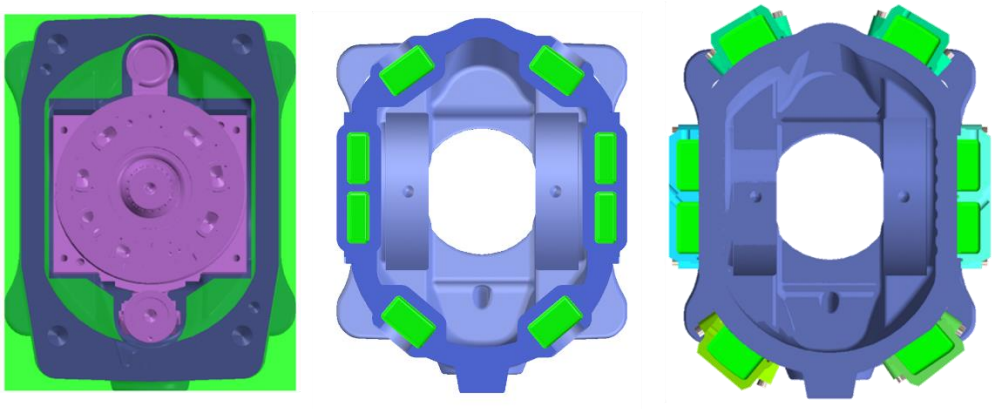

Figure 6: Left: Available construction space. Middle: concept for integrated particle dampers in casing. Right: corresponding design of attachable damper components

The design strategy for damper cavities as detailed above is constrained by practical considerations for pump design. Since the goal is to inspire an integrated design, the dimensions of the attachable dampers need to conform to these restrictions. In particular, it was determined that a significant increase of required space would not be acceptable for an industry adaptation. Therefore, the limits of the bounding box of the existing pumps were not to be exceeded.

A concept for placement of damping cavities in the casing under these constraints was developed, including preliminary sizing of the cavities – the final dimensioning being subject to the outcomes of the experimental study. These cavities were then offset towards the existing pump's surface, and attachable casings were constructed so as to enclose them, as depicted in Figure 6 for the casing; an analogous procedure was applied for the end case. A typical wall thickness of 5 mm was used, which corresponds to estimates for a later cast design. The casings are open towards the vibrating structure without a lid, thus allowing for direct transfer of the vibrational energy into the particle bed.

The final design for the attached dampers is shown in Figure 7. Each casing includes a filling bore for easy insertion of the particles during testing. Sealing cords are used where casings are mounted on raw cast surfaces, to prevent the escape of fine particles. From this base design, variations of the cavities inner structure, stiffening structures, curved surfaces etc. can be deduced for further study. The two pink-coloured casings attached to the front of the end case were included in order to take advantage of the considerable amounts of solid material currently present in these areas, where cavities could potentially be introduced with no additional space needed.

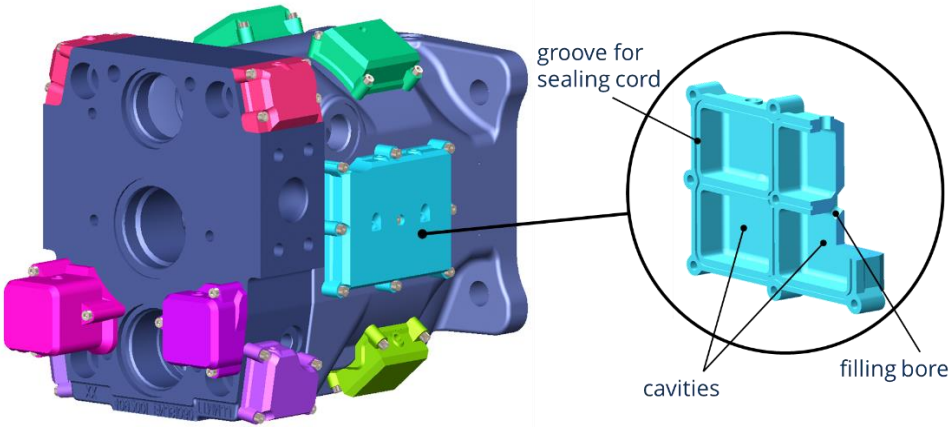

Figure 7: Pump with attached damper components

While the design aims to best simulate the integrated damper concept from Figure 6 (Middle), several differences are observed: there is only one direct interface between the particle bed and the oscillating pump structure; the transfer of momentum through the attachable casing walls may be less due to the transmission path which includes an additional contact and screw connection. The attachable casing material being different from that of the pump structure results in different contact behaviour and hence different transfer of momentum as well. Finally, the integrated cavities affect the pump casing stiffness properties significantly, leading to altered structural dynamic behaviour even before particle

damping; meanwhile the attached plastic casings are expected to only minimally affect these properties.

Finally the casings were manufactured on a 3D printer out of polylactic acid (PLA) material. The print was performed with a wall thickness of 1.2 mm and 20% filling in between walls, with reinforcement around the screw bores. This results in a highly lightweight design, reducing the risk of exciting resonant vibrations of the casings, however decoupling of their oscillation results difficult given their low mass. After PLA exhibited significant creep under pump operating temperatures, a second set of casings was printed from polyethylene terephthalate glycol (PET-G). Threaded holes were drilled on the pump casing and end case using a 5-axial CNC machine.

4. EXPERIMENTAL STUDY ON PARTICLE DAMPER PARAMETERS

The pump was newly installed on the test rig reported on in Section 2 for the assessment of particle damping parameter combinations. In order to test a wide variety of parameter sets, a limited number of operating points was scheduled, as listed in Table 4, each with one repeat measurement.

Table 4: Operating points for attachable particle damper assessment

Revolutions per minute	**Working pressure / bar**	**Relative swiveling / %**
1000, 1250, 1750, 2000	200	100
1500	100, 150, ... 300	100

In a first cycle, each particle type listed in Table 3 was to be tested for its. A filling ratio of 80% was set for these tests. Empty cavities would be dismounted. Further measurements were scheduled with all cavities left empty, in order to assess the effect on acoustics of the attachable casings themselves. Also, the performance of the regular – save for the threaded holes – pump without attached parts was measured to establish a baseline for acoustic performance.

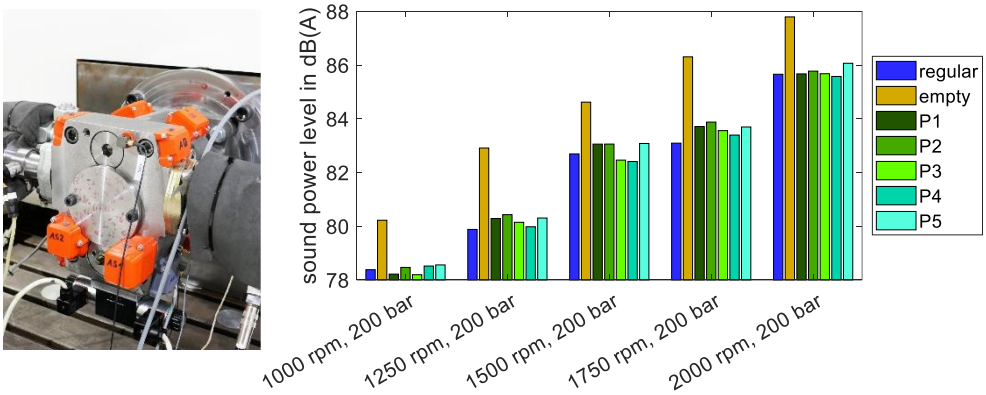

Figure 8: Test rig and performance of plastic made particle dampers depending on particle type (see Table 3 for particle types)

Figure 8 illustrates the experimental setup and the results of speed-dependent sound power level of this first cycle. It is apparent that the empty casings lead to an increase of sound power emission by about 2 dB across all operating points. Filling the cavities largely reverses that effect, returning to similar sound power levels as observed for the regular pump. This is mostly independent of the particle type, even though a tendency is observed for steel balls (P4) to perform slightly better than the others. To further investigate this behaviour, the dependency of the ratio of filling of the cavities was studied with steel balls for particles. The results are depicted in Figure 9. A gradual reduction of sound power is visible. The spectral distribution of sound power provides an explanation for these results: The additional sound power for the empty casings occurs cue to increases above 2.8 kHz, most prominently in the band from 2.8 to 3.5 kHz.

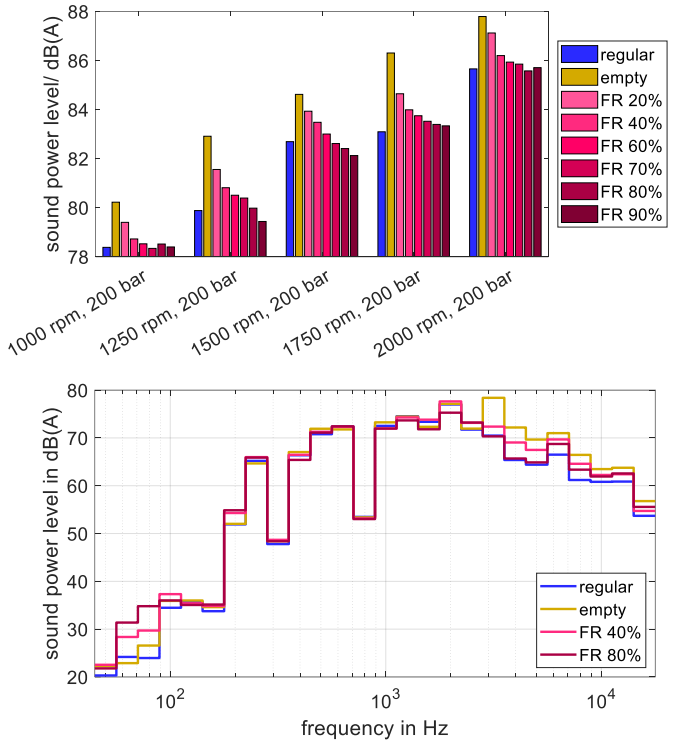

Figure 9: Performance of plastic made particle dampers filled with steel balls depending on cavity filling ratio. Top: integral values of sound power level. Bottom: tertiary band spectrum of sound power level for load case 1500 rpm / 200 bar.

An FEA of the plastic casings shows natural frequencies starting from 2.7 kHz. The analysis makes some simplifying assumptions: walls are modelled homogeneous and a substitute density is set as a quotient of actual weight and model volume, and rigid supports are set as boundary conditions for the nodes on the edges where the screw bores intersect with the contact area. Nevertheless, the result is consistent with the observed increase of sound power being due to resonance phenomena of the casing surfaces in that frequency range. The spectrum also shows these high frequency contributions being damped effectively with increasing cavity filling ratio. It is plausible that a high damping effect is achieved where

the casing walls perform high amplitude vibrations due to resonance. However, damping below the regular pump's sound power level occurs only minimally and not systematically across bands. It is also observed that at low frequency bands adding particles increases the emitted sound power measurably is measurably higher than for either the regular pump or the empty casings, even though the contribution to integral sound power is insignificant on the logarithmic scale. This may be explained as a rattling effect of the particles colliding with the cavity walls, which is prominent against the overall very low sound emission of the pump at these frequencies.

Upon review the unsatisfying results obtained with the plastic dampers, the design was revisited for metal casings. On the one hand, with natural frequencies predicted to start in the high 7 kHz range, sound emissions from casing resonances were expected to be much lower and shifted to a frequency range significantly above the one relevant for regular pump noise. On the other hand, it was expected that stiffer casing wall material would improve the momentum transfer between the oscillating structure and the particle bed, in particular at higher frequencies. Due to time constraints, a mix of 7 steel casings additively manufactured by laser powder bed fusion (LPBF), and 5 CNC milled aluminium casings were employed for the experimental study. Figure 11, left shows the test setup with metal casings from both manufacturing variants.

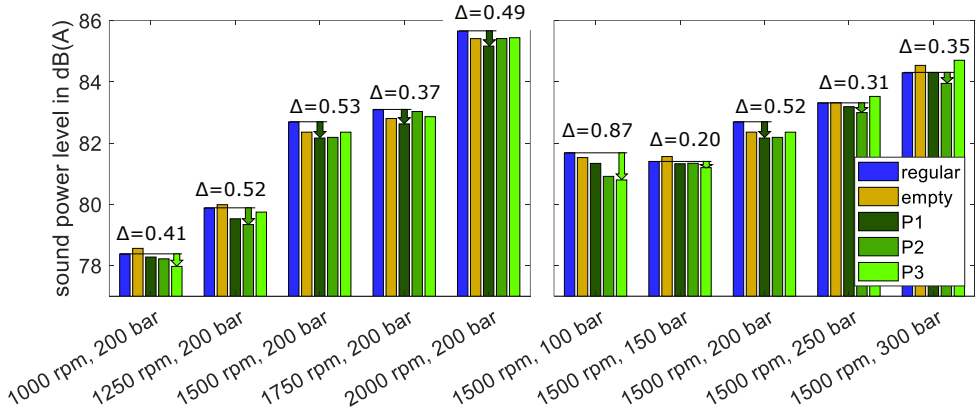

Figure 10: Performance of metal casing particle dampers depending on particle type (see Table 3 for particle types)

The integral sound power level values depending on particle types P1 to P3 (cast iron blasting agent of decreasing size) are shown in Figure 10. Compared with Figure 8, the damping configurations systematically yield lower sound power levels than the regular pump, with the exception of P3 at the two load cases > 200 bar. The reduction is meagre though, with typical values of $\Delta = 0.35\ldots0.5$ dB for the optimal particle type at each load case. A tendency is observed for the larger particles to perform better at higher pump speeds, and for the fine particles P3 at low power (low speed or pressure). As opposed to the plastic casings, their metal variants don't lead to significant increases of sound power when applied empty, and in fact provide a slight reduction for several load cases.

The spectral representation in Figure 11 shows that the empty casings still cause non-negligible sound emissions in the band starting at 5.6 kHz and above. However, they also

slightly reduce the levels in certain bands, leading to an overall lower sound power level for the considered load case. It can be suspected that these reductions are due to oscillation decoupling, such that vibration is not fully transmitted from the pump surface to the cavities at these frequencies. Again, the damping particles are most effective in the frequency bands where the empty casings introduced additional sound emissions.

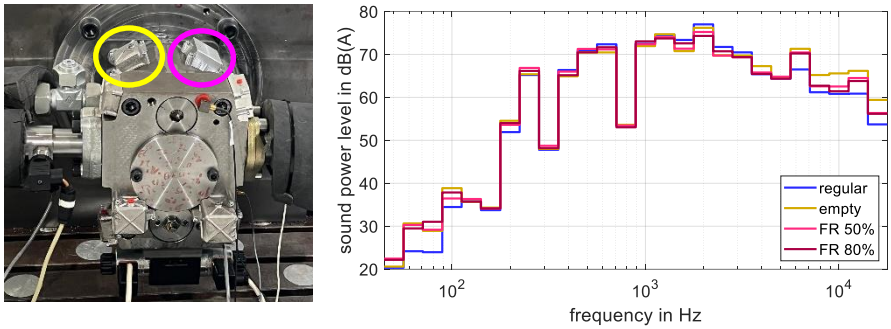

Figure 11: Left: Pump equipped with metal damper casings from additive manufacture (circled yellow) and CNC milling (pink). Right: Tertiary band spectrum of sound power level for load case 1500 rpm / 200 bar for particles P1 depending on filling ratio

5. CONCLUSION AND OUTLOOK

Particle dampers for vibration attenuation and consequential noise reduction were fitted to an existing axial piston pump using 3D printed attachable casings. Their design and particle preselection were informed by a literature survey in combination with an experimental and simulative assessment of the pump's vibration behaviour, with operational vibration measurements being the central piece. Experimental assessment of the damping properties showed slight reductions of pump sound power, especially for the revised design with metal casings. The spectral analysis indicates that these reductions are mainly due to oscillation decoupling of the damper casing surfaces, while the particle damping effect is clearly observable only for resonant vibration of the casings themselves.

The presented approach may yield more significant noise reduction when expanded to a larger share of the pump surface, combining a decoupling enclosure strategy with particle damping. The study yielded inconclusive results regarding the viability of integrated campers in the pump casing and further study is required.

6. ACKNOWLEDGMENT

The presented research activities are part of the project "Geräuschminderung in Verdrängereinheiten", funded by Forschungskuratorium Maschinenbau e.V. (FKM-Nr. 7052400). The authors would like to thank FKM and the Fluid Power Research Fund at VDMA for funding and support.

The authors would like to thank Prof. Fabian Riß of TH Rosenheim and his team for kindly providing additively manufactured steel casings for external cavities.

7. REFERENCES

[1] D. Becher, Untersuchungen an einer Axialkolbenpumpe mit Ringsystem zur Minderung von Pulsationen, PhD Thesis, TU Dresden, 2003.

[2] G. Kumar Seeniraj, M. Zhao and M. Ivantysynova, "Effect of combining precompression grooves, PCFV and DCFV on pump noise generation," *International journal of fluid power,* vol. 12 (3), pp. 53-63., 2011.

[3] D. Kim and M. Ivantysynova, "Valve plate optimization focusing on noise reduction in the axial piston machine with high volumetric efficiency," in *Proc. of the 7th FPNI PhD Symposium,* Reggio Emilia, 2012.

[4] T. Nishiumi, T. Ichiyanagi and T. Kuribayashi, "Development of a novel Helmholtz hydraulic silencer for attenuating the pressure ripple from a fixed displacement pump with variable rotational speed.," in *Proceedings of 11th IFK,* Aachen, 2018.

[5] T. Kim and M. Ivantysynova, "Active vibration/noise control of axial piston machine using swash plate control," *Fluid Power Systems Technology,* vol. Vol. 58332, 2017.

[6] N. Meyer and R. Seifried, "Systematic design of particle dampers for transient vertical vibrations," *Granular matter,* vol. 25 (1), p. 3, 2022.

[7] T. Ehlers, Auslegung partikelgedämpfter Strukturbauteile für die Additive Fertigung, PhD thesis, Leibniz Universität Hannover, 2023.

[8] H. Ye, Y. Wang, B. Liu and X. Jiang, "Experimental Study on the Damping Eect of Multi-Unit Particle Dampers Applied to Bracket Structure," *Applied Sciences,* vol. 9 (14), p. 2912, 2019.

[9] F. A. M. Vogel, S. Berger, E. Özkaya and D. Biermann, "Vibration Suppression in Turning TiAl6V4 Using Additively Manufactured Tool Holders with Specially Structured, Particle Filled Hollow Elements," *Procedia Manufacturing,* vol. 40, pp. 32-37, 2019.

[10] F. Duvigneau, S. Koch, E. Woschke and U. Gabbert, "An effective vibration reduction concept for automotive applications based on granular-filled cavities," *Journal of Vibration and Control,* vol. 24 (1), pp. 73-82, 2018.

[11] U. Bittner, Strukturakustische Optimierung von Axialkolbeneinheiten: Modellbildung, Validierung und Topologieoptimierung, PHD thesis, Karlsruhe Institute of Technology, 2012.

[12] N. J. Meyer, Systematic Design of Particle Dampers for Passive Vibration Attenuation, PhD thesis, TU Hamburg, 2023.

[13] N. Meyer and R. Seifried, “Toward a design methodology for particle dampers by analyzing their energy dissipation,” *Computational particle mechanics,* vol. 8, pp. 681-699, 2020.

[14] B. B. Prasad, F. Duvigneau, D. Juhre and E. Woschke, “Damping performance of particle dampers with different granular materials and their mixtures,” *Applied Acoustics,* vol. 200, p. 109059, 2022.

[15] Z. W. Xu, K. W. Chan and H. W. Liao, “An empirical method for particle damping design,” *Shock and Vibration,* Vols. 11 (5-6), pp. 647-664., 2004.

[16] G. Michon, A. Almajid and G. Aridon, “Soft hollow particle damping identification in honeycomb structures,” *Journal of Sound and Vibration,* vol. 332 (3), pp. 536-544, 2013.

[17] G. Jin, Z. Zhao, B. Liu, W. Cun, Z. Zhao, M. Hou and G. Chen, “Design of a particle damper and experimental study on vibration damping of the pipeline,” *Advances in Mechanical Engineering,* vol. 13 (9), p. 16878140211044923, 2021.

[18] T. Künneke and D. Zimmer, “Funktionsintegration additiv gefertigter Dämpfungsstrukturen bei Biegeschwingungen,” *Additive Fertigung von Bauteilen und Strukturen,* pp. 61-74, 2017.

[19] C. X. Wong, A. B. Spencer and J. A. Rongong, “Effects of Enclosure Geometry on Particle Damping Performance,” in *50th AIAA/ASME/ASCE/AHS/ASC Structures, Structural Dynamics, and Materials Conference*, Palm Springs, 2009.

[20] N. Meyer and R. Seifried, “Design of robust particle dampers using inner structures and coated container walls,” *Granular matter,* vol. 25 (1), p. 10, 2021.

Simultaneous Transfer Path Analysis of Axial Piston Pump Lumped Parameter Model Results

Dazhuang He[1], Antonio Masia[2], Yangfan Liu[3], Lizhi Shang[4], Daniel Dyminski[5]

[1] Ray W. Herrick Laboratories, Purdue University. 177 S Russell St, West Lafayette, IN 47907, USA. he385@purdue.edu

[2] Department of Agricultural & Biological Engineering, Purdue University Maha Fluid Power Research Center 1500 Kepner Drive, Lafayette, IN 47905 USA. amasia@purdue.edu

[3] Assistant Professor of Mechanical Engineering, Ray W. Herrick Laboratories, Purdue University. 177 S Russell St, West Lafayette, IN 47907, USA. yangfan@purdue.edu

[4] Assistant Professor of Mechanical Engineering and Agricultural & Biological Engineering, Purdue University Maha Fluid Power Research Center 1500 Kepner Drive, Lafayette, IN 47905 USA. shangl@purdue.edu

5 Principal Engineer, Hydraulic Pump and Power System Division Parker Hannifin Corporation. daniel.dyminski@parker.com

Abstract.

The recent trend in electrifying off-road vehicles has brought to light a critical issue – the noise emission of hydrostatic pumps and motors. In the transition from internal combustion engines (ICE) to electric motors, the previously masked noise from hydraulic pumps and motors has become significant in fluid power systems for off-road applications. The purpose of present study is to develop a analyzing tool of noise and vibration of hydrostatic pumps and motors. To achieve this goal, a dedicated lumped parameter model (LPM) was developed in Amesim. The numerical model takes into account various factors, including the fluid-dynamic path, unit kinematics, forces and moments acting on the main components. The lumped parameter model simulates the internal forces/moments/ripples that cause noise and vibration of the axial piston pump. The method of simultaneous transfer path analysis (sTPA) is then applied to the relation between internal forces/moments/ripples and consequent noise and vibration.

With simultaneous excitation information provided by LPM and operational measurement of acoustic/vibration responses, sTPA estimates the frequency response functions between the excitations and acoustical/vibrational responses. Path contribution information provided by sTPA characterizes the significance of individual transfer paths. A 45cc pump was subjected to testing enabling the collection of data of noise levels, vibrations and flow ripples over a large range of operating conditions. With both measurement and simulation results, sTPA is conducted to analyze how the pump internal excitations (forces, moments and ripples) correlate with pump noise and vibration. The results provided by sTPA highlights the critical path contributions and the main mechanisms that contribute to the noise emission

over a range of frequencies. A parameter sensitivity analysis based on sTPA results is conducted, in which the sensitivities of noise and vibration level of the piston pump to multiple design/operation parameters are investigated. In the case study, sTPA reveals that the moment oscillation exerted on the pump has the most significant impact on the overall vibration level, and the bearing force oscillation has the most significant impact on the overall noise level. In conclusion, sTPA is a tool that bridges the gap between LPM calculation results and air-borne noise/vibration performance of hydraulic pumps and provides insights to the root-cause of noise and vibration problems of axial piston pumps.

Keywords. Transfer path analysis, lumped parameter model, axial piston pump.

1. INTRODUCTION

Axial piston pumps are widely used in applications such as agricultural, construction and industrial vehicles. Due to the pulsive nature of the working principles of axial piston pumps, oscillatory forces, moments and pressure ripples are major sources of noise and vibration during the operation of piston units. In recent years, trend of electrification of off-road vehicles poses new challenges for the mitigation of noise and vibration of hydraulic units, because the quieter electrical powertrain accentuates the noise emitted from hydraulic units, which are otherwise masked by the noise from conventional ICE powertrain.

Despite the noise, vibration and harshness (NVH) performance of hydraulic pump/motor has been vastly improved over the course of fluid power technology development, the problem of noise and vibration generation remains a challenge. Specifically, the noise and vibration issue are more prominent for piston machines than gear or screw machine [1] due to its pulsive nature. Early efforts of noise reduction for piston machines focused mainly on *structure borne noise* (SBN) mainly induced by vibration of pump/motor components. Helgested *et al*. studied the effect of rate of pressurization on pump casing vibration and noise [2]. Yamauchi *et al*. investigated how factors such as pressurization rate, relief groove and dead volume affects swash plate vibration in piston pumps [3]. Kim and Ivantysynova designed a pump control system, in which an anti-moment is actively exerted on the swashplate to reduce its vibration [4]. *Fluid borne noise* (FBN) stem from the pressure and flow pulsations. As a result, the mitigation measures for FBN mainly focus on the reduction of flow/pressure ripples. Harrison *et al.* developed valve plates with a heavily damped check valve ahead of delivery port to reduce the flow ripple [5]. Ortwig installed a silencer in hydraulic circuit to reduce pulsations propagating through the hydraulic line [6]. Rebel attempted to introduce anti-noise, i.e., secondary pressure ripples that destructively interfere with the original ripples, to reduce FBN [7]. Techniques of FBN reduction has been comprehensively summarized by Harrison *et al.* [5].

In the aforementioned studies about noise reduction measures of piston pumps, the goal researchers attempted to achieve is always the reduction of pump internal force/moment/ripples. However, the oscillatory excitations, either structure borne or fluid borne, transmit differently through multiple paths and contribute to the noise level at designated locations, e.g., vehicle operator's ears. In order to conduct a thorough root-cause analysis for noise and vibration of piston units, a quantitative approach that correlates the internal excitations and perceivable noise and vibration of the pump is necessary. Such approach reveals how sources of noise and vibration transmit via different transfer paths. For this purpose, the method of simultaneous transfer path analysis (sTPA) is developed in

the present study and applied to piston units with internal excitations generated by a lumped parameter model (LPM) of axial piston pump.

LPM has been proven to be a reliable method to capture the internal force, moments and ripples of hydraulic units. In the work proposed by Manco *et al.*, [8] and [9] a lumped parameter model has been developed, showing remarkable agreement between simulation and measurements. A similar numerical model is available as a built-in component in the software Amesim. In the present study, a dedicated lumped parameter model is developed in Amesim to overcome the constraints of an imposed model, allowing the author the flexibility to access the source code to model the components that are the focus of interest for this study, which are not available in the current state of the art models. The numerical model takes into account the fluid-dynamic path, the unit kinematics and dynamics, and the forces and moments that are exerted on the main components, in particular, the forces and moments exerted on the port case of the pumps.

The conceptual LPM+sTPA framework is shown in the diagram in **Figure 1**. The pump sound and vibration measurement are carried out for multiple operation conditions, and LPM simulation is also conducted for the same operation conditions. sTPA is the processing tool for both the sound and vibration response data acquired in measurement and internal excitations data simulated using LPM. By feeding sTPA the excitation and response data for multiple operation conditions, sTPA estimates frequency response functions (FRFs) that characterize the transfer paths between excitation and response.

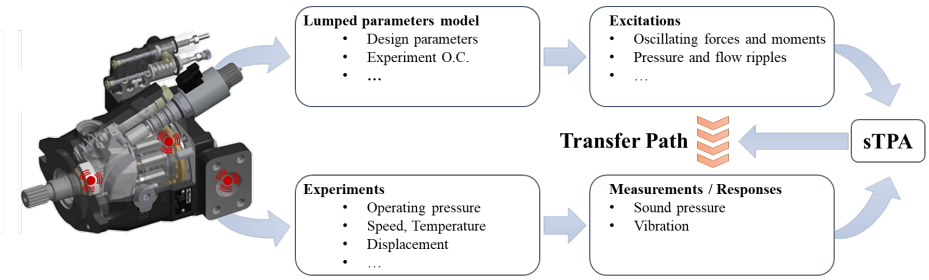

Figure 1 LPM+sTPA framework

Coupling LPM with sTPA has advantages in noise/vibration mitigation of pumps. sTPA requires simultaneous data of internal excitation, and LPM provides high fidelity data of internal excitations which is otherwise difficult to measure. With sTPA, the reductions in internal forces/moments/ripples can be quantified in terms of noise/vibration levels reductions. sTPA not only fills the gap between internal excitations and consequent noise/vibration level, but also provides guidelines on noise/vibration mitigation of the pump. By inspecting the FRF and path contributions, one can identify the critical paths. Once the critical paths are identified, noise/vibration mitigation measures can be explored using the estimated FRFs.

In this paper, the development of piston unit LPM is covered in the chapter 2. The methodology of sTPA is introduced in chapter 3. The results of transfer path FRF and path contributions are shown in chapter 4. Conclusions of the study is presented in the chapter 5.

2. LUMPED PARAMETER MODEL FOR PISTON UNIT

The mathematical model for simulating axial piston pump swashplate type is described in detail in this section. The model allows for the evaluation of the unit performance under both steady-state and dynamic conditions. It has been designed and implemented to be parametric, which means that it provides the flexibility to vary the geometric parameters of a unit or a specific feature and see their effects on the performances compared to a baseline design. **Figure 2** shows the cross-sectional view of an axial piston machine swashplate type with the main components considered for the model implementation labelled.

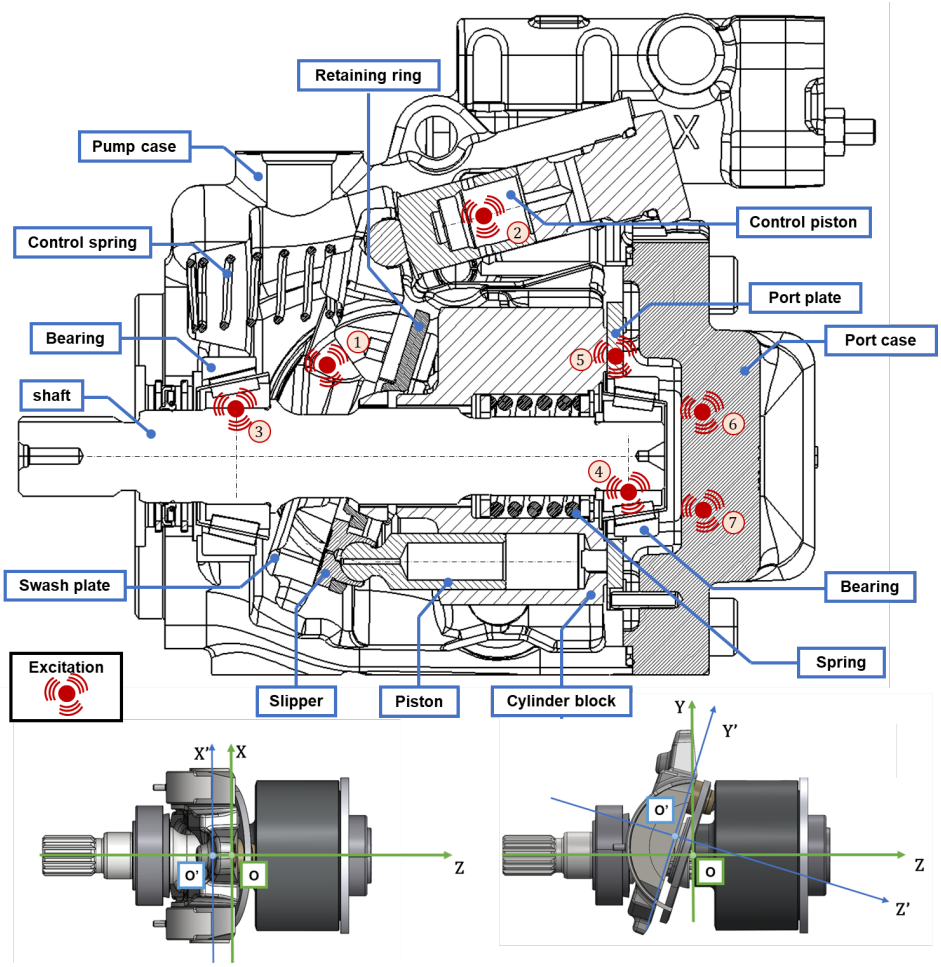

Figure 2 Axial piston pump cross-section and reference system

Two reference systems were selected. A fixed cartesian coordinate system is considered center at the center of the instantaneous rotation of the swashplate and a mobile coordinate system is considered center on the swashplate. The eccentricity of the swashplate is considered a design parameter as well. In **Figure 2** shows the main point that represents source of excitation that contribute to noise generation. Internal forces and moments have the potential to excite the pump housing, resulting in the pump vibration which results in

air-borne noise. The excitation includes ① the force from the swashplate, ② the pressure ripple in the swashplate control cylinder, ③ & ④ the force from the shaft through the two bearings, ⑤ the force on the port case from the cylinder block, and ⑥ & ⑦ the pressure ripples in the inlet and outlet port of the unit. In this study, the focus is only on ④, ⑤ which represents the excitation that most affects the port case of the pump. The swashplate force and the bearing force ③ are not considered because they are located next to the mounting interface where due to the rigid connection the housing is not free to deform. The pressure ripple in the swashplate control system is neglected because relatively low. The pressure ripple in the inlet and outlet port will results in more fluid-born noise, but limited air-borne.

2.1. Fluid Dynamic Model

To model the fluid dynamic behaviour of the unit, a lumped parameter method has been chosen. The first step is to discretize the unit into its equivalent fluid dynamic block diagram, shown in **Figure 3**. Where the entire pump fluid dynamic system is represented as a set of discrete components each characterized by lumped parameters such as volume, pressure, and flow rate. For simplicity is assumed that the unit is working in pumping mode, and the flow flows from left to right.

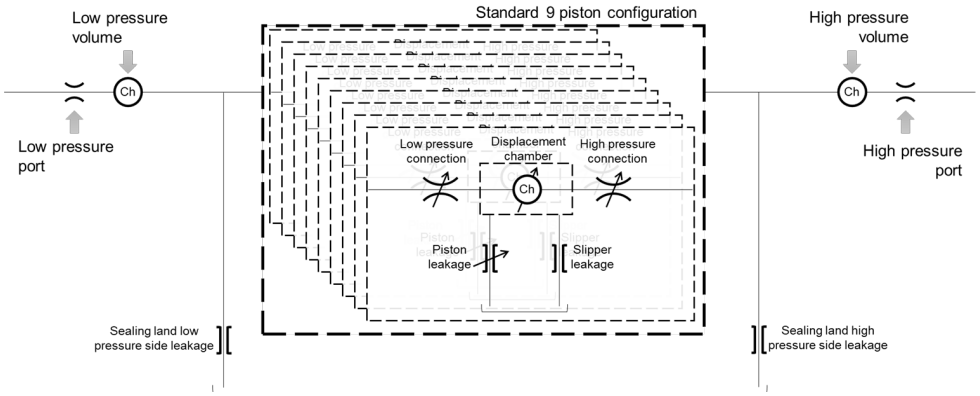

Figure 3 Axial piston pump fluid-dynamic block diagram.

To model the fluid dynamics within the axial piston machine, it is essential to analyse both its kinematic behaviour and the influence of component motion on the fluid path.

An axial piston pump typically features two ports: one for suction and one for delivery. In the pumping mode, the suction port operates at low pressure while the delivery port operates at high pressure. A fixed orifice is selected to model the ports, while a fixed volume is chosen to simulate the dead volume that is present inside the port-case. The structure of the pump's rotary group includes: shaft, cylinder block, pistons, and slippers. Traditionally, swashplate-type units feature configurations with nine pistons. During a single shaft revolution, each piston performs two primary actions: suction and delivery. In the suction phase, the piston moves out from the displacement chamber, allowing fluid to enter. In the delivery phase, the piston moves into the displacement chamber, pushing the fluid out. This process is repeated every shaft revolution, with the piston communicating with the low-pressure side during suction and the high-pressure side during delivery. A variable orifice is employed to model the opening and closing between the low and high-pressure sides of the pump.

The equation representing a variable orifice is the orifice equation, which can be expressed as follows:

$$Q_i = c_d \cdot A_i \cdot \sqrt{\frac{2 \cdot \Delta p}{\rho}} \tag{1}$$

The subscript "i" in the equation generalizes its form to a vectorial representation, where the "i" element corresponds to the "i-th" piston. A_i is the effective flow area for each piston. Its profile during a single revolution is crucial for replicating the proper behavior of the unit. The area profile depends on the design of the valve plate shown in **Figure 4**, which regulates the timing for connecting the displacement chamber with the low and high pressure.

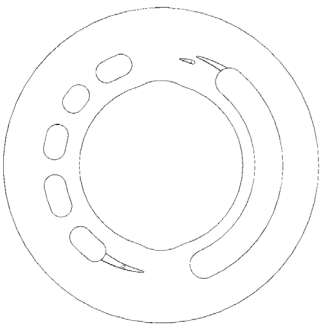

Figure 4 Valve plate

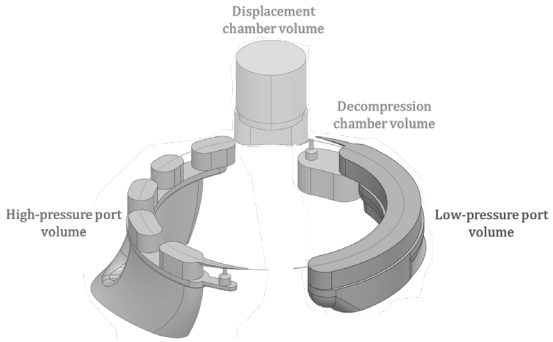

Figure 5 Fluid volume analysis

To evaluate the area profile, the AVAS toll was used. AVAS, expanded as Automated Valve Plate Area Search, is an in-house software that solves for a minimum area of cross-section of the fluid geometry (shown in **Figure 5**) normal to the flow streamline for every desired step angle in a shaft revolution. This area is the smallest opening between the cylinder clock and the valve plate in the direction of flow between the displacement chamber and the high-pressure or low-pressure ports.

The pressure within the displacement chamber changes and these variations can be described by the pressure build-up equation.

$$\frac{dp}{dt} = \frac{\beta}{V} \cdot \left(Q_{in} - Q_{out} - \frac{dV}{dt} \right) \tag{2}$$

This equation represents the instantaneous relationship that connects the pressure variation in the chamber to the sum of the flows and the volume variation It is also essential to consider the leakages from the three main lubricating interfaces. These leakages are approximated considering a laminar flow, with a constant gap height and with a linear or exponential pressure gradient. The laminar flow approximation, characterized by low Reynold number, simplifies its complexity making it suitable for a lumped parameter approach. The model considers the three main lubricating interfaces as a laminar interface with a constant gap height and their expression can be found analytically [10].

2.2. Mechanical Model

This section presents a simplified study of the mechanical components of the axial piston unit. For each individual component, equilibrium equations for translation and rotation were developed, allowing the evaluation of the forces and moments exerted on a single component. The reference coordinate systems and nomenclature of the main geometric points that define the motion of the pistons and slippers are shown in **Figure 2**. A free-body diagram approach has been used to define the equations that describe the kinematics and dynamics of the main elements. Particular attention was focused on the port case.

2.2.1. Port case

The displacement chamber exerts a pressure force acting against the cylinder block. This force is then transferred to the port case via the valve plate. A thorough evaluation of the equilibrium of forces and moments is performed to determine which component may be influencing the noise emission of the hydraulic machine. The valve plate is considered to be simplified to a two-dimensional plane. **Figure 6** shows how a reference system is set up in the center of the port case.

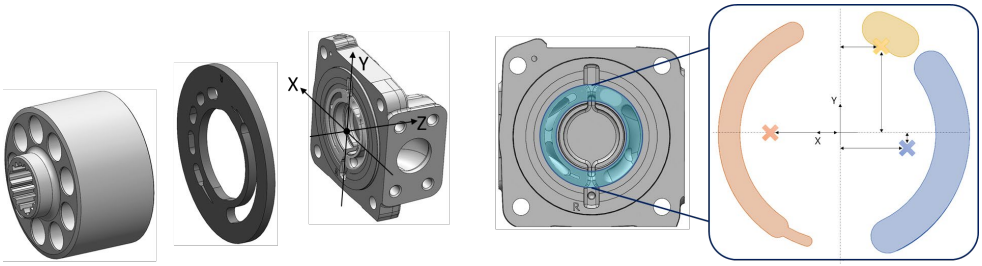

Figure 6 Port case notation

$$F_{pc} = \sum_{i=1}^{Np} -F_{p,i} + F_{vp} \tag{4}$$

Where F_{pc} represent the force applied on the port case, $F_{p,i}$ is the pressure force from the displacement chamber, and F_{vp} is the force from the valve plate. The force exerted by the valve plate is evaluated using three pressure values: low pressure, high pressure, and pressure within the inlet baffle chamber (Patent applied EP347171A1). Each of these pressures, multiplied by their corresponding area (as shown in **Figure 6**), produces a force opposite to the one generated by the cylinder block. The resulting force F_{pc} is expected to transfer to the port case. A three-dimensional computer-aided design (3D-CAD) study was used to determine the center of each region, resulting in coordinate coordinates relative to the x and y axes. A study of the moments operating on the port case was done assuming that the force generated by each area would is applied to its geometrical center.

$$M_{pc,x} = \sum_{i=1}^{Np} -F_{p,i} \cdot y_{p,i} + M_{vp,x} \tag{4}$$

Where $M_{pc,x}$ is the moment acting on the port case around the x-axis. A similar approach has been applied to determine the moment around the y-axis $M_{pc,y}$.

Another excitation to consider for the sTPA is the bearing force. The cylinder block and the shaft are assumed to be rigidly connected through a splined interface. The midpoint of the spline serves as the reference point. Using this reference, the force exerted by the cylinder block and the bearing location are employed to evaluate the force exerted on the bearing.

2.3. Experimental investigation and model validation

To validate the lumped parameter model, a series of experiments were run under steady-state conditions. These tests were primarily designed to measure the pressure ripple at 'he pump's outlet port. The experimental data were then compared to the simulated results generated by the model. The comparison aimed to evaluate the model's accuracy. The following **Figure 7** depicts the hydraulic schematic used for the experiments for model validation.

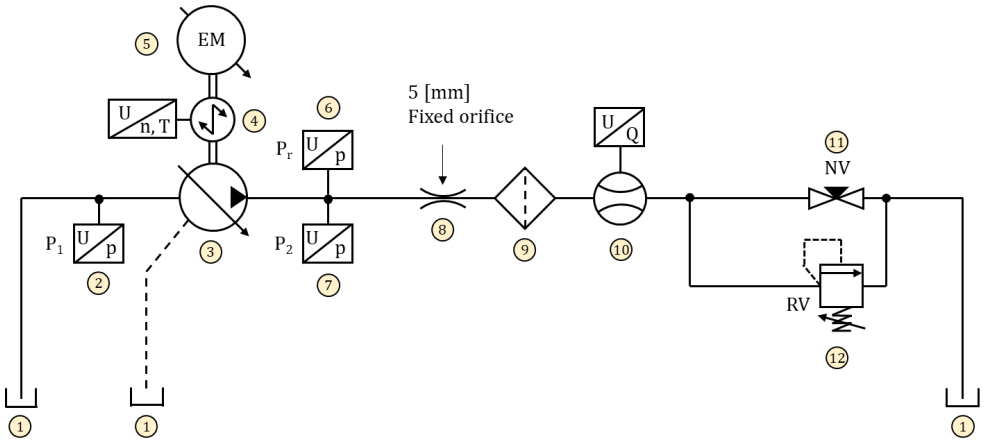

Figure 7 Hydraulic schematic.

A standard reservoir ① is connected to the unit under testing ③, which is driven by an electric motor ⑤. A torque meter ④ is used to monitor speed and torque. Two pressure sensors ② and ⑦ measure pressure differential throughout the unit, while a piezoelectric transducer ⑥ measures pressure ripple. The pump load is regulated by a fixed orifice ⑧, which is connected to the pressure sensors ⑥, ⑦ via a rigid pipe. Following the opening, a high-pressure filter ⑨ comes before the flow meter ⑩. Next, a needle valve ⑪ is added to regulate pump load. For safety, a pressure relief valve ⑫ is connected in parallel.

The tests analysed the hydraulic unit's performance at various operating speeds and pressure levels. The unit was operated at 1000, 1500, 2000 rpm, and 2500 rpm. The pressure within the system was monitored at each speed increment, with the needle valve fully open serving as the baseline. The pressure levels obtained by adjusting the needle valve opening to reach 75, 125, and 175 bar offered insight into the unit behavior across the speed range, assisting in the validation and calibration of the lumped parameter model.A series of custom components were developed to create a comprehensive library of components, which were then integrated into the Amesim environment. This new library contains customized

components modeled according to physical principles, with parametric and vectorial properties, including the parameter for the number of pistons. To consider the loading condition, the model use standard components already present in the Amesim library for modeling the rigid pipe and the orifice. Then, it is assumed that the pressure ripple is affected by orifice pressure drop, so a pressurized tank is used to generate the pump load. The validation of this model involves the comparison of the pressure ripple measured at the pump's outlet port. An FFT analysis was conducted on the measurements, revealing that 2000 rpm was the optimal configuration for validating the model due to its lower noise levels compared to other operating speeds. Additionally, the higher noise in the measurements might be attributed to the nonlinearity of the physical components present in the hydraulic circuit, which can be challenging to model using a lumped parameter approach. The following **Figure 8** and **Figure 9** show the comparison of the pressure ripple measured and the pressure ripple simulated.

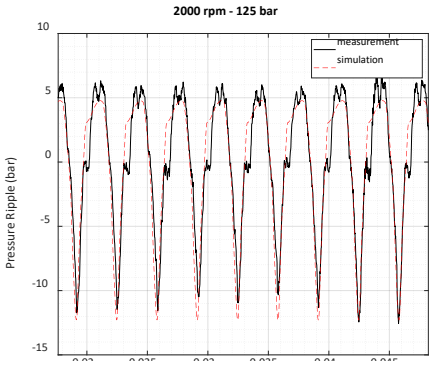

Figure 8 Sim–vs Mes - 1

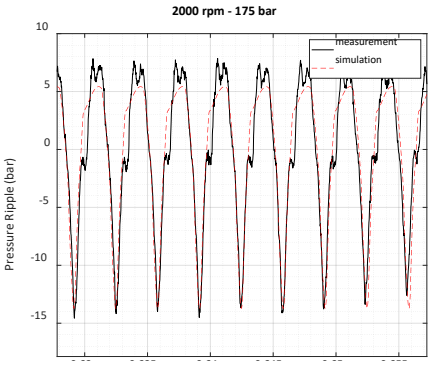

Figure 9 Sim–vs Mes - 2

As can be noticed, the model is able to capture the pressure ripple amplitude respect different level of pressure and follow the measurement profile. The comparison on the pressure ripple amplitude led to the following evaluation of the model accuracy

Speed [rpm]	**Pressure [bar]**	**Mes Δ ripple [bar]**	**Sim Δ ripple [bar]**	**Error [%]**
2000	175	20	19.14	4.30
2000	125	16	17	6.25
2000	75	13.5	14.3	5.93

The results show that the model can simulate the pressure ripple with an average error of 5.5% with respect the measurement results.

3. SIMULTANEOUS TRANSFER PATH ANALYSIS

Transfer path analysis (TPA) is a technique used to break down noise or vibration into its key contributors. The noise/vibration contributors are characterized using frequency response functions from excitations to the acoustic/vibration responses at target locations.

The three major components in the TPA calculation are:

- Excitations: The spectrum of forces/moments source that causes noise and vibration.
- Responses: The noise/vibration acquired at target locations.
- Transfer Paths: The mathematical relation that characterizes how noise and vibration are transferred from source excitation to the responses.

Figure 10 shows the relation of excitations, responses and the transfer paths in between for a mechanical system with 3 excitations, 2 responses and 6 transfer paths. In general, if there are r excitations and m responses, the number of transfer paths is r-by-m. The task of TPA is to determine the frequency response functions (transfer functions) for each transfer path mathematically.

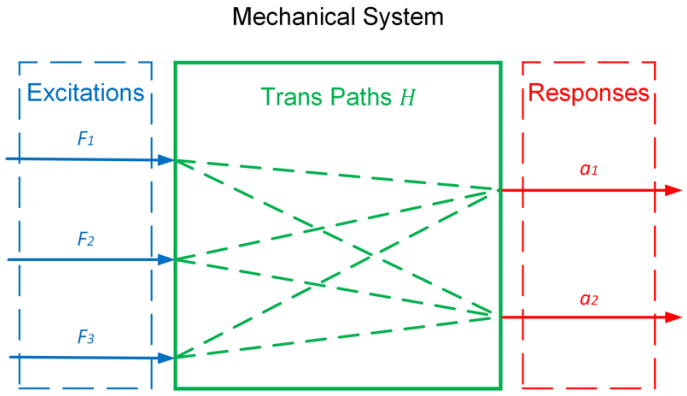

Figure 10 Excitations, responses and transfer paths in TPA

TPA has been a widely used engineering tool for the analysis of mechanical vibration transmissions for a variety of industrial products, and the methodologies of TPA has kept developing over time. Van der Seijs *et al*. provides a compressive review on the landscape of TPA methods [11]. In the conventional practice of TPA, the excitations are isolated and applied to the mechanical system individually. In the example shown in Figure 10, if excitation $\boldsymbol{F_1}$ is isolated and applied, then the frequency response function from $\boldsymbol{F_1}$ to responses $\boldsymbol{a_1}$ and $\boldsymbol{a_1}$ can be simply calculated as $\boldsymbol{H_{11} = a_1/F_1}$ and $\boldsymbol{H_{21} = a_2/F_1}$.

However, for axial piston pumps, it is difficult to isolate excitations and apply them individually. For example, in an operating hydraulic pump, the oscillatory fluid pressure ripples cause noise and vibration, yet it is difficult to investigate the fluid pressure related transfer path alone, without introducing other *simultaneous* excitations such as the bearing force due to pressure imbalance across cylinders. For this reason, a sub-category of TPA methodology, simultaneous TPA (sTPA, also referred to as operational TPA), is thus more suitable for the estimation of transfer path FRFs for such mechanical systems. sTPA has

gained popularity in multiple engineering areas as a NVH analysis tool [12-15], due to its ease to setup the measurement. Instead of isolating and applying excitations individually, in the practice of sTPA, multiple independent combinations of operational excitations are created by altering the operation conditions of the mechanical system. Assume the system is tested under n operation conditions, the mathematical relation of excitations, responses and transfer paths can be cast in a matrix form:

$$\begin{bmatrix} a_1^{(1)} & a_1^{(2)} & \cdots & a_1^{(n)} \\ a_2^{(1)} & a_2^{(2)} & \cdots & a_2^{(n)} \\ \vdots & \vdots & \ddots & \vdots \\ a_m^{(1)} & a_m^{(2)} & \cdots & a_m^{(n)} \end{bmatrix}_{m\times n} = \begin{bmatrix} H_{11} & H_{12} & \cdots & H_{1r} \\ H_{21} & H_{22} & \cdots & H_{2r} \\ \vdots & \vdots & \ddots & \vdots \\ H_{m1} & H_{m2} & \cdots & H_{mr} \end{bmatrix}_{m\times r} \begin{bmatrix} F_1^{(1)} & F_1^{(2)} & \cdots & F_1^{(n)} \\ F_2^{(1)} & F_2^{(2)} & \cdots & F_2^{(n)} \\ \vdots & \vdots & \ddots & \vdots \\ F_r^{(1)} & F_r^{(2)} & \cdots & F_r^{(n)} \end{bmatrix}_{r\times n} \tag{5}$$

$$[a]_{m\times n} = [H]_{m\times r}[F]_{r\times n} \tag{6}$$

in which $\boldsymbol{a_i^{(k)}}$ represents the i-th response at the k-th operation condition, $\boldsymbol{F_j^{(k)}}$ represents the j-th excitation at the k-th operation condition, and $\boldsymbol{H_{ij}}$ is the ratio of $\boldsymbol{a_i}$ to $\boldsymbol{F_j}$. For piston pumps, $\boldsymbol{a_i}$ can be responses that characterize noise/vibration of the unit, such as sound pressure or pump housing vibration acceleration. $\boldsymbol{F_j}$ can be variables such as pressure/flow ripples or bearing forces, which characterize noise/vibration inducing mechanisms of the pump. In sTPA, $\boldsymbol{a_i^{(k)}}$ is a frequency-dependent matrix containing responses such as sound acceleration, velocity or sound pressure, acquired by sound/vibration test. $\boldsymbol{F_j^{(k)}}$ is a frequency dependent matrix acquired from LPM simulation that contains the source magnitude and phase. The independence of excitations can be verified by stacking matrix $\boldsymbol{F_j^{(k)}}$ of different frequencies row-wise and calculating the rank of the stacked matrix. A rank equal to $\boldsymbol{r}$ indicates mutually independent operational excitations.

Given $\boldsymbol{a_i^{(k)}}$ and $\boldsymbol{F_j^{(k)}}$, the i-th row of $[\boldsymbol{H}]$ be estimated as

$$\begin{Bmatrix} H_{i1} \\ H_{i2} \\ \vdots \\ H_{ir} \end{Bmatrix} = ([A]^H[A])^{-1}[A]^H \begin{Bmatrix} a_i^{(1)} \\ a_i^{(2)} \\ \vdots \\ a_i^{(n)} \end{Bmatrix} \tag{7}$$

in which $[A] = [F]^T$. It should be noted that for equation (7) to be valid, the number of operation condition n needs to be greater than or equal to the number of excitations r.

Equation (7) provides a least-square estimate of $\{\mathbf{x}\}_i = [H_{i1} \quad H_{i2} \quad \dots \quad H_{ir}]^T$, such that norm $\|[A]\{\mathbf{x}\}_i - \{\mathbf{b}\}_i\|_2{}^2$ is minimized, in which $\{\mathbf{b}\}_i = \left[a_i^{(1)} \quad a_i^{(2)} \quad \dots \quad a_i^{(n)}\right]^T$. Since the number of operations conditions n is larger than the number of excitations r, overfitting of the transfer path FRF can occur. In order to avoid such overfitting of FRF, a regularized least-square formulation is used to replace equation 7. The regularized least square formulation minimizes $\|[A]\{\mathbf{x}\}_i - \{\mathbf{b}\}_i\|_2{}^2 + \lambda^2\|\{\mathbf{x}\}_i\|_2{}^2$, in which λ is the parameter of regularization. λ is chosen such that generalized cross validation (GCV) function

$$G(\lambda) = \frac{\|[A]\{\mathbf{x}\}_i - \{\mathbf{b}\}_i\|_2^{\,2}}{\left(tr(I - [A]([A]^H[A] + \lambda^2 I)^{-1}[A]^H)\right)^2} \tag{8}$$

is minimized.

It should be noted that different rows of matrix $[F]$ has different units. Consequently, when the least-square formulation is evaluated, the unit system applies different weights to rows of $[F]$. To eliminate the effect of unit system of choice, a normalization process is applied to matrix $[F]$ as

$$[\widetilde{F}] = \begin{bmatrix} F_1^{(1)}/\overline{F_1} & F_1^{(2)}/\overline{F_1} & \cdots & F_1^{(n)}/\overline{F_1} \\ F_2^{(1)}/\overline{F_2} & F_2^{(2)}/\overline{F_2} & \cdots & F_2^{(n)}/\overline{F_2} \\ \vdots & \vdots & \ddots & \vdots \\ F_r^{(1)}/\overline{F_r} & F_r^{(2)}/\overline{F_r} & \cdots & F_r^{(n)}/\overline{F_r} \end{bmatrix}, \tag{9}$$

in which $\overline{\boldsymbol{F_j}}$ are average values for j-th excitation over all operation conditions. Such normalization process makes $[\boldsymbol{A}] = [\widetilde{\boldsymbol{F}}]^{\boldsymbol{T}}$ dimensionless.

The method of sTPA is validated against analytical solutions of baffled pistons. The sound field of a baffled piston can be written as

$$P(\omega) = j\omega c \frac{Qk}{2\pi r} e^{-jkr} \left[\frac{2\mathrm{J}_1(ka\sin\theta)}{ka\sin\theta}\right]. \tag{10}$$

Therefore, the analytical FRF between piston volumetric displacement and radiated sound can be simply cast as P/Q. If r pistons are operating simultaneously with volumetric displacement Q_j respectively, the resulting sound field can be calculated at field points using Equation (10). Providing r different operation conditions of pistons (In this case, operation conditions is represented by independent combos of Q_j.), the problem can be formulated as in Equation (5), and the FRF can be found by sTPA. The results demonstrate total agreement as shown in **Figure 11**.

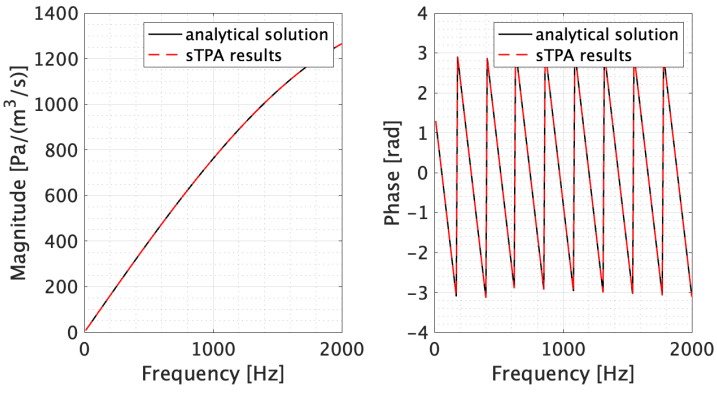

Figure 11 FRF of baffled pistons.

4. RESULTS

A 45cc pump was subjected to testing over 18 different operation conditions. The pump is set to run at a constant speed with two different configurations. Configuration A, a fixed orifice of 5 mm is located next to the outlet port of the pump, followed by a 3 m hose. In configuration B, the fixed orifice and the hose are switched in position. For both configurations, tests were run for three pressure level 50, 175, and 300 bar for three different swashplate angles, 0%, 50%, and 100%. It should be noted that the pump speed is kept constant in the case study, however, the method of sTPA is equally valid for any other pump speed.

In the pump test, two accelerations and a sound pressure are acquired. The placements of the sensors are shown in **Figure 12**. The two accelerometers measure horizontal (Z-axis) a_h acceleration and vertical (Y-axis) acceleration a_v respectively. Sound pressure p is measured 1 meter away at the same vertical level as the pump. An example of sound and vibration measurement results is shown in **Figure 13**.

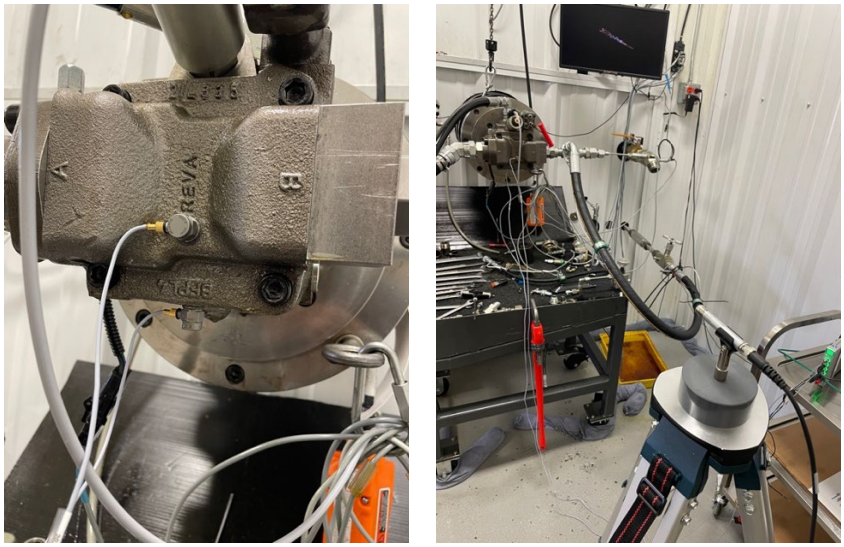

Figure 12 Sensor placement. Left: Accelerometers; Right: Microphone.

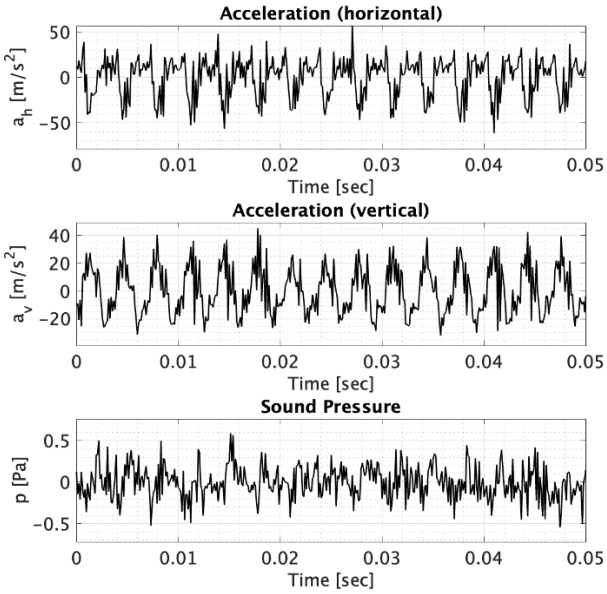

Figure 13 Noise and vibration measurement results. Operation condition: 300 bar, 50% swashplate angle, configuration B.

LPM simulations are conducted for all 18 different operation conditions. The excitations taking into consideration in present study are bearing force component in y-direction (see **Figure 6**) $F_{b,y}$, sealing land moments $M_{sl,x}$ and $M_{sl,y}$ and flow ripple Q_{out}. An example of excitation simulation results is shown in **Figure 14**.

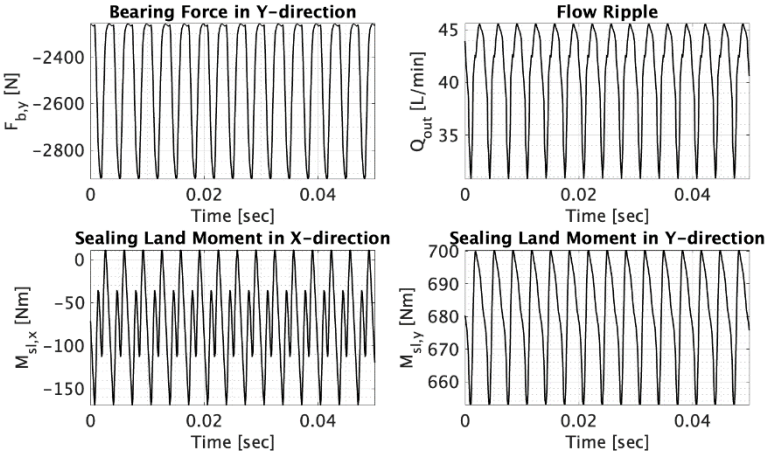

Figure 14 LPM simulation results of excitations. Operation condition: 300 bar, 50% swashplate angle, configuration B.

Due to the cyclic nature of pump operation, Fourier coefficients of both simulation and experiment data are estimated. The phase difference between simulated excitations (**Figure**

14) and sound and vibration measurement results (**Figure 13**) are estimated and compensated by introducing appropriate time delay to the results.

The FRF estimated using sTPA are shown in **Figure 15**. The colour indicates the magnitude of FRF in term of dB. Each value in **Figure 15** indicates the magnitude of noise or vibration caused by a unit of excitation. It can be noticed that the magnitude of FRF's take larger values at higher frequencies. However, larger magnitude of FRF does not necessarily mean the noise and vibration is more significant at particular frequencies. Because the excitations have dominant components at the frequency of piston passage (302 Hz in present study), the spectrum of noise and vibration is also dominated by the components at 302 Hz.

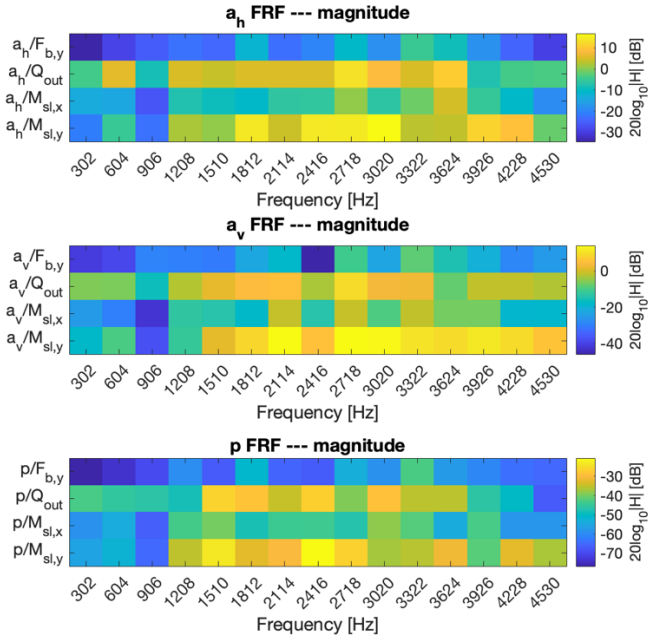

Figure 15 Frequency response functions between excitations ($F_{b,y}$, $M_{sl,x}$, $M_{sl,y}$ and Q_{out}) and responses (a_h, a_v and p).

4.1. Path Contribution

In order to analyse the root-cause of noise and vibration of piston pumps, path contributions are calculated using FRF estimated using sTPA. For the k-th operation condition, path contribution of the j-th excitation to the i-th response is simply $H_{ij}F_j^{(k)}$. The synthesized response is the summation of all the path contributions, that is, $a_i^{(k)} = \sum_{j=1}^{r} H_{ij}F_j^{(k)}$. Path contributions and synthesized responses are complex and can be drawn on complex plane. **Figure 16** shows the path contribution of a operation at piston frequency (302 Hz) as an example. Each solid arrow in the figure represents a contribution from an excitation (bearing force, sealing land moments or flow ripple) to either a vibrational or acoustical response. The solid arrows connect head-to-tail to form the synthesized response. The figure visualizes

the significance of individual transfer paths as well as the cancellation/enhancement between the paths. For instance, in the individual contributions of $F_{b,y}$ and $M_{sl,x}$ to a_h are both significant, yet they cancel against each other because of 130 degrees phase difference. The contributions to a_v, on the other hand, are in phase with each other and contributes evenly to the response. The measurement value is also shown in **Figure 16** for reference. **Figure 17** shows the comparison between synthesized response and measured response in time domain for the corresponding operation condition. The difference between measured response and synthesized response is due to the linear system for H_{ij} being overdetermined.

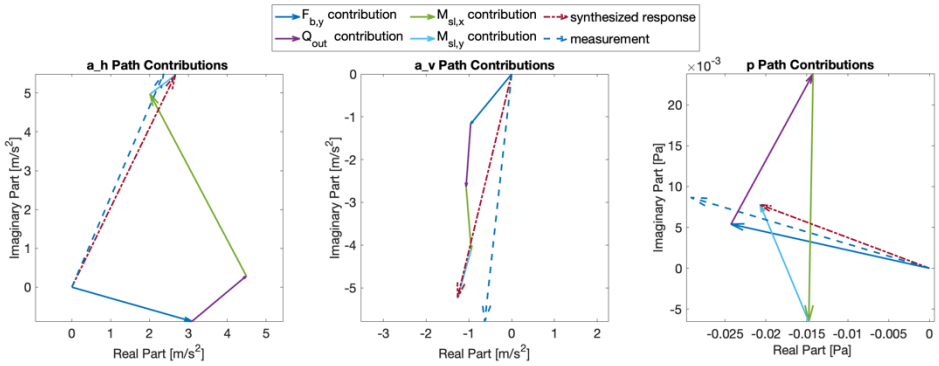

Figure 16 Path contributions. Operation condition: 300 bar, 50% swashplate angle, configuration B. Frequency = 302 Hz.

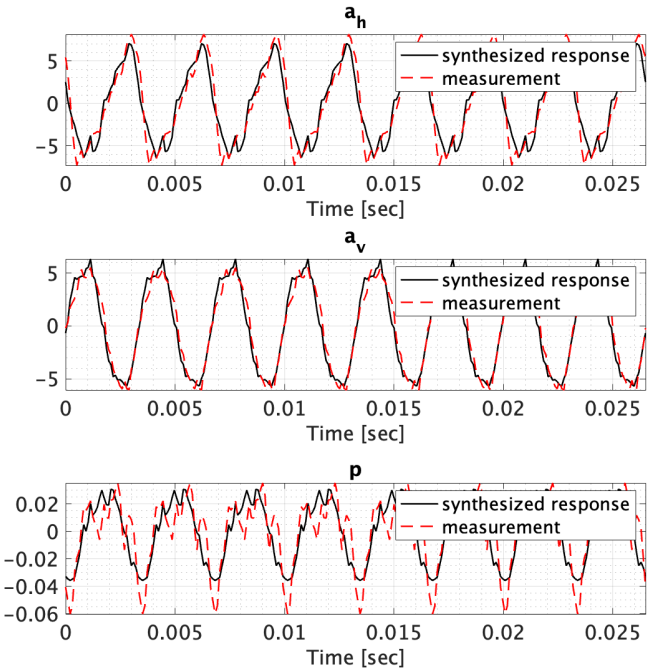

Figure 17 Time domain comparison between synthesized response and measurement.

4.2. Sensitivity analysis

Sensitivity analysis can be conducted based on the information of path contributions. In this study, the sensitivity of noise and vibration responses to excitation magnitudes are analysed. The overall sound pressure or acceleration level is used as the metric of noise/vibration performance of the pump. The overall level of the i-th response is calculated as

$$OL_i = 20\log_{10}\frac{a_{i,rms}}{a_{i,ref}},$$
$$a_{i,rms} = \frac{1}{n}\sum_{k=1}^{n}\sqrt{\sum_{l=-N_f}^{N_f}\left|a_i^{(k)}(f_l)\right|^2}. \tag{11}$$

$a_{i,ref}$ is the reference value for the i-th response and its value is 10 μm/s^2 and 20 μPa for acceleration and sound pressure respectively.

The sensitivities of the three responses (a_h, a_v and p) to the magnitude of the four excitations ($F_{b,y}$, $M_{sl,x}$, $M_{sl,y}$ and Q_{out}) are shown in **Figure 18** The magnitude of each excitation is set to independently vary over a ±20% range (the change of one excitation does not affect other excitations), and the overall levels of synthesized responses are evaluated. The red dashed lines in the figures indicate the reference point. As shown in the figure, all the curves are monotonically increasing, which implies the positive correlation between force/moment/ripple excitations and noise/vibration responses. The figure also indicates potentials of noise and vibration control. For example, overall sound pressure level can be decreased by 0.55 dB if the oscillations in bearing force decreases by 20%, overall horizontal acceleration decreases by 0.61 dB if X-moment oscillation decreases by 20%. Similar analysis can be conducted for excitation phase.

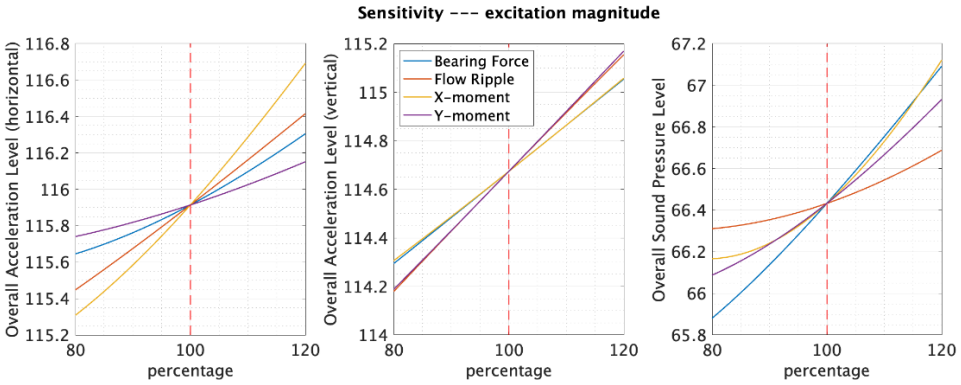

Figure 18 Sensitivity of noise and vibration response to excitation magnitudes.

A further comment on the generality of the sensitivity analysis needs to be emphasized. In such analysis, it is assumed that the transfer paths are not altered as parameters vary. For example, the graph shown in **Figure 18** can be interpreted as predictions of pump noise and vibration, only if the magnitude of excitations can increase/decrease without changing the characteristics of transfer paths. On the other hand, if the change of parameter is associated

with change in pump design, the parameter sensitives is not predictive, and sTPA can only be seen as an additional analysis to close the gap between LPM simulation and pump NVH.

5. CONCLUSION

sTPA is a tool that bridges the gap between LPM calculation results and air-borne noise/vibration performance of hydraulic pumps and provides insights to the root-cause of noise and vibration problems of axial piston pumps. The FRF estimated via sTPA indicates the quantitative relation between internal excitations (forces, moments, ripples etc.) calculated in LPM and consequent noise and vibration. Path contributions estimated in sTPA demonstrate how different sources of noise and vibration add up to the overall noise and vibration effect of the pump and highlights the most significant noise/vibration contributor. Based on the sensitivity analysis of sTPA, the potential pump noise/vibration control measures can be evaluated in terms noise/vibration level decrement.

6. REFERENCES

[1] Schleihs, C. (2017). Acoustic Design of Hydraulic Axial Piston Swashplate Machines. *Reihe Fluidtechnik*, 89. RWTH Aachen University.

[2] Helgestad, B. O., Foster, K. and Bannister, F. K. (1974). Pressure transients in an axial piston hydraulic pump. *Proceedings of Institution of Mechanical Engineers*. 188(1):189-199.

[3] Yamauchi, K. and Yamamoto, T. (1976). Noises generated by hydraulic pumps and their control method. *Mitsubishi technical review*, 13(1).

[4] Kim, T. and Ivantysynova, M. (2017). Active Vibration Control of Swash Plate-Type Axial Piston Machines with Two-Weight Notch Least Mean Square/Filtered-x Least Mean Square (LMS/FxLMS) Filters. *Energies*. 10(5):645.

[5] Harrison, A. M. and Edge, K. A. (2000). Reduction of axial piston pump pressure ripple. *Proceedings of Institution of Mechanical Engineers*, *Part I: Journal of Systems and Control Engineering*. 214(1):53-64.

[6] Ortwig, H. (2005). Experimental and analytical vibration analysis in fluid power systems. *International Journal of Solids and Structures*. 42:5821-5830.

[7] Rebel, J. (1977). Active liquid noise-suppressions in oil hydraulics. *VDI-Z*. 119:937-943.

[8] Manco, S., Nervegna, N., Lettini, A. and Gilardino, L. (1999). An experience in simulation: the case of a variable displacement axial piston pump. *JFPS International Symposium on Fluid Power.*

[9] Manco, S., Nervegna, N., Lettini, A. and Gilardino, L. (2002). Advances in the simulation of axial piston pumps. *JFPS International Symposium on Fluid Power*.

[10] Ivantysyn, J. and Ivantysynova, M. (2001). *Hydrostatic pumps and motors*.

[11] Van der Seijs, M., de Klerk, D. and Rixen, D. (2015). General framework for transfer path analysis: History, theory and classification of techniques. *Mechanical Systems and Signal Processing*. 68-69: 217-244.

[12] de Klerk, D. and Ossipov, A. (2010). Operational transfer path analysis. *Mechanical Systems and Signal Processing*. 24: 1950-1962.

[13] de Sitter, G., Devriendt, C., Guillaume, P. and Pruyt, E. (2010). Operational transfer path analysis. *Mechanical Systems and Signal Processing*. 24: 416-431.

[14] Roozen, N. B. and Leclère, Q. (2013). On the use of artificial excitation in operational transfer path analysis. *Applied Acoustics*. 74: 1167-1174.

[15] Sievi, A., Martner, O. and Lutzenberger, S. (2013). Noise Reduction of Trains Using the Operational Transfer Path Analysis – Demonstration of the Method and Evaluation by Case Study. In: Maeda, T., et al. Noise and Vibration Mitigation for Rail Transportation Systems. *Notes on Numerical Fluid Mechanics and Multidisciplinary Design*, vol 118. Springer, Tokyo.

Enhancing System Performance in Subsea and Off-Highway Applications: A High-Fidelity, Transient Dynamic CFD Analysis Approach

Vignesh Jeganathan[1,*], Rayhan Ahmed[1], Yawei Chen[1], Shyam Sundar Pasunurthi[1], Ashutosh Pandey[1], Emanuele Gnesi[2], Raju Kalidindi[2], Bipin Kashid[2], Howard Zhang[2]

[1]*Simerics, Inc.*
[2]*Parker Hannifin Corporation*
[*]*Corresponding Author, E-mail:* vj@simerics.com

Abstract

In hydraulic fluid power engineering, the need for reliability and high efficiency in system components, including valves and pumps, is paramount. This requirement becomes even more critical in tough operational environments, such as off-highway and subsea applications, which require both robust durability and optimal operational efficiency. Computational Fluid Dynamics (CFD) simulations are often used to address these demands and assume a pivotal role during product development. This paper demonstrates the use of CFD simulations as a tool to study the operations of a solenoid valve and a vane pump, which are used in subsea and off-highway applications. Our research employs 3D CFD simulations to examine complex transient dynamic phenomena such as two-piece poppet separation in solenoid valves and vane translation in the vane slots of vane pumps. By modeling these complex transient dynamics, we illustrate how CFD can identify problems that are difficult to test experimentally, and offer valuable insights for enhancing performance.

Keywords: subsea, off-highway, valves, vane pumps, CFD, cavitation, performance prediction, design improvement.

River Journal, 1–27.
© 2024 *River Publishers. All rights reserved.*

1 Introduction

Hydraulic systems are the critical infrastructure behind a wide array of industrial operations, powering machinery across the demanding landscapes of off-highway and subsea applications. The cornerstone of the effectiveness of these systems lies in the performance, reliability, and efficiency of key components, particularly pumps and valves. The pump is the main driving component that delivers the high pressure working fluid for the desired function of an hydraulic system, whereas the valves act as working fluid control components. The complexity of fluid behaviors and transient dynamics present in these components presents a significant challenge, often outpacing the capabilities of traditional design and testing methodologies to predict and mitigate issues that could undermine component functionality.

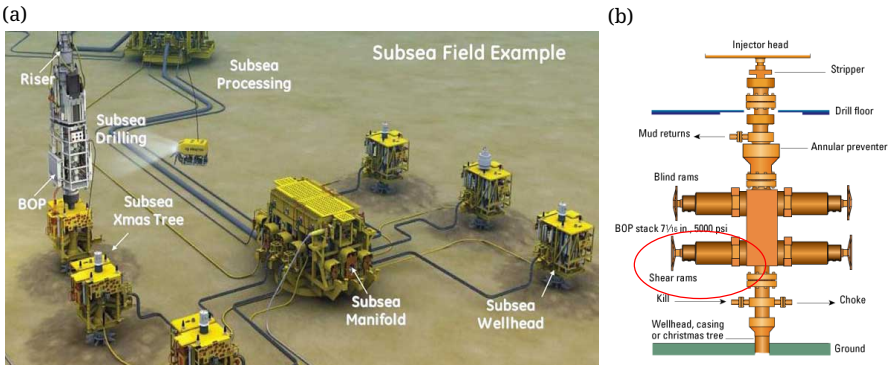

Figure 1 Components of (a) a subsea production system showing a Blow-Out Preventer (BOP), and (b) a BOP. Red circle highlights the shear ram which contains a pilot valve as one of its components.

The primary design criteria for components are determined by their unique applications and the variations among them. The components used in subsea applications (figure. 1 a) are required to resist extreme corrosive sea conditions, high deep-sea pressures, and severe temperatures, while also maintaining high levels of reliability and efficiency [1]. A range of proven and validated best practices [2–4] guide the design process of subsea valves and pump components. Off-highway hydraulic systems (figure. 2 a), which are used in sectors such as agriculture, construction, earth moving and material handling, have their unique design requirements. Given the substantial role of off-highway applications in total greenhouse gas emissions, it is crucial

to minimize fuel costs and emissions. Therefore, there are ongoing efforts to create cost-effective electric-hydraulic systems [5–7].

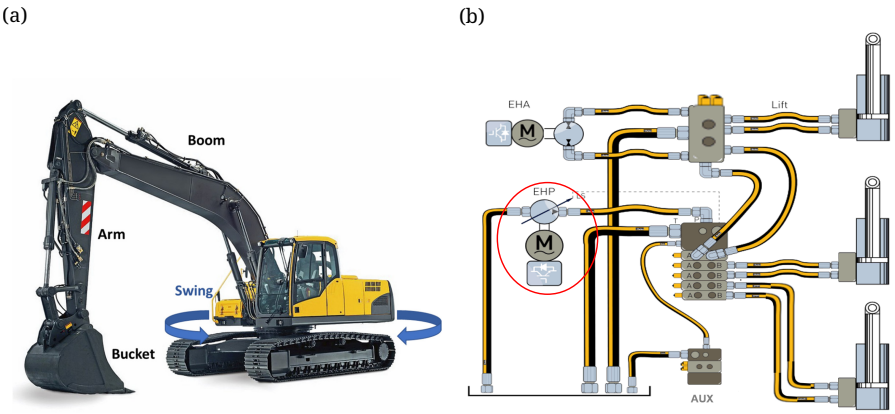

Figure 2 Schematic of (a) an off-highway equipment [7] and (b) hydraulic system used in the off-highway equipment. Red circle highlights the positive displacement pump studied in the current work.

In addition to adhering to design standards, it is crucial to optimize a component's fluid flow characteristics to ensure the optimal operation of both subsea and offshore equipment, considering their rigorous demands. CFD has been instrumental in achieving this for many years. A detailed investigation [8] using CFD on ball check valves has underscored the impact of cavitation on flow under varying pressure drop scenarios across the valve. Notably, it has revealed that the flow coefficient is not fixed but depends on the cavitation number. In a computational study of subsea safety valves [9], the integration of CFD with nonlinear finite element analysis (FEA) simulations has provided insight into the stresses triggered by high-pressure solid substances that could exceed design thresholds. The functionality of a two-way control valve in a hydraulic system is enhanced by applying CFD [10]. CFD has also been used to investigate the functioning of a double-acting vane pump, which incorporates vane dynamics [11], which has applicable benefits in power split transmission systems.

Parker Hannifin adopts an all-encompassing multiphysics simulation strategy to meticulously scrutinize and optimize hydraulic systems. Our methodology integrates 1D, FEA, 3D FEA, and CFD simulations, supplemented by co-simulations and proactive simulation-guided optimization studies. Central to our approach is a rigorous validation and verification

framework, which ensures that our simulations serve as accurate proxies for real-world performance [12]. This paper aims to showcase our endeavor to explore the intricate transient dynamic behavior of a solenoid valve and a vane pump, driven by flow, using the sophisticated 3D CFD software, Simerics MP+.

The solenoid valve presented in this study is a part of the shear ram, which in turn is an integral part of a Blow-Out Preventer (BOP) [13]. A BOP (as shown in the figure. 1 b) is a device used in subsea systems to prevent crude oil or natural gas from spilling uncontrollably from a well. In this paper, we study this specific solenoid valve also called the pilot valve for cavitation and valve body forces. The primary challenge addressed is the phenomenon of two-piece valve body separation during valve travel, a complex transient dynamic behavior difficult to predict and optimize in experiments.

The second device, a vane pump, is used in an off-highway electric-hydraulic mobile system, specifically coupled with an electric motor as shown in the figure. 2 b. In this section, our aim is to discuss the cavitation and flow characteristics of a vane pump design. after meticulous modeling of transient dynamics, such as vane motion within the slots.

1.1 Solenoid valve

The solenoid valve we discuss in the paper is solenoid operated and is shown in figure. 3a. The valve body comprises three disconnected parts: a solenoid, a pin, and a poppet whose diameters are around 0.2 m. The poppet is the actual body that seals the ports. The solenoid and poppet have pre-compressed springs that tend to push them inward towards the center of the valve. When the solenoid is deactivated, the spring forces position the valve bodies onto the right valve seat, meaning the right poppet seat blocks the flow between the inlet and intermediate pressure ports. This also connects the intermediate and outlet ports. When the solenoid is actuated to add additional force, the valve bodies move from right to left, and the left poppet seat sits on the left valve seat, sealing the intermediate port and the outlet, meanwhile, enabling the flow between the inlet and the intermediate ports. The spring and solenoid actuation forces are outlined in the free-body diagram depicted in the figure. 3b. The valve uses 95% water and 5% glycol mixture as a working fluid at 25 °C, whose properties are similar to water. The saturation pressure of this mixture is 3.169 kPa, which is required for cavitation study. The inlet is kept constantly at high pressure of 22.6 MPa, while the outlet is kept at atmospheric pressure of 101 kPa. The intermediate port is spring loaded and

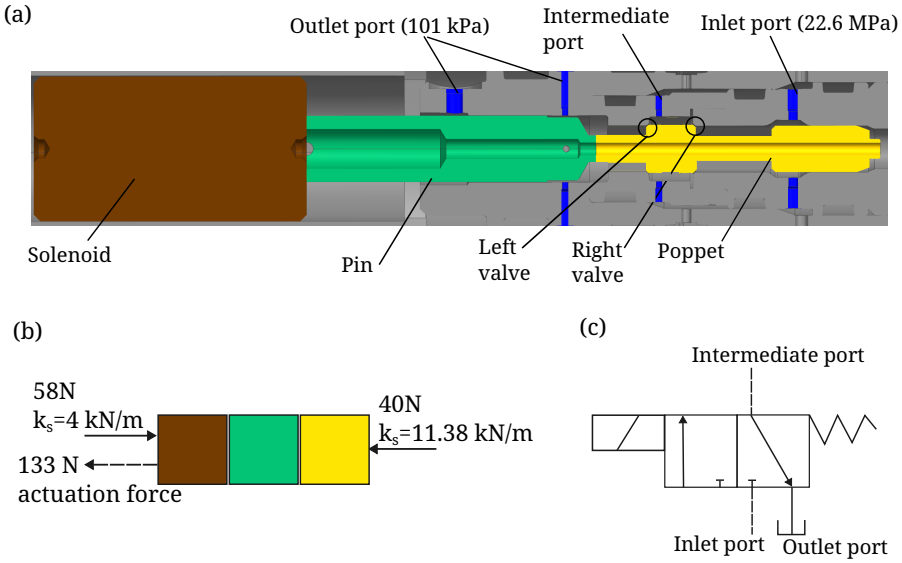

Figure 3 (a) Cross section of solenoid operated valve showing valve bodies and ports. (b) Free-body diagram showing the spring and solenoid forces, and the spring constants. (c) Hydraulic symbol of the pilot valve.

is either at high or atmospheric pressure depending on the position of the poppet. The valve can be represented using a hydraulic symbol as shown in figure. 3c.

1.2 Vane pump

The vane pump shown in figure. 4 comprises of a few parts: the inlet, the outlet, and the rotor chamber that houses the rotor and the vanes. The rotor has a radius of approximately 2.275×10^{-2} m. As the rotor rotates, the fluid is pressurized and displaced from the inlet to the outlet by vanes. The vanes move radially back and forth inside the vane slots based on pressure, spring, and centrifugal forces. The fluid volume inside the rotor chamber that depicts vane fluid volumes and cam profiles is shown in the figure. 4 b. The silicone fluid at 45 °C with a density of 857 kg.m^{-3} and a viscosity of 2.742 $\times 10^{-2}$ Pa.s is used as a working fluid. The saturation pressure required for cavitation study is set to be 133 Pa.

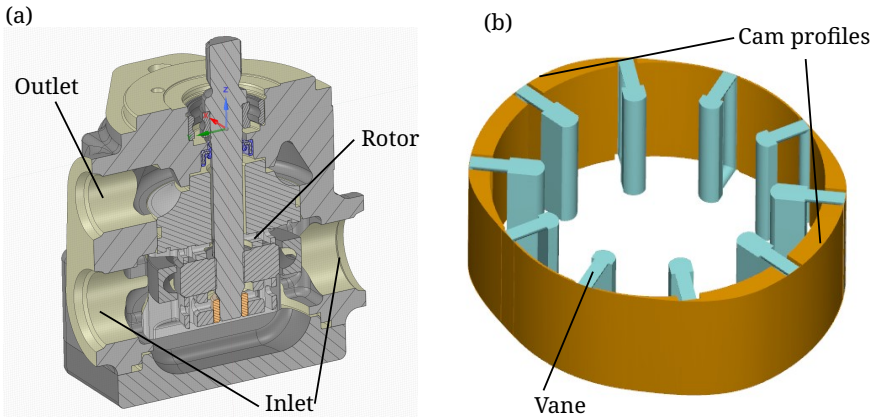

Figure 4 (a) Cross section of vane pump assembly. (b) Fluid volume enclosed in the rotor chamber

2 Numerical models

2.1 Computational Fluid Dynamics model

In a CFD simulation, Navier-Stokes equations that govern the fluid flow are solved numerically to determine the fluid velocity and pressure in the system.

The spatially averaged mass and momentum conservation equations can be written in integral form as follows:

$$\frac{\partial}{\partial t}\int_{\Omega(t)} \rho d\Omega + \int_{\sigma} \rho(v - v_\sigma).n d\sigma = 0, \tag{1}$$

and

$$\frac{\partial}{\partial t}\int_{\Omega(t)} \rho v d\Omega + \int_{\sigma} \rho v((v - v_\sigma).n) d\sigma = \int_{\sigma} \tau.n d\sigma - \int_{\sigma} P n d\sigma + \int_{\Omega} f d\Omega. \tag{2}$$

In the above equations, ρ is density of the working fluid, v is spatially averaged velocity vector, v_σ is velocity of a moving reference frame, τ is deviatoric stress tensor, P is the pressure and f represents the body force e.g. gravity. σ and Ω under the integral represent the surface and volume integrals respectively.

The standard $\kappa - \epsilon$ two equation model with wall function is used to account for turbulence as follows:

$$\frac{\partial}{\partial t}\int_{\Omega(t)} \rho\kappa d\Omega + \int_{\sigma} \rho((v - v_\sigma).n)\kappa d\sigma = \int_{\sigma} (\mu + \frac{\mu_t}{\sigma_\kappa})(\bigtriangledown\kappa.n)d\sigma + \int_{\Omega} (G_t - \rho\epsilon)d\Omega, \quad (3)$$

and

$$\frac{\partial}{\partial t}\int_{\Omega(t)} \rho\epsilon d\Omega + \int_{\sigma} \rho((v - v_\sigma).n)\epsilon d\sigma = \int_{\sigma} (\mu + \frac{\mu_t}{\sigma_\epsilon})(\bigtriangledown\epsilon.n)d\sigma + \int_{\Omega} (c_1 G_t \frac{\epsilon}{\kappa} - c_2\rho\frac{\epsilon^2}{\kappa})d\Omega. \quad (4)$$

κ is spatially averaged turbulent kinetic energy, ϵ is spatially averaged dissipation of turbulent kinetic energy, μ_t is turbulent viscosity, c_1 and c_2 are model constants, and G_t is a turbulent kinetic energy production source term.

To account for cavitation/aeration, the cavitation model proposed by Singhal et. al. [14] is implemented in Simerics-MP+. It accounts for real liquid properties, cavitation, aeration, and liquid compressibility. The following formulation describes the cavitation vapor distribution.

$$\frac{\partial}{\partial t}\int_{\Omega(t)} \rho f_v d\Omega + \int_{\sigma} \rho((v - v_\sigma).n)f_v d\sigma = \int_{\sigma} (D_{f_v} + \frac{\mu_c}{\sigma_{f_v}})(\bigtriangledown f_v.n)d\sigma + \int_{\Omega} (R_e - R_c)d\Omega \quad (5)$$

Where, f_v is volume fraction of vapor of the working fluid, D_f is the diffusivity of the vapor mass fraction and σ_f is the turbulent Schmidt number. In the present study, these two numbers are set equal to the mixture viscosity and unity, respectively. The vapor generation term, R_e and the condensation rate, R_c are modelled as follows:

$$R_e = C_e \frac{\sqrt{K}}{\sigma_l}\rho_l\rho_v \left(\frac{2}{3}\frac{(p - p_v)}{\rho_l}\right)^{1/2}(1 - f_v - f_g) \quad (6)$$

$$R_c = C_c \frac{\sqrt{K}}{\sigma_l}\rho_l\rho_v \left(\frac{2}{3}\frac{(p - p_v)}{\rho_l}\right)^{1/2}(f_v) \quad (7)$$

Where, model constants are $C_e = 0.02$ and $C_c = 0.01$. The final density calculation for the mixture is done by,

$$\frac{1}{\rho} = \frac{f_v}{\rho_v} + \frac{f_g}{\rho_g} + \frac{1 - f_v - f_g}{\rho_l} \tag{8}$$

Non-condensable gas (NCG) is considered as either a free gas or a combination of free gas and dissolved gas. Different models are implemented in Simerics-MP+ that account for both the components of NCG. More details are available in the software manual [15]. In the solenoid valve simulation, the constant gas mass fraction model is used which only captures the free gas component of the air. An equilibrium dissolved gas model is used in the simulation of the vane pump. The model captures both the free and the dissolved components of the air.

The above set of equations is discretized using a finite volume approach and solved using a pressure-based solution algorithm. Spatial terms and temporal terms are handled using second order upwind and second order explicit schemes, respectively. SIMPLE-S (Semi-Implicit Method for Pressure Linked Equations–Simerics) algorithm is used to solve the pressure-velocity coupling equation [16, 17].

2.2 Translation dynamics model

A rigid body motion without considering the fluid-structure interaction is implemented in Simerics-MP+. This kind of dynamics needs conservation of linear momentum equation to be solved for translation rigid body motion.

The governing equation based on the conservation of linear momentum is given as

$$m\frac{d^2s}{dt^2} = F_{hydrodynamic} - F_{damping} - F_{spring} - F_{friction} + F_{additional} \tag{9}$$

In Simerics-MP+, the governing equation is solved for the displacement of the moving body along with the flow and cavitation governing equations.

Where, m is the mass of the moving body, s is the displacement of the moving body under the influence of the net force, $F_{hydrodynamic}$ is the fluid force due to pressure and shear forces, $F_{damping}$ is a damping force that can be due to damping action of a spring (if any) or due to any other external component, F_{spring} is a spring force, which is usually an opposing force, $F_{friction}$, is an opposing force due to frictional contact between the moving

and the stationary bodies, $F_{additional}$ is any other external force acting on the moving body.

The displacement of the rigid body can also be prescribed as a constant value or a function of time. In this case, the linear momentum conservation equation is not solved.

2.3 Cavitation damage prediction model

Cavitation erosion, a phenomenon where high-energy release from imploding vapor bubbles can erode solid material, occurs under specific conditions. Bubbles form in zones where the pressure dips below the operating fluid's vapor pressure, only to collapse when they move to areas where the pressure exceeds this vapor pressure. This process of formation and implosion of bubbles in different pressure zones leads to cavitation erosion. In the solver, on a boundary of interest, the rate of change of cavitation bubble volume and bubble damage power are calculated. These two variables provide an indication of cavitation damage.

The rate of change of cavitation bubble volume is calculated as a total derivative with respect to time, which considers both the temporal and spatial variation of the bubble volume.

$$Bubble\ volume\ change\ rate = \frac{DV}{Dt} \tag{10}$$

Where, V is the volume of the bubble. The cavitation bubble damage power is calculated as

$$Cavitation\ bubble\ damage\ power = \frac{D(pV)}{Dt} \tag{11}$$

Where, p is the local pressure.

3 Mesh details

The fluid volumes are imported into Simerics-MP+ in stereolithography (STL) format. Fluid volume STLs are separated into stationary, moving (rotating or sliding), and deforming (valve ends) volumes. Fluid volumes are meshed using body-fitted binary tree mesh, which has several advantages [18] ranging from cubic cells offering orthogonality to an optimal transition between different length scales and resolutions. The Mismatched Grid Interface (MGI) feature in Simerics-MP+ is used to connect moving or stationary

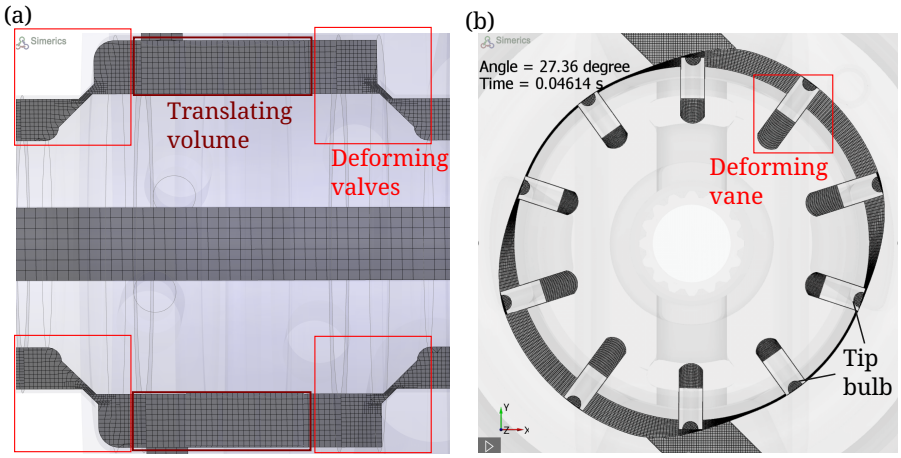

Figure 5 Cross section of (a) valve mesh showing translating and deforming meshes, and (b) vane mesh showing stationary, rotating and deforming meshes

neighbor mesh volumes. The deforming and moving meshes are changed internally every timestep by mapping the coordinates to a new coordinates based on the application by volume remeshing feature of Simerics MP+. For example, valves require expansion and contraction of the mesh coordinates, whereas pumps require rotation of the coordinates, which are handled internally by Simerics MP+ using volume remeshing feature.

Solenoid valves have valve bodies that translate in a single direction back and forth to seal the ports. In figure. 5 a, we point out the fluid volumes that are translating and deforming. The force interaction between the valve bodies and fluid is handled using the translation dynamic module. The translation module provides two methods for moving the valve bodies by remeshing: 1. Force balance mode that uses eqn. (9) where the valve moves on the basis of forces such as those of the spring and fluid acting on the valve bodies, and 2. prescribed motion mode that manually moves the valve body using valve displacement as a function of time.

A cross section of the vane pump mesh is shown in figure. 5 b. The vane pump model is setup using the “Vane” template of Simerics-MP+. The template enables the movement and deformation of the mesh in the vane volume as the vanes move with the rotor. In addition to remeshing volumes, it applies the appropriate boundary conditions, i.e. the rotation boundary condition, to the rotor surfaces. The template can also handle axial asymmetry in the rotor profiles with great ease. As the rotor rotates, the vane volume mesh com-

presses and expands depending on the distance between the cam, vane tip and rotor. The template can handle fixed-, variable-displacement, and balanced-vane configurations. In this study, we limit our scope to a balanced vane pump. The tip bulb dynamics is also simulated in this study using the "Radial Piston" template of Simerics-MP+. The Radial Piston template governs the mesh compression and expansion between the vane tip and the cam as the rotor rotates. The effect of spring loading on the vane motion and its effect of mesh compression and expansion between vane tip/cam as well as vane/rotor are also taken into account using the 1D translation dynamics module, similar to the valve mesh.

4 Results and discussion

In this section, we show the CFD simulation results of a few designs of a Parker Hannifin's valve and pump, used during the rigorous design process. Before the analysis, a grid independence study is performed to select the appropriate mesh for all the cases discussed. The appropriate mesh involves adequately resolving the annular, leakage, and side gaps in both the equipment. All the results presented have an error bar less than 5%, although they are not explicitly presented. All simulations are converged to 10^{-2} residual drop.

4.1 Solenoid Valve

4.1.1 Cavitation damage

In a solenoid valve, just when the valve body opens or closes the passages to allow or restrict flow, the flow velocity in the narrow passage is very high. Large velocities cause a massive pressure drop, and, when the pressure drops below the vapor pressure, cavitation bubbles form. This occurs predominantly in water-based equipment, such as this valve. The regions where such cavitation occurs is the narrow passage between the poppet seats and the cylinder surface as shown in the figure. 3, where the velocities are usually high. These cavitation bubbles often collapse when they enter the region of higher pressure. If cavitation bubbles collapse on the valve surfaces, they can damage the valve surfaces. When bubble collapses occur on poppet seats, sealing surfaces can be damaged, resulting in inadequate sealing. After repeated use of one of our prototype valves, we have observed cavitation damage marks on the sealing poppet surface, as shown in the figure. 6 a.

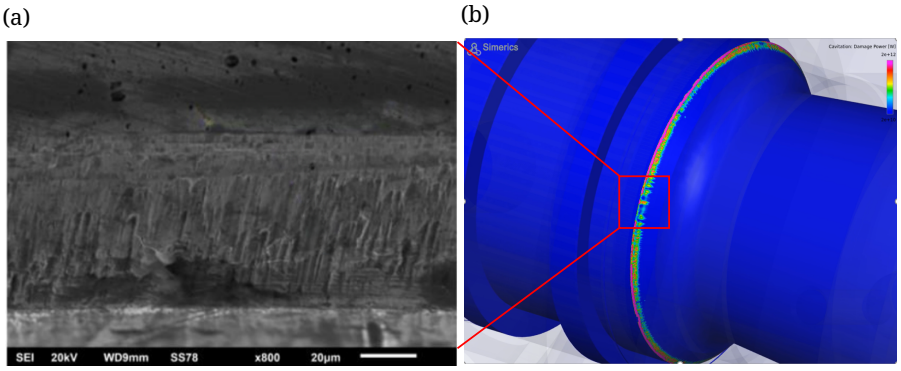

Figure 6 (a) Picture of pitting due to cavitation damage on the poppet surface removed from a valve after lab testing. (b) Cavitation damage power predicted by Simerics-MP+ on the poppet surface

Given that cavitation can shorten a valve's lifespan through metal surface erosion and induce high system vibration, it is crucial to engineer a valve design that minimally succumbs to cavitation. By leveraging 3D CFD, cavitation can be studied effectively using a variety of models coupled with the Navier-Stokes equation. We set out to use CFD to test the prototype that has shown cavitation damage in our experiments. The inlet boundary condition is kept at high pressure of 22.6 MPa, whereas the intermediate and outlet ports are at atmospheric pressure of 101 kPa. We use a constant gas cavitation model to account for cavitation and the translation dynamics model to move the valve bodies using prescribed motion. In this case, the valve body moves from right to left with reference to the figure 3.

We present the figure. 6 b that shows the damage power calculated by Simerics MP+ as a result of bubble collapse on the poppet, when the valve is just opening. The simulation clearly points out that the cavitation damage would occur on the poppet seat, which is in agreement with the pictures shown previously in the figure. 6 a. Since CFD can be a reliable tool for studying cavitation, it can be used to test various designs to find designs that show minimal cavitation damage. In addition to identifying potential cavitation damage areas, cavitation models contribute key physics to a CFD model that can improve overall accuracy of global parameters such as outlet pressures and volumetric flow rates.

4.1.2 Valve body forces

The forces that act on the valve bodies at any given time are the spring and fluid forces. Fluid forces can be categorized into shear forces and pressure forces. When the valve moves, the pressure forces dominate the shear forces due to the immense pressure range (22.6 MPa to 101 kPa) at which these valves operate. These pressure forces, in addition to the spring forces that act on the valve bodies, dictate whether a given valve would operate as expected. In other words, during the movement of the valve body, fluid pressure forces and spring forces can either support or oppose the valve motion. Hooke's law typically provides a straightforward calculation for the spring forces, leaving the fluid pressure forces as the only forces to be determined in order to predict the motion of the valve.

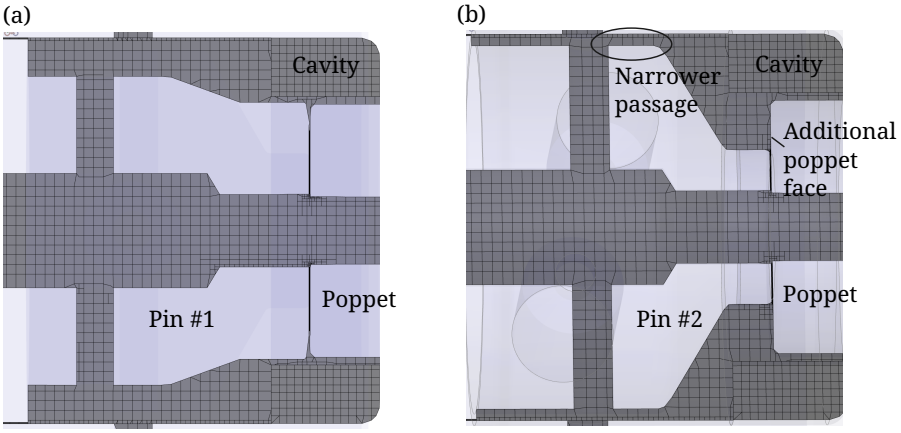

Figure 7 Mesh zone between pin and poppet of (a) #1 pin design, and (b) #2 pin design.

To highlight the importance of studying fluid pressure forces, we present two design concepts of the pin that have been used in Parker Hannifin's meticulous design process in figure. 7 a and b. The second design has two key differences: 1. an additional surface on the poppet body in the cavity where pin and poppet touch each other, and 2. the passage connecting the valve chamber and the intermediate ports is narrower. During laboratory tests, we have observed that when the solenoid is actuated, both designs work as expected, i.e. the valve bodies move from the right valve seat to the left with reference to the figure. 3. However, when the solenoid is turned off, the first design sometimes has difficulty moving the valve body from left to right due to valve instability and hence the inlet and the intermediate ports stay connected. This is not observed in the second design. Since the spring forces

are the same between the two designs, the fluid pressure force is the only difference between the two designs and needs to be investigated.

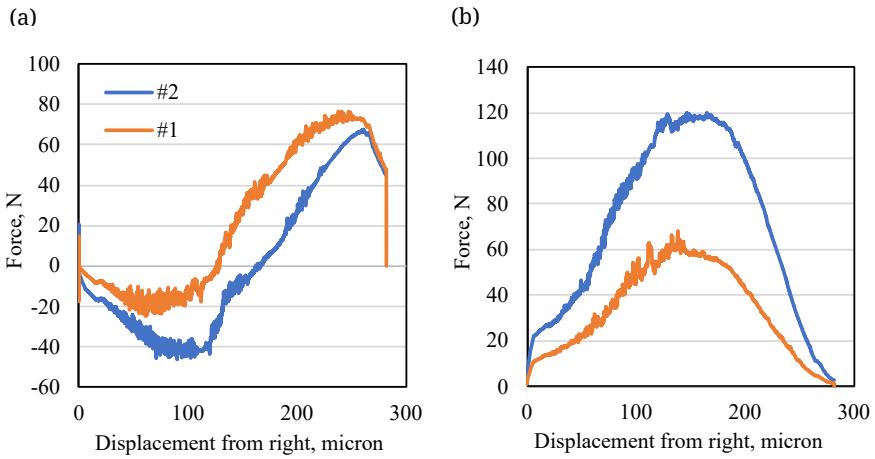

Figure 8 Forces on (a) the poppet and (b) the pin, for two pin designs when valve moves from right to left. Positive force promotes the valve motion in the desired direction

We have performed CFD simulations to predict fluid pressure forces on the valve bodies. To simplify the simulations, we assume that the three valve bodies move together, although it is possible for the valve bodies to separate and combine when traveling. Since we know the valve movement time from the tests, we have used prescribed motion to move the valve manually over $0.5s$, without considering any spring forces. For the intermediate, inlet and outlet port pressure boundary conditions, we use the test data measured by the pressure transducers. We use the same numerical models we used in the cavitation study shown in the previous section. To find the pressure forces on the valve body, we compute the integral of the pressure over the valve body area. We present forces with sign convention such that the positive force helps move the valve in the desired direction, whereas the negative force hinders the valve from moving in the desired direction.

In figure. 8a and b, we present the pressure force on poppet and pin bodies respectively as a function of valve displacement, when the solenoid is actuated i.e. when the valve bodies move from right valve seat to left valve seat. In both designs, fluid forces mostly encourage the solenoid to move the valve bodies in the desired direction. The forces on the poppet and the pin are different in magnitude but have the same direction meaning, there

is a possibility of valve bodies splitting but still moving in the desired direction. Note that the highest hindering force occurs in the poppet when the displacement is around 100 microns. We hypothesize that the hindering force can be overcome by the poppet's spring force of 40 N since they are of the same order. It is also important to note that during force-balanced valve body motion, the inertial forces of valve bodies can also work with spring force to overcome undesirable fluid forces. These reasons could potentially explain why both designs have performed well when the solenoid is actuated during lab tests.

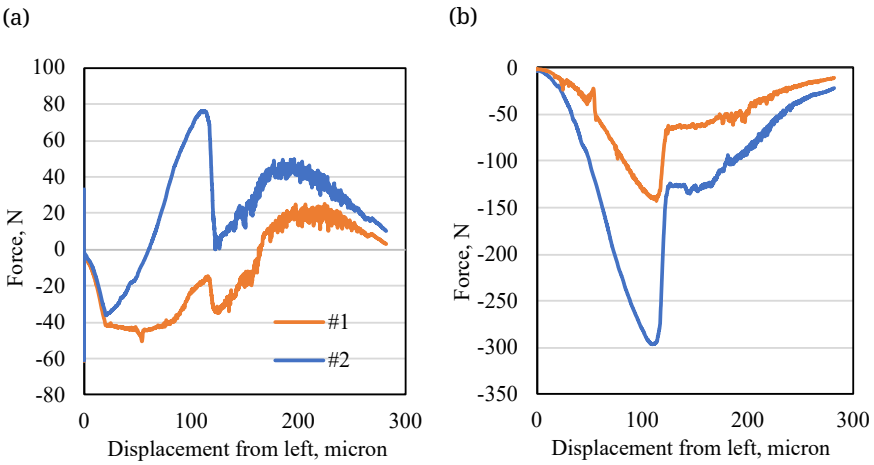

Figure 9 Forces on (a) the poppet and (b) the pin for two pin designs when valve moves from left to right. Positive force promotes the valve motion in the desired direction.

When the solenoid is switched off, there is no more solenoid force to keep the valve bodies on the left valve seat. The spring forces on the valve bodies will tend to push the valve back to the right. Figure 9 a shows the fluid forces on the poppet, for both designs. The poppet on the first design experiences a force that opposes the movement of the valve body. Unlike previously where the poppet's spring force has helped the poppet overcome fluid resistance, here the poppet's spring force is $-40N$, which does not help the poppet move in the desired direction. However, for the second design, the fluid forces mostly encourage the movement of the poppet. This could explain why the second design performed better than the first in the tests. In figure 9 b that shows the forces on the pin of two designs, we point out that the pin forces are acting in the undesired direction. The pin is pushed towards the left, while the poppet is moving towards the right, as we observe in Figure

9 a. These opposing forces can cause the poppet and pin to split and move in opposite directions. However, this will not affect the function of the valve because the poppet that does the actual sealing tends to move in the desired direction.

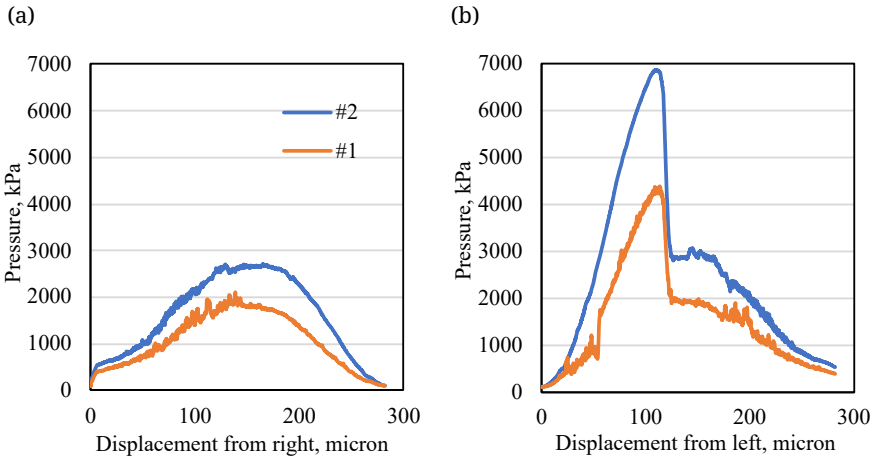

Figure 10 Cavity pressure as a function of displacement for two poppet designs when the solenoid is (a) on and (b) off

To explain the differences in forces between the pin and the poppet, we now examine the cavity between the poppet and the pin. In fact, the pressure built up in this cavity can influence the forces of the valve bodies, and therefore the splitting of the valve bodies. The figure. 10 a shows the cavity pressure of two designs when the valve body moves from right to left. Both designs show similar trends, and the second design has higher cavity pressures. We observe the same phenomenon in the figure. 10 b when the valve body moves from left to right. This can be explained by the narrow passage in the second design. The narrow passage of the second design can throttle the flow, resulting in pressures higher than those of the first design. Also, the higher cavity pressures in the second design is a plausible explanation for why we observe larger forces overall for the second design in the figures. 8 and 9. To visualize the high and low cavity pressures in the first and the second designs, respectively, we present the figure. 11 a and b when the valve bodies move from left to right at displacement of 100 microns from the left valve seat.

In both designs, when the valve bodies are moving towards the left, we hypothesize that the cavity pressure imparts forces on the valve bodies and

hence is responsible for splitting the valves. However, these cavity pressures are not high enough to impose opposing forces on the pin and the poppet to move them in the oppposite direction. When the valve bodies move towards the right, the cavity pressure reaches as high as 6894 kPa for the second design as shown in figures 10 b and 11 b. The second design also has an additional surface on the poppet side of the cavity as a design feature as seen in figure. 7 b. We hypothesize that high cavity pressures impart massive forces on the poppet's additional surface and the pin, as seen in figure 9 a and b. This could result in splitting of the pin and poppet, moving them in opposite directions, specifically pushing the poppet in the desired direction. Massive cavity pressure and an additional poppet surface are absent in the first design, as seen in the figures. 10 b, 11 b, and 7 c. Hence, the first design did not have adequate desirable force to move the poppet in the desired direction, when the solenoid is turned off.

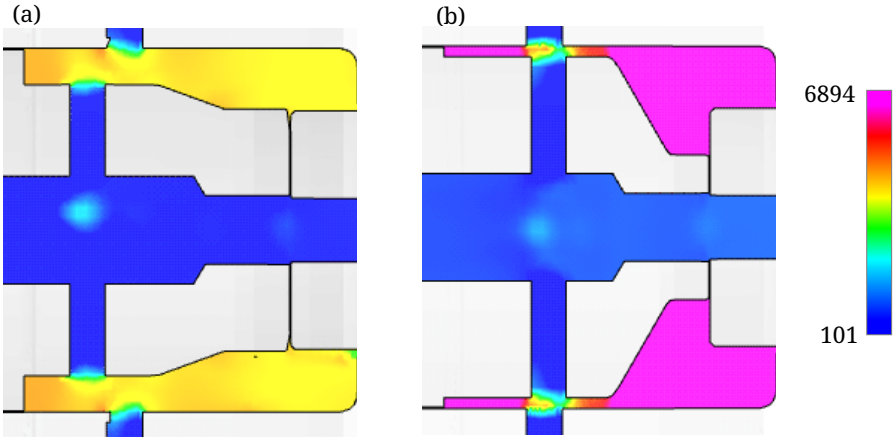

Figure 11 Comparison of cross sections of cavity pressure between designs (a) #1 and (b) #2 when displacement is 100 micron from the left. The unit for pressure used is kPa.

4.1.3 Valve separation

Since we have hypothesized that valve bodies can split based on cavity pressure in the previous section, it could be worthwhile to simulate valve separation and see what influence valve separation can have on flow dynamics. To demonstrate valve body separation, we have performed a transient dynamic simulation of a solenoid valve with the second poppet design shown in Figure 7 b, where the poppet and pin can split and combine depending

on the fluid forces. To do this, we alter the model to employ a translation dynamics model that incorporates force balance, as opposed to the previously used method of prescribed motion. The model now takes into account the forces of the spring and solenoid. The valve bodies now move solely as a result of spring, solenoid, and fluid forces. The starting position is the right, i.e. the solenoid is being actuated to move the valve bodies to the left with reference to figure. 3.

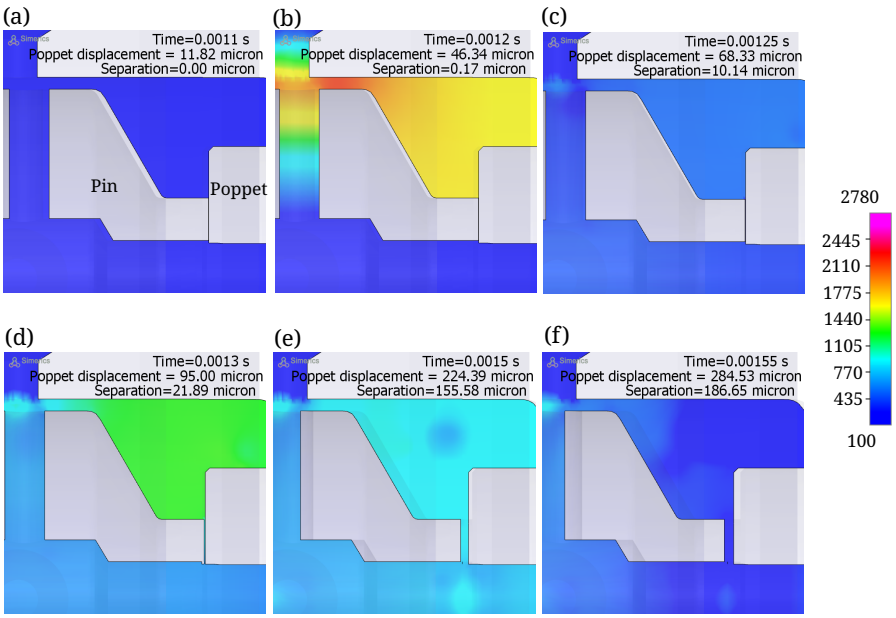

Figure 12 Cross sections showing cavity pressure and valve body splitting: (a) Cavity inadequately pressurized by inlet pressure due to small poppet displacement of 11.82 μm. (b, c, d, e) Cylclic increase and decrease in cavity pressure as the pin and poppet start separating. Cavity is adequately pressurized by inlet as the poppet is still traveling to the left, leaving cavity and inlet port connected. (f) Pressure is fully relieved as the high pressure source is disconnected by the poppet. The poppet has reached its final destination and the its displacement is 284.53 μm. Unit for pressure is kPa.

Figure. 12 a shows the pressure contour just when the poppet starts moving. At this point the cavity pressure is inadequate to cause valve splitting but that would change as the poppet moves. As time goes on and the poppet moves, the cavity pressure builds because the cavity is now connected to the high pressure inlet. This increase in cavity pressure leads to valve splitting and the pin moves further away as shown in figure 12 b. This valve body

separation is due to the balance of force between spring, solenoid, and fluid forces. As the valve splits, the cavity pressure starts to relieve itself through the central line. So, we notice a lower pressure in figure 12 c. Then the cavity is pressurized further by the inlet, and the pressure increases as we see in figure. 12 d which further causes more splitting. But this time, the leakage between the cavity and the central line is preventing the pressure from rising to larger pressures we observe in the figure. 12 b. This process of increasing pressure and moving the pin body only to relieve it happens again and again as shown in the figure. 12 b to e until the poppet finally reaches the other side and the pressure is completely relieved in the end.

It is important to note that, despite separation, both the poppet and pin move in the desired direction as evident in the figure. 12. This mirrors our earlier hypothesis from the previous section, where we calculated the forces exerted on the valve bodies as it moved from right to left in a prescirbed motion, without undergoing any separation. Although modeling valve body separation has not changed the earlier hypothesis, it could be a valuable modeling methodology to accurately predict valve body forces, since fluctuating cavity pressure seen in the figure. 12 could cause fluctuating valve body forces.

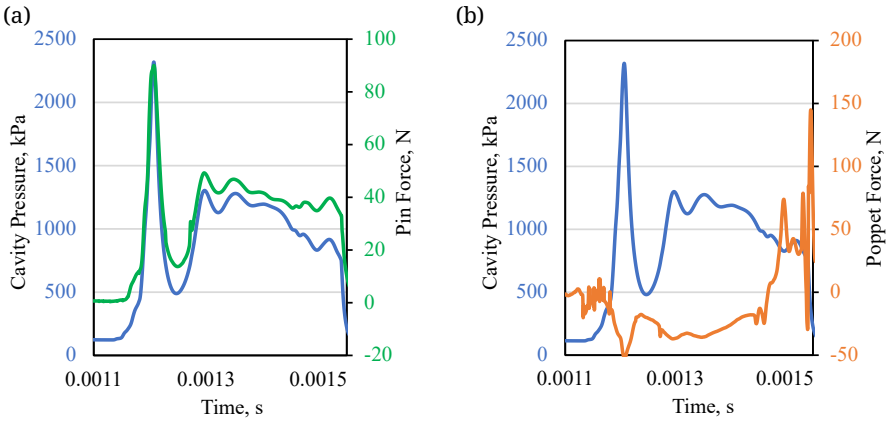

Figure 13 Cavity pressure during valve splitting period plotted against (a) the force on the pin and (b) the force on the poppet. Positive force promotes the valve body motion in the desired direction.

To show the fluctuating forces on the valve bodies: the pin and the poppet, due to fluctuations in the cavity pressure, we present the figure. 13. The cavity pressures and forces of the valve bodies are plotted for the duration

when valve separation occurs. Like mentioned previously, the positive force helps move the valve body in the desired direction. In figure. 13a, we have quantified the pressure fluctuation visualized in the figure. 12. In addition, the forces on the pin fluctuate in a similar fashion to the cavity pressure. The cavity pressure has a strong positive correlation with the forces on the pin. Similarly, the forces on the poppet fluctuate with cavity pressure as seen in the figure. 13b. However, the cavity pressure has a negative correlation with the forces on the poppet. This is understandable because the cavity pressure tends to push the valve bodies away from each other in opposite directions because of its location as seen in the figure. 12a. In other words, high cavity pressures push the pin towards the desired direction, whereas the poppet in the undesired direction. This becomes evident when the figures. 13a and b are compared.

4.2 Vane pump

In this section, we discuss the design improvement made by Parker Hannifin on one of the vane pumps after several CFD studies conducted in Simerics MP+. During the design process, we identify critical flow characteristics that need to be optimized and do several iterations of design change to arrive at a design that has improved performance.

4.2.1 Critical flow characteristics

To identify critical flow characteristics, we set out to perform a CFD simulation of the base design of a vane pump using the equilibrium dissolved gas cavitation and turbulence models for the flow; the translation model is used for the movement of the vane inside the slots.

Suction regions often experience pressures lower than the vapor pressure, resulting in cavitation. Figure 14 a shows this clearly in the suction region as large vapor volume fraction computed by CFD. In addition to typical cavitation in the suction region, the vane pump has an additional region where cavitation occurs. As the rotors rotate, the vanes can move radially due to the centrifugal, hydraulic pressure and spring forces. Using the dynamics model of Simerics MP+, we are able to appropriately model the vane motion as a result of force balance. During the motion of vanes, the pockets enclosed by the vane and rotor in the suction regions expand. Figure. 14 a and b show the expansion of a pocket based on rotation. In this zone, pressures can go below vapor pressure, and hence cavitation bubbles can form. The cavitation that occurs as a result of the expansion of the vane cavity can be realized when

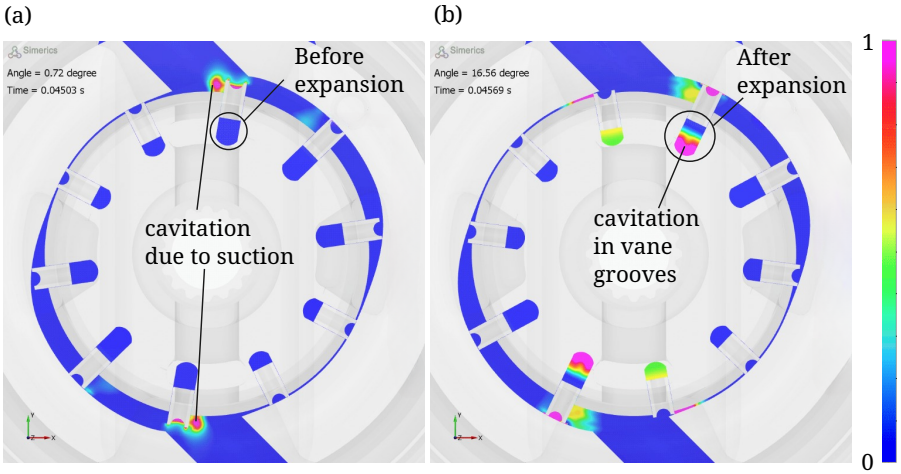

Figure 14 Cross section of vapor volume fraction of the base design of a vane pump. (a) Cavitation near suction port. (b) Cavitation in the vane slot as the vanes in suction region move outwards causing pressure drop.

the vapor volume fractions of the vane cavity before (figure. 14 a) and after expansion (figure. 14 b) are compared.

Another critical flow characteristic is the velocity profile at the inlet and outlet ports. Figure. 15 a shows the instantaneous velocity profiles for inlet and outlet ports. Although the inlet velocity profiles are smooth, the outlet velocity profiles are turbulent, and the local velocities are higher in certain regions. Turbulent vortices in the outlet can cause energy dissipation and therefore reduce the efficiency of the vane pump. The reasons for turbulent vortices and large local velocities are steps and narrow passages, respectively, as highlighted in the figure 15 a.

Lastly, leakage gaps also play a role in reducing efficiency. At higher speeds and pressure, leakages between the inlet and outlet ports become predominant and could largely reduce the volumetric flow rate of a pump. Leakages between the rotor and the housing and the vanes and the slots are shown in the figure. 15b.

By modifying the suction, discharge, and leakages appropriately in the base design, one can reduce cavitation, turbulent vortices, and high local velocities, and thereby improve the performance of the vane pump. After a rigorous parametric study on dimensions of vane grooves, inlet and outlet ports using CFD, we have arrived at an optimized design with higher efficiencies and discharge pressures. Using the base and optimized design,

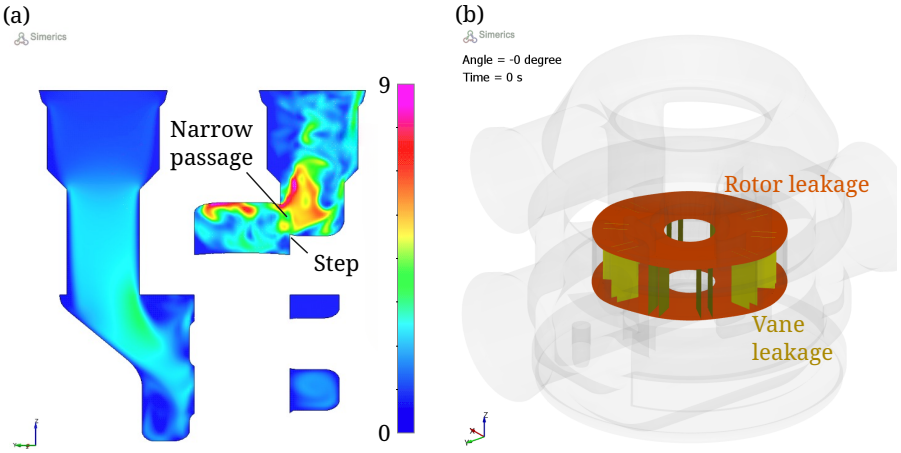

Figure 15 (a) Velocity patterns in inflow and outlflow. Unit of velocity is ms^{-1} (b) Rotor and vane leakage gaps.

prototypes have been built, and experiments have been conducted to verify the improvement in performance.

4.2.2 Comparison of base and optimized designs using experiments

In the experiments, we start by testing the dependence of discharge flow rates on rotation speeds at an suction pressure of 80 kPa. We anticipate the output flow to increase linearly with speed until a certain speed is reached, after which cavitation or leakages become predominant and the flow rate does not increase linearly anymore. We call that speed the maximum running speed of the base design and use it to non-dimensionalize the speed of both base and the improved design. We also call the flow rate that corresponds to this maximum speed the maximum flow rate since this is the highest flow rate one can expect from the base design before cavitation or leakages becomes predominant. We use this flow rate to non-dimensionalize the flow rate measured in both the base and the improved designs. We also non-dimensionalize discharge pressure by maximum operating discharge pressure of the base design. By non-dimensionalizing parameters based on the base design's maximum operating condition, we make it easier to visualize the improvements from the base design.

Figure. 16 a shows the non-dimensional flow rate (V') as a function of the non-dimenstional speed (ω') of the base (red) and optimized design (blue) at an intake pressure of 80 kPa and discharge pressure of 1500 kPa. We notice in

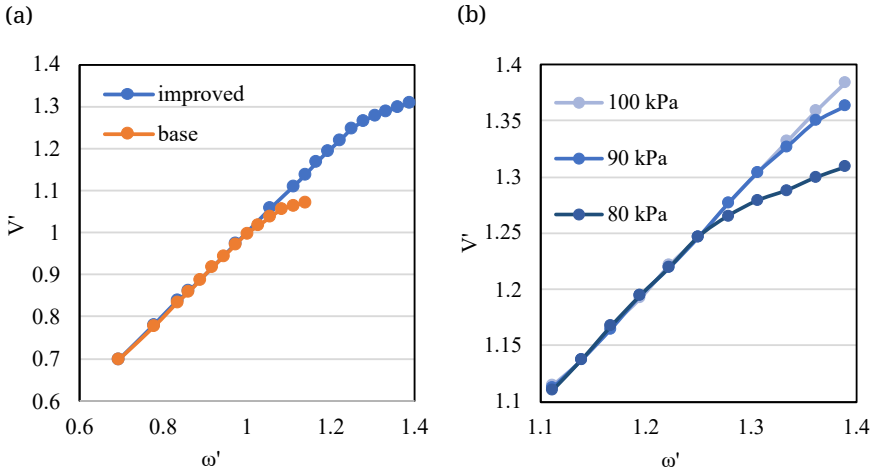

Figure 16 (a) Non-dimensional flow rate as a function of non-dimensional speed for base and improved design for suction pressure of 80 kPa. (b) Non-dimensional flow rate as a function of non-dimensional speed for various suction pressure in the extended working range.

the base design that the flow rate varies linearly with speed as intended until $(1, 1)$. Data corresponding to $(1, 1)$ of the base design belong to the maximum operating conditions above which cavitation and leakages becomes predominant. The data point in the improved design that is equivalent to $(1, 1)$ of the base design is $(1.138, 1.15)$. This signifies that the operating speed of the optimized design has increased by 13.8% and the highest volumetric flow rate by 15%, compared to the base design. To show the flow rate dependence on suction pressure in the extended operating range of the improved design, we present figure. 16 b. As expected, for higher inlet pressures, the performance drop does not occur until much later speeds, as larger suction pressures inhibit cavitation bubble formation and also cause smaller leakages.

To compare the effect of discharge pressures on efficiency, we have performed a different set of tests in which we vary the speed and discharge pressures to measure the volumetric flow rate in the outlet. We set the suction pressure at 100 kPa. Using the theoretical and measured volumetric flow rate, the volumetric efficiency is calculated and presented as a color contour for various non-dimensional speed (ω') and non-dimensional discharge pressures (P'_{out}) in the figure. 17. First, we point out that the improved design has an overall higher efficiency than the base design. Second, the operating speed and discharge pressure ranges have increased by 39% and 6% respectively, in the improved design, as seen in the figure 16 a. Finally, we see remark-

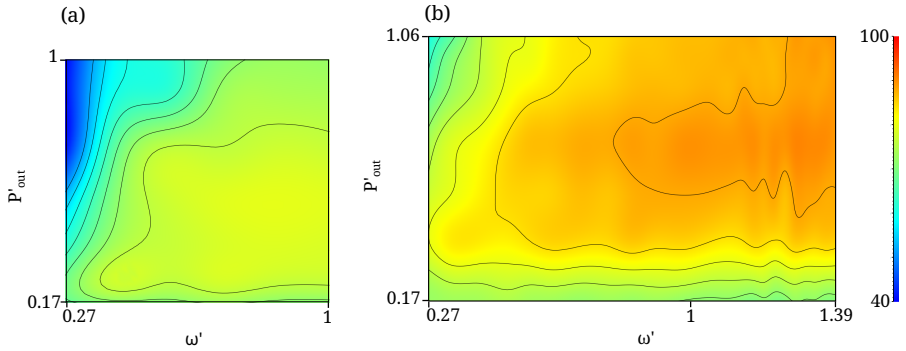

Figure 17 Contours showing efficiency for various discharge pressure and vane speed for (a) base design and (b) improved design. Improved design shows extended discharge pressure and working speed ranges.

ably higher efficiencies even at high discharge pressures and extended speed ranges.

To compare the simulation results with experimental data, we present non-dimensionalized volumetric flow rates of the improved design at different non-dimensionalized discharge pressures for experiments and simulations in the figure. 18a. The inlet is maintained at 101 kPa. At lower discharge pressures, the simulation results and the experimental results vary more than when the discharge pressures are higher. At low discharge pressure, the discharge velocities are usually large. The high discharge velocities cause swirling flows, which are often difficult to simulate. Nevertheless, the margin of error is very low, as shown in the figure. 18b. The highest percentage error observed between the simulations and the experiments is 2.50%, which is well within the acceptable range for engineering applications.

5 Conclusion

In this paper, we have discussed two hydraulic equipment: a solenoid valve and a vane pump that are being used in subsea and off-highway applications, respectively. All solenoid valve designs and vane pump designs used have been part of Parker Hannifin's rigorous design process.

In the solenoid valve section, we have shown how CFD can be used to predict cavitation damage in critical areas of the valve. It has also been shown that CFD serves as an instrument to elucidate the phenomena noted in the experimental studies of two valve designs. Simulations involving complex

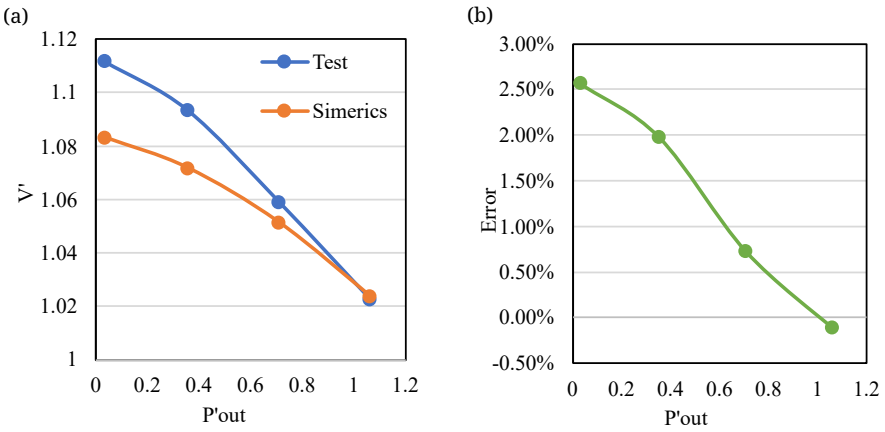

Figure 18 (a) Non-dimensionalized volumetric flow rate at different non-dimensionalized discharge pressures of the improved pump. (b) Difference between test and simulation results quantified as percentage change for various discharge pressures.

transient dynamics, such as valve separation, have been performed using the comprehensive rigid body dynamics offered by Simerics MP+. This only shows how advanced CFD along with transient dynamics and data analytics can be used to simulate phenomena that are nearly impossible to study in experiments. These studies have allowed Parker Hannifin to perform targeted optimizations, mitigating cavitation risks, a common issue in subsea applications that can lead to reduced efficiency and potential damage over time, and improving valve stability.

In the next section, we have modeled a vane pump and the transient dynamics of vane motion inside the slot, using pre-coded templates in Simerics MP+. This has helped identify flow attributes, notably cavitation within vane slots. By altering the geometries and utilizing CFD to choose a superior design, we have managed to enhance the total performance of a pump by boosting both the operational range and efficiency. This advancement propels us closer to realizing a cost-efficient off-road electric-hydraulic mobile system, marking a significant stride in Parker Hannifin's path towards electrification.

This paper has demonstrated the transformative impact of integrating advanced CFD simulation tools such as Simerics MP+ into the hydraulic fluid power engineering design process. Through meticulous validation and verification, upfront modeling of complex transient dynamics, and strategic optimization of key components, we have demonstrated the potential of

simulation-driven engineering to address and solve some of the most challenging problems in the field. Our successful application of these advanced techniques in comprehending the complex transient dynamic behavior in a subsea solenoid valve and a vane pump sets new benchmarks in product design and development of subsea and off-highway equipment.

References

[1] K. Sotoodeh, "A review on subsea process and valve technology," in *Marine Systems & Ocean Technology*, vol. 14, pp. 210–219, 2019.

[2] AMPP, "Nace standards resource," 2024. `https://www.ampp.org/standards/ampp-standards/standards-resources` [Accessed: April 8th 2024].

[3] API, "Api standard - 17f," 2024. `https://www.api.org/~/media/files/publications/whats%20new/17f%20e3%20pa.pdf` [Accessed: April 8th 2024].

[4] M. Solnørdal, "Hydrogen induced stress cracking (hisc) and dnv-rp-f112," in *Measurement and Control*, vol. 42, pp. 145–148, 2009.

[5] H. Zhang and R. Nagel, "Electrification challenges and solutions in mobile system design," 2023.

[6] F. Nishanth, G. Bohach, J. Van de Ven, and E. L. Severson, "Design of a highly integrated electric-hydraulic machine for electrifying off-highway vehicles," in *2019 IEEE Energy Conversion Congress and Exposition (ECCE)*, pp. 3983–3990, IEEE, 2019.

[7] F. Un-Noor, G. Wu, H. Perugu, S. Collier, S. Yoon, M. Barth, and K. Boriboonsomsin, "Off-road construction and agricultural equipment electrification: Review, challenges, and opportunities," *Vehicles*, vol. 4, no. 3, pp. 780–807, 2022.

[8] J. R. Valdes, J. M. Rodríguez, R. Monge, J. C. Peña, and T. Pütz, "Numerical simulation and experimental validation of the cavitating flow through a ball check valve," *Energy Conversion and Management*, vol. 78, pp. 776–786, 2014.

[9] L. Li, H. Zhang, G. Davis, F. Kalb, and S. Hamid, "Improving the closing characteristics of subsurface safety valve with combined fea and cfd modeling/numerical analysis," in *SPE western regional meeting*, pp. SPE–93941, SPE, 2005.

[10] E. Frosina, A. Senatore, D. Buono, M. Pavanetto, M. Olivetti, and I. Costin, "Improving the performance of a two way flow control valve, using a 3d cfd modeling," in *ASME International Mechanical Engineering Congress and Exposition*, vol. 46545, p. V007T09A085, American Society of Mechanical Engineers, 2014.

[11] E. Frosina, A. Senatore, D. Buono, K. A. Stelson, F. Wang, and H. Gao, "A three-dimensional cfd methodology to study vane-ring and vane-under-vane interactions of a vane pump power split transmission," in *Fluid Power Systems Technology*, vol. 50473, p. V001T01A042, American Society of Mechanical Engineers, 2016.

[12] B. Kashid and M. Eichler, "Lies, damned lies, and simulation results: How to change the conversation and build a thriving simulation ecosystem," in *Offshore Technology Conference*, p. D012S059R003, OTC, 2021.

[13] J. Azar, "Oil and natural gas drilling," in *Encyclopedia of Energy* (C. J. Cleveland, ed.), pp. 521–534, New York: Elsevier, 2004.

[14] A. K. Singhal, M. M. Athavale, H. Li, and Y. Jiang, "Mathematical basis and validation of the full cavitation model," *Journal of Fluids Engineering*, vol. 124, no. 3, pp. 617–624, 2002.

[15] Simerics Inc., "Simerics-MP+ user manual," 2024.

[16] A. Pandey, J. Wang, D. Maiti, and Y. Jiang, "Performance and validation of a segregated pressure-based solver for computations of low and high-speed compressible flows," in *AIAA SCITECH 2023 Forum*, p. 2274, 2023.

[17] S. Taghizadeh, K. C. Ng, J. Horen, and S. Dhar, "A 3d computational fluid dynamics and acoustics simulation approach for noise mitigation prediction in gerotor pumps," tech. rep., SAE Technical Paper, 2024.

[18] H. Ding, F. Visser, Y. Jiang, and M. Furmanczyk, "Demonstration and validation of a 3d cfd simulation tool predicting pump performance and cavitation for industrial applications," *Journal of Fluids Engineering*, 2011.

Analysis of the incomplete filling of a positive displacement pump due to undissolved gas involving experiments and simulations

Dinghao Pan, Andrea Vacca, and Daniel Gysling

Abstract

The analysis of the incomplete filling behavior of positive displacement machines requires considerations of the undissolved air (i.e. aeration) often associated with uncertainties in the evaluation of the air content within the working fluid and its dependencies with the suction pressure.

This study contributes to this topic by presenting an experimental analysis, as well as modeling considerations, based on an experimental set-up designed by the authors to measure the filling characteristics of an internal gear pump under induced gaseous cavitation. Measurements considered in the study include the pump flow rate vs. shaft speed, as well as the undissolved gas content at the inlet via an innovative solution by CorVera.

Experimental results show that with the same pump inlet pressure, low-speed operations present more tendency for incomplete filling, as compared to higher-speed conditions. This is due to the transient behavior of the air release process in the line connecting the reservoir to the pump, an effect often neglected in similar analyses. This observation is supported by the measured undissolved gas content, which decreases from 7% (at 500 rpm) to 1.5% at 1500 rpm, while the inlet pressure is maintained at 0.3 bar absolute. The measured air release was compared with analytical models, including the equilibrium model and the first-order dynamic model, where a good match was observed between the measurements and the first-order model results produced with an 8 s time constant for fluid with 6 % total air.

The incomplete filling behavior was further examined with a lumped parameter-based simulation model based on the equilibrium fluid model, showing that the total air content at the inlet condition greatly affects the accurate prediction of the pump's incomplete filling. A significant consistency was also found between the measured undissolved air content and the air content values that best predicted the incomplete filling phenomenon.

1 Introduction

Incomplete filling in a positive displacement pump means a situation where the displacement chambers of the pump can no longer be filled with the working fluid in the liquid state. When incomplete filling happens, there are significant volumes of gas in the displacement chambers, which is caused by the working fluid reaching a pressure lower than the saturation pressure (aeration) or, in extreme cases, vapor pressure (vapor cavitation). This phenomenon is associated with volumetric losses (or filling losses), as these gases eventually disappear at the delivery flow. Besides being an energy loss, incomplete filling should also be avoided because it is often associated with detrimental effects such as noise generation or mechanical damages caused by constant bubble collapsing.

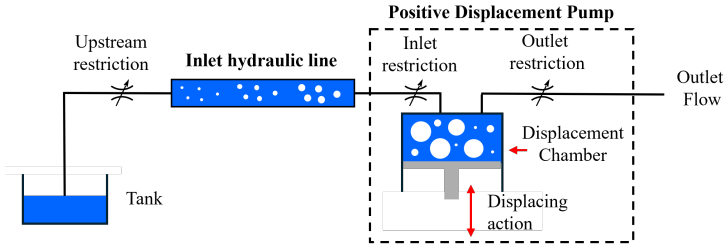

Figure 1: Hydraulic circuit for a positive displacement pump under induced incomplete filling

As Figure 1 illustrates, incomplete filling often occurs under an excessive pressure loss in a) the line connecting the reservoir to the pump inlet (equivalently caused by an upstream flow restriction) or b) between the pump inlet and its displacement chambers (caused both by the pump inlet restriction and the displacement chamber volume expansion related with the displacing action). Therefore, the phenomenon of incomplete filling is related to both the design of the suction circuit and the pump geometry. Certain pump designs are known for having better filling capabilities due to the minimum internal pressure loss while still suffering from incomplete filling under unfavorably high speeds or if an upstream restriction is present. Note that incomplete filling is related to the high operating speeds not only because of a higher pipe loss, but also because of a more rapid volume expansion in the displacement chambers, which gives higher pressure losses in both types a) and b). Additionally, fluid properties, namely the dissolved air content at the reservoir, where saturation conditions can usually be assumed, also heavily affect the incomplete filling behavior due to the effect of aeration. According to Henry-Dalton's law (fraction of air being released is proportional to the absolute liquid pressure if equilibrium), oil that dissolves more air at atmospheric pressure releases more air after the same pressure drop. Incomplete filling may also be caused by entrapped air (pseudo-cavitation), which is not associated with air release but rather with the air leakage into the suction circuit or tank design limitations[1]. Furthermore, an

incomplete filling may rise if the reservoir pressure is below the atmosphere. In fact, the incomplete filling issue in aviation lubricating pumps caused by a sub-atmosphere reservoir, known as the "lubrication ceiling", is a crucial consideration in designing aviation pumps[2]. Specifically, this work will neglect pseudo-cavitation phenomena and a sub-atmosphere tank and focus only on incomplete filling caused by the two types of pressure drops a) and b) mentioned above.

Past researchers have studied the pump incomplete filling behavior using experiments and different modeling techniques involving CFD and Lumped Parameter (LP) based models. Both simulation techniques are closely related to an important fluid property parameter known as the "total air". In this paper, "total air" is defined by the volume ratio between the total gas content and the total mixture volume after all dissolved and undissolved gas was separated from the liquid and stored at 1 atmosphere and T_0, which is 0 °C, as Equation (1) states. Note that such a definition is also often considered in engineering modeling utilities, such as Simcenter AMESim[3].

$$x_0 = \frac{V_{gas}(P_{atm}, T_0)}{V_{liq}(P_{atm}, T_0) + V_{gas}(P_{atm}, T_0)} \tag{1}$$

When simulating incomplete fillings, CFD simulations consider the gas presence with two approaches: equilibrium-CFD (where the undissolved gas fraction is determined from the pressure) and dynamic-CFD (which involves additional transport equations for gas or vapor content). Based on equilibrium-CFD, Altare and Rundo [4] showed that, with an unchanged sub-atmospheric pump inlet pressure, higher speeds lead to more severe incomplete filling in a Gerotor. Such speed dependency was also observed in other equilibrium-CFD-based studies, e.g., Hussain et al. for a Gerotor [5], Corvaglia et al. for an external gear pump [6]. Note this speed dependency was reported as negligible by Fresia et al.[7] for an internal gear pump running a high-viscosity fluid. Altare and Rundo noticed a total air setting of 2% in the simulation matched best with closed circuit experiments, indicating that the 7∼11% total air (which is commonly found for open reservoirs[8]) should not be generalized to various circuits. Fresia et al.[7] explained the better matching from the low air content as, before the pump inlet, the pump was only drawing the oil but without separating the air. Furthermore, based on equilibrium-CFD, Boland and Shang [9] studied the incomplete filling scalability, and Rundo et al.[10] investigated the impact of inlet geometries of a vane pump's filling capability under atmosphere inlet pressure. With the dynamic-CFD approach, on the other hand, Buono et al.[11] studied the incomplete filling of a Gerotor, reporting 8% total air simulation matching the measured flow saturation. Similar studies can be found by Stuppioni et al. [12] for a vane pump and by Yin et al. [13] for a piston pump. It should be pointed out that popular dynamic-CFD models, such as the 'full cavitation model' introduced by Singhal et al.[14], often require empirical time

constants to describe the speed of phase change processes, including vaporization/condensation and aeration/dissolution. Early experiments from Schweitzer and Szebehely[8] reported $\mathcal{O}(10^1)$ second half release time for dissolved air in hydraulic oils. Measurements from Kowalski et al.[15] showed that air release is much slower than vaporization if water is below vaporization pressure, and Yang et al. [16] reported that dissolution is further slower than the air release for the same pressure differential. Notable simulation-based work from Stuppioni et al.[17, 12] investigated how the outlet flow and pressure ripple of a pump with atmospheric inlet pressure could change under different time constant settings in the dynamic-CFD framework, reporting air release time $\mathcal{O}(10^{-2})$ and dissolution time $\mathcal{O}(10^0)$ matched best with measurements, and concluding these time constants as critical for describing the gas dynamics in the simulations. More details on different dynamic-CFD models can be found in the review paper from Orlandi et al.[18].

In studies that investigated the incomplete filling behavior with the LP simulation approach, there is also the static cavitation model (where the fractions of vapor and released gas are pressure-dependent) and the dynamic cavitation approach (where the vapor and released gas fraction are solved from the rate equations). Casoli et al. [19] formulated a static model to consider the fluid property change under sub-atmosphere conditions and noticed both a higher total air content and a higher saturation pressure emphasized the incomplete filling prediction. Vacca et al.[20] used a similar implementation to study the incomplete filling behavior of an axial piston pump, discussing the necessity of tuning the model parameters to achieve a higher fidelity compared to experiments. Also based on a static model, Pleskun et al.[21] reproduced the incomplete filling behavior for a screw pump. On the other hand, dynamic cavitation models have recently been explored for LP simulations, as can be found in the work from Zhou et al.[22], Shah et al.[23], and Mistry and Vacca[24], involving similar time constants discussed for dynamic-CFD as well. The work from Rundo et al. [25] detailed these time constants based on pump flow and pressure ripples and suggested release time $\mathcal{O}(10^{-3})$ and dissolution time $\mathcal{O}(10^1)$ for pumps with atmospheric inlet pressure. However, relevant studies on the incomplete filling behavior have not yet been presented from LP simulations based on dynamic cavitation considerations.

Previous studies on pump incomplete filling often focused on the pump side and didn't quantify the impact of the two types of pressure drops illustrated in Figure 1. Additionally, although past incomplete filling simulations have widely investigated the fluid settings such as total air and their effects on prediction accuracy, whether the best-matching fluid parameters (total air) can be justified with the design of the circuit has not been understood.

To investigate the incomplete filling behavior of a positive displacement pump, a test rig was set up in the authors' research lab to consider the two stages of pressure drops illustrated in Figure 1. Different operating speeds were measured,

including the measurement of the delivery flow, the pressure at the pump inlet, and the gas void fraction (GVF) in the hydraulic line before the pump inlet. The amount of gas content measured at the pump inlet was compared to the prediction from a first-order air release model. Furthermore, static cavitation-based simulations that utilize different total air settings were used to investigate the pump's incomplete filling behavior. The influence of total air setting will be discussed and compared with the total air which can be deduced from the gas content measurements. The comparison, as will be shown later, underscores the importance of both the inlet pressure and the total air in achieving good accuracy in predicting the incomplete filling phenomenon.

2 Experimental study on incomplete filling

2.1 Experimental set up

The setup for measuring the incomplete filling behavior for a reference 8 cc/rev internal gear pump [26] is illustrated in Figure 2. **Valve 1** regulates the pump inlet pressure, and **valve 2** is set to fully open to minimize the pressure load on the pump outlet. Such arrangements minimize the effect of pump internal viscous leakage when quantifying the incomplete filling. The test setup also includes an air valve, which was constantly closed during the test. Such a valve allows tests with entrained air, which will be the subject of future work. Pressure sensors $\boldsymbol{P}_1$ and $\boldsymbol{P}_2$ measure the pressure change along the hydraulic lines (**HL1** and **HL2**). More details regarding the components used in the measurements are given in Table 1.

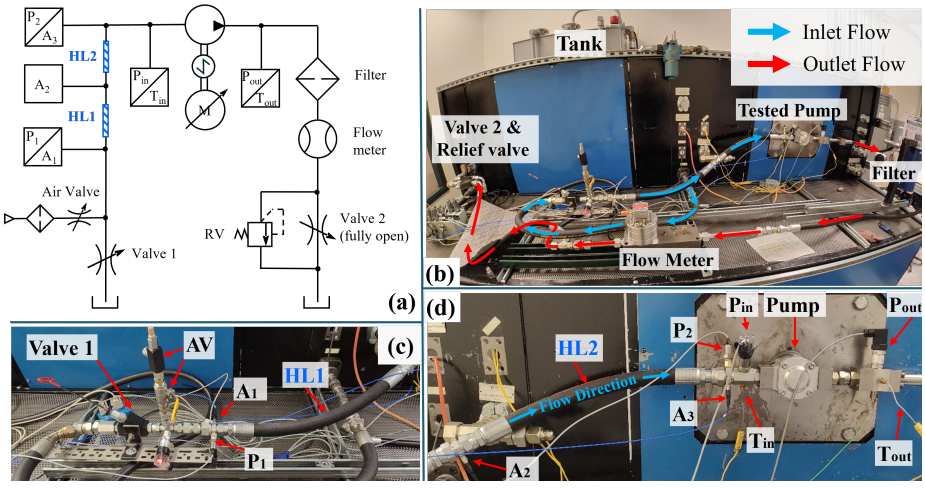

Figure 2: Test circuit to measure the incomplete filling behavior
(a: hydraulic circuit; b: overlook of the entire setup; c: inlet region; d: tested pump)

Components	Parts used	Accuracy
Pump	Eckerle EIPS2-008	N/A
Valve 1	Sun Hydraulics NFDD-KGN	N/A
Flow meter	VSEflow VS 2EPO 12V	0.3% measured value
P_{in}	WIKA S-20-1.6	0.003 bar
P_{out}	HAD 4745-B-006-00	0.25% measured value
A_1,A_2,A_3	PCB 102A44	0.07 bar
P_1,P_2	Keller America absolute type	0.25% measured value
HL1,HL2	DIN EN 856, inner diameter 1 inch, pipe length 2 feet	
Tank	Contains $\sim$ 290 liter hydraulic fluid	

Table 1: Component used in the test circuit

Notably, this work utilizes a non-intrusive, in-line, real-time, SONAR-based measurement system to quantify the gas void fraction (GVF) in the fluid entering the pump inlet. Based on beam-forming principles, the measurement system calculates the fluid's speed of sound utilizing the output of three acoustic pressure sensors ($\boldsymbol{A}_1$, $\boldsymbol{A}_2$, $\boldsymbol{A}_3$). The measured sound speed is then interpreted in terms of the gas void fraction utilizing Wood's equation[27]. For clarity, the GVF measured here is defined as the ratio of the gas volume to the total fluid volume. Note that this differs from the volumetric ratio between the gaseous and mixture flow rates. However, for homogeneous conditions where the velocity of the gas phase approaches that of the liquid phase (generally true for low GVF scenarios), the two definitions become equivalent. More details on the measurement approach can be found in Gysling[28].

2.2 Operating conditions

ISO-VG 46 hydraulic oil was used during the test, and measurements were taken at 23 °C inlet and outlet temperature. Four operating speeds (500, 1000, 1500, 2000 rpm) were tested with different pump inlet pressures (measured by $\boldsymbol{P}_{in}$), which were regulated by **valve 1**. During the test, a loud hissing noise was heard when the pump inlet pressure fell below $\sim$ 0.2 bar absolute, with spatial location near the outlet port on the pump body. Such pressure limit appeared to be lower for the low-speed conditions: for 500 rpm such limit was $\sim$ 0.18 bar absolute, whereas for 2000 rpm the limit was $\sim$ 0.3 bar absolute. The noise was believed to be related to the fierce vapor bubble collapsing process on the pump outlet side. All measurements discussed in this work are above this low pressure limit, to avoid extended pump operation in the possible damaging conditions.

The increase of the pump outlet pressure with the operating speed shown in Figure 3 is caused by the pressure loss characteristics of the outlet circuit. According to the pump specs [26], at 1500 rpm there is a decrease of volumetric efficiency of 0.2% every 8 bar of outlet pressure increase. This justifies that the effect of the measured increase of outlet pressure on the measured volumetric

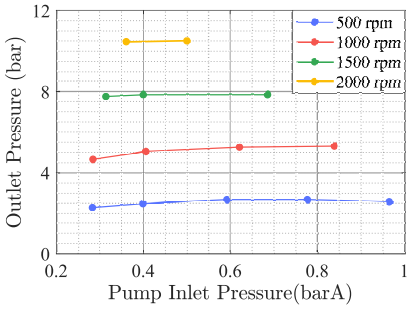

Figure 3: Pump outlet pressure

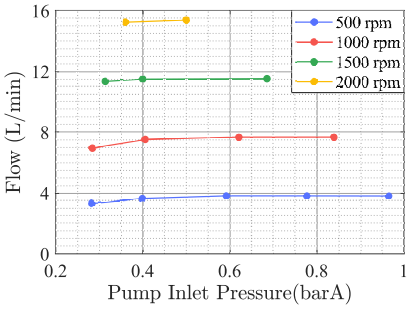

Figure 4: Pump Outlet flow

efficiency is minor, and major volumetric efficiency loss in the measurements should be associated with the incomplete filling phenomenon.

2.3 Incomplete filling flow measurement

As plotted in Figure 4, for constant operating speed, the measured pump outlet flow decreases with a lower pump inlet pressure. Significant flow rate drops happen at pressure values close to the limiting pressure ranges. The impaired outlet flow represents the incidence of incomplete filling inside the pump, which can be seen more clearly from the volumetric efficiency evaluated in Figure 5.

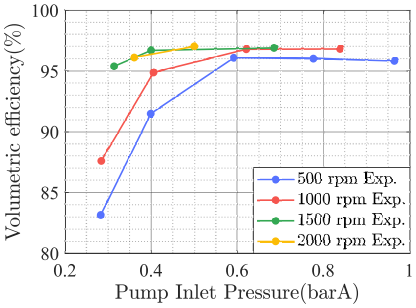

Figure 5: Volumetric efficiency

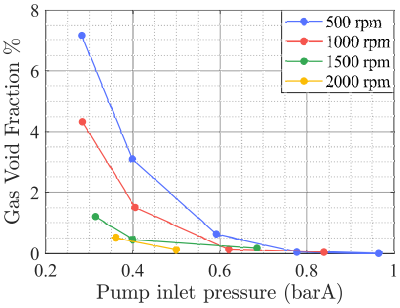

Figure 6: Measured GVF

Figure 5 shows an interesting trend where, as the speed increases from 500 to 2000 rpm, the incomplete filling becomes less obvious for the same inlet pressure. This trend appears to be in contrast with the common belief that higher speeds promote incomplete filling, as reported in several sources [1, 29] and recent works by Rundo[4] and Corvaglia et al.[6]. However, this paper will show how this trend does not contradict, but rather complement, the common understanding of incomplete filling. As mentioned in the first section, incomplete filling is

caused by the behaviors of both the inlet circuit and the pump design. In this test, the effect of the inlet circuit prevails, generating such a trend.

2.4 Gas content measurement

The Gas Void Fraction(GVF) measured with the CorVera system is plotted in Figure 6. Note the raw GVF was calculated by the measurement system around every 2 seconds, which involves instantaneous oscillations of absolute standard deviation $\sim$ 0.25%. The data reported in Figure 6 averaged a 2-minute period after the on-screen measurement stabilized (which takes about 1 minute). It should be carefully noted that the measured GVFs represent the volume of air at sub-atmospheric pressures, not the atmosphere pressure. Also note that the measured GVF can be considered as an averaged measurement at the middle position between hydraulic lines **HL1** and **HL2**, and the gaseous volume entering the pump inlet should be higher than the measured GVF, as the air release process develops along the length of the hydraulic lines.

The figure shows that as the operating speed increases, the gas volume in the inlet hydraulic lines becomes significantly lower. This trend can be explained as follows: for low speeds, due to the lower mean velocity, the fluid takes a longer time to pass the inlet hydraulic line (see Figure 1), and more air is therefore released into the fluid.

The GVFs for 1500 and 2000 rpm shown in Figure 6 give a clear clue about the low amount of released air at the pump inlet, which supports the assumption raised by Fresia et al.[7] that under higher flowrates very least air bubbles are released into the fluid before the pump inlet. This assumption well explains why equilibrium-CFD requires a lower total air setting to reproduce the incomplete filling. Particularly, for 500 rpm operating speed, it takes $\sim$ 10 seconds for the fluid to pass the total two hydraulic lines, whereas, for 2000 rpm, the travel time becomes $\sim$ 2.4 seconds. Such difference in the travel time indicates that the time scale of the air release process is on the order of magnitude of seconds, which is consistent with the value found in the measurements by Schweitzer and Szebehely[8]. Note Rundo et al.[25] and Stuppioni et al.[12] reported very fast air release constants ($10^{-2} \sim 10^{-3}$) that predicted experiment-matching pump outlet pressure ripples; however, we believe the time constants discussed in their work are more related to the fluid-dynamic process inside the pump domain (their work investigated pump with atmospheric inlet pressure), and the process of air release in the circuit upstream the pump inlet should involve a different time constant that is slower, because of less volume expansion or boundary perturbation in the region.

3 Analytical models of air release

3.1 Equilibrium fluid model

The air release measured can be compared with the results from an equilibrium fluid model, which states whenever a pressure change happens to the fluid, the air release and the volume change of the mixture are achieved instantly so that the fluid is always in the equilibrium state. Studies such as [10] and [19] have reported that the fluid equilibrium model when properly tuned, can give a good prediction for the incomplete filling behavior in positive displacement machines. According to the equilibrium fluid model, the volume of the air undissolved from the fluid (under the equilibrium state) $V_{g,undis,eq}$ can be determined according to Henry's law, as equation (2) gives. $P_{vap,H}$ is the high vaporization pressure [19]. P_{sat} is the saturation pressure above which all air is dissolved. Note equation (2) applies when the fluid pressure is between $P_{vap,H}$ and P_{sat} and if the fluid pressure is beyond the range, all or none air is released.

$$\frac{V_{g,undis,eq}(P_{sat}, T_0)}{x_0/(1-x_0) \cdot V_{liq}} = \frac{P_{sat} - P}{P_{sat} - P_{vap,H}} \tag{2}$$

The volume of the undissolved air evaluated in Equation (2) must be evaluated at the reference state (P_{sat}, T_0), as Henry's law quantifies about the amount of substance rather than the volume. The gas volume expansion caused by pressure decrease can be evaluated with equation (3) for a given polynomial coefficient κ, which is taken as 1.3 in this work. Note the temperature of the left-hand side fluid in equation (3) can be solved from κ based on the ideal gas law and is fundamentally different from the liquid temperature.

$$V_{g,undis,eq}(P) = \left(\frac{P_{sat}}{P}\right)^{1/\kappa} V_{g,undis,eq}(P_{sat}, T_0) \tag{3}$$

3.2 Dynamic air release model

The equilibrium fluid model assumes the air release process to happen instantly, whereas in reality, such equilibrium takes time to achieve. In fact, the air release process in hydraulic oils has been reported to have a proportional relationship with the extent of phase imbalance [8]. Based on this idea, a first-order model is often used to study the transient air release in fluid, of which the applications can be found in Simerics MP+[12], ANSYS CFX [16], and AMESim[3, 25].

The key idea of the first-order air release model can be expressed in the Lagrangian form for a moving fluid element with a specific mass δM (no mass transfer between surrounding fluid elements), as equation (4) gives. In the equation, $V_{g,undis}(t; P)$ is the volume of the gas released into the fluid element

after time t (at $t = 0$ no air is released) under pressure P. $V_{g,undis,eq}(P)$ is the equilibrium volume solved from equation (3). Equation (4) can also be alternatively expressed with mass terms; however, since the thermodynamic conditions are unified, the two ways of expression are equivalent. From equation (4), the volume of released air can be solved, as equation (5) gives, based on which the instantaneous void fraction f_{void} can be thus calculated by equation (6).

$$\left.\frac{dV_{g,undis}(t;P)}{dt}\right|_{\delta M} = \frac{V_{g,undis,eq}(P) - V_{g,undis}(t)}{\tau} \tag{4}$$

$$V_{g,undis}(t;P) = (1 - e^{(-t/\tau)}) \cdot V_{g,undis,eq}(P) \tag{5}$$

$$f_{void}(t;P) = \frac{V_{g,undis}(t;P)}{V_{g,undis}(t;P) + V_{liq}(P)} \tag{6}$$

Using a time constant $\tau = 8$ second, the transient gas void fractions were solved for a fluid with 6% total air (x_0) at different sub-atmospheric pressures, and results are plotted in Figure 7. Evident trends from the figure are: more air is released with time progressing; for a specific pressure, the rate of air release slows down with time; and the lower the pressure, the more air is released after the same amount of time. It should also be mentioned that if the pressure change caused by the air release is neglected, the air release process in the fluid that travels along the hydraulic lines can be predicted with constant-pressure curves given in Figure 7. Indeed, the inlet pressure change along the pipe was found to be low, as Figure 8 shows.

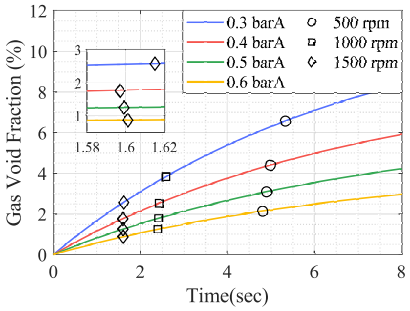

Figure 7: Void fraction predicted with 1st order air release ($x_0 = 6\%, \tau$=8s)

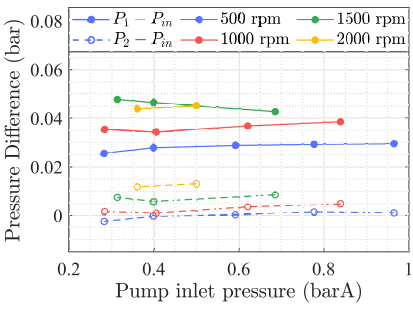

Figure 8: Measured inlet line pressure change ($\boldsymbol{P}_1$: pipe enter, $\boldsymbol{P}_2$: pipe end)

Apparently, the choice of τ affects the calculation in Equation (6): higher τ slower the air release, and it was noticed that a $\tau = 8$ provides the best

consistency with experiments. Specifically, the markers in Figure 7 highlight the predicted gas void fractions at the middle length of the hydraulic line (middle between **HL1** and **HL2**). The predicted GVF values are found to be consistent with the measured GVFs shown in Figure 6. Certain errors in the low GVF region can be explained by the first order being less accurate when the GVF is low, as a smaller bubble size hinders the air release process.

It is worth mentioning that computing the fluid travel time for the markers in Figure 7 involved two counter-acting considerations. On one hand, there is the compressibility-accelerate effect: air release along the pipe causes density to decrease, and to fulfill mass conservation, the flow is accelerated. The flow travel distance L after time t can be determined based on the void fraction history in the fluid element, as equation (7) gives by assuming the fluid starts from a location where no air is released. $\bar{u}_0$ is the mean flow velocity calculated based on the measured flow rate. This mean velocity is considered to happen at the starting location of the hydraulic pipe, assuming the density variation at the position to be negligible due to a minimal air release.

$$L(t) = \int_0^t \frac{\bar{u}_0}{1 - f_{void}(t)} dt \tag{7}$$

On the other hand, the incomplete-filling-decelerate effect also affects the evaluation of the travel time, where since a lower inlet pressure promotes incomplete filling, the mean velocity $\bar{u}_0$ which is calculated from the measured flow rate drops, thus giving a longer time for the fluid to reach the same distance. It was observed that such the incomplete-filling-decelerate effect wins over the compressibility-accelerate effect for 500 and 1000 rpm, explaining why for these speeds, the travel time for the fluid to reach the middle of the hydraulic lines becomes longer when the pump inlet pressure decreases. For 1500 rpm, on the other hand, Figure 7 shows that as the pressure decreases, the travel time first decreases and then increases. Such behavior is caused by a weaker incomplete-filling-decelerate effect under 1500 rpm, which loses its dominance to the compressibility-accelerate effect in higher pressure ranges.

4 Equilibrium-fluid-based pump simulation

4.1 Simulation setup and settings

The reference pump tested is a crescent-type internal gear pump with involute-type gear profiles. To study the pump incomplete filling behavior, isothermal lumped parameter-based pump simulations based on the circuit shown in Figure 9 were performed, considering the fluid with the equilibrium fluid model. In the simulation, the outlet pressure uses the measured values. The simulation model is a simplified version of a more complex model from the authors' previous work[30]. Particularly, the model used here neglects the viscous leakage

in the fluid films and across gear tips, since the outlet pressure was low. Radial micro-motion on the gear set was considered, as it affects the gear center distance and, hence, the effective displacement. The micro-motions of the two gears are solved based on the Ocvirk solution[31], considering both hydrostatic and contact loadings on the gear set[30]. More details on the coupled pump simulation model can be found in the authors' previous works[32, 30].

The pump was simulated up to 6 shaft revolutions, and the outlet flow rate averaged from the last 3 gear teeth period was considered to study the incomplete filling behavior. With such a time window, all performed simulations reported an absolute residue of less than 0.02 % in the volumetric efficiency. More details on the simulation settings can be found in table 2.

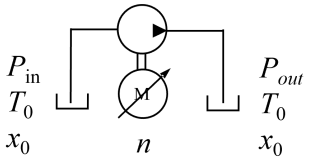

Figure 9: Simulated circuit

Sim. setting	**Value**
Fluid	ISO-VG46
$P_{vap,H}$	0.22 barA
P_{sat}	1 atm
T_0	23 $^\circ C$

Table 2: Simulation settings

4.2 Effect of total air in predicting incomplete filling

The pump volumetric efficiencies predicted by the simulation model considering different total air settings are compared with the measurements in Figure 10 for the four measured operating speeds.

Figure 10 shows a significant trend: for low speed (500 rpm) and low inlet pressure (0.3, 0.4 bar absolute), a higher total air gives a more accurate prediction in the impaired volumetric efficiency. When the inlet pressure is not very low ($>$ 0.6 bar absolute), low total air simulation gives better predictions. The trend also appears for 1000 rpm as the figure shows, whereas for higher speeds 1500 rpm and 2000 rpm, this trend was not observed. Instead, for the high speeds, simulation with very low total air appeared to match best with the measured volumetric efficiencies.

The underlying physics in different total air settings can be understood as follows. Due to the equilibrium fluid assumption, when the fluid pressure is below saturation, more air is released into a fluid if the fluid is defined with a higher total air. The higher amount of undissolved air leads to a lower bulk modulus of the fluid mixture, hence giving more density drops when the volume expansion happens inside the pump inlet and consequently a lower volumetric efficiency. On the other hand, the fact that such a trend is not evident for high speeds (1500, 2000 rpm) is that not much air was released for the speeds, which can be confirmed with the measurements in Figure 6.

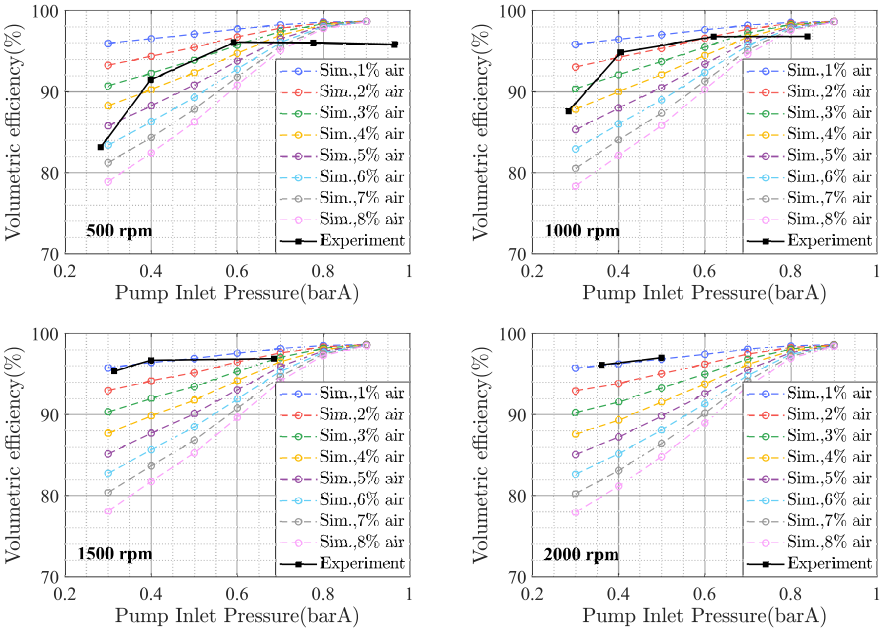

Figure 10: Measured pump volumetric efficiency compared with simulation results predicted based on fluids with different total air values

4.3 Speed dependency at higher speeds

As mentioned in section 2.3, Rundo et al.[10] and Corvaglia et al.[6] once noticed that for the same sub-atmosphere inlet pressure, the higher the operating speed, the more severe the incomplete filling becomes. Actually, such speed dependency can be reproduced from the simulation model used in this paper as well, as Figure 11 shows: for a certain total air, the pump volumetric efficiency drops with a higher speed, indicating a more severe incomplete filling. This speed dependency observed by earlier researchers can be explained as follows. As the flow rate becomes substantially high, the time for air release to happen becomes trivial such that only a very tiny amount of air can be released into the fluid before the pump inlet. Because the volume expansion process in the displacement chamber happens much faster ($\mathcal{O}(10^{-3}) \sim \mathcal{O}(10^{-2})s$) than the air release process ($\mathcal{O}(10^{1})$ s), the fluid that enters the pump, which is off-equilibrium (concerning the air release process), will not change its off-equilibrium status during the volume expansion stage. Such behavior gives a good rationale for considering the off-equilibrium fluid at the pump inlet as an "equivalent fluid" with less total air in the state of air-release equilibrium. In this way, for high-speed operations, the "equivalent fluids" that enter the pump inlet can be considered as not changing between different operating speeds, as they all equivalently contain a very small amount of total air. In this situation,

therefore, the primary cause of the incomplete filling becomes the pressure drop inside the gear displacement chambers, which is related to the volume expansion. Since a higher speed raises the expansion rate, a higher pressure drop can be expected in the displacement chambers and hence increases the volumetric loss for a higher operation speed.

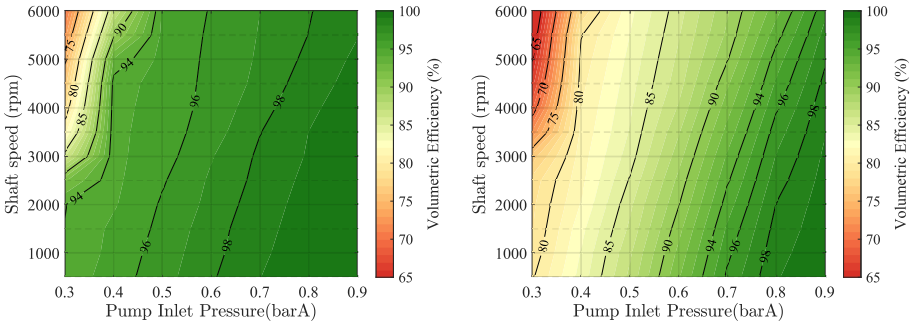

Figure 11: Simulated volumetric efficiency of a wider speed range (left: with 2% total air, right: with 8% total air)

The reason why such speed dependency seems to be reversed for lower speeds (see discussion in section 2.3) is as follows. A lower speed operation gives the fluid more time to release air; hence, the "equivalent fluid" that enters the pump inlet at low speeds has a significantly higher amount of total air when compared to the "equivalent fluid" at high speeds. This means that for a specific inlet pressure where incomplete filling happens, the pump volumetric efficiency should first increase and then decrease. Take 0.3 bar absolute pump inlet pressure shown in figure 11 as an example, when the speed increases from 500 rpm to 2000 rpm, the volumetric efficiency of a pump that is under incomplete filling condition should be first referred to a volumetric efficiency map predicted with a higher total air (e.g., 8 % in the right figure, where a low volumetric efficiency would be found) and then a map with a lower total air (e.g., 2% in the left figure, which gives a higher volumetric efficiency compared to the 8% map for the same speed). In the low-speed domain, the difference in the amount of air that is released into the upstream fluid is the main driving force in determining the incomplete filling, because the fluid compressibility upstream the pump inlet significantly varies in this speed domain. As the operating speed increases from 2000 rpm to higher, the map from where an accurate volumetric efficiency can be found gradually converges towards a map predicted with a trivial amount of total air (e.g., 2 % in the left figure), so that a higher speed gives a lower volumetric efficiency, due to a higher pump internal pressure drop becoming the dominant force in defining the incomplete filling phenomenon.

4.4 Air content comparison with measurement

The fluid at the pump inlet may carry a higher volume of released air than the measured value, which is a type of averaged GVF over the complete hydraulic lines. The increase in the GVF between the measured value and the value that should be expected at the pump inlet can be described with a factor. At first thought this factor should be slightly lower than 2 due to the non-linearity shown in Figure 7, but on the other hand, the non-linearity of the speed of sound (based on which the GVF is measured) with the gas presence involves an opposite effect which raises the factor. A more rigorous discussion on this factor is beyond the scope of this work. In this work, we assume the factor to be 2 for convenience.

In this way, the total air in the "equivalent fluid" at the pump inlet can be evaluated by back calculating x_0 from (3) and (2) where twice the measured GVF is used as the starting $V_{g,undis,eq}(P)$ value. Meanwhile, the equilibrium-state gas void fraction predicted from the equilibrium fluid model is given in Figure 12 so that the back-calculation can be conveniently achieved by looking up from the figure.

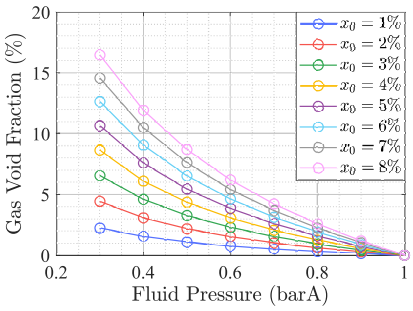

Figure 12: Equilibrium-state gas void fraction in sub-atmospheric fluids with different total airs

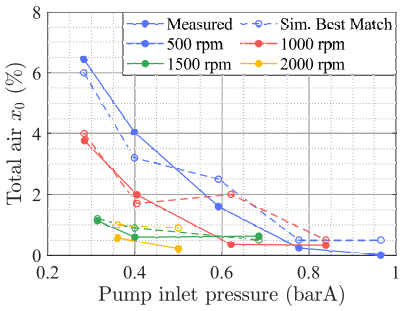

Figure 13: "Measured equivalent" versus "simulation proposed" total air

The total air in the "equivalent fluid" calculated from the measured GVF results is plotted in 13, labeled as "measured equivalent" total airs. Also plotted in Figure 13 are the "simulation proposed" total airs: the total air that gives the best volumetric efficiency predictions from the simulation which can be inferred from Figure 5. To account for possible inaccuracy in volumetric efficiency evaluations under higher inlet pressure conditions ($\geq$ 0.6 bar absolute), the "simulation proposed" total air is picked as 0.5 % in the higher pressure range. The comparison in Figure 13 gives a significant consistency between the "measured equivalent" and "simulation proposed" total air. Such consistency once again supports the validity of the gas void fraction measurements and also supports the earlier assumption stating that off-equilibrium fluid entering the pump inlet can be equivalently viewed as a fluid with a lower total air under

the equilibrium state.

Another important consideration can be made from Figure 13: the total air setting in pump incomplete filling simulations is an important and uncertain parameter that should be carefully considered based on the inlet circuit design. For higher flowrates or shorter inlet lines where less air release is expected, a lower total air might be accurate; however, when the air release upstream the pump is not negligible, the total air setting greatly affects the accuracy in predicting the incomplete filling behavior. Notably, our work not only identified the importance of the total air parameter but also for the first time measured its physical value in incomplete filling studies. This breakthrough suggests a promising direction for conditioning the inlet settings in future studies on positive displacement pumps, whether in simulation or tests.

5 Conclusion

This paper presented a study on the incomplete filling phenomenon of a positive displacement pump.

The study first experimentally investigated the reference pump incomplete filling under different inlet pressure and speed conditions. The measurements were achieved via a novel test rig setup in the authors' research lab, where two stages of pressure drops, including an upstream orifice and the pump internal inlet pressure drop, were simultaneously investigated. The measurement setup highlights an in-line gas void fraction measurement, the first time for an incomplete filling study to measure the fluid property that enters the pump inlet.

Measurements showed clear signs of incomplete filling when the pump inlet was subject to sub-atmosphere pressures. The measurements unveils the two factors that influence the incomplete filling characteristics of a pump:

(1) In the low speed operating domain, the amount of air released into the fluid upstream the pump inlet is the main driving force in determining the incomplete filling, as the fluid compressibility significantly varies in this speed domain. Since a lower speed gives more time for the air to release into the fluid before the pump inlet, a lower speed leads to a more severe incomplete filling.

(2) In the high speed operating domain, the pump inlet fluid contains a very small amount of undissolved air, so that the fluid compressibility becomes less important. Instead, the higher volume expansion rate inside the pump displacement chambers leads to a higher pressure drop in the displacement chambers, which predominantly defines a more severe incomplete filling situation.

This study also utilized simulations to study the incomplete filling behavior, involving a transient first order air release model to investigate the air release process in the pipe and an equilibrium-fluid-based LP pump simulation model

to investigate the pump's volumetric performance under incomplete filling.

The first order air release model with 6% total air and 8 second air release time constant showed a good accordance with the measured gas void fraction, supporting the validity of both the model and the gas void fraction measurements in studying the air release process in hydraulic lines.

Results from the equilibrium-fluid-based LP pump simulation showed that the total air setting greatly affects the prediction of the pump incomplete filling. Specifically, for low speed low inlet pressure conditions, simulation with higher total air gives more accurate volumetric efficiency predictions. The "equivalent" total air at the pump inlet, derived from the gas void measurement, was found to match well the total air settings that give the most accurate incomplete filling predictions. This finding confirms the importance of the total air, and also validates a crucial assumption that a fluid that has not reached air-release equilibrium at the pump inlet can be equivalently considered as a different fluid with less total air in the state equilibrium, and they can give the same effective prediction for the incomplete filling phenomenon. Notably, this work not only identified the importance of the "equivalent" total air concept but also measured it for the first time in incomplete filling studies. This breakthrough suggests a promising direction for conditioning the inlet settings in future studies on positive displacement pumps, whether in simulation or tests.

Acknowledgement

The authors would like to thank Prithvi Chandiramani, Seshan Suresh, and David Johnson for the inspiring discussions and valuable technical advice.

References

[1] Andrea Vacca and Germano Franzoni. *Hydraulic fluid power: fundamentals, applications, and circuit design*. John Wiley & Sons, 2021. ISBN: 978-1-119-56910-7.

[2] P. H. Schweitzer. "Effect of Aeration on Gear-Pump Delivery and Lubrication Ceiling". In: *Transactions of the American Society of Mechanical Engineers* (1945). DOI: 10.1115/1.4018189.

[3] Siemens PLM Software Inc. *Simcenter Amesim™ software User's guides: AHYD Advanced Fluid Properties Technical bulletin no. 117*. 2021.

[4] Giorgio Altare and Massimo Rundo. "Computational Fluid Dynamics Analysis of Gerotor Lubricating Pumps at High-Speed: Geometric Features Influencing the Filling Capability". In: *Journal of Fluids Engineering* (2016). DOI: 10.1115/1.4033675.

[5] Tarique Hussain et al. "A Simulation Study of Lubricating Oil Pump for an Aero Engine". In: *Journal of Mechanical Engineering (JMechE)* (2021). DOI: 10.24191/jmeche.v18i3.15417.

[6] Alessandro Corvaglia et al. "Simulation and Experimental Activity for the Evaluation of the Filling Capability in External Gear Pumps". In: *Fluids* (2023). DOI: 10.3390/fluids8090251.

[7] Paola Fresia et al. "CFD Modelling of an Internal Gear Pump for High Viscosity Fluids". In: *International Design Engineering Technical Conferences and Computers and Information in Engineering Conference*. 2023. DOI: 10.1115/DETC2023-111589.

[8] P. H. Schweitzer and V. G. Szebehely. "Gas evolution in liquids and cavitation". In: *Journal of Applied Physics* (1950). DOI: 10.1063/1.1699579.

[9] Hannah Boland and Lizhi Shang. "An Analysis of Cavitation Phenomena Scalability in Axial Piston Machine". In: *ASME/BATH 2023 Symposium on Fluid Power and Motion Control*. 2023. DOI: 10.1115/FPMC2023-113585.

[10] Massimo Rundo, Giorgio Altare, and Paolo Casoli. "Simulation of the filling capability in vane pumps". In: *Energies* (2019). DOI: 10.3390/en12020283.

[11] Dario Buono et al. "Modelling Approach on a Gerotor Pump Working in Cavitation Conditions". In: *Energy Procedia* (2016). DOI: 10.1016/j.egypro.2016.11.089.

[12] Umberto Stuppioni et al. "Computational Fluid Dynamics Modeling of Gaseous Cavitation in Lubricating Vane Pumps: On Metering Grooves for Pressure Ripple Optimization". In: *Journal of Fluids Engineering* (2022). DOI: 10.1115/1.4056416.

[13] Fang-long Yin et al. "Numerical and experimental study of cavitation performance in sea water hydraulic axial piston pump". In: *Proceedings of the Institution of Mechanical Engineers, Part I: Journal of Systems and Control Engineering* (2016). DOI: 10.1177/0959651816651547.

[14] A.K. Singhal et al. "Mathematical Basis and Validation of the Full Cavitation Model". In: *Journal of Fluids Engineering* (2002). DOI: 10.1115/1.1486223.

[15] Karoline Kowalski et al. "Experimental Study on Cavitation-Induced Air Release in Orifice Flows". In: *Journal of Fluids Engineering* (2018). DOI: 10.1115/1.4038730. URL: https://doi.org/10.1115/1.4038730.

[16] HQ Yang, AK Singhal, and M Megahed. "The full cavitation model". In: *Lecture seires - Von Karman Institute for fluid dynamics* 4 (2005). purchased on 2020 Sept. from VKI store, p. 10.

[17] Umberto Stuppioni et al. "Computational Fluid Dynamics Modeling of Gaseous Cavitation in Lubricating Vane Pumps: An Approach Based on Dimensional Analysis". In: *Journal of Fluids Engineering* (2020). DOI: 10.1115/1.4046480.

[18] Francesco Orlandi, Luca Montorsi, and Massimo Milani. "Cavitation analysis through CFD in industrial pumps: A review". In: *International Journal of Thermofluids* (2023). DOI: 10.1016/j.ijft.2023.100506.

[19] Paolo Casoli et al. "Modelling of fluid properties in hydraulic positive displacement machines". In: *Simulation Modelling Practice and Theory* (2006). DOI: 10.1016/j.simpat.2006.09.006.

[20] Richard Klop Andrea Vacca and Monika Ivantysynova. "A Numerical Approach for the Evaluation of the Effects of Air Release and Vapour Cavitation on Effective Flow Rate of Axial Piston Machines". In: *International Journal of Fluid Power* (2010). DOI: 10.1080/14399776.2010.10780996.

[21] H Pleskun, A Syring, and A Brümmer. "Transient chamber filling in rotary positive displacement vacuum pumps". In: *IOP Conference Series: Materials Science and Engineering* (2022). DOI: 10.1088/1757-899X/1267/1/012016.

[22] Junjie Zhou, Andrea Vacca, and Bernhard Manhartsgruber. "A Novel Approach for the Prediction of Dynamic Features of Air Release and Absorption in Hydraulic Oils". In: *Journal of Fluids Engineering* (2013). DOI: 10.1115/1.4024864.

[23] Yash Girish Shah, Andrea Vacca, and Sadegh Dabiri. "Air Release and Cavitation Modeling with a Lumped Parameter Approach Based on the Rayleigh–Plesset Equation: The Case of an External Gear Pump". In: *Energies* (2018). DOI: 10.3390/en11123472.

[24] Zubin Mistry and Andrea Vacca. "Cavitation Modeling Using Lumped Parameter Approach Accounting for Bubble Dynamics and Mass Transport Through the Bubble Interface". In: *Journal of Fluids Engineering* (2023). DOI: 10.1115/1.4062135.

[25] Massimo Rundo, Raffaele Squarcini, and Francesca Furno. "Modelling of a Variable Displacement Lubricating Pump with Air Dissolution Dynamics". In: *Source: SAE International Journal of Engines* (2018). DOI: 10.4271/03-11-02-0008.

[26] Eckerle Technologies GmbH. *EIPS segment pump - industrial design*. 2023. URL: https://eckerle.com/en/products/eips2-008ra04-1x-s111-eips-segment-pump-industrial-design.

[27] Albert Beaumont Wood and RB Lindsay. *A textbook of sound*. 1956.

[28] Daniel L. Gysling. "Accurate mass flow and density of bubbly liquids using speed of sound augmented Coriolis technology". In: *Flow Measurement and Instrumentation* (2023). DOI: 10.1016/j.flowmeasinst.2023.102358.

[29] Jaroslav Ivantysyn and Monika Ivantysynova. *Hydrostatic Pumps and Motors: Principles, Design, Performance, Modelling, Analysis, Control and Testing*. Tech Books International, 2003. ISBN: 81-88305-08-1.

[30] Dinghao Pan and Andrea Vacca. "Total Efficiency Prediction of Crescent-Type Internal Gear Pump Considering Floating Balancing Components". In: *ASME/BATH 2023 Symposium on Fluid Power and Motion Control*. Oct. 2023. DOI: 10.1115/FPMC2023-111553.

[31] Fred W. Ocvirk. *Short-bearing approximation for full journal bearings*. Tech. rep. NASA Technical Reports NACA-TN-2808, 1952.

[32] Dinghao Pan and Andrea Vacca. "Modeling of crescent-type internal gear pumps considering gear radial micromotion". In: *Chemical Engineering & Technology, special Issue: Digital, Reliable, Sustainable - Recent Innovations in Fluid Power* (). DOI: 10.1002/ceat.202200419.

Optimal designs of a hydromechanical hybrid transmission by minimizing fuel consumption and damage to human health

Nicola Andretta[1], Antonio Rossetti[2], Alarico Macor[1]

1-Department of Engineering and Management, University of Padua, Stradella San Nicola 3,36100 Vicenza, Italy; nicola.andretta.1@phd.unipd.it

2-Istituto per le Tecnologie della Costruzione, Consiglio Nazionale delle Ricerche (CNR), Corso Stati Uniti 4, 35127 Padova, Italy; antonio.rossetti@itc.cnr.it

Abstract.

The hybrid hydromechanical transmission must be sized by fully exploiting its strengths: the energy contribution of the hydraulic source and the possibility of managing the thermal source at the most convenient conditions.
Therefore, in this paper we propose a simulation-based optimisation which searches the design parameters values of both transmission and hydraulic source while minimizing the fuel consumption along a typical route.
A second objective function involving emissions was also considered. The difficulty of managing numerous chemical species with different dangers has been overcome by summarizing them in a single parameter: the damage to human health. In this way the concept of emission correspond with the concept of damage to health.
A study was carried out on a 12 m class urban bus.
The results of this study allow us to evaluate the effects of the hybridization of a hydromechanical transmission and the effects of the engine management criteria, not only on the optimal values of the design parameters, but also on fuel consumption and damage to human health.

Keywords. Hybrid hydromechanical transmission, Power-Split hydraulic hybrid, minimum fuel consumption criterion, minimum emissions criterion.

1. INTRODUCTION

Powertrain hybridization is a technique implemented by the automotive industry in recent years to reduce fuel consumption. Hydraulic hybridization, less widespread than electric hybridization, has some characteristics that make it interesting in some specific applications. In fact, the high energy density and low specific power of electric batteries direct electric

hybridization towards light vehicles, while the high specific power of hydraulic accumulators direct hydraulic hybridization towards applications characterized by frequent starts and stops, such as heavy vehicles [1, 2] and urban transport vehicles [3-8]. Hydraulic hybridization has been applied both to the classic hydrostatic transmission, showing significant consumption savings, and to the hydromechanical transmission [9]. The latter promises further efficiency benefits, although implementation of the hybridization could not be without problems, since this aspect was not faced thoroughly by literature. The need for sensors to measure the engine power and for a suitable control system to managing the engine and transmission leads to an increase in costs. This is a topic for future research development in this area. Additional hydraulic components, however, should not create reliability and cost issues, as it is a mature technology.

Ivantysynova patented the hybrid hydromechanical transmission in 2008 [10]. Van de Ven [11], Kumar and Ivantysynova [12], Kwon and Ivantysynova [13] studied it in the following years.

The hydromechanical transmission shows some advantageous features: it can recover the energy from braking, or it can level the engine operation to recharge the hydraulic source; as a continuous transmission, it allows the engine to operate at a speed independent of that of the wheels, leaving full freedom for its management. Thus the engine can be operated at speeds that minimize fuel consumption or emissions. However, the emissions are many and have opposing genesis. This creates difficulties in a management procedure and forces some compromises.

Some authors consider the emissions within the objective function as the sum of all emissions, implicitly considering them all equally dangerous [14-15]; Dollar et al. [16] only take into account NOx emissions, and Johri and Filipi [17] only NOx and PM, considering them the most dangerous, but neglecting the others. Masih-Tehrani considers emissions weighted on the basis of standard limits [18].

The authors proposed, instead, another way to take into account the emissions, which involves unifying emissions through a common parameter: the damage to human health caused by each of them [19]. In this way all emissions are summarized in a single parameter, which therefore becomes the basis for a procedure completely similar to that for fuel consumption [20].

The hydromechanical transmission, therefore, offers the possibility of producing the same power while producing fewer emissions. This aspect has a certain importance in light of the increasingly stringent regulations on emissions.

However, hybridization and engine management cannot be fully exploited without both entering into the transmission sizing procedure, which, given the complexity of the problem, must be transformed into an optimization process. Many authors in the literature have addressed sizing in these terms [21-26].

This work proposes an optimal sizing procedure that involves both the transmission with its components and the engine with its management criterion. The procedure, starting from some assigned data (engine, transmission layout, maximum vehicle speed, maximum torque at the wheels and typical load cycle), identifies the value of the design variables (gear ratios,

displacements of the hydraulic units, size of the hydraulic source) which minimize fuel consumption or emissions.

The aims of this study are to quantify the advantage of hybridization, and to evaluate the influence of the management criterion on design variables, consumption, and emissions.

2. THE HYDROMECHANICAL HYBRID TRANSMISSION

The hydromechanical transmission taken as the basis for the study is the classic Output Coupled (hereinafter referred to as OC) [9]. The hybrid transmission (hereinafter HOC) is derived from the latter by adding the hydraulic source and the related valves (Figure 2). The layout of both schemes is based on the one proposed by Kwon (13).

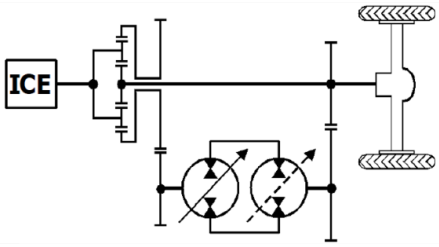

Figure 1. Scheme of the OC transmission.

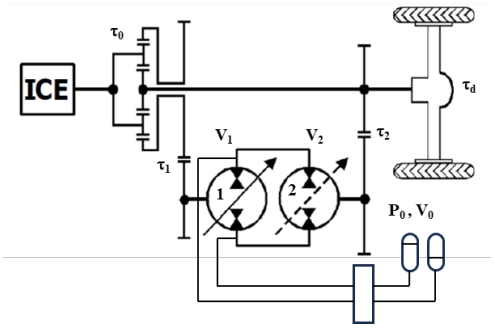

Figure 2. Scheme of the hybrid hydraulic transmission HOC.

The OC transmission works in the following modes.

- Power additive mode: the engine power is divided into the two branches of the transmission, the mechanical branch and the hydraulic branch; the two powers are then mixed in the final spur gear.
- Full mechanical point: all the power passes through the mechanical branch, since the epicyclic ring is stationary. It is the highest efficiency operation.
- Power recirculation mode: in order to increase the speed of the vehicle beyond the Full mechanical point speed value, the Unit 2 must invert its displacement, and transform from a motor to a pump. Therefore, some of the power flows back

through the hydrostatic group, in which the two machines have reversed their operation.

- Braking mode: Unit 1 is put at zero displacement while Unit 2, thanks to the inertia of the vehicle, transforms into a pump, raising the pressure of the low pressure branch. The safety valve laminates the flow rate, sending it to the other branch, creating the braking resistance. A mechanical brake integrates the hydraulic one to guarantee braking service in all conditions.

The HOC transmission has the same three modes of operation with some differences.

Starts and restarts occur solely through the power supplied by the accumulator, activated by the distributor; when the pressure in the accumulator reaches the pre-charge value it is no longer able to provide power and so the engine, previously at idle, is accelerated and the displacement of Unit 1 is increased. The braking phase occurs by setting the displacement of Unit 1 to zero and inverting the accumulator distributor. In this way the inertia of the vehicle transforms Unit 2 into a pump which charges the accumulator.

The sizing method of the OC transmission proposed by Blake [27] was used here in the optimization procedure.

3. ENGINE MANAGEMENT CRITERIA

The continuously variable transmission separates the engine angular velocity from the vehicle speed. This allows the engine to be managed according to various criteria. The first and most immediate is that of minimum fuel consumption.
In the engine map, the set of minimum points for BSFC (Brake-specific Fuel Consumption) can be identified and expressed as a function of the power

$$BSFC|_{min} = f(P|_{min}) \quad (1)$$

This set is defined as Optimal Operating Line (OOL) and can be used in the control system to force the engine to produce the required power at the minimum fuel consumption velocity [20], as shown in Figure 3.

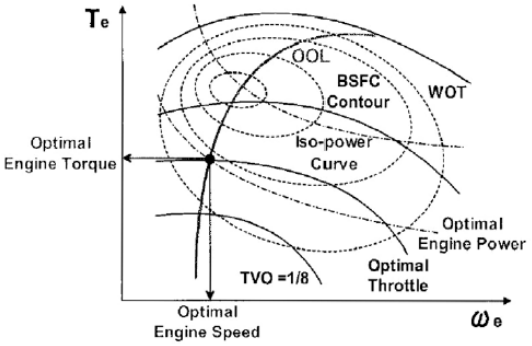

Figure 3. Engine map: iso-BSFC lines, iso-power lines, and optimal operating line [20].

A similar set of minimum is also possible for emissions, although they are divided into four groups (CO, H, NOx, and PM) and have different genesis. As the authors suggested in [19], the four groups of emissions can be unified through the concept of damage to human health that each of them produces. The damage to human health is quantified by the average number of years of life lost by a population due to premature death or disability caused by exposure to pollutants, and measured in DALY unit. The damage caused by the emission of a substance can be assessed according to the Jolliet methodology [28]:

$$D(T,n) = m(T,n) \cdot cf \cdot sd \tag{2}$$

where D [DALY] is the damage to human health due to the emission having mass m [kg]; cf [kg_{ref}/kg] is the characterization factor of the substance belonging to a certain impact category, sd [DALY/kg_{ref}] is the specific damage for that impact category. Summing the damage of all the emissions, a total damage is defined. In this way, a line of minimum total damage can be identified and used in the control system for minimal emission operation.

4. TRANSMISSION DESIGN AS AN OPTIMIZATION PROBLEM

The optimal design procedures are based on the classic optimization problem, which in more general terms can be generally stated as:

Find $x = \begin{bmatrix} x_1 & x_2 & .. & x_n \end{bmatrix}^T$ *minimizing* $f(x)$*; subject to the constraints* $g_j(x) \le 0 \; j = 1..m$ *and* $l_j(x) = 0 \; j = 1..p$

where:

- $x_1 \quad x_2 \quad .. \quad x_n$ are the nth free optimization variables (design variables);
- the equality constraints $l_j(x) = 0 \; j = 1..p$ are the design parameters;
- the inequality constraints $g_j(x) \le 0 \quad j = 1..m$ are the design constraints;
- $f(x)$ is the objective function of the problem.

For the case of the hybrid hydromechanical transmission, the objective function f(x) can be the engine fuel consumption or the total damage to human health.

The design variables are:

• the gear ratio of the planetary gear τ_0 (see Figure 2)

• ger ratio of the ordinary gears τ_1, τ_2, τ_d

• the displacement of the hydraulic units V_1, V_2

• the precharge pressure and the volume and of the accumulator p_0, V_0.

The design parameters are:

• engine maximum power and speed

• maximum vehicle speed

• maximum torque at wheel

• wheel radius.

The design constraints are:

• maximum pressure of hydraulic circuit

• maximum speed of hydraulic machines as a function of displacement.

The load cycle should consider a typical speed profile for the vehicle with starts and stops, and maximum power peaks.

5. THE CASE STUDY: THE CITY BUS

The study was conducted on a 12m class city bus, whose main characteristic data are shown in Table 1.

Table 1. Main data of the vehicle.

Engine- Turbodiesel	Max Power/Speed 228 kW/2200 rpm Max Torque/Speed 1300 Nm/1200 rpm Displacement/Cylinders 8600 cc/6
Vehicle Mass/max passengers	11000 kg/45x70kg
Wheel Radius	0.5281 m
Maximum Vehicle Speed	90 km/h
Maximum Pulling Torque	25000 Nm

6. THE VEHICLE MODEL

The city bus was modeled in the Amesim environment [29]. The complete model is composed by the sub-models of the engine, the hybrid transmission HOC (according to the layout in Figure 2), the load, and the sub-models of the control systems. The vehicle loads, i.e. the rolling friction and the aerodynamic friction, were respectively modelled according to $F_f = f\ m_v\ g$ and $F_{aer} = 0.5\ v^2 A\ \rho\ c_d$; where for the rolling resistance coefficient, the drag coefficient, frontal area the following values were respectively assumed: $f = 0.01$, c_d=1,17, $A = 7$ m^2. The mass m_v is equal to the constant mass of the vehicle and passengers (see Table 1), plus the transmission variable mass as detailed in point 6.4.

As regards the losses in the gears, a constant efficiency equal to 0.98 was assumed for each spur gear, while for the planetary gear, an efficiency equal to 0.97 was assumed for each pair of engaged wheels.

The non-hybrid hydromechanical transmission model (OC, Figure 1), which is taken here as a reference for comparisons, was obtained from the previous hybrid transmission model, leaving the accumulator directional valve always closed.

6.1. Control strategy

The transmission control strategy involves separating the energy contributions of the two energy sources: the starting and pickup are assigned to the hydraulic source, the rest to the thermal source. Therefore two control systems in sequence were adopted: the first one, based on the vehicle speed error signal, manages only the displacement of Unit 2 to pursue the desired speed; the second one, on the basis of the same signal, acts sequentially first on the displacement V_1 and then on the displacement V_2.

In OC transmission only the second control works.

6.2. Minimum fuel consumption and minimum emission lines

The OOL line was obtained from the engine map by crossing the isopower hyperbolas with the isoconsumption curves (Figure3). Figure 4 shows the map with the OOL line.

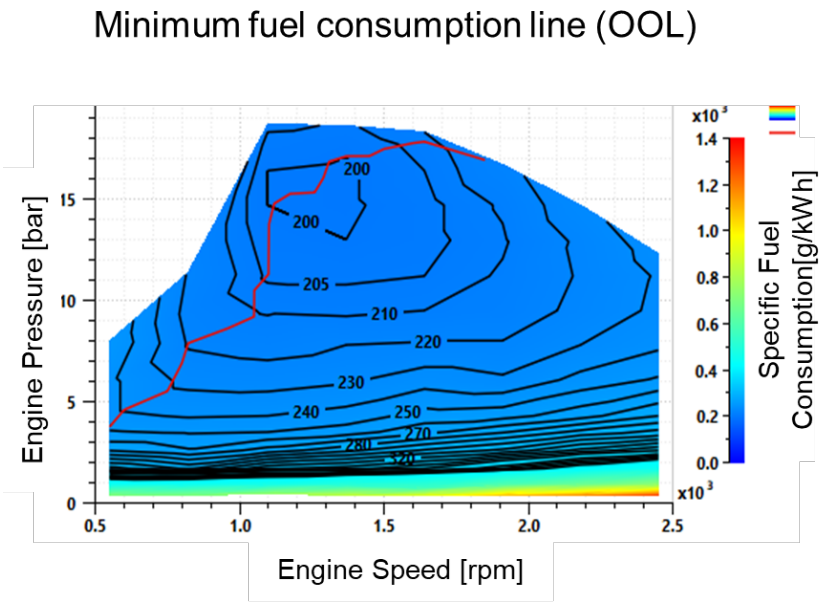

Figure 4. Engine map: iso-BSFC lines, and optimal operating line.

Figure 5 shows the maps of the four emission groups: NO, HC, PM and NOx. For each of them, the minimum emission line was obtained by crossing the isopower and iso-emission curves. The four isocurves are distant from each other, especially that of the minimum NOx, effectively preventing the formation of a single minimum line.

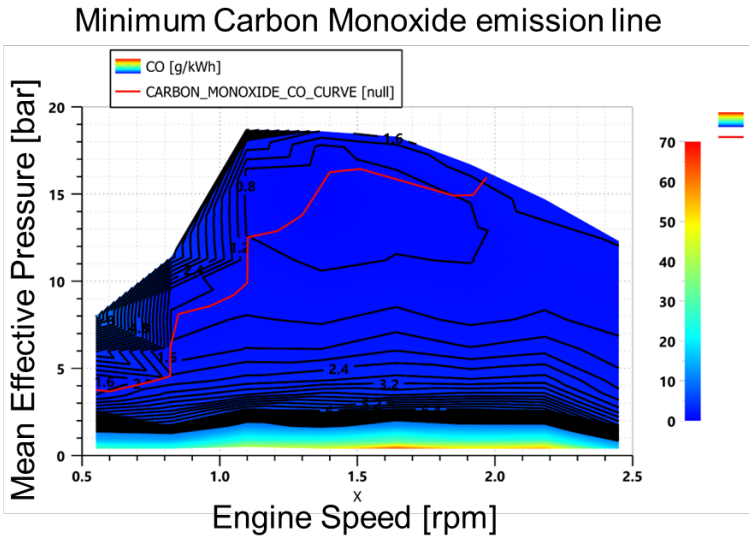

A)

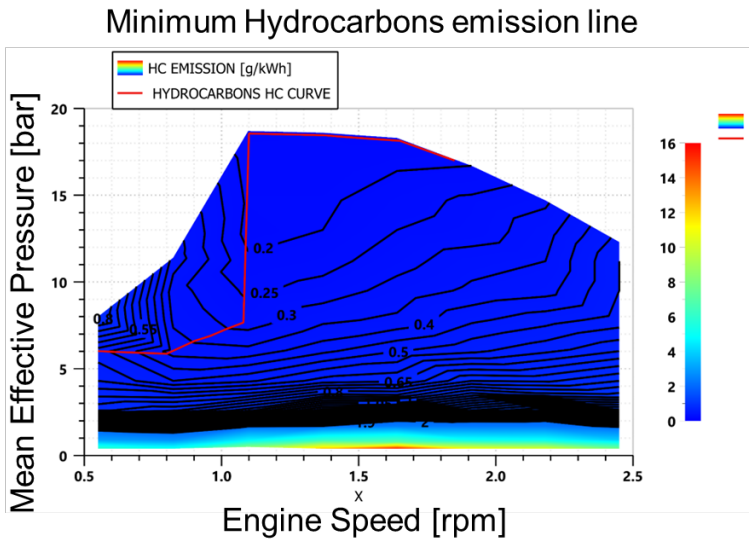

B)

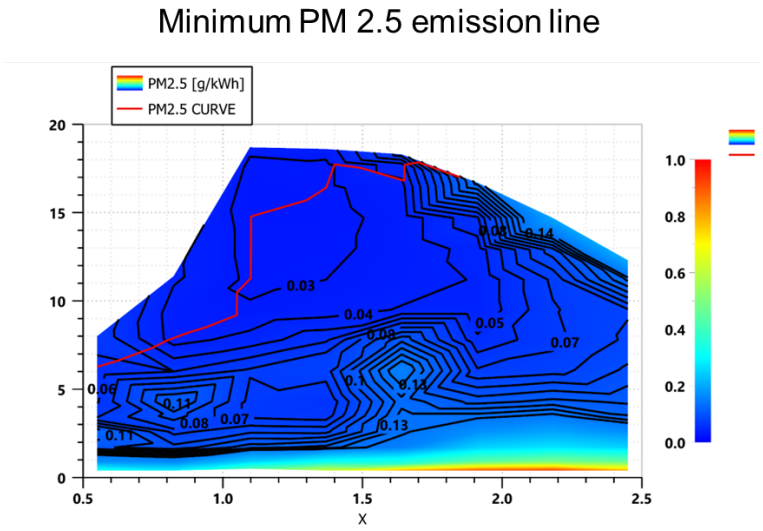

C)

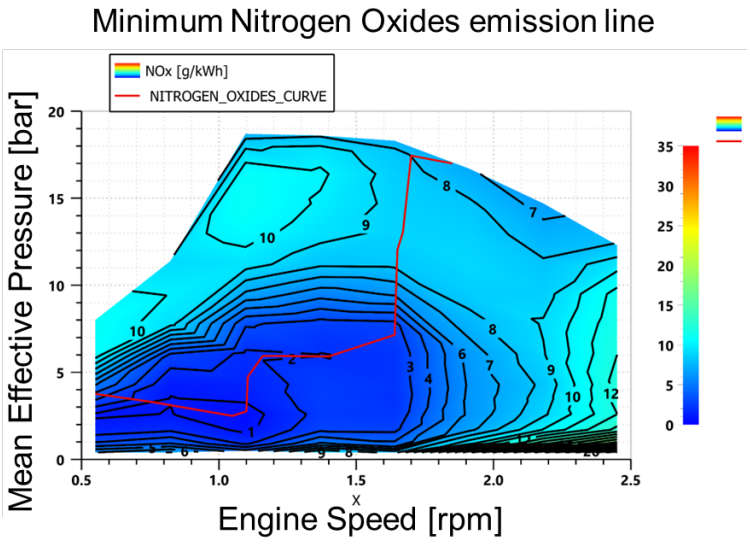

D)

Figure 5. Emission maps and minimal emission lines: A) CO, B) HC, C) PM, D) NOx.

The total damage to human health is the sum of the damage caused by each emission calculated with the procedure illustrated in Section 3. Also in this case the line of minimum total damage (MTDL) can be identified by crossing the isopower curves with the isodamage curves (Figure 6). The two lines, OOL and MDL, are distant from each other and allow two different engine managements.

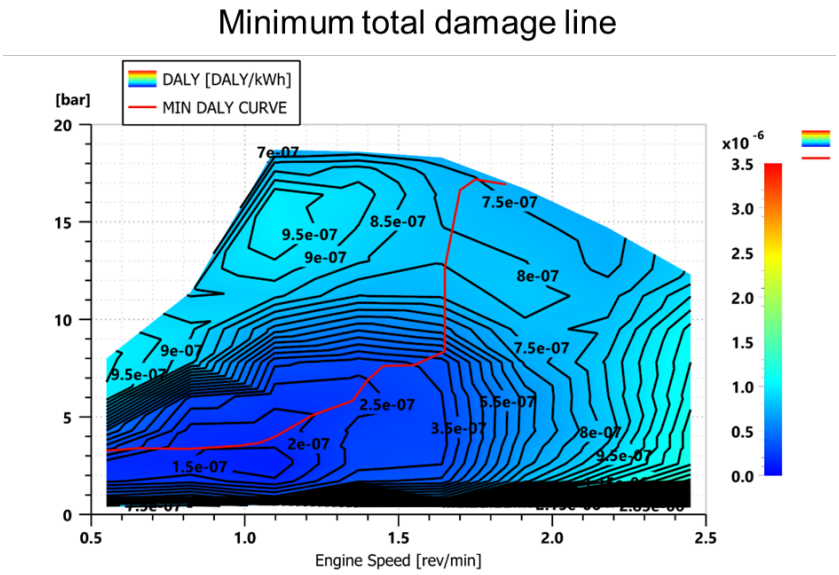

Figure 6. Total damage map and minimal total damage line (MTDL)

6.3. Hydraulic Pump and motor modelling

The accuracy of the models of the hydraulic units affects the reliability of global simulation results. Therefore the volumetric and hydromechanical losses were evaluated using scaling laws starting from values experimentally obtained from a reference machine, as suggested in [25, 30].

Linear scaling laws are based on the assumption that scaling units operate at the same maximum pressures and maximum speeds. Volumetric losses can be summarized by the flow rate flowing between two cylindrical surfaces, which depends on cube of the linear dimensions, as shown by the Poiseuille's law. Torque losses can be summarized by the torque generated by the friction force occurring between two flat surfaces in relative motion, which linearly depends on the linear dimension [30].

Therefore, the losses for a generic unit can be expressed as a function of the losses of the reference unit as follows:

$$Q_{loss} = Q_{loss_ref} \cdot \lambda^3 \quad (3)$$

$$T_{loss} = T_{loss_ref} \cdot \lambda^2 \quad (4)$$

where Q_{loss_ref} and T_{loss_ref} are the reference volumetric and hydromechanical losses expressed by polynomials as a function of pressure, speed and displacement fraction, while λ is the scale parameter.

$$\lambda = \sqrt[3]{\frac{V}{V_{ref}}} \quad (5)$$

6.4. Size and weight of transmission and accumulators

The transmission and accumulators weights were also evaluated in the transmission model. It is very difficult to predict the weight of a hydromechanical transmission since geometric, layout and mechanical resistance factors are involved in its definition. In this work a law was adopted that expresses the approximate weight of the transmission in this way:

$$m_{tr} \cong m_0 + (m_1 + m_2) \quad (6)$$

Where m_o = 600 kg is the mass of a commercial transmission of equal power [31] minus the weights of its two hydraulic units. m_1 and m_2 are the masses of the hydraulic units taken from the catalog of a well-known manufacturer. This transmission weight has been reduced by the powershift transmission weight supplied with the bus in question (Voith Diwa 6 model) equal to 350 kg. The final weight of the transmission also includes the weight of the oil, which varies between 20 and 35 kg. Both the displacements of the hydraulic units and the size of the accumulators refer to the catalog data offered by well-known manufacturers. Table 2 shows the displacement, maximum velocity and weight data for the pumps and motors; Table 3 shows the dimensions and weights of the accumulators.

In the vehicle model, a special control rejects cycles in which at least one of the two units runs at speeds higher than that recommended by the manufacturer.

Table 2. Pump and motor characteristics for 500 bar maximum operating pressure.

V_1 - cm^3	56	71	90	110	125	145	175	210	280
n_{1max} - rpm	3900	3600	3300	3250	3150	3000	2800	2650	2550
m_1 - kg	38	50	60	84	88	106	115	152	160
V_2 - cm^3	80	107	140	160	200	250	255	500	
n_{2max} - rpm	6150	5600	5150	4900	4600	3300	2650	2400	
m_2 - kg	36	46	61	62	78	100	170	210	

Table 3. Standard bladder accumulators - maximum pressure 400 bar.

V_0 - L	10	13	20	32	50	2x50	2x50+20
m_{acc} - kg	41	49	71	104	137	274	345

6.5. Mission profile

The vehicle model was subjected to the standard WLTP cycle for hybrid vehicles, limited to the low and medium segments of the conventional cycle for class 3 vehicles (first 1000 s in figure 7) [32]. These two segments show the characteristics of a city route with stops and starts and with speed peaks close to the maximum. Furthermore, sudden accelerations allow the engine to reach maximum power.

In the simulations the vehicle speed follows the mission profile with a maximum error of 1.8%.

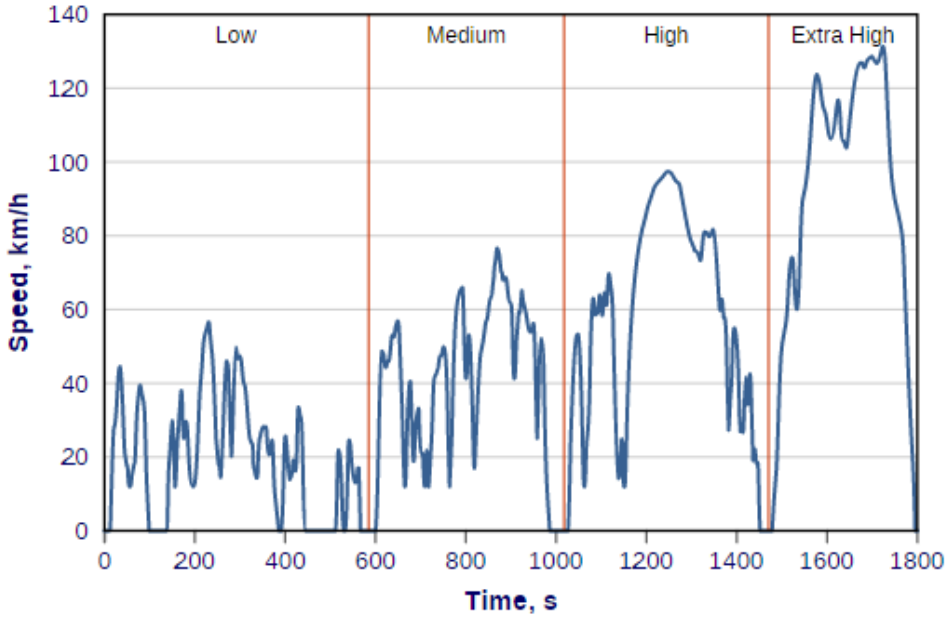

Figure 7. Mission profile based on WLTP cycle for class 3 vehicles.

7. SIMULATIONS AND OPTIMIZATIONS

As already mentioned, the bus models were used to size the transmissions OC and HOC as seen in Section 4. Two engine management criteria were considered. The first one requires the engine to follow the minimum consumption line (OOL, Figure 4), therefore in the following it will be indicated with MinC criterion; the second criterion requires the engine to follow the line of minimum total damage (MDL, Figure 6), hereinafter indicated as MinD criterion. The optimizations performed are summarized in Table 4.

Table 4. Optimizations carried out in this study.

	MinC	MinD
OC	x	
HOC (continuous variables)	x	x
HOC (discrete variables)	x	x

The design variables for each of the optimizations are as follows:

- OC transmission: τ_o, τ_1, τ_2, τ_d, V_1, V_2

- HOC transmission: τ_o, τ_1, τ_2, τ_d, V_1, V_2, p_0, V_0

The accumulator starts and ends the cycles at the same pressure, with a deviation of less than 1%. In this way, comparisons between different solutions are not distorted by a net contribution of energy due to the hydraulic source.

The search for the optimum was carried out using the genetic algorithm, a method particularly suitable for solving problems not well suited for standard optimization algorithms, including problems with discontinuous objective function, nondifferentiable, stochastic, or highly nonlinear.

The algorithm parameters were assumed based on literature recommended values. Population size was assumed equal to 30 and 40 respectively for the OC and HOC optimizations (recommended value 4.5* number of design variables); the reproduction rate was assumed 80% to assure a fast convergence limiting the risk of a local minima (recommended values 50- 85%); the number of generations was assumed equal to 30, with recommended value over 10.

The machine time to reach the solution was approximately 10 hours for each of the optimizations on a Windows I9 machine.

8. RESULTS AND DISCUSSIONS

Figure 8 shows the power contributions of the hydraulic source and the thermal source in a part of the work cycle. The first source only contributes to the start as long as the gas pressure in the accumulator allows it. After which only the thermal source will provide the required power. During the deceleration phase, the engine is idled and the kinetic energy of the vehicle is used to recharge the accumulator. During the energy sources shift, there is a power deficit which causes a small deceleration of the vehicle.

Figure 9 shows the evolution of the objective function, fuel consumption, and displacements during the optimization process of the OC transmission with MinC criterion.

Similar evolutions occurred for the HOC transmission.

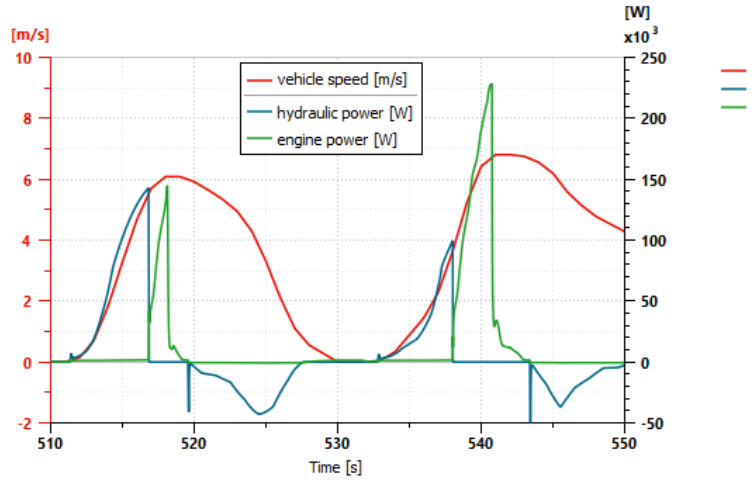

Figure 8. Hydraulic and engine power contributions during acceleration and braking phases.

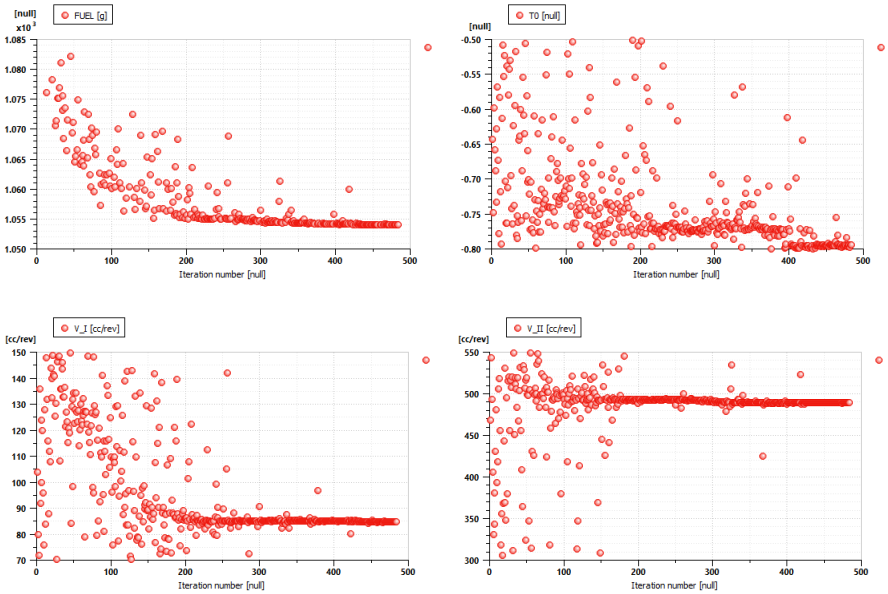

Figure 9. Evolution of the objective function (minimum fuel consumption) and the design variables during the optimization of OC transmission with MinC criterion.

8.1. Effect of the hybridization

Table 5 compares the optimization results of the OC and HOC transmissions both subjected to MinC criterion.

Table 5. Optimal design variables for OC and HOC transmissions (MinC)

	τ_0	V_1	V_2	p_0	V_0	τ_1	τ_2	τ_d	m_{fuel}	damage
	/	cm^3	cm^3	bar	L	/	/	/	g	DALY
OC	-0.849	84.7	489	/	/	1,12	0.84	8.2	1054	3.80E-6
HOC	-0.828	94.9	510	255	129.3	1.01	0.8	8.3	916	3.23E-6
Δ %									-13%	-15%

As can be seen, hybridization, i.e. the addition of the two accumulators, does not significantly change the optimal values of the design variables, only the displacement of the Unit 1 increases by approximately 10%, indicating that transmission and accumulators are practically independent functional groups.

Hybridization, however, increases the average transmission efficiency from 0.74 to 0.89, and leads to marked reductions in fuel consumption and damage, equal to 13% and 15% respectively. In a previous study [33], the authors found on a reach stacker a fuel consumption reduction due to hybridization of 21%.

The energy contribution of the hydraulic source was found to be equal to 24% of the total energy entering the transmission, while the additional weight due to the accumulators, approximately 750 kg, produces an increase in fuel consumption of 3%.

Note the high value of the accumulator pre-charge pressure. This is explained by the transmission management criterion adopted here, which provides for starting via the accumulator alone, without the contribution of the engine.

8.2. Effect of the management criterion on HOC transmission

Figure 10 shows the operating points in the engine map for a HOC simulation with the engine managed according to MinC criterion (red dots) and MinD criterion (black dots). The two trends are consistent with those of the OOL (Figure 4) and MDL (Figure 6), a sign that the control system acts correctly in forcing the engine towards those two conditions. In the medium-high speed area the two curves differ more from each other and therefore here the difference in damage caused is more marked.

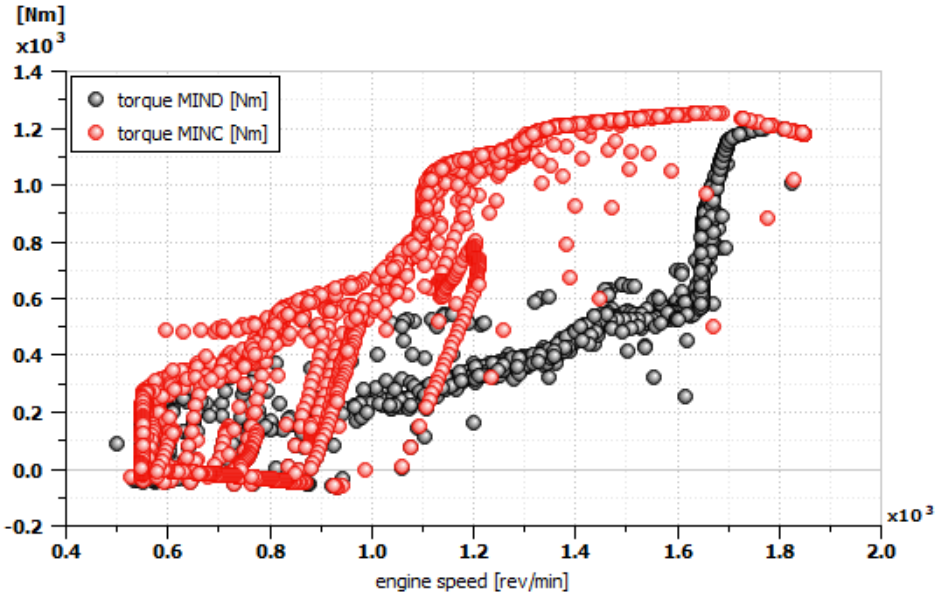

Figure 10. Operating points of the engine operated according to MinC criterion (red points) and MinD criterion (black points).

Table 6 shows the optimal parameters provided by the optimization procedure for the HOC transmission managed with MinC and MinD criteria.

Table 6. Optimal design variables for HOC transmission with the engine managed at MINC and MIND criteria.

	τ_0	V_1	V_2	p_0	V_0	τ_1	τ_2	τ_d	m_{fuel}	damage
	/	cm^3	cm^3	bar	L	/	/	/	g	DALY
MinC	-0.828	94.9	510	255	129.3	1.01	0.8	8.3	917	3.24E-6
MinD	-0.849	116	514	270	90	0.82	0.80	8.2	947	2.43E-6
Δ %									+3 %	-25%

The comparison shows that the management criterion moderately influences the optimal values of the design variables, only the Unit 1 displacement increases significantly. What is evident, however, is the difference in consumption and damage: the minimum damage criterion, compared to an increase in consumption of 3%, produces a reduction in the damage produced by emissions of approximately 25%.

8.3. Effect of component discretization

We now want to examine how and to what extent the choice of components from the catalogue, i.e. which vary in discrete steps, influences the optimal values of the design variables and the performance of the HOC transmission. Therefore the optimization processes were repeated considering the displacements and the volume of the accumulator varying according to the catalog values reported in Tables 2 and 3.

Table 7. Optimal design variables for HOC transmission with the engine managed at MinC and MinD conditions and discrete values for displacements and accumulator volumes.

	τ_0	V_1	V_2	p_0	V_0	τ_1	τ_2	τ_d	m_{fuel}	damage
	/	cm^3	cm^3	bar	L	/	/	/	g	DALY
MinC	-0.796	110	500	256	120	0.89	0.8	8.5	917	3.24E-6
MinD	-0.65	110	500	279	100	0.97	0.71	9.5	953	2.46E-6
Δ %									+4%	-24%

For both criteria, both the displacements and the volume of the accumulator settle on the values closest to those obtained in Table 6, without this causing significant deviations in consumption and damage. This concept is reiterated in Table 8, in the continuous-discrete comparison of the design variables.

Table 8. Continuous-discrete comparison for the management criteria MinC and MinD

	τ_0	V_1	V_2	p_0	V_0	τ_1	τ_2	τ_d	m_{fuel}	damage
	/	cm^3	cm^3	bar	L	/	/	/	g	DALY
MinC										
cont	-0.828	94.9	510	255	129.3	1.01	0.8	8.3	917	3.24E-6
disc	-0.796	110	500	256	120	0.89	0.8	8.5	917	3.24E-6
Δ %									0.0%	0.0%
MinD										
cont	-0.849	116	514	270	90	0.82	0.80	8.2	947	2.43E-6
disc	-0.65	110	500	279	100	0.97	0.71	9.5	953	2.46E-6
Δ %									+0.6%	-1.2%

From these comparisons it can be deduced that the usual practice in hydraulic design also applies in delicate cases like this one, i.e. proceeding with the theoretical calculation of the size and then adopting the closest catalog value.

9. CONCLUSIONS

In this work the hybrid hydromechanical transmission was investigated with particular reference to its sizing.

The sizing involved both the transmission and the engine in order to exploit the advantage afforded by the continuous transmission of engine management according to the most convenient criteria.

The criteria adopted here are the minimum fuel consumption criterion and the minimum emissions criterion. This second criterion was achieved by unifying emissions into a single parameter: the damage to human health.

Given the complexity of the transmission and the high number of variables, sizing was transformed into a mathematical programming problem.

The proposed sizing procedure was applied to a 12 m class city bus, of which a model including engine, transmission, control systems and load was prepared. The model was inserted into an optimization process that used the genetic algorithm as a search strategy for the optima.

For this vehicle, the study highlighted some points that can be summarized as follows:

- the hybridization of a powersplit transmission leads to a decrease in consumption of approximately 13% and a decrease in damage to human health by 15%.

-The optimal values of the transmission variables are not significantly affected by hybridization, indicating that the transmission and accumulators are practically independent functional groups.

-The management criterion of minimizing damage to human health, compared to an increase in consumption of 3%, reduces the damage caused by emissions by approximately 25%.

-The use of catalog components, i.e. with discretely variable dimensional values, does not lead to a substantial reduction in efficiency compared to the optimal solution obtained with continuous variation.

It is worth underlining that the results obtained are to be considered valid for this type of vehicle. For other vehicles, subject to different duty cycles, the results may be different.

10. NOMENCLATURE

cf	characterization factor of a substance belonging to an impact category	[kg_{ref}/kg]
D	damage to human health	[DALY]
m	emission mass	[kg]
m_{acc}	accumulator mass	[kg]
m_{tr}	transmission mass	[kg]
n,ω	engine rotational speed	[RPM, rad/s]
P	power	[kW]
p_0	accumulator precharge pressure	[bar]
Q_{loss_ref}	experimental volumetric losses of a reference hydraulic unit	[L/min]
Q_{loss}	volumetric losses of a generic hydraulic unit	[L/min]
sd	specific damage of a impact category	[DALY/kg_{ref}]
T	torque	[Nm]
T_{loss}	volumetric losses of a generic hydraulic unit	[L/min]
T_{loss_ref}	experimental hydromechanical losses of a reference hydraulic unit	[L/min]
v	vehicle speed	[m/s]
V	maximum unit displacement of a hydraulic unit	[cm^3]
V_1	maximum unit displacement of Unit 1	[cm^3]
V_2	maximum unit displacement of Unit 2	[cm^3]
V_0	accumulator volume	[L]
λ	scaling parameter	[-]
τ_0	standing gear ratio of the planetary gear (see Figure 2)	[-]
τ_1	gear ratio of the Unit 1 gear (see Figure 2)	[-]
τ_2	gear ratio of the Unit 2 gear (see Figure 2)	[-]
τ_d	rear axle gear ratio (see Figure 2)	[-]

acronyms

BSFC	Brake-specific fuel consumption	[g/kWh]
MTDL	minimum total damage line	
MinC	minimum fuel consumption engine management criterion	
MinD	minimum health damage engine management criterion	
HOC	Hydraulic hybrid Output Coupled	
OC	Output Coupled	
OOL	Optimal operating line in the engine map	

Funding: This research was funded by the University of Padua through the DOR 2023 fund.

11. REFERENCES

[1] Wang J., Yang Z., Liu S., Zhang Q. and Han Y., "A comprehensive overview of hybrid construction machinery". Advances in Mechanical Engineering 2016, Vol. 8(3) 1–15) 2016. DOI: 10.1177/1687814016636809

[2] Chen, Q.; Lin, T.; Ren, H.; Fu, S. "Novel potential energy regeneration systems for hybrid hydraulic excavators". Math. Comput. Simul. **2019**, 163, 130–145.

[3] R. Ramakrishnan, Somashekhar S. Hiremath and M. Singaperumal, "Theoretical investigations on the effect of system parameters in series hydraulic hybrid system with hydrostatic regenerative braking". Journal of Mechanical Science and Technology 26 (5) (2012) 1321~1331- DOI 10.1007/s12206-012-0321-y

[4] Ramdan M I and Stelson K A 2016 "Optimal design of a power-split hybrid hydraulic bus" Proc IMechE Part D: J Automobile Engineering, Vol. 230(12) 1699–1718. DOI: 10.1177/0954407015621817

[5] Prado Barbosa T P, Rodrigues da Silva L A, Pacheco Pujatti F J, Horta Gutierrez J C 2022 "Hydraulic hybrid passenger vehicle: Fuel savings possibilities" Mechanics Based Design of Structures and Machines An International Journal Volume 50, 2022 - Issue 1 https://doi.org/10.1080/15397734.2020.1714447

[6] Bender, F.A.; Bosse, T.; Sawodny, O. "An investigation on the fuel savings potential of hybrid hydraulic refuse collection vehicles". Waste Manag. **2014**, 34, 1577–1583.

[7] Wen Q, Wang F, Xu B and Sun Z "Improving the Fuel Efficiency of Compact Wheel Loader with a Series Hydraulic Hybrid Powertrain" IEEE Transactions On Vehicular Technology, Vol. 69, No. 10, October 2020.

[8] Karl Pettersson, Kim Heybroek, Per Mattsson & Petter Krus (2017) "A novel hydromechanical hybrid motion system for construction machines", International Journal of Fluid Power, 18:1, 17-28, DOI: 10.1080/14399776.2016.1210423

[9] Renius KT and Resch R 2005 "Continuously variable tractor transmissions" ASAE Disting. Lect. 29 (2005).

[10] Ivantysynova M M, Carl, B A and Williams, K R 2008 "Power split transmission with energy recovery" US Patent 20080081724

[11] Van de Ven J D, Olson M W, and Li P Y 2008 "Development of a Hydro-Mechanical Hydraulic Hybrid Drive Train with Independent Wheel Torque Control for an Urban Passenger Vehicle" Proc. of International Fluid Power Exhibition, Las Vegas, Nevada, United States.

[12] Kumar R and Ivantysynova M 2010 “Investigation of various power management strategies for a class of hydraulic hybrid powertrains: Theory and experiments” Proc. of the 6th FPNI PhD Symposium, p. 87–99.

[13] Kwon, H.; Ivantysynova, M. “System Characteristics Analysis for Energy Management of Power-Split Hydraulic Hybrids”. *Energies* **2020**, *13*, 1837. https://doi.org/10.3390/en13071837

[14] Hu, X.; Zhang, X.; Tang, X.; Lin, X. “Model predictive control of hybrid electric vehicles for fuel economy, emission reductions, and inter-vehicle safety in car-following scenarios”. Energy 2020, 196, 117101.

[15] Tang, X.; Chen, J.; Liu, T.; Qin, Y.; Cao, D. “Distributed Deep Reinforcement Learning-Based Energy and Emission management Strategy for Hybrid Electric vehicles”. IEEE Trans. Veh. Technol. 2021, 70, 9922–9934.

[16] R. A. Dollar, L. Thibault, M. Laraki and A. Sciarretta, “Eco-Driving of Compression-Ignition Vehicles to Minimize Nitrogen Oxide Emissions” in *IEEE Transactions on Control Systems Technology*, vol. 30, no. 5, pp. 2084-2099, Sept. 2022, doi: 10.1109/TCST.2021.3133867..

[17] Johri, R.; Filipi, Z. “Optimal energy management of a series hybrid vehicle with combined fuel economy and low-emission objectives”. Proc. IMechE Part D J. Automob. Eng. 2014, 228, 1424–1439.

[18] Masih-Tehrani, M.; Ebrahimi-Nejad, S.; Dahmardeh, M. “Combined fuel consumption and emission optimization model for heavy construction equipment”. Autom. Constr. 2020, 110, 103007.

[19] Rossetti, A.; Andretta, N.; Macor, A. “On the Use of the Disability-Adjusted Life Year (DALY) Estimator as a Metric to Optimally Manage ICE Emissions”. Energies 2022, 15, 4386. https://doi.org/10.3390/ en15124386.

[20] R. Pfiffner*, L. Guzzella, C.H. Onder. “Fuel-optimal control of CVT powertrains. Control Engineering Practice” 11 (2003) 329–336.

[21] Katharina Baer, Liselott Ericson & Petter Krus “Framework for simulation-based simultaneous system optimization for a series hydraulic hybrid vehicle”, International Journal of Fluid Power, DOI: 10.1080/14399776.2018.1527122

[22] Uebel K, Raduenz H, Krus P and de Negri V J 2018 “Design optimisation strategies for a hydraulic hybrid wheel loader” Proceedings of the BATH/ASME Symposium on Fluid Power and Motion Control FPMC2018 September 12-14, 2018, Bath, UK

[23] S. Ahn, J. Choi, S. Kim, J. Lee, C. Choi and H. Kim. “Development of an integrated engine-hydro-mechanical transmission control algorithm for a tractor” Advances in Mechanical Engineering 2015, Vol. 7(7) 1–18 DOI: 10.1177/1687814015593870

[24] Li C T and Peng H 2010 “Optimal Configuration Design for Hydraulic Split Hybrid Vehicles” 2010 American Control Conference Marriott Waterfront, Baltimore, MD, USA June 30-July 02, 2010 pag. 5812-5217.

[25] Andretta N 2022 “Design methods for hybrid hydro-mechanical transmissions for heavy-duty vehicles”. Ph.D. Dissertation. Department of Management and Engineering, course in Mechatronics and Product Innovation Engineering. University of Padua 2022.

[26] N Andretta *et al* 2022 *J. Phys.: Conf. Ser.* **2385** 012031 **DOI** 10.1088/1742-6596/2385/1/012031

[27] Blake C, Ivantysynova M, Williams K. “Comparison of Operational Characteristics in Power Split Continuously Variable Transmissions”. SAE 2006 Commercial Vehicle Engineering Congress & Exhibition, October 2006, *SAE Techical Paper series 2006-01-3468*

[28] Jolliet, O., Margni, M., Charles, R., Humbert, S., Payet, J., Rebitzer, G., et al. IMPACT 2002+: A New Life Cycle Impact Assessment Methodology. 2003. doi:10.1007/BF02978505

[29] *Amesim*; 2021-2022; Siemens Industry Software NV: Plano, TX, USA, 2021.

[30] L. Shang, M. Ivantysynova “An Investigation of Design Parameters Influencing the Fluid Film Behavior in Scaled Cylinder Block/Valve Plate Interface” FPNI2016-1540, V001T01A027. https://doi.org/10.1115/FPNI2016-1540

[31] Mercati S, Panizzolo F, Profumo G 2016 “Power split Hydro-mechanical Variable Transmission (HVT) for off-highway application”, 10th International Fluid Power Conference (10. IFK) March 8 - 10, 2016, Vol. 3, pp. 69-80.

[32] https://dieselnet.com/standards/cycles/index.php

[33] Andretta N, Rossetti A and Macor A 2019 “Optimal design of a hybrid hydromechanical transmission for a reach stacker” AIP Conference Proceedings 2191, 020010 (2019); https://doi.org/10.1063/1.5138743.